

Minu Gupta Bhowmik
Sabina Jhaumeer-Lal
Henri Li Kam Wah
Ponnadurai Ramasami

Chemistry
for Sustainable

Chemistry for Sustainable Development

Minu Gupta Bhowon • Sabina Jhaumeer-Laulloo
Henri Li Kam Wah • Ponnadurai Ramasami
Editors

Chemistry for Sustainable Development

 Springer

Editors

Dr Minu Gupta Bhowon
Department of Chemistry
University of Mauritius, Réduit
Mauritius
mbhowon@uom.ac.mu

Dr Sabina Jhaumeer-Laulloo
Department of Chemistry
University of Mauritius, Réduit
Mauritius
sabina@uom.ac.mu

Dr Henri Li Kam Wah
Department of Chemistry
University of Mauritius, Réduit
Mauritius
lkwah@uom.ac.mu

Dr Ponnadurai Ramasami
Department of Chemistry
University of Mauritius, Réduit
Mauritius
p.ramasami@uom.ac.mu

ISBN 978-90-481-8649-5 e-ISBN 978-90-481-8650-1

DOI 10.1007/978-90-481-8650-1

Springer Dordrecht Heidelberg London New York

Library of Congress Control Number: 2011939768

© Springer Science+Business Media B.V. 2012

No part of this work may be reproduced, stored in a retrieval system, or transmitted in any form or by any means, electronic, mechanical, photocopying, microfilming, recording or otherwise, without written permission from the Publisher, with the exception of any material supplied specifically for the purpose of being entered and executed on a computer system, for exclusive use by the purchaser of the work.

Printed on acid-free paper

Springer is part of Springer Science+Business Media (www.springer.com)

Preface

The International Conference on Pure and Applied Chemistry (ICPAC 2010) was held from 26th to 30th July 2010 at La Plantation Resort and Spa, Balaclava, in Mauritius. The theme of the conference was “Chemistry for Sustainable Development”. ICPAC 2010 was attended by about 160 participants coming from 30 countries. The conference featured 100 oral and 85 poster presentations.

The participants of ICPAC 2010 were invited to submit full papers. The latter were subsequently peer reviewed and the selected papers are collected in this volume.

This book of proceedings encloses 31 presentations covering wide ranging topics from organic chemistry to material science and nanotechnology, and from computational chemistry to agricultural chemistry.

We would like to thank all those who submitted the full papers and the reviewers for their timely help in assessing these papers for publication.

We would like to pay a special tribute to all the sponsors of ICPAC 2010.

Chemistry is being increasingly recognised as a central discipline that encompasses several areas of medicine, agriculture, biology, environment, physics and material science. Therefore, as we celebrate the International Year of Chemistry (IYC 2011) and the 100th anniversary of the Noble prize awarded to Marie Curie, we hope that this collection of papers will serve as a useful reference set for researchers.

Gupta Bhowon, M
Jhaumeer-Laulloo, S
Li Kam Wah, H
Ramasami, P

Contents

1	Investigation of Dissolved Nutrients in Tropical Coastal Waters in Mauritius	1
	Zaynab B. Bissembur, Janita Balgobin, Archana Anjore, Roshan T. Ramessur, and Kishore Boodhoo	
2	The Influence of the Cage Effect on the Mechanism of Multistage Chemical Reactions in Solutions	11
	Alexander B. Doktorov and Stanislav G. Fedorenko	
3	Photoionization Studies of Reactive Intermediates of Importance in the Atmosphere	35
	John Dyke	
4	Synthesis and Applications of Nano Size Titanium Oxide and Cobalt Doped Titanium Oxide	57
	Revannath D. Nikam, Sharad S. Gaikwad, Ganesh E. Patil, Gotan H. Jain, and Vishwas B. Gaikwad	
5	Development of Novel Insect Growth Regulators: Effect of 1-(Substitutedbenzoyl)-3-[(2'-Isopropyl-5'-Methylphenoxy) Acetamino] Thiourea and Urea Derivatives on Total Haemocyte Count of <i>Dysdercus koenigii</i>	69
	Chetan M. Zade, Umesh D. Pete, Megharaj S. Kadam, and Ratnamala S. Bendre	
6	Preliminary Catalytic Studies Using Tyrosine and Phenylalanine Analogues on Selected Baylis-Hillman and Michael Reactions	81
	Prakashanand Caumul, Nausheen Joondan, Anuradha Tuhaloo, and Thavinash Jhowry	

7	Synthesis, Structure and Characterization of New Amic Acid Derivatives of 3-Amino-1,2,4-Triazole and Their Complexes with Some Metal Ions	103
	Ahlam J. Abdulghani and Suad M. Sahan	
8	Regioselective Synthesis of Polyfluorinated Pyrazoles and Evaluation of Antimicrobial Activity	121
	Madhukar N. Jachak, Dilip R. Birari, Deepak P. Shelar, Sandeep R. Patil, Ramhari V. Rote, Santosh S. Shinde, and Sandip M. Bagul	
9	Trapping of Organomanganese Generated Enolates with an Aldehydes in the Presence of $\text{Cu}(\text{NCMe})_4[\text{BF}_4]$	143
	Sunil D. Jadhav and Madhukar B. Deshmukh	
10	Radial and Electron Correlation Effects for Helium and Some Helium Like Ions	153
	Khalil H. AL-bayati and Esraa F. Saeed	
11	Dynamical Role of the Fictitious Orbital Mass in Car-Parrinello Molecular Dynamics	171
	Sheau-Wei Ong, Eng-Soon Tok, and H. Chuan Kang	
12	Novel Liquid Diffusion Tube Determines Electrolytes' Relative Free Diffusion Velocities, Hydration Numbers and Overwhelmingly Revalidates Electrolytic Diffusion Law	193
	Abul Khair, Golam M. Golzar Hossain, Mohammad S. Alam, Mahammad M. Hossain, Mohammad H. Kabir, Mohammad H. Rahman, and Amal Halder	
13	Reverse Phase Extraction Chromatographic Separation of Trivalent Bismuth Using Liquid Anion Exchanger	209
	Sachin R. Phule, Haribhau R. Aher, Shamrao P. Lawande, and Shashikant R. Kuchekar	
14	Dry Sliding Wear Behavior of Ultrafine-Grained Mild Steel Processed Using Multi Axial Forging	219
	Aditya K. Padap, Gajanan P. Chaudhari, and Sumeer K. Nath	
15	Thiocyanato Bridged Heterodinuclear Complex $[\text{Cu}(\text{bpy})_2(\mu\text{-NCS})\text{Ru}(\text{bpy})_2(\text{NO}_3)](\text{PF}_6)_2$ and Its Binding with Cd(II), Hg(II), Pb(II) and Ag(I) Ions	231
	Niraj Kumari, Mudit Dixit, Herbert W. Roesky, and Lallan Mishra	

16 Using Electrochemical Impedance Spectroscopy of Methylene Blue and Ferricyanide for DNA Sensing Surface Characterization	249
Suthisa Leasen, Kallaya Sritunyalucksana-Dangtip, Jose H. Hodak, Jiraporn Srisala, Chadin Kulsing, and Waret Veerasia	
17 An Investigation into the Use of the Concept Attainment Model in Teaching the “Periodic Table” at ‘O’-Level Through an Action Research	265
Mokshada Luckpoteea and Fawzia B. Narod	
18 Synthesis, Spectral Characterization and Anticancer Screening of Triorganotin(IV) Carboxylates	301
Mala Nath, Monika Vats, and Partha Roy	
19 Nonequilibrium Ultrafast Charge Transfer Reactions in Photoexcited Donor-Acceptor Pairs	317
Valentina A. Mikhailova, Sergey V. Feskov, Vladimir N. Ionkin, Vladislav V. Yudanov, and Anatoly I. Ivanov	
20 Adsorption Studies of Lead, Copper and Cadmium Ions in Aqueous Solution by Ethylene Diamine Modified Amberlite XAD-1180	335
Isaac W. Mwangi, Jane C. Ngila, Joseph Kamau, and Jonathan Okonkwo	
21 Theoretical Study of Structure, Vibration Spectra and Thermodynamic Properties of Cluster Ions in Vapors over Potassium, Rubidium and Cesium Chlorides	353
Tatiana P. Pogrebnaya, Jean B. Hishamunda, Camille Girabawe, and Alexander M. Pogrebnoi	
22 Environmental Threat to Photochemical and Photobiological Reactions	367
Rafia Azmat	
23 Neutral-Neutral Direct Hydroamination Reactions of Substituted Alkenes: A Computational Study on the Markovnikov Selection Rule	375
Sanyasi Sitha and Linda L. Jewell	
24 Preparation and Characterization of TiO₂ – ZrO₂ Mixed Oxide Catalysts for Photocatalytic Reduction of Carbon Dioxide	389
Simona Krejčikova, Kamila Koci, Lucie Obalova, Libor Capek, and Olga Solcova	

25	Modification of Anthraquinone-2-Carboxylic Acid with Multiwalled Carbon Nanotubes and Electrocatalytic Behavior of Prepared Nanocomposite Towards Oxygen Reduction ..	399
	Ida Tiwari, Manorama Singh, and Mandakini Gupta	
26	Synthesis and Biological Activity of Derivatives of 2,2'-Dithiobisbenzamides ..	411
	Roumilla Gungah, Salma Moosun, Sabina Jhaumeer-Laulloo, and Minu G. Bhowon	
27	Spectral Studies of Solar Radiation Induced Dye Decoloration in Aqueous Solution ..	419
	Fahim Uddin, Rafia Azmat, and Tehseen Ahmed	
28	Optimization of Process Parameters for Enhanced Decolorization of NOVASOL Direct Black Textile Dye by <i>Agaricus bitorqus</i> ..	433
	Haq N. Bhatti and Ismat Bibi	
29	Chemical Composition and Antimicrobial Activity of Comorian <i>Ocimum canum</i> Essential Oil Harvested in the Region of Maweni Dimani-Grande Comoros.....	443
	S.O.S. Hassane, A. Farah, B. Satrani, M. Ghanmi, N. Chahmi, S.H. Soidrou, and A. Chaouch	
30	Synthesis of Five-, Six- and Seven-Membered Hetero Ring Annulated Imidazo[4,5-b] carbazoles and Azacarbazoles of Medicinal Interest ..	453
	Bhawani Singh, Bharti Vashishtha, and D. Kishore	
31	Screening Biochemical Markers for the Prevention of Coronary Heart Disease ..	473
	Deepuk Albana and Marie Chan Sun	
	Index ..	481

Contributors

Ahlam J. Abdulghani Department of Chemistry, College of Science, University of Baghdad, Jaderiya, Baghdad, Iraq, prophahlam@yahoo.com

S. M. Achmet School of Chemistry, University College of Science, University of Tehran, Tehran, Iran

Haribhau R. Aher P. G. Department of Analytical Chemistry, P. V. P. College Pravaranagar, At/Po. Loni (Kd), Tal. Rahata, Dist. Ahmednagar, 413713 Maharashtra, India, h_aher@yahoo.com

Tehsenn Ahmed Department of Chemistry, University of Karachi, Karachi, 75270 Pakistan, chemist_physical@yahoo.com

Khalil H. AL-bayati Department of Physics, College of Science for Women, Baghdad University, Aljadyria, Baghdad, Iraq, drkhalilhadi@yahoo.com

Mohammad S. Alam Department of Applied Chemistry & Chemical Engineering, Noakhali Science and Technology University, Sonapur, Noakhali, Bangladesh

Deepuk Albana C/o mr Ravin Albana, 122 Caroline Road, Vallee des Pretres, Port Louis, Mauritius

Archana Anjore Department of Chemistry, University of Mauritius, Réduit, Mauritius

Rafia Azmat Department of Chemistry, Jinnah University for Women, 5C Nazimabad, Karachi, 74600 Pakistan, rafiasaeed200@yahoo.com

Sandip M. Bagul Organic Chemistry Research Centre, Department of Chemistry, K. T. H. M. College, Gangapur Road, Nashik 422 002, Maharashtra, India, sandipbagul@gmail.com

Janita Balgobin Department of Chemistry, University of Mauritius, Réduit, Mauritius, j1.balgobin@yahoo.com

Ratnamala S. Bendre School of Chemical Sciences, North Maharashtra University, Jalgaon, 425 001 India, bendrs@rediffmail.com

Haq N. Bhatti Department of Chemistry & Biochemistry, University of Agriculture, Faisalabad, 38040 Pakistan, hnbhatti2005@yahoo.com

Minu G. Bhowon Department of Chemistry, Faculty of Science, University of Mauritius, Réduit, Mauritius, mbhowon@uom.ac.mu

Ismat Bibi Department of Chemistry & Biochemistry, University of Agriculture, Faisalabad, 38040 Pakistan, ismat16_08_1982@yahoo.com

Dilip R. Birari Organic Chemistry Research Centre, Department of Chemistry, K. T. H. M. College, Gangapur Road, Nashik 422 002, Maharashtra, India, dilip.birari@cipl.com

Zaynab B. Bissemur Department of Chemistry, University of Mauritius, Réduit, Mauritius, zeinabiss72@yahoo.com

Kishore Boodhoo Department of Chemistry, University of Mauritius, Réduit, Mauritius, kishore.boodhoo@uom.ac.mu

Libor Capek Faculty of Chemical Technology, Univerzity of Pardubice, Studentská, 95, Pardubice, Czech Republic, libor.capek@upce.cz

Prakashanand Caumul Department of Chemistry, Faculty of Science, University of Mauritius, Réduit, Mauritius, p.caumul@uom.ac.mu

N. Chahmi National Institute of Medicinal and Aromatic Plants – Taounate, BP 159, Tounate Principale, Sidi Mohamed Ben Abdallah University, Fes Maroc

A. Chaouch Laboratory of Applied Chemistry and Quality Control, Faculty of Science, Université Ibn Tofail, BP133 Kenitra, Morocco

Gajanan P. Chaudhari Department of Metallurgical and Materials Engineering, Indian Institute of Technology Roorkee, Roorkee, Uttarakhand, 247667 India, chaudfmt@iitr.ernet.in

Madhukar B. Deshmukh Department of Chemistry, Shivaji University, Belgaum Road, 416004 Kolhapur, India, m.deshmukh1@rediffmail.com

Mudit Dixit Electronic Structure and Theory Group, National Chemical Laboratory, 441008 Pune, India, dixitmuditk@gmail.com

Alexander B. Doktorov Laboratory of Theoretical Chemistry, Institute of Chemical Kinetics and Combustion SB RAS, Institutskaya 3, 630090 Novosibirsk, Russia, doktorov@kinetics.nsc.ru

John Dyke School of Chemistry, University of Southampton, Southampton, SO17 1BJ UK, jmdyke@soton.ac.uk

A. Farah Department of Chemistry, CCB124, York University, 4700 Keele St., Toronto, ON, M3J1P3 Canada

Stanislav G. Fedorenko Laboratory of Theoretical Chemistry, Institute of Chemical Kinetics and Combustion SB RAS, Institutskaya 3, 630090 Novosibirsk, Russia, fedorenk@kinetics.nsc.ru

Sergey V. Feskov Physical-Technical Institute, Volgograd State University, University Avenue, 400062 Volgograd, Russia, serguei.feskov@volsu.ru

Sharad S. Gaikwad Department of Chemistry, K.T.H.M.College, Gangapur Road, Nashik, Maharashtra, 422 002 India, gaikwad.sharad85@gmail.com

Vishwas B. Gaikwad Chemistry Materials Research Laboratory, K. T. H. M. College, Nashik, Maharashtra, 422 022 India, dr.gaikwadvb@rediffmail.com

M. Ghanmi Laboratoire de Chimie des Plantes et Synthèse organique et Bioorganique, Faculté des Sciences, Université Mohammed V-Agdal, BP1014 Rabat, Morocco

Camille Girabawe Roumilla Gungah Department of Chemistry, Faculty of Science, University of Mauritius, Reduit, Mauritius, rumilla_777@yahoo.com

Mandakini Gupta Department of Chemistry, Faculty of Science, Banaras Hindu University, Varanasi, 221005 India, mandakini1710@gmail.com

Amal Halder Department of Chemistry, University of Burdwan, Bardhaman, India

S. O. S. Hassane Faculty of Science and Technology, University of the Comoros, BP 2585 Moroni, Comoros, Comorossaid_omar2000@yahoo.fr

Jean B. Hishamunda Physics Department, Brandeis University, Waltham, MA 02453, USA

Jose H. Hodak Facultad de Ciencias Exactas y Naturales, Ciudad Univeritaria Pab., Universidad de Buenos Aires, 1428 Buenos Aires, Argentina, josew3@yahoo.com

Golam M. Golzar Hossain School of Chemistry, Cardiff University, Cardiff, CF10 3AT UK

Mahammad M. Hossain Department of Chemical Engineering, Mohamed Sathak Engineering College, Kilakarai, 623 806 India

Vladimir N. Ionkin Physical-Technical Institute, Volgograd State University, University Avenue, 400062 Volgograd, Russia, ionya@mail.ru

Anatoly I. Ivanov Physical-Technical Institute, Volgograd State University, University Avenue, 400062 Volgograd, Russia, Anatoly.Ivanov@volsu.ru

Madhukar N. Jachak Organic Chemistry Research Centre, Department of Chemistry, K. T. H. M. College, Gangapur Road, Nashik 422 002, Maharashtra, India, mnjachak@hotmail.com

Sunil D. Jadhav Department of Chemistry, Dada Patil Mahavidyalaya, Karjat, 414402 Maharashtra, India, jadhav.sd@rediffmail.com

Gotan H. Jain Department of Physics, Arts, Commerce & Science College, Nandgaon, Nashik, Maharashtra, 423 106 India, gotanjain@rediffmail.com

Linda L. Jewell School of Chemical and Metallurgical Engineering, University of the Witwatersrand, Private Bag 3, Wits 2050 Johannesburg, South Africa, linda.jewell@wits.ac.za

Sabina Jhaumeer-Laulloo Department of Chemistry, Faculty of Science, University of Mauritius, Réduit, Mauritius, sabina@uom.ac.mu

Thavinash Jhowry Department of Chemistry, Faculty of Science, University of Mauritius, Réduit, Mauritius

Nausheen Joondan Department of Chemistry, Faculty of Science, University of Mauritius, Réduit, Mauritius

Mohammad H. Kabir Department of Microbiology, University of Dhaka, Dhaka, Bangladesh

Megharaj S. Kadam School of Life Sciences, North Maharashtra University, Jalgaon, 425 001 India, ms.kadam@gmail.com

Joseph Kamau School of Chemistry, University of KwaZulu-Natal, University Road, Westville, P/Bag X45001, Durban, 4000 South Africa, josephkamau@yahoo.com

H. Chuan Kang Department of Chemistry, National University of Singapore, 3 Science Drive 3, 117543 Singapore, Singapore, chmkhc@nus.edu.sg

Abul Khair Department of Chemistry, University of Dhaka, Dhaka, 1000 Bangladesh, profabulkhair@gmail.com

D. Kishore Department of Chemistry, Banasthali University, Banasthali, Rajasthan, 304022 India, kishoredharma@yahoo.co.in

Kamila Koci Department of Physical Chemistry and Theory of Technological Processes, Technical University of Ostrava, 17. Listopadu, 15, Ostrava, Czech Republic, kamila.koci@vsb.cz

Simona Krejčikova Department of Catalysis and Reaction Engineering, Institute of Chemical Process Fundamentals of the ASCR, v.v.i., Rozvojova, 135, Prague 6, Czech Republic, krejčikova.simona@icpf.cas.cz

Shashikant R. Kuchekar P. G. Department of Analytical Chemistry, P. V. P. College Pravaranagar, At/Po. Loni (Kd), Tal. Rahata, Dist. Ahmednagar, 413713 MS, India, shashi17@gmail.com

Chadin Kulsing IFEC-MU, Mahidol University, Rama VI Road Thung Phyathai Rachadevi, 10400 Bangkok, Thailand, payoonum@yahoo.com

Niraj Kumari Department of Chemistry, Banaras Hindu University, 221005 Varanasi, India, nirajchem@gmail.com

Shamrao P. Lawande P. G. Department of Analytical Chemistry, P. V. P. College Pravaranagar, At/Po. Loni (Kd), Tal. Rahata, Dist. Ahmednagar, 413713 MS, India

Suthisa Leasen Department of Physics, Mahidol University, Rama VI Road Thung Phyathai Rachadevi, 10400 Bangkok, Thailand, sainub@gmail.com

Mokshada Luckpoteea Simadree Virahsawmy State Secondary School, Rivière du Rempart, Mauritius, mokshada25@hotmail.com

Valentina A. Mikhailova Physical-Technical Institute, Volgograd State University, University Avenue, 400062 Volgograd, Russia, mixailova.va@mail.ru

Lallan Mishra Department of Chemistry, Banaras Hindu University, 221005 Varanasi, India, lmishrabhu@yahoo.co.in

Salma Moosun Department of Chemistry, Faculty of Science, University of Mauritius, Reduit, Mauritius, salma2410@gmail.com

Isaac W. Mwangi School of Chemistry, University of KwaZulu-Natal, University Road, Westville, P/Bag X45001, Durban, 4000 South Africa, isaacwaweru2000@yahoo.co.uk

Fawzia B. Narod Department of Science Education, Mauritius Institute of Education, Mauritius, Mauritius, zia373@eudoramail.com

Mala Nath Department of Chemistry, Indian Institute of Technology Roorkee, Roorkee 247667, India, malanfcy@iitr.ernet.in

Sumeer K. Nath Department of Metallurgical and Materials Engineering, Indian Institute of Technology, Roorkee, Uttarakhand, 247667 India, indiafmt@iitr.ernet.in

J. Catherine Ngila School of Chemistry, University of KwaZulu-Natal, University Road, Westville, P/Bag X45001, Durban, 4000 South Africa, ngila@ukzn.ac.za

Revannath D. Nikam Department of Chemistry, K.T.H.M.College, Gangapur Road, Nashik, Maharashtra, 422 002 India, nikam.revan@rediff.com

Lucie Obalova Dept.of Physical Chemistry and Theory of Technological Processes, Technical University of Ostrava, 17. Listopadu, 15, Ostrava, Czech Republic, lucie.obalova@vsb.cz

Jonathan Okonkwo Department of Environmental, Water & Earth Science, Faculty of Science, Tshwane University of Technology, 175 Nelson Mandela Drive, P/Bag X680, Pretoria, 0001 South Africa, OkonkwoJ@tut.ac.za

Sheau-Wei Ong Department of Chemistry, National University of Singapore, 3 Science Drive 3, 117543 Singapore, Singapore, chmosw@nus.edu.sg

Aditya K. Padap Department of Metallurgical and Materials Engineering, Indian Institute of Technology Roorkee, Roorkee, Uttarakhand, 247667 India

Ganesh E. Patil Department of Physics, Arts, Commerce & Science College, Nandgaon, Nashik, Maharashtra, 423 106 India, ganeshpatil.phy@rediffmail.com

Sandeep R. Patil Organic Chemistry Research Centre, Department of Chemistry, K. T. H. M. College, Gangapur Road, Nashik 422 002, Maharashtra, India, dr.sandeepatil28@gmail.com

Umesh D. Pete School of Chemical Sciences, North Maharashtra University, Jalgaon, 425 001 India, umeshdpete@rediffmail.com

Sachin R. Phule Department of Chemistry, P. V. P. College Pravaranagar, At/Po. Loni (Kd), Tal. Rahata, Dist. Ahmednagar, 413713 Maharashtra, India, sachinphule55@yahoo.co.in

Tatiana P. Pogrebnya Ivanovo State University of Chemical Technology, Ivanovo, Russia

Alexander M. Pogrebnoi Department of Applied Physics, Kigali Institute of Science and Technology, Kigali, Rwanda, pgamtp@mail.ru

Mohammad H. Rahman Dr. Panjwani Center for Molecular Medicine and Drug Research (PCMD); International Center for Chemical and Biological Sciences (ICCBS), University of Karachi, Karachi, 75270 Pakistan, hafizur.rahman@iccs.edu

Roshan T. Ramessur Department of Chemistry, University of Mauritius, Réduit, Mauritius, ramessur@uom.ac.mu

H. W. Roesky Institute of Inorganic Chemistry, Goettingen University, Goettingen, Germany, hroesky@gwdg.de

Ramhari V. Rote Organic Chemistry Research Centre, Department of Chemistry, K. T. H. M. College, Gangapur Road, Nashik 422 002, Maharashtra, India, rote.ramhari509@rediffmail.com

Partha Roy Department of Biotechnology, Indian Institute of Technology Roorkee, Roorkee 247667, India, paroyfbs@iitr.ernet.in

Esraa F. Saeed Department of Physics, College of Science, Hahrain University, Aljadyria, Baghdad, Iraq, israa_physics2006@yahoo.com

Suad M. Sahan Department of Chemistry, College of Science, University of Baghdad, Jaderiya, Baghdad, Iraq

B. Satrani Centre de recherche forestière, BP 763, Agdal, 10050 Rabat, Morocco

Deepak P. Shelar Organic Chemistry Research Centre, Department of Chemistry, K. T. H. M. College, Gangapur Road, Nashik 422 002, Maharashtra, India, deeprity83@gmail.com

Santosh S. Shinde Organic Chemistry Research Centre, Department of Chemistry, K. T. H. M. College, Gangapur Road, Nashik 422 002, Maharashtra, India, sss.3s@rediffmaill.com

Bhawani Singh Department of Chemistry, Banasthali University, Banasthali, Rajasthan, 304022 India, bsyadav2000@gmail.com

Manorama Singh Department of Chemistry, Faculty of Science, Banaras Hindu University, Varanasi, 221005 India, manoramabhu@gmail.com

Sanyasi Sitha School of Chemical and Metallurgical Engineering, University of the Witwatersrand, Private Bag 3, Wits 2050 Johannesburg, South Africa, sanyasi.sitha@wits.ac.za

S. H. Soidrou Olga Solcova Department of Catalysis and Reaction Engineering, Institute of Chemical Process Fundamentals of the ASCR, v.v.i., Rozvojova 135, Prague 6, Czech Republic, solcova@icpf.cas.cz

Jiraporn Srisala National Science and Technology Development Agency, National Center for Genetic Engineering and Biotechnology, Klongluang Province, 12120 Pathumthani, Thailand, jsrisala@gmail.com

Kallaya Sritunyalucksana-Dangtip Centex Shrimp, Mahidol University, Rama VI Road Thung Phyathai Rachadevi, 10400 Bangkok, Thailand, tekst@mahidol.ac.th

Marie Chan Sun Department of Medicine, University of Mauritius, Réduit, Mauritius, lan.sun@uom.ac.mu

Ida Tiwari Department of Chemistry, Faculty of Science, Banaras Hindu University, Varanasi, 221005 India, idatiwari_2001@rediffmail.com

Eng-Soon Tok Department of Physics, National University of Singapore, 3 Science Drive 3, 117543 Singapore, Singapore, phytokes@nus.edu.sg

Anuradha Tuhalo Department of Chemistry, Faculty of Science, University of Mauritius, Réduit, Mauritius

Fahim Uddin Department of Chemistry, University of Karachi, Karachi, 75270 Pakistan, fahim_Uddin01@yahoo.com

Bharti Vashishtha Department of Chemistry, Banasthali University, Banasthali, Rajasthan, 304022 India, bhartivashishtha.chem@gmail.com

Monika Vats Department of Chemistry, Indian Institute of Technology Roorkee, Roorkee 247667, India, mona2k42000@gmail.com

Waret Veerasia IFEC-MU, Mahidol University, Rama VI Road Thung Phyathai Rachadevi, 10400 Bangkok, Thailand, scwvr@mahidol.ac.th

Vladislav V. Yudanov Physical-Technical Institute, Volgograd State University, University Avenue, 400062 Volgograd, Russia, Yudanov-VolsU@yandex.ru

Chetan M. Zade School of Chemical Sciences, North Maharashtra University, Jalgaon, 425 001 India, zadecm2007@rediffmail.com

Chapter 1

Investigation of Dissolved Nutrients in Tropical Coastal Waters in Mauritius

Zaynab B. Bissembur, Janita Balgobin, Archana Anjore,
Roshan T. Ramessur, and Kishore Boodhoo

Abstract This study investigated the concentration ratios of dissolved nitrate: phosphate in tropical coastal waters in Mauritius (1,850 km², 20°S and 57°E, Western Indian ocean) during winter 2008 and summer 2009 arising from both surface and submarine groundwater sources. Dissolved nutrients in lagoon waters were statistically compared between winter and summer periods and between urban and rural estuaries at Grand River North West (GRNW), Albion and Flic en Flac. A low ratio of 5 was computed for dissolved [nitrate]: [phosphate] for the Flic en Flac lagoon situated in a rural area, lying in the range from 2 to 15 as usually found for coastal waters globally suggesting denitrification whereas the ratio of dissolved [nitrate]: [phosphate] in lagoon waters computed for GRNW and Albion situated in urban areas were lower and less than 2 and may be attributed to possible high phosphate input. The sources of dissolved phosphate may come from the run-off of phosphate fertilisers from sugar cane plantations and submarine groundwater discharges. This high concentration of dissolved phosphate in the freshwater system can be harmful as it can cause an algal bloom. A high concentration of dissolved phosphate was recorded in September during a flood. The mean values for dissolved nitrate were $11.8 \pm 11.0 \mu\text{mol/L}$ during winter and $11.7 \pm 5.0 \mu\text{mol/L}$ during summer at Flic en Flac. Dissolved nitrate levels were observed to be abnormally high which probably were due to the lagoon water being mixed with the submarine groundwater discharge in the lagoon. In addition, a strong positive correlation was observed between phosphate and nitrate ($R^2 = 0.74$) during the period of winter 2009 to summer 2010 for all the stations at Flic en Flac.

Z.B. Bissembur • J. Balgobin • A. Anjore • R.T. Ramessur • K. Boodhoo (✉)
Department of Chemistry, University of Mauritius, Réduit, Mauritius
e-mail: zeinabiss72@yahoo.com; j1_balgobin@yahoo.com; ramessur@uom.ac.mu;
kishore.boodhoo@uom.ac.mu

1.1 Introduction

The coastal zone has evolved in response to individual sectorial interests which plan development independently and which do not adequately consider the effects of one form of exploitation upon another development activity. Consequently, many of our coastal resources are susceptible to negative impact. At present, the surface drainage patterns of Mauritius have been classified into 25 major drainage areas, defined as catchment areas ranging from 10.4 to 164.8 km² [1]. The river resources used for recreation spaces and consumptive uses conflict with environmental protection as many of the rivers in Mauritius receive diffuse urban and land runoff. The threat of contamination of surface waters in Mauritius and deterioration in water quality by urban runoff, in particular, metal pollution is only relatively recent as compared to industrialized countries as the Mauritian economy underwent a rapid phase of urbanization during the 1980s. Previous studies have showed that estuaries are particularly vulnerable to trace metal contamination [2–7] hence highlighting the need to monitor these aspects of pollution in estuarine regions.

Based on the increasing population growth in Mauritius and the significant use of pesticides and fertilisers, it is concluded that dissolved nutrients may pose the greatest present and future threat to the marine environment. The responses of both flora and fauna span an array of ecosystems and organizational hierarchies, from the species to the community levels. Although we are only at an early stage in the projected trends of global warming, ecological responses to recent climate change are already clearly visible [8]. The intensity and quantity of phosphorus losses have been found to vary as a function of numerous factors, including phosphorus application rate, rainfall intensity, the form of phosphorus applied, and the method of application. Since occurrence of rainfall along with rainfall-derived run-off is generally unpredictable, incidental phosphorus losses make the dominant (20–98%) contribution to measured phosphorus loads in run-off from fields when rainfall interacts directly with topsoil receiving applied fertilisers or manure. In agricultural landscape there are two major local sources of nitrogen. One is rather constant in time and space and consists of animal housing, dung reservoir and other point sources. The second source is very diffuse and is formed by nitrogen emission from the application of mineral and organic fertilisers, especially slurry [9, 10]. Contamination from industrial discharges and urban runoff represent a risk to surface and groundwater quality. The accumulation of toxic and persistent substances in the coastal environment continuously increases owing to anthropogenic activities as the estuaries and their adjacent coasts are the focus for many economic activities [11–14].

The coastal zone of Mauritius (1,850 km², 20°S and 57°E, Western Indian ocean) is made up of terrestrial and marine interfaces where industrial and urban activities and baseline investigations carried out on the west coast of Mauritius have highlighted the susceptibility of local estuaries and lagoons to metal and dissolved nutrient inputs by both surface runoff and submarine groundwater discharge [15, 16]. The heavy use of leaded fuel by vehicles up to 2001 has been potentially

dangerous both as an atmospheric pollutant and through its introduction into food chains via rain induced road run-off and it has become necessary to introduce unleaded petrol [1, 4, 17].

In Mauritius, estuaries are sensitive areas with a very sensitive and ecologically important fauna and flora. Sediment serves as a source and a removal mechanism for some contaminants, and as a vehicle for contaminant transport downstream. Industrial development coupled with a rise in the tourism industry have led to major concerns in pollution problems, especially in estuaries with fishermen communities giving rise to conflicts amongst the various coastal stakeholders. This study was carried out to determine dissolved nitrate and phosphate in coastal waters from an urban estuary at Grand River North West and statistically compared to Albion and Flic en Flac situated in a rural area in order to assess eutrophication from dissolved nutrients in coastal waters along the western coast of Mauritius during winter and summer from August 2008 to February 2009. The objective of this study was to monitor dissolved nutrients (nitrates and phosphates) in an industrial, touristic and agricultural area during winter (August – October) and summer (November – February) months. Consequently, with the collected data, we would be able to check if there are any significant differences in dissolved nitrate and phosphate during winter (dry) and summer (wet) periods at GRNW, Albion and Flic en Flac situated in rural estuary. In addition, from the calculated concentration ratios of nitrate: phosphate we would determine if there has been any denitrification at GRNW, Albion and Flic en Flac.

1.2 Methodology

1.2.1 Study Sites

The three stations along the western coast of Mauritius are shown in Fig. 1.1 as follows:

1.2.2 Grand River North West (GRNW) (Station 1)

The GRNW which discharges south of Port Louis has a catchment area of 116 km² and is fed by small southern tributaries from Upper Plaines Wilhems and Moka district. The GRNW estuary receives wastewater from St Louis River. The latter receives wastewater from domestic and industrial origins such as dye-houses, battery manufacturers, galvanizing and electroplating plants, paint manufacturers and other chemical industries. River St Louis at its mouth merges into GRNW and both discharge their waters directly into the sea. The annual average rainfall in the Port Louis area is 1,160 mm.

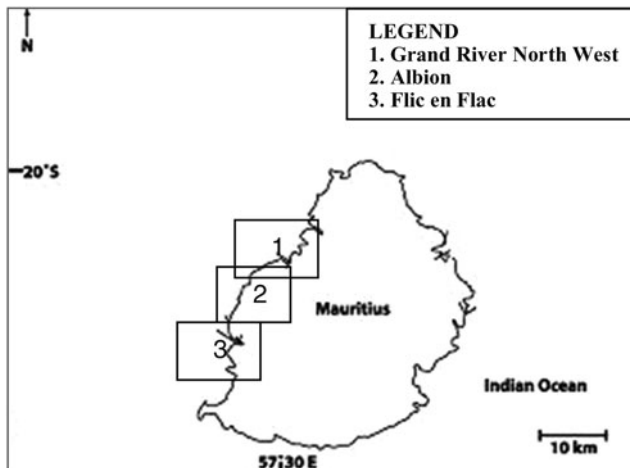


Fig. 1.1 Sampling stations along the western coast of Mauritius (An urban estuary at Grand River North West, station 1, Albion, station 2 and a rural estuary at Flic en Flac, station 3)

1.2.3 *Albion (Station 2)*

The Belle Eau estuary is situated at the southern end of the Albion Public Beach and is fed by the Belle Eau River. It is bordered by the Albion Fisheries Research Centre on one side and on the other by the main road and a small residential community. The water quality of the Belle Eau River is being influenced by the inputs derived from land use and human activities in the surrounding region from non-point sources. These land uses include agriculture, animal farming and residential development. Surface water canals, rivulets and streams flow into the river after crossing sugar-cane fields and land under crop cultivation. Surface runoff from these areas carry animal wastes, fertilisers, pesticides and silt into the river and finally to the estuary.

1.2.4 *Flic en Flac (Station 3)*

Flic en Flac ($20^{\circ}16'S$, $57^{\circ}22'E$) is found in the district of Black River on the western coast of the island of Mauritius. Flic en Flac is a non-industrial area with 2,000 inhabitants. It has a coastline of 13×0.5 km with 9 large hotels extending from Flic en Flac to Wolmar and the beach has 0.5 million of visitors yearly. Flic en Flac covers an area of about 13 km^2 . An area of 4 km^2 is under plantation, particularly sugar cane plantation. The maximum atmospheric temperature at Flic en Flac is 31.6°C in February and 28.4°C in August. The mean monthly rainfall during the period of August 2008 – February 2009 is in the range of 9.7–167.1 mm. Water in

the minor aquifer in Curepipe tends to move towards the west going to Flic en Flac and La Ferme Reservoir through the Pierrefond tunnel. In addition to surface flow in River Rempart (West) there is groundwater flow through the aquifer producing a freshwater spring in the lagoon and marshes in the Flic en Flac coastal region. Seven stations were selected at Flic en Flac to see whether the region was contaminated by anthropogenic activities.

1.2.5 Dissolved Nutrient Analysis

Replicate samples of water were collected in 200 ml plastic bottles (dissolved nitrate) and glass bottles (reactive phosphate) in the coastal area in GRNW, Albion and Flic en Flac. Samples were stored at 4°C and analyzed within 24 h. The concentration of dissolved nitrite, dissolved nitrate, and dissolved phosphate were determined using standard spectrophotometric methods [18] at 543 and 882 nm respectively using a PU 8710 spectrophotometer and a UNICAM 8700 Series UV/VIS spectrometer following calibration using known standard solutions. Quality control was achieved by analyzing an internal reference independently prepared from the standard and the standard curves were verified after ten successive runs by analysis of one standard solution within the linear range for each nutrient.

1.2.6 Dissolved Nitrate Analysis

Dissolved nitrate in the samples were reduced almost quantitatively to nitrite by running samples and standards through a column containing commercially available cadmium granules coated with metallic copper. The nitrite produced was determined by diazotising with sulphanilamide and coupling with N-(1-naphthyl)-ethylenediamine dihydrochloride to form a highly coloured azo dye which was measured spectrophotometrically in 10 cm cuvettes at 543 nm after 15 min. The reduction efficiency of the Cd column was determined by comparing the amount after reduction with the calculated amount supplied to the column. A correction was made for the nitrite present in the sample by analyzing without the reduction step. The precision of nitrate determination was at the 1 $\mu\text{mol L}^{-1}$.

1.2.7 Dissolved Phosphate Analysis

Samples for reactive phosphate analysis were immediately filtered after collection. In a suitably acidified solution, phosphate reacted with molybdate to form molybdo-phosphoric acid, which was then reduced to the intensely coloured molybdenum blue complex after 5 min. The absorbance of the latter was measured at 882 nm in a 10 cm cell. The precision was at the 0.1 $\mu\text{mol L}^{-1}$.

1.3 Results and Discussion

The mean values for dissolved nitrates and phosphates during winter and summer at GRNW, Albion and Flic en Flac are shown in Table 1.1 and nitrate-phosphate plots are shown in Figs. 1.2–1.4, as follows:

A low dissolved nitrate: phosphate concentration ratio of 7 was computed for the Flic en Flac lagoon situated in a rural area which lie in the range from 2 to 15, as found for coastal waters globally according to Tyrell and Law [19] suggesting denitrification whereas the concentration ratios of dissolved nitrate: phosphate in coastal waters computed for GRNW and Albion situated in urban areas were smaller than two and were attributed to denitrification, algal blooms. A strong positive correlation between nitrate and phosphate ($R^2 = 0.78$) was obtained at GRNW during winter, as shown in Fig. 1.2.

A strong positive correlation was observed between phosphate and nitrate ($R^2 = 0.74$) during the period of winter 2009 to summer 2010 for all the stations at Flic en Flac, as shown in Fig. 1.4.

Table 1.1 Mean and standard deviation of dissolved nitrate, dissolved phosphate in coastal waters during winter and summer at GRNW, Albion and Flic en Flac

Stations	Dissolved nitrate ($\mu\text{mol/L}$)	Dissolved phosphate ($\mu\text{mol/L}$)
GRNW downstream		
Winter 2008	12.6 ± 0.2	1.0 ± 0.6
Summer 2009	7.8 ± 5.6	3.9 ± 5.2
Mean	10.2 ± 3.4	2.4 ± 2.0
GRNW estuary		
Winter 2008	2.7 ± 0.4	1.5 ± 0.9
Summer 2009	3.2 ± 0.5	3.3 ± 4.7
Mean	3.0 ± 0.3	2.4 ± 1.3
Albion downstream		
Winter 2008	12.7 ± 1.6	2.7 ± 0.5
Summer 2009	5.9 ± 0.6	5.4 ± 0.4
Mean	9.3 ± 4.8	4.1 ± 1.9
Albion estuary		
Winter 2008	10.8 ± 0.7	3.0 ± 2.0
Summer 2009	5.9 ± 0.6	3.8 ± 0.4
Mean	8.3 ± 3.5	3.4 ± 0.6
Flic en Flac lagoon		
Winter 2008	11.8 ± 11.0	1.7 ± 0.6
Summer 2009	11.7 ± 5.0	2.9 ± 0.6
Mean	11.8 ± 0.1	2.3 ± 0.8
Flic en Flac lagoon		
Winter 2009	10.6 ± 8.2	2.4 ± 1.3
Summer 2010	4.1 ± 3.3	1.0 ± 0.6
Mean	7.4 ± 3.6	1.7 ± 1.0

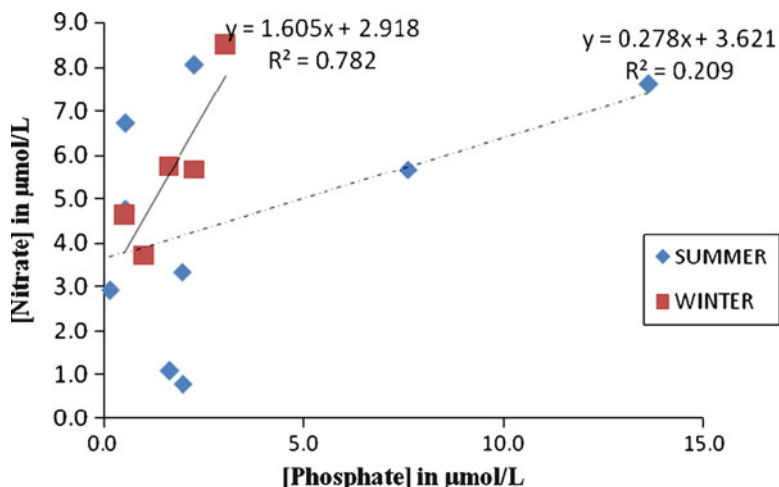


Fig. 1.2 Correlations between dissolved phosphate and dissolved nitrate at GRNW for summer and winter (August 2008 – February 2009)

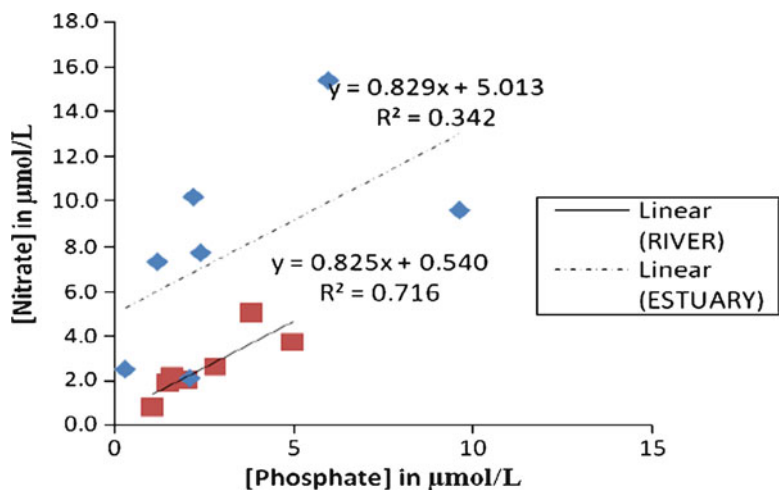


Fig. 1.3 Correlations between dissolved phosphate and dissolved nitrate at Albion (August 2008 – February 2009)

This indicated that biological activities in water for phosphate and nitrate are linked. The concentration ratio of dissolved nitrate: phosphate was 1.6 for GRNW during winter. Moreover at Albion in the estuary, a strong positive correlation ($R^2 = 0.72$) was obtained between nitrate and phosphate which were linked to biological activities of the nutrients in the estuarine system. The concentration ratio of nitrate: phosphate was 0.8 at Albion in the estuary. The low concentration ratio of

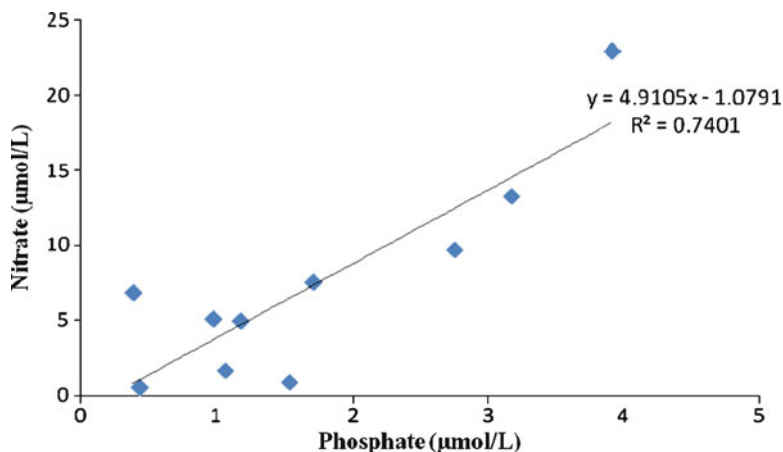


Fig. 1.4 Correlation of dissolved nitrate and dissolved phosphate at Flic en Flac (September 2009 – February 2010)

nitrate: phosphate is associated with low oxygen concentrations and is probably caused by denitrification as reported by Tyrrell and Law [19] with algal bloom observed during this period.

The mean values for dissolved phosphate were $1.7 \pm 0.6 \mu\text{mol/L}$ during winter and $2.9 \pm 0.6 \mu\text{mol/L}$ during summer at Flic en Flac. The comparison of phosphate between winter and summer showed no significant difference using t-test at 5% significance level. The comparison of phosphate between the different stations showed no significant difference at 5% significance level. The mean concentration of dissolved phosphate was higher during the wet period due to heavy rainfall recorded by the meteorological services as similarly stated by Bellos et al. [20]. Much of the dissolved phosphate was eventually washed into the water from agricultural runoff. This is in accordance with Ashraf et al. [21] who observed a similar situation in Cochin, India. Dissolved phosphate obtained at Flic en Flac lagoon was much higher than values $1.6 \pm 1.5 \mu\text{mol/L}$ during winter and $0.6 \pm 0.4 \mu\text{mol/L}$ during summer as indicated by Ramessur et al. [22] in the lagoon of Flic en Flac a decade ago indicating input from anthropogenic sources with an increase in residential development. The sources of dissolved phosphate may come from the run-off of phosphate fertilisers from sugar cane plantations and submarine groundwater discharges as reported by Burnett et al. [16]. This high concentration of dissolved phosphate in the freshwater system can be harmful as it can cause an algal bloom [23, 24]. A high concentration of dissolved phosphate was recorded in September during a flood.

The mean values for dissolved nitrate were $11.8 \pm 11.0 \mu\text{mol/L}$ during winter and $11.7 \pm 5.0 \mu\text{mol/L}$ during summer at Flic en Flac. Dissolved nitrate levels were observed to be abnormally high which probably were due to the lagoon water being mixed with the submarine groundwater discharge in the lagoon [20, 21]. The

comparison of nitrate between winter and summer showed no significant difference at 5% significance level. Nitrate concentration in the south end was significantly higher at 5% significance level compared to mid lagoon waters because of the freshwater and nutrient input from the rivulet in the south. The mean concentration was found to be higher in winter than in summer, unlike phosphate. This may be explained by the increase in temperature in summer which results in an increase in the rate of photosynthesis and thus an increase of uptake of nitrate by aquatic organisms. Further, this increase of nitrate concentration in winter may result from winter-time additions of fertilisers to sugarcane plants in the watershed with the plantation of sugarcane crops and the latter being irrigated during winter season. The maximum mean concentration of dissolved nitrate was observed in the south end of the lagoon. The high concentration of dissolved nitrate in the south end of the lagoon could be due to the rivulet passing through the coastal grazing lands where animal wastes could enter the stream. Furthermore, it could be possible that nitrates from fertilisers leach from inland sugarcane plantations into groundwater and eventually into the rivulet.

1.4 Conclusions

Excessive nutrients at GRNW, Albion and Flic en Flac can promote algal blooms, leading to oxygen depletion and severe deterioration of water quality as well as fish mortality. It can be argued that agricultural, urbanization and tourism activities have contributed to an increase in anthropogenic activities and hence have increased the potential for increased sewage effluent and urban runoff in this area. An estuarine model for nutrient and trace metal fluxes from the estuary to the lagoon could then be developed following measurement of currents, tides and river flow. A computer assisted budget analysis could then help in the understanding of biogeochemical fluxes for effective integrated coastal management of small island states.

Acknowledgements Thanks to Mr V. Ramsahye and Mr S. Radha for assistance during sampling work and analysis of samples in the Chemistry Labs at the University of Mauritius. At the same time we are very grateful to the University of Mauritius for providing the necessary funding to carry out this project.

References

1. Anonymous (1998) Mauritius Neap II: environmental strategy option report. Environmental Resources Management, London, p 173
2. Seitzinger SP, Nixon SW, Pilson MEQ (1984) Denitrification and nitrous oxide production in a coastal marine ecosystem. *Limnol Oceanogr* 29:73–83
3. Carpenter EJ, Dunham S (1985) Nitrogenous nutrient uptake, primary production, and specicomposition of phytoplankton in the Carmans River estuary, Long Island, New York. *Limnol Oceanogr* 30:513–526

4. Ramessur RT (2004) Statistical comparison and correlation of Zn and Pb in estuarine sediments along the western coast of Mauritius. *Environ Int* 30:1039–1044
5. Balgobin J (2009) Variations of dissolved nutrients, lead and zinc in the coastal system at Flic en Flac, Mauritius. BSc thesis, University of Mauritius, Mauritius, p 89
6. Bissemur ZB (2009) A comparative study of lead and zinc in sediments and some nutrients at GRNW and Albion. BSc thesis, University of Mauritius, Mauritius, p 83
7. Ramessur RT, Boodhoo K, Balgobin J, Aurelio A (2010) Statistical comparison between consecutive winter and summer concentrations in zinc and lead from sediments in a tropical urban estuary in Mauritius. *Environ Monit Assess* 168:345–351
8. Walther GR (2002) Ecological responses to climate change. *Nature* 416:389–395
9. Carpenter SR, Caraco NF, Correll DL, Howart RW, Sharpley AN, Smith VH (1998) Non point pollution of surface water with phosphorus and nitrogen. *Ecol Appl* 8:559–568
10. Verhagen R, Van Diggelen R (2006) Spatial variation in atmospheric nitrogen deposition on low canopy vegetation. *Environ Pollut* 144:826–832
11. Chiffolleau JF, Cossa D, Auger D, Truquet I (1994) Trace metal distribution, partition and fluxes in the Seine estuary (France) in low discharge regime. *Mar Chem* 47:145–158
12. Pereira ME, Duarte AC, Millward GE, Abreu SN, Vale C (1998) Tidal export of particulate mercury from the most contaminated area of Aveiro's lagoon, Portugal. *Sci Total Environ* 213:157–163
13. Williams MR, Millward GE (1998) Dynamics of particulate trace metals in the tidal reaches of the Ouse and Trent, U.K. *Mar Pollut Bull* 37:306–315
14. Singh AM, Singh M (2006) Lead decline in the Indian environment resulting from the petrol-lead phase-out programme. *Sci Total Environ* 368:686–694
15. Anonymous (2005) Assessment and management implications of submarine groundwater discharge into the coastal zone. ICAM-IHP-IAEA, p 52
16. Burnett WC, Aggarwal PK, Aureli A, Bokuniewicz H, Cable JE, Charette MA, Kontar E, Krupa S, Kulkarni KM, Loveless A, Moore WS, Oberdorfer JA, Oliveira J, Ozyurt N, Povinec P, Privitera AMG, Rajar R, Ramessur RT, Scholten J, Stieglitz T, Taniguchi M, Turner JV (2006) Quantifying submarine groundwater discharge in the coastal zone via multiple methods. *Sci Total Environ* 367:498–543
17. Ramessur RT, Ramjeawon T (2002) Determination of Pb, Cr and Zn from an urbanized river in Mauritius. *Environ Int* 28:315–324
18. Parsons T, Maita Y, Lalli CM (1984) Chemical and biological methods for sea water analysis. Pergamon Press, Oxford, UK
19. Tyrrell T, Law CS (1997) Low [nitrate]:[phosphate] ratios in the global ocean. *Lett Nat* 387:793–796
20. Bellos D, Sawidis T, Tsekos I (2003) Nutrient chemistry of river Pinios. *Environ Int* 30:105–115
21. Ashraf M, Edwin L, Meenakumari B (2006) Studies on the seasonal changes of phosphorus in the marine environment off Cochin. *Environ Int* 32:159–164
22. Ramessur RT, Parry SJ, Ramjeawon T (2001) The relationship of dissolved Pb to some dissolved trace metals (Al, Cr, Mn and Zn) and to dissolved nitrate and phosphate in a freshwater aquatic system in Mauritius. *Environ Int* 26:223–230
23. Prayag R, Jootun L, Bheeroo RA (1995) Integrated coastal zone management. Protection and management of marine and coastal areas of the Eastern African Region. Report prepared for UNEP/FAO/IOC/IUCN EAF5 project. Ministry of Environment and Quality of Life, Mauritius, p 92
24. Botte MDM (2001) Monitoring of coral bleaching at four sites around Mauritius. BSc thesis. University of Mauritius, Mauritius

Chapter 2

The Influence of the Cage Effect on the Mechanism of Multistage Chemical Reactions in Solutions

Alexander B. Doktorov and Stanislav G. Fedorenko

Abstract Manifestations of the cage effect on the encounters of reactants are treated theoretically with elementary and multistage irreversible reactions in liquid solutions as an example. The cage effect is shown to give rise to some essential effects not inherent in reactions in gases or reactions in solutions proceeding in the kinetic regime. Among such effects, the change in multistage reaction mechanism showing itself as new reaction channels and the corresponding transformation rate constants of reactants is most important. This substantially affects experimental kinetic evidence processing in determining rate constants of multistage reaction elementary stages.

2.1 Introduction

It is generally accepted that the mechanism of multistage reaction (a combination of successive and parallel elementary reactions) unambiguously specifies the form of the set of kinetic equations of formal chemical kinetics [1] based on the use of the kinetic law of mass action. By this law, concentration variation rate of any of the reactants is determined by the sum of its variation rates in the process of all elementary reactions resulting in the decay or production of this reactant. For bimolecular reactions, when the reaction involves two molecules only, the variation rate (negative for reactant decay and positive for product formation) is proportional to the concentration product of reactants entering into the elementary reaction. For rather rarefied gases commonly considered in the framework of the Collision Theory [2, 3] the kinetic law of mass action represents the fact that reactants in free walk (the mean time of which exceeds significantly the mean collision time) are spatially (and

A.B. Doktorov (✉) • S.G. Fedorenko

Laboratory of Theoretical Chemistry, Institute of Chemical Kinetics and Combustion SB RAS, Institutskaya 3, 630090 Novosibirsk, Russia

e-mail: doktorov@kinetics.nsc.ru; fedorenk@kinetics.nsc.ru

chemically) uncorrelated; this is expressed via the product of bulk concentrations of reactants involved in collision. The efficiency of such a collision (the reaction rate constant value) is determined by inelastic scattering cross-section of two reactants upon collision [4].

For reactions in solutions (even dilute) substantiation of the kinetic law of mass action and determination of kinetic coefficients (reaction rate constants) even for elementary irreversible reactions is a problem. Beginning with the Smoluchowski work [5] dealing with instantaneous irreversible contact reaction on the surface of a “black” sphere and the subsequent generalizations of the theory to the general case of reacting contact sphere [6, 7] or remote reactions [8–11], traditional approach to the derivation of kinetic equations in the theories of reactions in solutions was based on the concepts of independent pairs (“free pairs”) [12, 13]. The evolution of such pairs can be brought about both by the elementary event of chemical conversion (defined by the elementary event rate (sink term)), and by stochastic motion (often treated as continual diffusion) of reactants dissolved in chemically inert continual solvent. In the framework of such concepts, the kinetic equations have the form of differential ones (rate equations) quite similar to those of formal chemical kinetics equations. The only difference is that the rate constant is time dependent; this is interpreted as non-stationary diffusion in the ensemble of pairs. At small concentrations the substantiation of the kinetic equation for the simplest irreversible reaction based on the examination of a many-particle system was first performed using the superposition decoupling in hierarchies for Reduced Distribution Functions (RDF) [14, 15]. Note that the smallness of concentration of reactants in the development of a general theory of reactions is also necessary because at large concentrations the reactants move in solution the composition of which is affected by the reaction. However, even at small concentrations of reactants application of this method to more complicated physicochemical processes (determined, in particular, by the dynamic evolution of quantum states) or to multistage reactions becomes difficult if possible at all.

The exact many-particle substantiation of the above theories of irreversible reactions based on the concepts of independent pairs was made in the framework of the so-called “target model” [12, 13]. This model referring to luminescence quenching was used to consider the reaction of immobile donor reactant and point moving acceptors in excess. Due to the independence of donor quenching by any of the acceptors and independence of changes in acceptor position relative to the donor, the problem admits the exact solution for any concentration of point acceptors. Similar result is also obtained for pressure broadening of the Doppler spectra in gases [16]. However, the advantages of this model are lost if any of the above assumptions (leading to the violation of the notion of independent pairs) is abandoned. The derivation of kinetic equations based on such concepts, even at small density parameter, becomes impossible. So to consider physicochemical processes in liquid solutions, the approach has been proposed based on the fact that in the case of a traditional treatment of a solvent as a continual medium, dilute solutions resemble a “gas” of reactants dissolved in the homogeneous chemically inert medium. So development of the kinetic theory of physicochemical processes

in solutions may be based [17, 18] on the analogy with the Collision Theory (CT) in gases [2, 3], when reacting particles are for the most part in the process of free pass, and the reaction occurs upon their collisions the characteristic duration of which is essentially less than the mean time between them. As in gases, in dilute solutions the reactants are almost all the time in the process of free random walks at the distances too long for the elementary event of chemical conversion to occur. The only difference is in the character of motion of reactants due to a solvent (commonly such a motion is treated as continual diffusion). However, it is essential that the change in the character of the relative motion of reactants affects the course of chemical conversion on the approach of reactants. This is most easily shown with contact reactions as an example, i.e., the reactions proceeding between reactants separated by the distance equal to the sum of van der Waals radii. The point is that reactants that came into contact resulting in chemical conversion event do not escape from the cage when the contact is over by virtue of the cage effect [19, 20], but can re-contact which leads to further chemical transformation. Only after a series of re-contacts the reactants move apart; this corresponds to the escape from the cage, i.e., the products begin walking freely. Thus the process that in a gas is considered as collision, in solution is treated as residence in the cage – the encounter of reactants consisting of re-contacts (analog of “scattering”). Exactly for this reason the theory based on representing a solution as a “gas” of reactants has received the name the Encounter Theory [17, 18].

Thus though the course of rather fast reactions (for example, reactions between radicals) in liquid solutions depends on the mobility of reactants responsible for their approach that is sufficient for chemical conversion elementary event, and the solution resembles a “gas” of reactants dissolved in chemically inert solvent, there is a fundamental difference between reactions in gases and solutions.

The cage effect is responsible for some specific features of the multistage reaction course in liquid solutions, and this is the subject of the present paper. In particular, for successive multistage reaction the influence of reactant mobility does not reduce solely to traditional redefinition of elementary stage rate constants [21], but can change radically the set of formal chemical kinetics equations, i.e., it gives rise to extra terms in kinetic equations completely defined by the motion of reactants. Since the analysis of such kinetic equations is used both to determine the rate constants from experimental kinetics form, and to find particular systems able to abruptly change the process under the change of the system parameters (diffusion coefficients, external electric or magnetic fields), therefore, the above-mentioned changes in the equations may turn out to be critical.

It is important that the above effects can be interpreted not only in the framework of the Encounter Theory but also on the basis of simple kinetic schemes often used in chemistry. One of the aims of this contribution is to show the equivalence of these two approaches.

In Sect. 2.2 we show that for the well-known simplest irreversible reaction $A + B \rightarrow \text{products}$ the Encounter Theory in the case of short-range reaction corresponds to simple kinetic schemes of the “cage complex” with appropriately defined kinetic parameters, and give the explanation of the fact. On the same basis

in Sect. 2.3 the irreversible two-stage reaction will be considered to demonstrate that the cage effect can change the reaction mechanism. In connection with this, in Sect. 2.4 the detailed analysis is given of the possibilities of rate constants determination by experimentally observed kinetics and possible errors due to the change of the reaction mechanism. In Sect. 2.5 the results of the investigation are generalized to a multistage irreversible reaction in which the number of new reaction channels increases quadratically with increasing number of elementary stages. The results are summarized in Conclusion.

2.2 The Cage Effect in Elementary Irreversible Reaction

Consider the elementary (one stage) irreversible reaction



corresponding, for example $[B]_t$, to luminescence quenching reaction [7] or catalytic cis-trans isomerization. The kinetic equation for such a reaction in liquid solutions

$$\frac{d}{dt}[A]_t = -K(t)[A]_t[B]_t \quad (2.2)$$

was derived in all traditional theories mentioned in the Introduction. The same equations are also obtained in the Encounter theory [17, 18] that provides most general, natural and transparent physical interpretation of the cage effect influence. The derived equation has the form of a differential equation quite similar to the equation of formal chemical kinetics but with time dependent rate constant. In traditional theories such a dependence (non-Markovian character of the theory [22]) is interpreted as a non-stationary diffusion in the ensemble of reacting pairs, while in the Encounter Theory (just as in the Collision Theory) – as a consequence of the encounter incompleteness on the Gibbs ensemble [22]. This reaction constant is

$$K(t) = \int w(q) n^+(q, t) \varphi(q) dq, \quad (2.3)$$

where $w(q)$ is the elementary event rate (sink term) depending in the general case on configuration space coordinates that include both relative-position vector of reactants and angles of their orientation, $\varphi(q)$ is the equilibrium configuration space distribution in the thermodynamic limit, and $n^+(q, t)$ is a joint pair density that obeys the equation

$$\frac{\partial}{\partial t} n^+(q, t) = -w(q) n^+(q, t) + \hat{\mathcal{L}}_q^+ n^+(q, t) \quad (2.4)$$

with the initial condition $n^+(q, t) = 0$. Here $\hat{\mathcal{L}}_q^+$ is the operator that determines the stochastic motion (translation and rotation) of reactants in a solvent (considered as chemically inert continuous medium). The first term on right-hand-side of Eq. 2.4 is “reaction” origin and the second one is “stochastic motion” (e.g. diffusion) origin.

As time increases, the rate constant attains its steady-steady value

$$k = \lim_{t \rightarrow \infty} K(t) \quad (2.5)$$

and the equation takes the form of formal chemical kinetics equation corresponding to the kinetic law of mass action

$$\frac{d}{dt}[A]_t = -k[A]_t[B]_t \quad (2.6)$$

with the steady-state reaction rate constant (Markovian constant [22]) defined by expression similar to Eq. 2.3

$$k = \int w(q) n^+(q) \varphi(q) dq, \quad (2.7)$$

where $n^+(q) = \lim_{t \rightarrow \infty} n^+(q, t)$ is the stationary value of the pair density. This stationary pair density obeys the stationary equation (Eq. 2.4 at $\frac{\partial}{\partial t} n^+(q, t) = 0$) that can be rewritten in the integral form

$$n^+(q) = 1 - \int g_0(q'|q) w(q') n^+(q') \varphi(q') dq', \quad (2.8)$$

using the free Green function $g_0(q'|q)$. This function obeys the well-known equation

$$-\hat{\mathcal{L}}_q^+ g_0(q'|q) = \delta(q - q') \quad (2.9)$$

and satisfies the detailed balance relation

$$g_0(q'|q) \varphi(q) = g_0(q|q') \varphi(q'). \quad (2.10)$$

This function is readily seen to describe the free motion (without the reaction), translational and rotational, and is the time integral

$$g_0(q|q') = \int_0^{\infty} \varphi(q, t | q', 0) dt \quad (2.11)$$

of the conditional probability density $\varphi(q, t | q', 0)$ to have configuration coordinate q at the time moment t if it was q' at the initial time moment $t = 0$.

Let us introduce the reaction constant

$$k^0 = \int w(q) \varphi(q) dq, \quad (2.12)$$

that is (as follows from Eqs. 2.7 and 2.8) the reaction rate constant in the kinetic regime ($w(q) \rightarrow 0$), when the elementary event rate is small as compared to the rate of reactant approach enough to control chemical transformation. Then we define the function $\psi(q)$ by the identity

$$w(q) \equiv k^0 \psi(q). \quad (2.13)$$

We shall call this function normalized to unity

$$\int \psi(q) \varphi(q) dq = 1 \quad (2.14)$$

the shape of the reaction zone.

Then let us introduce the averaging of some quantity $A(q)$ over the reaction zone

$$\langle A(q) \rangle \equiv (A(q) | \psi(q)) = \int A(q) \psi(q) \varphi(q) dq, \quad (2.15)$$

It can be considered as a scalar product of the functions $A(q)$ and $\psi(q)$ with the weight $\varphi(q)$. Now we can define the quantities

$$\nu = \langle \psi(q) \rangle^{-1} \equiv (\psi(q) | \psi(q))^{-1}, \quad \tau_c(q) = \nu \int \psi(q') g_0(q'|q) dq', \quad (2.16)$$

that are the reaction zone volume and the mean residence time in the reaction zone for the starting position q . Note that for traditional stepwise spherical symmetric reactivity near rigid sphere of the radius R

$$w_{AB}(r) = \begin{cases} w_0 & \text{at } R \leq r \leq R + \Delta \\ 0 & \text{otherwise} \end{cases}, \quad \varphi(r) = \begin{cases} 1 & \text{at } R \leq r \\ 0 & \text{at } r < R \end{cases} \quad (2.17)$$

(where $\Delta \ll R$ is the width of a thin reaction layer) we obtain from Eq. 2.17 the usual definitions of the geometric volume of the reaction zone $\nu = 4\pi R^2 \Delta$, and (in view of Eq. 2.11) the usual definition of the residence time in this volume [23].

Using definitions (2.16), (2.7) and (2.12) and averaging both parts of Eq. 2.8 with allowance for Eq. 2.10 we can rewrite the basic equations as

$$k = k^0 \langle n^+(q) \rangle, \quad k^0 = \langle w(q) \rangle \nu \quad (2.18)$$

and

$$\langle n^+(q) \rangle = 1 - \frac{k^0}{\nu} \langle \tau_c(q) n^+(q) \rangle \quad (2.19)$$

Now we use the decoupling procedure

$$\langle \tau_c(q)n^+(q) \rangle \approx \langle \tau_c(q) \rangle \langle n^+(q) \rangle \equiv \tau_c \langle n^+(q) \rangle, \quad (2.20)$$

where $\tau_c = \langle \tau_c(q) \rangle$ is the complete mean residence time in the reaction zone (the mean residence time in the reaction zone for the starting position q averaged over the starting positions in the reaction zone). Note that procedure (2.20) is exact in the case of spherically symmetric contact reactivity

$$w_{AB}(r) = k_{\text{int}} \frac{\delta(r-R)}{4\pi r R} \quad \left(k_{\text{int}} = 4\pi \int_{R-0}^{\infty} w(r)r^2 dr \right) \quad (2.21)$$

(k_{int} is the intrinsic constant that coincides with the reaction constant k^0 only for $\varphi(q)$ defined in Eq. 2.17).

When the reaction takes place in a narrow reaction zone, Eq. 2.20 is the approximation that can be shown to require that the dispersion of the mean residence times $\tau_c(q)$ be small compared to the square of complete mean residence time

$$d = \langle \tau_c^2(q) \rangle - \langle \tau_c(q) \rangle^2 = \langle (\tau_c(q) - \langle \tau_c(q) \rangle)^2 \rangle \ll \langle \tau_c(q) \rangle^2 = \tau_c^2 \quad (2.22)$$

Decoupling (2.20) is the basis of the so-called kinematic approximation used in the theory of mobility influenced reactions [24, 25]. In this approximation we can introduce, along with representation (2.18) for the reaction constant k^0 , similar representation for the reaction rate constant in mobility controlled regime (diffusion constant in the case of continues diffusion) [24, 25]

$$k_d = \frac{v}{\tau_c} \quad (2.23)$$

Then Eq. 2.19 (taking account of Eqs. 2.20 and 2.23) can be written as

$$(k_d + k^0) \langle n^+(q) \rangle = k_d, \quad (2.24)$$

Using the definition of the reaction rate constant k (2.18), this immediately gives

$$k = \frac{k_d k^0}{k_d + k^0} \quad \left(\frac{1}{k} = \frac{1}{k_d} + \frac{1}{k^0} \right) \quad (2.25)$$

This expression is formally similar to the well-known expression for spherically symmetric contact reactions [6]. However expression (2.25) is an essential generalization to the case of arbitrary non-isotropic reactivity and mobility of reactants (including rotation).

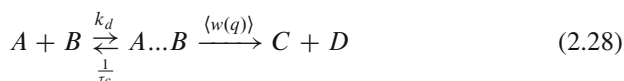
It is very interesting that taking into consideration Eqs. 2.18 and 2.23 and introducing the concentration $[A\dots B]_t$ of the “cage complex” $A\dots B$,

$$[A\dots B]_t = \nu \langle n^+(q) \rangle [A]_t [B]_t \quad (2.26)$$

Eqs. 2.6 and 2.24 can be recast as

$$\begin{aligned} \partial_t [A]_t &= -k^0 \langle n^+(q) \rangle [A]_t [B]_t = -k_d [A]_t [B]_t + \frac{1}{\tau_c} [A\dots B]_t \\ \partial_t [A\dots B]_t &\approx 0 = k_d [A]_t [B]_t - \left(\frac{1}{\tau_c} + \langle w(q) \rangle \right) [A\dots B]_t \end{aligned} \quad (2.27)$$

which corresponds to quasi-stationary (with respect to the concentration of the “cage complex”) equations of the formal chemical kinetics for simple reaction scheme



Similar reaction schemes are often used in chemical kinetics for empirical calculations of reaction rate constants in gases (e.g., for reactions proceeding via long-lived complex). However a remarkable advantage of the reaction scheme with appropriately defined kinetic coefficients k_d , τ_c and $\langle w(q) \rangle$ that are determined by the reaction sink term $w(q)$ and the operator $\hat{\mathcal{L}}_q^+$ of reactants mobility is the possibility to solve (with the controlled accuracy) a complicated problem of mobility influenced reactions in solutions, and give a clear interpretation of the results derived.

This scheme agrees with the Encounter Theory concepts. Its left side describes the reactants in free walk that approach each other due to diffusion to produce a cage (with the rate constant k_d) and the reactants escape from the cage at the rate τ_c^{-1} .

Note that the applicability of the above simple kinetic scheme means that the distribution $f(\tau)$ in complete residence times in the reaction zone (the “cage complex” lifetimes) is Poisson $\left(f(\tau) = \frac{1}{\tau_c} \exp\left(-\frac{\tau}{\tau_c}\right) \right)$. Such notions correspond to the familiar exponential model. Though the distribution in the encounter times (residence in the cage) is not exponential, its applicability is related to the fact that in the absence of physicochemical processes between re-contacts the efficiency of a quasi-steady reaction is determined by the complete residence time τ_c of all contacts on the encounter; and the distribution in such times is exponential. We shall call the above method of the derivation of the Markovian kinetic equations based on a simple formal kinetic scheme of the reaction course the cage complex method.

It is seen that in the case at hand the cage effect manifests itself in the fact that the reaction rate constant depends entirely on the reaction constant k^0 in the kinetic regime only ($k^0 \ll k_d$, $k \approx k^0$). In the opposite situation the mobility control of the reaction takes place ($k_d \ll k^0$, $k \approx k_d$). Thus in the general case, the motion

of reactants results in redefinition (2.25) of the reaction rate constant that may be represented as

$$k = k_d p = k^0 \Omega \equiv k^0 (1 - p) \quad (2.29)$$

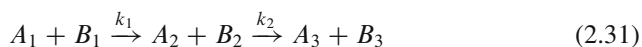
The first definition (2.29) is in full agreement with the concepts of the Encounter Theory, according to which the reaction rate $k[B]$ is specified by the frequency of their encounters multiplied by the encounter efficiency (the probability of reaction in a cage)

$$p = \frac{k^0}{k_d + k^0} \equiv 1 - \int_0^{\infty} \exp(-\langle w(q) \rangle \tau) f(\tau) d\tau \quad (2.30)$$

It shows (in view of Eqs. 2.18 and 2.23) that complete residence time distribution $f(\tau)$ must be Poisson. The second definition (2.29) shows that at the same time this rate constant is defined by the reaction constant multiplied by the probability to escape from the cage due to diffusion without reaction (escape probability). Note that, unlike the first definition, the second one is also applicable (under appropriate definition of the probability Ω to remote reactions, and, in the general case, to the calculation of the non-Markovian (time dependent) reaction rate constant (2.3)). This procedure of redefinition of kinetic constants (2.25) or (2.29) is well-known [5, 6, 21, 26], and is used to describe the reactions depending on reactants mobility.

2.3 Irreversible Two-Stage Reaction

Consider now irreversible two-stage reactions



for which the set of equations of formal chemical kinetics is of the form

$$\begin{aligned} \frac{d}{dt}[A_1]_t &= -k_1[A_1]_t[B_1]_t \\ \frac{d}{dt}[A_2]_t &= k_1[A_1]_t[B_1]_t - k_2[A_2]_t[B_2]_t \\ \frac{d}{dt}[A_3]_t &= k_2[A_2]_t[B_2]_t \end{aligned} \quad (2.32)$$

To derive the kinetic equations for this reaction influenced by the mobility of reactants, only the Encounter Theory [17, 18] can be used. According to the Encounter Theory, let us introduce the column vectors of concentrations

$[A_i]_t$ ($i = 1, 2, 3$), $[B_k]_t$ ($k = 1, 2, 3$), elementary event rates and motion operators matrices (Liouvillians) in the collective states basis (ik): (11) = I , (22) = II , (33) = III

$$[\mathbf{A}]_t = \begin{pmatrix} [A_1]_t \\ [A_2]_t \\ [A_3]_t \end{pmatrix} \quad [\mathbf{B}]_t = \begin{pmatrix} [B_1]_t \\ [B_2]_t \\ [B_3]_t \end{pmatrix}, \quad (2.33a)$$

$$\hat{\mathbf{W}} = \begin{pmatrix} -w_1(q) & 0 & 0 \\ w_1(q) & -w_2(q) & 0 \\ 0 & w_2(q) & 0 \end{pmatrix} \quad \hat{\mathbf{L}}_q = \begin{pmatrix} \hat{\mathcal{L}}_q^{(1)} & 0 & 0 \\ 0 & \hat{\mathcal{L}}_q^{(2)} & 0 \\ 0 & 0 & \hat{\mathcal{L}}_q^{(3)} \end{pmatrix} \quad (2.33b)$$

where $w_1(q)$ and $w_2(q)$ are elementary event rates of the first and the second elementary stages of reaction (2.31), and $\hat{\mathcal{L}}_q^{(i)}$ is the relative motion operator of reactants A_i and B_i ($i = 1, 2, 3$). Then we have the vector kinetic equation of the Encounter Theory [18]

$$\frac{d}{dt}[\mathbf{A}]_t = Tr_B \int \hat{\mathbf{W}}(q) \hat{\mathbf{G}}(q) dq ([\mathbf{A}]_t \otimes [\mathbf{B}]_t), \quad (2.34)$$

where \otimes means the direct product of concentration vectors, Tr_B is the trace (summation) over states B_i . The steady-state Liouvillian of pair densities is the stationary solution $\hat{\mathbf{G}}(q) = \lim_{t \rightarrow \infty} \hat{\mathbf{G}}(q, t)$ of the matrix equation

$$\frac{\partial}{\partial t} \hat{\mathbf{G}}(q, t) = \hat{\mathbf{W}}(q) \hat{\mathbf{G}}(q, t) + \hat{\mathbf{L}}_q \hat{\mathbf{G}}(q, t) \quad (\hat{\mathbf{G}}(q, 0) = \hat{\mathbf{E}}), \quad (2.35)$$

where $\hat{\mathbf{E}}$ is a unity matrix.

Let us introduce the notations for the matrix elements of the Liouvillian $\hat{\mathbf{G}}(q)$

$$G_{I \ I}(q) = n_1(q) \quad G_{II \ II}(q) = n_2(q) \quad G_{II \ I}(q) = m(q) \quad (2.36)$$

Then we obtain from Eq. 2.34

$$\begin{aligned} \frac{d[A_1]_t}{dt} &= -k_{11}[A_1]_t[B_1]_t \\ \frac{d[A_2]_t}{dt} &= k_{21}[A_1]_t[B_1]_t - k_{22}[A_2]_t[B_2]_t \\ \frac{d[A_3]_t}{dt} &= k_{31}[A_1]_t[B_1]_t + k_{32}[A_2]_t[B_2]_t, \end{aligned} \quad (2.37)$$

where

$$\begin{aligned} k_{11} &= \int w_1(q) n_1(q) dq, & k_{21} &= \int w_1(q) n_1(q) dq - \int w_2(q) m(q) dq, \\ k_{22} &= k_{32} = \int w_2(q) n_2(q) dq, & k_{31} &= k_{11} - k_{21} = \int w_2(q) m(q) dq, \end{aligned} \quad (2.38)$$

and $n_1(q)$, $n_2(q)$, and $m(q)$ are the stationary solutions of the equations

$$\begin{aligned} \frac{\partial}{\partial t} n_1(q, t) &= -w_1(q) n_1(q, t) + \hat{\mathcal{L}}_q^{(1)} n_1(q, t), \\ \frac{\partial}{\partial t} n_2(q, t) &= -w_2(q) n_2(q, t) + \hat{\mathcal{L}}_q^{(2)} n_2(q, t), \\ \frac{\partial}{\partial t} m(q, t) &= -w_2(q) m(q, t) + w_1(q) n_1(q, t) + \hat{\mathcal{L}}_q^{(2)} m(q, t), \end{aligned} \quad (2.39)$$

with the initial conditions $n_1(q, 0) = n_2(q, 0) = 1$, $m(q, 0) = 0$.

Now using the free Green functions $g_{01}(q|q')$ and $g_{02}(q|q')$ defined similar to Eq. 2.9, we can rewrite Eq. 2.39 in the integral form

$$\begin{aligned} n_1(q) &= \varphi_1(q) - \int g_{01}(q|q') w_1(q') n_1(q') dq', \\ n_2(q) &= \varphi_2(q) - \int g_{02}(q|q') w_2(q') n_2(q') dq', \\ m(q) &= - \int g_{02}(q|q') w_2(q') m(q') dq' + \int g_{02}(q|q') w_1(q') n_1(q') dq', \end{aligned} \quad (2.40)$$

where $\varphi_1(q)$ and $\varphi_2(q)$ are the corresponding equilibrium distributions in the space of reaction configuration coordinates (static counters)

$$\hat{\mathcal{L}}_q^{(1)} \varphi_1(q) = 0, \quad \hat{\mathcal{L}}_q^{(2)} \varphi_2(q) = 0. \quad (2.41)$$

Let us represent the elementary event rates similar to Eq. 2.13 in the form

$$w_1(q) = k_1 \psi_1(q), \quad w_2(q) = k_2 \psi_2(q), \quad (2.42)$$

introducing the reaction zone shapes of the corresponding reaction stages normalized to unity

$$\int \psi_1(q) \varphi_1(q) dq = 1, \quad \int \psi_2(q) \varphi_2(q) dq = 1. \quad (2.43)$$

and perform averaging over reaction zones as in the previous Section. Introducing the adjoint quantities $n_1^+(q)$, $n_2^+(q)$, and $m^+(q)$ as

$$\begin{aligned} n_1(q) &= n_1^+(q)\varphi_1(q), & n_2(q) &= n_2^+(q)\varphi_2(q), \\ m(q) &= m^+(q)\varphi_2(q), \end{aligned} \quad (2.44)$$

multiplying the first of Eq. 2.40 by $\psi_1(q)$, and the second and the third equations by $\psi_2(q)$, integrating over q and using decoupling procedures similar to Eq. 2.20, we obtain

$$\begin{aligned} \langle n_1^+(q) \rangle &= 1 - k_1 \frac{\tau_1}{v_1} \langle n_1^+(q) \rangle, & \langle n_2^+(q) \rangle &= 1 - k_2 \frac{\tau_2}{v_2} \langle n_2^+(q) \rangle, \\ \langle m(q) \rangle &= -k_2 \frac{\tau_2}{v_2} \langle m(q) \rangle + k_1 \frac{\tau_2}{v_2} \langle n_1^+(q) \rangle, \end{aligned} \quad (2.45)$$

where

$$\begin{aligned} v_1 &= \langle \psi_1(q) \rangle^{-1} \equiv (\psi_1(q) | \psi_1(q))^{-1}, & v_2 &= \langle \psi_2(q) \rangle^{-1} \equiv (\psi_2(q) | \psi_2(q))^{-1}, \\ \tau_1 &= \langle \tau_1(q) \rangle, & \tau_2 &= \langle \tau_2(q) \rangle \\ \tau_1(q) &= v_1 \int \psi_1(q') g_{01}(q'|q) dq', & \tau_2(q) &= v_2 \int \psi_2(q') g_{02}(q'|q) dq'. \end{aligned} \quad (2.46)$$

Averaging the quantities with the lower index 1 is performed over the reaction zone $\psi_1(q)$, and the quantities with the lower index 2 – over the reaction zone $\psi_2(q)$. Strictly speaking, the residence time τ_2 in the last term in the right hand side of the third of Eq. 2.45 must be calculated by averaging $\tau_2(q)$ over the reaction zone $\psi_1(q)$. However due to condition (2.22) dispersion of the residence time $\tau_2(q)$ with the starting point q inside any reaction zone must be neglected, and the value of the complete residence time in the great extent is determined by the distribution of the final points.

Introducing the reaction constants and the reaction rate constants in mobility controlled regime (mobility constants), by analogy with Eqs. 2.18 and 2.23

$$k_1 = \langle w_1(q) \rangle v_1, \quad k_2 = \langle w_2(q) \rangle v_2, \quad k_{d_1} = \frac{v_1}{\tau_1}, \quad k_{d_2} = \frac{v_2}{\tau_2}, \quad (2.47)$$

we can write Eq. 2.45 as

$$\begin{aligned} k_1 \langle n_1^+(q) \rangle &= k_{d_1} - k_{d_1} \langle n_1^+(q) \rangle, & k_2 \langle n_2^+(q) \rangle &= k_{d_2} - k_{d_2} \langle n_2^+(q) \rangle, \\ k_{d_2} \langle m^+(q) \rangle &= k_1 \langle n_1^+(q) \rangle - k_2 \langle m^+(q) \rangle \end{aligned} \quad (2.48)$$

Then for reaction rate constants (2.38) we have

$$\begin{aligned}
 k_{11} &= k_1 \langle n_1^+(q) \rangle = k_{d_1} - k_{d_1} \langle n_1^+(q) \rangle, \\
 k_{21} &= k_1 \langle n_1^+(q) \rangle - k_2 \langle m^+(q) \rangle = k_{d_2} \langle m^+(q) \rangle \\
 k_{22} &= k_{32} = k_2 \langle n_2^+(q) \rangle = k_{d_2} - k_{d_2} \langle n_2^+(q) \rangle, \\
 k_{31} &= k_{11} - k_{21} = k_2 \langle m^+(q) \rangle
 \end{aligned} \tag{2.49}$$

and kinetic equations (2.37), in view of Eqs. 2.49 and 2.47, take the form

$$\begin{aligned}
 \frac{d[A_1]_t}{dt} &= -k_{d_1}[A_1]_t[B_1]_t + \frac{1}{\tau_1}[A_1\dots B_1]_t, \\
 \frac{d[A_2]_t}{dt} &= -k_{d_2}[A_2]_t[B_2]_t + \frac{1}{\tau_2}[A_2\dots B_2]_t, \\
 \frac{d[A_3]_t}{dt} &= \langle w_2(q) \rangle [A_2\dots B_2]_t \equiv -k_{d_3}[A_3]_t[B_3]_t + \frac{1}{\tau_3}[A_3\dots B_3]_t,
 \end{aligned} \tag{2.50}$$

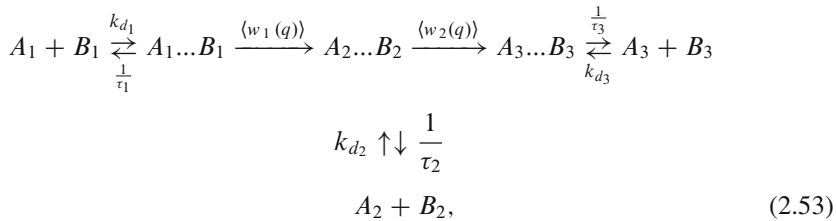
where we introduce concentrations of the ‘‘cage complex’’ states

$$\begin{aligned}
 [A_1\dots B_1]_t &= \nu_1 \langle n_1^+(q) \rangle [A_1]_t [B_1]_t, \\
 [A_2\dots B_2]_t &= \nu_2 (\langle m^+(q) \rangle [A_1]_t [B_1]_t + \langle n_2^+ \rangle [A_2]_t [B_2]_t)
 \end{aligned} \tag{2.51}$$

and formally some concentration $[A_3\dots B_3]_t$ of additional ‘‘cage complex’’ states, as well as complete residence time τ_3 in this complex and the constant k_{d_3} . From Eq. 2.49 and the identity introduced in the third equation of Eq. 2.50, we obtain, in view of Eq. 2.47, the quasi-stationary equations for concentrations in the ‘‘cage complex’’

$$\begin{aligned}
 \frac{d[A_1\dots B_1]_t}{dt} &\approx 0 = k_{d_1}[A_1]_t[B_1]_t - \left(\frac{1}{\tau_1} + \langle w_1(q) \rangle \right) [A_1\dots B_1]_t \\
 \frac{d[A_2\dots B_2]_t}{dt} &\approx 0 = k_{d_2}[A_2]_t[B_2]_t - \left(\frac{1}{\tau_2} + \langle w_2(q) \rangle \right) [A_2\dots B_2]_t + \langle w_1(q) \rangle [A_1\dots B_1]_t \\
 \frac{d[A_3\dots B_3]_t}{dt} &\approx 0 = k_{d_3}[A_3]_t[B_3]_t - \frac{1}{\tau_3}[A_3\dots B_3]_t + \langle w_2(q) \rangle [A_2\dots B_2]_t
 \end{aligned} \tag{2.52}$$

Equations 2.50 and 2.52 correspond to quasi-stationary equations (with respect to the concentration of the ‘‘cage complex’’) of formal chemical kinetics for a simple reaction scheme



consistent with the concepts of the Encounter Theory. In this case the cage complex $A_1 \dots B_1 \xrightarrow{\langle w_1(q) \rangle} A_2 \dots B_2 \xrightarrow{\langle w_2(q) \rangle} A_3 \dots B_3$ has three states corresponding to different reactants A_i ($i = 1, 2, 3$) the sequential transition between which due to chemical conversion occurs at the rates $\langle w_1(q) \rangle$ and $\langle w_2(q) \rangle$. Coming to the cage complex and the escape from it are determined by diffusion constants k_{d_i} , and rates $\frac{1}{\tau_i}$ ($i = 1, 2, 3$) depending on the cage complex state.

Eventually, solving the set of algebraic equations obtained from Eq. 2.52 after substitution of the calculated quasi-steady concentration values in the cage complex in Eq. 2.50, we derive the equations of formal chemical kinetics (2.37), where, as for a single-stage irreversible reaction (see. Eqs. 2.25 and 2.29) we introduce the rate constants of elementary stages

$$\begin{aligned}
 k_{11} &= \frac{k_1 k_{d_1}}{k_1 + k_{d_1}} = k_{d_1} p_1 = k_1 \Omega_1 \equiv k_1 (1 - p_1), \quad p_1 = \frac{k_1}{k_1 + k_{d_1}}, \\
 k_{32} = k_{22} &= \frac{k_2 k_{d_2}}{k_2 + k_{d_2}} = k_{d_2} p_2 = k_2 \Omega_2 \equiv k_2 (1 - p_2), \quad p_2 = \frac{k_2}{k_2 + k_{d_2}},
 \end{aligned} \tag{2.54}$$

Thus the diffusion cage effect leads to redefinition of kinetic constants of each of elementary irreversible stages similar to that in a single-stage irreversible reaction.

However, this is not the only problem. Comparison of the derived kinetic equations with kinetic equations (2.32) corresponding to the mechanism of a two-stage reaction (2.31) shows that when diffusion is taken into account, a new accumulation channel of A_3 reactant arises due to the encounters of A_1 and B_1 reactants, though direct transformation of A_1 reactant into A_3 reactant by elementary event of chemical conversion is impossible for the given mechanism of the reaction. The rate constant of the new channel is

$$k_{31} = \frac{k_1 k_{d_1} k_2}{(k_1 + k_{d_1})(k_2 + k_{d_2})} \equiv k_{11} p_2. \tag{2.55}$$

It goes to zero when the reaction is kinetically controlled by the second channel of the two-stage reaction in question, i.e., on condition that

$$k_2 \ll k_{d_2} \tag{2.56}$$

The new reaction channel also affects the accumulation rate constant of A_2 reactant due to the encounters of A_1 reactant with B_1 reactants that is defined now by the difference between rate constants of appropriate elementary stage and the new channel

$$k_{21} = k_{11} - k_{31} = k_{11} (1 - p_2). \quad (2.57)$$

The last relation is to take place because of the preservation of total concentration of reactants $[A_1]_t + [A_2]_t + [A_3]_t = [A_1]_0 + [A_2]_0 + [A_3]_0 = \text{const}$ ($-k_{11} + k_{21} + k_{31} = 0$). This result can easily be explained from the standpoint of the cage complex theory (and the Encounter Theory). When in the cage (and in the cage complex), A_1 reactant is transformed (the change in the cage complex state) into A_3 reactant which escapes from the cage and goes to the volume in the state of free random walk. From the standpoint of the Encounter Theory this means the transformation of A_1 reactant into A_3 reactant during one encounter. It follows from Eq. 2.55 that at the given rate of the course of the first stage (the given value of the rate constant k_{11}) the rate of such a transformation is fully determined by the efficiency of the second stage p_2 attaining the maximum value ($p_2 = 1$) in the case of the diffusion control of this stage $k_{d_2} \ll k_2$. In this situation the elementary rate of A_2 reactant transformation into A_3 is so high that the rate constant k_{21} (2.57) of the formation of A_2 from A_1 goes to zero. So if A_2 was absent at the initial instant of time, then the reaction proceeds without this reactant in the volume, though it exists in the cage complex as an intermediate.

However, if the second stage of the reaction is kinetically controlled ($p_2 \ll 1$), then the new channel of the product accumulation is absent ($k_{31} \approx 0$). The set of kinetic equations (2.37) reduces to (2.32) corresponding to the mechanism of reaction (2.31) with the only difference that instead of the kinetic (reaction) constant k_1 they involve the rate constant k_{11} determined with allowance for the cage effect, according to Eq. 2.54, as in the corresponding single-stage irreversible reaction. Note that in this case, in accordance with Eq. 2.57, $k_{21} = k_{11}$, in full agreement with the material balance.

As for the kinetics of the reaction in question, it can easily be found in the case when reactants B_1 and B_2 are in excess ($[B_i]_t \approx \text{const}$ ($i = 1, 2$)) from the solution of the set of linear equations (2.37). Solving it with the initial conditions $[A_2]_0 = [A_3]_0 = 0$ we find

$$\begin{aligned} \frac{[A_1]_t}{[A_1]_0} &= \exp(-k_{11} [B_1] t) \\ \frac{[A_2]_t}{[A_1]_0} &= \xi [\exp(-k_{11} [B_1] t) - \exp(-k_{22} [B_2] t)] \\ \frac{[A_3]_t}{[A_1]_0} &= 1 - (1 + \xi) \exp(-k_{11} [B_1] t) + \xi \exp(-k_{22} [B_2] t) \end{aligned} \quad (2.58)$$

It is seen that in the general case the kinetics depends on the values of rate constants k_{11} and k_{22} of sequential channels, as well as on the only parameter

$$\begin{aligned}\xi &= \frac{k_{21}[B_1]}{k_{22}[B_2] - k_{11}[B_1]} = \frac{(k_{11} - k_{31})[B_1]}{k_{22}[B_2] - k_{11}[B_1]} = \\ &= \frac{k_{11}[B_1](1 - p_2)}{k_{22}[B_2] - k_{11}[B_1]} \equiv \frac{(1 - p_2)}{\frac{k_{22}[B_2]}{k_{11}[B_1]} - 1}.\end{aligned}\quad (2.59)$$

Thus the qualitative form of the kinetic curves is almost the same both in the case of the kinetic control and in the more general situation.

In the case of the kinetic control of both channels, when a new channel does not arise, the value of the parameter ξ is completely specified by the ratio between the values of the channel kinetic rates $k_{11}[B_1] = k_1[B_1]$, $k_{22}[B_2] = k_2[B_2]$

$$\xi = \frac{k_1[B_1]}{k_2[B_2] - k_1[B_1]} = \frac{1}{\frac{k_2[B_2]}{k_1[B_1]} - 1}\quad (2.60)$$

and may be negative at $k_2[B_2] < k_1[B_1]$.

When only the second channel is kinetically controlled, the new channel also does not arise, and the value of the parameter ξ is defined by the ratio between the kinetic (reaction) constant of the second channel and the reaction rate constant in the first channel:

$$\xi = \frac{k_{11}[B_1]}{k_2[B_2] - k_{11}[B_1]} = \frac{1}{\frac{k_2[B_2]}{k_{11}[B_1]} - 1}\quad (2.61)$$

Since $k_{11} \leq k_1$, this parameter may become positive even at $k_2[B_2] < k_1[B_1]$.

In the case of diffusion control in the second channel ($p_2 \rightarrow 1$), when the new accumulation channel related to the cage effect is of first importance, the parameter ξ goes to zero, and the kinetics of the process takes a simple form

$$\frac{[A_1]_t}{[A_1]_0} = \left(1 - \frac{[A_3]_t}{[A_1]_0}\right) = \exp(-k_{11}[B_1]t), \quad [A_2]_t \equiv 0.\quad (2.62)$$

imitating the course of elementary irreversible reaction (2.1). It is seen from Eq. 2.61 that in the general case the sign of the parameter ξ depends on the ratio of channel rates $k_{22}[B_2]$ and $k_{11}[B_1]$, while its absolute value is defined (apart from this ratio) by the efficiency p_2 of the second channel.

As the parameter ξ goes to infinity in a specific degenerate case $k_{11}[B_1] \equiv k_{d_1}p_1[B_1] = k_{22}[B_2] \equiv k_{d_2}p_2[B_2] = K$ it is interesting to consider the kinetics for this situation:

$$\begin{aligned}\frac{[A_1]_t}{[A_1]_0} &= \exp(-Kt) \\ \frac{[A_2]_t}{[A_1]_0} &= Kt(1 - p_2) \exp(-Kt) \\ \frac{[A_3]_t}{[A_1]_0} &= 1 - [1 + Kt(1 - p_2)] \exp(-Kt),\end{aligned}\quad (2.63)$$

Instead of the parameter ξ , it involves the efficiency p_2 of the second channel.

2.4 Determination of Irreversible Two-Stage Reaction Rate Constants from Experimental Kinetics

Consider the possibility and methods of experimental determination of rate constants k_{11} , $k_{22} = k_{32}$, k_{21} , and k_{31} in kinetic equations (2.37) of formal kinetics. As an example we consider the case when reactants B_i are in excess. To find these constants, it is sufficient to use just time dependences of two concentrations, for definiteness $[A_1]_t$ and $[A_2]_t$, since concentration of the third reactant is determined from the material balance preservation, i.e., the third equation depends linearly on other two equations. First, examine the case where the second stage of the two-stage reaction (2.31) is diffusion controlled ($k_{d_2} \ll k_2$, $p_2 \rightarrow 1$). In this case $k_{21} = 0$ ($\xi = 0$), and the rate constant of extra channel attains its limiting value $k_{31} = k_{11}$, so only two rate constants k_{11} and $k_{22} \equiv k_{d_2}$ are to be found. Equations 2.58 or 2.62 give the only equation defining the concentration $[A_1]_{t_0}$ of A_1 reactant at a given instant of time t_0 , while the concentration of the second reactant (the intermediate) is equal to zero:

$$\frac{[A_1]_{t_0}}{[A_1]_0} = \exp(-k_{11}[B_1]t_0) \equiv \exp(-a) \quad ([A_2]_{t_0} \equiv 0), \quad (2.64)$$

For the prescribed concentration $[B_1]$ and the moment t_0 of measurement this equation defines unambiguously the rate constant k_{11} by measurable concentration $[A_1]_{t_0}$

$$k_{11}[B_1]t_0 \equiv a = \ln \frac{[A_1]_0}{[A_1]_{t_0}}. \quad (2.65)$$

As for the rate constant $k_{22} \equiv k_{d_2}$, it can only be found if a chemical nature of the intermediate (chemical reactant A_2) is known (for example, from chemical considerations, or if the reactant is observed when the reaction proceeds not in diffusion controlled regime of the second stage). Adding this reactant at $[A_2]_0$

concentration to solution at the initial instant of time, we have for its concentration at the moment t_0

$$\frac{[A_2]_{t_0}}{[A_2]_0} = \exp(-k_{22}[B_2]t_0) \equiv \exp(-k_{d_2}[B_2]t_0) \equiv \exp(-b), \quad (2.66)$$

The desired rate constant is determined from the relation similar to Eq. 2.65

$$k_{22}[B_2]t_0 \equiv k_2[B_2]t_0 \equiv b = \ln \frac{[A_2]_0}{[A_2]_{t_0}}. \quad (2.67)$$

Now consider the general case of a two-stage reaction ($p_2 < 1$). Here the quantity a , and, correspondingly, the rate constant k_{11} of the first stage are defined by relation (2.65). Therefore another two rate constants should be found, i.e., the rate constant k_{22} of the second stage and the rate constant $k_{31} = k_{11}p_2$ of the new reaction channel, or, generally speaking, its efficiency p_2 . To determine them, we use Eq. 2.58 that gives, in view of (2.61), the only equation

$$\frac{[A_2]_{t_0}}{[A_1]_{t_0}a(1-p_2)} = \frac{1}{z}(1 - \exp(-z)) \equiv f(z), \quad (2.68)$$

where $f(z)$ is a monotonically decreasing function of the parameter

$$z = \left(\frac{k_{22}[B_2]}{k_{11}[B_1]} - 1 \right) a, \quad (2.69)$$

varying over the range $-a \leq z < \infty$. The value of this function attains its maximum at the boundary of the variation interval of the quantity z , i.e., at $z = -a$:

$$f_{\max} = f(-a) = \frac{1}{a}(\exp(a) - 1) \geq 1 \quad (2.70)$$

In the last inequality we use the relation $\exp a \geq 1 + a$. At $z = 0$ the value of the function is equal to unity $f(0) = 1$, and at $z \rightarrow \infty$ $f(z) \rightarrow 0$.

The parameter z contains the ratio of rate constants, and, since the rate constant k_{11} (as well as the value of a) are found from (2.65), its value defines the rate constant value of the second stage. As is seen from Eq. 2.68, this value corresponds to the z -coordinate of the intersection point of the curve $f(z)$ with horizontal straight line parallel to the axis z that cuts a section on the ordinate axis specified by the left-hand side of Eq. 2.68. Its length, and, hence, the intersection point coordinate depends on the efficiency p_2 . So unambiguous definition of the quantities k_{22} and p_2 based on concentration measurements at the instants of time t_0 is only possible if it is known that the second stage of the reaction proceeds in the kinetic regime ($k_2 \ll k_{d_2}$). Then $p_2 \rightarrow 0$, the reaction rate constant at the second stage of the reaction is equal to the reaction constant $k_{22} \approx k_2$, and there is no extra reaction

channel $k_{31} \approx 0$. In this case the value of the parameter z (and, therefore, the desired rate constant $k_{22} \approx k_2$) is unambiguously defined by the equation obtained from (2.68) at $p_2 = 0$:

$$\frac{[A_2]_{t_0}}{[A_1]_{t_0} a} = \frac{1}{z} (1 - \exp(-z)) \quad (2.71)$$

Determination of all rate constants on the basis of relation (2.68) is also possible if both reaction stages proceed at the same rate ($k_{22} = k_{11}$ ($z = 0$)), that can be found from Eq. 2.65. In this case relation (2.68) reduces to the relation

$$\frac{[A_2]_{t_0}}{[A_1]_{t_0} a (1 - p_2)} = 1, \quad (2.72)$$

that follows immediately from kinetic dependences (2.63) for this degenerate case. It allows one to find the desired efficiency p_2 .

Returning to relation (2.71), note that it could also take place in the more general case of diffusion controlled reaction at the second stage, if the cage effect led to ordinary redefinition (2.54) of rate constants of some stages, and did not give rise to a new channel rate constant (2.55) of which calls for the knowledge of the efficiency p_2 . Just the change in the reaction “mechanism” due to extra reaction channel that cannot arise from direct chemical transformation makes the determination of all the necessary rate constants in kinetic equations (2.37) impossible on the basis of reactant concentration values at some instant of time t_0 , as in traditional set of kinetic equations (2.32) corresponding to a two-stage irreversible reaction mechanism.

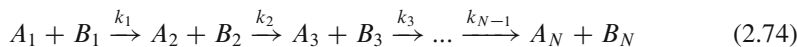
However, if the experiment is processed by formula (2.71) ignoring extra reaction channel, then the value of the parameter z will exceed the correct value obtained from (2.68). This means that the value of the rate constant k_{22} of the second stage of the reaction found from (2.71) will exceed the true one, and the difference between these values will be the greater, the greater the extent of diffusion control of the second stage (i.e., the greater the value of p_2). In the general case correct determination of all kinetic parameters calls for the use of kinetic dependences of concentrations, rather than the use of their values in arbitrary cross-section t_0 . For example, calculation of the time derivative of the kinetics $[A_2]_t$ (2.58) at the initial instant of time (concentration increase rate) gives

$$\frac{1}{[A_1]_0} \frac{d}{dt} [A_2]_t \Big|_{t=0} = k_{11} [B] (1 - p_2), \quad (2.73)$$

that makes possible independent determination of the efficiency p_2 , i.e., rate constant (2.55) of the new reaction channel. With this value of p_2 in Eq. 2.68, one can find the value of the parameter z , i.e., the rate constant k_{22} .

2.5 Irreversible Multistage Reaction

The obtained results can easily be extended to a multistage irreversible reaction



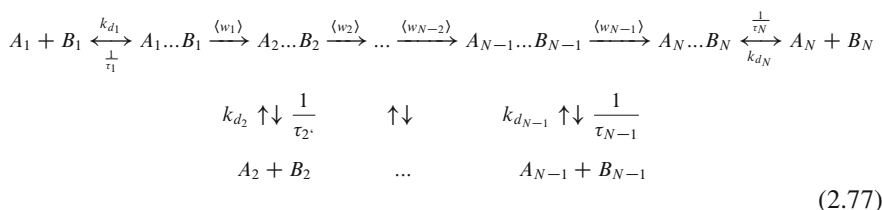
In the kinetic control the equations of formal chemical kinetics may be written in a matrix form

$$\frac{d}{dt}[\mathbf{A}]_t = \mathbf{K}[\mathbf{AB}]_t, \quad (2.75)$$

by introducing concentration vector $[\mathbf{AB}]_t$ (vector-column) with the coordinates $[A_i]_t, [B_i]_t$ ($i = 1, 2, \dots, N$) and near-diagonal matrix of kinetic coefficients:

$$\mathbf{K} = \begin{pmatrix} -k_1 & 0 & 0 & 0 & \dots & 0 \\ k_1 & -k_2 & 0 & 0 & \dots & 0 \\ 0 & k_2 & -k_3 & 0 & \dots & 0 \\ 0 & 0 & k_3 & -k_4 & \dots & 0 \\ \dots & \dots & \dots & \dots & \dots & \dots \\ \dots & \dots & \dots & \dots & \dots & \dots \\ \dots & \dots & \dots & \dots & \dots & \dots \\ 0 & 0 & 0 & \dots & k_{N-1} & 0 \end{pmatrix} \quad (2.76)$$

In the cage complex method describing the transition to diffusion control, reaction (2.74) corresponds to the kinetic scheme



Writing the kinetic equations of the cage complex method according to the above kinetic scheme, putting concentrations in all its states quasi-steady, solving the set of all algebraic equations for quasi-steady concentrations of the complex, and using the relations:

$$k_i = \langle w_i \rangle v_i, \quad k_{d_i} = \frac{v_i}{\tau_i} \quad (i = 1, 2, \dots, N-1), \quad (2.78)$$

we derive the set of kinetic equations:

$$\frac{d}{dt}[\mathbf{A}]_t = \mathbf{K}_{AA}[\mathbf{AB}]_t, \quad (2.79)$$

where $[\mathbf{A}]_t$ is still the concentration vector-column of reactants $[A_i]_t$ ($i = 1, 2, \dots, N$), and the matrix \mathbf{K}_{AA} with elements k_{ij} ($i, j = 1, 2, \dots, N$) is:

$$\begin{pmatrix} -(1-p_1)k_1 & 0 & 0 & 0 & \dots 0 \\ (1-p_1)(1-p_2)k_1 & -(1-p_2)k_2 & 0 & 0 & \dots 0 \\ (1-p_1)p_2(1-p_3)k_1 & (1-p_2)(1-p_3)k_2 & -(1-p_3)k_3 & 0 & \dots 0 \\ (1-p_1)p_2p_3(1-p_4)k_1 & (1-p_2)p_3(1-p_4)k_2 & (1-p_3)(1-p_4)k_3 & -(1-p_4)k_4 & \dots 0 \\ \dots & \dots & \dots & \dots & \dots \\ \dots & \dots & \dots & \dots & \dots \\ \dots & \dots & \dots & \dots & \dots \\ (1-p_1)p_2\dots p_{N-1}k_1 & (1-p_2)p_3\dots p_{N-1}k_2 & (1-p_3)p_4\dots p_{N-1}k_3 & \dots & 0 \end{pmatrix} \quad (2.80)$$

Thus the near-diagonal matrix of kinetic (reaction) constants (2.76) with allowance for the cage effect caused by diffusion is transformed into a triangle matrix, i.e., the matrix containing extra rate constants k_{i+n} ($i = 1, 2, \dots, N-1$, $2 \leq n \leq N-i$) corresponding to $(N-1)(N-2)/2$ new transformation channels of reactants that cannot result from the elementary event of chemical conversion.

It is seen that if all stages of the multistage reaction at hand are kinetically controlled $p_i \ll 1$ ($i = 1, 2, \dots, N-1$), matrix (2.80) is transformed into matrix (2.76), just as it should be. If all stages except the first one are kinetically controlled ($p_i \ll 1$ ($i = 2, 3, \dots, N-1$)), the matrix of kinetic coefficients is of the form of Eq. 2.76, but with the reaction rate constant k_{11} being defined by Eq. 2.54, i.e., at the first stage of the reaction the cage effect is taken into account by simple redefinition, as in the elementary reaction.

Unlike the case with a two-stage reaction, in the multistage reaction the dependence of rate constants of new channels on the efficiencies p_i ($i = 2, 3, \dots, N-1$) of all channels except the first channel is more complicated. As these efficiencies increase, only constants k_{ii} ($i = 2, \dots, N-1$) and k_{Ni} ($i = 1, 2, \dots, N-1$) in the last line of matrix (2.80) increase monotonically attaining their limiting values at $p_i \rightarrow 1$ ($i = 2, 3, \dots, N-1$). All other constants (except k_{11}) go to zero, just as all near-diagonal elements of matrix (2.80) (except the last element). In other words, the set of kinetic equations takes the form

$$\begin{aligned} \frac{d[A_1]_t}{dt} &= -k_{11}[A_1]_t[B_1]_t \\ \frac{d[A_i]_t}{dt} &= -k_{d_i}[A_i]_t[B_i]_t \quad (i = 2, 3, \dots, N-1) \\ \frac{d[A_N]_t}{dt} &= k_{11}[A_1]_t[B_1]_t + \sum_{i=2}^{N-1} k_{d_i}[A_i]_t[B_i]_t. \end{aligned} \quad (2.81)$$

This means that in this case the rate of sequential transformation of reactants in the cage is so high that, when any reactant A_i ($i = 1, 2, 3, \dots, N - 1$) finds itself in the cage (encounters B_i reactant), it inevitably transforms into the final A_N reactant during the encounter at the rates determined by the rate constant k_{11} in the first channel and appropriate diffusion constants k_{d_i} in all other channels. If initial concentrations of reactants A_i ($i = 2, 3, \dots, N$) are equal to zero, they will remain unchanged, and the solution of set (2.81) is of a simple form quite similar to Eq. 2.62

$$\frac{[A_1]_t}{[A_1]_0} = \left(1 - \frac{[A_N]_t}{[A_1]_0} \right) = \exp(-k_{11}[B_1]t), \quad [A_i]_t \equiv 0 \quad (i = 2, 3, \dots, N - 1) \quad (2.82)$$

In this case a multistage irreversible reaction becomes an elementary one.

2.6 Conclusions

It is shown that the cage complex method (method of quasi-stationary concentrations of "collision" complex) fully agrees with the concepts of the Encounter Theory that is the analog of the Collision Theory in gases. However, there is a fundamental difference between collisions of reactants in a gas and the encounters of reactants (residence in a cage) in liquid solutions. Unlike time distribution of collisions in gases, the time distribution of encounters (consisting of a series of re-contacts) is not Poisson. Nevertheless, when applied to elementary irreversible reaction, the cage complex method reproduces the familiar result of reacting contact spheres corresponding to the exponential model. The reason is that by the cage complex we mean not the entire encounter of reactants but just a part of it corresponding to the contact of reactants resulting in elementary event of chemical conversion. In the absence of physicochemical processes in the intervals between re-contacts the quasi-stationary reaction efficiency is specified by complete residence time in the reaction zone (duration of all contacts on the encounter), and the time distribution of contacts is established to be exponential.

Thus the derived expressions correspond to the so-called kinematic approximation in the theory of reactions proceeding in a narrow reaction zone. It is important that the complete escape from the cage complex also means the escape from the cage into solution, since, otherwise, the residence time in the contacts will be affected by subsequent re-contacts. Despite the exponential type of the distribution in complete residence times on contacts, the stochastic character of motion in the cage (giving rise to a series of re-contacts) essentially increases the residence time in the cage complex as compared to the time of collision in gases. This is responsible for specific features of reactions in solutions not typical of reactions in gases. The most prominent example is the appearance of extra channels of reactant transformation in multistage (in particular, sequential) reactions which cannot result

from chemical conversion elementary event. Rate constants of the new channels depend considerably on the regimes of intermediate and final reaction stages. In the case of the kinetic regime these rate constants go to zero, and formal chemical kinetics equations retain their traditional form corresponding to a given reaction mechanism (combination of elementary stages). Note that the rate constant of the initial stage of irreversible multistage reaction is redefined with allowance for diffusion in a traditional way, as in a single-stage irreversible reaction. However, rate constants of extra channels differ from zero if the above stages are affected by diffusion motion. Rate constant values of extra channels increase and attain their maximum when intermediate and final stages are diffusion controlled. In this situation there are no intermediates of a multistage irreversible reaction in solution (if they were absent at the initial instant of time), and can be found just in the cage complex.

The above peculiarities of multistage sequential reactions affecting kinetic equations of formal chemical kinetics should be taken into consideration in finding rate constants on the basis of experimental kinetics analysis.

Acknowledgments The authors are grateful to the Russian Foundation for Basic Research for financial support (Project 09-03-00456).

References

1. Eyring H, Lin SH, Lin SM (1980) Basic chemical kinetics. Wiley, New York
2. Kolb A, Griem H (1958) Theory of line broadening in multiplet spectra. *Phys Rev* 111:514–521
3. Chen S, Takeo M (1958) Broadening and shift of spectral lines due to the presence of foreign gases. *Uspekhi Fizicheskikh nauk* 66:391–478, in Russian
4. Taylor JR (1972) Scattering theory. Wiley, New York/London/Sydney/Toronto
5. Smoluchowski M (1917) Versuch einer mathematischen Theorie der Koagulationskinetik kolloider Lösungen. *Zeitschrift Physisch Chemie* 92:129–168
6. Collins FC, Kimball GE (1949) Diffusion-controlled reaction rates. *J Colloid Sci* 4:425–437
7. Sveshnikov BY (1952) Fluorescence quenching of solutions by foreign substances as the method of investigation of bimolecular reaction kinetics in solutions. *Uspekhi Fizicheskikh nauk* 46:331–347, in Russian
8. Tunitskii NN, Bagdasar'yan HS (1963) On resonance intermolecular excitation transfer with regard to diffusion. *Optika i Spektroskopiya* 15:100 (in Russian); (1963) *Opt Spectr* 15:303
9. Kilin SF, Mikhelashvili MS, Rozman IM (1964) On the transfer of electronic excitation energy in liquid solutions. *Optika i Spektroskopiya* 16:1063 (in Russian); (1964) *Opt Spectr* 16:576
10. Vasil'ev II, Kirsanov BP, Krongaus VA (1964) A study into energy transfer mechanism in liquid organic scintillators. *Infl diffus* 5:792; *Kinetika i kataliz* (in Russian)
11. Yokota M, Tanimoto O (1967) Effects of diffusion on energy transfer by resonance. *J Phys Soc Japan* 22:779–785
12. Steinberg IZ, Katchalski E (1968) Theoretical analysis of the role of diffusion in chemical reactions, fluorescence quenching, and nonradiative energy transfer. *J Chem Phys* 48:2404–2410
13. Tachiya M (1983) Theory of diffusion-controlled reactions: formulation of the bulk reaction rate in terms of the pair probability. *Radiat Phys Chem* 21:167–185

14. Waite TR (1957) Theoretical treatment of the kinetic of diffusion-limited reaction. *Phys Rev* 107:463–470
15. Waite TR (1958) General theory of bimolecular reaction rates in solids and liquids. *J Chem Phys* 28:103–106
16. Andersen PW (1949) Pressure broadening in the microwave and infra-red regions. *Phys Rev* 76:647–661
17. Doktorov AB, Burshtein AI (1976) Quantum theory of diffusion accelerated remote transfer. *Sov Fiz JETP* 41:671–677
18. Doktorov AB (1978) The impact approximation in the theory of bimolecular quasi-resonant processes. *Phys A* 90:109–136
19. Frank J, Rabinowich E (1934) Some remarks about free radicals and the photochemistry of solutions. *Trans Faraday Soc* 30:120–130
20. Noyes RM (1955) Kinetics of competitive processes when reactive fragments are produced in pairs. *J Am Chem Soc* 77:2042–2045; 78:5486–5490
21. Gopich IV, Szabo A (2002) Kinetics of reversible diffusion influenced reactions: the self-consistent relaxation time approximation. *J Chem Phys* 117:507–517
22. Doktorov AB, Kipriyanov AA (2007) Deviation from the kinetic law of mass action for reactions induced by binary encounters in liquid solutions. *J Phys Condens Matter* 19:065136–29
23. Kac M (1959) Probability and related topics in physical sciences. Interscience, London
24. Berdnikov VM, Doktorov AB (1982) Steric factor in diffusion-controlled chemical reactions. *Chem Phys* 69:205–212
25. Doktorov AB, Yakobson BI (1981) Averaging of the reactivity anisotropy by the reactant translation motion. *Chem Phys* 60:223–230
26. Rice SA (1985) Diffusion-limited reactions. Elsevier, Amsterdam

Chapter 3

Photoionization Studies of Reactive Intermediates of Importance in the Atmosphere

John Dyke

Abstract Studying a reactive intermediate in the gas-phase with photoionization provides an important way of obtaining information on neutral and ionic bond energies and cationic vibrational constants, as well as more generally of providing insight into its electronic structure and reactivity.

This presentation provides an overview of the information that can be obtained by taking recent examples of research investigations from the Southampton PES group, notably

- (i) Preparation of reactive intermediates for study using gas-phase reactions, taking the ClO and BrO radicals as examples. A review is given of the use of atom-molecule reactions to prepare reactive intermediates for study by PES, the experimental steps which are necessary to establish the presence of a reactive intermediate, and the importance of electronic structure and Franck-Condon factor calculations in assigning the PE spectral bands to a particular reactive intermediate.
- (ii) Measurement of reaction rate coefficients, using the atmospherically important reaction $\text{Cl}_2 + \text{DMS}$ as an example. A summary is given of how a flow-tube can be interfaced to a photoelectron spectrometer to obtain rate coefficients of bimolecular reactions. This is exemplified by considering the reaction $\text{Cl}_2 + \text{DMS}$. This reaction proceeds via a reactive intermediate, Me_2SCL_2 , and the final products are $\text{CH}_3\text{SCH}_2\text{Cl} + \text{HCl}$. The reaction rate coefficient has been determined at room temperature and the implications of the value obtained to atmospheric chemistry are considered. Also, the structure of the reactive intermediate has been established. It can be thought of as a trigonal bipyramidal structure with the Cl atoms in axial positions, and the methyl groups and the S lone pair in equatorial positions.

J. Dyke (✉)

School of Chemistry, University of Southampton, Southampton, SO17 1BJ, UK

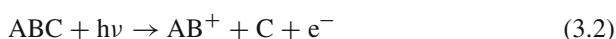
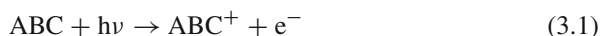
e-mail: jmdyke@soton.ac.uk

- (iii) Study of reactive intermediates of atmospheric importance with synchrotron radiation, using atomic nitrogen as an example. The advantages of using synchrotron radiation to study reactive intermediates compared to using a fixed frequency photon source from an inert gas discharge are summarised. The extra information to be obtained from angularly resolved constant-ionic-state (CIS) and threshold photoelectron spectroscopy are illustrated by considering recent studies on atomic nitrogen, a reactive intermediate which is important in the upper atmosphere.

3.1 Introduction

The most obvious application of photoionization studies on reactive intermediates is in determining ionization energies. These can be used in thermodynamic cycle calculations to yield heats of formation, which are in turn valuable in calculations of relevance to atmospheric chemistry, combustion, plasma science and other areas. Photoelectron (PE) spectra of reactive intermediates have a major application in the determination of bond strengths in molecules and the heats of formation of reactive intermediates [1, 2]. Specifically, the first adiabatic ionization energy (AIE) of a reactive intermediate is equal to the difference in the heats of formation of the cation and the neutral molecule. If the heat of formation of the cation is available from other sources, for example from proton affinity studies, the heat of formation of the neutral molecule is obtained.

If a stable molecule ABC is considered with reactive fragments AB and C, which are usually fragments with unpaired electrons called free radicals, then the following ionization processes are possible:-



If the adiabatic ionization energies (AIEs) of ABC and AB can be measured for processes (3.1) and (3.3), and the appearance energy (AE) of AB^+ can be measured for step (3.2), then from the AE of AB^+ and the AIE of ABC, the dissociation energy of $AB^+ - C$, $D(AB^+ - C)$, can be calculated, using Eq. 3.4:-

$$D(AB^+ - C) = AE(AB^+) - AIE(ABC) \quad (3.4)$$

Also, from the $AE(AB^+)$ in Eq. 3.2 and the AIE of AB in Eq. 3.3, the neutral dissociation energy $D(AB - C)$ can be calculated

$$D(AB - C) = AE(AB^+) - AIE(AB) \quad (3.5)$$

Thermodynamic cycle calculations of this type have been used extensively to determine heats of formation of reactive intermediates and bond strengths in molecules and ions [3–5]. This information is important in modelling the atmosphere and other environments, and in benchmarking theoretical methods used to calculate these quantities.

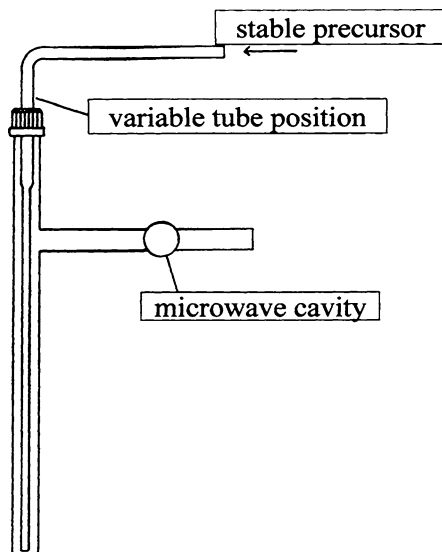
For example, modelling of ozone in the stratosphere requires its ionization energy and electron affinity, and also modelling the role of ozone in the lower ionosphere requires knowledge of direct and dissociative ionization by photons and electrons. The first adiabatic ionization energy of ozone was not unambiguously determined until 2005 [6]. Prior to that, in u.v. photoelectron spectroscopy (PES) studies, Dyke et al. [7] and Katsumata et al. [8] observed a weak band at (12.44 ± 0.01) eV which was assigned to ionization to the vibronic ground state of the cation. This weak band was not observed in other studies [9, 10], which reported a value of 12.52 eV in agreement with the result of (12.519 ± 0.004) eV obtained by photoionization mass spectrometry [11]. A value near 12.52 eV has also been suggested on the basis of an analysis of relevant thermochemical cycles [12, 13]. In 2005, this discrepancy was resolved by Willitsch et al. [6] in a pulsed-field-ionization zero-kinetic-energy (PFI-ZEKE) photoelectron study of jet-cooled ozone which gave a value for the first adiabatic IE of ozone as (12.52495 ± 0.00006) eV, indicating that the earlier value of (12.44 ± 0.01) eV arises from ionization of vibrationally excited ozone. The highly precise value of the AIE determined in this PFI-ZEKE study also allowed a determination of a more accurate value for the lowest dissociation threshold of O_3^+ , $\text{D}(\text{O}_2^+-\text{O})$ as $(4,898 \pm 3)$ cm^{-1} .

3.2 Preparation of Reactive Intermediates for Study by PES Using Gas-Phase Reactions, Taking the ClO and BrO Radicals as Examples

One of the main methods used to prepare reactive intermediates for study with PE spectroscopy is atom-molecule or molecule-molecule reactions, although other methods such as photolysis [14], pyrolysis [15] and microwave discharge of a flowing gas mixture [16] are also used. In the Southampton PES group, an inlet system of the type shown in Fig. 3.1 is used. This is positioned on the top of the ionization chamber of the spectrometer and the photon beam passes just below the lower end of the inlet system where photoionization of the reaction mixture occurs. Separate diffusion pumps are used for the analyser and ionization chambers, and the reagent gases flowing through this inlet system are mainly pumped by the diffusion pump on the ionization chamber which is positioned immediately below the inlet system.

As shown in Fig. 3.1, a microwave discharge is used to produce a source of atoms by discharging a flowing inert gas/parent molecule mixture to produce atoms in high yield (e.g. F, Cl or O atoms; for example chlorine atoms are produced by discharging a flowing Cl_2/Ar mixture) and the atoms pass between the two inlet tubes to react

Fig. 3.1 Inlet system used to study atom-molecule reactions by PES



with the target molecules, which pass down the central inlet tube, just above the photon source. By moving the inner inlet tube upwards above the photon beam, spectra can be recorded as a function of mixing distance (i.e. reaction time), with 1 cm mixing distance corresponding to ca. 0.5 ms reaction time with the simple inlet system and the pumping system used. The aim is usually first to record a spectrum of the selected reactive intermediate at low reaction times and then to record spectra at longer times. This gives information on how the reactive intermediates decrease with reaction time and what products are formed. The observed behaviour at longer reaction times provides important information which assists assignment of the spectra at short reaction times to a particular reaction intermediate. In selecting a gas-phase reaction to prepare a particular reactive intermediate for study, it is important to consider the rate coefficient of the reaction that produces the reactive intermediate as well as the rate coefficient of the fastest reaction that removes it in the reaction system used. If two consecutive reactions are considered:-



where C is produced by reaction (3.6) and removed by reaction (3.7), then in order to produce C with sufficient number density to be detected by PES (detection limit with the spectrometer and photon source used is 10^{10} – 10^{11} molecules. cm^{-3}), the rate coefficient at room temperature for reaction (3.6) should ideally be 10^{-10} – 10^{-11} cm^3 . molecule $^{-1}$ s $^{-1}$ and the rate coefficient for reaction (3.7) at room temperature should be 10^{-12} – 10^{-13} cm^3 .molecule $^{-1}$ s $^{-1}$ or lower.

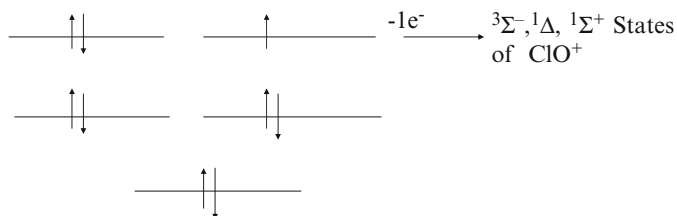


Fig. 3.2 Valence electronic structure of ClO and the ionic states obtained on ionization from the outermost occupied orbital

ClO and BrO are both key reactive intermediates in the atmosphere being involved as intermediates in the catalytic destruction of ozone by chlorine and bromine atoms respectively. Their first AIEs are important

- (i) in determining energies of electron transfer processes in the atmosphere,
- (ii) in determining energies of ion-molecule reactions in the upper atmosphere, and
- (iii) in thermochemical cycles which can be used to determine bond dissociation energies.

For ClO, an efficient way to prepare this radical is from the $\text{Cl} + \text{ClO}_2$ reaction (3.8). However, as described above, the main removal reaction must also be considered. The production and removal reactions are:-



The room temperature rate coefficients for these reactions are $k_8 = 6.0 \times 10^{-11} \text{ cm}^3 \cdot \text{molecule}^{-1} \text{ s}^{-1}$ and $k_9 = 4.8 \times 10^{-15} \text{ cm}^3 \cdot \text{molecule}^{-1} \text{ s}^{-1}$ which fit the general requirements outlined above with k_8 being very much greater than k_9 . This proved to be a very good way of preparing ClO for PE study.

Another important point to bear in mind is that reactive intermediates often have characteristic “fingerprints” which can be predicted before the PE spectrum of a reactive intermediate is recorded, and these are very important in terms of associating spectral bands, observed at short reaction times and which disappear at longer reaction times, with a particular reactive intermediate. For example, ClO and BrO are valence isoelectronic with O_2^- . They have three electrons in the outermost π antibonding orbital and have a $^2\Pi$ ground state. One electron ionization from this outermost orbital will give rise to three ionic states ($X^3\Sigma^-$, $a^1\Delta$, $b^1\Sigma^+$) with a relative degeneracy ratio of 3:2:1 (see Fig. 3.2). Three bands are therefore expected associated with this one electron ionization with an intensity ratio of 3:2:1, each with a vibrational constant, ω_e , which is greater than that in the neutral molecule because an antibonding electron has been removed. The vibrational constants of the three ionic states will also be approximately equal. These expectations were confirmed in the spectra obtained for the first three bands of ClO where the experimental

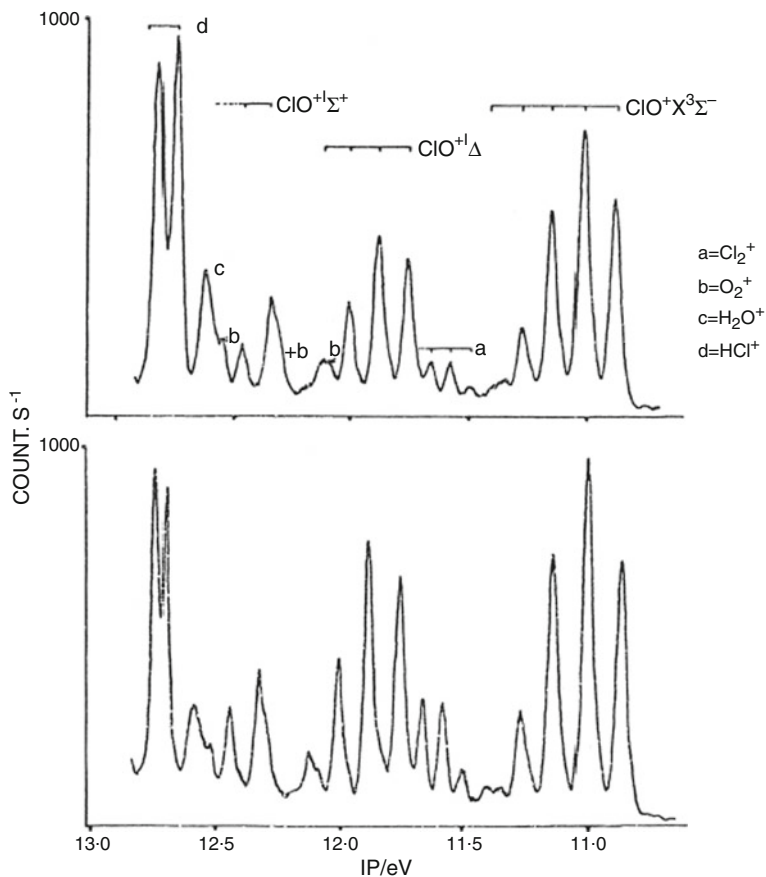


Fig. 3.3 PE spectra obtained from the Cl + ClO₂ reaction, showing the first three PE bands of ClO. The lower spectrum has slightly better resolution than the upper spectrum, but has a slightly higher oxygen level

intensity ratios of the first three bands was measured as $(2.9 \pm 0.1) : (2.0 \pm 0.1) : 1.0$. The first AIE of ClO was measured as (10.95 ± 0.01) eV [17]. Spectra obtained for the Cl + ClO₂ reaction showing the first three bands of ClO are shown in Fig. 3.3. The vibrationally resolved band envelopes were very similar in all three bands and as expected in each band the vibrational separations led to an ionic state vibrational constant which was greater than that in the neutral molecule, and approximately the same in each ionic state.

In the case of BrO, two main production routes were considered Br + O₃ and O + Br₂. For these reactions, the production and removal reactions are:-



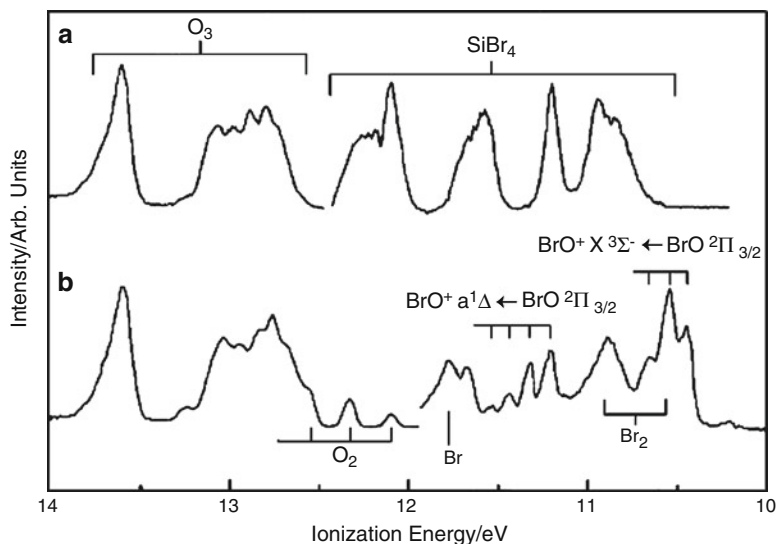


Fig. 3.4 The HeI PE spectrum obtained for the Br + O₃ reaction at a mixing distance of 15 cm above the photon beam. (b) Br atoms were obtained by discharging a flowing Ar/SiBr₄ mixture. (a) was obtained with the discharge off

and



For Br + O₃, the room temperature rate coefficients are $k_{10} = 1.2 \times 10^{-12} \text{ cm}^3 \cdot \text{molecule}^{-1} \text{ s}^{-1}$ and $k_{11} < 2 \times 10^{-17} \text{ cm}^3 \cdot \text{molecule}^{-1} \text{ s}^{-1}$, and for O + Br₂ the room temperature rate coefficients are $k_{12} = 1.1 \times 10^{-11} \text{ cm}^3 \cdot \text{molecule}^{-1} \text{ s}^{-1}$ and $k_{13} = 4.1 \times 10^{-11} \text{ cm}^3 \cdot \text{molecule}^{-1} \text{ s}^{-1}$. Inspection of these rate coefficients indicated that although the production route for Br + O₃ reaction (3.10) has a rate coefficient which is an order of magnitude lower than the “target values” for the production reaction outlined above (10^{-10} – $10^{-11} \text{ cm}^3 \cdot \text{molecule}^{-1} \text{ s}^{-1}$), the removal rate coefficient is very low with at least five orders of magnitude difference between k_{10} and k_{11} . In contrast, for O + Br₂ the production reaction is very favourable with $k_{12} = 1.1 \times 10^{-11} \text{ cm}^3 \cdot \text{molecule}^{-1} \text{ s}^{-1}$ but the removal rate coefficient is also very high ($k_{13} = 4.1 \times 10^{-11} \text{ cm}^3 \cdot \text{molecule}^{-1} \text{ s}^{-1}$). Therefore, the Br + O₃ reaction was selected for initial study as the most favourable preparative route to give a PE spectrum of BrO [18].

Figure 3.4b shows the u.v. photoelectron spectrum obtained from the Br + O₃ reaction, recorded at a mixing distance of 15 cm above the photon beam. Br atoms were prepared in this study by microwave discharge of a flowing SiBr₄/Ar mixture.

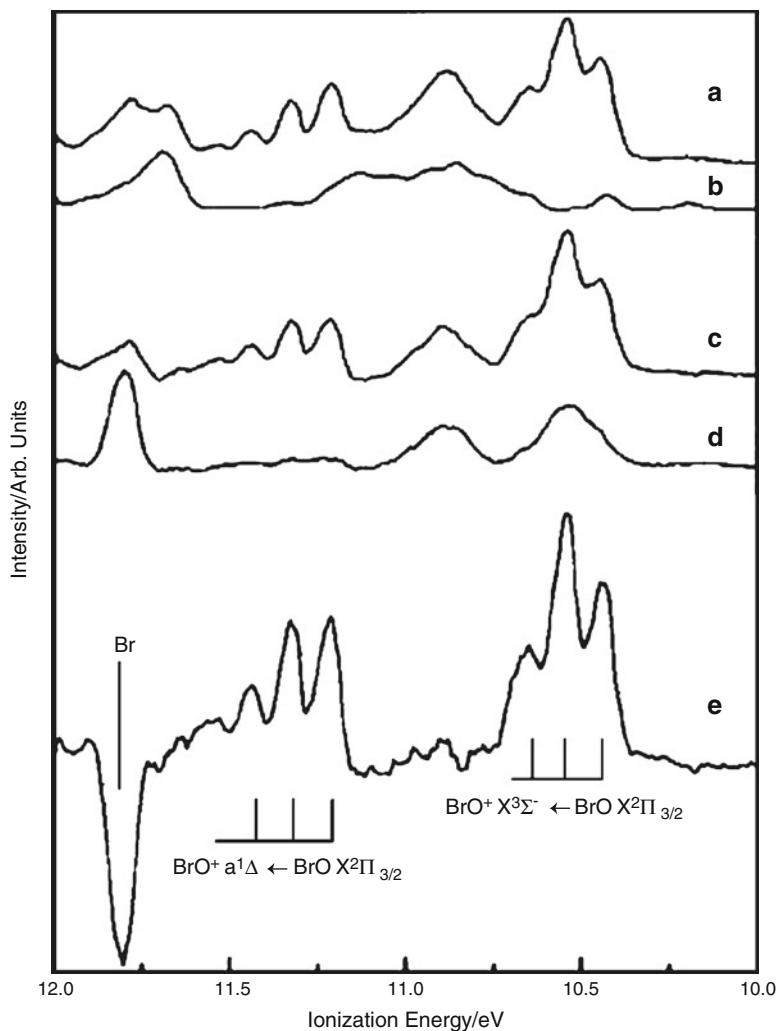


Fig. 3.5 Part (e) shows the first two PE bands of BrO. The parts of this figure are as follows: (a) HeI PE spectrum recorded in the 10.0–14.0 eV IE region for the Br + O₃ reaction at 15 cm mixing distance (b) HeIβ signals arising from O₃ and O₂ in the 10.0–14.0 eV IE region. (c) The PE spectrum obtained by subtracting (b) from (a). (d) HeI PE spectrum recorded in the 10.0–14.0 eV IE region for discharged SiBr₄/Ar showing bands from Br₂ and Br. (e) HeI spectrum obtained by subtracting (d) from (c)

Two bands attributed to BrO are marked on this figure. Increasing the mixing distance at constant reagent partial pressures resulted in a decrease in intensity of these BrO bands. Figure 3.4a was obtained for the same reaction mixture as Fig. 3.4b but with the microwave discharge turned off. It therefore only shows bands of ozone and SiBr₄. Figure 3.4b also shows bands from Br₂ which arise from Br

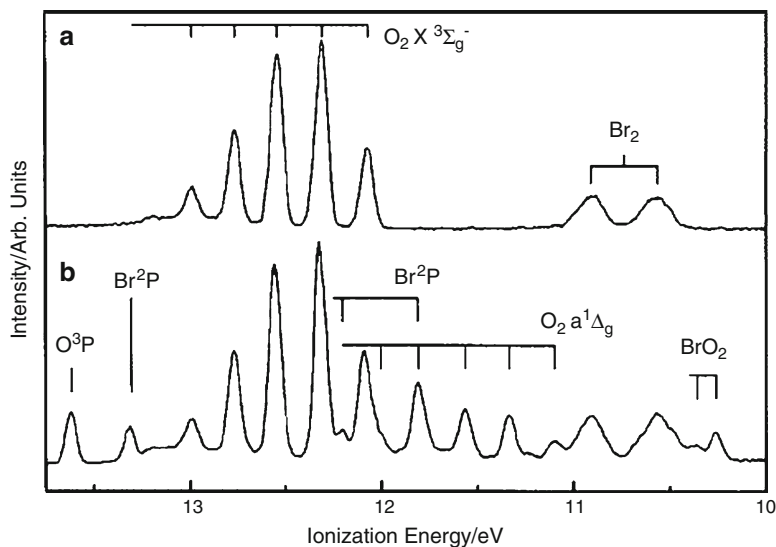


Fig. 3.6 HeI PE spectra recorded in the 10.0–13.8 eV IE region for Br_2 reacted with discharged oxygen at a mixing distance of 10 cm above the photon beam. (a) and (b) were recorded with the oxygen discharge off and on respectively

atom recombination. When these Br_2 bands are subtracted off, the spectrum shown in Fig. 3.5e in the ionization energy region 10.0–11.8 eV was obtained.

As outlined above, ionization from the outermost π -antibonding orbital of BrO is expected to give three bands with intensity ratios 3:2:1. Unfortunately, the third band of BrO , corresponding to the ionization $\text{BrO}^+(\text{b}^1\Sigma^+) \leftarrow \text{BrO}(\text{X}^2\Pi)$, could not be observed because of overlap with more intense bands in the 11.9–12.6 eV ionization energy region, notably bands of Br , O_2 and O_3 . (The bands in the 11.9–14.0 eV region in Fig. 3.4b were more intense than those in the 10.0–11.9 eV region; it is important to note that the count-rate used to record the 11.90–14.0 eV region of Fig. 3.4b was ten times higher than that used to record the 10.0–11.9 eV region). The relative intensity of the two bands shown in Fig. 3.5e was measured as $(2.6 \pm 0.2): 2.0$ in reasonable agreement with the expected ratio of 3:2. Also, for each band the vibrational constant, ω_e , obtained from the vibrational separations in Fig. 3.5e was greater than that in the neutral molecule as expected for ionization from an antibonding orbital. The values of ω_e in each band were also equal within experimental error. The first AIE of BrO obtained from this work is (10.46 ± 0.02) eV.

The $\text{O} + \text{Br}_2$ reaction was also investigated, although this was not expected to show evidence of the BrO radical. The spectrum obtained is shown in Fig. 3.6b recorded at a mixing distance of 10 cm above the photon beam [18]. For this reaction, atomic oxygen was obtained by discharging flowing molecular oxygen and a spectrum obtained under the same conditions as used to obtain Fig. 3.6b but with

the discharge off is shown in Fig. 3.6a. A band, associated with a short-lived reactive intermediate, was observed at (10.26 ± 0.02) eV which decreased in intensity as the mixing distance was increased above ~ 7 cm.

Clearly this band could not be associated with BrO. It was assigned to BrO₂ by a series of *ab initio*/Franck-Condon calculations [19] on BrO₂ and Br₂O with different structures. Good agreement was obtained in both band position and structure for a BrO₂ C_{2v} structure. The observed vibrational structure was assigned to excitation of the ν_1 mode in the ground state of BrO₂⁺ (see Fig. 3.7). The first adiabatic ionization energy of BrO₂ was obtained as (10.26 ± 0.02) eV. It is clear that the BrO₂ must be produced from the O + BrO reaction to give vibrationally excited BrO₂^{*} which is then collisionally deactivated by third body collisions i.e.



3.3 The Use of PES to Measure Reaction Rate Coefficients, Using the Atmospherically Relevant Reaction Cl₂ + DMS as an Example

PES has recently been developed to allow rate coefficients of bimolecular reactions to be measured [20–22]. It has an advantage over mass spectrometry in that it does not suffer from fragmentation problems. Also, it has the potential to observe reactants, intermediates and products, and to measure branching ratios between reaction channels which give different intermediates and/or final products.

PES has recently been used by the Southampton group to measure the rate coefficient of the DMS + Cl₂ reaction at room temperature [20]. This reaction was found to proceed via an intermediate to give monochloro DMS and HCl. The overall reaction is



Figure 3.8b shows spectra obtained at different mixing distances. The bands labelled as “Intermediate” show a distance dependence which is characteristic of a reaction intermediate.

The presence of a reaction intermediate can be seen from Fig. 3.8. In Fig. 3.8b, bands of the reagents (Cl₂ and DMS), the intermediate and the products monochloroDMS (MDMS) and HCl are present. As expected the reagent bands decrease in intensity from 15 to 25 cm and to 45 cm mixing distance whereas the product bands increase over these mixing distances. In contrast, the bands of the intermediate are low in intensity at 15 cm, are larger at 25 cm and are low again at 45 cm, as expected for a reaction intermediate. Based on computed vertical IEs for possible structures, the observed PE spectrum for the intermediate is consistent with

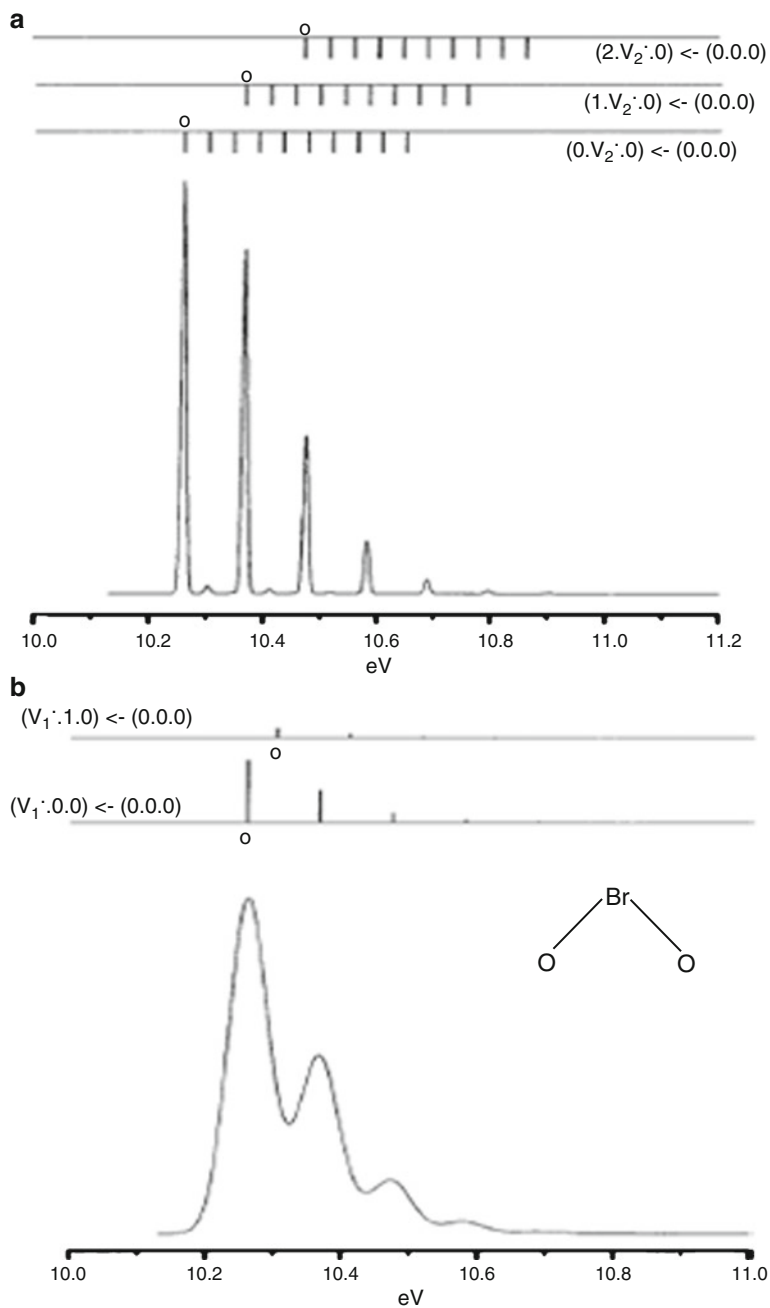


Fig. 3.7 Comparison of the observed (*lower*) and simulated (*upper*) first PE band of BrO_2 . The simulated spectrum was obtained using *ab initio*/Franck Condon calculations

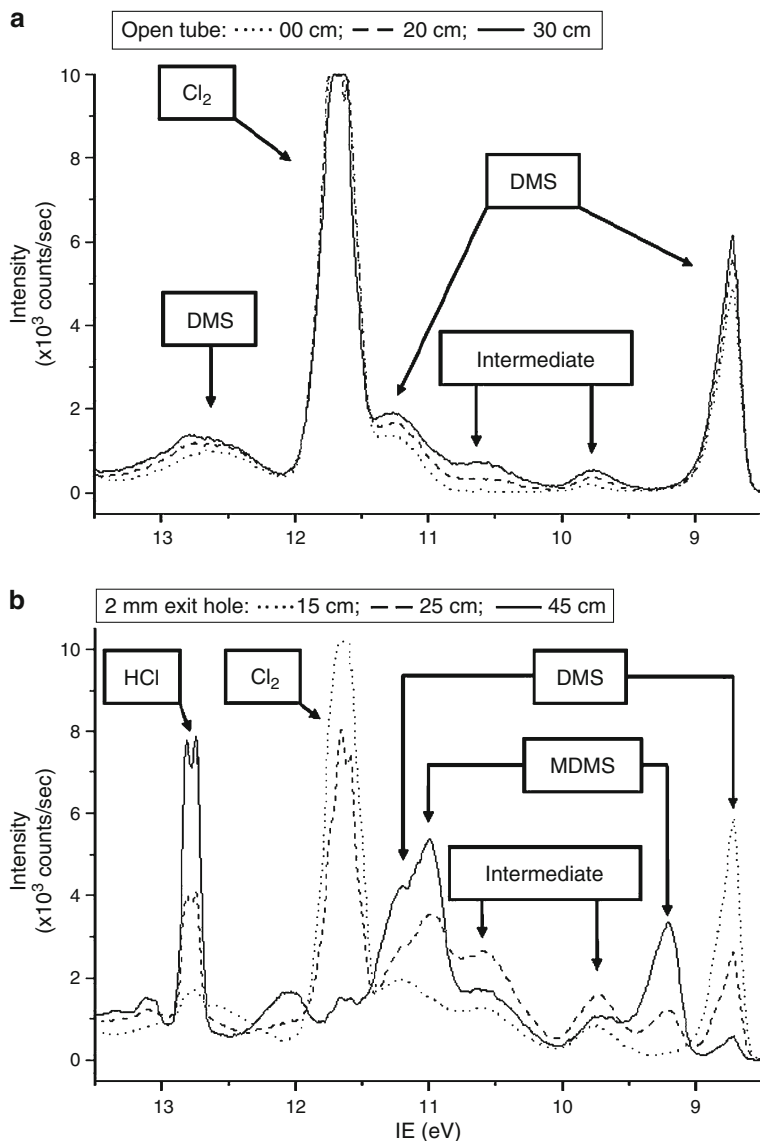


Fig. 3.8 PE spectra which show the presence of an intermediate in the $\text{Cl}_2 + \text{DMS}$ reaction. In this figure, *MDMS* represents monochlorodimethylsulphide

a covalently bound structure $(\text{CH}_3)_2\text{SCl}_2$ where the sulphur atom is four coordinate and bonded to two methyl groups and two chlorine atoms [20]. In terms of the Valence Shell Electron Pair (VSEPR) repulsion model, this structure has four bond pairs and one lone pair (from the S atom). The structure, which is similar to that of

SF₄, can therefore be viewed as a trigonal pyramidal structure with two long S-Cl bonds in axial positions, the two methyl groups in equatorial positions, and the third equatorial position occupied by a S non-bonding lone pair.

In the atmosphere, the interaction of DMS with Cl₂, and other halogens such as Br₂ and I₂, are thought to lead ultimately to SO₂ production. If the rate coefficients of the reactions of DMS with molecular halogens can be measured then these rate coefficients can be built in to atmospheric models of SO₂ production. At present, the calculated levels of SO₂ are lower than the observed levels and including these extra sources may be a way of reducing the difference between the calculated and observed levels. The main ways of DMS oxidation in the atmosphere are reaction with the OH radical during the day and the NO₃ radical at night. Subsequent oxidation in the atmosphere leads to formation of species such as SO₂, H₂SO₄ and CH₃SO₃H (methanesulphonic acid). These species may contribute significantly to the acidity of the atmosphere and, in the case of sulphuric acid, to cloud formation. Recently, molecular chlorine has been observed in coastal marine air. It is produced at night, as well as during the day, from heterogeneous reactions of ozone with wet sea-salt. Employing a high-pressure chemical ionization mass spectrometer, Spicer et al. [23] measured Cl₂ levels ranging from < 15 to 150 pptv. Night-time mixing ratios were in the range 40–150 pptv, with the highest value being observed near midnight which dropped to 15 pptv at sunrise.

In order to measure rate coefficients, a differentially pumped, flow-tube, operated under laminar flow conditions, has been interfaced to a PE spectrometer as shown in Fig. 3.9. The basic assumptions of the method are:-

- (i) that the reactants are mixed homogeneously with the carrier gas (helium),
- (ii) the carrier gas flow velocity is the transport velocity of the reactants (typically 3–20 m.s⁻¹) and
- (iii) the reaction distance and time are proportional to each other in the flow-tube.

The kinetics experiments were performed under pseudo-first-order conditions. Chlorine, the reactant in excess, was added through the central movable injector and DMS was introduced to the flow-tube through a fixed side-arm, as shown in Fig. 3.9. Contact times were between 20 and 150 ms. The pseudo first-order rate coefficient was determined by measuring the relative concentration of DMS, from the intensity of its first PE band, with the movable injector at several different positions while the chlorine partial pressure was in excess and held constant. This was then repeated at different chlorine partial pressures. The flow rates of all the gases were regulated using mass-flow controllers, which were calibrated for each individual gas mixture used. Typical first order plots at different excess chlorine partial pressures are shown in Fig. 3.10, where the intensity of the first band of DMS measured at different times is used to obtain a plot of $\log_e([DMS]_0/[DMS]_t)$ against contact time. The slope of each of these lines gives the pseudo first-order rate coefficient which can be plotted against the chlorine concentration used, to obtain the second order rate coefficient (see Fig. 3.11). The value obtained is $k = (3.4 \pm 0.7) \times 10^{-14} \text{ cm}^3 \cdot \text{molecule}^{-1} \text{ s}^{-1}$ at $T = (294 \pm 2) \text{ K}$.

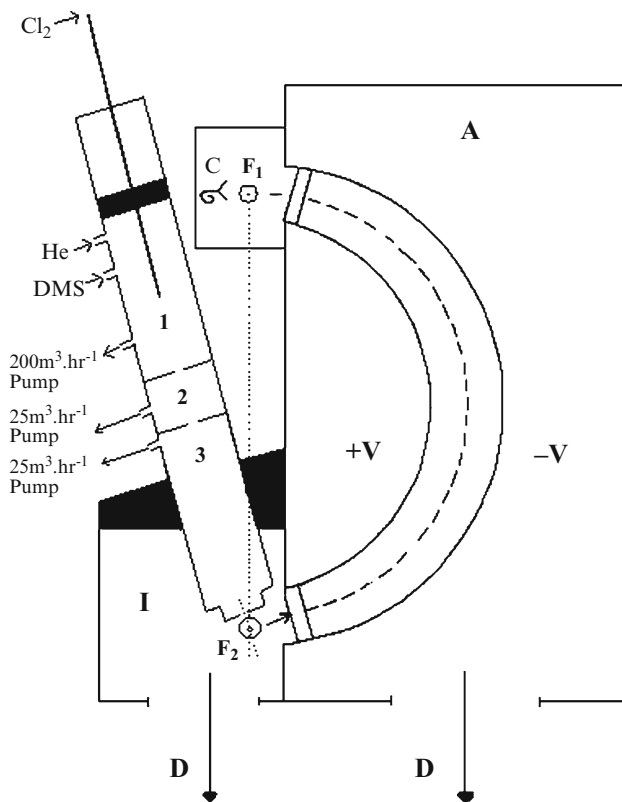
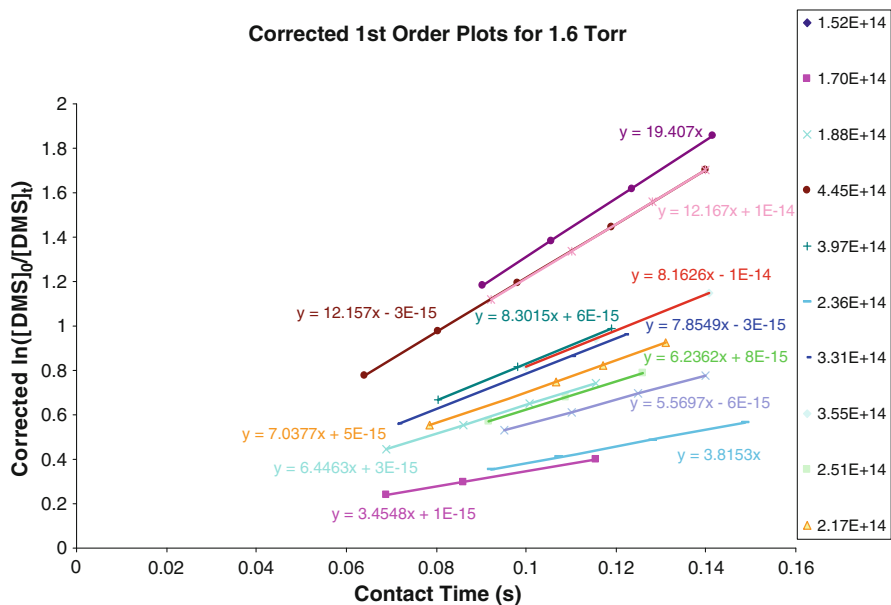


Fig. 3.9 Schematic diagram showing a flow-tube interfaced to a PE spectrometer for kinetics studies

This bimolecular rate coefficient has been used [20–22] to investigate the atmospheric implications of including the DMS + Cl₂ reaction in an SO₂ production model. If it assumed that the [Cl₂] and [DMS] are ~50 pptv at night, and these levels are replenished at night to maintain these levels, then using the bimolecular rate coefficient derived in this work, ~40 pptv of CH₃SCH₂Cl would be generated over a 6 h period. During the day CH₃SCH₂Cl would either be photolysed or react with OH. Photolysis of CH₃SCH₂Cl would lead via several steps to SO₂ production. Therefore, the night-time interaction between Cl₂ and DMS may well provide a mechanism to speed up SO₂ production in the day and go some way towards explaining the discrepancy between DMS decay rates and SO₂ production rates during the day. These results mean that interaction between DMS and halogens cannot be ignored in climate modelling studies. Related work is currently underway on the reactions DMS + Br₂ and DMS + I₂.



$$\ln\left(\frac{[A]_0}{[A]_t}\right) = (k_w + k'_2)t \quad \text{where } k_w \text{ is the wall loss rate constant (s}^{-1}\text{)}$$

Fig. 3.10 Typical first order plots for the $\text{Cl}_2 + \text{DMS}$ reaction

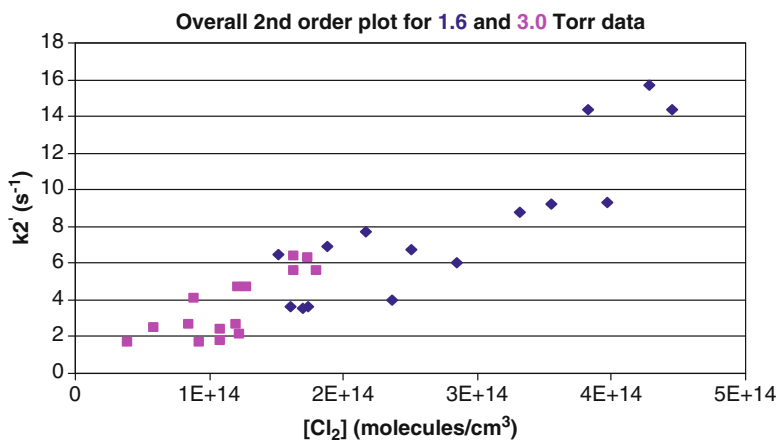


Fig. 3.11 Second order plot for the $\text{Cl}_2 + \text{DMS}$ reaction

3.4 Photoionization of Reactive Intermediates of Atmospheric Importance with Synchrotron Radiation, Using Atomic Nitrogen as an Example

The study of a reactive intermediate with PES using monochromatized synchrotron radiation should allow more information to be obtained on the molecular ionic states and the associated photoionization processes than a PES study with a low pressure discharge of an inert gas as the photon source. In particular

- (i) because the photon source is tunable it will be possible to identify autoionization resonances, and, once identified, they can give rise to extra vibrational structure in a molecular PE spectrum over that observed in a PE spectrum recorded off resonance,
- (ii) because the photon source is polarized, angular distribution measurements are possible and this allows information on photoionization dynamics to be obtained,
- (iii) a study of the relative band intensities in the valence PE spectra of an atom or molecule as a function of photon energy can provide valuable information to assist in band assignment, and
- (iv) by sweeping the photon energy and detecting threshold electrons, threshold photoelectron (TPE) spectra can be obtained. These are higher resolution than conventional PE spectra and hence provide more information on the ionization process and the ionic states accessed.

It was the first feature which initially attracted the Southampton group to use synchrotron radiation because in a number of previous investigations some of the valence PE bands of the reactive intermediate studied, when recorded with a inert gas discharge source, showed an intense adiabatic component with very little intensity in other vibrational components. This is the case for radicals such as OH, SH, N₃ and CH₃O. Such an observation for the first PE band of a reactive intermediate is particularly disappointing, since measurement of the vibrational level separations in the ground ionic state is usually one of the main experimental objectives. Also, the intensity of a PE band from a reactive intermediate, recorded at a non-resonant photon energy, in a given reaction system may be low and monitoring it at a photon energy corresponding to an autoionization resonance should enhance its intensity.

A PE spectrometer has been built in the Southampton group to study reactive intermediates with synchrotron radiation [24–26]. Three types of spectra can be recorded with this instrument:-

- (a) angularly resolved PE spectra;
- (b) angularly resolved constant-ionic-state (CIS) spectra; a CIS spectrum is obtained by monitoring the intensity of a selected PE band as a function of photon energy.
- (c) threshold PE spectra.

Some of the capabilities of this instrument, notably in areas (a) and (b), to study reactive intermediates of atmospheric importance can be demonstrated by considering angularly resolved PE spectra and CIS spectra of nitrogen atoms.

Photoionization of atomic nitrogen is an important process in the physics and chemistry of the upper atmosphere.

Angle resolved PE and CIS measurements were made on N atoms using the Elettra synchrotron radiation source (near Trieste in Italy) on the beamline BL 4.2R [27]. The degree of linear polarization ($P = 1$) of the radiation is well established. The asymmetry parameter (β) was measured for nitrogen atoms at selected photon energies and over a photon energy range, by recording CIS spectra at two different angles θ (0° and $54^\circ 44'$) at each photon energy. The angle $54^\circ 44'$ corresponds to the angle at which the measurement is independent of β , thereby, permitting a straightforward determination of the relative partial photoionization cross-section. β was then determined from $\beta = R - 1$, where $R = I_0/I_{54^\circ 44'}$ is the ratio of the experimental intensities at these two angles.

Nitrogen atoms were produced by passing a flowing mixture of molecular nitrogen mixed with helium through a microwave discharge in a glass inlet tube attached to the ionization chamber of the spectrometer. A PE spectrum recorded for discharged nitrogen is shown in Fig. 3.12 (upper panel). This shows the first band of N atoms at 14.54 eV corresponding to the ionization $N^+(2s^2 2p^3, ^3P) \leftarrow N(2s^2 2p^4, ^4S)$. The corresponding spectrum obtained with the discharge off is also shown in Fig. 3.12 (lower panel).

The CIS spectrum of N atoms at $\theta = 54^\circ 44'$ is shown in Fig. 3.13. This is the relative cross-section for N atoms plotted as a function of photon energy. This is obtained by monitoring the intensity of the first N atom PE band at 14.54 eV as a function of photon energy. The resonances seen in this plot correspond to excitation to $N^*(2s 2p^3, ^5S), np)$ states from the $N(2s^2 2p^3, ^4S)$ ground state followed by autoionization to the $N^+(2s^2 2p^3, ^3P)$ state. The resonances seen in this plot show an asymmetric profile. This is due to interference between the direct and indirect (resonance plus autoionization) ionization processes and results in a characteristic Fano profile. Each resonance can be fitted to a Fano profile to obtain Fano parameters which provide information about the excited state lifetime and the interaction of the excited state with the continuum. Specifically, the resonance position E_n , the natural line-width, Γ , and line-shape parameters q and ρ^2 , and the discrete oscillator strength f have been determined for the $N^*(2s 2p^3, ^5S), np) \leftarrow N(2s^2 2p^3, ^4S)$ autoionization resonances for $n = 5-10$, and explanations of the changes in these parameters with principal quantum number have been proposed [27]. Fitting the resonance energies, E_n , obtained to the Rydberg energy expression

$$E_n = E_\infty - \frac{R}{(n - \delta_n)^2} \quad (3.17)$$

where E_∞ is the ionization energy, R is the Rydberg constant and δ is the quantum defect, gave $E_\infty = 20.39$ eV for the $(2s)^{-1}$ ionization and $\delta = (0.61 \pm 0.01)$. This δ value is consistent with the value expected for a p Rydberg orbital of a first row element.

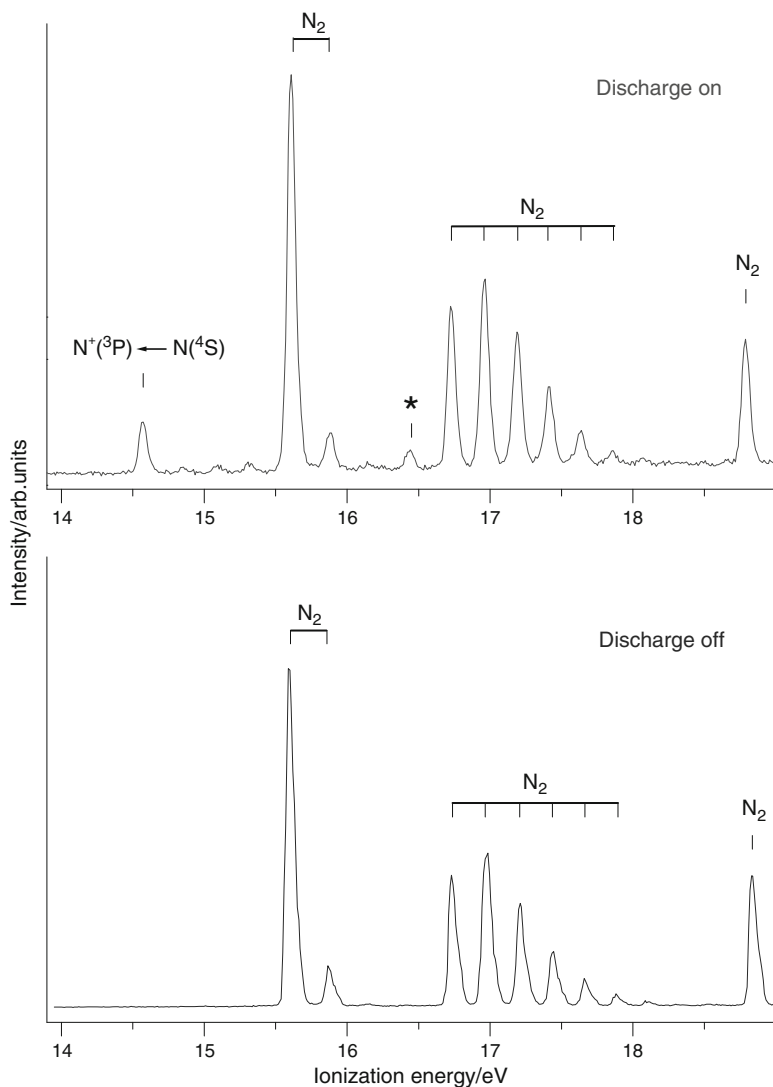


Fig. 3.12 PE spectrum recorded at photon energy $h\nu = 21.22$ eV with the microwave discharge on (*upper panel*) and off (*lower panel*) of a He/N₂ mixture. The peak labelled with (*) at 16.45 eV is a “hot-band” associated with the ionization $N_2^+(A^2\Pi_u, v^+ = 0) \leftarrow N_2(X^1\Sigma_g^+, v'' = 1)$

The β -parameter plot is shown in Fig. 3.14. As can be seen, resonances are observed in this plot in the same positions as are observed in the CIS plot shown in Fig. 3.13. β values are in general in the range -1 to $+2$ and interpretation of a β -plot of the type shown in Fig. 3.14 provides information about the angular momentum carried away by the free electron. For an electron with orbital angular momentum quantum number l in an atom before photoionization, free electron waves with $l-1$

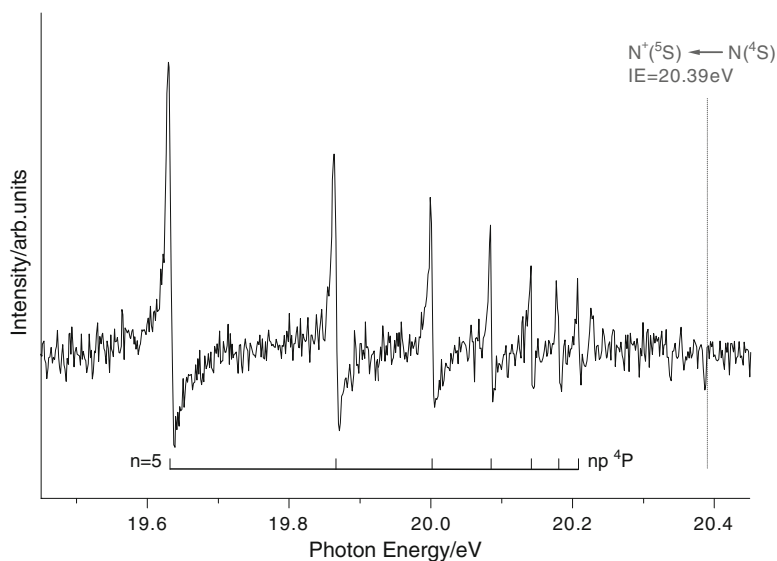


Fig. 3.13 Relative integrated cross section of atomic nitrogen across the $N^+(2s^22p^3, ^3P) \leftarrow N^*(2s2p^3(^5S) np)^4P \leftarrow N(2s^22p^3, ^4S)$ autoionizing resonances for $n \geq 5$, over the photon energy range 19.4–20.5 eV. The spectrum was recorded at $\theta = 54^\circ 44'$

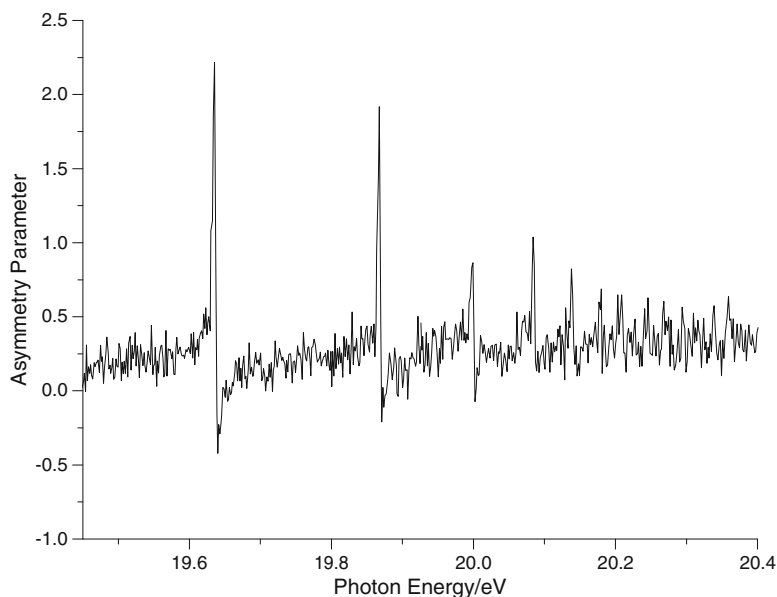


Fig. 3.14 Asymmetry parameter for atomic nitrogen across the $N^+(2s^22p^3, ^3P) \leftarrow N^*(2s2p^3(^5S) np)^4P \leftarrow N(2s^22p^3, ^4S)$ autoionizing resonances for $n \geq 5$, over the photon energy range 19.4–20.5 eV

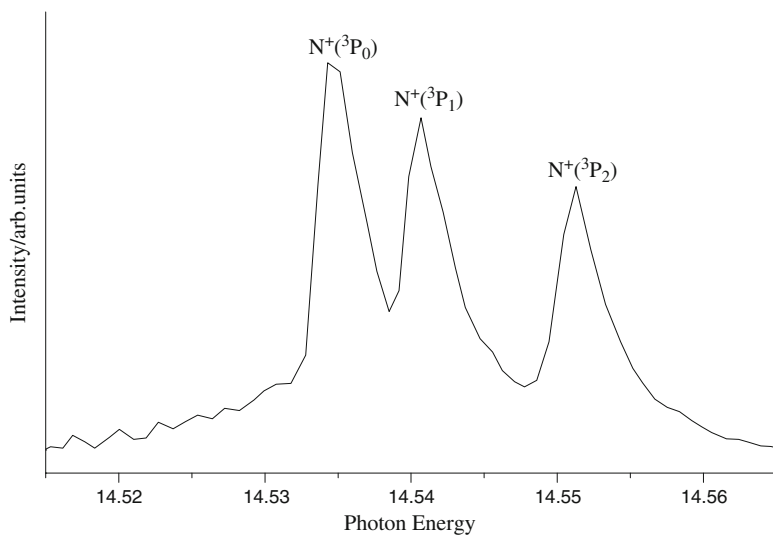


Fig. 3.15 TPE spectrum recorded for the $N^+(^3P_{2,1,0}) \leftarrow N(^4S)$ ionization showing ionization to the three ionic state components 3P_0 , 3P_1 and 3P_2

and $l + 1$ will be produced on photoionization. The value of β depends not only on the strengths of the two partial waves but also on their phases, which control the interference between them.

For non-resonant ionization of a 2p electron in nitrogen, both an s and a d free electron wave can be produced. For a $p \rightarrow s$ ionization $\beta = 0$ and for a $p \rightarrow d$ ionization $\beta = 1.00$. The off-resonant background level in Fig. 3.14 of approximately $\beta = +0.2$ indicates that both s and d free electron waves are contributing off resonance. Further insight into the values of β both on and off resonances can be obtained by using angular momentum transfer theory, for the angular momentum transferred between the molecule, and the ion and photoelectron. This has been applied to the results shown in Fig. 3.14 for N atoms and has also recently applied to similar angular distribution plots obtained for atomic iodine [28].

An example of the use of threshold PE spectroscopy is shown in Fig. 3.15, where the first photoelectron band of N atoms is shown. This corresponds to the $N^+(^3P_{0,1,2}) \leftarrow N(^4S_{3/2})$ ionization. The resolution is 3 meV and as can be seen bands corresponding to ionization to the spin-orbit components of the 3P ionic state, at 14.534, 14.540 and 14.550 eV, are resolved. This illustrates the extra information that can be obtained from TPES studies.

3.5 Conclusions

In this review lecture, an attempt has been made to demonstrate the range and detail that can be obtained on studying atmospherically important reactive intermediates with photoionization methods. Much of the information obtained is relevant to

understanding the photoionization, and reactivity of reactive intermediates and their ions in the atmosphere as well as in deriving thermochemical quantities which can be used in calculations relevant to atmospheric chemistry.

Acknowledgements I would like to thank EPSRC and NERC (UK), and the many co-workers who have collaborated in this research. I am particularly indebted to Dr Edmond Lee and Dr Alan Morris with whom I have collaborated over a significant number of years. Ed has been responsible for most of the theory and calculations and Alan has designed and built all of the spectrometers used. I am also very grateful to the organisers of ICPAC 2010 for the opportunity to present this paper.

References

1. Dyke JM, Jonathan N, Morris A (1982) Recent progress in the study of transient species with vacuum ultraviolet photoelectron spectroscopy. *Int Rev Phys Chem* 2:3
2. Dyke JM, Jonathan N, Morris A (1979) Vacuum ultraviolet photoelectron spectroscopy of transient species. In: Brundle CR, Baker AD (eds) *Electron spectroscopy*, vol 3. Academic, London, p 189
3. Cockett MCR, Dyke JM, Zamapour H (1991) Photoelectron spectroscopy of short-lived molecules. In: Ng CY (ed) *Vacuum ultraviolet photoionization and photodissociation of molecules and clusters*. World Scientific Co., Teaneck
4. Dyke JM (1987) Properties of gas-phase ions. *JCS Faraday II* 83:67
5. Chen P (1994) Photoelectron spectroscopy of reactive intermediates. In: Ng CY, Baer T, Powis I (eds) *Unimolecular and bimolecular reaction dynamics*. Wiley, New York, p 372
6. Willitsch S, Innocenti F, Dyke JM, Merkt F (2005) High-resolution pulsed-field-ionization zero-kinetic-energy photoelectron spectroscopic study of the two lowest electronic states of the ozone cation O_3^+ . *J Chem Phys* 122:024311
7. Dyke JM, Golob L, Jonathan N, Morris A, Okuda M (1974) Vacuum ultraviolet photoelectron spectroscopy of transient species: part 4 difluoromethylene and ozone. *JCS Faraday Trans I* 70:1828
8. Katsumata S, Shiromaru H, Kimura T (1984) Photoelectron angular distributions and assignment of photoelectron spectrum of ozone. *Bull Chem Soc Jpn* 57:1784
9. Brundle CR (1974) He(I) and He(II) photoelectron spectrum of ozone. *Chem Phys Lett* 26:25
10. Frost DC, Lee ST, McDowell CA (1974) High resolution photoelectron spectroscopy of ozone. *Chem Phys Lett* 24:149
11. Weiss MJ, Berkowitz J, Appelman EH (1977) Photoionization of ozone: formation of O_4^+ and O_5^+ . *J Chem Phys* 66:2049
12. Moseley JT, Ozenne JB, Crosby PC (1981) Photofragment spectroscopy of O_3^+ . *J Chem Phys* 74:337
13. Probst M et al (2002) Ionization energy studies of ozone and OCIO monomers and dimers. *J Chem Phys* 116:984
14. Willitsch S, Dyke JM, Merkt F (2004) Rotationally resolved photoelectron spectrum of the lowest singlet electronic state of NH_2^+ and ND_2^+ . *Mol Phys* 102:1543
15. Dyke JM, Morris A, Josland G, Hastings MP, Francis PD (1986) High-temperature photoelectron spectroscopy: an increased sensitivity spectrometer for studying vapor-phase species produced at furnace temperatures >2000 K high temperature. *Science* 22:95
16. Innocenti F, Eyyper M, Lee EPF, Stranges S, Mok DKW, Chau FT, King GC, Dyke JM (2008) Difluorocarbene studied with threshold photoelectron spectroscopy (TPES): measurement of the first adiabatic ionization energy (AIE) of CF_2 . *Chem Eur J* 14:11452

17. Bulgin DK, Dyke JM, Jonathan N, Morris A (1979) Vacuum ultraviolet photoelectron spectroscopy of transient species: part 9 the ClO radical. *JCS Faraday II* 75:456
18. Dyke JM, Gamblin SD, Hooper N, Lee EPF, Morris A, Mok DKW, Chau FT (2000) A study of BrO and BrO₂ with vacuum ultraviolet photoelectron spectroscopy. *J Chem Phys* 112:6262
19. Mok DKW, Lee EPF, Chau FT, Wang DC, Dyke JM (2000) A new method of calculation of Franck-Condon factors which includes allowance for anharmonicity and the Duschinsky effect: simulation of the He I photoelectron spectrum of ClO₂. *J Chem Phys* 113:5791
20. Dyke JM, Ghosh MV, Kinnison DJ, Levita G, Morris A, Shallcross DE (2005) A kinetics and mechanistic study of the atmospherically relevant reaction between molecular chlorine and dimethyl sulphide (DMS). *PCCP* 7:866
21. Dyke JM, Ghosh MV, Goubet M, Lee EPF, Levita G, Miqueu K, Shallcross DE (2006) A study of the atmospherically relevant reaction between molecular chlorine and dimethyl sulphide (DMS): establishing the reaction intermediate and measurement of absolute photoionisation cross-sections. *Chem Phys* 324:85
22. Beccaceci S, Ogden JS, Dyke JM (2010) Spectroscopic study of the reaction between Br₂ and dimethyl sulphide (DMS), and comparison with a parallel study made on Cl₂ + DMS: possible atmospheric implications. *PCCP* 12:2075
23. Spicer CW, Chapman EG, Finlayson-Pitts BJ, Platridge RA, Hubbe JM, Fast DJ, Berkowitz CM (1998) Unexpectedly high concentrations of molecular chlorine in coastal air. *Nature* 394:353
24. Innocenti F, Eypper M, Beccaceci S, Morris A, Stranges S, West JB, King GC, Dyke JM (2008) A study of the reactive intermediate IF and I atoms by photoelectron spectroscopy. *J Phys Chem A* 112:6939
25. West JB, Dyke JM, Morris A, Wright TG, Gamblin SD (1999) Photoelectron spectroscopy of short-lived molecules using synchrotron radiation. *J Phys B* 32:2763
26. Dyke JM, Gamblin SD, Morris A, Wright TG, Wright AE, West JB (1998) A photoelectron spectrometer for studying reactive intermediates with synchrotron radiation. *J Electron Spectrosc Relat Phenom* 97:5
27. Innocenti F, Zuin L, Costa ML, Dias AA, Morris A, Paiva ACS, Stranges S, West JB, Dyke JM (2005) Photoionization studies of the atmospherically important species N and OH at the Elettra synchrotron radiation source. *J Electron Spectrosc Relat Phenom* 142:241
28. Eypper M, Innocenti F, Morris A, Stranges S, West JB, King GC, Dyke JM (2010) Photoionization of iodine atoms: Rydberg series which converge to the I⁺(¹S₀) ← I(²P_{3/2}) threshold. *J Chem Phys* 132:244304

Chapter 4

Synthesis and Applications of Nano Size Titanium Oxide and Cobalt Doped Titanium Oxide

Revannath D. Nikam, Sharad S. Gaikwad, Ganesh E. Patil, Gotan H. Jain, and Vishwas B. Gaikwad

Abstract Using titanium isopropoxide the nano size TiO_2 was prepared by new sol-gel method. The nano size structure of TiO_2 was confirmed by ultra-violet diffuse reflectance spectroscopy (UV-DRS), X-Ray Diffraction (XRD) Spectroscopy, Field Emission Scanning Electron Microscopy (FESEM) and Transmission Electron Microscopy (TEM). The gas sensitivity of material was tested by preparing thick film by screen printing technique. For this the thixotropic paste of material was prepared by using ethyl cellulose and butyl cellulose. The gas sensing performance of this thick film was tested for gases like ethanol, CO_2 , H_2S , NH_3 , CO , Cl_2 and maximum sensitivity was observed for H_2S gas. The H_2S gas sensing ability was also improved by doping of cobalt into TiO_2 by hydrothermal method. The cobalt doped TiO_2 showed sensitivity for minimum 100 ppm of H_2S at 300°C .

4.1 Introduction

Metal oxide semiconductors are widely used as gas sensor materials since they show change in conductance on exposure to gases [1]. The scientific literatures showed that TiO_2 is used as a gas sensing material in many devices [2]. The gas sensing

R.D. Nikam • S.S. Gaikwad
Department of Chemistry, K.T.H.M. College, Gangapur Road, Nashik,
422 002 Maharashtra, India
e-mail: nikam.revan@rediff.com; gaikwad.sharad85@gmail.com

G.E. Patil • G.H. Jain
Department of Physics, Arts, Commerce & Science College, Nandgaon, Nashik,
423 106 Maharashtra, India
e-mail: ganeshpatil_phy@rediffmail.com; gotanjain@rediffmail.com

V.B. Gaikwad (✉)
Chemistry Materials Research Laboratory, K.T.H.M. College, Nashik,
422 022 Maharashtra, India
e-mail: dr.gaikwadvb@rediffmail.com

ability of nano size TiO_2 can be increased through doping of other atoms such as Pt, Mn, Co, Cu, Cr and Nb [3]. Hydrogen sulfide is a toxic gas generally released from industrial effluents and coal mining processes. The permissible limit of H_2S gas in clean environment is about 15 ppm [4]. Concentration of H_2S of more than 156 ppm is very hazardous to human health, so the measurement of released H_2S gas is environmentally important. Numerous H_2S gas sensing devices are available in the market, but have drawbacks of slow response and low sensitivity. This paper presents a method of preparation of nano size TiO_2 [2] and cobalt doped TiO_2 , the semi-conducting material utilized for manufacturing the H_2S gas sensor with maximum sensitivity for lower concentration of H_2S .

4.2 Methodology

4.2.1 Synthesis of Nano Size TiO_2 by Sol-Gel Method

Titanium isopropoxide (2 ml) and dodecylamine (0.5 ml) were added to NaCl (3.9 g) in 95% ethanol (30 ml) and the mixture was stirred for about 3 h at room temperature. The rate of reaction was slowed down with the addition of ethanol: NaCl mixture to obtain the product with smaller sized particle dimensions. Then the pH of the reaction mixture was adjusted to 6.0 using 0.1 M HCl and the whitish gel thus formed was again stirred for 2 h. The unwanted salt from gel material was removed by washing it with a mixture of *p*-toluene sulphonic acid in distilled water. The gel was dried overnight at 250°C in an electric oven. The obtained gel was annealed at various temperatures. The first fraction of gel annealed at 400°C showing black colour. The second fraction of gel annealed at 500°C showing gray coloured product. The third fraction annealed at 600°C showing a white coloured product [2]. The colour change of material was due to phase change of TiO_2 from anatase to rutile. The reaction scheme is shown in Fig. 4.1.

4.2.2 Doping of Cobalt into Nano Size TiO_2 by Hydrothermal Method

The cobalt doping to nano size TiO_2 was carried out by hydrothermal method by using Teflon bottle [5, 6]. In this method 0.1 M cobalt(II) chloride solution (125 ml) was mixed into 0.1 M NaOH solution (125 ml) in a Teflon bottle and nano TiO_2 (1 g) was added. The bottle was kept in an electric oven for about 2 h. Due to the internal pressure created on the crystal lattice of titanium oxide, the cobalt got doped. The doped material was taken into a beaker and stirred for 30 min. The product was dried after washing it with distilled water and was fired at 250°C for removal of unused reagents. The cobalt doping was tested by comparing the IR absorption frequency of doped and undoped TiO_2 .

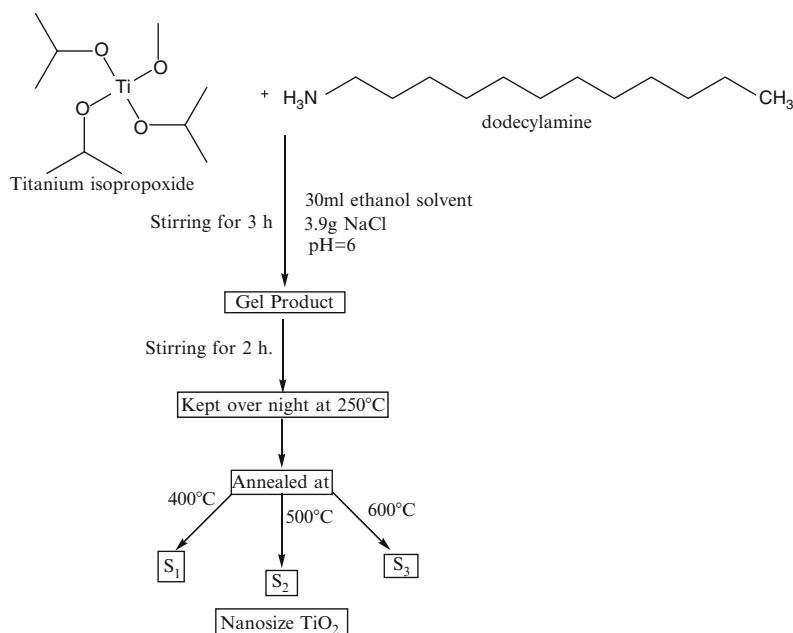


Fig. 4.1 The scheme for formation of nano size TiO₂

4.2.3 Preparation of Thick Film

The gas sensitivity of prepared material was tested for various gases using thick film. The thick film of material was prepared by screen printing technique [7]. First the thixotropic paste was prepared by mixing of the synthesized semi-conducting nano TiO₂ material (1.0 mg) with a solution of 1.0 g ethyl cellulose (binder) and 1 ml mixture of organic solvents with the following composition [Butyl cellulose (4 parts) + Butyl carbitol acetate (3 parts) + Terpenol (3 parts)]. The film was made uniform by application of pressure on it. The film was then fired at 475°C to remove organic matter. The thick film of Co-TiO₂ was prepared similarly. The gas sensing ability of both of these films was tested by their explosion with gaseous ethanol, H₂S, NH₃, Cl₂, CO and CO₂ gases.

4.3 Results and Discussion

4.3.1 X-Ray Diffraction Analysis

The crystal structures of all samples were studied by X-ray diffraction technique [8] (XRD Make-BRUKER) and the patterns are shown in Fig. 4.2. The Cu-Kα

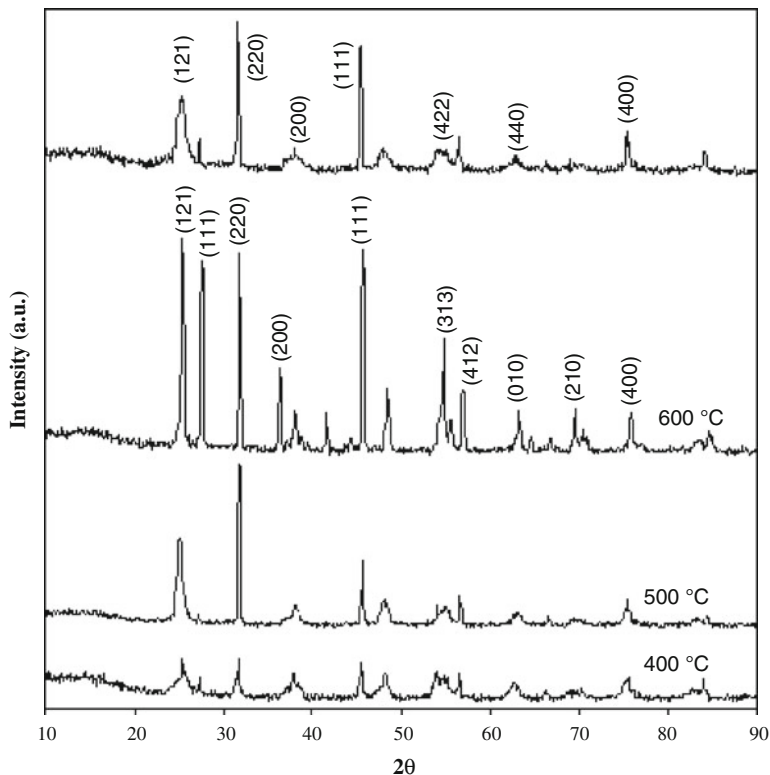


Fig. 4.2 XRD patterns of nano size TiO_2 annealed at 400°C , 500°C , 600°C and Co-doped- TiO_2

radiation was used with $10\text{--}90^\circ$ angular region for identification of the specific phase formed after heat treatment. The obtained XRD pattern of nano TiO_2 was matched with JCPDS data card no. (21–1272) and the XRD pattern of Co-doped TiO_2 was matched with JCPDS data card no. (29–0516). The comparative study showed that the XRD pattern of sample annealed at 400°C exhibited only anatase phase peak at 25.5° with (121) plane, but the peak intensity was low because of the amorphous nature of this material. The sample annealed at 500°C showed anatase phases with increase in peak intensity due to increase in crystallinity. The XRD pattern of sample annealed at 600°C showed both anatase and rutile phases corresponding to the peak at 25.5° with (121) plane and 27.4° with (111) plane. The XRD analysis of cobalt doped material indicated the presence of crystalline Co, judged by the diffraction signals arising from the (111) plane and (200) plane of cobalt lattice. The XRD pattern of cobalt doped TiO_2 exhibited rutile as well as anatase peak. Overall the rutile phase formation was found to increase with increase in annealing temperature. This effect was observed due to the increase in surface energy with increasing annealing temperature. In gas sensing, rutile phase was preferred because of its higher semi-conducting property [9].

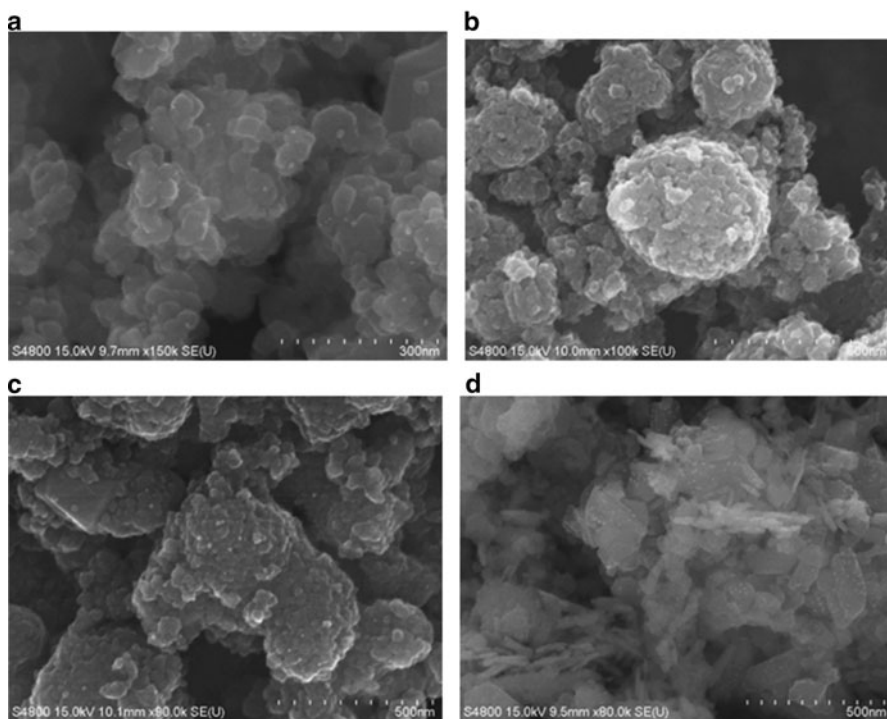


Fig. 4.3 FESEM images of nano size TiO_2 annealed at (a) 400°C , (b) 500°C , (c) 600°C and (d) Co-doped TiO_2

4.3.2 Field Emission Scanning Electron Microscopy Analysis

The nano size structures of TiO_2 annealed at 400°C , 500°C and 600°C and cobalt doped- TiO_2 were studied by FESEM spectroscopy. The sample for this analysis was prepared by coating the sample of any thickness on alumina stub. The electron beam was scanned over the surface of sample to obtain the image of surface. Due to this, the size measured by FESEM was greater than the size measured by TEM. The result of this analysis is represented in Fig. 4.3. When TiO_2 was annealed at 400°C , the spherical morphology of nano TiO_2 was observed with particle dimensions equal to 28 nm (Fig. 4.3a). The particle dimensions of nano material were observed to increase with rise in annealing temperature due to coarsening of particle. Fig. 4.3b elucidates that, when TiO_2 was annealed at 500°C , the spherical nature of the particle changed and its size was increased to 36 nm. Similarly, the TiO_2 annealed at 600°C showed particle dimension equal to 56 nm with coagulated particles (Fig. 4.3c). The FESEM image (Fig. 4.3d) of Co doped TiO_2 showed spherical morphology of particle with size 28 nm.

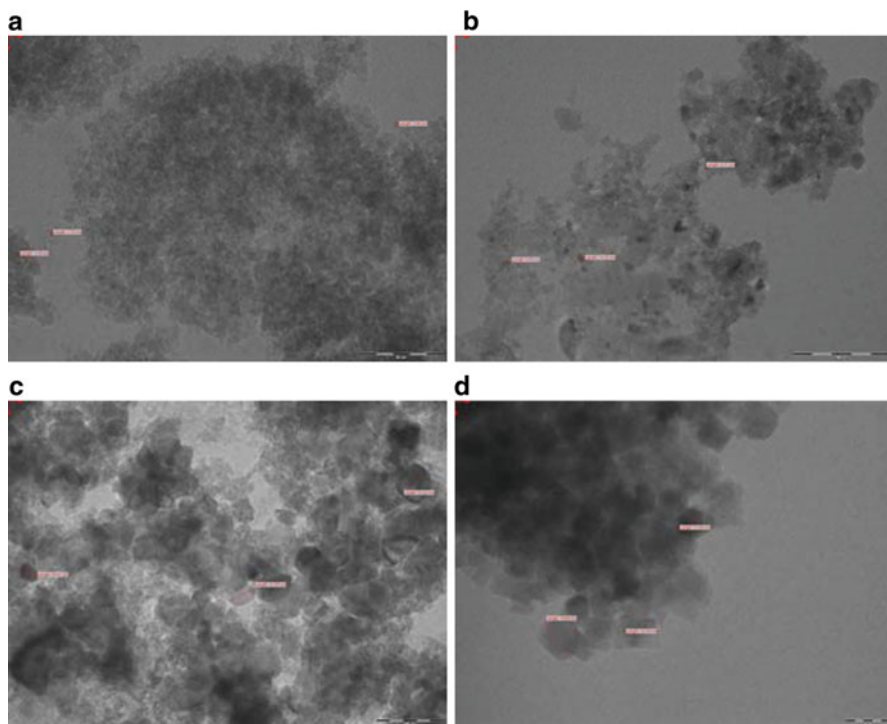


Fig. 4.4 TEM images of nano size TiO_2 annealed at (a) 400°C , (b) 500°C , (c) 600°C and (d) Co-doped- TiO_2

4.3.3 Transmission Electron Microscopy Analysis

Transmission Electron Microscopy (TEM) images were recorded using a CM-200, Make-PHILIPS instrument. The sample was supported on TEM grid for this analysis. The electron beam was passed through thin sample to obtain two dimensional image of sample. Due to this the result obtained by TEM analysis was superior to FESEM. The result of this analysis is represented in Fig. 4.4. When TiO_2 was annealed at 400°C the average grain size was equal to 2.37 nm (Fig. 4.4a). The average grain size of nano material was observed to increase with rise in annealing temperature due to increasing rate of coarsening [10]. When TiO_2 was annealed at 500°C the grain size changed to 8.57 nm (Fig. 4.4b). The TiO_2 annealed at 600°C showed increasing grain size to 51.33 nm (Fig. 4.4c). For Co doped- TiO_2 the grain size observed was 16.16 nm (Fig. 4.4d).

Thus overall observation indicates that the average grain size increases with increasing temperature due to increasing coarsening rate.

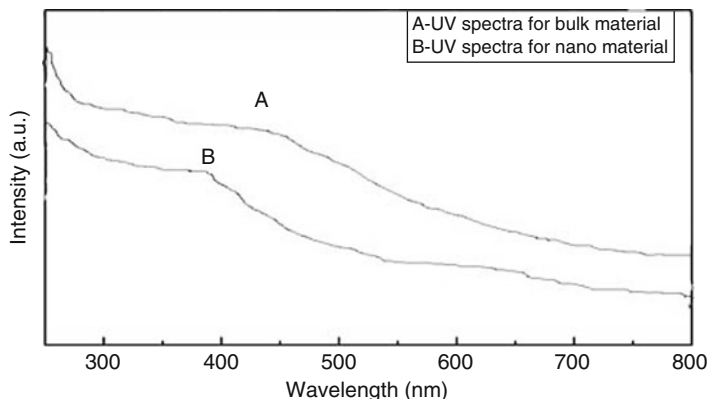


Fig. 4.5 UV-Spectrum of nano TiO₂ and bulk TiO₂

4.3.4 UV-Spectroscopic Study

Primarily the nano TiO₂ was characterized by UV-spectrophotometry by determination of the band gap between the valence band and conduction band [11]. Using DRS assembly the absorption spectra of sample material and standard TiO₂ (bulk TiO₂) were taken. The UV-absorption peak for bulk TiO₂ and nano size TiO₂ were observed at 410 and 370 nm respectively (Fig. 4.5), revealing a blue shift. This blue shift was observed because of reduction in particle dimension and indicates the formation of nano size TiO₂. The band gap of both nano and bulk TiO₂ is calculated by the equation $E = hc/\lambda$.

The band gap for bulk TiO₂ was found to be 3.72 eV and for nano TiO₂ 3.36 eV. This value is used for calculation of the average particle size of nano TiO₂ by the following effective mass approximation formula:

$$E = E_g + \frac{h^2\pi^2}{2R^2} \left\langle \frac{1}{m_e} + \frac{1}{m_h} \right\rangle - \frac{1.8e^2}{4\pi \epsilon_0 R}$$

where E is the band gap of nano TiO₂, E_g is the band gap of bulk TiO₂, h is the Planck's constant, R is the radius of the nano particle, m_e is the effective mass of electron, m_h is the effective mass of hole, and ϵ_0 is the permittivity of free space. The average size for nano TiO₂ calculated by this formula was found to be 46 nm.

4.3.5 IR Spectroscopic Study

The IR spectrum of TiO₂ without annealing was taken (Fig. 4.6), the various peaks indicating that the prepared material was not in a pure form and required further calcinations. The peak at 356.84 cm⁻¹ was due to a Ti-O stretching, 1020.38 cm⁻¹ due

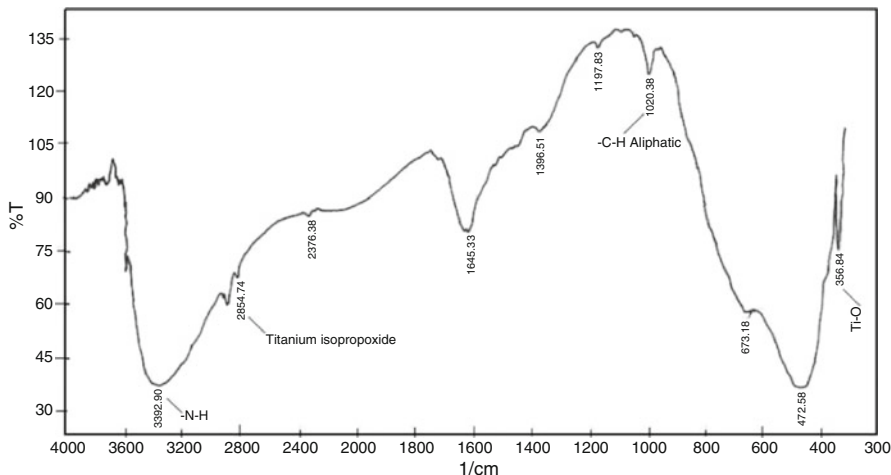


Fig. 4.6 The IR spectrum of pure nano size TiO_2

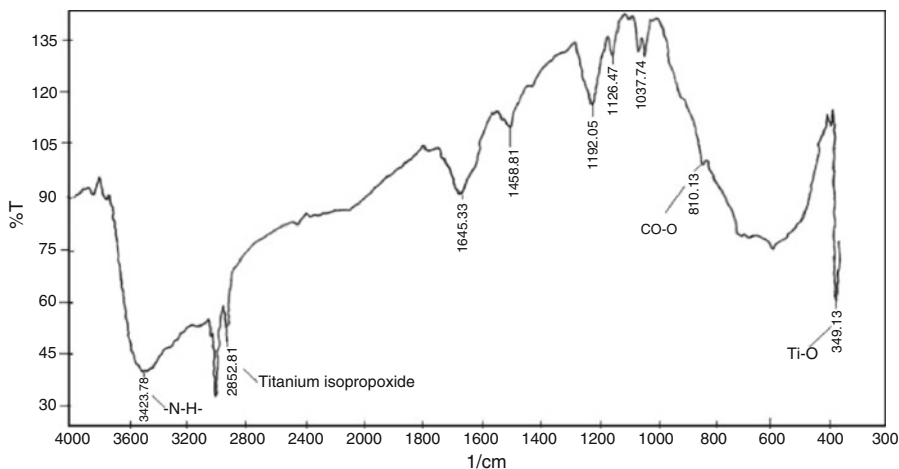


Fig. 4.7 The IR spectrum of nano TiO_2 doped with cobalt

to aliphatic C-H stretching, 3392.90 cm^{-1} due to -NH stretching, and 2854.74 cm^{-1} due to titanium isopropoxide. The data showed that further calcinations were required to obtain pure TiO_2 . The peaks obtained due to titanium isopropoxide, -NH, and -CH aliphatic were found to disappear during the calcinations.

The IR spectrum of doped TiO_2 fired at 250°C (Fig. 4.7) showed peaks at 349.13 cm^{-1} due to a Ti-O stretching, 810.13 cm^{-1} due to Co-O stretching, 1037.34 cm^{-1} due to aliphatic C-H stretching, 3423.78 cm^{-1} due to -NH stretching, and 2852.81 cm^{-1} due to titanium isopropoxide. The data showed that further calcinations were required to obtain pure Co- TiO_2 . The peaks due to titanium isopropoxide, -NH, and -CH aliphatic disappeared during the calcinations.

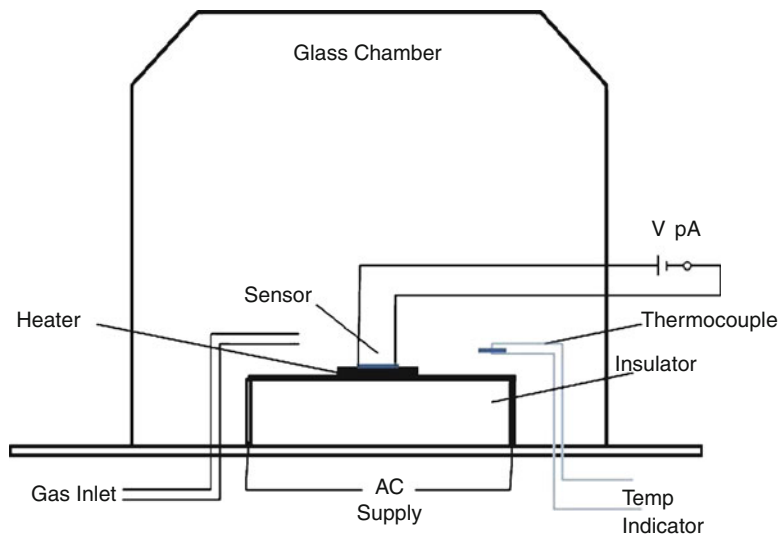


Fig. 4.8 Static gas sensing unit

4.3.6 Gas Sensing Performance of Nano Size TiO_2 and Co-doped TiO_2

4.3.6.1 Details of Gas Sensing System

The gas sensing performance of the thick film was measured by using a static gas sensing unit (Fig. 4.8). This apparatus consists of a heater plate fixed on the base plate to heat the sample under set up to the required temperature. The Cr-Al thermocouple was used to sense the gas at operating temperature of the sensor [3]. The output of the thermocouple was connected to a digital temperature recorder. A gas inlet valve was fitted at one of the ports of the base plate. The required gas concentration inside the static system was achieved by injecting a known volume of a test gas using a gas injecting syringe. A constant voltage was applied to the sensor and current was measured by a digital Pico ammeter. Air was allowed to pass into every gas exposure cycle.

4.3.6.2 Gas Sensitivity of Nano TiO_2 and Co-doped TiO_2 . Mechanism of Gas Sensing

The gas sensing performance of any semi-conducting material depends on factors such as type of semi-conducting material (n-type or p-type), rate of adsorption-desorption process and nature of test gas. In this work the nano TiO_2 which is an n-type semiconductor was prepared. In n-type semiconductors, the electrons are the

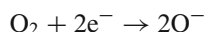
major charge carriers and the holes are the minor charge carriers [3]. When TiO₂ film was exposed to atmospheric oxygen, the oxygen got adsorbed on it by process of reduction to form O⁻ species [12]. The reduction process reduces the electron and conductance decreases. When test gases like H₂S, NH₃, CO, CO₂, and ethanol were exposed on this film, reaction took place between O⁻ species and test gas giving electron back. This increases the conductance of the film. The conductance of all gases between temperature range 100–600°C was measured. The sensitivity was then determined from conductance measurement using the following formula [3]:

$$S = \frac{(R_a - R_g)}{R_a} = \frac{\Delta R_a}{R_a}$$

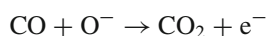
where R_a and R_g are the resistances of the sensor in air and in the test gas, respectively.

For the gas sensing, the sample annealed at 600°C was used because it consisted of the rutile phase of TiO₂ which showed higher semi-conducting property than anatase phase.

The process of adsorption by reduction of oxygen [9] is given by:



In the second step, desorption of O⁻ took place by reaction with various test gases [9, 13] such as:



The gas sensitivity for different gases was determined by passing known amount of gas about 100 ppm in gas sensing system between temperature ranges 100–600°C. The sensitivity for all gases was higher at 300°C as compared to other temperatures because at that temperature the rate of desorption was higher than other temperatures. Thus sensitivity for all gases was measured at 300°C. Among all the gases, H₂S showed the highest sensitivity. The adsorption-desorption is a surface phenomenon which depends on type of surface [4, 14]. In case of nano-TiO₂ surface, the rate of adsorption-desorption would be more for H₂S gas compared to other interfering gases. Hence the change of conductance during oxidation of H₂S gas would be more, which results in greater sensitivity to the H₂S gas [15, 16]. The sensitivity for all gases at 300°C is shown in Fig. 4.9.

The sensitivity of nano TiO₂ was increased by surface modification [17, 18]. The modification was performed by cobalt. Due to surface modification the rate of desorption was increased and the presence of cobalt also increases the semi-conducting

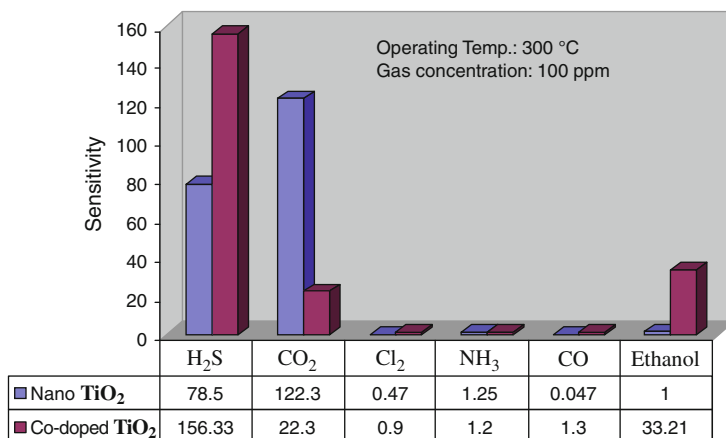


Fig. 4.9 Selectivity of nano TiO₂ and Co-doped nano TiO₂

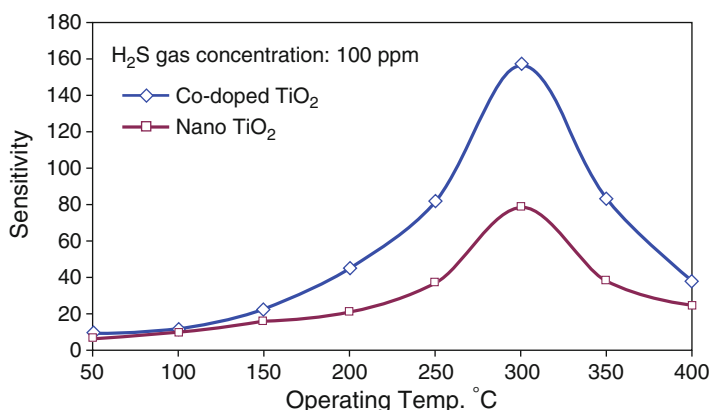


Fig. 4.10 Sensitivity of nano TiO₂ and Co-doped nano TiO₂ at various operating temperatures

property of TiO₂ [7]. Thus Co-TiO₂ showed higher sensitivity for H₂S gas at 300°C than undoped nano TiO₂. The sensitivity for Co doped TiO₂ and for nano TiO₂ was measured for various temperatures. The variation of sensitivity with temperature to both is shown in Fig. 4.10.

4.4 Conclusions

This study shows that cobalt doped material exhibits an increase in gas sensitivity especially for H₂S gas. Compared to doped material, the undoped material showed less response for H₂S. The sol-gel method of synthesis of TiO₂ is very easy as

compared to other methods. The hydrothermal method of doping required less time than other methods and also required amount of metal can be doped by this method.

Acknowledgements The authors thank Dr. V N Pawar and the managing committee of M.V.P. Samaj, Nashik for providing the necessary infrastructure and UGC, New Delhi for providing the funds. Thanks are also due to C-MET Pune and IIT Mumbai for extending the analysis facilities.

References

1. Kohl D (2001) Function and applications of gas sensors. *J Phys D* 34:125–149
2. Han CH, Lee HS, Han SD (2008) Synthesis of nano crystalline TiO_2 by sol-gel combustion hybrid method and its application to dye solar cells. *Bull Korean Chem Soc* 29:1495–1498
3. Gaikwad VB, Kajale DD, Baste YR, Shinde SD, Khanna PK, Pawar NK, Chavan DN, Deore MK, Jain GH (2009) Studies on gas sensing performance of pure and surface modified SrTiO_3 thick film resistors. *Sens Transduc* 6:57–68
4. Kim S (2006) CNT sensor for detecting gases with low adsorption energy by ionization. *J Sens* 6:503–513
5. Kim D-S, Yang J-H, Balaji S, Cho H-J, Kim M-K, Kang D-U, Djaoued Y, Kwon Y-U (2009) Hydrothermal synthesis of anatase nanocrystals with lattice and surface doping tungsten species. *CrystEngComm* 11:1621–1629
6. Jeong ED, Borse PH, Jang JS, Lee JS, Jung O-S, Chang H, Jin JS, Won MS, Kim HG (2008) Hydrothermal synthesis of Cr and Fe co-doped TiO_2 nanoparticle photocatalyst. *J Ceram Process Res* 9:250–253
7. Gaikwad VB, Deore MK, Khanna PK, Kajale DD, Shinde SD, Chavan DN, Jain GH (2009) Studies on gas sensing performance of pure and nano-Ag doped ZnO thick film resistors. *Recent Advances in Sensing Technology Lecture Notes in Electrical Engineering, Part 12*, 49:293–307
8. Cullity BD (1978) *Elements of X-ray diffraction*, 2nd edn. Addison-Wesley Publishing Company Inc., London
9. Shriver DF, Atkins PW (2002) *Inorganic chemistry*, 2nd edn. Oxford University Press, Oxford
10. Ponce MA, Parra R, Savu R, Joanni E, Bueno PR, Cilense M, Varela JA, Castro MS (2009) Impedance spectroscopy analysis of TiO_2 thin film gas sensors obtained from water-based anatase colloids. *Sens Actuat B* 139:447–452
11. Kulkarni SK (2007) *Nanotechnology principles and practices*. Revised edition. Capital Publishing House, New Delhi
12. Jain GH, Gaikwad VB, Kajale DD, Chaudhari RM, Patil RL, Pawar NK, Patil LA (2008) Gas sensing performance of pure and modified barium strontium titanate thick film resistors. *Sens Transduc* 90:160–173
13. Jain GH, Patil LA (2007) CuO-doped BSST thick film resistors for ppb level H_2S gas sensing at room temperature. *Sens Actuat B* 123:246–253
14. Patil DR, Patil LA (2007) Room temperature chlorine gas sensing using surface modified ZnO thick film resistors. *Sens Actuat B* 123:546–553
15. Nakagomi S, Okuda K, Kokubun Y (2003) Electrical properties dependent on H_2 gas for new structure diode of Pt-thin WO_3 -SiC. *Sens Actuat B* 96:364–371
16. Arbab A, Spetz A, Lundstrom I (2008) Evaluation of gas mixtures with high temperature gas sensors based on silicon carbide. *Sens Actuat B* 18–19:562–565
17. Sonawane PS, Patil LA (2007) Effect of nanostochiometry on structural and optical properties of nanostructured Bi_2S_3 thin films prepared chemically at room temperature. *Mater Chem Phys* 105:157–161
18. Jain K, Pant RP, Lakshmikummar ST (2006) Effect of Ni doping on thick film SnO_2 gas sensor. *Sens Actuat B* 113:823–829

Chapter 5

Development of Novel Insect Growth Regulators: Effect of 1-(Substitutedbenzoyl)-3-[(2'-Isopropyl-5'-Methylphenoxy) Acetamino] Thiourea and Urea Derivatives on Total Haemocyte Count of *Dysdercus koenigii*

Chetan M. Zade, Umesh D. Pete, Megharaj S. Kadam,
and Ratnamala S. Bendre

Abstract Insect growth regulators (IGRs) are receiving more practical attention due to low mammalian toxicity and specificity in action. Benzoyl phenyl ureas (BPUs) and N,N'-diacylhydrazines are the two prominent types of IGRs. Hence in present work these two important functional linkages have been assembled with a biologically active natural monoterpene, thymol (2-isopropyl-5-methyl phenol) to generate two novel series of substituted benzoyl thiourea acetyl thymoxy hydrazine (BTATH) [IVa-f] and benzoyl urea acetyl thymoxy hydrazine (BUATH) [Va-f], with aim to generate more target specific molecules for control of different types of insects by keeping ecosystem undisturbed. The synthesized derivatives have been characterized by elemental analysis, IR, mass spectroscopy, ^1H & ^{13}C NMR. All the laboratory experiments were conducted to study the effect of the synthesized compounds on Total Haemocyte Count (T.H.C.) of *Dysdercus koenigii*. T.H.C. in the treated insects increases up to 48 h and then declines upto 96 h. The series exhibited parallel pattern as that of Penfluron a standard IGR. The T.H.C. count is found to be dependent on number, position and type of substituent. Among all the derivatives 2,6-diF-BUATH compound caused a greater reduction in haemocytes in both the sexes at 72 and 96 h after treatment.

5.1 Introduction

Insect growth regulators (IGRs) are considered as new generation of insecticides having great prospects for insect control due to their low mammalian toxicity, biodegradability and specificity in action [1]. The 1-tert-butyl-1,2-diacylhydrazines,

C.M. Zade • U.D. Pete • R.S. Bendre (✉)
School of Chemical Sciences, North Maharashtra University, 425 001 Jalgaon, India
e-mail: zadecm2007@rediffmail.com; umeshdpete@rediffmail.com; bendrs@rediffmail.com

M.S. Kadam
School of Life Sciences, North Maharashtra University, 425 001 Jalgaon, India
e-mail: ms.kadam@gmail.com

discovered by Rohm and Haas Company in the mid-1980s, is a promising class of chemically and mechanistically novel insect control agents first to be commercialized as a lepidopteron-specific insecticide, with a low toxicity profile towards mammals, birds and fishes, as well as towards non target arthropods such as insect pollinators, predators and parasitoids [2, 3].

IGRs mainly affect the development of immature stages and disrupt metamorphosis and reproduction [4, 5] and are becoming more important in the management of insect pests [6]. IGRs include various chemical categories like juvenile hormones, benzoyl phenyl ureas (BPUs), *N,N'*-diacylhydrazines as chitin synthesis inhibitors and nonsteroidal ecdysone agonist as well as triazine derivatives with different modes of action [7–14]. Most of the insect growth regulators (IGRs) with juvenile hormone activity are derived from terpenes and sesquiterpenes [15]. Therefore, as an extension of our work to develop novel IGRs by derivatizing natural monoterpenoids [16], with the aim to produce ecofriendly pest management agents, we have constructed two series viz. benzoyl thiourea acetyl thymoxy hydrazine (BTATH) [IVa-f] and benzoyl urea acetyl thymoxy hydrazine (BUATH) [Va-f] by introducing benzoyl phenyl ureas (BPUs) and *N,N'*-diacylhydrazines linkages in the thymol moiety. The synthesized series of compounds have been fully characterized by spectral methods and investigated to study their effect on Total Haemocyte Counts (T.H.C.), since as a new trend, workers are now trying to use the haemolymph as a medium for controlling insect pest because the changes occurring in the haemolymph are expected to get transferred to other portions of the body. And any change in T.H.C. of particular insect directly or indirectly affects the insect adversely [17, 18].

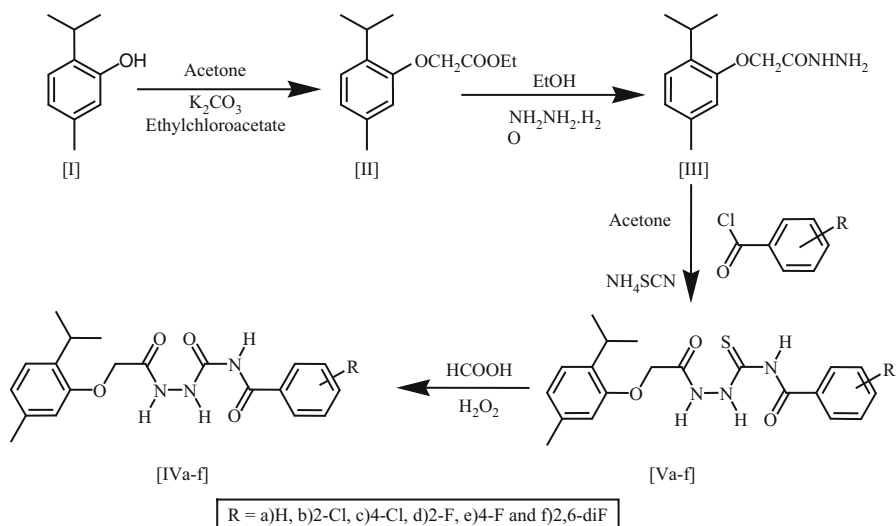
5.2 Methodology

5.2.1 Synthesis and Characterization

A naturally occurring monoterpenoid thymol (2-isopropyl-5-methyl phenol) is suitably derivatized to its thymoxy ethyl acetate, thymoxy acetyl hydrazine and further to a series of substituted BTATH [IVa-f] and BUATH [Va-f] [19–22]. The synthesized compounds have been characterized by IR, ^1H and ^{13}C NMR, LC-MS and elemental analysis (Scheme 5.1).

5.2.2 Synthesis of Ethyl-2(2-Isopropyl-5-Methyl Phenoxy) Acetate (II)

A mixture of thymol (0.1 mol) and anhydrous K_2CO_3 (0.15 mol) in an excess of dry acetone (375 mL) was reflux for 4 h with constant stirring. Into the stirred



Scheme 5.1 Synthetic route for substituted BTATH and BUATH

suspension, ethyl chloroacetate (0.10 mol) in dry acetone (50 mL) was added drop wise during 1 h and the reaction was continued for 4 h. After keeping the reaction temperature overnight, the excess of solvent was removed and the residue was poured onto crushed ice. Further the reaction mixture was stirred for half hour, extracted with diethyl ether, dried with Na_2SO_4 and the solvent was recovered under vacuum to obtain a yellowish oil (Yield: 84.10%) [19].

5.2.3 Synthesis of Ethyl-2(2-Isopropyl-5-Methyl Phenoxy) Acetyl Hydrazine (III)

To the suspension of (II) (0.1 mol) in ethanol was added 99% hydrazine hydrate 5 g (0.1 mol) and the reaction mixture was refluxed for 2 h. The resulting clear solution was concentrated under vacuum to small volume. The suspension was poured on crushed ice and the solid separated was filtered, washed thoroughly with cold water, dried and recrystallized with ethanol (Yield: 72%) [20].

5.2.4 General Synthetic Procedure for BTATH (IVa-f)

To a hot, vigorously stirred solution of ammonium thiocyanate (0.011 mol), in dry acetone (20 mL) was added dropwise substituted benzoyl chloride (0.011 mol) in

dry acetone (10 mL). The reaction mixture was stirred on a hot plate for 1.5 h and to it was added an equimolar quantity of the III (0.011 mol) in dry acetone (10 mL). The mixture was refluxed for 5–6 h at 55°C. The solvent was then removed under reduced pressure and the reaction mixture was diluted with ice cold water (50 mL) to afford the product. The separated solid was purified by recrystallization from hexane-ethyl acetate mixture [21].

Data for BTATH (IVa): Yield 72.00%; white solid. ^1H NMR (300 MHz, CDCl_3): δ 1.237 (6H, d, $(\text{CH}_3)_2\text{CH}$), 1.643 (1H, s, NH-NH-CS), 2.329 (3H, s, CH_3 -Ar), 3.33 (1H, m, Ar- $\text{CH}(\text{CH}_3)_2$), 5.438 (2H, s, Ar-O- CH_2 -CO-), 6.78 (1H, s, Ar-H), 6.84 (1H, d, Ar-H), 7.14 (1H, d, Ar-H), 7.54 (2H, t, Ar-H), 7.64 (1H, t, Ar-H), 8.21 (2H, d, Ar-H), 11.98 (1H, s, Ar-CO-NH-CS). ^{13}C NMR 21.42, 22.93, [2C, $\text{CH}(\text{CH}_3)_2$], 26.74 [1C, Ar- $\text{CH}(\text{CH}_3)_2$], 65.21, (Ar-O- CH_2 -CO-), 154.77, 133.47, 126.43, 122.64, 136.64, 112.48 (Ar-O- CH_2), 134.52, 128.60, 129.02, 131.13 (Ar-C=O), 162.34 (NH-CO-Ar), 165.48 (HN-CS-NH), LC-MS m/z calcd for $\text{C}_{20}\text{H}_{23}\text{N}_3\text{O}_3\text{S}$ (M-H) 384, found 384.1

Data for 2Cl-BTATH (IVb): Yield 74.00%; white solid, ^1H NMR (300 MHz, CDCl_3): δ 1.22 (6H, d, $(\text{CH}_3)_2\text{CH}$), 1.62 (1H, s, NH-NH-CS), 2.33 (3H, s, CH_3 -Ar), 3.29 (1H, m, Ar- $\text{CH}(\text{CH}_3)_2$), 5.37 (2H, s, Ar-O- CH_2 -CO-), 6.74 (1H, s, Ar-H), 6.84 (1H, d, Ar-H), 7.13 (1H, d, Ar-H), 7.42 (1H, t, Ar-H), 7.44 (1H, t, Ar-H), 7.50 (1H, d, Ar-H), 7.89 (1H, d, Ar-H), 11.43 (2H, s, CO-NH-NH-, CS-NH-CO). LC-MS m/z calcd for $\text{C}_{20}\text{H}_{22}\text{ClN}_3\text{O}_3\text{S}$ (M+H) $^+$ 420, found 420.1

Data for 4Cl-BTATH (IVc): Yield 75.00%; white solid, ^1H NMR (300 MHz, CDCl_3): δ 1.23 (6H, d, $(\text{CH}_3)_2\text{CH}$), 1.57 (1H, s, NH-NH-CS), 2.33 (3H, s, CH_3 -Ar), 3.30 (1H, m, Ar- $\text{CH}(\text{CH}_3)_2$), 5.44 (2H, s, Ar-O- CH_2 -CO-), 6.78 (1H, s, Ar-H), 6.84 (1H, d, Ar-H) 7.14 (1H, d, Ar-H), 7.51 (2H, d, Ar-H), 8.15 (2H, d, Ar-H), 11.88 (1H, s, CO-NH-NH-), 13.98 (CS-NH-CO). LC-MS m/z calcd for $\text{C}_{20}\text{H}_{22}\text{ClN}_3\text{O}_3$ (M+H) $^+$ 420, found 420

Data for 2F-BTATH (IVd): 70.00%; white solid, ^1H NMR (300 MHz, CDCl_3): δ 1.25 (6H, d, $(\text{CH}_3)_2\text{CH}$), 1.57 (1H, s, NH-NH-CS), 2.32 (3H, s, CH_3 -Ar), 3.32 (1H, m, Ar- $\text{CH}(\text{CH}_3)_2$), 5.45 (2H, s, Ar-O- CH_2 -CO-), 6.76 (1H, s, Ar-H), 6.83 (1H, d, Ar-H) 7.12 (1H, d, Ar-H), 7.30 (1H, d, Ar-H), 7.14 (1H, t, Ar-H), 7.65 (1H, m, Ar-H), 8.21 (1H, d, Ar-H), 10.08 (1H, s, CS-NH-CO). LC-MS m/z calcd for $\text{C}_{20}\text{H}_{22}\text{FN}_3\text{O}_3\text{S}$ (M+H) $^+$ 403, found 403.8

Data for 4F-BTATH (IVe): Yield 76.00%; white solid, ^1H NMR (300 MHz, CDCl_3): δ 1.23 (6H, d, $(\text{CH}_3)_2\text{CH}$), 2.33 (3H, s, CH_3 -Ar), 3.38 (1H, m, Ar- $\text{CH}(\text{CH}_3)_2$), 4.71 (2H, s, Ar-O- CH_2 -CO-), 6.64 (1H, s, Ar-H), 6.84 (1H, d, Ar-H), 7.14-7.26 (3H, m, Ar-H), 7.93 (2H, m, Ar-H), 9.00 (1H, s, CO-NH-NH-CS), 10.25 (1H, s, CO-NH-NH-CS), 13.36 (1H, s, CS-NH-CO). LC-MS m/z calcd for $\text{C}_{20}\text{H}_{22}\text{FN}_3\text{O}_3\text{S}$ (M+H) $^+$ 404, found 404

Data for 2,6-diF-BTATH (IVf): Yield: 73.00%; white solid, ^1H NMR (300 MHz, CDCl_3): δ 1.22 (6H, d, $(\text{CH}_3)_2\text{CH}$), 1.66 (1H, s, NH-NH-CS), 2.34 (3H, s, CH_3 -Ar), 3.33 (1H, m, Ar- $\text{CH}(\text{CH}_3)_2$), 5.30 (2H, s, Ar-O- CH_2 -CO-), 6.72 (1H, s, Ar-H),

6.84 (1H, d, Ar-H), 7.04 (1H, m, Ar-H), 7.14 (1H, d, Ar-H), 7.72 (2H, m, Ar-H), 12.75 (1H, s, CO-NH-NH-CS), 13.64 (1H, s, CS-NH-CO). LC-MS m/z calcd for C₂₀H₂₁F₂N₃O₃S (M-H)⁻ 421.47, found 420

5.2.5 General Synthetic Procedure for BUATH (Va-f)

Benzoyl thymoxy acetyl hydrazine thioureas were dissolved in mixture of DMF (10 mL) and formic acid (1 mL). After addition of hydrogen peroxide (30%, 2.5 mL), the solution was stirred for 24 h at room temperature and poured onto crushed ice. The precipitate was collected, dried and recrystallized from ethanol [22].

Data for BUATH (Va): Yield 78.00%; white solid, ¹H NMR (300 MHz, CDCl₃): δ 1.23 (6H, d, (CH₃)₂ CH), 1.58 (2H, s, CO-NH-NH-CO, CO-NH-NH-CO), 2.33 (3H, s, CH₃-Ar), 3.33 (1H, m, Ar-CH(CH₃)₂), 5.26 (1H, s, CO-NH-CO), 5.44 (2H, s, O-CH₂-CO), 6.77 (1H, s, Ar-H), 6.84 (1H, d, Ar-H), 7.14 (1H, d, Ar-H), 7.54 (2H, t, Ar-H), 7.64 (1H, d, Ar-H), 8.14 (2H, m, Ar-H). LC-MS m/z calcd for C₂₀H₂₃N₃O₄ (M+H)⁺ 369.42, found 370

Data for 2Cl-BUATH (Vb): Yield 74.00%; white solid, ¹H NMR (300 MHz, CDCl₃): δ 1.22 (6H, d, (CH₃)₂ CH), 1.56 (2H, s, CO-NH-NH-CO, CO-NH-NH-CO), 2.32 (3H, s, CH₃-Ar), 3.29 (1H, m, Ar-CH(CH₃)₂), 5.39 (2H, s, O-CH₂-CO), 6.74 (1H, s, Ar-H), 6.82 (1H, d, Ar-H), 7.12 (1H, d, Ar-H), 7.40-7.47 (2H, m, Ar-H), 7.50 (1H, d, Ar-H), 7.88 (1H, d, Ar-H), 10.90 (1H, s, CO-NH-CO). LC-MS m/z calcd for C₂₀H₂₂ClN₃O₄ (M-H)⁻ 403.87, found 401.9

Data for 4Cl-BUATH (Vc): Yield 75.00%; white solid, ¹H NMR (300 MHz, CDCl₃): δ 1.23 (6H, d, (CH₃)₂ CH), 2.32 (3H, s, CH₃-Ar), 3.28 (1H, m, Ar-CH(CH₃)₂), 4.68 (2H, s, O-CH₂-CO), 6.67 (1H, s, Ar-H), 6.84 (1H, d, Ar-H), 7.13 (1H, d, Ar-H), 7.44 (2H, m, Ar-H), 7.87 (2H, m, Ar-H), 8.36 (1H, d, CO-NH-NH-CO), 9.19 (1H, s, CO-NH-NH-CO), 10.37 (1H, s, CO-NH-CO). LC-MS m/z calcd for C₂₀H₂₂ClN₃O₄ (M-H)⁻ 403.87, found 401.8

Data for 2F-BUATH (Vd): Yield 70.00%; white solid, ¹H NMR (300 MHz, CDCl₃): δ 1.23 (6H, d, (CH₃)₂ CH), 1.63 (1H, s, CO-NH-NH-CO), 2.33 (3H, s, CH₃-Ar), 3.32 (1H, m, Ar-CH(CH₃)₂), 5.45 (2H, s, O-CH₂-CO), 6.77 (1H, s, Ar-H), 6.80 (1H, d, Ar-H), 7.13 (1H, d, Ar-H), 7.23 (1H, d, Ar-H), 7.37 (1H, t, Ar-H), 7.65 (1H, m, Ar-H), 8.21 (1H, m, Ar-H), 10.90 (1H, s, CO-NH-CO). LC-MS m/z calcd for C₂₀H₂₂ClN₃O₄ (M+H)⁺ 387.41, found 388

Data for 4F-BUATH (Ve): Yield 76.00%; white solid, ¹H NMR (300 MHz, CDCl₃): δ 1.23 (6H, d, (CH₃)₂ CH), 1.63 (3H, s, CO-NH-NH-CO), 2.33 (3H, s, CH₃-Ar), 3.33 (1H, m, Ar-CH(CH₃)₂), 5.43 (2H, s, O-CH₂-CO), 6.78 (1H, s, Ar-H), 6.84 (1H, d, Ar-H), 7.14-7.22 (3H, m, Ar-H), 8.28 (2H, m, Ar-H). ¹³C NMR 21.19, 22.69, [2C,CH-(CH₃)₂], 26.49 [1C, Ar-CH-(CH₃)₂], 65.00, (Ar-O-CH₂-

CO-), 154.58, 134.23, 126.13, 122.32, 136.38, 112.33 (Ar-O-CH₂), 127.64, 131.03, 115.56, 162.15, 115.85, 131.15 (Ar-C=O), 164.43 (N-CO-Ar), 161.37 (HN-CO-NH), LC-MS m/z calcd for C₂₀H₂₂FN₃O₄ (M-H)⁻ 387.41, found 387

Data for 2,6-diF-BUATH (Vf): Yield: 73.00%; white solid, ¹H NMR (300 MHz, CDCl₃): δ 1.22 (6H, d, (CH₃)₂ CH), 1.66 (1H, s, CO-NH-NH-CO), 2.34 (3H, s, CH₃-Ar), 3.32 (1H, m, Ar-CH(CH₃)₂), 5.31 (2H, s, O-CH₂-CO), 6.71-7.52 (6H, m, Ar-H), 12.54 (2H, s, CO-NH-NH-CO, CO-NH-CO). LC-MS m/z calcd for C₂₀H₂₁F₂N₃O₄ (M+H)⁺ 405.40, found 404

5.3 Biological Activities

5.3.1 Effect of Synthesized Compounds (BTATH & BUATH) on Total Haemocyte Count of *Dysdercus koenigii*

Fully matured adult bugs (*Dysdercus koenigii*) were reared in laboratory at 28°C and a photoperiod of 14–16 h day length. The insects were treated by applying topically (on the ventral side) 2 μl 100 ppm solution of each compound. Concentration was prepared by dissolving 0.001 g in 10 cc of acetone. Treated insects were taken at 24, 48, 72 and 96 h interval and haemocyte slides were prepared for both living and fixed conditions for Total Haemocyte Count [18, 23].

5.4 Results and Discussion

Effect on T.H.C.: In the case of control males the T.H.C. was 8,000 ± 200 cells/mm³ and in females it was 10,000 ± 200 cells/mm³. The T.H.C. was always higher in females as compared to males. During the course of study after treatment with each derivative a considerable increase in the T.H.C. was observed up to 48 h, and then a significant decrease in T.H.C. up to 96 h was noted in both the sexes (Tables 5.1 and 5.2). It is interesting to note that the T.H.C. in males was lower than that of the female bugs, and it remained same so even after the treatment. The pattern of results, as depicted in Figs. 5.1 and 5.2, is found to be similar to the results observed in *Dysdercus koenigii* after microwave exposure [24], treatment with *T. arjuna* barks extract [23] as well as Penfluron, a standard IGR known for chitin inhibiting activity having similar structural units to our compounds [16, 18]. The solvent acetone was found to be totally ineffective in showing any effect on haemocyte count.

From the results it can be observed that both substituted benzoyl thiourea acetyl thymoxy hydrazine (BTATH) [IVa-f] and benzoyl urea acetyl thymoxy hydrazine (BUATH) [Va-f] show remarkable effect on T.H.C. at lower doses. Based on the total haemocyte count and its comparison with the standard IGR, Penfluron, the following structure activity relationship could be established.

Table 5.1 Effect of synthesized compounds (BTATH) (I Va-f) on total haemocyte count (cells/mm³) in adult *Dysdercus koenigii*

Derivative code	Species	Time period after treatment					
		0 h	24 h	48 h	72 h	96 h	
BTATH	Male	8,000 ± 250	8,800 ± 500	9,600 ± 400	5,600 ± 500	3,000 ± 200	
	Female	10,200 ± 300	10,850 ± 300	12,100 ± 300	6,650 ± 400	6,200 ± 400	
2Cl- BTATH	Male	8,200 ± 200	9,800 ± 360	11,270 ± 120	4,300 ± 240	2,100 ± 300	
	Female	10,400 ± 200	11,300 ± 320	13,800 ± 350	5,800 ± 580	4,200 ± 140	
4Cl- BTATH	Male	8,000 ± 300	9,000 ± 300	10,750 ± 240	5,150 ± 300	2,600 ± 150	
	Female	10,200 ± 100	11,000 ± 100	12,500 ± 200	6,200 ± 200	4,950 ± 160	
2F- BTATH	Male	8,200 ± 340	10,950 ± 160	12,400 ± 170	4,040 ± 150	1,700 ± 100	
	Female	10,400 ± 100	11,850 ± 100	14,700 ± 300	5,650 ± 200	3,750 ± 200	
4F- BTATH	Male	8,200 ± 390	10,700 ± 130	11,650 ± 200	4,100 ± 140	2,000 ± 400	
	Female	10,200 ± 340	11,400 ± 150	14,230 ± 400	6,600 ± 260	3,900 ± 330	
2,6di-F- BTATH	Male	8,400 ± 400	11,800 ± 360	13,200 ± 250	3,370 ± 400	1,600 ± 100	
	Female	10,600 ± 300	12,600 ± 400	15,920 ± 180	4,800 ± 100	3,120 ± 170	

Table 5.2 Effect of synthesized compounds (BUATH) on total haemocyte count (cells/mm³) in adult *Dysdercus koenigii*

Derivative code	Species	Time period after treatment					
		0 h	24 h	48 h	72 h	96 h	
BUATH	Male	8,000 ± 300	8,800 ± 220	9,600 ± 450	5,160 ± 300	2,800 ± 500	
	Female	10,200 ± 200	10,850 ± 150	12,100 ± 380	6,050 ± 400	4,460 ± 350	
2Cl-BUATH	Male	8,200 ± 500	9,800 ± 100	11,270 ± 300	4,000 ± 100	2,040 ± 160	
	Female	10,400 ± 300	11,300 ± 360	13,800 ± 200	5,100 ± 130	3,300 ± 180	
4Cl- BUATH	Male	8,000 ± 340	9,000 ± 230	10,750 ± 350	4,050 ± 300	2,080 ± 450	
	Female	10,200 ± 120	11,000 ± 250	12,500 ± 100	5,240 ± 400	3,480 ± 400	
2F- BUATH	Male	8,200 ± 140	10,950 ± 100	12,400 ± 450	3,850 ± 100	1,670 ± 200	
	Female	10,400 ± 280	11,850 ± 150	14,700 ± 230	4,550 ± 490	3,020 ± 300	
4F- BUATH	Male	8,200 ± 250	10,700 ± 200	11,650 ± 140	3,900 ± 170	1,890 ± 160	
	Female	10,200 ± 540	11,400 ± 430	14,230 ± 300	4,760 ± 400	3,100 ± 150	
2,6di-F- BUATH	Male	8,400 ± 300	11,800 ± 190	13,200 ± 100	3,080 ± 200	1,300 ± 170	
	Female	10,600 ± 540	12,600 ± 100	15,920 ± 340	4,330 ± 120	2,850 ± 400	
Thymol (SM)	Male	8,400 ± 200	8,600 ± 180	8,800 ± 160	6,400 ± 150	4,800 ± 170	
	Female	10,200 ± 100	10,400 ± 300	10,600 ± 160	7,200 ± 210	6,400 ± 500	
Acetone	Male	8,000 ± 200	8,200 ± 420	8,200 ± 280	8,000 ± 130	7,800 ± 300	
	Female	10,000 ± 300	10,400 ± 100	10,400 ± 100	10,200 ± 600	10,000 ± 300	
Std (Penfluron)	Male	8,200 ± 100	13,000 ± 150	17,400 ± 100	3,400 ± 200	1,000 ± 210	
	Female	10,600 ± 100	15,400 ± 360	21,400 ± 100	7,200 ± 240	3,200 ± 100	

Fig. 5.1 Effect of synthesized compounds (BTATH and BUATH) on total haemocyte count (Cells/mm³) in male *Dysdercus koenigii*

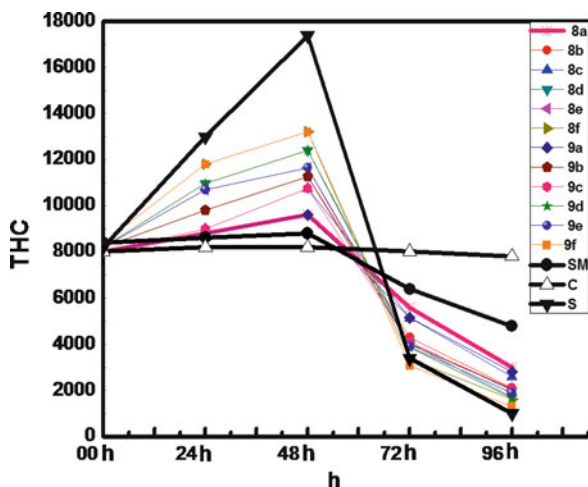
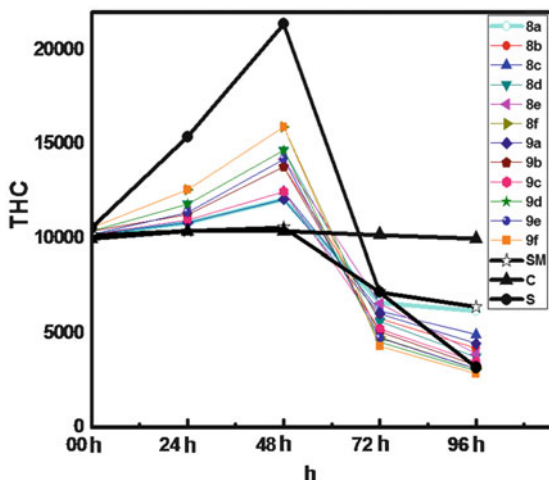


Fig. 5.2 Effect of synthesized compounds (BTATH and BUATH) on total haemocyte count (Cells/mm³) in female *Dysdercus koenigii*



5.4.1 Structural Activity Relationship

1. Benzoyl urea acetyl thymoxy hydrazine (BUATH) compounds showed higher T.H.C. value than benzoyl thiourea acetyl thymoxy hydrazine (BTATH) compounds at 48 h and similarly BUATH also showed lower T.H.C. value than BTATH compounds at 96 h.
2. In both the series the F-substituted derivatives exhibited higher and lower T.H.C. value than Cl-substituted derivatives at 48 and 96 h respectively.
3. As far as both the series are concerned, ortho substitution has given higher and lower T.H.C. value than para substitution at 48 and 96 h respectively.

4. 2,6-diF-derivatives showed the highest effect on T.H.C. amongst respective series.
5. All the derivatives have conferred higher activity than parent compound thymol.
6. In both the series 2,6-diF-benzoyl urea acetyl thymoxy hydrazine (2,6-diF-BUATH) demonstrated highest effect while benzoyl thiourea acetyl thymoxy hydrazine (BTATH) lowest effect on T.H.C.

Penfluron, a well known IGR has been studied in detail for its mechanism of action and it has been mentioned that Penfluron which has a chitin inhibiting activity probably functions like toxins [25]. Penfluron inhibiting the formation of chitin in insects might utilize the haemocytes from haemolymph thus causing decline in T.H.C. All the compounds studied here have demonstrated similar pattern of effect on T.H.C. as that of Penfluron. Therefore, it can be concluded that they have similar mechanism of action as that of Penfluron [18].

The parent compound thymol exhibited the least effect on T.H.C. count indicating that its structural modification to BUATH and BTATH has substantially improved the effectiveness as pest management agents.

Acknowledgement We are thankful to University Grants Commission, New Delhi, India, for the (UGC-RFSMS) Research Fellowship for Sciences and Meritorious Students and Research funding.

References

1. Fournet F, Sannier C, Money N (1993) Effect of insect growth regulators OMS 2017 and Diflubenzuron on the reproductive potential of *Aedes aegypti*. *J Am Mosq Control Assoc* 9:426–430
2. Wing D (1988) RH5849, a nonsteroidal ecdysone agonist effects on a *Drosophila* cell line. *Science* (Washington, District of Columbia) 241:467–469
3. Wing D, Slaweki A, Carlson R (1988) RH5849, a nonsteroidal ecdysone agonist effects on *Lepidoptera*. *Science* (Washington, District of Columbia) 241:470–472
4. Graf F (1993) The roles of insect growth regulators in arthropod control. *Trends Parasitol* 9:471–474
5. Retnakaran A, Granett J, Ennis T (1985) Insect growth regulators. *Comprehensive insect physiology, biochemistry and pharmacology*. Pergamon Press, New York
6. Grenier S, Grenier M (1993) Fenoxycarb a fairly new insect growth regulator a review of its effects on insects. *Ann Appl Biol* 122:369–403
7. Cao S, Qian H, Song H (2001) *N'*-*tert*-Butyl-*N'*-aroyl-*N'*-(alkoxycarbonylmethyl)-*N'*-aroylhydrazines, a novel nonsteroidal ecdysone agonist syntheses, insecticidal activity, conformational and crystal structure analysis. *Can J Chem* 79:272–278
8. Chen H, Zhang N (1999) The synthesis and larvicidal activity of *N*-aroyl-*N'*-(5-aryl-2-furoyl) ureas. *Pestic Sci* 52:282–286
9. Li H, Ling Y, Yang L (2003) Synthesis of novel benzoyl ureas containing thiadiazole and their insecticidal activity. *Huaxue Tongbao* 66:333–336
10. Oberlander H, Silhacek L (1998) Mode of action of insect growth regulators in lepidopteran tissue culture. *Pestic Sci* 54:300–302
11. Qian H (1996) Molecular modeling study on the structure–activity relationship of substituted dibenzoyl-1-*tert*-butylhydrazines and their structural similarity to 20-hydroxyecdysone. *J Agric Food Chem* 44:1538–1542

12. Qian H (1999) Quantitative studies on structure-activity relationship of sulfonylurea and benzoylphenylurea type pesticides and their substituents bioisosterism using synthons activity contribution. *J Agric Food Chem* 47:4415–4418
13. Xu Y, Qian H, Li Z, Huang C, Chen G (2003) Synthesis and insecticidal activity of new substituted *N*-aryl-*N'*-benzoylthiourea compounds. *J Fluor Chem* 121:51–54
14. Zhao L, Li J, Yang F (2007) Synthesis and insecticidal activity of chromanone and chromone analogues of diacylhydrazines. *Bioorg Med Chem* 15:1888–1895
15. Pallos F, Letchworth P, Menn J (1976) Novel nonterpenoid insect growth regulators. *J Agric Food Chem* 24:218–221
16. Zade C, Pete U, Dikundwar A, Bendre R (2010) (Z)-2-(2-Isopropyl-5-methylphenoxy)-N-(2-oxoindolin-3-ylidene) acetohydrazide. *Acta Crystallogr E* 66:01614
17. Pugazhvendan S, Soundararajan M (2009) Effect of penfluron on total haemocyte count of *Chrysocoris purpureus*. *Middle East J Sci Res* 4:338–340
18. Prakash B, Bhargava S, Rawat K (2007) Effect of penfluron on total haemocyte count of *Dysdercus koenigii*. *Asian J Exp Sci* 21:151–154
19. Shah H, Vashi S, Mehta S (1996) Synthesis of 2,5-disubstituted-1,3,4-oxadiazole, 1,5-disubstituted -2-mercapto-1,3,4-triazole and 2,5-disubstituted-1,3,4-thiadiazole as potential antimicrobial agents. *Indian J Chem* 35B:111–115
20. Nargud G, Reddy N, Hariprasad V (1996) Synthesis and antibacterial activity of a series 1-aryl-2-mercapto-5-[4-acetamido phenoxyethyl]-1,3,4-triazoles and 2-[4-(acetamido phenoxy) carbonyl]-3,4,5-trisubstituted pyrazoles. *Indian J Chem* 35B:499–502
21. Kachroo P, Kapoor K, Somal P, Gupta R (1991) Synthesis and antimicrobial activity of some 5-Aryl-2-[*N*-(5-nitrofurfurylidene)amino] and 5-Aryl-2-(*N*-thiocarbonylamino)-1,3,4-oxadiazoles. *J Indian Chem Soc* 68:104–106
22. Muccioli G, Fazio N, Scriba GK, Poppitz W, Cannata F, Poupaert JH, Wouters J, Lambert D (2006) Substituted 2-thioxolidin-4-ones and imidazolidin-2,4-diones as fatty acid amide hydrolase inhibitors templates. *J Med Chem* 49:417–425
23. Karnavat A (2004) Effect of bark extract of *Terminalia arjuna* on various biological activities of *Dysdercus koenigii*. PhD thesis, Maharshi Dayanand Saraswati University, Ajmer
24. Bhalerao S. (1992) Use of Microwaves an alternative safe technology for insect pest control. PhD thesis, Maharshi Dayanand Saraswati University, Ajmer
25. Lim J, Lee S (1982) The toxicity of difluorobenzuron to *Oxya japonica* (Willemse) and its effects on moulting. *Pestic Sci* 13:537–544

Chapter 6

Preliminary Catalytic Studies Using Tyrosine and Phenylalanine Analogues on Selected Baylis-Hillman and Michael Reactions

Prakashanand Caumul, Nausheen Joondan, Anuradha Tuhadoo, and Thavinash Jhowry

Abstract A range of surfactant analogues were synthesized from *L*-Tyrosine and *L*-Phenylalanine and tested for their catalytic and biological activity. Analogues (6)–(9) were synthesized using the *L*-Tyrosine backbone whilst (10)–(12) were synthesized from *L*-Phenylalanine. Preliminary catalytic studies using both the analogues of *L*-Tyrosine and *L*-Phenylalanine were carried out on three main reactions: Baylis-Hillman, Michael addition and dipolar additions. For the Baylis-Hillman, the reaction between benzaldehyde and methyl acrylate was investigated where yields as high as 15% were generated when using (9) as catalyst. A phase-transfer solvent system was found to be the best medium to carry out these reactions. For the Michael addition reactions between dialkyl malonates and cyclic pentenones, the best yield was 70%, using *L*-Phenylalanine as catalyst. Selectivity enhancement was observed when adding an extended chain onto cyclopentenone where values of up to 69% e.e to the *S*-isomer were obtained using (12). Interestingly for the reaction between cyclopentenone and diethylmalonate higher and reversed selectivities (as high as 76% e.e, *R*-isomer) were observed using the Tyrosine analogues (6) and (8). The phenylalanine analogues (10)–(12) were found to enhance the dipolar addition reaction between sarcosine and *N*-ethyl maleimide generating yields as high as 85% when using catalytic amounts of (12). Finally biological analysis showed that *L*-phenylalanine and *N*-propanoyl *L*-phenylalanine gave moderate activity for a range of gram (+) and gram (–)-bacteria.

6.1 Introduction

Surfactants are amphiphilic molecules that have gained increasing importance in the field of asymmetric synthesis [1–3]. The use of micellar media as a synthetic tool can be used to generate reaction control and selectivity as a result of their

P. Caumul (✉) • N. Joondan • A. Tuhadoo • T. Jhowry
Department of Chemistry, Faculty of Science, University of Mauritius, Réduit, Mauritius
e-mail: p.caumul@uom.ac.mu

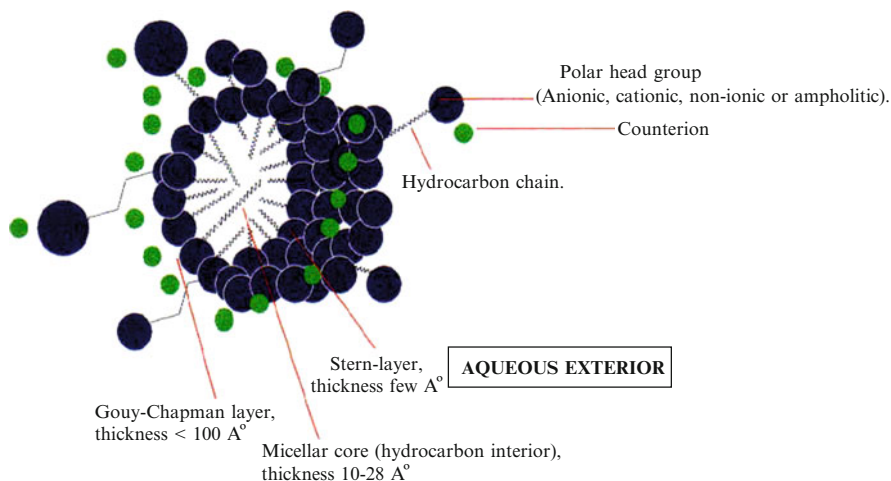


Fig. 6.1 Representation of surfactant aggregation to form a micelle in aqueous media

properties in substrate solubilisation, pre-orientation and cage effects to generate chiral products (Fig. 6.1). This method can thus provide a cleaner and viable alternative to generate chiral systems which are important in the areas of catalysis as well as medicine (in making bioactive drugs) [1–3].

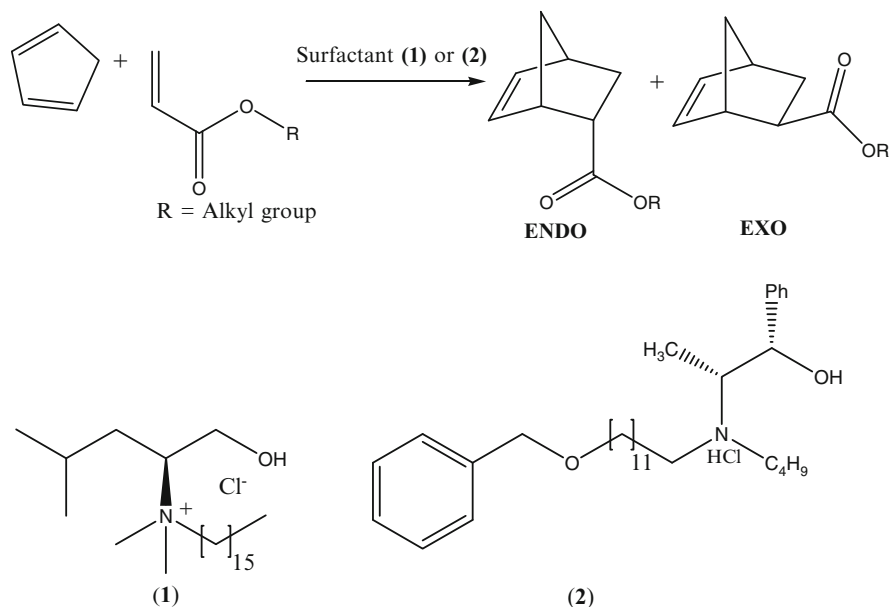
The amphiphilic nature of surfactants makes them useful in making drug carrier lipids as well as in environmental research to generate metal chelating ligands in order to bind onto heavy metals for their elimination from contaminated aqueous media [4–8].

Over the years, organic chemistry has generally relied on significant quantities of toxic solvents and reagents such as Lewis acids, e.g. TiCl_4 to enhance enantiomeric reactions. Hence a more environmentally friendly technology in chemistry is now required to run key reactions which can be carried out in aqueous media. This is of particular importance since there is pressing need by both the government and industry to develop more environmentally friendly technology in organic synthesis [3]. There are two advantages of using surfactants to enhance this. Firstly they are cheap to make and secondly, they can be recycled and re-used.

In addition, they have been reported to provide good enantioselectivity, regioselectivity, and stereochemistry when used as catalysts. The concentrations at which surfactants have been used catalytically are at or above the critical micelle concentration (CMC), i.e. the concentration at which micelles have been formed after the surfactant molecule has aggregated onto the surface to form one monolayer [3].

Micelles have also been reported to produce a number of effects that can influence the reaction outcome. This includes pre-orientation, and cage effects. From this and their amphiphilic nature, surfactants have the ability to solubilise substrates, as well as concentrate and pre-orientate reactants within the micellar core [3].

Currently, there are very few reported applications using chiral micellar media as catalysts. However, examples of their uses have included some excellent work carried out by Hailes and Diego-Castro on Diels-Alder reactions [1] as well as studies on the diethyl zinc addition of benzaldehyde carried out by Hailes and Madden [2]. In these cases, the surfactants were used at concentrations above the CMC level generating very good yields and selectivity. It is worth noting that Hailes et al. designed a range of surfactants using the β -amino alcohol backbone [1, 2] (Scheme 6.1).



Scheme 6.1 Using micellar media as catalyst for the Diels-Alder reaction between cyclopentadiene and alkyl acrylate

This was because substantial work had been carried out by Soai and Kitamura in the early 1990's using β -amino alcohols as catalysts [9–12]. These types of materials were found to be excellent chiral catalytic systems generating high enantioselectivities especially when they were used for the addition reaction between benzaldehyde and diethyl zinc [9–13]. It was therefore envisaged that by addition of aliphatic chains to a β -amino alcohol backbone, the reaction rate and selectivity would be enhanced due to substrate solubilisation within the micellar core of the catalyst.

Since several publications in the early 1990s have made use of derivatives of ephedrine and norephedrine as catalysts [9, 10], investigations were underway to synthesise derivatives similar to these compounds. Hence phenylalanine was selected which consists of the aromatic moiety similar to that of both ephedrine and norephedrine (2) since it was important to know what effect the absence and presence of an extra OH functional moiety attached to the aromatic ring has on reaction selectivity as well as on biological activity. With this view, tyrosine was selected.

The catalytic and biological activity of each of the derivatives of phenylalanine and tyrosine *en-route* to the synthesis of the final analogues were tested to identify which functional groups were responsible for yield and enantioselectivity enhancement as well as biological activity.

6.2 Materials and Methods

The chemicals and reagents used were of analytical grade and were purchased from Sigma-Aldrich Co. Ltd and Acros-Fisher Scientific, UK. All the chemicals were purified before use. THF was freshly distilled and dried using molecular sieves (4 Å) prior to use. Both ethyl acetate and hexane were distilled prior to use. All air and moisture sensitive reactions were carried out under an inert nitrogen atmosphere.

Infrared spectra (IR) were recorded on an Avarar 320 FTIR spectrometer in the range of 4,000–500 cm^{-1} . ^1H NMR and ^{13}C NMR spectra were recorded in 5 mm outer diameter tubes in CDCl_3 , or D_2O as solvent at room temperature using a FT Bruker 250 MHz spectrometer. The chemical shift (δ) of each peak was assigned relative to tetramethylsilane (TMS). Elemental analysis was obtained using a LECO 932 CHNS Mattson 1,000 Spectrophotometer. Melting point analysis was carried out using an Electrothermal melting point apparatus and the value was quoted uncorrected to the nearest degree. Optical rotations were determined using a Billingham-Stanley Model D optical activity polarimeter.

Chromatography refers to using a “flash column” technique over silica gel (70–230 mesh). Thin layer chromatography (TLC) was performed on a glass backed or on plates precoated with silica. Visualisation was achieved by exposure to an iodine atmosphere or with ultraviolet light (254 nm).

6.2.1 Propanoyl Chloride (4)

Thionyl chloride (40 ml, 536 mmol) was added dropwise to propanoic acid (40 ml, 402 mmol) at room temperature. The reaction mixture was refluxed for 3 h under inert atmosphere.

The resulting solution was then distilled to obtain the title compound as a colourless solution (6.2 g, 85%).

$\nu_{\text{Max}}/\text{cm}^{-1}$: 2989, 1788.

^1H NMR (CDCl_3) δ (ppm): 1.15 (3H, t, J 7.3 Hz) 2.87 (2H, m).

^{13}C NMR (CDCl_3) δ (ppm): 9.7, 41.1, 174.9.

6.2.2 Bromoheptane (5)

To heptanol (10 ml, 86 mmol) in toluene (50 ml), hydrogen bromide (60% aq solution) (68 ml, 90 mmol) was added and the mixture was heated at reflux for 24 h.

The reaction was monitored by TLC. The organic layer was extracted with ether (3 × 50 ml) and washed with sodium hydroxide (1 M) and saturated brine (10 ml).

The organic layer was removed under *vacuo* and purified by flash chromatography to yield the title compound as a pale brown liquid (9 g, 75%). R_f 0.5 Hexane:ethyl acetate 1:2.

$\nu_{\max}/\text{cm}^{-1}$: 2958, 2856.

$^1\text{H NMR}$ (CDCl_3) δ (ppm): 0.89 (2H, d, J 6.75 Hz), 1.31 (8H, m), 1.85 (2H, m), 3.44 (2H, t, J 7 Hz).

$^{13}\text{C NMR}$ (CDCl_3) δ (ppm): 14.1, 22.6, 28.2, 28.5, 31.7, 32.9, 34.1.

6.2.3 *L*-Tyrosine methyl Ester Hydrochloride (6)

To a stirred, ice cold suspension of *L*-tyrosine (10.05 g, 50 mmol) in absolute methanol (200 ml), thionyl chloride (10 ml, 138 mmol) was added dropwise. The temperature of the reaction mixture was maintained below 0°C during addition. The pale yellow solution was left to stir for 18 h at room temperature and then the excess methanol was evaporated in *vacuo* to give the crude product.

The material was purified by washing with diethyl ether to give a white solid. This was recrystallised from ethyl acetate to yield the title compound as colourless crystals (12.50 g, 95%). M.pt. 191–193°C.

$\nu_{\max}/\text{cm}^{-1}$ (KBr): 3382, 2906, 1742, 1591, 832.

$^1\text{H NMR}$ (D_2O) δ (ppm): 2.95 (1H, m, J 14.7 Hz), 3.18 (1H, m, J 14.7 Hz), 3.67 (3H, s, OCH_3), 4.20 (1H, m, J 13 Hz), 6.72 (2H, d, J 8.2 Hz), 7.02 (2H, d, J 8.2 Hz).

$^{13}\text{C NMR}$ (D_2O) δ (ppm): 34.8, 53.5, 54.2, 115.9, 125.4, 130, 155.2, 170.3.

Anal. calc. for $\text{C}_{10}\text{H}_{14}\text{O}_3\text{N}^+\text{Cl}^-$: C, 51.94; H, 6.06; N, 6.06; found C, 51.01, H 5.90; N, 6.50%.

$[\alpha]_{\text{D}} = +75.0^\circ$ (c 3 in pyridine at 25°C).

6.2.4 *N*-(Propanoyl) Tyrosine Methyl Ester (7)

L-Tyrosine methyl ester hydrochloride (6) (1.0 g, 4.3 mmol) was dissolved in THF (Tetrahydrofuran) (75 ml) at room temperature. Triethylamine (0.9 ml, 6.5 mmol) was added and was left to stir for 1 h. Propanoyl chloride (0.4 ml, 4.4 mmol) was added dropwise over a period of 10 min. When the addition was completed, a catalytic amount of DMAP (4-dimethyl amino pyridine) was added to the mixture and the reaction was heated at reflux for 3 h. The reaction mixture was quenched with water (100 ml) and the aqueous and organic layers were separated. The aqueous layer was washed with ethyl acetate (4 × 50 ml) and the combined organic extracts were washed with sodium hydrogen carbonate (5%, 50 ml). The organic layer was dried over anhydrous magnesium sulphate and the solvent was removed in *vacuo*

and purified using flash chromatography (petroleum: ethyl acetate, 1:1) to yield the title compound as a pale cream solid (0.08 g, 8%) R_f 0.30, petroleum: ethyl acetate, 1:1. M.pt. 60–63°C.

$\nu_{\max}/\text{cm}^{-1}$ (KBr): 3316, 3252, 1734, 1655, 1620, 1260, 835.

$^1\text{H NMR}$ (CDCl_3) δ (ppm): 1.09 (3H, t, J 7.5 Hz), 2.17 (2H, m), 2.99 (2H, m), 3.71 (3H, s, OCH_3), 4.83 (1H, m), 5.90 (1H, d, J 7.5 Hz, N-H), 6.69 (2H, d, J 8.5 Hz), 6.89 (2H, d, J 8.5 Hz).

6.2.5 *N-Propanoyl O-Propanoyl Tyrosine Methyl Ester (8)*

L-Tyrosine methyl ester hydrochloride (**6**) (3.01 g, 13 mmol) was dissolved in THF (75 ml) at room temperature. Triethylamine (3.6 ml, 25.6 mmol, 2 eq) was added and was stirred for 1 h. A further 2 equivalents of triethylamine (3.6 ml, 25.6 mmol) followed by 2 equivalents of propanoyl chloride (2.3 ml, 26 mmol) was used. When the addition was completed, a catalytic amount of DMAP was added to the mixture and the reaction was refluxed at 70°C for 12 h. The reaction mixture was quenched with water (100 ml) and the aqueous and organic layers separated. The aqueous layer was washed with ethyl acetate (4×100 ml) and the combined organic extracts were washed with sodium hydrogen carbonate (5%, 50 ml). The organic layer was dried over anhydrous magnesium sulphate and the solvent was removed in *vacuo* and purified by flash chromatography (R_f 0.82), (hexane: ethyl acetate, 1:4) to yield a pale brown oil. This material was precipitated in hexane and filtered to yield the title compound as a light brown solid (2.37 g, 60%). M.pt. 69–71°C

$\nu_{\max}/\text{cm}^{-1}$ (KBr): 3330, 2921, 1745, 1645, 1625, 1548, 1250, 815.

$^1\text{H NMR}$ (CDCl_3) δ (ppm): 1.28 (3H, t, J 6 Hz), 1.47 (3H, t, J 6 Hz), 2.38 (2H, m), 2.77 (2H, m), 3.23 (2H, m), 3.91 (3H, s, OCH_3); 5.04 (1H, m); 6.10 (1H, d, J 7 Hz, N-H); 7.17 (2H, d, J 8.6 Hz), 7.25 (2H, d, J 8.6 Hz).

$^{13}\text{C NMR}$ (CDCl_3) δ (ppm): 9.2, 9.8, 27.9, 29.7, 37.4, 52.6, 53.1 (OCH_3), 121.8, 130.4, 133.6, 150.6, 172.3, 173.2, 173.6.

Anal. Calc. for $\text{C}_{16}\text{H}_{21}\text{O}_5\text{N}$: C, 62.59; H, 6.84; N 4.56; found C, 61.90, H 7.10; N, 4.60%.

$[\alpha]_{\text{D}} = +48.2^\circ$ (c 1.0 in chloroform at 25°C).

6.2.6 *N-(Propanoyl–Heptyl)-O-Propanoyl Tyrosine Methyl Ester (9)*

N-Propanoyl *O*-propanoyl tyrosine methyl ester (**8**) (1.0 g, 3.27 mmol) was dissolved in THF (75 ml). Triethylamine (0.68 ml, 4.88 mmol) was added to the reaction mixture and stirred for 2 h at room temperature. 1-Bromoheptane was then added (0.75 ml, 4.88 mmol) together with a catalytic amount of DMAP to the

mixture. The reaction was heated at reflux for 72 h. The reaction was then quenched with water (20 ml). The organic layer was extracted with ethyl acetate (4 × 25 ml) and the combined organic layer was washed with sodium hydrogen carbonate (5%, 50 ml). The combined organic extracts were then dried over magnesium sulphate, and the solvent was removed in *vacuo* to yield the title product as crude. The crude product was then purified via flash chromatography (hexane: ethyl acetate, 1:1) to yield the title compound as a yellow paste (0.38 g, 30%). R_f 0.4, hexane: ethyl acetate, 1:1.

$\nu_{\max}/\text{cm}^{-1}$ (KBr): 2921, 1745, 1645, 1620, 1230, 820.

$^1\text{H NMR}$ (CDCl_3) δ (ppm): 0.86 (6H, m), 1.10 (3H, t, J 7.5 Hz), 1.26 (8H, m), 1.83 (2H, m), 2.20 (2H, m), 2.57 (2H, m), 3.01 (2H, m), 3.38 (2H, m), 3.70 (3H, s, OCH_3), 4.87 (1H, d, J 7.5 Hz), 6.90 (2H, d, J 8.2 Hz), 7.02 (2H, d, J 8.2 Hz).

$^{13}\text{C NMR}$ (CDCl_3) δ (ppm): 9.0, 9.8, 14.0, 22.7, 27.5, 28.3, 28.6, 29.7, 31.8, 33.0, 34.2, 37.4, 52.3, 53.1 (OCH_3): 121.8, 130.4, 133.6, 150.1, 172.0, 173.1, 173.5.

$[\alpha]_{\text{D}} = +40.2^\circ$ (c 1.0 in chloroform at 25°C).

6.2.7 *L*-Phenylalanine Methyl Ester (10)

L-phenylalanine (1.02 g, 6.14 mmol) was dissolved in dry methanol (20 ml) and the solution cooled to -5°C . The mixture was stirred and thionyl chloride (1.0 ml, 13.7 mmol) was added dropwise. The temperature of the mixture was kept below 0°C during the addition. The colourless solution formed was then stirred for 18 h at room temperature. Excess methanol was removed in *vacuo* to give the crude product.

The material was purified by washing with methanol (3 × 50 ml) to give a white solid. The latter was recrystallised from ethyl acetate to yield the title product as colourless crystals (1.19 g, 90%). M.pt. 156°C .

$\nu_{\max}/\text{cm}^{-1}$ (KBr): 3337, 2922, 1741, 1613, 1591.

$^1\text{H NMR}$ (D_2O) δ (ppm): 3.29 (2H, m), 3.86 (3H, s, OCH_3), 4.46 (1H, m), 7.33 (2H, d, J 1.8 Hz), 7.42 (3H, d, J 2.0 Hz).

$^{13}\text{C NMR}$ (D_2O) δ (ppm): 35.5, 53.3, 55.0, 128.8, 132.9, 134.1, 169.2.

Anal. calc. for $\text{C}_{10}\text{H}_{14}\text{O}_2\text{N}^+\text{Cl}^-$: C, 55.64; H, 6.49; N, 6.49; found C, 54.86; H, 5.90; N, 6.60%.

$[\alpha]_{\text{D}} = +35.0^\circ$ (c 2 in ethanol at 25°C).

6.2.8 *N*-Propanoyl-*L*-Phenylalanine Methyl Ester (11)

L-Phenylalanine methyl ester hydrochloride (1.02 g, 4.6 mmol) was dissolved in THF (75 ml) at room temperature. Triethylamine (1 ml, 7.12 mmol) was added to the mixture and left to stir for 1 h. Dropwise addition of propanoyl chloride

(0.4 ml, 4.4 mmol) was carried out over a period of 10 min. When the addition was completed, a catalytic amount of DMAP was added to the mixture and the latter was refluxed for 3 h. The mixture was then quenched with water (50 ml) and the aqueous layer was extracted with ethyl acetate (4 × 25 ml). The combined organic extracts were washed with sodium hydrogen carbonate (5%, 25 ml) and the organic layer was dried over anhydrous sodium sulphate. The solvent was removed in *vacuo* to yield a crude product which was purified via flash chromatography (petroleum ether: ethyl acetate, 1:1) to give the title compound as a pale yellow oil (0.75 g, 77%).

$\nu_{\max}/\text{cm}^{-1}$: 3272, 2949, 1742, 1649, 1536, 745.

$^1\text{H NMR}$ (CDCl_3) δ (ppm): 1.08 (3H, t, J 7.5 Hz), 2.16 (1H, dd, J 6.3 Hz), 2.25 (1H, dd, J 4.8 Hz), 3.12 (2H, q, J 8.0 Hz), 3.72 (3H, s, OCH_3), 4.90 (1H, m), 6.07 (1H, br, N-H), 7.09–7.28 (5H, m, Ph).

$^{13}\text{C NMR}$ (CDCl_3) δ (ppm): 12.5, 32.3, 40.7, 55.1, 55.9, 129.9, 131.4, 132.1, 138.9, 175.2, 176.4.

6.2.9 *L*-Phenylalaninol (12)

The reaction was carried out under an inert nitrogen atmosphere. Sodium borohydride (1.14 g, 30.3 mmol) was dissolved in 40 ml THF (freshly distilled and predried over sodium). *L*-Phenylalanine (2.01 g, 12.11 mmol) was added in small portions. The mixture was cooled to 0°C.

A solution of iodine (2.9 g, 27.35 mmol dissolved in 20 ml THF) was added slowly over 30 min resulting in vigorous evolution of hydrogen. After addition of iodine, the mixture was heated to reflux for 22 h and then cooled to room temperature. Methanol was added until a clear mixture was obtained. The resulting mixture was left to stir for 30 min and the solvent was removed in *vacuo* leaving a white paste that was dissolved in 30 ml of 20% KOH. The solution was stirred for 4 h and extracted with 4 × 25 ml of DCM. The organic extracts were dried over anhydrous sodium sulphate, filtered and concentrated in *vacuo* to give a crude solid (1.270 g, 8.41 mmol) which was recrystallised from toluene (10 ml) to yield the title compound as white crystals (1.20 g, 60%). M.pt. 89–90°C.

$\nu_{\max}/\text{cm}^{-1}$: 3438, 3355, 2938, 1633, 1579, 1454, 753.

$^1\text{H NMR}$ (CDCl_3) δ (ppm): 2.48 (3H, br, s), 2.81 (1H, m), 2.83 (1H, m), 3.10 (1H, m), 3.63 (1H, m), 3.67 (1H, m), 7.17 (1H, t, J 6.0 Hz); 7.20 (2H, d, J 6.8 Hz); 7.26 (2H, t, J 7 Hz).

$^{13}\text{C NMR}$ (CDCl_3) δ (ppm): 36.3, 54.3, 54.8, 128.8, 130.0, 130.1, 134.0, 170.7.

Anal. calc. for $\text{C}_9\text{H}_{13}\text{ON}$: C, 71.51; H, 8.61; N, 9.26; found C, 70.92; H, 8.75; N, 9.24%.

$[\alpha]_{\text{D}} = -22.8^\circ$ (c 1.2, 1 M HCl).

6.2.10 Methyl Acrylate

Thionyl chloride (5.00 ml, 69.3 mmol) was added dropwise to a stirred solution of acrylic acid (4.76 ml, 69.3 mmol) and stirred for 1 h at 25°C. Dry methanol (9 ml, 70 mmol) in dichloromethane (10 ml) together with triethylamine (5 ml, 35.9 mmol) was added to the reaction mixture. The mixture was then heated at reflux for 18 h under anhydrous conditions. The solvent was removed in *vacuo* and the product was purified via flash chromatography (R_f 0.5, petroleum spirit: ethyl acetate, 1:3) to give the title compound as a yellow oil (2 g, 49%).

$\nu_{\max}/\text{cm}^{-1}$: 2957, 1724, 1640, 1057.

$^1\text{H NMR}$ (CDCl_3) δ (ppm): 3.72 (3H, s, OCH_3), 5.76 (1H, d, J 10 Hz), 6.07 (1H, m), 6.34 (1H, d, J 17.3 Hz).

$^{13}\text{C NMR}$ (CDCl_3) δ (ppm): 51.8, 128.4, 130.9, 166.9.

6.2.11 2-(1-Hydroxy-1'-Phenylmethyl)-Acrylic Acid Methyl Ester

The catalyst (0.2 g, 4 mmol) was stirred in acidified water (pH 1) (25 ml) and THF (25 ml) solution at room temperature. Benzaldehyde (2 ml, 19 mmol) and methyl acrylate (1.7 ml, 19 mmol) were then added. The reaction was stirred at room temperature for 72 h. The mixture was washed with water (100 ml) and the organic phase was extracted using ethyl acetate (4×25 ml). The organic layer was dried over magnesium sulphate, filtered and concentrated in *vacuo*. The crude oil was purified by flash chromatography (hexane: ethylacetate, 6:1) to afford the title compound as a brown oil (0.15 g, 15%). R_f 0.6, hexane: ethyl acetate, 6:1.

$\nu_{\max}/\text{cm}^{-1}$: 3452, 3019, 1712, 1631.

$^1\text{H NMR}$ (CDCl_3) δ (ppm): 3.55 (1H, br, OH), 3.86 (3H, s, OCH_3), 5.24 (1H, d, J 1.5 Hz), 5.55 (1H, d, J 1.5 Hz), 6.45 (1H, s), 7.26–7.37 (5H, m, Ph).

$^{13}\text{C NMR}$ (CDCl_3) δ (ppm): 51.00 (OCH_3), 72.4, 125.6, 126.9, 127.5, 129.9, 140.3, 141, 166.8.

$[\alpha]_D = +14.0^\circ$ (c 1.0 in methanol at 25°C).

6.2.12 3-[Bis(Ethoxycarbonyl)Methyl] Cyclopentanone

Diethyl malonate (0.38 ml, 2.50 mmol), cyclopentenone (0.25 ml, 2.50 mmol) and potassium carbonate (0.1066 g, 1.09 mmol) were stirred together with surfactant CTAB (cetyl trimethyl ammonium bromide) (0.1138 g, 0.45 mmol) in distilled water (25 ml) and heated at reflux for 48 h. The reaction mixture was then cooled to room temperature and extracted with ethyl acetate (3×25 ml). The combined organic extracts were dried over sodium sulfate and the solvent removed in *vacuo*. The crude

product was purified by flash chromatography (hexane: ethyl acetate:1:1) to afford the desired product as a colourless oil (0.260 g, 43%).

$\nu_{\max}/\text{cm}^{-1}$: 1730, 2983, 1372, 1465.

^1H NMR (250 MHz; CDCl_3) δ (ppm): 1.26 (6H, m), 1.60–2.00 (2H, m), 2.24–2.40 (4H, m), 2.85 (1H, m), 3.35 (1H, d, J 6.2 Hz), 4.20 (4H, m).

^{13}C NMR (CDCl_3) δ (ppm): 13.3, 26.5, 35.7, 37.4, 42.2, 55.6, 60.5, 167.2, 167.3.

6.2.13 3-[Bis(Methoxycarbonyl) Methyl]-2-Pentyl-2-Cyclopentan-1-one

Dimethyl malonate (0.29 ml, 2.50 mmol), 2-pentyl-2-cyclopent-1-enone (0.42 ml, 2.54 mmol) and potassium carbonate (0.34 g, 2.47 mmol) were stirred together with *L*-phenylalanine (0.025 g, 0.15 mmol) in distilled water (25 ml) at room temperature for 48 h. The reaction mixture was extracted with diethyl ether (3 \times 20 ml). The organic layer was washed with 0.1 M HCl (2 \times 5 ml), distilled water (5 ml) and brine (2 \times 5 ml). The combined organic extracts were dried over sodium sulfate, filtered and concentrated in *vacuo*. The crude oil was then purified by column chromatography (dichloromethane: hexane, 2:1) to give the desired product as a colourless oil (0.494 g, 70%).

$\nu_{\max}/\text{cm}^{-1}$: 2958, 2250, 1715, 1466, 1378, 1255, 909.

^1H NMR (CDCl_3): δ (ppm) 0.84–0.94 (6H, m), 1.25–1.27 (6H, m), 1.36–1.45 (2H, m), 2.10–2.13 (3H, m), 2.38–2.56 (6H, m).

^{13}C NMR (CDCl_3): δ (ppm) 13.0, 21.4, 23.7, 25.4, 26.4, 30.6, 33.6, 75.6, 76.2, 76.7, 145.5, 156.3.

$[\alpha]_{\text{D}} = +5^\circ$ (c 3.0 in CHCl_3 at 25°C).

6.2.14 1-Ethyl-7-Methyl-cis-3,7-Diazabicyclo-[3.3.0]Octane-2,4-Dione

Sarcosine (534 mg, 6 mmol), *L*-phenylalaninol (20 mg, 0.134 mmol), *N*-ethylmaleimide (900 mg, 7.2 mmol) and paraformaldehyde (1.35 g, 15 mmol) were added to toluene (40 ml) with an azeotropic mixture of water. The mixture was heated under reflux for 10 h. The solvent was then removed under *vacuo* and the residue was purified by flash chromatography (dichloromethane: methanol; 95:5) to give the title compound as a crude yellow oil (0.87 g, 85%).

$\nu_{\max}/\text{cm}^{-1}$: 2949, 2789, 1769, 1688, 1443, 1402, 1344, 1223, 1122, 1046.

$^1\text{H NMR}$ (CDCl_3) δ (ppm): 1.13 (3H, t, J 8.0 Hz, 6-H), 2.21 (3H, s, 1-H), 2.54–2.70 (1H, m, 2-H), 3.11–3.13 (2H, m, 3-H), 3.19–3.23 (2H, d, J 9.7 Hz), 3.44–3.53 (2H, q, J 7.5 Hz, 5-H).

$^{13}\text{C NMR}$ (CDCl_3) δ (ppm): 12.8, 33.9, 40.7, 44.9, 58.4, 179.0.

6.2.15 Biological Analysis Using Disc Diffusion Method

Muller Hinton agar (38 g/dm^3) and Muller Hinton broth (52 g/dm^3) were prepared. After autoclaving, 20 ml of agar was poured in sterilized Petri plates and left to solidify at room temperature.

The inocula of the test strains were prepared by touching an inoculating loop to 4 or 5 isolated colonies of the pathogen growing on agar. This was then used to inoculate a test tube of culture broth containing Muller Hinton broth (4 ml). The cultures were plugged with cotton wool and incubated at 37°C for 24 h. The bacteria were transferred from Muller Hinton broth to the Petri plates using sterilized cotton swabs, ensuring that the Muller Hinton broth containing the bacteria was spread all over the plates. Various concentrations of the tested samples were prepared in the range of 25–100 mg/ml in DMSO. Sterilized paper disc (6 mm) was placed on the seeded plates and 20 μL of test solution was placed on the sterilized paper disc. The plates were incubated at 37°C in sterile conditions.

The diameter of the zone of inhibition including the diameter of the disc was measured to the nearest whole millimetre.

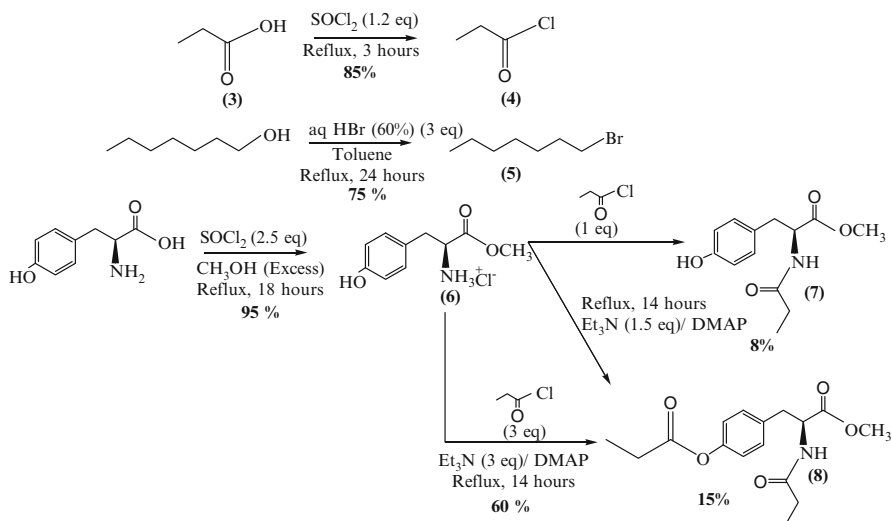
6.3 Results and Discussion

6.3.1 Synthesis of Selected Tyrosine Analogues

A propanoyl chain was selected in order to compare its results to that of butyryl chained systems which have previously been successfully reported in the making of asymmetric catalysts. With this in mind the propanoyl chloride chain was synthesised. This was done by acylating propanoic acid using thionyl chloride to give (**4**) in 85% yield.

A 7-chain aliphatic lipophilic system was selected for completing the synthesis of our surfactant analogue. This chain length was selected in order to investigate micellar aggregation. Heptanol was therefore chosen and subsequently brominated using the conditions underlined in Scheme 6.2, to give (**5**) in 75% yield.

In order to make our tyrosine analogues, *L*-tyrosine was first esterified so as to increase the ease and yield of conversion. It was observed that direct reduction of



Scheme 6.2 Synthesis of the surfactant intermediates derived from *L*-Tyrosine

tyrosine became very problematical. Hence its esterification was carried out using thionyl chloride and methanol to yield the resulting hydrochloride salt (**6**) in 95% yield.

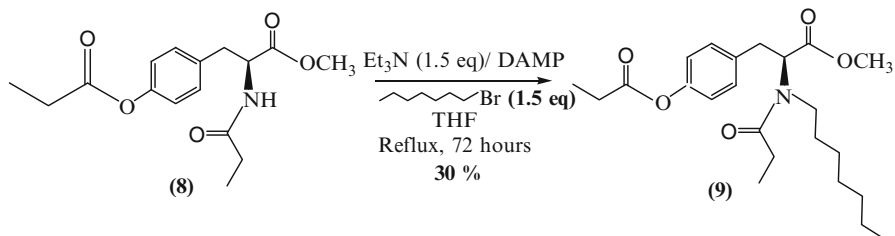
Introduction of the propanoyl chain was explored via amide formation and subsequent reduction was carried out in order to avoid polyalkylation.

It was initially decided to react (**6**) with propanoyl chloride (**4**) using triethylamine base (1.5 equivalents), which subsequently gave compounds (**7**) and (**8**) in disappointing yields of 8% and 15% respectively. However, increasing the amount of triethylamine base to 3 equivalents generated compound (**8**) exclusively in 60% yield. This did not come as a surprise since the pK_a of R-NH₂ (10.7) is very similar to that of the phenolic OH which is about 10.19 [14].

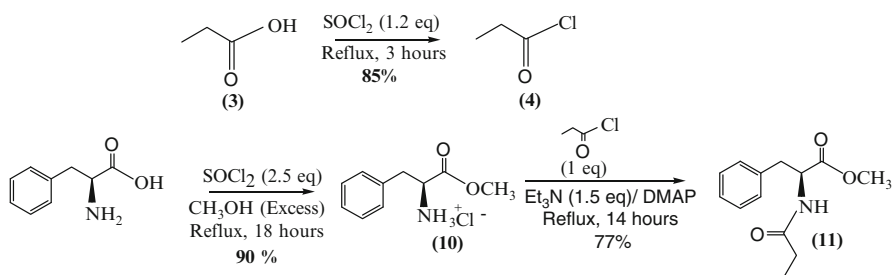
A reduction of (**8**) was next carried out using lithium aluminium hydride. NMR analysis confirmed the loss of the propanoyl chain on the phenolic end of the tyrosine molecule. However, isolation of the resulting products after reduction was problematical.

An alternative strategy was sought and although this would involve the blocking of the phenolic group, investigations were carried out to see what happens when the heptyl chain is added onto the intermediate (**8**) to verify if this analogue is catalytically or biologically active and provide us with a clearer picture of determining which functional group is responsible for these activities.

Hence bromoheptane (1.5 equivalents) was reacted with analogue (**8**) using triethylamine base and a catalytic amount of DMAP in THF solvent to give the resulting surfactant analogue (**9**) in 30% (Schemes 6.3 and 6.4).



Scheme 6.3 Synthesis of surfactant, *N*-(propanoyl-heptyl) *O*-propanoyl tyrosine methyl ester

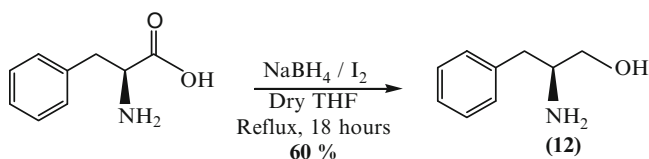


Scheme 6.4 Synthesis of the surfactant intermediates derived from *L*-phenylalanine

6.3.2 Synthesis of Intermediates Derived from Phenylalanine

L-Phenylalanine was initially esterified using similar conditions to that carried out on *L*-tyrosine to give the resulting methyl ester hydrochloride (10) in 90% yield. This was subsequently reacted with propanoyl chloride using 3 equivalents of triethylamine and a catalytic amount of DMAP to give compound (11) in 77% yield.

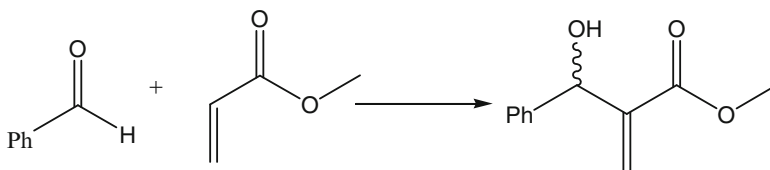
The catalytic and biological effects of phenylalaninol were also studied since verification was required on whether there was any correlation between the aliphatic OH moiety and reaction selectivity as well as biological activity. As a result, phenylalanine was subsequently reduced using sodium borohydride and iodine in dry THF to yield (12) in 60% yield (Scheme 6.5).



Scheme 6.5 Reduction of phenylalanine to phenylalaninol

6.3.3 Catalytic Studies – The Baylis-Hillman Reaction

The Baylis-Hillman reaction is a carbon-carbon bond forming reaction which involves the coupling of activated alkenes with carbon electrophiles containing electron-deficient sp^2 carbon atoms using a catalyst [15] (Scheme 6.6).



Scheme 6.6 Baylis-Hillman reaction between benzaldehyde and methyl acrylate

Previous reports have shown the use of DABCO (1,4-diazabicyclo[2.2.2]octane), DBU (1,8-diazabicyclo[5.4.0]undec-7-ene, quinidine and various chiral catalysts such as (*S*)-BINAP (2,2'-bis(diphenylphosphino)-1,1'-binaphthyl) giving varying yields and selectivities in organic media [15]. However limited work has been carried out on these reactions in water. More recently though, a variety of Baylis-Hillman reactions was successfully carried out using a range of surfactants successfully synthesised from cinchonine [16]. It was observed that carrying out the reaction under acidic conditions helps drive the reaction, enhancing productivity. It was postulated that this was due to the protonation of the acrylate which enhances the reaction (as shown below, Fig. 6.2). It was also observed that yield enhancement was possible using electron withdrawing groups attached to the acrylic moiety.

Till date however, very few of these reactions have been carried out using amino acids. As a result, a successfully reported Baylis-Hillman reaction was reported between methyl acrylate and benzaldehyde [15] using the synthesised *L*-tyrosine and *L*-phenylalanine analogues (Table 6.1).

Promising results were observed when using (9) in water and under phase-transfer conditions. Addition of a lipophilic chain resulted in both reaction yield and selectivity increase, especially when the reaction was carried out in a phase-transfer system due to the amphiphilic nature of surfactants which enhances substrate solubilisation at the reaction interface.

Interestingly lower selectivity values than expected were observed. A postulated model was designed to try and rationalise the above behaviour indicating that there is presence of π -stacking and hydrogen bonding between the substrate and catalyst showing also a free rotation of the aldehyde as it interacts with the reacting substrate leading to a lack of enantiomeric control (Fig. 6.3).

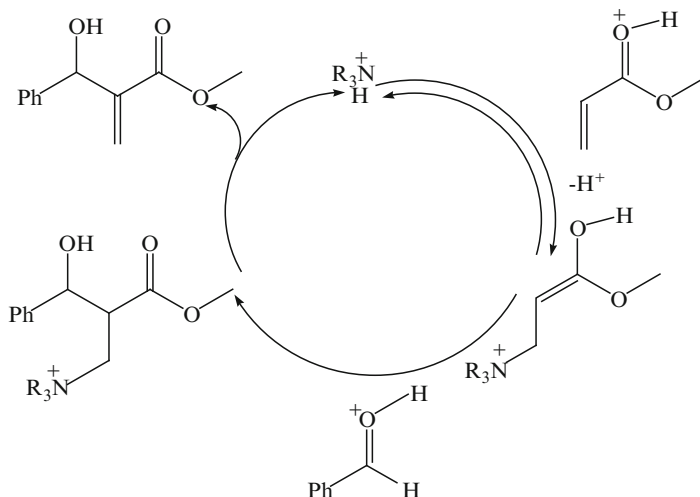


Fig. 6.2 Baylis-Hillman cycle

Table 6.1 Results from the Baylis-Hillman reaction between benzaldehyde and methyl acrylate in H_2O

Catalyst	% yield	$[\alpha]_D$
DABCO	47	–
DBU	56	–
9	9	+10°
9 ($H_2O:THF = 1:1$)	15	+14°

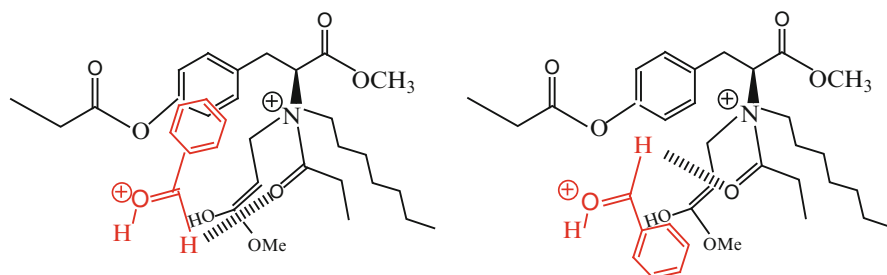
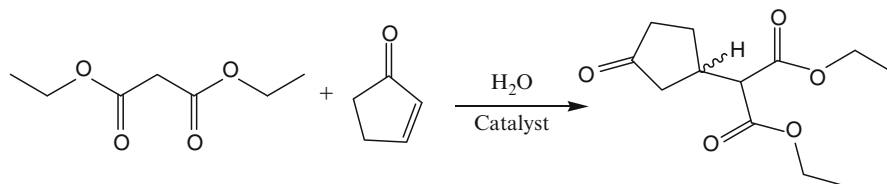


Fig. 6.3 Postulated model showing the interactions between *L*-tyrosine catalyst (9) and benzaldehyde and methyl acrylate substrates

6.3.4 Catalytic Studies – Michael Addition Reaction

Another reaction which was used to monitor the efficacy and influence of micellar catalysis in aqueous media was the Michael-addition [17, 18] reaction between diethyl malonate and cyclopenten-2-one (Scheme 6.7).



Scheme 6.7 Michael addition between diethyl malonate and cyclopenten-2-one

Table 6.2 Results from the Michael addition reaction between cyclopenten-2-one and diethyl malonate in H₂O

Catalyst	Time (h)	Temperature (°C)	% yield	[α] _D	e.e.
No catalyst	48	100	5	–	–
CTAB	48	100	43	–	–
SDS	48	100	22	–	–
<i>L</i> -Tyrosine	48	100	38	+19.4°	56 (<i>R</i>)
6	48	100	14	+21.2°	61 (<i>R</i>)
8	48	100	34	+26.5°	76 (<i>R</i>)
<i>L</i> -Phenylalanine	48	100	45	+13.5°	39 (<i>R</i>)
10	48	100	5	+15.9°	46 (<i>R</i>)
11	48	100	34	+14.6°	42 (<i>R</i>)
12	48	100	43	–10.5°	30 (<i>S</i>)

Lit [17]: [α]_D²⁵ = +28.35° (*c* = 1.89, CHCl₃) 82% ee, *R*-isomer

Previous reports on these reactions have been carried out using chiral catalysts such as BINOL (1,1'-bi-2-naphthol) in organic media generating good selectivity [17]. However till date limited work has been carried out on these reactions in aqueous media. As a result, a range of catalysts were used which included two commercially available surfactants, i.e. CTAB (cetyltrimethylammonium bromide) and SDS (sodium dodecyl sulphate) as well as the synthesised tyrosine and phenylalanine analogues. The summary of results is shown in Table 6.2.

Both the use of CTAB and SDS showed yield enhancement compared to when no catalyst was used where only 5% of the Michael product was generated. When using the synthesised tyrosine and phenylalanine analogues, it was observed that esterification of the carboxylic group, (**6**) and (**10**) produced a drop in the reaction yield but an increase in enantioselectivity.

Addition of the propanoyl chain to the ester moiety (**8**) and (**11**) was found to increase the reaction yield indicating that the chain in part is responsible for yield enhancement due to increasing hydrophobic interactions between the chains, resulting in an aggregate intermediate.

Interestingly when using phenylalanine analogues, two points were noted. Firstly that slightly lower selectivity values were observed using phenylalanine compared to tyrosine indicating that perhaps the phenolic OH of tyrosine has a direct impact on reaction selectivity. Secondly, when reducing phenylalanine to phenylalaninol (**12**), a reversal in the reaction selectivity was observed.

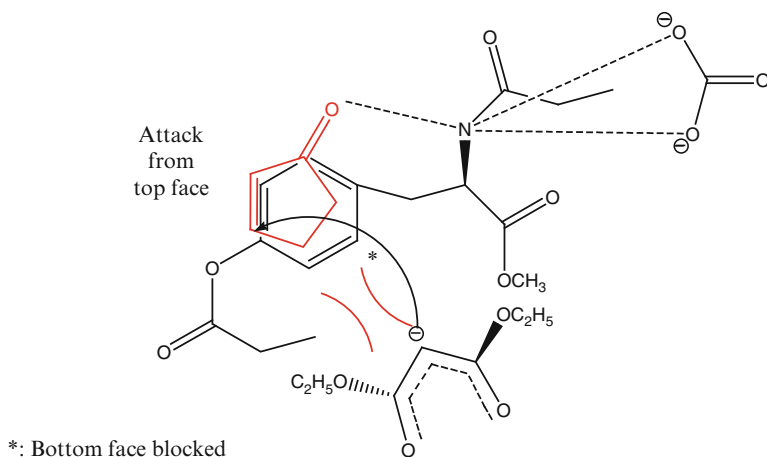


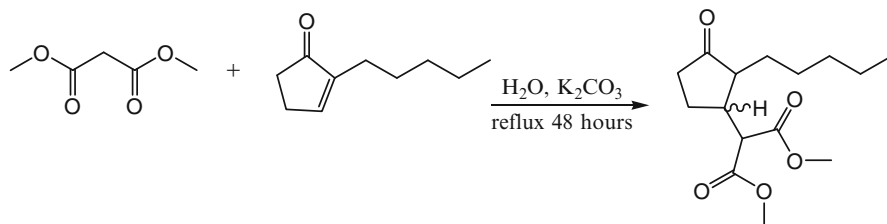
Fig. 6.4 Postulated model showing the interaction between *L*-tyrosine catalyst (**8**) and cyclopenten-2-one and diethyl malonate

Yields as high as 45% for the Michael reaction (using phenylalanine) and selectivities as high as 76% e.e. (using *N*-propanoyl, *O*-propanoyl tyrosine methyl ester) (**8**) were generated.

A transition state was postulated to rationalise the enhanced selectivities. This can be seen in Fig. 6.4 which shows a possible π - π stacking between cyclopenten-2-one and tyrosine where the bottom *re*-face is blocked by the catalyst, which enables attack from the top *si*-face generating the *R*-isomer.

Further investigation on the stereoselectivity of the Michael reaction by using a substituted cyclopentenone compound was carried out to create a greater facial stereo-differentiation.

2-Pentyl-2-cyclopenten-1-one was used, which is a commercially available conjugate addition system which leads to the production of jasmonate precursors. Perrard and co-workers reported high e.e. values of up to 90% for the reaction between dimethyl malonate and 2-pentyl-2-cyclopenten-1-one using cinchonine, quinine and quinidine derived catalysts under solvent free conditions [18] (Scheme 6.8).



Scheme 6.8 Michael addition between dimethyl malonate and 2-pentyl-2-cyclopenten-1-one

Table 6.3 Results from the Michael addition reaction between 2-pentyl-2-cyclopenten-1-one and dimethyl malonate in H₂O

Catalyst	Time (h)	Temperature (°C)	% yield	[α] _D	e.e.
–	48	100	5	–	–
CTAB	48	100	40	–	–
SDS	48	100	46	–	–
<i>L</i>-Tyrosine	48	100	51	+3.3°	15 (<i>R</i>)
6	48	100	46	+3.3°	15 (<i>R</i>)
8	48	100	43	+8.3°	38 (<i>R</i>)
<i>L</i>-Phenylalanine	48	100	69.5	+5.0°	23 (<i>R</i>)
10	48	100	41	+13.3°	61 (<i>R</i>)
11	48	100	32	+13.3°	61 (<i>R</i>)
12	48	100	32	–15.0°	69 (<i>S</i>)

Lit [18]: [α]_D²⁰ = +19.7° (c = 3, CHCl₃) 90% ee, *R*-isomer

The reaction was repeated using the synthesised catalytic analogues under aqueous conditions (Table 6.3).

Similar trends to that of the cyclopentenone and diethyl malonate reaction were observed. Using the esterified amino acid analogues resulted in a drop in yield but gave an increase in enantioselectivity of products when using phenylalanine methyl ester. Methylating the tyrosine molecule had surprisingly no effect on reaction selectivity. Incorporation of the propanoyl chain to its ester resulted in an increase in selectivity for the Michael reaction but surprisingly a drop in reaction yield was observed. Interestingly just like with the cyclopenten-2-one addition to diethyl malonate, a reversal in the selectivity was noted using *L*-phenylalaninol as catalyst.

Yields as high as 70% to the *R*-isomer were observed using *L*-phenylalanine. The highest selectivity was observed at 69% to the *S*-isomer using *L*-phenylalaninol. When using phenylalanine methyl ester, a selectivity as high as 61% e.e. to the *R*-isomer was observed. Surprisingly no increase in the selectivity was observed when adding the propanoyl chain onto phenylalanine.

A transition state model was postulated to account for this. Apart from the expected π - π stacking between the aromatic rings of the catalyst and the reacting substrate, favourable van der Waals forces between the respective chains of the catalyst and substrate were observed which would favour and enhance the reaction and favour the formation of the *R*-isomer as shown in Fig. 6.5.

6.3.5 Preliminary Studies on Dipolar Trappings

Initial investigations are outlined on the dipolar trapping reaction involving sarcosine, *N*-ethylmaleimide and paraformaldehyde using toluene as solvent, a reaction which was initially carried out by Lubineau et al. (1995) [19] (Table 6.4; Scheme 6.9).

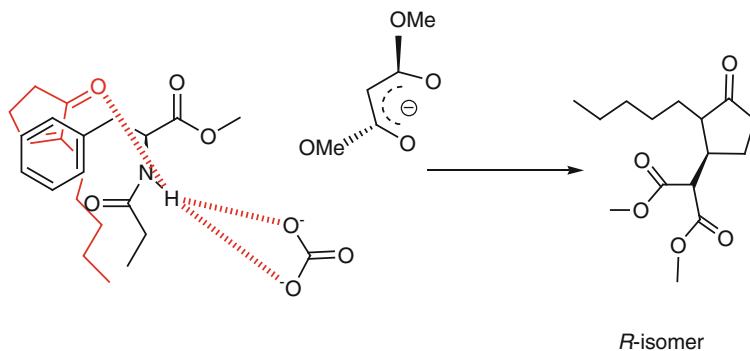
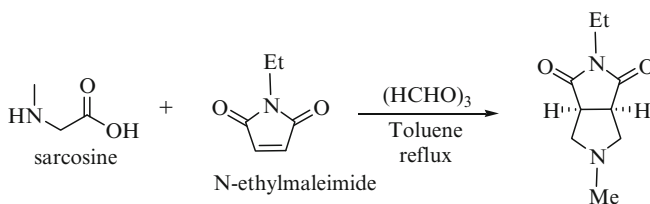


Fig. 6.5 Postulated model showing the interaction between *L*-phenylalanine catalyst (**11**) and 2-pentyl-2-cyclopenten-1-one and dimethyl malonate

Table 6.4 Results from the dipolar addition between sarcosine and N-ethylmaleimide

Catalyst	Time (h)	% yield	$[\alpha]_D$
–	10	0	–
SDS	10	Mixtures	
CTAB	10	Mixtures	
10	10	74	+3.3°
11	10	63	+3.1°
12	10	85	+3.7°



Scheme 6.9 Dipolar addition between sarcosine and N-ethylmaleimide

Initial studies showed that the reaction did not proceed in the absence of any catalyst. Both commercially available surfactants SDS and CTAB as catalysts generated mixtures that were difficult to isolate. However a good conversion was observed using the synthesised phenylalanine analogues albeit in low selectivity. Interestingly *L*-phenylalaninol (**12**) generated the best yield at 85%, signifying that the aliphatic OH group may be integral for dipolar addition.

6.3.6 Preliminary Biological Studies on Tyrosine and Phenylalanine Analogues

Biological studies were carried out on the tyrosine and phenylalanine analogues. Previous reports have demonstrated that alpha-alkyl amino acids are biologically active [20]. Four pathogenic bacteria were investigated. These were gram (+)-*Staphylococcus aureus*, gram (-)-bacteria- *Klebsiella pneumonia*, *Shigella* and *Pseudomonas aeruginosa*. Upon using the synthesised analogues for biological activity, only *N*-propanoyl *L*-phenylalanine (**11**) and *L*-phenylalaninol (**12**) were moderately active.

It was deduced from initial findings that the aliphatic OH substituent in *L*-phenylalanine is vital for inducing antibacterial activity. It can also be postulated that the presence of the *N*-propanoyl chain is also responsible for its activity perhaps due to its ability to disrupt the membrane of the bacterial cell. Further work is underway to confirm and rationalise these findings.

6.4 Conclusions

A range of surfactant analogues derived from *L*-tyrosine and *L*-phenylalanine had been successfully synthesized which were used for catalytic and biological analysis. The best results were obtained using the *L*-tyrosine analogue (**9**) which gave yields of up to 15% for the Baylis-Hillman reaction between benzaldehyde and methyl acrylate. The best conditions were found to be in phase-transfer solvent system. These results were encouraging since there have been virtually no reported cases of yield enhancement using amino acid derivatives as catalysts for Baylis-Hillman reactions.

For the Michael reactions, yields as high as 45% using *L*-phenylalanine as catalyst were obtained for the reaction between cyclopentenone and diethylmalonate. Interestingly, yield enhancement of up to 70% was observed when a pentyl cyclopent-2-enone substrate was used. Selectivity as high as 70% e.e. to the *S*-isomer was obtained using (**12**) as catalyst.

The phenylalanine analogues were found to generate encouraging yields when used as catalyst for the dipolar addition between sarcosine and *N*-ethylmaleimide where yields as high as 85% were obtained when a catalytic amount of (**12**) was used.

Finally initial biological studies on the tyrosine and phenylalanine analogues showed moderate activity using both *N*-propanoyl *L*-phenylalanine (**11**) and *L*-phenylalaninol (**12**).

Acknowledgements We are grateful to the following technical staff at the University of Mauritius: Mr B. Jokhun and Miss S. L'Omelette, for the running of NMR, Mr V. Ramsahye for assistance during the polarimetry studies and Mrs M. Bissoondoyal for assistance during the biological studies.

References

1. Diego-Castro MJ, Hailes HC (1998) Novel applications of chiral micellar media to the Diels-Alder. *J Chem Soc Chem Commun* 15:1549–1550
2. Hailes HC, Madden J (1999) Novel recyclable aminoalcohol salts in catalytic asymmetric inductions. The addition of diethylzinc to aromatic aldehydes. *Synlett* 1:105–109
3. Tascioglu S (1996) Micellar solutions as reaction media. *Tetrahedron* 52:11113–11151
4. Discher DE, Eisenberg A (2002) Polymer vesicles. *Science* 297:967–973
5. Shin M, Barrington S (2005) Effectiveness of the iodide ligand along with two surfactants on desorbing heavy metals from soils. *Water Air Soil Pollut* 161:193–208
6. Zhang L, Eisenberg A (1995) Multiple morphologies of “crew-cut” aggregates of polystyrene-*b*-poly(acrylic acid) block copolymers. *Science* 268:1728–1731
7. Torchilin VP, Lukyanov AN, Gao Z, Papahadjopoulos-Sternberg B (2003) Immunomicelles: targeted pharmaceutical carriers for poorly soluble drugs. *Proc Nat Acad Sci USA* 100:6039–6044
8. Jones MC, Leroux JC (1999) Polymeric micelles. A new generation of colloidal drug carriers. *Eur J Pharm Biopharm* 48:101–111
9. Noyori R, Kitamura M (1991) Enantioselective addition of organometallic reagents to carbonyl compounds: chirality transfer, multiplication and amplification. *Ang Chem Int Ed* 30:49–69
10. Noyori R, Suga S, Kawai K, Ohada S, Kitamura M (1990) Enantioselective addition of diorganozincs to aldehydes catalysed β -amino alcohols. *J Organomet Chem* 382:19–37
11. Watanabe M, Soai K (1994) Enantioselective addition of diethylzinc to aldehyde using chiral polymer catalysts possessing a methylene spacer. *J Chem Soc Perkins Trans I* 1:837–842
12. Soai K, Niwa S (1992) Enantioselective addition of organozinc reagents to aldehydes. *Chem Rev* 92:833–856
13. Soai K, Niwa S, Yamada Y, Inoue H (1987) Chiral piperazine as a new chiral catalyst for the enantioselective addition of dialkylzincs to aryl aldehydes. *Tetrahedron Lett* 28:4841–4842
14. Sykes P (1986) A guidebook to mechanisms in organic chemistry, 6th edn. Longman, London
15. Basaviah D, Rao PD, Hyma RS (1996) The Baylis-Hillman reaction: a novel carbon-carbon bond forming reaction. *Tetrahedron* 52:8001–8062
16. Caumul P, Hailes HC (2005) Baylis-Hillman reactions in aqueous acidic media. *Tetrahedron Lett* 46:8125–8127
17. Manickam G, Sundararajan G (1997) A new C_2 -symmetric heterobimetallic complex as a promoter for asymmetric Michael addition reactions. *Tetrahedron Asym* 8:2271–2278
18. Perrard T, Plaquevent JC, Desmurs JR, Hébrault D (2000) Enantioselective synthesis of both enantiomers of methyl dihydrolasmonate using solid-liquid asymmetric phase-transfer catalysis. *Org Lett* 2:2959–2962
19. Lubineau A, Bouchain G, Queneau Y (1995) Reactivity of the carbonyl group in water. Generation of azomethine ylides from aqueous formaldehyde: Michael addition versus dipolar trapping. *J Chem Soc Perkins Trans I* 19:2433–2437
20. Lubec B, Herkner KR, Brückner H, Höger H, Gialamas J, Adamiker D, Lubec G (1991) Biological activity of alpha-alkyl amino acids. *Amino Acids* 1:289–292

Chapter 7

Synthesis, Structure and Characterization of New Amic Acid Derivatives of 3-Amino-1,2,4-Triazole and Their Complexes with Some Metal Ions

Ahlam J. Abdulghani and Suad M. Sahan

Abstract Three new amic acid ligands namely: 2-(1H-1,2,4-triazol-3-ylcarbamoyl) benzoic acid (HL_I), 2-(1H-1,2,4-triazol-3-ylcarbamoyl)-3,4,5,6-tetrachlorobenzoic acid (HL_{II}) and 3-(1H-1,2,4-triazol-3-ylcarbamoyl) propanoic acid (HL_{III}) were synthesized by condensation reaction of 3-amino-1,2,4-triazole (3-AT) with phthalic anhydride, 2,3,4,5-tetrachlorophthalic anhydride and succinic anhydride respectively in refluxing dry methanol, dimethylformamide (DMF) or ethanol respectively. Metal complexes were synthesized by heating each ligand with Co(II), Ni(II), Cu(II), and Zn(II) acetates in dry ethanol or dimethylacetamide (DMA). Structures of the studied compounds were characterized by CHN and thermogravimetric analyses, ¹H n.m.r., IR, and mass spectrometric analyses as well as metal percentage, electronic spectra, magnetic moments and electrical conductivity measurements for the metal complexes. Band energies and ligand field transitions obtained from the electronic spectra, together with magnetic moment values of metal complexes showed that coordination of all metal ions with ligand donor atoms acquired octahedral geometry. The ligands and some selected metal complexes were tested for antibacterial activity.

7.1 Introduction

The synthesis of amic acids attracted the attention of chemists due to their importance in polymer industries in the manufacture of modified resins [1], wetting agents [2], photopolymers [3] and curing catalysts [4]. Some amic acid derivatives have been used as corrosion inhibitors of metals and metal alloys [5, 2b]. In biology, amic acids including those containing heterocyclic rings (i.e. quinoline, thiazole, imidazole rings) have been used as protecting agents for amino sugars [6],

A.J. Abdulghani (✉) • S.M. Sahan

Department of Chemistry, College of Science, University of Baghdad, Jaderiya, Baghdad, Iraq

e-mail: prophahlam@yahoo.com

aminopeptides [4, 6, 7], amino acids [5, 8, 9], and as enzyme models [10]. In medicine, amic acids have shown anti-inflammatory [8, 11], antitumor [9b], anticonvulsant [11, 12a], antibacterial [12a] and analgesic activity [12b]. Some phthalamic acid derivatives have been used as potent agrochemicals [13].

Amitrole is a well known herbicide with toxic effect on plants and animals [14, 15]. It has been reported to cause thyroid and liver tumors to experimental animals [14, 15]. On the other hand several derivatives of 1,2,4-triazoles have been reported to exhibit antibacterial [16], antifungal and anticonvulsant activities [17]. Amitrole possesses more than one nitrogen atom that can be involved in chelation with metal ions, showing monodentate, bidentate and bridging ligand behaviours [18–21]. Coordination of amitrole with various metal ions have been suggested to be responsible for its toxicity and regulating activities in plants and animals [9, 11]. In this work we study the synthesis and coordination chemistry of new amic acids derived from condensation of phthalic anhydride, tetrachlorophthalic anhydride and succinic anhydride with the heterocyclic amine, 3-amino-1,2,4-triazole (3-At, amitrole).

7.2 Methodology

Melting points of compounds (uncorrected) were measured by using a Gallenkamp MFB 600 010f m.p. apparatus. Elemental CHN analyses were undertaken with EA-1108 Carlo Erba elemental analyzer. Metal contents of complexes were measured by atomic absorption technique using Shimadzu – 680 GAA EE spectrophotometer. Mass spectra were recorded on a Jeol mass spectrometer 700. ^1H n.m.r and ^{13}C n.m.r were recorded on J300 MHz n.m.r spectrometer. Thermal analyses were performed by Stanton Rodcorts TG 760 and NETZCH Geratebau GmbH STA 40 thermal analysers. IR spectra were recorded on a Perkin Elmer 1310 spectrophotometer and vector 22-FTIR spectrophotometer. Electronic spectra in the region (200–1100 nm) of products in DMF were recorded on a Shimadzu u.v-visible spectrophotometer. Electrical conductivity measurements of complexes in DMF (10^{-3} M) were carried out by using Elekter Lietfahgkeit conductometer (SIEMENS). Magnetic moment (μ_{eff} , BM) of solid complexes were determined by using Johnson Matthey magnetic balance and Bruker magnet BM6.

All chemicals were of high purity and were used as received except methanol, ethanol and DMF which were dried and distilled prior to use [22].

7.2.1 Preparation of Ligands

A solution of 3-At (0.01 mol, 0.84 g) in hot dry methanol, DMF or ethanol (10, 5, 10 ml respectively) was added to a solution of phthalic, tetrachlorophthalic, and succinic anhydride respectively (0.01 mol, 2.32, 3.76, 1.84 g respectively) in the

same solvents (10, 5, 10 ml). The mixture was heated under reflux for 2 h, 30 min, and 1 h respectively. After cooling to room temperature a white precipitate was formed. The products were filtered, washed with DMF, ethanol, methanol followed by ether and vacuum dried, giving white to colourless microcrystals.

2-(1H-1,2,4-triazol-3-ylcarbamoyl)benzoic acid (HL_I) Yield 72.64%, m.p > 300°C, IR(KBr) $\nu(\text{cm}^{-1})$: 3425 (νNH triazole ring), 3270–3108 (νNH amide), 2970–2617, 1190 (νOH , CO acid), 1743–1710 (νCO acid), 1681 (νCO amide), 1575, 1520, 1287 ($\nu\text{C}=\text{N}$, $\text{N}=\text{C}-\text{N}$, $\text{N}-\text{N}=\text{C}$ of triazole ring), ^1H n.m.r. (DMSO) $\delta(\text{ppm})$: 7.5–7.9 (m, 4H, aromatic H), 8.75 (s, 1H, triazole N–H), 8.05 (s, 1H, amide N–H), 8.0 (s, 1H, triazole 5'-H), 14.55 (s, br, 1H, COOH), MS, m/z (I%) for $\text{C}_{10}\text{H}_8\text{N}_4\text{O}_3$, mwt 232 g/mol: 215 [$\text{M}-\text{OH}$] $^+$ (23), 214 [$\text{M}-\text{H}_2\text{O}$] $^+$ (100), 181(13), 173(22), 146(5), 104(83), 76(50), 50(12). CHN: Calculated for $\text{C}_{10}\text{H}_8\text{N}_4\text{O}_3$: C, 51.73; H, 3.44; N, 24.13%; found: C, 51.56; H, 3.84; N, 24.565.

2-(1H-1,2,4-triazole-3-ylcarbamoyl)-3,4,5,6-tetrachlorobenzoic acid (HL_{II}) Yield 79.43%, mp >300°C; IR (KBr) $\nu(\text{cm}^{-1})$: 3480 (νNH , triazole), 3330–3100 (νNH amide) 2950–2550, 1180 (νOH , CO acid) 1680 (νCO acid), 1630 (νCO amide) 1580, 1525, 1275 ($\nu\text{C}=\text{N}$, $\text{N}=\text{C}-\text{N}$, $\text{N}-\text{N}=\text{C}$ of triazole ring). ^1H n.m.r. (DMSO), $\delta(\text{ppm})$: 13.6–14.4 (1H, s, br, NH triazole), 11.35 (1H, s, OH), 8.79 (1H, s, amide NH), 7.62 (1H, s, CH triazole); ^{13}C n.m.r. $\delta(\text{ppm})$: 129.20 (C_6-Cl), 129.89 (C_3-Cl), 183.72 (C_5-Cl), 134.96 (C_4-Cl), 134.05 (C_2), 128.60 (C_1), 164.70 (CONH), 164.95 (COOH), 161.84 (C_3' triazole) 145.97 (C_5' triazole). CHN(%): Calculated for $\text{C}_{10}\text{H}_4\text{N}_4\text{O}_3\text{Cl}_4$: C, 32.80; H, 1.09; N, 15.12%, found: C, 32.34; H, 1.14 N, 15.08%.

3-(1H-1,2,4-triazol-3-ylcarbamoyl)propanoic acid (HL_{III}) Yield, 60%; m.p 150°C, IR(KBr) $\nu(\text{cm}^{-1})$: 3400 (NH triazole), 3240–3170 (NH amide), 2970–2860 (νCH_2 methylene) 2760–2575, 1190 (νOH , CO) 1691–1688 (νCO), 1630–1616 (νCO amide), 1570, 1520, 1275–1270 ($\nu\text{C}=\text{N}$, $\text{N}=\text{C}-\text{N}$, $\text{N}-\text{N}=\text{C}$ of triazole ring), ^1H n.m.r. (DMSO), δ (ppm), 2.41 (s, 2H, $\alpha\text{-CH}_2$), 2.50 (s, 2H, βCH_2), 5.76 (s, 2H, triazole ring NH and amide NH), 7.44 (s, 1H, 5'-H of triazole ring), 11.7–12.6 (s, broad 1H, COOH), ^{13}C n.m.r. (DMSO) $\delta(\text{ppm})$, 28.84 (2C, α and βCH_2); 147.66 (2C, triazole ring), 157.89 (1C, CONH), 173.67 (1C, COOH); MS, m/z(I%) for $\text{C}_6\text{H}_8\text{N}_4\text{O}_3$ (m.wt 184 g/mol): 184(1)[M] $^+$, 166 [$\text{M}-\text{H}_2\text{O}$] $^+$ (63) 156 [$\text{M}-\text{N}_2$] $^+$ (61), 151 (34) 111 (100), 110 (26); 84 (100), 55 (33), 45 (49), 43 (25), 28 (52). Calculated for $\text{C}_6\text{H}_8\text{N}_4\text{O}_3$: C, 39.13; H, 4.34; N, 30.43%; found: C, 38.88; H, 4.48; N, 30.22%.

7.2.2 Preparation of Metal Complexes

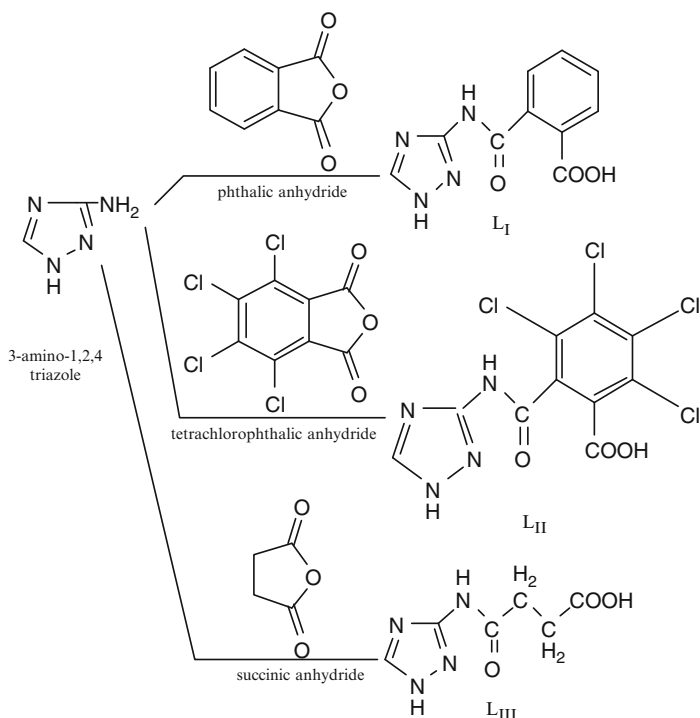
To a solution of amic acid (2 mmol) in methanol (HL_I and HL_{III}) and dimethyl acetamide (DMA, HL_{II}) (5 ml) was added a solution of one of the following metal acetates: $\text{Co}(\text{CH}_3\text{COO})_2 \cdot 6\text{H}_2\text{O}$, $\text{Ni}(\text{CH}_3\text{COO})_2 \cdot 6\text{H}_2\text{O}$, $\text{Cu}(\text{CH}_3\text{COO})_2 \cdot 2\text{H}_2\text{O}$,

$\text{Zn}(\text{CH}_3\text{COO})_2 \cdot 6\text{H}_2\text{O}$ (0.02 mmol) in the same solvent (5 ml). The mixture was heated under reflux with continuous stirring. Precipitation of products took place immediately for (CoL_I , C_1 ; NiL_{II} , C_5 ; ZnL_{III} , C_{10}); within 10 min for (NiL_I , C_2); 30 min (CuL_{III} , C_9); 1 h for ZnL_I , CoL_{II} , CuL_{II} , and NiL_{III} (C_3 , C_4 , C_6 and C_8 respectively) and 2 h for (CoL_{III} , C_7). In all cases heating was continued for 2 h for complete precipitation. The products were filtered, washed with hot methanol and DMA respectively followed by cold methanol and ether and vacuum dried.

7.3 Results and Discussion

7.3.1 Synthesis

The reaction involves nucleophilic attack of amine on carbonyl of acid anhydride followed by elimination of a water molecule (Scheme 7.1). The reaction requires anhydrous conditions to proceed successfully. The three ligands gave satisfactory elemental analyses, IR, ^1H n.m.r. and ^{13}C n.m.r. spectra. Protons of carboxylic



Scheme 7.1 Synthesis of N-3-triazolylic acids

acid groups exhibited shifts at lower fields [1b, 6, 23]. The signals assigned to CH protons of triazole ring appeared in their usual positions at 7.44–8.00 ppm while the positions of NH proton signals varied with the structure of the ligands [24]. Chemical shifts related to CH₂ protons of succinyl moiety of HL_{III} appeared at higher fields [1c]. The signal observed at 28.84 ppm in ¹³C n.m.r. of HL_{III} was assigned to the two CH₂ carbons of succinyl group [23]. Chemical shifts of COOH, CONH and triazole ring carbons were also observed [23–25].

Fragmentation of the two ligands HL_I and HL_{II} by EI mode of mass spectrum showed peaks corresponding to [M-OH]⁺ or [M-H₂O]⁺ or both molecular fragments which are characteristic of carboxylic acid behaviors [23]. Smaller molecular ions obtained from fragmentation of triazole and aromatic rings were also observed. Fragmentation of HL_{III} involved also the departure of succinyl carboxylic group moiety.

7.3.2 Physical Properties and Elemental Analyses

The colours, m.p or decomposition temperatures and CHN analysis of all compounds together with metal content of studied metal complexes are described in Table 7.1. The analytical data are in agreement with the calculated values. The molecular formulae were suggested according to these results together with those obtained from thermal analyses, spectral data as well as magnetic moments and conductivity measurements of metal complexes.

7.3.3 IR Spectra

The important vibrations and assignments of the studied ligands and their metal complexes are described in Table 7.2. The spectra of the ligands exhibited stretching vibrations of NH groups for both triazole ring and amide NH at 3480–3425 and 3330–3110 cm⁻¹ respectively [1a]. The OH stretching vibration of carboxylic group was observed in the range 2970–2550 cm⁻¹ [23]. Bands related to stretching modes of carbonyl groups for COOH and amide groups were located at 1743–1680 [13a] and 1681–1630 cm⁻¹ [1c] respectively. Peaks assigned to stretching modes of aromatic C=C for both HL_I and HL_{II} were observed at 1600–1450 and 1600–1500 cm⁻¹ respectively [23a]. The band related to aromatic CH of HL_I was observed at 3030 cm⁻¹. The spectrum of HL_{II} exhibited stretching vibration of aromatic C-Cl band at 720 cm⁻¹ [23, 26]. The spectrum of HL_{III} exhibited multiple bands related to asymmetric symmetric methylene linkage at 2970–2860 cm⁻¹ together with CH₂ bending and rocking vibrations at 1480, 1255 and 960, 800 cm⁻¹ respectively [23c]. Bands of triazole ring stretching vibrations (C=N, N=C-N and N-N=C) were slightly affected by amide linkage and were observed at the frequency ranges 1580–1570, 1525–1520 and 1295–1270 cm⁻¹ respectively [19].

Table 7.1 Physical properties and analytical data of N-3(1,2,4-triazolyl)amic acids and their metal complexes

Formula (color)	Comp. no.	m.p °C	Yield %	Elemental analyses % found (calculated)			
				C	H	N	M
C ₁₀ H ₈ N ₄ O ₃ (white)	HL _I	>300	72.64	51.56 (51.73)	3.84 (3.44)	24.65 (24.13)	–
[CoHL _I (OAc) ₂]·H ₂ O (purple)	C ₁	>300	58.58	38.85 (39.35)	3.50 (3.74)	12.93 (13.11)	13.61 (13.80)
NiHL _I (H ₂ O) ₂ (OAc) ₂ (sky blue)	C ₂	>300	83.93	37.30 (37.77)	4.20 (4.04)	11.60 (12.59)	13.08 (13.19)
Zn(HL _I)(OAc) ₂ (white)	C ₃	>300	63.17	39.11 (39.79)	4.76 (4.16)	13.40 (13.26)	15.40 (15.48)
C ₁₀ H ₄ N ₄ O ₃ Cl ₄ (white)	HL _{II}	>300	79.43	32.34 (32.60)	1.14 (1.08)	15.08 (15.21)	–
[CoL _{II} (OAc)] (reddish brown)	C ₄	>300	89.38	30.07 (29.57)	1.25 (1.23)	11.8 (11.50)	12.00 (12.10)
[Ni(HL _{II})(OAc) ₂]·H ₂ O (blue)	C ₅	>300	55.11	30.76 (29.75)	2.44 (2.12)	9.48 (9.91)	10.45 (10.39)
[Ni(HL _{II})(OAc)] (bluish green)	C ₆	>300	73.53	30.07 (29.30)	1.36 (1.22)	11.15 (11.39)	12.84 (12.96)
C ₆ H ₈ N ₄ O ₃ (white)	HL _{III}	150	60.00	38.88 (39.13)	4.48 (4.34)	30.22 (30.43)	–
[Co(HL _{III})(H ₂ O) ₂ OAc]OAc·H ₂ O (brown)	C ₇	>300	60.10	28.90 (28.92)	4.76 (4.82)	13.76 (13.49)	14.10 (14.20)
Ni(HL _{III})(H ₂ O) ₂ (OAc) ₂ (blue)	C ₈	>300	70.61	30.23 (30.45)	4.76 (4.53)	13.84 (14.11)	14.63 (14.79)
Cu ₂ (HL _{III})(H ₂ O) ₆ (OAc) ₄ (greenish blue)	C ₉	>300	30.48	25.74 (25.65)	4.59 (4.88)	9.30 (8.55)	19.63 (19.39)
Zn(HL _{III})(H ₂ O) ₂ (OAc) ₂ (white)	C ₁₀	>300	70.67	29.18 (29.74)	4.20 (4.46)	14.08 (13.88)	16.40 (16.20)

Table 7.2 Characteristic stretching vibrations (cm^{-1}) for triazolylamic acids and their metal complexes

No.	vNH tr (amide)	Acid v OH (vCO)	vC=O acid (amide)	Triazole ring		vN=C-N	vN-N=C	H ₂ O coord. (lattice)	vM-N amide (triazole)	vM-O	vOAc
				vC=N	vN=C-N						
HL _I	3425 (3270– 3108)	2970–2617 (1190)	1743–1710 (1681)	1575	1520	1287	–	–	–	–	–
C ₁ CoL _I	3425 (3240– 3128)	2940–2600 (1180)	1712 (1650)	1577	1520	1288	3620–3500	432	–	–	1722, 1286 ^d
C ₂ NiL _I	3424 (3272– 3152)	2980–2600 (1170)	1705–1690 (1680)	1577	1520	1288	3580, 780, 650	–	500 ^a	–	1650, 1257 ^d
C ₃ ZnL _I	3425 (3230– 3130)	2950–2600 (1160)	1720–1680 (1650)	1577	1520	1284	–	460	–	–	1640, 1314 ^d
HL _{II}	3480 (3330– 3100)	2950–2550 (1180)	1680 (1630)	1580	1525	1275	–	–	–	–	–
C ₄ CoL _{II}	3400 (3325– 3100)	2910–2490 (1198)	1640 (1630)	1560	1510	1295	–	400	320 ^b , 360 ^c , 390	–	1610, 1420 ^e
C ₅ NiL _{II}	3430–3410 (3350– 3100)	2910–2490 (1190)	1635 (1630)	1555	1510	1305	3600–3500	440	330 ^b , 370 ^e	–	1710, 1240 ^d
C ₆ CuL _{II}	3417 (3247– 3085)	(1195)	1635 (1629)	1550	1510	1285	–	355	305 ^c , 393 ^b	–	1730, 1220 ^e
HL _{III}	3400 (3240– 3170)	2760–2573 (1190)	1691–1688 (1630– 1616)	1570	1520	1275– 1270	–	–	–	–	–
C ₇ CoL _{III}	3400 (3320– 3200)	2725–2530 (1180)	1640 (1630– 1610)	1570	1525	1270	3500–3480, 780, 810	–	470 ^a , 350 ^b , 367 ^c	–	1620, 1240 ^e 1580, 1410 ^f

(continued)

Table 7.2 (continued)

No.	ν NH tr (amide)	Acid ν OH (ν CO)	ν C=O acid (amide)	Triazole ring			H ₂ O coord. (lattice)	ν M-N amide (triazole)	ν M-O	ν OAc
				ν C=N	ν N=C-N	ν N=N=C				
C ₈ NiL _{III}	3452 (3350– 3200)	2740–2540 (1170)	1641 (1630– 1607)	ν C=N 1570	ν N=C-N 1520	ν N=N=C 1270	3600–3500 740 660	–	400 ^a , 305 ^c , 350 ^b	1710, 1240 ^d
C ₉ CuL _{III}	3480 (3380– 3250)	2740–2540 (1170)	1650 (1630– 1610)	ν C=N 1570	ν N=C-N 1520	ν N=N=C 1270	3500–3480 890, 850	–	450 ^a , 310 ^c , 370–350 ^b	1710, 1430 ^d
C ₁₀ ZnL _{III}	3450 (3320– 3240)	2720–2520 1160	1640 (1630– 1610)	ν C=N 1570	ν N=C-N 1525	ν N=N=C 1270	3560–3480 570, 530	–	430 ^a , 330 ^b , 320 ^c	1740, 1290 ^d

^aOxygen of coordinated water^bOxygen of COOH^cOxygen of acetate^dMonodentate^eBidentate^fIonic

The spectra of metal complexes exhibited shifts of the carbonyl stretching vibrations of carboxylic groups to lower frequencies referring to coordination with metal ions [27]. Bands assigned to OH stretching vibrations disappeared in the spectra of CoL_{II}, CuL_{II}, (C₄, C₆), while shifted to lower frequencies in the spectra of the other metal complexes. Such changes were combined with shift of ν C–O bands to higher frequencies. Such changes refer to carboxylate ion bonding in the former and COOH bonding in the latter. Bands assigned to NH and C=O stretching modes of amide group in the spectra of CoL_I and ZnL_I were shifted to lower frequencies indicating the involvement of amide group in the complexation process [27a], while that of NiL_I remained unchanged. Vibrational modes of triazole ring in the spectra of HL_{II} complexes (C₄–C₆) showed shifts of ν NH, ν C=N, ν N=C–N to lower frequencies and ν N–N=C to higher frequencies as a result of coordination of triazole nitrogens with the metal ions [19, 20a]. The acetate anion exhibited vibrational modes of monodentate ligand with metal complexes of HL_I (C₁–C₃), NiL_{II} (C₅), NiL_{III}, CuL_{III}, ZnL_{III} (C₈–C₁₀) complexes, bidentate with CoL_{II} and CuL_{II} (C₄, C₆) and both bridging and ionic ligand with CoL_{III} (C₇) [26]. Bands assigned to lattice water (CoL_I, NiL_{II}) and coordinated water (NiL_I, CoL_{III}, NiL_{III}, CuL_{III} and ZnL_{III}) were also observed [26b]. Bands assigned to M–N and M–O for metal complexes were located at lower frequencies depending on coordinating groups.

7.3.4 Thermal Analyses

Thermal behaviour of the ligands and their metal complexes at temperature range (30–1,000°C) following the TG modes showed that the weight loss in the three ligands involved departure of COOH groups, or CO₂ gas [28]. Liberation of N₂ molecules of triazole ring was observed which confirms what is reported in the literature [28, 1b]. Endothermic changes shown by DTG for L_I, L_{II} and L_{III} were observed at 350°C, 400°C and 150°C, respectively which may correspond to the melting points of the ligands.

Thermal behaviour of metal complexes depended mainly on type of coordination and bonding nature between the metal ions and donor atoms (metal-ligand affinity) [28, 29]. The early stages of thermal decomposition involve loss of lattice water (C₁ and C₇), counter ion outside the coordination sphere (C₇) and uncoordinated organic fragments. The final decomposition products of CoL_I, CuL_{II} and CuL_{III} (C₁, C₆ and C₉ respectively) were mainly metal oxides [28a,c]. The complexes CoL_{III} (C₇) and NiL_{III} (C₈) were incompletely decomposed while CoL_{II} (C₄) sublimed at the end stages. Thermograms of the ligands and some selected metal complexes are shown in Figs. 7.1 and 7.2 respectively.

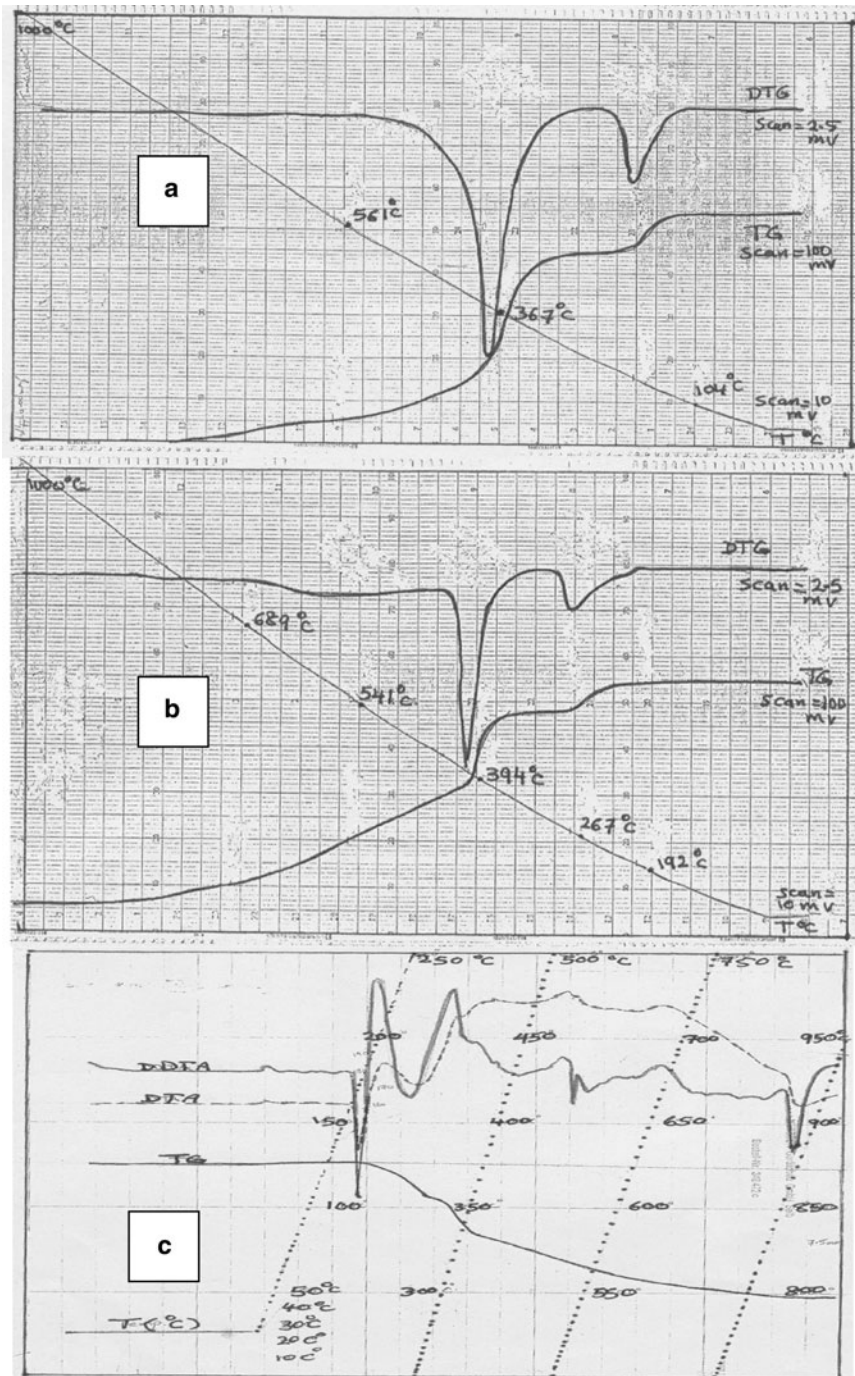


Fig 7.1 Thermographs of (a) HL_I, (b) HL_{II} and (c) HL_{III}

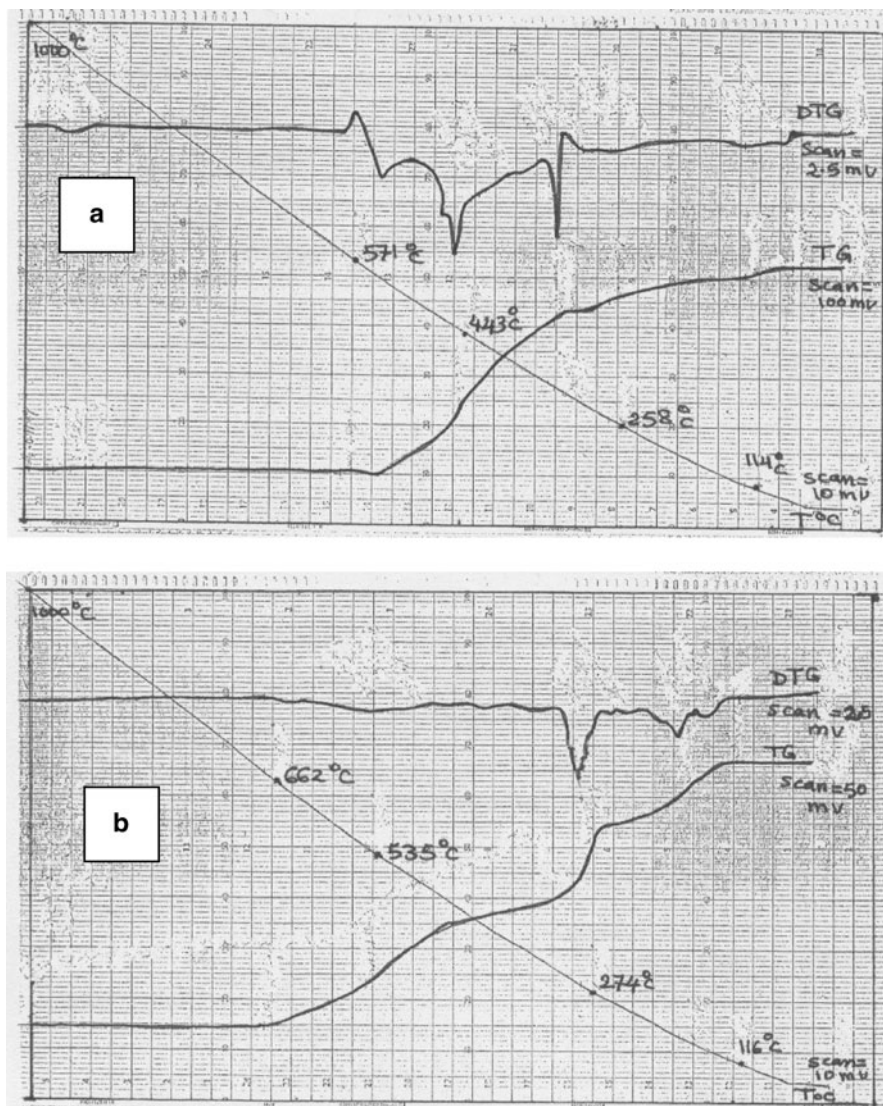


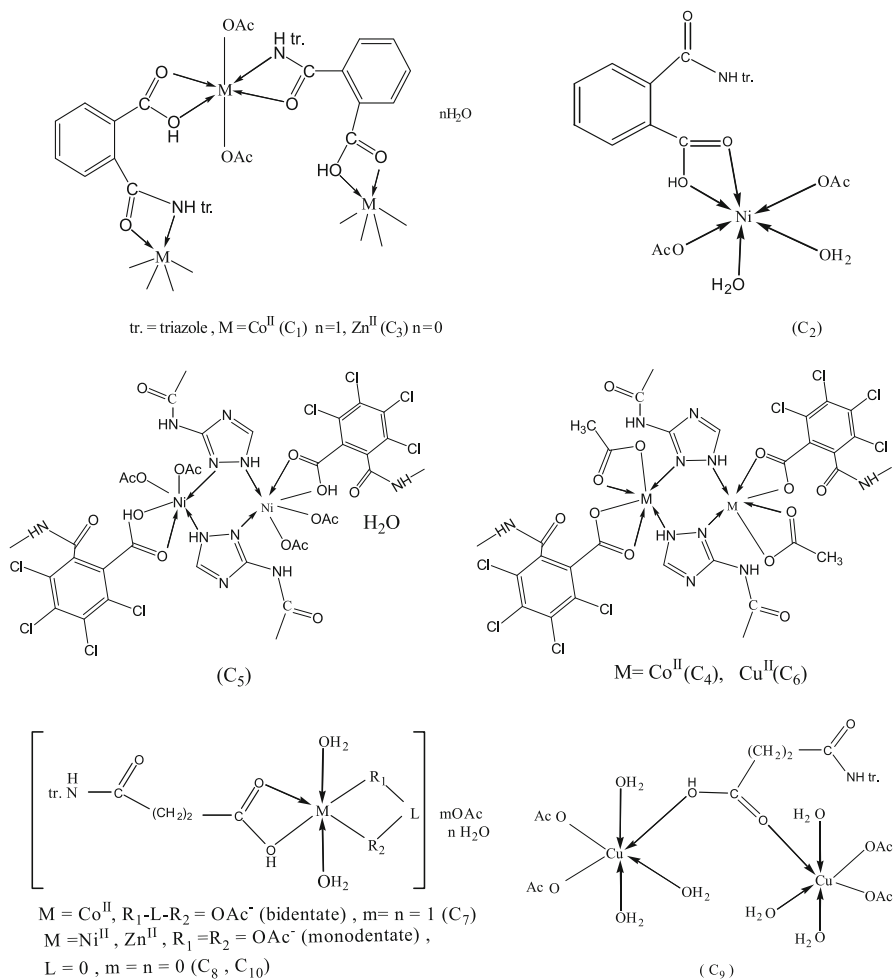
Fig 7.2 Thermographs of (a) CoL_I and (b) CuL_{III}

7.3.5 Electronic Spectra, Magnetic Moments and Conductivity Measurements

The electronic spectra of the three ligands in DMF exhibited high intensity bands appeared at 35890 , 36100 and 35970 cm^{-1} for HL_I , HL_{II} and HL_{III} respectively with shoulders at 29762 , 28571 and 30570 , 27502 cm^{-1} and were assigned to

Table 7.3 Electronic spectra, spectral parameters, molar conductance and magnetic moments for triazolylamic acid metal complexes

Symbol	Band energy (cm ⁻¹)	Assignment	B' (cm ⁻¹) (β)	10Dq (cm ⁻¹)	Molar cond. S.mol cm ²	μ _{eff} (BM)
CoL _I (C ₁)	v ₁ 6562(cal.)	4T _{1g} → 4T _{2g}	930	7654	0.0	5.28
	v ₂ 15322	4T _{1g} → 4A _{2g}	(0.957)			
	v ₃ 20833	4T _{1g(F)} → 4T _{1g}				
	v ₄ 25575	L → MCT				
NiL _I (C ₂)	v ₁ 10255	3A _{2g} → 3T _{2g}	959.2	10152	46.0	3.45
	v ₂ 16924	3A _{2g} → 3T _{1g}	(0.931)			
	v ₃ 28205	3A _{2g} → T _{1g(F)}				
ZnL _I (C ₃)	v ₁ 35129	IL π → π*	-	-	4.0	Diamagnetic
	v ₂ 25906	L → MCT				
	v ₃ 20000					
CoL _{II} (C ₄)	v ₁ 5886(cal.)	4T _{1g} → 4T _{2g}	910	8026	13.0	4.85
	v ₂ 14186	4T _{1g} → 4A _{2g}	(0.937)			
	v ₃ 18500	4T _{1g(F)} → 4T _{1g(F)}				
NiL _{II} (C ₅)	v ₁ 10142	3A _{2g} → 3T _{2g}	621	10244	3.0	3.17
	v ₂ 15848	3A _{2g} → 3T _{1g(F)}	(0.603)			
	v ₃ 24840(cal.)	3A _{2g} → 3T _{1g(F)}				
CuL _{II} (C ₆)	v ₁ 13178	2B _{1g} → 2B _{2g}	-	-	12.0	2.125
	v ₂ 15600	2B _{1g} → 2Eg				
	v ₃ 2582(cal.)	4T _{1g} → 4T _{2g}	783	11119	62.2	5.36
CoL _{III} (C ₇)	v ₁ 10204	4T _{1g} → 4A _{2g}	(0.806)			
	v ₂ 18401(cal.)	4T _{1g} → 4A _{2g}				
	v ₃ 20755	4T _{1g(F)} → 4T _{1g(F)}				
NiL _{III} (C ₈)	v ₁ 10281	3A _{2g} → 3T _{2g}	723.2	10333	14.0	3.27
	v ₂ 16370	3A _{2g} → 3T _{1g(F)}	(0.702)			
	v ₃ 2582(cal.)	3A _{2g} → 3T _{1g(F)}				
CuL _{III} (C ₉)	v ₂ 15552	2Eg → 2T _{2g}	-	-	34.0	2.53
	v ₁ 34000	IL π → π*			5.0	Diamagnetic
	v ₂ 28947	L → MCT				
ZnL _{III} (C ₁₀)	v ₃ 25575					



Scheme 7.2 Suggested structures of metal complexes of HL_I , HL_{II} and HL_{III}

$\pi \rightarrow \pi^*$ transitions of aromatic and heterocyclic rings as well as carbonyl groups [23]. Low intensity bands appeared at lower wavenumbers in the visible region at 23810 and 23057 cm^{-1} in the spectra of HL_{II} and HL_{III} and were assigned to $n \rightarrow \pi^*$ transitions [23].

Complexation with metal ions caused bathochromic shifts of the $\pi \rightarrow \pi^*$ transition bands except NiL_{III} (C_8) which showed hypsochromic shifts. The spectral parameters (B' , β , and $10Dq$) and energies of unobserved ligand field bands in the spectra of $\text{Co}(\text{II})$ and $\text{Ni}(\text{II})$ complexes were calculated by applying observed band energies on Tanabe – Sugano diagrams of the two ions [30]. These data together with band assignments are described in Table 7.3. Values of magnetic moments (μ_{eff}) of complexes in the solid state showed high spin octahedral coordination behavior [30].

The electronic spectra of copper complexes indicate spin orbital contribution with distorted octahedral geometry [29, 30]. The Zn(II) complexes (C₃ and C₁₀) showed absorption bands assigned to L → M charge transfer [30b]. All complexes showed non-electrolytic nature in DMF (10⁻³ M) except CoL_{III} (C₇) which exhibited ionic behaviour of 1:1 [31] (Table 7.3). According to these data and both elemental and thermal analyses the structures of the metal complexes of the three triazolylamic acids may be suggested as illustrated in Scheme 7.2.

7.3.6 Antibacterial Activities

The growth inhibition tests of the three ligands against the bacterial cultures *Proteus mirabilis*, *Escherichia coli*, *Staphylococcus aureus*, *Pseudomonas aeruginosa* and *Klebsiella pneumonia* showed that they were all inactive except HL_{II} which showed inhibition zones of 18 mm diameter against *Pseudomonas aeruginosa* and 12 mm against both *Staphylococcus aureus* and *Klebsiella pneumonia*. Among the Cu(II) and Co(II) complexes, only the Cu(II) complex of HL_{II} (C₆) showed inhibition zone of 18 mm against *Staphylococcus aureus*.

7.4 Conclusions

The three amic acid derivatives showed potent chelating behaviors due to the presence of various donor atoms forming bi, tri and polynuclear metal complexes.

References

1. (a) Pyriadi TM, Abdulameer I (2000) Preparation of phenol formaldehyde resin containing pendant isoimides and their isomerization to stable resins. *J Polymer Sci A Polymer Chem* 38:3244–4252; (b) Al-Azawi Ah (1998) Synthesis and polymerization of N-substituted citraconimide acrylates and their copolymers with N-substituted maleimides. PhD thesis, Chemistry department, College of Science, Baghdad University; (c) Al-tememy EO (1998) Synthesis of poly(allylamines), their derived amic acids and imides. Curing the unsaturated products via grafting and crosslinking. PhD thesis, College of Science, Chemistry Department, Baghdad University
2. (a) Xu X, Xu S, Wang Z (1984) *Huanong Huamgong Xueyuan Xuebao* 4:485–93 (ch). *Chemical Abstract* (1985) 103:38978 h; (b) *Farbenindustrie A-G* (1936) *Wetting agents* *chemical abstract* (1936) 30:7727
3. Japan Kokai Tokkyo Koho (1936) Photopolymers for printing plate fabrication Japan Patent 59, 218 440 [84, 218, 440] Application 83, 92, 035 25 May 1983 6 pp; *Chem Abstr* (1985) 102:229494 m
4. Li S, Xie J, Zhao S (1987) Epoxy resin potting composition foaming. *Zhaon lishen-qing Coongkai Shouomingshu*, CN 86, 100, 232, Application 1986; *Chem Abstr* (1987) 107:155569 u

5. Hans B, Hans G (1984) β -(Benzothiazolythio) and β -(benzimidazolylthio) carboxylic acid. European Patent, Application EP 126, 030, 4 pp; Chem Abstr (1985) 102:1320282
6. Elsadek MM, Muhyf M, Jomy AA (1989) Synthesis and spectra of phthalimido derivatives. J Chem Eng Data 34:257–259
7. David S, Felix B (1941) Condensation of heterocyclic amines with dicarboxylic anhydrides. J Org Chem 6:774–780
8. (a) Loktyushkina MB, Glotova RV (1982) Monitoring of the preparation of bis maleimino acids. Khim Prom – st ser. Metody Anal. Kontrol'ya Kach Prod. Khim Prom-sti 2:26–27; Chem Abstr (1983) 96:163880h; (b) Katagi T, Inoi T (1985) Synthesis and anti inflammatory activity of malonamic acid, malonamate, and malonamide derivatives of some heterocyclic compounds. Chem Pharm Bull 33:4878–4888; (c) Werbin H, Spoerri P (1947) Cyclization of N-succinyl glycine dimethyl ester. J Am Chem Soc 69:1981–1984
9. (a) Balasubramaniyan V, Argade NP (1989) Reaction of cyclic anhydrides XVI: a novel approach to angular oxygenated pyrrolobenzoxy azinones. Tetrahedron 45:835–842; (b) ElSaadek MM, Werren CD, Jeanloz RW (1982) New synthesis of benzylated chitabiose derivatives employing 4-acetyl-3,6-di-O-benzyl-2-deoxy-2-phthalimido- α -D-glucopyranosyl chloride. Carbohydr Res 100:C35–C38; (c) King FE, Clark-Lewis JW, Wade R, Swinden WA (1957) Synthesis from phthalimido acids Pt VII: oxazolones and other intermediates in the synthesis of phthalyleptides and an investigation of maleic acid derivatives of amino acids. J Chem Soc:873–879; (d) Ondrus V, Fisera L (1997) Synthesis and 1,3-dipolar cycloaddition reactions of chiral maleimides. Molecules 2:49–50
10. Suh J, Kim MJ, Seong NJ (1981) Ionization and intramolecular reaction of N, N-bis[(2-pyridyl)ethyl] and N, N-bis[(2-pyridyl)methyl] maleamic acids, an enzyme model. J Org Chem 46:4354–4358
11. (a) Joshi B, Joy D, Dilip HG (1983) Synthesis and anticonvulsant activity of 7-oxobicyclo [2.2.1] heptane derivatives Part II: N-Alkyl, N-Aryl and N-heteroaryl derivatives of 3,6-epoxyhexa hydro-phthalic acid amide. Indian J Chem 22B:136–139; (b) Miller CA, Long LM (1951) Anticonvulsant I. An investigation of N-R- α -R₁- α -phenyl succinimide. J Am Chem Soc 73:4895–4898
12. (a) Morgan GT, Watton E (1931) New derivative of p-arsanilic acid, Pt I: p-Arsanosuccinilic acid and related compounds. J Chem Soc 615–619; (b) Correa R, Filho VC, Rosa PW, Pereira CI, Schlemper V, Nunes RJ (1997) Synthesis of new succinimides and sulphonated derivatives with analgesic action on mice. Pharm Sci 3:67–71
13. Ching-Hua Huang, Stone Alan T (1999) Hydrolysis of naptalam and structurally amides inhibition by dissolved metal ions and metal (hydr.) oxide surfaces. J Agric Food Chem 47:4425–4434
14. (a) Klaus U, Oesterreich T, Volk M, Splitter MG (1998) Interaction of aquatic dissolved organic matter with amitrole, the nature of bound residues. Acta Hydrochim Hydrobiol 26:311–317; (b) Lynch DE, Smith G (1992) Molecular co-crystal of carboxylic acids. 8-Structure of the 1:1 dduct of 3,5-dinitrobenzoic acid with 3-amino-1,2,4-triazole. Acta Crystallogr C48:1265–1267
15. (a) Tephly TR, Hasegawa E, Baron J (1971) Effect of drugs on heme synthesis in the liver. J Clinical Exp Biochem, Part II 20:200–214; (b) Casarett LJ, Doull J (1980) Toxicology the basic science of poisons, 3rd edn. McMillan Publishing company, New York, pp 131–559
16. (a) Vissler PT, Taylor BF (1993) A new mechanism for the aerobic catabolism of dimethyl sulphocide. Appl Environ Microbiol 59:3784–3789; (b) Honlinger C, Hampel WA, Rohr M, Kubicek CP (1988) Differential effect of general amino acid control of lysine biosynthesis on penicillin formation in strains of Penicillium chrysogenum. J Antibiot XLI 2:255–257; (c) Bekircan O, Bektas H (2006) Synthesis of new bis-1,2,4-triazole derivatives. Molecules 11:469–477; (d) Hui XP, Zhang Lin-Mie, Zhang Zi-Yi, Wang Fang (2000) Synthesis and antibacterial activity of 5-triazoles. J Chin Chem Soc 47:535–539; (e) Molina J, Martins Filho O, Berner Z, Romanha AJ, Loebenbeog D, Urbina JA (2000) Activities of triazoles derivatives against drug resistant strains of protozoan parasite Trypanosoma cruzi in immuno competent and immuno suppressed murin hosts. Antimicrob Agents Chemother 44:150–155

17. Salama SM, Atwal H, Gandhi A, Simon J, Poglod M, Montasari H, Khan JK, Furkawa T, Saito H, Nishida K (2001) In vitro and in vivo activities of *Syn* 2836, *Syn* 2869, *Syn* 2903, and *Syn* 2921. New series of triazole antifungal agents. *Antimicrob Agents Chemother* 45:2420–2426
18. Onary Y (1986) Chelating polymers bearing triazolylazophenol moiety as the functional group. *J Appl Polym Sci* 31:1663–1670
19. (a) Vassilev GN, Davarski K, Petrova A, Berberova P (1994) Chemical structure and herbicidal activity of some new metal coordination compounds of 3-amino-1,2,4-triazole (amitrole). *Comptes rendus de l'Academie Bulgare des Sciences Tome* 47(4):53–56; (b) Gabryszewski M (1998) Synthesis and characterization of the copper(II) complexes with 3-amino-1,2,4-Triazole and 3-amino-5-methylthio-1,2,4-triazole. *Pol J Chem* 72(12):2519–2523; (c) Leonava TG, Larinov SV, Sheladyakova L A, Ikorskii VN (1984) Complexes of metal nitrates with 3,5-diamino-1,2,4-triazole. *Izvestia Sibirskogo Otdeleniia Akademii Nauk USSR, Seriiia Khimii Nauk* 17:65–70; *Chem Abstr* (1984), 100: 150068a; (d) Haasnoot JG (2000) Mononuclear oligonuclear and polynuclear metal coordination compounds with 1,2,4-triazole derivatives as ligand. *Coord Chem Rev* 200–202:131–185
20. (a) Petra JVK, Dante G, Rudolf AGD, Haasnoot J, Reedijk J, Claudia Z (1995) Isotopic and anisotropic, magnetic exchange interaction through μ -N, N2-1,2,4-triazole and μ -sulfato bridges. *Inorg Chem* 34:5175–5180; (b) Navarro JAR, Romero MA, Salas JM, Quiros M, El Bahraoui J, Molina J (1996) Binuclear platinum(II) triazolopyrimidine bridged complexes: preparation, crystal structures, NMR spectroscopy and ab initio MO investigation on the bonding nature of Pt(II). Pt(II) interaction in the model compound $[Pt_2(NHCHNC(CH_2)(CH_3))_4]$. *Inorg Chem* 35:7829–7835
21. (a) Fredrick JF, Gentile AC (1960) The stability constants of manganese chelate of 3-amino-1,2,4-triazole. *Arch Biochem Biophys* 91:178; (b) Magos L, Sugata Y (1974) Effects of 3-amino-1,2,4-triazole on mercury uptake by in vitro human blood samples and by whole rats. *Toxicol Appl Pharm* 28:367–373
22. (a) Perrin DD, Armarego WLF (1980) Purification of laboratory chemicals, 2nd edn. Pergamon Press, New York; (b) Vogel AI (1972) A textbook of practical organic chemistry, 3rd edn. Longman, London
23. (a) Pretsch E, Buhlmann PA (2000) Structure determination of organic compounds, 3rd edn. Springer, Berlin; (b) Silverstein RM, Webster FX (1997) Spectrometric identification of organic compounds, 6th edn. Wiley, New York
24. (a) Daoud KM, Eisa MA (2002) Synthesis of some new 3-(arylaminoethyl)4(H)-1,2,4-triazole-5-thiol. *Nat J Chem* 5:107–114; (b) Emilsson H, Selander H (1988) Spectroscopic identification of some derivatives of 3,4-diamino-4-H-1,2,4-triazole and 3-hydrazine. *J Heterocycl Chem* 25:565
25. (a) Berez G, Pongo L, Koresdi I, Reiter J (2002) On Triazoles XLV[II]. Synthesis of 5,7-Diamino-1,2,4-triazole [1,5-a] [1,3,5] triazines. *J Heterocycl Chem* 39:327–333; (b) Abul Haj M, Salas JM, Quiros M, Mohlina J, Faures R (2000) 5-oxo and 7-oxoderivatives of [1,2,4] triazolo-[1,5-a] pyrimidine characterization and theoretical study. *J Mol Struct* 519:165–172
26. Nakamishi K (1962) Practical infrared absorption spectroscopy. Nanked Company Ltd, Tokyo
27. (a) Adams TA (1967) Metal – ligand and related vibrations. Edward Arnold Ltd, London; (b) Nakamoto K (1997). Infrared and Raman spectra of inorganic and coordination compounds, 5th edn. Wiley, New York
28. (a) Hemminger, W (1980) Thermal analysis, vol 2. Birkhauser, Budapest; (b) Al – Ansari RM (1984) Thermoanalytical investigation on heterocyclic organic compounds Pt IV. Thermal decomposition of 1,2,3- triazolino-4,5-(N-phenyl) dicarboximides. *Thermochim Acta* 19:139–147; (c) Duval C (1963) Inorganic thermogravimetric analysis, 2nd edn. Elsevier, London
29. (a) Dubey SN, Beena K (1985) Triazole as complexing agents, synthesis and characterization of Co(II), Ni(II), Cu(II), Zn(II), and Cd(II) complexes with 4-amino-5-mercapto-3-n-propyl-5-triazole and 5-mercapto-3-n-propyl-4-salicylidene amino-5-triazole. *Indian J Chem* 24A:950–953; (b) Allan JR, Baillie GM, Banner JG (1989) Thermal studies on maleic acid compounds of manganese (II), nickel(II), copper(II) and zinc (II). *Thermochim Acta* 143:283–288

30. (a) Lever ABP (1968) *Inorganic electronic spectroscopy*. Elsevier publishing company, Amsterdam/London/New York; (b) Figgis BN (1966) *Introduction to ligand fields*. Inter-Science Publishers, A division of John Wiley and Sons, New York/London-Sydney; (c) Bruger K (1967) *Coordination chemistry – experimental methods*. Butterworth, London; (d) Sutton D (1968) *Electronic spectra of transition metal complexes*, 1st edn. McGraw Hill Publishing Company Ltd, New York; (e) Miessler GA, Tarr DA (1999) *Inorganic chemistry*, 2nd edn. Prentice Hall, Upper Saddle River
31. Geary WJ (1971) The use of conductivity measurements in organic solvents for the characterization of coordination compounds. *Coord Chem Rev* 7:81–122

Chapter 8

Regioselective Synthesis of Polyfluorinated Pyrazoles and Evaluation of Antimicrobial Activity

Madhukar N. Jachak, Dilip R. Birari, Deepak P. Shelar, Sandeep R. Patil, Ramhari V. Rote, Santosh S. Shinde, and Sandip M. Bagul

Abstract A series of 1,3,5-trisubstituted pyrazole derivatives were prepared from asymmetrical polyfluorinated 1,3-diketone. The reactivity of substituted hydrazines towards the diketone compound is studied leading to the formation of regioisomers. The polyfluorinated pyrazoles were utilized for the alkylation with N-aryl acetamides to yield N-alkyl products. Then they were hooked with amino acid esters such as L-phenylalanine, L-proline, L-tyrosine, and L-norvaline by multistep process. The antimicrobial activities of the synthesized pyrazoles were evaluated. All synthesized compounds were characterized by spectroscopic and analytical methods.

8.1 Introduction

Pyrazoles have been widely described as pharmaceutical therapeutic agents, including anti-inflammatory and anti-diabetic agents. Formation of halogenated 1-arylbutane-1,3-diones has been described [1–3]. In addition the preparation of pyrazoles by the condensation of diketones and hydrazines has also been reported [4–6]. Poly and perfluoroalkyl derivatives of aromatic and heteroaromatic compounds are intensively studied [7–11]. The 1,3,5-trisubstituted pyrazole structural motif is found in numerous drug targets. A common approach into these systems including commercial process is to react substituted hydrazine with diketone [12]. The π -excessive five membered nitrogen heterocycles such as pyrazole have

M.N. Jachak (✉) • D.R. Birari • D.P. Shelar • S.R. Patil • R.V. Rote • S.S. Shinde • S.M. Bagul
Organic Chemistry Research Centre, Department of Chemistry, K. T. H. M. College, Gangapur
Road, Nashik 422 002, Maharashtra, India
e-mail: mnjachak@hotmail.com; dilip.birari@cipla.com; deeprity83@gmail.com;
dr.sandeepatil28@gmail.com; rote.ramhari509@rediffmail.com; sss.3s@rediffmaill.com;
sandipbagul@gmail.com

been extensively used in transition metal chemistry because pyrazoles are poorer π -acceptor and behave as π -donor sites [13, 14]. Pyrazole derivatives possess anti-inflammatory and antitumor activity. Pyrazoles also are of particular interest to the chemical community because they exhibit pesticide properties and there is increasing interest on biological model systems containing pyrazole chelates [15–28]. The synthesis of pyrazoles remains of great interest due to the wide application of such heterocycles in the pharmaceutical and agrochemical industry. The most important methods for preparing this class of heterocycles are reactions between hydrazines with β -difunctional compounds [29–31]. The polyfluoro 1,3-diketones function as metal chelating agents and have been shown to act as hydrogen ionophores, disrupting intercellular pH gradients. This results in an uncoupling of mitochondrial oxidative phosphorylation, thus disrupting energy production. Various members of this class of compounds have been shown to exhibit antibacterial, antiviral, anthelmintic, fungicide and/or herbicidal activity [32–39].

8.2 Methodology

Regioisomers of pyrazoles were obtained by reaction of an asymmetrical polyfluorinated 1,3-diketone with monosubstituted hydrazines under mild conditions. Antimicrobial activities of the synthesised pyrazoles were evaluated.

8.3 Results and Discussion

There are several methods described in the literature to prepare the pyrazole ring, the condensation of 1,3-dicarbonyl compounds with hydrazines and its variations remain the most common and efficient method to construct these five membered heterocyclic systems i.e. Knorr pyrazole synthesis. In case of unsymmetrical 1,3-diketones, the 3,5-dihydroxypyrazolidine and hydrazone intermediates have been isolated in some cases [40].

The regioisomers of pyrazole formation depend on enolisation of dione. Recently Singh et al. summarized the mechanism of pyrazole formation *via* Knorr reaction between 1,1,1-trifluoropentane-2,4-dione with monosubstituted hydrazines [41]. The study of ^{19}F NMR showed greater enolization of trifluoromethyl ketone versus the methyl ketone. Thus free NH_2 of hydrazine reacts with ketone rather than enol as revealed by NMR studies and the carbonyl group reacts faster than enol form [42–44].

The rates of dehydration of 3,5-dihydroxy pyrazolidine intermediates of the two isomers of unsymmetrical diketone decide the product distribution ratio. Computational studies were done to show the effect of hydrazine substituent on the dehydration in conjunction with semi-empirical calculations [41].

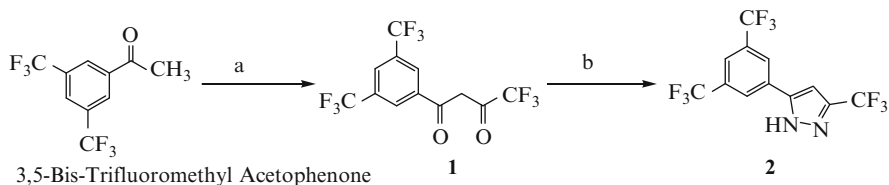
In the case of unsymmetrical diketone, definitely there is potential of producing regioisomers as well as the effect of hydrazine substituent on the rate of dehydration. Many efforts have been done and reported in the literature to mitigate the difficulty to isolate the single pure regioisomer by enhancing the selectivity of product formation. The methods like masking of either counterpart i.e. hydrazine or diketone and made available *in situ* during the course of reaction by releasing from the masked derivative directs the Knorr pyrazole synthesis to the formation of major product. Another method which enhances the selectivity is the green solventless process of getting the pyrazole derivative by mixing equimolar amounts of 1,3-dicarbonyl compound with the hydrazine with a drop of sulfuric acid [45].

Although these methods increased the selectivity of product formation up to 85–95%, they still could not guarantee to furnish either regioisomer as a single exclusive product. The increasing demand of many pharmaceutical active ingredients, dyes, and chelates insists on single exclusive regioisomer because of the total bioactivity that resides in a required isomer and another may have toxicity. Hence we have tried to synthesize a single exclusive product in this communication.

8.3.1 Synthesis of 1-(3,5-Bis(Trifluoromethyl)Phenyl)-4,4,4-Trifluorobutane-1,3-Dione (1)

The starting material unsymmetrical 1,3-diketone **1** bearing trifluoromethyl substituents as a light yellow oil in 90% yield was prepared from 3,5-bis-trifluoromethyl acetophenone upon Claisen condensation with ethyl trifluoroacetate using sodium methoxide as base in methyl tert-butyl ether.

The IR spectrum of this oil showed the presence of two broad bands at 1823 and 1745 cm^{-1} corresponding to the carbonyls of aryl and trifluoromethyl substituted ketones. The broad bands at 3345 cm^{-1} indicated that enol form was also present in this compound. The ^1H NMR spectrum showed tautomeric signals at δ 8.63 and δ 8.42 ppm in the downfield region for aromatic protons. It was interesting to note that the compound showed a sharp singlet at δ 7.23 ppm for olefinic proton (in case of enolised form) and a singlet at δ 2.70 ppm for methylene protons which was flanked between by two carbonyls indicative that compound exists in keto-enol form. The structure was also supported by ^{13}C NMR spectrum which showed signals in the downfield region at δ 196, 194 and 182 ppm for two carbonyl carbons and one for its tautomer. The signals for quaternary carbons, methylene carbons and CH carbons were identified by DEPT experiment. The compound showed signal at δ 94.6 ppm for CH carbon of the enol form whereas the reverse signal for CH_2 group appeared at δ 53.1 ppm indicating the presence of keto form.



Scheme 8.1 Synthesis of pyrazole **2**. Conditions: (a) $\text{CF}_3\text{COOCH}_2\text{CH}_3$, NaOMe/MeOH , TBME, 90%; (b) $\text{N}_2\text{H}_4 \cdot \text{H}_2\text{O}$, EtOH/AcOH , 92%

8.3.2 Synthesis of 5-(3,5-Bis(Trifluoromethyl)Phenyl)-3-(Trifluoromethyl)-1H-Pyrazole (2)

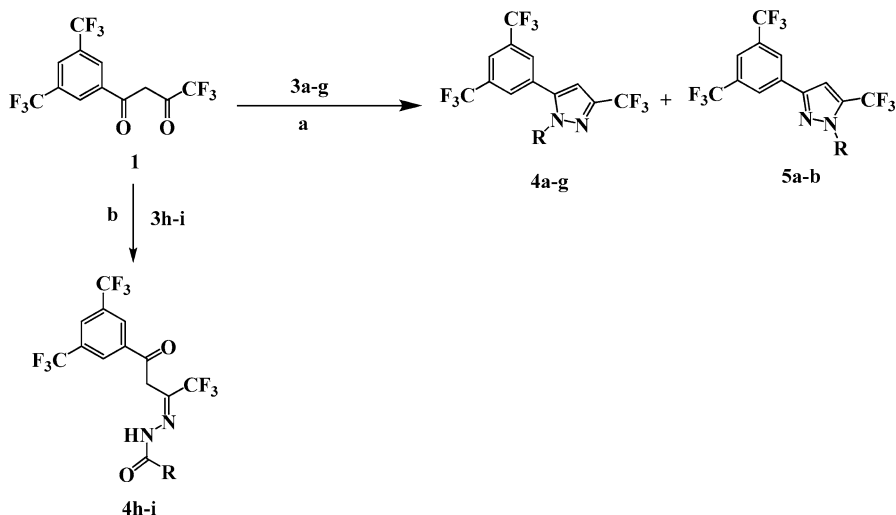
The analytically confirmed 1,3-diketone **1** having two electrophilic centers was reacted with bidentate nucleophiles like hydrazine hydrate or substituted hydrazines to construct electron rich five-membered heterocycles. Thus, compound **1** was reacted with hydrazine hydrate in ethanol in the presence of catalytic amounts of acetic acid at reflux temperature for 20 h (Scheme 8.1). The residue obtained after evaporation of the solvent was purified by column chromatography eluting with dichloromethane. The pure fractions were collected and evaporated under reduced pressure to furnish colourless needles in 92% yield, and the structure was assigned on the basis of spectral and analytical data (Data are given in experimental section).

8.3.3 Synthesis of *N*-Substituted Pyrazoles 4 and 5; Study of Regioisomer Formation

We extended this methodology to a series of substituted pyrazoles using mono-substituted hydrazines **3a-g**. Thus, solution of **1** in ethanol was treated with **3a** in the presence of a catalytic amount of acetic acid at reflux temperature for 20 h (Scheme 8.2). As revealed by TLC two products were formed in this reaction and were separated by column chromatography eluting with dichloromethane. The pure fractions were collected and evaporated completely to obtain two compounds as major and minor derivatives in 80% and 4% yield respectively. The major compound was assigned structure **4a** and compound obtained in small quantity was characterized as a regioisomer of **4a** and was assigned structure **5a** on the basis of spectral and analytical data (Data are given in experimental section).

The following substituted hydrazines **3a-i** were used for the formation of pyrazoles **4a-g**, **5a-b** and acyl hydrazones **4h-i** (Table 8.1).

Analogously reaction of **3b** produced two compounds in 77% and 8% yield respectively and which were characterized by spectral and analytical methods. However, only single major products **4c-g** were obtained from the reactions of **1** with **3c-g**.



Scheme 8.2 Synthesis of pyrazoles **4a-g** and **5a-b** as well as acyl hydrazones **4h-i**. Conditions: (a) RNHNH₂, EtOH/AcOH; (b) RCONHNH₂, EtOH/AcOH

Table 8.1 Synthesis of compounds **4a-i** and **5a-b**

3	R	4 (% yield)	5 (% yield)
a	4-(H ₃ CNHSO ₂ CH ₂ CH ₂)C ₆ H ₄	80 ^a	4.0 ^a
b	4-(H ₃ CNHSO ₂ CH ₂)C ₆ H ₄	77 ^a	8.0 ^a
c	4-(HOOC)C ₆ H ₄	85 ^b	–
d	4-(H ₃ CCH ₂ COCO)C ₆ H ₄	61 ^a	–
e	4-(H ₂ NSO ₂)C ₆ H ₄	85 ^a	–
f	C ₆ H ₅	79 ^c	–
g	2,4-DichloroC ₆ H ₃	94 ^b	–
h	H ₃ CCOCO	76 ^a	–
i	C ₆ H ₅ CO	83 ^a	–

^aIsolated yields after recrystallization from ethanol

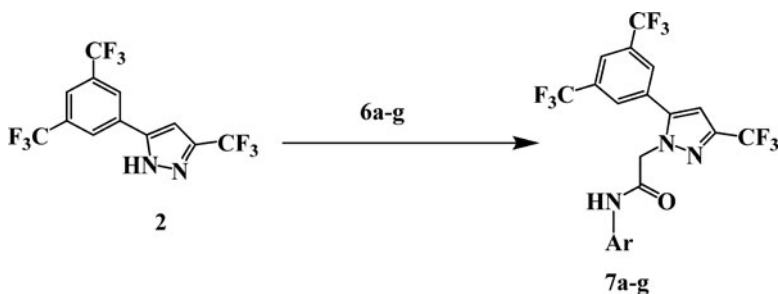
^bIsolated yields after recrystallization from acetone

^cIsolated yields after recrystallization from ethyl acetate

The condensation of **1** with substituted hydrazides **3h-i** in an analogous way produced the compounds as uncyclised derivatives (Scheme 8.2). The structures of these compounds were deduced from spectral and analytical data which are given in the experimental section.

8.3.4 Alkylation of 5-(3,5-Bis(Trifluoromethyl)Phenyl)-3-(Trifluoromethyl)-1H-Pyrazole (**2**); Synthesis of **7a-g**

The pyrazole **2** was studied for the alkylation with N-aryl acetamides. Thus, compound **2** was reacted with 2-bromo-N-aryl acetamide compounds **6** in DMF at room temperature under basic condition of potassium carbonate for 3 h (Scheme 8.3).



Scheme 8.3 Synthesis of N-alkylated pyrazoles **7a-g**. Conditions: ArNHC(=O)CH₂Br, K₂CO₃, DMF, 25–30°C

Table 8.2 Synthesis of compounds **7a-g**

6, 7	Ar	% yield ^a	m.p. (°C)
a	2-Chloro-6-fluoro	76	202–204
b	2,4-Dichloro	74	198–200
c	4-Methyl	72	235–237
d	4-Chloro	81	193–195
e	4-Chloro-3-trifluoromethyl	77	158–160
f	4-Fluoro	87	243–245
g	2,5-Bis(trifluoromethyl)	85	184–186

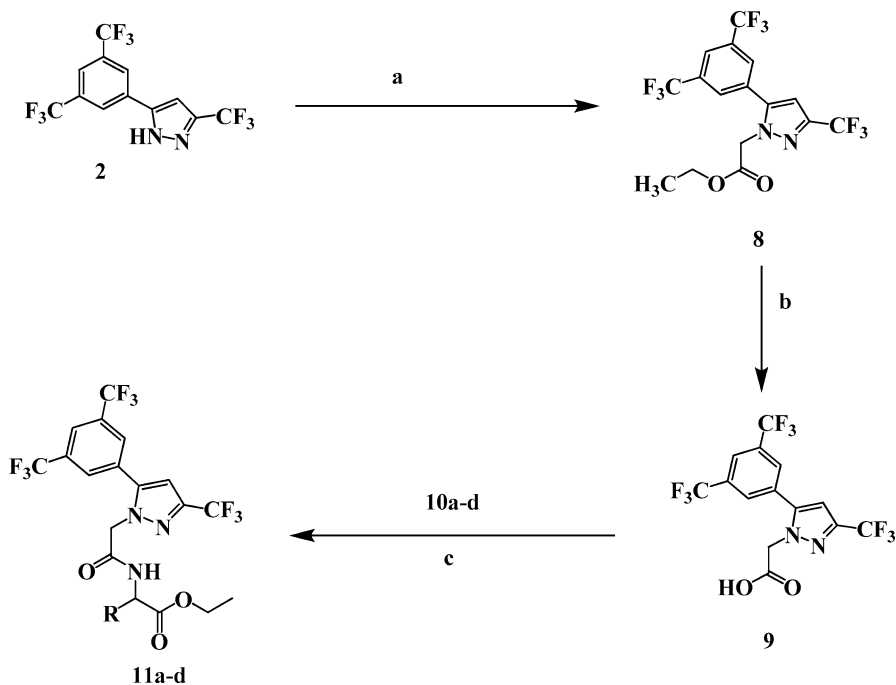
^aIsolated yields after recrystallization from ethanol

The colourless solids obtained after quenching the reaction mass in ice cold water were isolated and recrystallized from ethanol to furnish colourless solids in 72–87% yield (Table 8.2). The obtained solids were characterized by spectral and analytical methods.

We planned the third protocol to obtain the pyrazole derivatives using an aprotic polar solvent. It is interesting to observe that using an aprotic polar solvent and lower temperature for alkylation of 3,5-disubstituted pyrazole **2**, only one isomer was obtained exclusively as 1,3,5-trisubstituted derivatives **7a-g** in good yield. All the reactions were carried out at room temperature in dimethyl formamide and using potassium carbonate as base.

8.3.5 Attachment of Amino Acid Linkers to 5-(3,5-Bis (Trifluoromethyl)Phenyl)-3-(Trifluoromethyl)-1H-Pyrazole **2**; Synthesis of **11a-d**

The polyfluorinated pyrazole **2** was utilized further for hooking the amino acids with a similar methodology adopted for compounds **7**. In this protocol the pyrazole **2** was linked to amino acid esters through multistep process (Scheme 8.4). The pyrazole was first reacted with ethyl 2-bromo acetate to obtain the N-linked acetate in 96.3%



Scheme 8.4 Synthesis of amino acid linked pyrazoles **11a-d**. Conditions: (a) $\text{BrCH}_2\text{COOCH}_2\text{CH}_3$, K_2CO_3 , ACN, Reflux, 96%; (b) 2N NaOH/THF, 2N HCl, 90%; (c) amino acid esters **10a-d**, TBTU/DIEA/DCM

Table 8.3 Synthesis of compounds **11a-d**

10, 11	Amino acid ester	% yield ^a	m.p. (°C)
a	L-phenyl alanine ethyl ester	83	50–53
b	L-proline ethyl ester	84	35–38
c	L-tyrosine ethyl ester	88	43–45
d	L-norvaline ethyl ester	78	63–65

^aIsolated yields from hexane

yield after recrystallization from ethanol as colourless needles. The colourless needles were characterized by ^1H NMR and mass analysis (Table 8.3).

Hydrolysis of pure **8** was carried out in tetrahydrofuran in the presence of 2N NaOH. Thus, compound **8** was dissolved in tetrahydrofuran and treated with 2N NaOH for 5 h at 50°C. Colourless material was isolated on acidification of the reaction mass in 90% yield. The obtained colourless solid was characterized by proton NMR and mass analysis.

Acid **9** was then coupled with the amino acid esters **10a-d** of the L-series using TBTU as peptide coupling reagent to furnish colourless solids in 78–88% yield. Thus, compound **9** was reacted with **10d** in the presence of peptide coupling reagent and diisopropyl ethylamine (DIEA). After stirring at room temperature

Table 8.4 Antimicrobial activity of compounds **1**, **2**, **4**, **7** and **11**

Cpd	Inhibition zone (in mm)					
	<i>S. aureus</i>	<i>E. coli</i>	<i>B. subtilis</i>	<i>P. aeruginosa</i>	<i>A. niger</i>	<i>C. albicans</i>
1	11.11	7.56	13.12	7.8	–	–
2	12.11	8.21	7.56	8.23	–	–
4a	7.23	8.16	8.34	–	–	–
4b	–	7.43	–	8.12	–	–
4c	8.92	9.12	7.23	7.34	–	–
4e	7.34	8.11	9.12	–	8.12	8.34
4f	7.33	8.19	12.34	11.21	–	–
7a	–	7.34	–	7.8	–	–
7b	–	8.12	–	7.23	–	–
7c	7.11	–	8.34	–	7.28	8.18
7d	8.76	–	7.12	–	–	–
7e	7.25	–	8.23	–	7.12	8.27
7f	–	8.23	7.26	–	–	–
7g	11.04	–	–	9.08	8.06	–
11a	–	9.08	–	–	–	–
11c	9.31	–	8.69	7.29	9.12	–
11d	8.67	–	8.36	–	–	–
Nystatin (100U/disc)	NA	NA	NA	NA	22.02	22.28
Chloramphenicol	32.91	30.04	29.81	25.17	NA	NA

for 2 h the solid was isolated by concentrating the reaction mass and purified by column chromatography eluting with dichloromethane. The desired fractions were collected and evaporated completely to furnish colourless solid in 78% yield and were characterized by spectral and analytical methods. The amino acid esters were used as their hydrochlorides, hence the base *N,N'*-diisopropyl ethylamine was used during the coupling reaction. The by-product urea and the unreacted starting material contamination were removed by acidic and basic washings. All the *N*-linked products **11a-d** were isolated and recrystallized from hexane as colourless solids.

8.3.6 Antimicrobial Activity

8.3.6.1 Results of Antimicrobial Activity

The synthesized compounds **1**, **2**, **4a-c**, **e-f**, **7a-g** and **11a, c-d** were tested against microorganism species at 1,000 ppm concentration. The observed results of antibacterial screening reported in Table 8.4 indicated that pyrazole compounds **1**, **2**, **4c** and **4f** were active against *S. aureus*, *E. coli*, *B. subtilis* and *P. aeruginosa* bacterial species whereas compounds **4a** and **4e** showed activity against *B. subtilis*, *S. aureus* and *E. coli* species. Compounds **4b**, **7a** and **7b** were active against *E. coli* and *P. aeruginosa*. Compounds **7c-e**, **11c-d** were active against *S. aureus* and *B. subtilis*.

From the antifungal assays it has been observed that whereas compounds **7g** and **11c** were found to be active against *A. niger* species only, compounds **4e**, **7c** and **7e** were active against the two fungal species. However compounds **1**, **2**, **4a-c**, **4f**, **7a-b**, **7d**, **7f**, **11a** and **11d** were totally inactive against the two fungal species.

From the above observations, it is clear that the pyrazoles containing aryl functionality bearing trifluoromethyl substituents **1**, **2**, and **7g** showed significant antibacterial activity but were less active than chloramphenicol.

8.4 Experimental

8.4.1 General Methods

Melting points (uncorrected): *Gallenkamp* melting point apparatus; IR Spectra (KBr-compression mould): Shimadzu IR-408; ^1H NMR (300 MHz), ^{13}C NMR (75 MHz) spectra: Varian XL-300, DMSO- d_6 , CDCl_3 , TMS, ^1H and ^{13}C chemical shifts are quoted in ppm; Mass spectra: Shimadzu GC-MS QP 2010A mass spectral instrument with an ionization potential of 70 eV; Elemental analyses (C, H, N, S) were conducted using the HOSLI CH-Analyzer; the results were in agreement with calculated values. HPLC solvents were HPLC grade and were filtered through 0.45 μm filters (Supelco, Bellefonte, PA) prior to use. Analytical HPLC analysis was carried out using the following set of conditions: HP Hypersil ODS- C_{18} reverse phase column (4.6 \times 250 mm, 5 μm), flow rate 1.2 mL/min, linear gradient from 100%A to 60%A/40% (v/v) B in 40 min, UV monitored at $\lambda = 266$ and 254 nm, at 55°C.

8.4.2 Synthesis of 1-(3,5-Bis(Trifluoromethyl)Phenyl)-4,4,4-Trifluorobutane-1,3-Dione (**1**)

Ethyl trifluoroacetate (22.7 g, 160.0 mmol) was dissolved in methyl tert-butyl ether (70 ml) and cooled to 0–5°C. Twenty-five percentage sodium methoxide (36.2 ml, 168.0 mmol) was then added to it with stirring. 3,5-bis(trifluoromethyl)acetophenone (38.5 g, 160.0 mmol) diluted in methyl tert-butyl ether (20 ml) was added dropwise into the reaction mass over a period of 30 min at 0–5°C. The reaction mass was then stirred at 25–30°C for 14 h. Reaction was monitored by TLC (CHCl_3 : MeOH 9.5:0.5). After completion of reaction 4N hydrochloric acid (40 ml, 160 mmol) was added to adjust the pH to 4–5. Water was added and the layers were separated. The organic layer was dried over sodium sulfate and evaporated completely under reduced pressure to obtain the brown oil. The oil was purified by column chromatography eluting with dichloromethane. The pure fractions were collected and evaporated under reduced pressure to obtain a light yellow oil. IR (Nujol): 3345,

1823, 1745, 1546, 1485, 1356 cm^{-1} ; ^1H NMR (300 MHz, $\text{DMSO-}d_6$): δ 8.25(s, 2H, Ar-H), 7.91(s, 1H, Ar-H), 7.23(s, 1H, =CH), 2.70(s, 2H, CH_2); ^{13}C NMR (75 MHz, $\text{DMSO-}d_6$): δ 206.0(C=O), 201.1(C=O), 137.3, 131.2, 128.4, 127.5, 124.4(q, 2Ar- CF_3 , $^2J_{\text{CF}} = 32.6$ Hz), 117.2(q, C- CF_3 , $^2J_{\text{CF}} = 36.6$ Hz), 35.1(CH_2); MS: 352 $[\text{M}]^+$, 333, 283, 241, 213, 187, 75, 69; Anal. calcd. for $\text{C}_{12}\text{H}_5\text{F}_9\text{O}_2$: C, 40.93; H, 1.43; Found: C, 41.09; H, 1.82.

8.4.3 Synthesis of 5-(3,5-Bis(Trifluoromethyl)Phenyl)-3-(Trifluoromethyl)-1H-Pyrazole (2)

To a solution of compound **1** (1.0 g, 2.84 mmol) in ethanol (20 ml), hydrazine hydrate (2.90 mmol) was added along with a catalytic amount of acetic acid. The resulting solution was refluxed at 80°C for 20 h. Reaction was monitored by TLC (CHCl_3 : MeOH 9:1). After completion of reaction the solvent was removed under reduced pressure and the compound was purified by column chromatography eluting with dichloromethane. The pure fractions were collected and evaporated under reduced pressure to obtain NH-pyrazole **2** as colourless needles. m.p. $128\text{--}130^\circ\text{C}$; IR (KBr): 3272, 1566, 1455, 1376 cm^{-1} ; ^1H NMR (300 MHz, $\text{DMSO-}d_6$): δ 12.62(bs, 1H, NH), 8.52(s, 2H, Ar-H), 8.08(s, 1H, Ar-H), 7.60(s, 1H, Pyrazole-CH); ^{13}C NMR (75 MHz, $\text{DMSO-}d_6$): δ 141.5, 131.5(q, 3,5-di-C- CF_3 , $^2J_{\text{CF}} = 33$ Hz), 128.6, 126.1, 124.9, 123.2, 121.8(q, pyrazole C3- CF_3 , $^2J_{\text{CF}} = 36$ Hz), 103.2(Pyrazole-CH); MS: 348 $[\text{M}]^+$, 329, 279, 250, 144, 69, 44; Anal. calcd. for $\text{C}_{12}\text{H}_5\text{F}_9\text{N}_2$ C, 41.40; H, 1.45; N, 8.05; Found: C, 41.59; H, 1.32; N, 7.91.

8.4.4 General Procedure for the Synthesis of Compounds 4 and 5

To a solution of compound **1** (1.0 g, 2.84 mmol) in ethanol (20 ml), hydrazines **3a-i** (2.90 mmol) were added along with a catalytic amount of acetic acid. The resulting solution was refluxed at 80°C for 20 h. Reaction was monitored by TLC (CHCl_3 : MeOH 9:1). After completion of reaction the solvent was removed under reduced pressure and the compounds were purified by column chromatography eluting with dichloromethane. The pure fractions were collected and evaporated under reduced pressure to obtain 1,3,5-substituted pyrazoles **4a-g** as white solids (70–85%) along with the regioisomers **5a-b** (4–10%) and the uncyclised hydrazone derivatives **4h-i** in 65–75% yield.

8.4.4.1 2-(4-(5-(3,5-Bis(Trifluoromethyl)Phenyl)-3-(Trifluoromethyl)-1H-Pyrazol-1-yl)Phenyl)-N-Methyl Ethane Sulfonamide (4a)

M.p. 143–145°C; IR (KBr): 3263, 1571, 1472, 1367 cm^{-1} ; ^1H NMR (300 MHz, DMSO- d_6): δ 8.12(s, 1H, Ar-H), 7.89(s, 2H, Ar-H), 7.55(s, 1H, Pyrazole-CH), 7.40(d, 2H, Ar-H, $J = 9.0$ Hz), 7.35(d, 2H, Ar-H, $J = 9.0$ Hz), 7.03(q, 1H, NH, $J = 6.0$ Hz), 3.24(t, 2H, $\text{SO}_2\text{-CH}_2$, $J = 6.0$ Hz), 3.02(t, 2H, CH_2 , $J = 6.0$ Hz), 2.59(d, 3H, N- CH_3 , $J = 6.0$ Hz); ^{13}C NMR (75 MHz, DMSO- d_6): δ 141.7, 141.2, 140.3, 136.5, 130.5(q, 2Ar C- CF_3 , $^2J_{\text{CF}} = 21$ Hz), 129.4, 128.2, 126.2, 124.6, 122.4(q, Pyrazole-C- CF_3 , $^2J_{\text{CF}} = 40$ Hz), 120.9, 119.4, 117.4, 106.9(Pyrazole-CH), 50.2($\text{SO}_2\text{-CH}_2$), 28.8(N- CH_3), 28.6(Ar- CH_2); MS: 545 $[\text{M}]^+$, 526, 450, 429, 103, 77, 65; Anal. calcd. for $\text{C}_{21}\text{H}_{16}\text{F}_9\text{N}_3\text{O}_2\text{S}$ C, 46.24; H, 2.96; N, 7.70; Found: C, 46.58; H, 2.69; N, 7.56.

8.4.4.2 2-(4-(3-(3,5-Bis(Trifluoromethyl)Phenyl)-5-(Trifluoromethyl)-1H-Pyrazol-1-yl)Phenyl)-N-Methyl Ethane Sulfonamide (5a)

M.p. 150–152°C; IR (KBr): 3276, 1549, 1468, 1389 cm^{-1} ; ^1H NMR (300 MHz, DMSO- d_6): δ 8.55(s, 2H, Ar-H), 8.12(s, 1H, Ar-H), 8.08(s, 1H, Pyrazole-CH), 7.53(s, 4H, Ar-H), 7.03(q, 1H, NH, $J = 6.0$ Hz), 3.34(t, 2H, $\text{SO}_2\text{-CH}_2$, $J = 6.0$ Hz), 3.07(t, 2H, CH_2 , $J = 6.0$ Hz), 2.62(d, 3H, N- CH_3 , $J = 6.0$ Hz); ^{13}C NMR (75 MHz, DMSO- d_6): δ 141.7, 141.2, 140.3, 136.5, 132.8(q, 2 Ar C- CF_3 , $^2J_{\text{CF}} = 21$ Hz), 129.4, 128.2, 126.2, 124.6, 123.8(q, Pyrazole-C- CF_3 , $^2J_{\text{CF}} = 40$ Hz), 120.9, 119.4, 118.2, 107.2(Pyrazole-CH), 51.4($\text{SO}_2\text{-CH}_2$), 27.5(N- CH_3), 25.9(Ar- CH_2); MS: 545 $[\text{M}]^+$, 526, 450, 429, 142, 77, 44; Anal. calcd. for $\text{C}_{21}\text{H}_{16}\text{F}_9\text{N}_3\text{O}_2\text{S}$ C, 46.24; H, 2.96; N, 7.70; Found: C, 46.58; H, 2.69; N, 7.56.

8.4.4.3 2-(4-(5-(3,5-Bis(Trifluoromethyl)Phenyl)-3-(Trifluoromethyl)-1H-Pyrazol-1-yl)Phenyl)-N-Methyl Methane Sulfonamide (4b)

M.p. 115–117°C; IR (KBr): 3276, 1549, 1482, 1375 cm^{-1} ; ^1H NMR (300 MHz, DMSO- d_6): δ 8.13(s, 1H, Ar-H), 7.96(s, 2H, Ar-H), 7.52(s, 1H, Pyrazole-CH), 7.45(m, 4H, Ar-H), 6.95(q, 1H, NH, $J = 6.0$ Hz), 4.40(s, 2H, $\text{SO}_2\text{-CH}_2$), 2.70(d, 3H, N- CH_3 , $J = 6.0$ Hz); ^{13}C NMR (75 MHz, DMSO- d_6): δ 141.9, 141.7, 141.4, 137.7, 131.6(q, 2Ar C- CF_3 , $^2J_{\text{CF}} = 23.25$ Hz), 129.7, 128.2, 126.5, 125.8, 124.5, 122.6(q, Pyrazole-C- CF_3 , $^2J_{\text{CF}} = 25.5$ Hz), 120.9, 119.4, 117.4, 107.3(Pyrazole-CH), 55.5($\text{SO}_2\text{-CH}_2$), 28.9(N- CH_3); MS: 531 $[\text{M}]^+$; 512, 415, 367, 129, 89, 44; Anal. calcd. for $\text{C}_{20}\text{H}_{14}\text{F}_9\text{N}_3\text{O}_2\text{S}$ C, 45.2; H, 2.66; N, 7.91; Found: C, 45.45; H, 2.51; N, 7.58.

8.4.4.4 2-(4-(3-(3,5-Bis(Trifluoromethyl)Phenyl)-5-(Trifluoromethyl)-1H-Pyrazol-1-yl)Phenyl)-N-Methyl Methane Sulfonamide (5b)

M.p. 132–135°C; IR (KBr): 3291, 1563, 1482, 1399 cm^{-1} . ^1H NMR (300 MHz, DMSO- d_6): δ 8.43(s, 1H, Ar-H), 8.18(s, 2H, Ar-H), 7.74(q, 1H, NH, $J = 9.2$ Hz), 7.50(d, 2H, Ar-H, $J = 8.5$ Hz), 7.23(d, 2H, Ar-H, $J = 8.5$ Hz), 6.51(s, 1H, Pyrazole-CH), 4.32(s, 2H, $\text{SO}_2\text{-CH}_2$), 2.47(d, 3H, N- CH_3 , $J = 9.2$ Hz); ^{13}C NMR (75 MHz, DMSO- d_6): δ 153.6(Pyrazole-C- CF_3), 143.5, 141.7, 136.7, 133.6, 131.8(C- CF_3), 130.7, 129.8, 129.6, 125.1, 124.7(2Ar- CF_3), 123.1, 117.3(Pyrazole- CF_3), 107.5(Pyrazole-CH), 65.7($\text{SO}_2\text{-CH}_2$), 25.4(N- CH_3); MS: 531 $[\text{M}]^+$; 512, 437, 415, 367, 129, 89, 44; Anal. calcd. for $\text{C}_{20}\text{H}_{14}\text{F}_9\text{N}_3\text{O}_2\text{S}$ C, 45.20; H, 2.66; N, 7.91; Found: C, 45.45; H, 2.51; N, 7.58.

8.4.4.5 4-(5-(3,5-Bis(Trifluoromethyl)Phenyl)-3-(Trifluoromethyl)-1H-Pyrazol-1-yl)Benzoic Acid (4c)

M.p. 213–215°C; IR (KBr): 3279, 1561, 1469, 1387 cm^{-1} ; ^1H NMR (300 MHz, DMSO- d_6): δ 12.8(bs, 1H, COOH), 8.15(s, 1H, Ar-H), 8.00(d, 2H, Ar-H, $J = 7.5$ Hz), 7.94(s, 2H, Ar-H), 7.55(s, 1H, Pyrazole-CH), 7.52(d, 2H, Ar-H, $J = 7.5$ Hz); ^{13}C NMR (75 MHz, DMSO- d_6): δ 166.2(COOH), 153.6(C- CF_3), 142.4(Ar-C-N), 141.2(Ar-C-N-Pyrazole), 131.1(Ar-C-Pyrazole), 130.5(q, Ar-C- CF_3 , $^2J_{\text{CF}} = 12$ Hz), 130.2, 129.6, 128.2(Ar-C- CF_3), 125.9(2Ar- CF_3), 124.5, 122.8(q, Pyrazole-C- CF_3 , $^2J_{\text{CF}} = 9.75$ Hz), 120.9, 119.3, 107.6(Pyrazole-CH); MS: 468 $[\text{M}]^+$, 447, 207, 134, 106, 65, 44; Anal. calcd. for $\text{C}_{19}\text{H}_9\text{F}_9\text{N}_2\text{O}_2$ C, 48.73; H, 1.94; N, 5.98; Found: C, 48.51; H, 2.10; N, 5.66.

8.4.4.6 Ethyl-4-(5-(3,5-Bis(Trifluoromethyl)Phenyl)-3-(Trifluoro-Methyl)-1H-Pyrazol-1-yl)Benzoate (4d)

M.p. 105–107°C; IR (KBr): 3286, 1551, 1476, 1391 cm^{-1} . ^1H NMR (300 MHz, DMSO- d_6): δ 8.17(s, 1H, Ar-H), 8.03(s, 2H, Ar-H), 8.00(d, 2H, Ar-H, $J = 7.5$ Hz), 7.56(d, 2H, Ar-H, $J = 7.5$ Hz), 7.53(s, 1H, Pyrazole-CH), 4.34(q, 2H, $J = 6.0$ Hz, Ester CH_2), 1.30(t, 3H, $J = 6.0$ Hz, Ester CH_3); ^{13}C NMR (75 MHz, DMSO- d_6): δ 164.6(Ester C=O), 142.4(Ar-C-N), 141.5(Ar-C-N-Pyrazole), 131.0(Ar-C-Pyrazole), 130.2, 130.0(C- CF_3), 129.7, 126.0(Ar-C- CF_3), 124.5(2Ar- CF_3), 122.8, 119.3(Pyrazole- CF_3), 107.5(Pyrazole-CH), 61.3(ester CH_2), 14.1(Ester CH_3); MS: 496 $[\text{M}]^+$; Anal. calcd. for $\text{C}_{21}\text{H}_{13}\text{F}_9\text{N}_2\text{O}_2$ C, 50.82; H, 2.64; N, 5.64; Found: C, 50.57; H, 2.38; N, 5.89.

8.4.4.7 4-(5-(3,5-Bis(Trifluoromethyl)Phenyl)-3-(Trifluoromethyl)-1H-Pyrazol-1-yl)Benzene Sulfonamide (4e)

M.p. 148–150°C; IR (KBr): 3276, 1561, 1472, 1394 cm^{-1} ; ^1H NMR (300 MHz, DMSO- d_6): δ 8.18(s, 1H, Ar-H), 8.01(s, 2H, Ar-H), 7.87(d, 2H, Ar-H, $J = 9.0$ Hz), 7.62(d, 2H, Ar-H, $J = 9.0$ Hz), 7.59(s, 1H, Pyrazole-CH) 7.55(bs, 2H, NH_2); ^{13}C NMR (75 MHz, DMSO- d_6): δ 144.5, 142.9, 142.4, 141.4, 140.3, 130.6(C- CF_3), 129.8, 128.2, 126.7(2Ar- CF_3 , $^2J_{\text{CF}} = 36$ Hz), 124.6, 122.9(Pyrazole- CF_3), 120.9, 119.3, 117.3, 115.7, 107.8(Pyrazole-CH); MS: 503 $[\text{M}]^+$, 484, 439, 423, 403, 329, 309, 75, 63; Anal. calcd. for $\text{C}_{18}\text{H}_{10}\text{F}_9\text{N}_2\text{O}_2\text{S}$, 42.95; H, 2.00; N, 8.35; Found: C, 42.68; H, 2.37; N, 8.17.

8.4.4.8 5-(3,5-Bis(Trifluoromethyl)Phenyl)-1-Phenyl-3-(Trifluoro-Methyl)-1H-Pyrazole (4f)

M.p. 160–162°C; IR (KBr): 3291, 1548, 1469, 1388 cm^{-1} ; ^1H NMR (300 MHz, DMSO- d_6): δ 8.43(s, 1H, Ar-H), 8.31(s, 2H, Ar-H), 8.10(s, 1H, Pyrazole-CH), 7.50(d, 2H, Ar-H, $J = 9.0$ Hz), 7.33(t, 2H, Ar-H, $J = 9.0$ Hz), 7.07(t, 1H, Ar-H, $J = 9.0$ Hz) ^{13}C NMR (75 MHz, DMSO- d_6): δ 144.4, 141.7, 133.9, 130.9, 130.5, 130.1, 128.4, 125.7, 124.9(2Ar- CF_3), 122.8, 121.8(Pyrazole- CF_3), 121.3, 119.3, (Pyrazole-CH), 94.1, 93.6; MS: 424 $[\text{M}]^+$; Anal. calcd. for $\text{C}_{18}\text{H}_9\text{F}_9\text{N}_2$ C, 50.96; H, 2.14; N, 6.60; Found: C, 50.74; H, 2.37; N, 6.83.

8.4.4.9 5-(3,5-Bis(Trifluoromethyl)Phenyl)-1-(2,4-Dichlorophenyl)-3-(Trifluoromethyl)-1H-Pyrazole (4g)

M.p. 130–132°C; IR (KBr): 3281, 1555, 1476, 1395 cm^{-1} ; ^1H NMR (300 MHz, DMSO- d_6): δ 8.13(s, 1H, Ar-H), 7.88(s, 2H, Ar-H), 7.69(s, 1H, Ar-H), 7.50(d, 1H, Ar-H, $J = 7.5$ Hz), 7.41(s, 1H, Pyrazole-CH), 7.37(d, 1H, Ar-H, $J = 7.5$ Hz); ^{13}C NMR (75 MHz, DMSO- d_6): δ 143.5, 141.7, 134.9, 133.6, 133.2(C-Cl), 131.8(C- CF_3), 129.8, 127.5, 124.7(2Ar- CF_3), 123.1, 122.7, 117.3(Pyrazole- CF_3), 107.5 (Pyrazole-CH); MS: 493 $[\text{M}] + 2$, 491 $[\text{M}]^+$; Anal. calcd. for $\text{C}_{18}\text{H}_7\text{Cl}_2\text{F}_9\text{N}_2$ C, 43.84; H, 1.43; N, 5.68; Found: C, 43.61; H, 1.72; N, 5.42.

8.4.5 General Procedure for the Synthesis of Compounds 4h-i

To a solution of compound **1** (1.0 g, 2.84 mmol) in ethanol (20 ml), hydrazines **3h-i** (2.90 mmol) were added along with a catalytic amount of acetic acid. The resulting solution was refluxed at 80°C for 20 h. Reaction was monitored by TLC (CHCl_3 :

MeOH 9:1). After completion of reaction the solvent was removed under reduced pressure and the compounds were purified by column chromatography eluting with dichloromethane. The pure fractions were collected and evaporated under reduced pressure to obtain 1,3,5-substituted pyrazoles **4h-i** as white solids (75–83%).

8.4.5.1 N'-(4-(3,5-Bis(Trifluoromethyl)Phenyl)-1,1,1-Trifluoro-4-Oxobutane-2-Ylidine) Acetohydrazide (**4h**)

M.p. 113–115°C; IR (KBr): 3278, 1698, 1554, 1471, 1398 cm^{-1} ; ^1H NMR (300 MHz, DMSO- d_6): δ 10.48(bs, 1H, NH), 8.23(s, 1H, Ar-H), 7.98(s, 2H, Ar-H), 4.21(s, 2H, CH_2), 2.29(s, 3H, CH_3); ^{13}C NMR (75 MHz, DMSO- d_6): δ 187.1(C=O), 153.6(C- CF_3), 145.9(Ar-C-N), 143.5, 137.5, 131.8(C- CF_3), 130.5, 129.8, 127.7(Ar-C- CF_3), 124.7(2Ar- CF_3), 123.1, 64.1(CH_2), 13.8(CH_3); MS: 408 $[\text{M}]^+$, 355, 328, 249, 151, 89, 59, 44; Anal. calcd. for $\text{C}_{14}\text{H}_9\text{F}_9\text{N}_2\text{O}_2$ C, 41.19; H, 2.22; N, 6.86. Found: C, 41.67; H, 2.34; N, 6.61.

8.4.5.2 N'-(4-(3,5-Bis(Trifluoromethyl)Phenyl)-1,1,1-Trifluoro-4-Oxobutane-2-Ylidine)Benzohydrazide (**4i**)

M.p. 189–191°C; IR (KBr): 3282, 1667, 1556, 1475, 1396 cm^{-1} ; ^1H NMR (300 MHz, DMSO- d_6): δ 11.03(bs, 1H, NH), 8.41(s, 1H, Ar-H), 8.14(s, 2H, Ar-H), 7.86(d, 2H, Ar-H, $J = 9.0$ Hz), 7.56–7.50(m, 3H, Ar-H), 4.30(s, 2H, $-\text{CH}_2$); ^{13}C NMR (75 MHz, DMSO- d_6): δ 165.0(C=O), 140.6, 137.5, 134.5, 133.6, 131.8, 131.1, 130.6, 129.8, 128.3(C- CF_3), 126.7(2Ar- CF_3), 125.1, 122.5, 121.4, 64.1(CH_2); MS: 470 $[\text{M}]^+$, 374, 359, 249, 151, 105, 77, 51; Anal. calcd. for $\text{C}_{19}\text{H}_{11}\text{F}_9\text{N}_2\text{O}_2$ C, 48.52; H, 2.36; N, 5.96; Found: C, 48.71; H, 2.13; N, 5.64.

8.4.6 General Procedure for the Synthesis of N-Alkylated Pyrazole Derivatives (**7a-g**)

To a suspension of **2** (0.5 g, 1.42 mmol), K_2CO_3 (0.25 g, 1.86 mmol) and DMF (10 ml) at room temperature was added **6** (1.42 mmol). The reaction mass was then stirred at the same temperature for 3 h (monitored by TLC, CHCl_3 : MeOH 9:1). Reaction mass was then quenched in ice-cold water and solid obtained was filtered, washed with water, dried and was recrystallized from ethanol to give **7a-g** as white solids in 72–87% yields.

8.4.6.1 2-(5-(3,5-Bis(Trifluoromethyl)Phenyl)-3-(Trifluoromethyl)-1H-Pyrazol-1-yl)-N-(2-Chloro-6-Fluorophenyl)Acetamide (7a)

IR (KBr): 3118, 1654, 1540 cm^{-1} ; ^1H NMR (300 MHz, $\text{DMSO-}d_6$): δ 10.24(bs, 1H, NH), 8.53(s, 1H, Ar-H), 8.08(s, 2H, Ar-H), 7.46(m, 3H, Ar-H), 7.37(s, 1H, Pyrazole-CH), 4.94(s, 2H, N- CH_2); ^{13}C NMR (75 MHz, $\text{DMSO-}d_6$): δ 165.2(C=O), 160.2(C-F), 142.6, 140.6(Pyrazole-C- CF_3), 133.2, 132.9(C-Cl), 131.3(Ar-C- CF_3), 128.8, 128.1, 126.2, 125.4, 123.7(2Ar- CF_3), 123.2, 120.7(Pyrazole- CF_3), 113.8, 107.2(Pyrazole-CH), 54.3(N- CH_2); MS (ESI): 535 [M] + 2, 533 [M]⁺; Anal. calcd. for $\text{C}_{20}\text{H}_{10}\text{ClF}_{10}\text{N}_3\text{O}$ C, 45.00; H, 1.89; N, 7.87; Found: C, 45.27; H, 1.58; N, 7.53.

8.4.6.2 2-(5-(3,5-Bis(Trifluoromethyl)Phenyl)-3-(Trifluoromethyl)-1H-Pyrazol-1-yl)-N-(2,4-Dichlorophenyl)Acetamide (7b)

IR (KBr): 3285, 1687, 1576, 1495, 1399 cm^{-1} ; ^1H NMR (300 MHz, $\text{DMSO-}d_6$): δ 10.24(bs, 1H, NH), 8.51(s, 1H, Ar-H), 8.28(s, 2H, Ar-H), 7.57(m, 2H, Ar-H), 7.35(d, 1H, Ar-H, $J = 8.4$), 7.27(s, 1H, Pyrazole-CH), 4.85(s, 2H, N- CH_2); ^{13}C NMR (75 MHz, $\text{DMSO-}d_6$): δ 166.2(C=O), 144.6, 142.3(Pyrazole-C- CF_3), 134.6, 133.5, 131.2(Ar-C- CF_3), 130.2(C-Cl), 130.1, 129.4, 127.8(C-Cl), 126.7, 123.9(2Ar- CF_3), 123.1, 120.7(Pyrazole- CF_3), 121.0, 107.5(Pyrazole-CH), 51.8(N- CH_2); MS: 552 [M] + 2, 550 [M]⁺; Anal. calcd. for $\text{C}_{20}\text{H}_{10}\text{Cl}_2\text{F}_9\text{N}_3\text{O}$ C, 43.66; H, 1.83; N, 7.64; Found: C, 43.84; H, 1.98; N, 7.85.

8.4.6.3 2-(5-(3,5-Bis(Trifluoromethyl)Phenyl)-3-(Trifluoromethyl)-1H-Pyrazol-1-yl)-N-(4-Methylphenyl)Acetamide (7c)

IR (KBr): 3272, 1687, 1566, 1386 cm^{-1} ; ^1H NMR (300 MHz, $\text{DMSO-}d_6$): δ 10.25(bs, 1H, NH), 8.48(s, 1H, Ar-H), 7.97(s, 2H, Ar-H), 7.26(d, 2H, Ar-H, $J = 5.5$ Hz), 7.11(d, 1H, Ar-H, $J = 8.5$ Hz), 6.87(s, 1H, Pyrazole-CH), 4.85(s, 2H, N- CH_2), 2.45(s, 3H, Ar- CH_3); ^{13}C NMR (75 MHz, $\text{DMSO-}d_6$): δ 165.2(C=O), 164.2(C-F), 144.6, 142.3(Pyrazole-C- CF_3), 135.8, 134.5, 133.4, 132.7, 131.2(Ar-C- CF_3), 129.5, 128.8, 127.3, 125.6, 123.7(2Ar- CF_3), 123.2, 121.7(Pyrazole- CF_3), 121.2, 112.9, 107.1(Pyrazole-CH), 51.8(N- CH_2), 21.5(CH_3); MS (ESI): 495 [M]⁺; Anal. calcd. for $\text{C}_{21}\text{H}_{14}\text{F}_9\text{N}_3\text{O}$ C, 50.92; H, 2.85; N, 8.48; Found: C, 50.68; H, 2.57; N, 8.74.

8.4.6.4 2-(5-(3,5-Bis(Trifluoromethyl)Phenyl)-3-(Trifluoromethyl)-1H-Pyrazol-1-yl)-N-(4-Chlorophenyl)Acetamide (7d)

IR (KBr): 3283, 1687, 1596, 1387 cm^{-1} ; ^1H NMR (300 MHz, $\text{DMSO-}d_6$): δ 10.6(bs, 1H, NH), 8.50(s, 2H, Ar-H), 7.92(s, 1H, Ar-H), 7.57(s, 1H, Pyrazole-CH),

7.55(d, 2H, Ar-H, $J = 8.2$ Hz), 7.35(d, 2H, Ar-H, $J = 8.5$ Hz), 5.30(s, 2H, N-CH₂); ¹³C NMR (75 MHz, DMSO-*d*₆): δ 164.1(C=O), 147.2, 137.2, 133.8(C-Cl), 131.6(Ar-C-CF₃), 128.8, 128.5, 127.3, 125.5, 124.9(2Ar-CF₃), 121.8(Pyrazole-CF₃), 120.7, 117.8, 107.0(Pyrazole-CH), 54.3(N-CH₂); MS: 517 [M] + 2, 515 [M]⁺, 361, 154, 126, 99, 75, 63, 44; Anal. calcd. for C₂₀H₁₁ClF₉N₃O C, 46.57; H, 2.15; N, 8.15; Found: C, 46.82; H, 2.39; N, 8.51.

8.4.6.5 2-(5-(3,5-Bis(Trifluoromethyl)Phenyl)-3-(Trifluoromethyl)-1H-Pyrazol-1-yl)-N-(4-Chloro-3-Trifluoromethylphenyl)Acetamide(7e)

IR (KBr): 3262, 1687, 1586, 1376 cm⁻¹; ¹H NMR (300 MHz, DMSO-*d*₆): δ 10.73(bs, 1H, NH), 8.52(s, 1H, Ar-H), 8.49(s, 2H, Ar-H), 8.06(s, 1H, Ar-H), 8.11(d, 1H, Ar-H, $J = 8.2$ Hz), 8.05(d, 1H, Ar-H, $J = 8.2$ Hz), 7.93(s, 1H, Ar-H), 7.68(s, 1H, Pyrazole-CH), 5.36(s, 2H, N-CH₂); ¹³C NMR (75 MHz, DMSO-*d*₆): δ 163.2(C=O), 144.6, 142.6(Pyrazole-C-CF₃), 135.2, 133.6, 129.5, 129.3, 129.1(Ar-C-CF₃), 128.5(C-Cl), 127.2, 125.7, 123.3(2Ar-CF₃), 123.1, 121.7(Pyrazole-CF₃), 118.8, 113.8, 107.3(Pyrazole-CH), 55.3(N-CH₂); MS: 585 [M] + 2, 583 [M]⁺; Anal. calcd. for C₂₁H₁₀ClF₁₂N₃O C, 43.21; H, 1.73; N, 7.20; Found: C, 43.56; H, 1.98; N, 7.51.

8.4.6.6 2-(5-(3,5-Bis(Trifluoromethyl)Phenyl)-3-(Trifluoromethyl)-1H-Pyrazol-1-yl)-N-(4-Fluorophenyl)Acetamide (7f)

IR (KBr): 3272, 1677, 1546, 1384 cm⁻¹; ¹H NMR (300 MHz, DMSO-*d*₆): δ 10.42(bs, 1H, NH), 8.48(s, 1H, Ar-H), 7.98(s, 2H, Ar-H), 7.54(m, 2H, Ar-H), 7.28(m, 2H, Ar-H), 7.25(s, 1H, Pyrazole-CH), 4.75(s, 2H, N-CH₂); ¹³C NMR (75 MHz, DMSO-*d*₆): δ 164.7(C=O), 162.7(C-F), 144.6, 142.5(Pyrazole-C-CF₃), 133.1, 132.5(C-Cl), 131.5(Ar-C-CF₃), 129.7, 128.1, 126.8, 125.5, 124.6(2Ar-CF₃), 123.2, 121.4(Pyrazole-CF₃), 120.3, 114.4, 107.5 (Pyrazole-CH), 53.3(N-CH₂); MS: 499 [M]⁺; Anal. calcd. for C₂₀H₁₁F₁₀N₃O C, 48.11; H, 2.22; N, 8.42; Found: C, 48.42; H, 2.57; N, 8.81.

8.4.6.7 N-(2,5-Bis(Trifluoromethyl)Phenyl)-2-(5-(3,5-Bis(Trifluoromethyl)-Phenyl)-3-(Trifluoromethyl)-1H-Pyrazol-1-yl)-Ethanamide (7g)

IR (KBr): 3285, 1679, 1586, 1,379 cm⁻¹; ¹H NMR (300 MHz, DMSO-*d*₆): δ 10.95(bs, 1H, NH), 8.50(s, 2H, Ar-H), 8.12 (s, 1H, Ar-H), 8.10(s, 1H, Ar-H), 7.94(s, 1H, Pyrazole-CH), 7.78(d, 1H, Ar-H, $J = 8.5$ Hz), 7.69(d, 1H, Ar-H, $J = 8.4$ Hz), 5.35(s, 2H, N-CH₂); ¹³C NMR (75 MHz, DMSO-*d*₆): δ 164.7(C=O), 147.3, 137.5, 133.7, 132.3(C-CF₃), 131.1(Ar-C-CF₃), 130.7, 126.9, 125.6, 124.9(CF₃),

124.4(2Ar-CF₃), 123.9(CF₃), 121.8(Pyrazole-CF₃), 117.6, 107.0(Pyrazole-CH), 54.1(N-CH₂); MS: 617 [M]⁺; Anal. calcd. for C₂₂H₁₀F₁₅N₃O C, 42.80; H, 1.63; N, 6.81; Found: C, 42.57; H, 1.91; N, 6.54.

8.4.7 Synthesis of Ethyl 2-(5-(3,5-Bis(Trifluoromethyl)Phenyl)-3-(Trifluoromethyl)-1H-Pyrazol-1-yl)Acetate (8)

To a magnetically stirred suspension of **2** (5 g, 14.3 mmol), K₂CO₃ (3.3 g, 23.9 mmol) and DMF (100 ml) at room temperature was added 2-bromo ethyl acetate (2.5 g, 15.0 mmol). The reaction mass was then stirred at the same temperature for 3 h (monitored by TLC, CHCl₃: MeOH 9:1). Reaction mass was then quenched in ice-cold water and extracted with ethyl acetate (50 ml). The ethyl acetate layer was then washed with saturated sodium chloride solution and dried over sodium sulfate. The solvent was removed under reduced pressure to obtain a viscous oil which on trituration with ethanol yielded white needles. Yield 6.0 g (96%), m.p. 35–38°C; IR (KBr): 1731, 1557, 1481, 1386 cm⁻¹; ¹H NMR (300 MHz, DMSO-*d*₆): δ 8.30(s, 1H, Ar-H), 8.23(s, 2H, Ar-H), 7.28(s, 1H, Pyrazole-CH), 5.34(s, 2H, N-CH₂), 4.06(q, 2H, *J* = 3.0 Hz, Ester CH₂), 1.06(t, 3H, *J* = 3.0 Hz, Ester CH₃); ¹³C NMR (75 MHz, DMSO-*d*₆): δ 168.1(Ester C=O), 154.5(C-CF₃), 145.3(Ar-C-N), 143.6(Ar-C-N-Pyrazole), 136.5, 132.4(Ar-C-Pyrazole), 130.7(C-CF₃), 130.2, 128.5, 127.8(Ar-C-CF₃), 124.8(2Ar-CF₃), 122.8, 121.9(Pyrazole-CF₃), 107.4(Pyrazole-CH), 64.4(Ester CH₂), 53.7(N-CH₂), 15.4(Ester CH₃); MS: 434 [M]⁺, 415, 361, 341, 213, 69, 43; Anal. calcd. for C₁₆H₁₁F₉N₂O₂ C, 44.25; H, 2.55; N, 6.45; Found: C, 44.57; H, 2.87; N, 6.77.

8.4.8 Synthesis of 2-(5-(3,5-Bis(Trifluoromethyl)Phenyl)-3-(Trifluoromethyl)-1H-Pyrazol-1-yl)Acetic Acid (9)

The above obtained compound **8** (6.0 g, 13.82 mmol) was dissolved in tetrahydrofuran (65 ml) at room temperature and NaOH solution (2 N, 7.5 ml, 15.2 mmol) added to it. The reaction mass was heated to 50°C for 5 h (monitored by TLC, CHCl₃: MeOH 9:1). The reaction mass was evaporated completely to obtain a residue. The residue was dissolved in water (25 ml) and acidified with 2 N HCl to pH 1–2. The product was extracted with ethyl acetate (25 ml) and washed with saturated sodium chloride solution. The ethyl acetate extracts were dried over sodium sulfate and evaporated completely to obtain a white solid. Yield: 90.0%; m.p. 35–38°C; IR (KBr): 3552, 1725, 1524 cm⁻¹; ¹H NMR (300 MHz, CDCl₃): δ 13.57(bs, 1H, COOH), 8.52(s, 2H, Ar-H), 8.24(s, 2H, Ar-H), 7.94(s, 1H, Pyrazole-CH), 5.23(s, 2H, N-CH₂); ¹³C NMR (75 MHz, DMSO-*d*₆): δ 178.3(Acid C=O), 155.4(C-CF₃), 147.6(Ar-C-N), 144.7(Ar-C-N-Pyrazole), 136.8, 134.9(Ar-C-Pyrazole), 131.7(C-

CF₃), 130.6, 128.5, 127.1(Ar-C-CF₃), 123.9(2Ar-CF₃), 123.2, 122.3(Pyrazole-CF₃), 106.8(Pyrazole-CH), 55.2(N-CH₂); MS: 406 [M]⁺, 387, 361, 341, 213, 144, 75, 69, 45; Anal. calcd. for C₁₄H₇F₉N₂O₂ C, 41.40; H, 1.74; N, 6.90; Found: C, 41.76; H, 1.53; N, 6.61.

8.4.9 General Procedure for the Synthesis of Amino Acid Linked Pyrazole Derivatives (11a-d)

To a magnetically stirred suspension of **9** (0.5 g, 1.6 mmol) and dichloromethane (20 ml) at room temperature was added **10** (1.6 mmol) and TBTU (0.64 g, 2.0 mmol). To this was added a solution of N,N-diisopropyl ethyl amine (0.774 g, 6.0 mmol) in dichloromethane (10 ml) dropwise at room temperature. The reaction mass was then stirred further for 2 h (monitored by TLC, CHCl₃: MeOH, 8:2). It was then washed twice with water (20 ml) followed by phosphoric acid (20 ml, 1%) then with saturated sodium bicarbonate solution (20 ml) and finally with saturated sodium chloride solution (20 ml). The dichloromethane layer was then dried over sodium sulfate and evaporated completely and recrystallized from hexane to obtain **11a-d** in 78–88% yield as white solids.

8.4.9.1 Ethyl-2-(2-(5-(3,5-Bis(Trifluoromethyl)Phenyl)-3-(Trifluoromethyl)-1H-Pyrazol-1-yl) Acetamido)-3-Phenyl Propionate (11a)

IR (KBr): 3266, 1736, 1697, 1666, 1622, 1605, 1548 cm⁻¹; ¹H NMR (300 MHz, DMSO-d₆): δ 8.86(d, 1H, NH), 8.50(s, 2H, Ar-H), 8.12(s, 1H, Ar-H), 7.89(s, 1H, Pyrazole-CH), 7.29–7.21(m, 5H, Ar-H), 5.07(s, 2H, N-CH₂), 5.01(dd, 1H, *J* = 8.4 and 8.0 Hz), 4.51(q, 2H, ester O-CH₂, *J* = 8.0 Hz), 4.06(dd, 1H, *J* = 5.5 and 5.5 Hz, Bn-H_a), 3.07(dd, 1H, *J* = 8.2 and 8.3 Hz, Bn-H_b), 1.10(t, 3H, *J* = 7.1 Hz ester CH₃); ¹³C NMR (75 MHz, DMSO-d₆): δ 172.7(Amide C=O), 171.5(Ester C=O), 164.2(C-F), 145.6, 142.6(Pyrazole-C-CF₃), 136.6, 135.5, 133.6, 132.1, 131.8(Ar-C-CF₃), 129.2, 128.6, 127.7, 125.9, 124.7(2Ar-CF₃), 123.1, 121.7(Pyrazole-CF₃), 121.5, 113.8, 105.3(Pyrazole-CH), 61.0(Ester CH₂), 59.3(N-CH₂), 56.7(CH), 36.8(CH₂), 14.1(Ester CH₃); MS: 581 [M]⁺, 508, 488, 361, 341, 213, 176, 148, 120, 83, 65, 43; Anal. calcd. for C₂₅H₂₀F₉N₃O₃ C, 51.64; H, 3.47; N, 7.23; Found: C, 51.95; H, 3.58; N, 7.61.

8.4.9.2 Ethyl-1-(2-(5-(3,5-Bis(Trifluoromethyl)Phenyl)-3-(Trifluoromethyl)-1H-Pyrazol-1-yl)Acetyl) Pyrrolidine-2-Carboxylate (11b)

IR (KBr): 3263, 1726, 1687, 1652, 1612, 1595, 1542 cm⁻¹; ¹H NMR (300 MHz, DMSO-d₆): δ 8.23(s, 2H, Ar-H), 8.03(s, 1H, Ar-H), 7.83(s, 1H, Pyrazole-CH),

5.02(s, 2H, N-CH₂), 4.29(dd, 1H, *J* = 8.4 Hz, 8.0 Hz), 4.21(q, 2H, *J* = 7.1 Hz ester O-CH₂), 3.51–3.41(m, 2H, N-CH₂), 2.44–2.19(m, 2H, ring CH₂), 2.02–1.92(m, 2H, ring CH₂), 1.24(t, 3H, *J* = 7.1 Hz ester CH₃); ¹³C NMR (75 MHz, DMSO-d₆): 172.7(Amide C=O), 171.5(Ester C=O), 164.2(C-F), 145.6, 142.6(Pyrazole-C-CF₃), 136.6, 135.5, 133.6, 132.1, 131.8(Ar-C-CF₃), 129.2, 128.6, 127.7, 125.9, 124.7(2Ar-CF₃), 123.1, 121.7(Pyrazole-CF₃), 121.5, 113.8, 105.3(Pyrazole-CH), 65.7(CH), 61.0(Ester CH₂), 57.5(N-CH₂), 49.6(N-CH₂), 28.9(CH₂), 24.5(CH₂), 14.1(Ester CH₃); MS: 531 [M]⁺, 512, 361, 341, 183, 142, 70, 41; Anal. calcd. for C₂₁H₁₈F₉N₃O₃ C, 47.47; H, 3.41; N, 7.91; Found: C, 47.86; H, 3.82; N, 7.61.

8.4.9.3 Ethyl-2-(2-(5-(3,5-Bis(Trifluoromethyl)Phenyl)-3-(Trifluoromethyl)-1H-Pyrazol-1-yl) Acetamido)-3-(4-Hydroxyphenyl) Propionate (11c)

IR (KBr): 3263, 1746, 1685, 1667, 1632, 1602, 1538 cm⁻¹; ¹H NMR (300 MHz, DMSO-d₆): δ 9.27(bs, 1H, OH), 8.80(d, 1H, NH), 8.51(s, 2H, Ar-H), 8.29(s, 1H, Ar-H), 7.89(s, 1H, Pyrazole-CH), 7.00(d, 2H, *J* = 7.5 Hz, Ar-H), 6.67(d, 2H, *J* = 7.5 Hz, Ar-H), 5.08(s, 2H, N-CH₂), 4.43(dd, 1H, *J* = 8.4 Hz, 8.0 Hz), 4.21(q, 2H, ester O-CH₂), 3.23(dd, 1H, *J* = 5.5 Hz, 5.5 Hz, Bn-H_a), 2.85(dd, 1H, *J* = 8.2 Hz, 8.3 Hz, Bn-H_b), 1.29(t, 3H, *J* = 7.0 Hz ester CH₃); ¹³C NMR (75 MHz, DMSO-d₆): δ 172.7(Amide C=O), 171.5(Ester C=O), 155.7(Ar-C-OH), 145.6, 142.6(Pyrazole-C-CF₃), 136.6, 135.5, 133.6, 132.1, 131.8(Ar-C-CF₃), 130.2, 129.2, 127.7, 125.9, 124.7(2Ar-CF₃), 123.1, 121.7(Pyrazole-CF₃), 121.5, 115.8, 105.3(Pyrazole-CH), 61.0(Ester CH₂), 59.3(N-CH₂), 56.7(CH), 36.8(CH₂), 14.1(Ester CH₃); MS: 597 [M]⁺, 470, 438, 419, 244, 216, 188, 145, 117, 77, 63, 51; Anal. calcd. for C₂₅H₂₀F₉N₃O₄ C, 50.26; H, 3.37; N, 7.03; Found: C, 50.47; H, 3.71; N, 7.24.

8.4.9.4 Ethyl-2-(2-(5-(3,5-Bis(Trifluoromethyl)Phenyl)-3-(Trifluoromethyl)-1H-Pyrazol-1-yl) Acetamido)-Pentanoate (11d)

IR (KBr): 3258, 1729, 1685, 1654, 1624, 1615, 1541 cm⁻¹; ¹H NMR (300 MHz, DMSO-d₆): δ 8.78(d, 1H, NH), 8.51(s, 2H, Ar-H), 8.28(s, 1H, Ar-H), 7.90(s, 1H, Pyrazole-CH), 5.12(s, 2H, N-CH₂), 4.24(dd, 1H, CH, *J* = 8.4 Hz, 8.0 Hz), 4.08(q, 2H, *J* = 7.1 Hz ester O-CH₂, *J* = 8.0 Hz), 1.64(q, 2H, CH₂, *J* = 8.4 Hz), 1.33(m, 2H, CH₂), 1.17(t, 3H, *J* = 7.1 Hz ester CH₃, *J* = 8.4 Hz), 0.88(t, 3H, CH₃, *J* = 8.4 Hz); ¹³C NMR (75 MHz, DMSO-d₆): δ 171.5(Ester C=O), 166.5(Amide C=O), 164.2(C-F), 145.6, 142.6(Pyrazole-C-CF₃), 136.6, 135.5, 133.6, 132.1, 131.8(Ar-C-CF₃), 129.2, 128.6, 127.7, 125.9, 124.7(2Ar-CF₃), 123.1, 121.7(Pyrazole-CF₃), 121.5, 113.8, 105.3(Pyrazole-CH), 55.9(CH), 61.3(Ester CH₂), 59.7(N-CH₂), 33.4(CH₂), 18.8(CH₂), 14.1(Ester CH₃), 13.8(Terminal CH₃). MS: 533 [M]⁺, 514, 491, 361, 341, 213, 144, 116, 84, 55, 41; Anal. calcd. for C₂₁H₂₀F₉N₃O₃ C, 47.29; H, 3.78; N, 7.88; Found: C, 47.16; H, 3.54; N, 7.49.

8.5 Conclusions

A series of 1,3,5-trisubstituted pyrazole derivatives were prepared from asymmetrical polyfluorinated 1,3-diketone **1**. The reactivity of substituted hydrazines towards the dioxo compound was studied leading to the formation of regioisomers **4** and **5**. The pyrazole unsubstituted at nitrogen was linked to N-arylacetamides **7**. It is interesting to observe that using aprotic polar solvent and lower temperature for alkylation of 3,5-disubstituted pyrazole **2**, only one isomer was obtained exclusively as 1,3,5-trisubstituted derivatives **7a-g** in good yields. All the reactions were carried out at room temperature in dimethyl formamide and using potassium carbonate as base as well as amino acids to furnish the peptide linked pyrazoles **11**. The amino acid esters were used as their hydrochlorides hence the base N,N'-diisopropyl ethyl amine was used during the coupling reaction. The by-product urea and the unreacted starting material contamination were removed by acidic and basic washings. All the N-linked products **11a-d** were isolated and recrystallized from hexane as colourless solids.

Acknowledgements The authors gratefully acknowledge financial support of this project by UGC, New Delhi, BCUD, University of Pune, India and Principal, K. T. H. M. College, Nashik – 422 002 for facilities.

References

1. Joshi KC, Pathak VN, Grover V (1979) Studies in potential organo-fluorine antibacterial agents. Part 2: synthesis and antibacterial activity of some new fluorine-containing 3,5-disubstituted isoxazoles. *Pharmazie* 34:68–69
2. Joshi K (1983) Formation of halogenated 1-arylbutane-1,3-diones. *J Indian Chem Soc* 60:1074–1076
3. Ho RKY, Livingstone SE (1968) Thio derivatives of β -diketones and their metal chelates. IX. Nickel and copper complexes of some new fluorinated monothio- β -diketones. *Aust J Chem* 21:1781–1787
4. Nishiwaki T (1969) Studies on heterocyclic chemistry. IV. Preparation of several trifluoromethyl-substituted heterocyclic compounds and observation of metastable ion in the mass spectra of trifluoromethyl-pyrazoles. *Bull Chem Soc Jpn* 42:3024–3026
5. Wright JB, Dulin WE, Markillie JH (1964) The antidiabetic activity of 3,5-dimethylpyrazoles. *J Med Chem* 7:102–105
6. Soliman R, Feid-Allah H (1980) Preparation and antidiabetic activity of new 3-methyl-5-phenylpyrazolesulfonylurea derivatives. *J Pharm Sci* 70:602–605
7. Sauter F, Stanetty P, Ramer W, Sittenthaler W (1991) Fungizide Pyridinderivate, 4. Mitt. α -Trifluormethyl-3-pyridinmethanole. *Monatsh Chem* 122:879–885
8. Tordeux M, Francesc C, Wakselman C (1990) Reactions of trifluoromethyl bromide and related halides: Part 9. Comparison between additions to carbonyl compounds, enamines, and sulphur dioxide in the presence of zinc. *J Chem Soc Perkin Trans 1*:1951–1957
9. Sugimori A, Yamada T, Ishida H, Nose M, Terashima K, Oohata N (1986) Radiation-induced alkylation of quinoline derivatives with alcohol. *Bull Chem Soc Jpn* 59:3905–3909
10. Linderman RJ, Graves DM (1989) Oxidation of fluoroalkyl-substituted carbinols by Dess-Martin reagent. *J Org Chem* 54:661–668

11. Yemets SV (2000) Alkylation of 1-phenyl-3,5-disubstituted pyrazole with polyfluorinated aliphatic aldehydes: properties of 1-phenyl-4-(1-hydroxypolyfluoroalkyl)pyrazole derivatives. *J Fluor Chem* 101:111–116
12. Lynette MO (2006) Synthesis of celecoxib via 1,3-dipolar cycloaddition. *Tetrahedron Lett* 47:7943–7946
13. Trofimenko S (1986) The coordination chemistry of pyrazole-derived ligands. *Prog Inorg Chem* 34:115–210
14. Mukherjee R (2000) Coordination chemistry with pyrazole-based chelating ligands: molecular structural aspects. *Coord Chem Rev* 203:151–218
15. Naito T, Yoshikawa T, Kitahara S, Aoki N (1969) Studies on pyrimidinylpyrazoles. I. Syntheses of 1- and 2-pyrimidinyl-3-methylpyrazolin-5-one derivatives. *Chem Pharm Bull* 17:1467–1478
16. Miyashita Y, Seki T, Yotsui Y, Yamazaki K, Sano M, Abe H, Sasaki S (1982) Quantitative structure-activity relations in pyrazolopyrimidine derivatives for their analgesic activities. *Bull Chem Soc Jpn* 55:1489–1492
17. Molla MC, Garcia J, Borrás J, Foces-Foces C, Cano FH, Ripoll MM (1985) Crystal structure and electronic properties of bis(mepirizole) copper(II) perchlorate. Correlation between the electronic spectrum and CuN₄ chromophore distortion from tetrahedral symmetry. *Trans Met Chem* 10:460–463
18. Soto L, Legros JP, Molla MC, Garcia J (1987) Dichloro(mepirizole)copper(II). *J Acta Crystallogr C* 43:834–836
19. Sakai K, Tomita Y, Ue T, Goshima K, Ohminato M, Tsubomura T, Matsumoto K, Ohmura K, Kawakami K (2000) Syntheses, antitumor activity, and molecular mechanics studies of *cis*-PtCl₂(pzH)₂ (pzH = pyrazole) and related complexes. Crystal structure of a novel Magnus-type double-salt [Pt (pzH)₄][PtCl₄][*cis*-PtCl₂(pzH)₂]₂ involving two perpendicularly aligned 1D chains. *Inorg Chim Acta* 197:64–71
20. Broomhead JA, Rendina LM, Webster LK (1993) Binuclear complexes of platinum having anticancer properties. DNA-binding studies and biological activity of bis(4,4'-dipyrazolylmethane-N, N')-bis[dichloroplatinum(II)] and related complexes. *J Inorg Biochem* 49:221–234
21. Broomhead JA, Lynch MJ (1995) The synthesis and characterization of dinuclear platinum complexes bridged by the 4,4'-dipyrazolylmethane ligand. *Inorg Chim Acta* 240:13–17
22. Ona GB, Moreno V, Font-Bordia M, Solans X, Pirez JM, Alonso C (1999) Structural and cytotoxic study of new Pt(II) and Pd(II) complexes with the bi-heterocyclic ligand mepirizole. *J Inorg Biochem* 75:205–212
23. Pons J, Ros J, Llagostera M, Perez JA, Ferrer M (2003) Regioselective formation of *N*-alkyl-3,5-pyrazole derived ligands. A synthetic and computational study. Spanish Patent No.01494
24. Ware G (1999) Introduction to insecticides, 3rd edn. University of Minnesota, St Paul
25. Haga T, Toki T, Koyanagi T, Okada H, Imai O, Morita M (1990) Regioselective formation of *N*-alkyl-3,5-pyrazole derived ligands. A synthetic and computational study. Japan Patent No.02040380
26. Constable EC, Steel PJ (1989) *N*, *N'*-Chelating biheteroaromatic ligands: a survey. *Coord Chem Rev* 93:205–223
27. Bowman E, Drissen WL, Reedijk J (1990) Model systems for type I copper proteins: structures of copper coordination compounds with thioether and azole-containing ligands. *Coord Chem Rev* 104:143–172
28. Mani F (1992) Model systems containing pyrazole chelates and related groups: recent developments and perspectives. *Coord Chem Rev* 120:325–359
29. Elguero J (1984) In: Katritzky A (ed) *Comprehensive heterocyclic chemistry*, vol 5. Pergamon Press, Oxford, pp 277–282
30. Elguero J (1966) In: Shinkai I (ed) *Comprehensive heterocyclic chemistry II*, vol 3. Elsevier, Oxford, pp 3–75
31. Kost AN, Grandberg II (1966) Progress in pyrazole chemistry. *Adv Heterocycl Chem* 6: 347–429

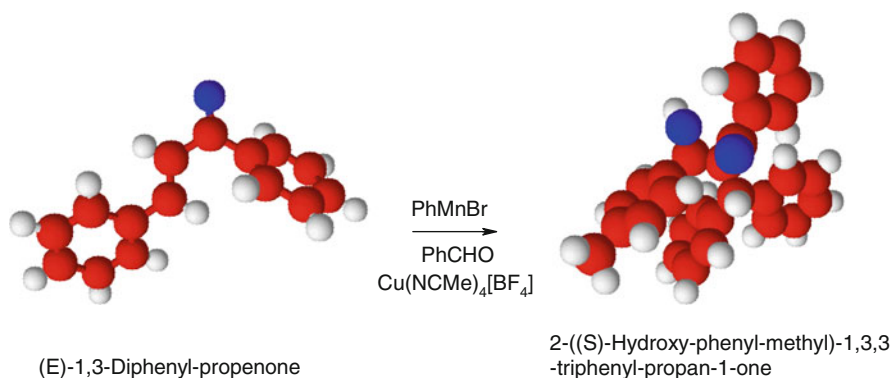
32. Boisvenue RJ, Crouse GD, Kramer KE (1988) Control of ectoparasites. European Patent 202903
33. Reid JC, Calvin M (1950) Some new β -diketones containing the trifluoromethyl group. *J Am Chem Soc* 72:2948–2952
34. Lucid MF (1973) Mixtures of alcohols and fluorinated β -diketones useful as extractant in recovery of vanadium. US Patent 3647712
35. Van de Bossche H (1972) In: Van de Bossche H (ed) *Biochemistry of parasites and host-parasite relationships*, vol 1076. North Holland, Amsterdam, pp 553–572
36. Mitchell P (1961) Coupling of phosphorylation to electron and hydrogen transfer by a chemi-osmotic type of mechanism. *Nature (London)* 191:144–148
37. Brickl R, Eberhardt H, Appel KR, Lechner U, Merk W (1980) (1976) Substituted fluoracylresorcinols. US Patent 4225619 and 4229479
38. Diana GD, Carabateas PM, Johnson RE, Williams GL, Poncee F, Collins JC (1978) Antiviral activity of some beta-diketones. 4. Benzyl diketones. In vitro activity against both RNA and DNA viruses. *J Med Chem* 21:889–894
39. Van De Bossche H, Verboeven H, Vanparijs O, Lauwers H, Thienpont D (1979) Guidelines for the efficacy evaluation of equine anthelmintics. Food and Drug Administration. *Arch Int Physiol Biochim* 7:851–852
40. Osadchii SA, Barkhash VA (1971) Reaction of perfluorodibenzoylmethane with hydrazines. *Ser Khim* 8:1721–1723
41. Singh SP, Kumar D, Batra H, Naithani R, Rozas I, Elguero J (2000) The reaction between hydrazines and dicarbonyl compounds: proposal for a mechanism. *Can J Chem* 79:1109–1120
42. Zefirov NS, Kozhushkov SI, Kuznetsova TS (1996) Rearrangements and cyclization-XVII: Mechanism of the formation of 1,2-azoles in reactions of 1,1-diacyclopropanes with hydrazine and hydroxylamine. *Tetrahedron* 42:709–713
43. Singh SP, Kumar D, Jones BJ, Threadgill MD (1999) Formation and dehydration of a series of 5-hydroxy-5-trifluoromethyl-4,5-dihydropyrazoles. *J Fluor Chem* 94:199–203
44. Song L, Zhu S (2001) Regioselective synthesis of fluorinated pyrazole derivatives from trifluoromethyl-1,3-diketone. *J Fluor Chem* 111:201–205
45. Burness DM (1956) β -keto acetals. I. Synthesis of pyrazoles and pyrimidines and the steric inhibition of resonance in 5-alkyl-1-*p*-nitrophenylpyrazoles. *J Org Chem* 21:97–101

Chapter 9

Trapping of Organomanganese Generated Enolates with an Aldehydes in the Presence of $\text{Cu}(\text{NCMe})_4[\text{BF}_4]$

Sunil D. Jadhav and Madhukar B. Deshmukh

Graphical Abstract



Abstract The enolates produced from the conjugate addition of phenyl manganese bromide with α,β -unsaturated carbonyl compounds were trapped with electrophiles like aromatic aldehydes in presence of a catalyst *tetrakis* (acetonitrile) copper (I) tetrafluoroborate by varying temperature, time and ethereal solvents to give overall β -phenyl α -hydroxy aryl compounds in 32–98% yield. Reaction of these enolates when trapped with allyl bromide produced 34–88% *C*-alkylated product. It was found that, enolates of *trans*-chalcone, benzylidene acetone and *trans*-cinnamaldehyde were trapped with 1–10 equivalents of an aromatic aldehyde in

S.D. Jadhav (✉)

Department of Chemistry, Dada Patil Mahavidyalaya, Karjat, 414402 Maharashtra, India
e-mail: jadhav.sd@rediffmail.com

M.B. Deshmukh

Department of Chemistry, Shivaji University, Belgaum Road, 416004 Kolhapur, India
e-mail: m.deshmukh1@rediffmail.com

the presence of 5 mol % of $\text{Cu}(\text{NCMe})_4[\text{BF}_4]$, in excellent yield. When enolate of mesityl oxide was tried to trap with *p*-tolualdehyde, only conjugated product was formed.

9.1 Introduction

The use of lithium organocuprate reagents in conjugate addition reaction is widely recognized as a powerful synthetic method in organic synthesis [1]. The mechanism for these reactions is still not fully resolved although there are strong evidences that they proceed by an electron transfer process [2]. The intermediate formed has an anionic character as shown by the isolation of various enol derivatives following treatment with appropriate electrophilic reagents [3] and, although this intermediate has been thoroughly examined [4], some differences in chemical reactivity from a lithium enolate have been noted.

Early work carried out by Noyori indicated that aldehydes are suitable electrophilic traps for Zn enolates [5]. There has been also report about the reactivity of enolate in the formation of syn- or anti diols [6]. Following on from work within our own group we have reported the catalytic activity of $\text{Cu}(\text{NCMe})_4[\text{BF}_4]$ and $\text{Cu}(\text{NCMe})_2(\text{PPh}_3)_2[\text{BF}_4]$ in conjugate addition and substitution reaction with α,β -unsaturated carbonyl compounds, acylals and allylic halide [7]. We became interested in trapping the enolate formed during the addition of organomanganese reagent to enone and enal in presence of $\text{Cu}(\text{NCMe})_4[\text{BF}_4]$ catalyst [8] in a subsequent carbon-carbon bond formation reaction. Herein, we outline our initial findings on enolate trapping with aldehydes.

During the period of this investigation several reports have appeared of similar synthetic schemes using alkyl halides [9] and Mannich bases [10]. The use of ZnCl_2 in enolate trapping has also been reported [11]. Cu(I) catalyzed phosphorylation and trapping with diethyl phosphochloridate has appeared in literature [12].

9.2 Results and Discussion

We found that **A**, (Scheme 9.1) produced from the reaction of enone substrate with phenyl manganese bromide in THF reacted with aldehydes under various conditions of temperature and concentration giving β -hydroxy ketones in the presence of 5–10 mol % $\text{Cu}(\text{NCMe})_4[\text{BF}_4]$ as catalyst (see Table 9.1). Reaction of 10 equivalents of aldehydes with **A** in presence of 5 mol % $\text{Cu}(\text{NCMe})_4[\text{BF}_4]$ gave **2a** and **2d** in acceptable yields (entries 1 & 4). The yields were lowered from 99 to 63% when 5 equivalents of aldehyde were used to form **2b** and **2c** in presence of 10 mol % of $\text{Cu}(\text{NCMe})_4[\text{BF}_4]$ catalyst.

Table 9.1 Enolate trapping with aldehydes

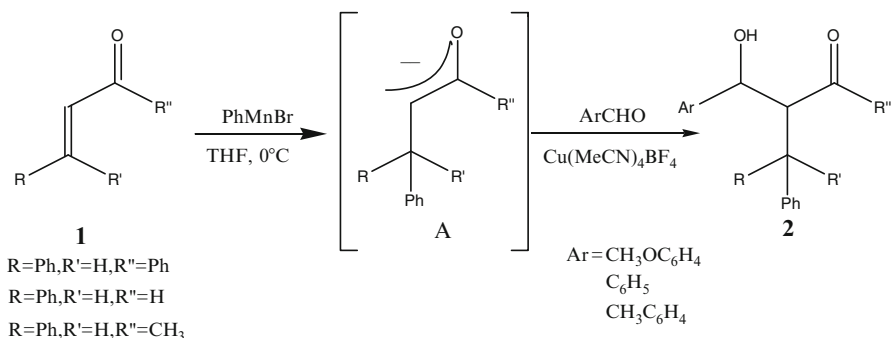
Entry	Enone	Ar	Solvent	Temp (°C)	Product	β -ketols % yield	Cu(I) mol %	Time h
1	<i>Trans</i> -chalcone	OCH ₃ -C ₆ H ₄	THF	0	2a	99 ^a	5	2
2	<i>Trans</i> -chalcone	C ₆ H ₅	THF	0	2b	64 ^b	10	2
3	<i>Trans</i> -chalcone	C ₆ H ₅	THF	-10	2c	63 ^b	10	2
4	<i>Trans</i> -chalcone	CH ₃ -C ₆ H ₄	THF	5	2d	98 ^a	5	1
5	<i>Trans</i> -cinnamal	OCH ₃ -C ₆ H ₄	Et ₂ O	5	2e	68 ^c	5	0.5
6	<i>Trans</i> -cinnamal	C ₆ H ₅	Et ₂ O	0	2f	46 ^c	5	0.5
7	<i>Trans</i> -cinnamal	C ₆ H ₅	THF	0	2g	78 ^c	5	1
8	<i>Trans</i> -cinnamal	CH ₃ -C ₆ H ₄	Et ₂ O	0	2h	58 ^c	10	2.30
9	Benzylidene acetone	CH ₃ -C ₆ H ₄	THF	0	2i	79 ^c	5	3
10	Benzylidene acetone	C ₆ H ₅	THF	0	2j	72 ^c	10	1
11	Mesityl oxide	C ₆ H ₅	Et ₂ O	0	2k	32 ^b	10	2
12	Mesityl oxide	CH ₃ -C ₆ H ₄	Et ₂ O	0	2l	48 ^c	10	0.5

All reactions were carried out on 5-mmol scale. Mass balance is starting material or other side reactions

^a10 equivalents of Ar-CHO were used

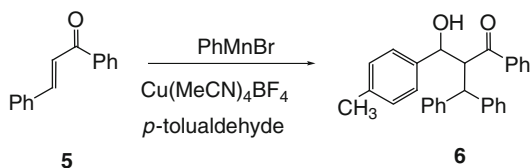
^bCu(I): Cu(NCMe)₄[BF₄]

^cReaction with 1 equivalent of Ar-CHO



Scheme 9.1 Organomanganese generated enolate trapping with aromatic aldehydes

Fig. 9.1 Enolate trapping of *trans*-chalcone with *p*-tolualdehyde



The enolate generated from *trans*-cinnamaldehyde afforded low β ketols (entries 5–7), due to other side reactions. When the reaction was performed with 1 equivalent of aldehyde in THF, the yield of **2g** was increased from 46% to 78% (entries 6 & 7). However, when 10 mol % of catalyst was used, there was not quantitative increase of **2h** in ether even after prolonged stirring of reaction mixture (entry 8).

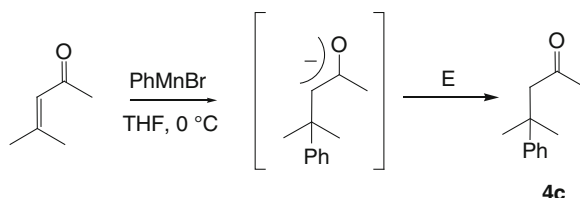
Benzylidene acetone enolate when reacted with 1 equiv. of aldehyde in THF produced **2i** and **2j** in 72–79% yield in presence of 5–10 mol % of $\text{Cu}(\text{NCMe})_4[\text{BF}_4]$ catalyst. When enolate derived from mesityl oxide was trapped with an aldehyde, the yields of **2k** and **2l** were not quantitative (entries 11 & 12) (Fig. 9.1).

In another attempt of enolate trapping with allyl bromide, we observed low yield of β -ketols (see Table 9.2). When the enolate derived from *trans*-chalcone was trapped with 10 equiv. of allyl bromide in Et_2O , the yield of **4a** was 71% (entry 1). However, by changing the solvent from Et_2O to THF, the yield of **4a** was increased from 71% to 88% (entry 2). Trapping of enolate of *trans*-cinnamaldehyde with allyl bromide afforded only 34% of **4b** (entry 3) afforded. It was observed that there was not clean enolate trapping with allyl bromide. There has been report of **A** produced from the reaction of enone substrate with lithium dialkyl cuprates (R_2CuLi) in Et_2O that it was inert towards normally reactive alkylating reagents (e.g. MeI , $\text{CH}_2=\text{CH-I}$) [13]. This is in agreement with the original report by House et al. [2]. The enolate of mesityl oxide when trapped with allyl bromide, in the presence of 10 mol % $\text{Cu}(\text{NCMe})_4[\text{BF}_4]$ catalyst gave more conjugate addition product **4c** in 54% yield (entry 6 Table 9.2, Fig. 9.2), than that of trapping with an aldehyde indicating this catalyst is probably not involved in this reaction but the Cu^+ is acting as stabilizing chelating metal center (as outlined by House et al. [2] with Zn enolate).

Table 9.2 Enolate trapping with allyl bromide

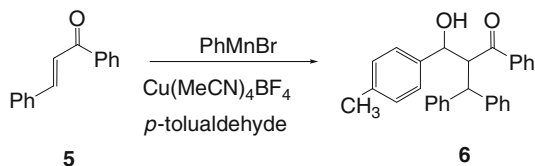
Entry	Enone	Solvent	Temp. (°C)	Product	% yield
1	<i>Trans</i> -chalcone	Et ₂ O	0	4a	71
2	<i>Trans</i> -chalcone	THF	0	4a	88
3	<i>Trans</i> -cinnamal	Et ₂ O	0	4b	34
4	<i>Trans</i> -cinnamal	THF	0	4b	74
5	Mesityl oxide	Et ₂ O	0	4c	<i>c</i>
6	Mesityl oxide	THF	0	4c	<i>c</i>

All reactions were carried out on 5 mmol scale, *c*= conjugated products resulted

Fig. 9.2 Conjugate addition product**Table 9.3** *p*-tolualdehyde enolate trapping with an aldehyde

<i>p</i> -tolualdehyde (equivalent)	Reaction time (min)	Temp. (°C)	% yield	
			(6)	(5)
10	15	0	99	1
10	15	5	75	3
5	15	0	79	18
5	90	0	42	52

All reactions were carried out on 5 mmol scale in THF

Fig. 9.3 *p*-tolualdehyde enolate trapping with an aldehyde

We have also investigated the enolate trapping of *trans*-chalcone with variation of temperature and reaction time in presence of 5 mol % Cu(NCMe)₄[BF₄] catalyst (Table 9.3, Fig. 9.3).

A brief study of **6** (Table 9.3) showed that, temperature and reaction time are very important parameters in determining conditions for optimum yield. When the reaction was performed with *p*-tolualdehyde, an excess (10 equiv.) of aldehyde was generally used. In the formation of **6**, use of 5 equiv. of *p*-tolualdehyde lowered the yield from 99% to 79%. When the reaction time was increased again the yield of **6** was dropped to only 42%. We noticed that these results were excellent from the preparative point of view.

IR spectra were obtained on Perkin Elmer FTIR spectrometer. Solid samples were examined in Nujol and liquid samples as liquid films unless stated other-

wise. ^1H NMR spectra were recorded with a SFX 400 MHz and ^{13}C NMR spectra on 100 MHz SFX spectrometer in CDCl_3 solution using TMS as an internal standard. The chemical shifts (δ) are quoted in ppm downfield from TMS. Spectra are reported according to the conventions. Chemical shift (number of protons, multiplicity, observed coupling constant (Hz), assignment). Multiplicities are reported as: s, singlet; d, doublet; t, triplet; q, quartet; m, multiplet.

Chromatography (a) Analytical TLC were obtained using Merck TLC aluminum foil silica gel $^{60}\text{F}_{254}$ strips with a layer thickness of 0.20 mm. (b) Preparative layer chromatograms (plc) were obtained on glass plates (20 cm \times 20 cm or 20 cm \times 50 cm) coated with Merck Silica gel PF $_{254+366}$ with a layer thickness of 1.25 mm.

Reactions involving organometallic reagents were performed under an atmosphere of dry, oxygen free N_2 in 3-necked round-bottomed flasks, dried by heating at 110°C and cooling under N_2 or alternatively by heating with a flame under a stream of N_2 equipped with septum stoppers.

Na-dried diethyl ether was refluxed with LAH under N_2 for 1–2 h and distilled directly into the reaction flask. THF was refluxed with Na under N_2 in the presence of small quantities of benzophenone until a blue colour appeared, then the solvent distilled directly into the reaction flask. $\text{Cu}(\text{NCMe})_4[\text{BF}_4]$ was prepared according to the literature procedure [14]. Molarity of phenyl magnesium bromide was determined according to the Gilman double titration method [15]. All organic reactants were commercial samples or prepared using standard procedures and were redistilled or recrystallised before use.

9.3 Li_2MnCl_4 (Dilithium Tetrachloro Manganate)

Manganese(II) chloride (1M) and lithium chloride (2M) were vacuum dried in oven at 120°C for 3 h and then Na dried THF was added to form “ate” complex of Li_2MnCl_4 . Organomanganese reagents are prepared by adding Grignard reagent to the “ate” complex prior to use.

9.4 Typical Procedure

9.4.1 Aldol Condensation Reactions of Enolates with Aldehydes in the Presence of $\text{Cu}(\text{NCMe})_4[\text{BF}_4]$ Complex

To a cooled solution of Li_2MnCl_4 (5 mmol, 1 M, 5 mL), phenyl magnesium bromide (5.1 mmol, 1 M, 5.1 mL) in 2 mL dry THF was added at 0°C . The reaction mixture was stirred till black brown suspension of PhMnBr resulted. Then benzylidene acetone (5 mmol, 0.73 g) in 1 mL of THF was added and the content was stirred for 30 min. 10 mol % of $\text{Cu}(\text{NCMe})_4[\text{BF}_4]$ (50 mg) was added and the solution was

further agitated for 15–20 min. Then benzaldehyde (5 mmol, 0.511 mL) in 1 mL THF was added over 5 min. Progress of the reaction was monitored by TLC. The reaction mixture was poured into 10% NH₄Cl (100 mL), which gave a blue aqueous phase and the mixture was then extracted with ether. After evaporating ether the crude liquid was purified on column chromatography.

9.5 Characterization of Products

Specified spectral data are recorded on pure isomers. In a few cases it was not possible to obtain single isomers (**2k**, **2l** and **4c**) and in these cases the ¹³C NMR spectra were recorded from a mixture.

2a ¹³C NMR δ ppm: 190.5, 164.50, 144.62, 132.61, 131.77, 130.38, 129.87, 129.36, 128.80, 128.58, 128.47, 128.32, 127.9, 126.93, 122, 115.31, 114.19, and 55.37.

IR (KBr) ν_{max}: 3307, 2936, 1684, 1459, 1314, 1181, 1024, 833 cm⁻¹

2b ¹³C NMR δ ppm: 206.46, 171.21, 143.5, 141.80, 138.84, 133.68, 132.63, 130.21, 129.37, 128.67, 128.26, 127.88, 127.15, 126.70, 125.98, 124.98, 124.62, 60.83, 56.73, 52.65.

IR (KBr) ν_{max}: 3384, 2926, 1649, 1596, 1450, 1257, 1065, 941 cm⁻¹

2c ¹³C NMR δ ppm: 141.34, 132.68, 132.41, 130.08, 129.04, 128.78, 128.31, 127.92, 127.70, 127.21, 126.58, 125.20, 73.15, 56.94, 56.10.

IR (KBr) ν_{max}: 3684, 3018, 1687, 1659, 1597, 1482, 1319, 1219, 1074, 927, 848, 759 cm⁻¹

2d ¹³C NMR δ ppm: 191.81, 145.43, 144.72, 134.31, 132.77, 130.52, 129.77, 125.13, 128.95, 128.85, 128.76, 128.62, 128, 127, 125, 122, 21.70.

IR (KBr) ν_{max}: 3386, 3029, 1688, 1605, 1577, 1449, 1387, 1215, 1168, 1017, 846, 809, 758 cm⁻¹

2e ¹H NMR (CDCl₃) δ ppm: 1.5 (t, 1H, J = 7.5 Hz), 3.8 (s, 3H), 4.5 (s, 1H), 5.4 (d, 1H, J = 7.2 Hz), 6.9–7.9 (m, 15H), 9.6 (d, 1H, J = 7.2 Hz).

¹³C NMR δ ppm: 190.62, 164.44, 152.59, 145.81, 144.65, 136.45, 132.4, 131.35, 130.16, 129.43, 128.65, 127.97, 126.86, 121.90, 79.12, 74.68, 55.24.

IR (KBr) ν_{max}: 3362, 2968, 2740, 1683, 1509, 1393, 1255, 1161, 1070, 970 cm⁻¹

2f ¹H NMR (CDCl₃) δ ppm: 5.1 (t, 1H, J = 7.5 Hz), 5.35 (d, 1H, J = 7.1 Hz), 5.8 (s, 1H), 7.0–7.1 (m, 16H), 9.65 (d, 1H, J = 7.3 Hz).

IR (KBr) ν_{max}: 3400, 2814, 2750, 1687, 1560, 1459, 1314, 1181, 1033, 838 cm⁻¹

2h ¹³C NMR δ ppm: 191.68, 145.24, 142.79, 140.98, 136.46, 134.69, 132.52, 131.34, 130.29, 130.98, 129.44, 128.70, 127.43, 126.60, 74.75, 69.77, 21.36.

IR (KBr) ν_{max}: 3448, 3028, 1702, 1686, 1577, 1449, 1387, 1216, 1168, 1018, 847, 809, 758 cm⁻¹

2i ^1H NMR (CDCl_3) δ ppm: 2.30 (s, 3H), 2.32 (s, 3H), 3.58 (t, 1H, $J = 7.5$ Hz), 5 (s, 1H), 6.41–6.45 (d, 1H, $J = 5.6$ Hz), 6.6–8.2 (m, 15H).

IR (KBr) ν_{max} : 3479, 3062, 1701, 1652, 1597, 1455, 1390, 1359, 1203, 1166, 1072, 827, 745, 688, 650 cm^{-1}

2j ^{13}C NMR δ ppm: 198.35, 143.84, 141.14, 136.40, 133.18, 130.72, 129.62, 128.68, 127.46, 127.05, 126.75, 125.26, 115.45, 74.46, 49.5, 30.9, 29.71.

IR (KBr) ν_{max} : 3448, 3029, 1702, 1608, 1494, 1359, 1258, 1167, 1072, 974, 827, 740 cm^{-1}

2k ^{13}C NMR δ ppm: 215, 149, 147.62, 144, 136.2, 132.32, 129.56, 128.19, 126.12, 125.61, 73.85, 56.76, 40.82, 33.51, 28.79.

IR (KBr) ν_{max} : 3471, 3030, 1710, 1597, 1482, 1390, 1359, 1203, 1167, 1071, 897, 827, 745 cm^{-1}

2l ^{13}C NMR δ ppm: 215, 147.66, 141.03, 136.04, 134.01, 129.5, 128.56, 127.69, 126.75, 125.78, 124.95, 76.88, 70.01, 40.68, 35.01, 27.30.

IR (KBr) ν_{max} : 3466, 3030, 1708, 1605, 1577, 1482, 1385, 1266, 1168, 1075, 1030, 904, 846, 758 cm^{-1}

4a ^{13}C NMR δ ppm: 197.91, 144.75, 141.18, 133.1, 133.5, 132.67, 130.44, 129.9, 129.4, 128.68, 127.9, 127.1, 126.3, 75.2, 54.6, 53.8, 49, 44.6.

IR (KBr) ν_{max} : 3024, 2928, 1722, 1578, 1452, 1382, 1218, 1172, 1028, 848, $809,752\text{ cm}^{-1}$

4b ^{13}C NMR δ ppm: 193.87, 152.93, 145, 142.8, 141.2, 136.59, 132.79, 131.58, 130.52, 128.7, 127.8, 126.60, 49.2, 25.1.

IR (KBr) ν_{max} : 3442, 3059, 1674, 1577, 1493, 1372, 1231, 1177, 1027, 915, 845, 739 cm^{-1}

4c ^1H NMR (CDCl_3) δ ppm: 1.48 (s, 6H), 1.83 (s, 2H), 2.2 (s, 3H), 7.2–7.6 (m, 5H).

IR (KBr) ν_{max} : 3059, 1704, 1598, 1495, 1444, 1357, 1287, 1181, 1076, 1009, 905, 842, 781, 764, 738 cm^{-1}

9.6 Conclusions

We have shown that, enolate generated from *trans*-chalcone, *trans*-cinnamaldehyde and benzylidene acetone with phenyl manganese bromide can be trapped with aldehydes in presence of 5–10 mol % $\text{Cu}(\text{NCMe})_4[\text{BF}_4]$ catalyst in THF solvent. The reaction conditions are gentle, yields are moderate to good. This approach complements existing methods for producing β -ketols, in many cases offers definite advantages in terms of the scope of application and conditions of reaction.

Acknowledgements We thank BCUD University of Pune, for financial support to this project.

References

1. Posner GH (1972) Conjugate addition reactions of organocopper reagents. *Org React* 19:1–113
2. House HO, Wilkins JM (1976) The chemistry of carbanions & the nature of the enolate formed by addition of lithium dimethylcuprate to enones. *J Org Chem* 41:4031–4033
3. Binkley ES, Heathcock CH (1975) Regiospecific alkylation of enolate ions in liquid ammonia-tetrahydrofuran. *J Org Chem* 40:2156–2160
4. Heng KK, Smith RAJ (1978) An organocuprate conjugate addition-Aldol condensation synthetic procedure for sequential formation of two carbon-carbon bonds. *Tetrahedron* 35:425–435
5. Kitamura M, Miki T, Nakano K, Noyori R (2000) 1,4-addition of diorganozincs to α,β -unsaturated ketones catalyzed by a copper(I)-sulfonamide combined system. *Bull Chem Soc Jpn* 73:999–1006
6. Alexandre A, Trevitt GP, Bernardinelli G (2001) Tandem enantioselective conjugate addition: electrophilic trapping reactions. Application in the formation of syn or anti aldols. *J Am Chem Soc* 123:4358–4359
7. (a) Deshmukh MB, Jadhav S, Anbhule PV, Mali AR, Suryawanshi AW (2006) A remarkable catalytic activity of $\text{Cu}(\text{NCMe})_2(\text{PPh}_3)_2[\text{BF}_4]$ in conjugate addition of organomanganese to α,β -unsaturated enone and allyl chloride. *J Chem Res* 4:248–250 (b) Deshmukh MB, Jadhav SD, Kadam SV (2007) Copper catalyzed substitution reactions of acylal with organomanganese reagents. *Indian J Chem* 47B:989–994
8. Jason G, Sinn E, Woodward S (1993) Mechanistic insights into catalytic cyclopropanation by copper(I) phosphine complexes. X-ray crystal structures of $[\text{Cu}(\text{F}-\text{BF}_3)(\text{PCy}_3)_2]$ (Cy = cyclo- C_6H_{11}) and $[\text{Cu}(\text{MeCN})_2\{1,2\text{-C}_6\text{H}_4\text{CH}_2\text{NMe}_2(\text{PPh}_2)\}_2]\text{BF}_4$. *Polyhedron* 12:991–1001
9. Boeckwan RK Jr (1973) Regiospecific alkylation of organocopper enolates. *J Org Chem* 38:4450–4452
10. Holy NL, Wang YF (1977) New applications of the Mannich reaction. Use of dimethyl (methylene) ammonium trifluoroacetate for regiospecific carbanion quenching. A new route to α -methylene- γ -butyrolactone. *J Am Chem Soc* 99:944–950
11. Heng KK, Simpson J, Smith RAJ (1981) Trapping of a homocuprate-generated enolate with an aldehyde in the presence of ZnCl_2 . *J Org Chem* 46:2932–2934
12. Muchmore DC (1972) Synthesis of an enol phosphate. *Org Synth* 52:109–114
13. Coates RM, Sowerby RL (1971) Site-selective germinal alkylation of ketones. Reduction-alkylation of n-butylthiomethylene derivatives. *J Am Chem Soc* 93:1027–1031
14. Kubas GJ (1990) Tetrakis(acetonitrile)copper(1+) hexafluorophosphate(1-). *Inorg Synth* 28:68–71
15. Gilman H, Cartledge FK (1964) The analysis of organolithium compounds. *J Organomet Chem* 2:447–450

Chapter 10

Radial and Electron Correlation Effects for Helium and Some Helium Like Ions

Khalil H. AL-bayati and Esraa F. Saeed

Abstract The radial and electronic correlation effects for intra-electronic shell have been examined within two-electron system, helium atom, and compared with two helium like ions, Li^+ and Be^{++} using the uncorrelated Hartree Fock wave function published by Clementi and Roetti (At Data Nucl Data Tables 14:177, 1974) and the correlated configuration interaction wave function published by Weiss (Phys Rev 122:1826, 1961). Some atomic properties have been studied to examine the radial correlation effects such as: (i) one-particle radial distribution function and one-particle expectation value when $k = -2$ to 2, (ii) two-particle radial distribution function and two-particle expectation value when $k = -2$ to 2, (iii) the inter-particle distribution function and inter-particle expectation value when $k = -2$ to 2, and, (iv) the partial distribution function. In addition to these atomic properties, coulomb hole, partial coulomb hole, the radial correlation for one and two-particles distribution function and the radial correlation energy are very important in studying the physical and chemical properties of these ions or atoms. The results were compared with that calculated in previous published work using partitioning technique.

10.1 Introduction

Any system can be described by a wave function $\psi(r_1, r_2, \dots, r_N)$; it is a mathematical expression to describe the system properties such as position, momentum, energy etc. The exact calculation of wave functions for many electron atoms becomes

K.H. AL-bayati (✉)

Department of Physics, College of Science for Women, Baghdad University, Al-jadyria, Baghdad, Iraq

e-mail: drkhalilhadi@yahoo.com

E.F. Saeed

Department of Physics, College of Science, Hahrain University, Al-jadyria, Baghdad, Iraq

e-mail: israa_physics2006@yahoo.com

difficult because of the many electron–electron repulsions that should be ignored for simplicity. There are two main kinds of wave function approximation methods which are used in this research, the first one is the uncorrelated wave function approximation Hartree-Fock (HF), and the second one is the correlated wave function approximation Configuration Interaction (CI). The aim of this research is to calculate the radial correlation for He-like atoms using Schrödinger wave function with two approximations: the uncorrelated HF wave function and the correlate CI wave function.

In many electron systems, many investigators in position space have studied the atomic properties. In majority of these theoretical studies, different approximations were applied. In this section we will review some of them, which are relevant to the present research. Roothaan et al. [1] have obtained an accurate wave function for the ground state of helium-like systems. They have found that one of the most successful models is the Hartree-Fock approximation. Weiss [2] has done successful approaches to many-particle quantum mechanics for the ground and excited state of helium, lithium and beryllium atoms using a configuration interaction approximation. Banyard [3] has analysed and compared several wave functions for H^- , based on the single determinant independent-particle model and correlated wave functions. He has discussed the two-particle density $D(r_1, r_2)$ and the radial density $D(r_1)$. Banyard and Baker [4] have studied the electron correlation of an isoelectronic series possessing electrons with antiparallel spins H^- , He, and Li^+ . The correlation within the wave functions was demonstrated by presenting two-particle density difference maps, $\Delta D(r_1, r_2)$ relative to the uncorrelated approach, and graphs of the radial density $D(r_1)$. The maxima values of $D(r_1)$ were decreased with increasing nuclear charge (atomic number Z) increasing [4]. AL-Khafaji [5] examined the influence of electron correlation on the K-shell within the ground state of a series of He-like ions and for each individual electronic shell of series of Li-like ions using the correlated wave function. Coulson and Neilson [6] have obtained formulae for the distribution function $f(r_{12})$ of the inter-electronic distance r_{12} in the ground state of helium, and for the mean value of r_{12} . Five different wave functions were considered, showing varying degrees of electron correlation. They have also evaluated the Coulomb hole [6]. Curl and Coulson [7] have calculated the Coulomb hole $\Delta f_c(r_{12})$ in the ground state of two-electron atoms, where the Coulomb hole was defined by Coulson and Neilson [6]. Banyard and Seddon [8] have examined, in depth, several wave functions for the two-electron systems H^- , He, Li^+ , and Be^{++} . They have calculated the inter-particle distribution function $f(r_{12})$, by comparing the results for different wave functions. Some insights were obtained into the roles played by different types of correlation factor [8]. The Coulomb hole and several two-electron expectation values were calculated using a series of Configuration Interaction (CI) wave function of differing accuracy for helium like ions reported by Seddon and Banyard [9]. Boyd [10] has discussed the radius of the Coulomb hole in an atom or molecule in general terms and illustrated in detail for the ground state of the helium isoelectronic sequence. Aman Alla [11] had examined the atomic properties in closed-shell system in the form of He-like ions, and open-shell systems in the form of Li-like ions position

space [11]. The aim of this research is to calculate the radial correlation for He-like atoms using the uncorrelated HF wave function and the correlate CI wave function and study the atomic properties for both approximations and compare between the He atom and its positive ions, Li^+ and Be^{++} .

10.2 The Correlation Energy

The correlation energy is the energy recovered by fully allowing the electrons to avoid each other, and is defined as the difference between the energy in the HF limited and the exact non relativistic energy (E_0) of a system [12]:

$$E_{corr} = E_0 - E_{HF} \quad (10.1)$$

E_{corr} will always be negative because the HF energy is an upper bound to the exact energy. A full CI in a complete one-electron basis set can calculate the exact non-relativistic energy. Where the energy predicted by a correlated wave function takes into account all the instantaneous particle interactions which occurred within a many electron system, therefore, such calculations go well beyond the description provided by independent-particle model.

10.3 The Uncorrelated Wave Function

From the mathematical point of view, many body wave functions are written as [13–15]:

$$\Psi_{HF}(1, 2, 3 \dots N) = \frac{1}{\sqrt{N!}} \begin{vmatrix} \phi_1(1) & \dots & \phi_1(1) \\ \vdots & \ddots & \vdots \\ \phi_N(N) & \dots & \phi_N(N) \end{vmatrix} \quad (10.2)$$

where the multiplying factor ($1/\sqrt{N!}$) introduced to ensure that the wave function Ψ is normalized, and $\phi_i(i)$ is referred to as Spin-orbital. Any spin-orbital may be written as the product of a space function ϕ_i , and a spin function α or β .

$$\phi_i(i) = \varphi(r, \theta, \phi) \delta(s) \quad (10.3)$$

where $\varphi_i(i)$ is the spatial part, $\delta(s)$ the spin part the numbers in the parentheses denote the particle, and the subscripts 1, 2... N denotes the eigen state. The special function φ_{nl} is defined by [2]:

$$\varphi_{nl} = \sum_j^j c_n^j \chi_{nlm} \quad (10.4)$$

$$\chi_{nlm}(r, \theta, \phi) \stackrel{\text{def}}{=} R_{nl}(r) Y_{lm}(\theta, \phi) \quad (10.5)$$

$R_{nl}(r)$ is the radial part of special part of the total wave function.

$Y_{lm}(\theta, \phi)$ is the angular part of the total wave function.

$$R_{nl}(r) = N_{nlm} S_{nl}(r) \quad (10.6)$$

N_{nlm} is the normalization constant, and given as

$$N_{nlm} = \sqrt{\frac{(2\xi)^{2n+1}}{(2n)!}} \quad (10.7)$$

Then

$$S_{nl}(r) = r^{n-1} e^{-\xi r} \quad (10.8)$$

where $S_{nl}(r)$ is called the Slater-Type-Orbital's (STO's). c_n in [4] represents the coefficients of $\chi_{nlm}(r)$ and $Y_{lm}(\Omega)$. Finally, ξ is the orbital exponent.

10.4 The Correlated Wave Function

One method of correcting the shortcomings of Hartree-Fock approximation is the Configuration Interaction (CI) which is used to study the effect of the electron correlation in term of correlation energy. The correlation description of the ground state of He⁻ ions had been taken from Weiss [16].

The correlated wave function is expanded as a linear combination of Slater determinants [16]

$$\Psi_{CI} = \sum_i c_i \phi_i \quad (10.9)$$

where each of ϕ_i (configurations) is antisymmetrized product of one-electron functions (spin orbital), and the coefficients c_i are taken as those which minimize the total energy. By applying the variation theorem and solving an infinite set of secular equations to obtain the exact wave function is obtained.

The specific form of the configuration used for the two-electron system studied here is the following linear combination of single Slater determinant using 15 configuration of s symmetry.

$$(\varphi\chi) = \frac{1}{\sqrt{2}} \sum |\varphi(1)\alpha\chi(2)\beta| \quad (10.10)$$

The basis set of one-electron function chosen is consisted of the normalized Slater-type orbital defined by [17, 18].

$$\chi_{nlm} = \frac{(2\xi)^{n+0.5}}{[(2n)!]^{0.5}} r^{n-1} e^{-\xi r} Y_{lm}(\theta, \varphi) \quad (10.11)$$

10.5 Two-Particle Density Distribution

For any N-electron system, the two-particle density $\Gamma(\chi_m, \chi_n)$ can be written as [19, 20]

$$\Gamma(\chi_m, \chi_n) = \binom{N}{2} \int \Psi^*(\chi_m, \chi_n, \dots, \chi_N) \Psi(\chi_m, \chi_n, \dots, \chi_N) d\chi_m, \dots, d\chi_N \quad (10.12)$$

where χ_m stands for the spin and space coordinate of electrons and $d\chi_m$ indicates that the integration performed for all electrons within system except m and n, while the binomial factor $\binom{N}{2}$ is introduced to ensure that the second order density matrix $\Gamma(\chi_m, \chi_m)$ is normalized to the number of electron pairs in the system.

10.5.1 Two-Particle Density Distribution in HF Approximation

For two-electrons in K-shell $\Gamma_{HF}(\chi_m, \chi_n)$ function is defined as:

$$\Gamma_{HF}(X_m, X_n) = \frac{1}{2} [\phi_{1s}(1)\alpha(1)\phi_{1s}(2)\beta(2) - \phi_{1s}(1)\beta(1)\phi_{1s}(2)\alpha(2)] \quad (10.13)$$

$$\Gamma_K(^1S)(1, 2) = [\phi_{1s}(1)\phi_{1s}(2)]^2 \left[\frac{\alpha(1)\beta(2) - \beta(1)\alpha(2)}{\sqrt{2}} \right] \quad (10.14)$$

10.5.2 The Two-Particle Density $\Gamma''_{corr}(1, 2)$ in CI Approximation

The two particle density function $\Gamma'_{corr}(1, 2)$ for K-shell for He-like ions can be derived as [11]:

$$\Psi = (\varphi\chi) = \frac{1}{\sqrt{2}} |\varphi(1)\chi(2)| \quad (10.15)$$

where $\varphi(i)$ and $\chi(i)$ refer to the one particle function.

By integrating the overall spin and angular parts we get:

$$\Gamma''_{corr}(r_1, r_2) = 0.5 \left[R_\varphi^2(1)R_\chi^2(2) + R_\varphi^2(2)R_\chi^2(1) \right] \quad (10.16)$$

10.6 The Change in Two-Particle Density

For N-electron system, the change in the two-particle density due to the electron correlation can be written as follows [21]:

$$\Delta\Gamma_{ij}(\chi_m, \chi_n) = \Gamma_{ij}^{corr}(\chi_m, \chi_n) - \Gamma_{ij}^{HF}(\chi_m, \chi_n) \quad (10.17)$$

10.7 Two-Particle Radial Distribution Function $D(r_1, r_2)$

For each individual electronic shell, the two-particle density distribution function $D(r_1, r_2)$ is defined as [21]

$$D(r_1, r_2) \int \int \Gamma(r_1, r_2) r_1^2 r_2^2 d\Omega_1 d\Omega_2 d\sigma_1 d\sigma_2 \quad (10.18)$$

where $d\Omega_i$ denotes that the integration is over all angular coordinates of the position.

The function $D(r_1, r_2)$ tells us how the motion of the two different electrons is correlated as a result of their interaction and it is a measure of the probability of finding two electrons simultaneously with radial coordinates enclosed between r_1 to $r_2 + dr_1$ and r_2 to $r_2 + dr_2$ respectively.

10.8 Two-Particle Radial Distribution Functions by Using HF Approximation

For K-shell using HF method $D_{HF}(r_1, r_2)$ can be written as

$$D(r_1, r_2) \int \int [\phi_{1s}(1)\phi_{1s}(2)]^2 \left[\frac{\alpha(1)\beta(2) - \beta(1)\alpha(2)}{\sqrt{2}} \right]^2 r_1^2 r_2^2 d\Omega_1 d\Omega_2 d\sigma_1 d\sigma_2 \quad (10.19)$$

10.9 Two-Particle Radial Distribution Functions by Using CI Approximation

The two-particle radial density distribution function of correlated wave function can be defined by

$$D_{K(1S)}^{CI}(r_1, r_2) = 0.5 \left[R_\phi^2(r_1)R_x^2(r_2) + R_\phi^2(r_2)R_x^2(r_1) \right] r_1^2 r_2^2 \quad (10.20)$$

10.10 One-Particle Radial Distribution Function $D(r_1)$

The radial density distribution function $D(r_1)$ is of extreme importance in the study of atom and ions because it measures the probability of finding an electron in each shell, and it is defined as

$$D_{HF}(r_1) = R_{1s}^2(r_1)r_1^2 \quad (10.21)$$

10.11 One-Particle Radial Distribution Functions by Using CI Approximation

The one particle radial distribution function in CI approximation can be defined by

$$D_{CI}(r_1) = 0.5r_1^2 \left[R_{\varphi}^2(r_1) + R_x^2(r_1) \right] \quad (10.22)$$

10.12 One Particle Expectation Values $\langle r_1^K \rangle$

The one particle expectation value $\langle r_1^K \rangle$ is given by using both CI and HF approximations [21]:

$$\langle r_1^K \rangle_{CI, HF} = \int_0^{\infty} r_1^K D_{CI, HF}(r_1) dr_1 \quad (10.23)$$

The Eq. 10.23 indicates that the expectation values are calculated to various radial locations and for the sake of comparison of different probabilities of electron locations in the regions near the nucleus and of distant electron charge cloud for every electronic shell; for example $k = -1$ is employed in determination of expectation values of electronic-nuclear attraction potential energy and in determination of nuclear magnetic shielding constants of various shells and states while $k = +2$ is essential for calculating the diamagnetic susceptibility [11].

The radial correlation of the one-particle expectation value is the change between the configuration interaction approximation and the Hartree-Fock approximation.

$$\Delta \langle r_1^K \rangle = \langle r_1^K \rangle_{CI} - \langle r_1^K \rangle_{HF} \quad (10.24)$$

10.13 Two-Particle Expectation Values $\langle r_1^K r_2^K \rangle$

Two-particle expectation values $\langle r_1^K r_2^K \rangle$ are defined as [4]

$$\langle r_1^K r_2^K \rangle = \int_0^\infty \int_0^\infty D(r_1, r_2) r_1^K r_2^K dr_1 dr_2 \quad (10.25)$$

The function $\langle r_1^K r_2^K \rangle$ is calculated when $-2 \leq K \leq 2$.

The radial correlation for the two-particle expectation values $\Delta \langle r_1^K r_2^K \rangle$:

$$\Delta \langle r_1^K r_2^K \rangle = \langle r_1^K r_2^K \rangle_{CI} - \langle r_1^K r_2^K \rangle_{HF} \quad (10.26)$$

10.14 The Inter-Particle Distribution Function $f(r_{12})$

Coulson and Neilson [6] proposed a distribution function for inter-electronic separation of $f(r_{12})$ of s-states associated with spin – orbital pair (i, j).

$$f_{ij}(r_{12}) = \int \Gamma_{ij}(r_1, r_2) dr_1 dr_2 \quad (10.27)$$

where the function $f_{ij}(r_{12})$ is the probability distribution distance between electron 1 and electron 2; this function is of great importance in both Fermi and Coulomb holes and r_{12} is the distance between the two electrons. This function satisfies the normalization condition [6].

$$\int f(r_{12}) dr_{12} = 1 \quad (10.28)$$

Then $f(r_{12})$ can be as follows

$$f(r_{12}) = 8\pi^2 r_{12} \{J_1 + J_2\} \quad (10.29)$$

where

$$\begin{aligned} J_1 &= \int_0^{r_{12}} r_1 \int_{|r_{12}-r_1|}^{|r_{12}+r_1|} \Gamma'(r_1, r_2) r_2 dr_2 dr_1 \\ J_2 &= \int_{r_{12}}^\infty r_1 \int_{|r_1-r_{12}|}^{|r_1+r_{12}|} \Gamma'(r_1, r_2) r_2 dr_2 dr_1 \end{aligned} \quad (10.30)$$

10.15 The Inter-Particle Distribution Function $f(r_{12})$ in HF Method

The inter-particle distribution function for HF, and correlated wave function for He-like ions can be obtained [6]

$$f_{CI, HF}(r_{12}) = 0.5r_{12} \left[\int_0^{r_{12}} r_1 \int_{|r_{12}-r_2|}^{|r_{12}+r_2|} \Gamma'_{CI, HF}(r_1, r_2) r_2 dr_2 dr_1 + \int_{r_{22}}^{\infty} r_1 \int_{|r_1-r_{22}|}^{|r_1+r_{22}|} \Gamma'_{CI, HF}(r_1, r_2) r_2 dr_2 dr_1 \right] \quad (10.31)$$

10.16 Calculation of Coulomb Hole $\Delta f_{coul}(r_{12})$

Coulomb hole $\Delta f_{coul}(r_{12})$ was introduced for the first time by Coulson and Neilson which is defined as a difference between the correlated CI and uncorrelated HF wave functions normalized distribution function and mathematically it given by:

$$\Delta f_{coulomb}(r_{12}) = f_{CI}(r_{12}) - f_{HF}(r_{12}) \quad (10.32)$$

While the inter particle separation is $r_{12} = |r_1 - r_2|$. This equation provides a simple physical picture of the average extent to which electronic charge is pushed away from a selected electron as a result of its instantaneous (rather average) interaction with other electrons [12].

10.17 The Inter-Particle Expectation Value $\langle r_{12}^K \rangle$

The expectation value of two-electron separation is given by [6]

$$\langle r_{12}^K \rangle = \int_0^{\infty} f(r_{12}) r_{12}^K dr_{12} \quad (10.33)$$

when $-2 \leq k \leq 2$.

The change of the inter-particle expectation value is given by

$$\Delta \langle r_{12}^K \rangle = \langle r_{12}^K \rangle_{CI} - \langle r_{12}^K \rangle_{HF} \quad (10.34)$$

10.18 Partial Distribution Function $g(r_{12}, r_1)$

The partial distribution function $g(r_{12}, r_1)$ represents the probability of finding an inter-electronic separation r_{12} given by the relationship

$$g(r_{12}, r_1) = 8\pi^2 r_1 r_{12} \int_{|r_{12}-r_1|}^{|r_{12}+r_1|} \Gamma'(r_1, r_2) r_2 dr_2 \quad (10.35)$$

This function depends upon both electronic separation (r_{12}) and the position of the first electron. The function $g(r_{12}, r_1)$ is useful to illustrate the behavior of the test electron “reference electron”, and the change in distance occurs when the location of electron 1 from nucleus is fixed. This function is used to study the partial Fermi and Coulomb holes.

10.18.1 Partial Distribution Function $g(r_{12}, r_1)$ in HF Method

For the K-shell by substituting Eq. 10.14 in Eq. 10.35 the result is [11]

$$g_{k(1s)}^{HF}(r_{12}, r_1) = 0.5 r_1 r_{12} \int_{|r_{12}-r_1|}^{|r_{12}+r_1|} R_{1s}^2(r_1) R_{1s}^2(r_2) r_2 dr_2 \quad (10.36)$$

10.18.2 The Partial Distribution Function $g(r_{12}, r_1)$ in CI Method

For the K-shell by substituting Eq. 10.16 in Eq. 10.35 the result is

$$g(r_{12}, r_1) = 0.5 r_1 r_{12} \int_{|r_{12}-r_1|}^{|r_{12}+r_1|} \left[R_{\varphi}^2(1) R_{\chi}^2(2) + R_{\varphi}^2(2) R_{\chi}^2(1) \right] r_2 dr_2 \quad (10.37)$$

10.18.3 Calculation Method of Partial Coulomb Hole $\Delta g(r_{12}, r_1)$

The partial Coulomb hole $\Delta g(r_{12}, r_1)$ allows us to analyze the effect of the coulomb hole when the test (reference) electron say particle 1 at specific radial distance from the atomic nucleus [11] $\Delta g(r_{12}, r_1)$ is defined as

$$\Delta g(r_{12}, r_1) = g_{CI}(r_{12}, r_1) - g_{HF}(r_{12}, r_1) \quad (10.38)$$

The partial distribution function $g(r_{12}, r_1)$ for both CI and HF wave function K-shell is given by

$$g_{CI,HF}(r_{12}, r_1) = 0.5r_1r_{12} \int_{|r_{12}-r_1|}^{|r_{12}+r_1|} \Gamma'_{CI,HF}(r_1, r_2)r_2dr_2 \quad (10.39)$$

10.19 Results and Discussion

10.19.1 The Two-Particle Radial Density Distribution $D(r_1, r_2)$

The two-particle radial density distribution function $D(r_1, r_2)$ is particularly sensitive to radial correlation. Table 10.1 shows that as the atomic number Z increases, the two-particle radial density distribution function $D(r_1, r_2)$ is increased at $r_1 = r_2$ and because of the symmetry state of K-shell, the maximum values of $D(r_1, r_2)$ are always located along diagonal when $r_1 = r_2$. The effect of electron correlation upon the electron density shows that the location and the maximum value of two-particle density distribution function $D_{HF}(r_1, r_2)$ is greater than $D_{CI}(r_1, r_2)$.

10.19.2 The One Particle Radial Distribution Functions $D(r_1)$

Table 10.2 shows the maximum value of the one particle radial densities distribution function $D(r_1)$ and its location for the considered atomic system in HF and CI approximations. From this table the following notes can be found: The one particle density $D(r_1)$ in both wave functions increases with increasing the atomic number Z , whereas the values of locations r_1 decrease with increasing the atomic number Z

Table 10.1 Maximum value of the two-particle radial density distribution function and the location for He-series in the Hartree-Fock (HF) wave function and configuration-interaction (CI) wave function

Atom or ion	Wave function	$r_1 = r_2 = r_k$	Max. $D(r_1, r_2)$	Radial corr. %*
He	HF	0.569	0.750	93.866
	HF [18]	0.575	0.75	
	CI	0.521	0.704	
Li ⁺	HF	0.363	1.981	85.714
	HF [18]	0.36	1.981	
	CI	0.343	1.698	
Be ⁺⁺	HF	0.266	3.796	83.219
	HF [18]	0.27	3.796	
	CI	0.256	3.159	

All results are expressed in a.u

*Radial corr. % = $(D_{CI}(r_1, r_2)/D_{HF}(r_1, r_2)) * 100$

Table 10.2 The one particle radial densities $D(r_1)$ in HF and CI approximations for K-shell of the He-Like atoms and the maximum locations r_1

Atom or ion	Wave function	r_1	Max $D(r_1)$	Radial corr. %
He	HF	0.5692	0.8663	97.12
	HF [18]	0.5692	0.8663	
	CI	0.5217	0.841	
Li^+	HF	0.3634	1.407	93.24
	HF [18]	0.3634	1.4074	
	CI	0.3434	1.312	
Be^{++}	HF	0.2668	1.949	92.25
	HF [18]	0.2667	1.9487	
	CI	0.2562	1.804	

Table 10.3 The one particle expectation value $\langle r_1^k \rangle$ and standard deviation for both HF and CI approximation

Atom or ions	Wave function	$\langle r_1^k \rangle$						Δr_1
		$\langle r_1^{-2} \rangle$	$\langle r_1^{-1} \rangle$	$\langle r_1^0 \rangle$	$\langle r_1^1 \rangle$	$\langle r_1^2 \rangle$	$\langle r_1^3 \rangle$	
He	HF	5.995	1.687	1	0.927	1.184	1.94	0.570
	HF [22]	5.981	1.68	1	0.919	1.169	—	0.569
	CI	6.438	1.702	1	0.945	1.254	2.180	0.625
	CI [23]	6.018	1.688	1	0.929	1.192	—	—
Li^+	HF	14.910	2.687	1	0.572	0.445	0.439	0.343
	HF [22]	14.912	2.687	1	0.572	0.444	—	0.342
	CI	15.456	2.668	1	0.596	0.502	0.559	0.408
	CI [23]	14.929	2.687	1	0.572	0.446	—	—
Be^{++}	HF	27.829	3.680	1	0.414	0.231	0.163	0.245
	HF [22]	27.829	3.687	1	0.414	0.231	—	0.245
	CI	28.335	3.641	1	0.433	0.264	0.212	0.295

as a result from the attraction force of the nucleus to the electrons. Also for all Z, the maximum value of $D(r_1)$ in CI wave function is less than in HF wave function due to radial correlation effect.

10.19.3 One-Particle Expectation Value $\langle r_1^k \rangle$

Table 10.3 shows the following statements for all atom and ions under investigation. For both HF and CI wave functions, the largest value of $\langle r_1^1 \rangle$ is in the He-atom, because it has the smallest atomic number with respect to other ions, leading to smallest Coulombs attraction between the nucleus and the electron in the K-shell. As the atomic number is increased the Coulombs attraction force is also increased. This leads to decrease of the one particle expectation value which means that moving region for electrons will be smaller and smaller with increasing atomic number Z and the uncertainty (i.e.) $\Delta x \Delta p \geq \hbar/2$ of finding the electronic position will

Table 10.4 The two-particle expectation values $\langle r_1^k r_2^k \rangle$ in both HF and CI wave functions

Atom or ions	Wave function	$\langle r_1^k r_2^k \rangle$					
		$\langle r_1^{-2} r_2^{-2} \rangle$	$\langle r_1^{-1} r_2^{-1} \rangle$	$\langle r_1^0 r_2^0 \rangle$	$\langle r_1^1 r_2^1 \rangle$	$\langle r_1^2 r_2^2 \rangle$	$\langle r_1^3 r_2^3 \rangle$
He	HF	35.946	2.846	1	0.859	1.403	3.765
	CI	39.049	3.021	1	0.883	1.615	4.945
Li ⁺	HF	222.3	7.368	1	0.327	0.198	0.192
	CI	247.7	7.223	1	0.369	0.267	0.293
Be ⁺⁺	HF	774.4	13.543	1	0.172	0.054	0.027
	CI	845.2	13.597	1	0.196	0.073	0.042

decrease and the certainty of finding r_1 will be increased. It is obvious that Δr_1 in CI is greater than in HF approximations because the wave function of CI has more terms than HF wave function.

10.19.4 The Two Particle Expectation Value

The amounts of the two-particle expectation values $\langle r_1^k r_2^k \rangle$ have been evaluated and tabulated in Table 10.4. One may find the following notes: (1) For both wave functions the largest value of $\langle r_1^1 r_2^2 \rangle$ is in the He-atom, and this result is similar to that found in $\langle r_1^1 \rangle$ for the same region. (2) Two particle expectation values for CI approximation are greater than HF approximation because of the radial correlation of the two particle radial distribution function. The two particle expectation value is the square of the one particle expectation value for both HF and CI approximations because of the symmetry.

10.19.5 Function $f(r_{12})$ for He-Like Atoms

The probabilities of the inter particle distribution function $f(r_{12})$ for both HF and CI wave functions are tabulated in Table 10.5 for He-like atoms. The results show that the maximum value of the inter particle distribution function for both HF and CI approximation is increased and is closer to the nucleus as the atomic number (Z) increases because the distance between electrons r_{12} decreases. This behavior shows that the K-shell density shrinkage toward the nucleus due to the Coulomb repulsion force will be greater than the Coulomb attraction force. In each Z, the inter particle distribution function in $f_{HF}(r_{12})$ is greater than in $f_{CI}(r_{12})$, and the radial correlation percent for $f(r_{12})$ is 98.9%, 91.7% and 88.9% for Z = 2, 3 and 4 respectively. The value of r_{12} such that $f(r_{12}) = 0$ may be interpreted as the radius of Coulomb hole in Table 10.6. The result of He-like atoms shows that the addition of radial correlation has reduced, as atomic number Z increases, the depth increases while the radius decreases.

Table 10.5 The inter particle distribution function $f(r_{12})$ in maximum location for the inter particle distance

Atom or ions	Wave Function	r_{12}	Max. $f(r_{12})$	$\frac{f(r_{12})}{z}$	Radial corr. %
He	HF	0.995	0.629	0.314	98.9
	HF [22]	0.995	0.629	0.314	
	CI	0.921	0.622	0.311	
Li^+	HF	0.623	1.029	0.343	91.7
	HF [22]	0.623	1.029	0.343	
	CI	0.580	0.943	0.314	
Be^{++}	HF	0.455	1.439	0.359	88.9
	HF [22]	0.454	1.427	0.356	
	CI	0.423	1.279	0.319	

Table 10.6 The radius of Coulomb hole r_{12} and its area $\Delta f(r_{12})$

Atom or ions	Radius of coulomb hole	Area of the coulomb hole
He	1.198	0.008
Li^+	1.195	0.055
Be^{++}	0.845	0.07

Table 10.7 The inter-particle expectation values $\langle r_{12}^k \rangle$ of the HF and CI approximation for He-like atoms and the standard deviation

Atom or ions		$\langle r_{12}^k \rangle$					Δr_{12}
		$\langle r_{12}^{-2} \rangle$	$\langle r_{12}^{-1} \rangle$	$\langle r_{12}^0 \rangle$	$\langle r_{12}^{-2} \rangle$	$\langle r_{12}^{-1} \rangle$	
He	HF	1.842	1.025	1	1.362	2.3695	0.717
	HF [18]	1.8421	1.0258	1	1.3621	2.3697	0.7171
	CI	1.815	1.017	1	1.396	2.549	0.774
Li^+	HF	4.726	1.651	1	0.838	0.8906	0.433
	HF [18]	4.7264	1.6517	1	0.8381	0.8906	0.4334
	CI	4.473	1.583	1	0.907	1.0791	0.506
Be^{++}	HF	8.934	2.261	1	0.609	0.4681	0.310
	HF [18]	8.944	2.277	1	0.6058	0.4637	0.3109
	CI	8.311	2.158	1	0.663	0.5729	0.364

All values are in a.u

10.19.6 Inter Particle Expectation Value $\langle r_{12}^k \rangle$ and Standard Deviation

The inter-particle expectation values $\langle r_{12}^k \rangle$ of the HF and CI approximation for He-like atoms have been tabulated in Table 10.7. One may conclude that the different regions of $f(r_{12})$ will be emphasized by the function $\langle r_{12}^k \rangle$ when k takes positive, and negative values ($-2 \leq k \leq 2$). A particularly useful concept displaying the spread of position density $f(r_{12})$ about inter particle distance is the standard deviation Δr_{12} . For each Z the inter-particle expectation values $\langle r_{12}^k \rangle$ increase when electrons

Table 10.8 The maximum location of the partial distribution function $g(r_{12}, r_1)$ for both the HF and CI wave functions and the maximum location for r_{12} when $r_l = r_k$

Atom or ions	Wave function	r_{12}	$r_l = r_k$	Maximum $g(r_{12}, r_1)$
He	HF	0.7575	0.569	0.761
	CI	0.6912	0.521	0.739
Li	HF	0.4843	0.363	1.991
	CI	0.4385	0.343	1.798
Be^{++}	HF	0.3578	0.266	3.819
	CI	0.3264	0.2562	3.338

All results are expressed in a.u

Table 10.9 The maximum location of the partial distribution function $g(r_{12}, r_1)$ for both the HF and CI wave functions and the maximum location for r_1 when $r_{12} = r_k$

Atom or ions	Wave function	$r_l = r_k$	r_l	Maximum $g(r_{12}, r_1)$
He	HF	0.995	0.685	0.690
	CI	0.921	0.693	0.681
Li	HF	0.623	0.363	1.991
	CI	0.580	0.438	1.648
Be^{++}	HF	0.455	0.312	3.523
	CI	0.423	0.316	3.089

are located in the region near the nucleus (when k goes from -1 to -2), while $\langle r_{12}^k \rangle$ increases (when k goes from 1 to 2) for (He, Li^+) and decreases for (B^{++}) because the electron cloud is further away than the nucleus. As Z increases the inter-particle expectation values $\langle r_{12}^k \rangle$ decrease, and $\langle r_{12}^k \rangle_{CI}$ is greater than $\langle r_{12}^k \rangle_{HF}$ at negative values of k whereas at positive values of k we find opposite behavior that means the values of $\langle r_{12}^k \rangle_{HF}$ are greater than $\langle r_{12}^k \rangle_{CI}$. The standard deviation results indicate that each $f(r_{12})$ distribution function has become less diffuse when electrons correlated and it has therefore sharpened up about its maximum. As Z is increased Δr_{12} decreases for both HF and CI wave functions.

10.19.7 Partial Distribution Function $g(r_{12}, r_1)$

The influence of the correlation in partial distribution function $g(r_{12}, r_1)$ of r_{12} and r_1 for $Z = 2, 3$ and 4 in the K-shell is shown in Tables 10.8 and 10.9 for the HF and CI wave functions. We notice that as Z increases the maximum value $g(r_{12}, r_1)$ for both HF and CI approximations increases because the Coulomb attraction forces is greater than the Coulomb repulsion forces in positive ions so the probability density of finding pair electrons in the region near the nucleus in positive ions is larger than that in He-atom. As expected $g_{CI}(r_{12}, r_1)$ is less than $g_{HF}(r_{12}, r_1)$ because in HF the approximation each electron move independently of each other, so this hypothesis neglects the details of the electronic repulsion which will reduces the HF results, while CI approximation takes it in account. The $g(r_{12}, r_1)$ surface shows that the maximum density is always located along the diagonal such that $r_{12} > r_1$.

10.20 Conclusions

From the present work, all atomic properties obtained with HF and CI wave functions are Z dependent. As the atomic number Z increases, for both approximations the one, two-particle radial density distribution function $D(r_1)$, $D(r_1, r_2)$, the electron density at r_k , the inter particle distribution function $f(r_{12})$ and the partial distribution function $g(r_{12}, r_1)$ are increased. For both HF and CI wave functions, the largest value of $\langle r_1^1 \rangle$, $\langle r_1^1 r_2^1 \rangle$ and $\langle r_{12}^1 \rangle$ is in the He-atom, because it has the smallest atomic number with respect to other ions. This leads to smallest Coulombs attraction between the nucleus and the electron in the K-shell for this ground state element (Z goes from 2 to 4). The inter particle distribution function and the magnitude density of $g(r_{12}, r_1)$ for both approximations are increased and are closer to the nucleus as the atomic number (Z) is increased and the distance between electrons r_{12} is decreased. This behavior shows the K-shell density shrinkage toward the nucleus because the Coulomb repulsion force will be less than the Coulomb attraction force. The one, two-particle, inter-particle and partial distribution functions are systematically shifted for He-like atoms when they are plotted as functions of the atomic number. The radial correlation of one, two-particle radial density distribution functions $\Delta D(r_1, r_2)$ and $\Delta D(r_1)$ are increased as Z increases and closer to the nucleus. The Coulomb hole and partial Coulomb hole are increased as Z increases, whereas the radius of Coulomb hole is decreased and the depth is increased Z increases.

References

1. Roothaan CCJ, Sachs L, Weiss AW (1960) Rev Mod Phys 32:186
2. Weiss AW (1961) Phys Rev 122:1826
3. Banyard KE (1968) J Chem Phys 48:2121
4. Baker CC, Banyard KE (1969) Phys Rev 188:57–62
5. AL-Khafaji KS (2005) A study of correction function to Hartree-Fock orbitals derived from correlated wave function. PhD thesis, Al-Mustansiriyah university, Baghdad, Iraq
6. Coulson CA, Neilson AH (1961) Proc Phys Soc 78:831
7. Curl RF, Coulson CA (1965) Proc Phys Soc 85:647
8. Banyard KE, Seddon GJ (1973) J Chem Phys 58:1132
9. Seddon GJ, Banyard KE (1973) J Chem Phys 59:572
10. Boyd RJ (1975) J Chem Phys 53:592
11. Aman Alla SM (2007) Electron correlation for many atomic and ionic system. MSc thesis, College of Education (Ibn AL-Haitham). University of Baghdad, Baghdad, Iraq
12. AL-Robayi EM (2002) A study of Coulomb hole for the ground state in momentum space for He-like and Li-like ions. MSc thesis, College of Education (Ibn AL-Haitham), University of Baghdad, Bagdad, Iraq
13. Zielinski TJ, Barnett MP (2003) Development and dissemination of mathcad; see reference no. 44 therein
14. Lopez EP (1995) Physical chemistry: a practical approach. Williamstown, MA 01267
15. Avery J (1980) The quantum theory of atoms, molecules, and photons. Mc Graw Hill, New York

16. Wiess AW (1963) *J Chem Phys* 39:1262
17. Clementi E, Roetti J (1974) Roothaan-Hartree-Fock atomic wave functions: basis functions and their coefficients for ground and certain excited states of neutral and ionized atoms, $Z \geq 54$. *At Data Nucl Data Tables* 14:177
18. AL-Tamimeh NC (2005) Calculation of effect of electronic correlation force on the energy of some atoms. MSc thesis, College of Science for Women, Baghdad University, Baghdad, Iraq
19. McWeeny R, Sutcliffe BT (1969) *Method of molecular quantum mechanics*. Academic, New York
20. Banyard KE, Mobbs RJ (1981) *J Chem Phys* 75(7):3433
21. Banyard KE, Al-Bayati KH (1986) *J Phys B At Mol Phys* 19:2211
22. AL-Meshhedany WA (2006) A study for nuclear magnetic shielding constant for $Z = 2$ to 10. MSc thesis, College of Science, Nahrain university, Baghdad, Iraq
23. Banyard KE, Baker CC (1969) *J Chem Phys* 51:2680

Chapter 11

Dynamical Role of the Fictitious Orbital Mass in Car-Parrinello Molecular Dynamics

Sheau-Wei Ong, Eng-Soon Tok, and H. Chuan Kang

Abstract We investigate ion-orbital interaction in Car-Parinello molecular dynamics (CPMD) analytically and numerically in order to probe the role of the fictitious orbital mass. We show analytically that this interaction can be described by linearly coupled oscillators when the system is sufficiently close to the ground state. This leads to ionic vibrational modes with frequency ω_M that depends upon the ionic mass M and the orbital mass μ as $\omega_M = \omega_{0M}[1 - C(\mu/M)]$ in the limit of zero μ/M ; ω_{0M} is the Born-Oppenheimer ionic frequency and C depends upon the ion-orbital coupling force constants. This analysis provides new insight on the orbital mass dependence of the dynamics, and suggests a rigorous method of obtaining accurate ionic vibrational frequency using CPMD. We verify our analytical results with numerical simulations for N_2 , and discuss in detail the dynamical interaction between the ionic and the fictitious orbital modes in CPMD. Our results demonstrate that displacement from the ground state significantly affects ionic frequencies. In the linear regime this results in the linear dependence of ionic vibrational frequency upon μ/M . In the non-linear regime, even the ionic geometry deviates from the correct ground-state structure, highlighting the importance of staying close to the ground state in CPMD calculations.

S.-W. Ong • H.C. Kang (✉)

Department of Chemistry, National University of Singapore, 3 Science Drive 3,
117543 Singapore, Singapore

e-mail: chmosw@nus.edu.sg; chmkhc@nus.edu.sg

E.-S. Tok

Department of Physics, National University of Singapore, 3 Science Drive 3, 117543 Singapore,
Singapore

e-mail: phytokes@nus.edu.sg

11.1 Introduction

The Car-Parrinello molecular dynamics (CPMD) method [1] initiated the field of *ab initio* molecular dynamics and is an important technique applied to a wide range of problems. Originally introduced to investigate problems involving electronic structure in condensed matter within the framework of density functional theory it has been applied to other ways of solving electronic structure problems [2, 3], and also to other problems [4, 5] where the forces acting on the interesting degrees of freedom are determined by underlying fast degrees of freedom. Within density functional theory applications the central idea in CPMD is the simultaneous propagation of the Kohn-Sham (KS) orbital degrees of freedom along with the ionic degrees of freedom. This is achieved by treating the orbitals as a set of generalized classical displacements each with an associated fictitious mass μ , thereby reducing the problem to one where Newtonian dynamics is used to relax the ionic positions and the electronic structure simultaneously [1]. This introduces fictitious ion-orbital interactions that affect the real dynamics of the ions because during a CPMD simulation the orbitals are not exactly on the Born-Oppenheimer surface, but oscillate about it. It has been shown that the error in the CPMD trajectory relative to the true trajectory on the Born-Oppenheimer surface is bounded by μ , and thus the adiabatic limit is reached when μ goes to zero. In calculations the choice of μ , necessarily finite, is made by balancing the computational cost and the accuracy both of which increase as μ decreases.

The basic idea is that although the forces at any instant in a CPMD calculation are different from the forces calculated using the ground state electronic structure, these instantaneous differences average to zero over a time-scale relevant to investigations of ionic dynamics because the fictitious orbital dynamics are much faster [6] and their fluctuations have much shorter time-scales [7, 8]. Although the CPMD method has been successfully and widely used, and the important work in Ref. [6] has provided a heuristic understanding of the dynamics, the current understanding of the interaction between the ionic and the orbital degrees of freedom is not satisfactory. In particular, recent work [9, 10] demonstrates that the forces in CPMD, even when averaged over fluctuations due to the orbital motion, are not equal to the ground-state forces. It is commonly held that the motion of the ions in the field due to the rapidly fluctuation electronic structure effectively rescales the mass of the ions. This mass rescaling can be estimated within a rigid-ion approximation which is rigorous only for weakly-interacting ions.

Even with rescaled ionic masses taken into consideration in calculating the ion trajectories, it was found that the forces on the ions are still not correctly calculated [10]. This is problematic since it implies that the ionic forces in CPMD deviate from the actual forces in ways that are not understood currently, even though it is pointed out that the errors are systematically reduced when the orbital mass is decreased [9]. In addition, significant systematic drift in the fictitious electronic kinetic energy is observed in simulations when μ is large. For instance, in liquid water calculations

with $\mu = 400$ au, the drift is considerable, demonstrating that smaller values of the fictitious mass than that need to be used at least for liquid water [11, 12]. Thus, it is important to establish quantitative relationships between μ and dynamical quantities that are to be calculated using CPMD so that the extrapolation to zero fictitious mass can be rigorously made and accurate dynamical quantities extracted from CPMD. There is thus a need for a better understanding of the interaction between the ionic degrees of freedom and the fictitious orbital dynamics.

11.2 Theoretical Analysis

We have recently examined the ion-orbital interaction by deriving equations of motion describing the ionic displacement and the orbital displacement away from the ground state [13], and showing that the ion-orbital interaction has the form of coupled linear oscillators when sufficiently close to the ground state. Thus, the calculated ionic vibrational frequencies in CPMD deviate from their adiabatic values by an amount linearly proportional to the mass ratio μ/M . We verified our analysis through numerical simulations of N_2 , Sn_2 and hydrogen adsorbed on Si(100)-(2 × 1) surface [13]. Here we examine the orbital dynamics in detail.

In CPMD the equations of motion are derived [1] from the classical Lagrangian

$$L = \mu \sum_i \left\langle \dot{\phi}_i \mid \dot{\phi}_i \right\rangle + \frac{1}{2} \sum_I M_I \dot{R}_I^2 - E[\{\phi_i\}, \{R_I\}] + \sum_{i,j} \lambda_{ij} (\langle \phi_i \mid \phi_j \rangle - \delta_{ij}).$$

where the Kohn-Sham energy E is a functional of the orbitals ϕ_i and the ionic coordinates R_I . In CPMD, it plays the role of a classical potential energy for the system that includes the fictitious dynamical degrees of freedom from the orbitals. The Lagrange multipliers λ_{ij} keep the latter orthonormal. The Car-Parrinello orbital can be written as $\delta\phi_i = \phi_i - \phi_i^0$ where ϕ_i^0 is the ground state orbital and $\delta\phi_i$ is the deviation of ϕ_i from the ground state [14]. The ground state orbital $\phi_i^0(r)$ is parametrically dependent upon and completely specified by the positions R_I of the ions. Taylor expansions in $\delta\phi_i$ and δR_I of the derivatives of E about the Born-Oppenheimer surface lead to:

$$\begin{aligned} \delta\ddot{R}_I &= -\frac{1}{M_I} \left(\frac{\partial E}{\partial R_I} \right)_{\{\phi_i\}} \\ &= -\sum_J \frac{1}{M_I} \left(\frac{d^2 E}{dR_I dR_J} \right) \Bigg|_{\{R_I^0\}, \{\phi_i^0\}} \delta R_J + \sum_{i,j} \int dr dr' \frac{1}{M_I} \left(\frac{d\phi_i^0(r)}{dR_I} \right) \\ &\quad \times \left(\frac{\delta^2 E}{\delta\phi_i(r) \delta\phi_{ij}(r')} \right) \Bigg|_{\{R_I\}, \{\phi_i^0\}} \delta\phi_j \end{aligned} \quad (11.1)$$

$$\begin{aligned}
\delta\ddot{\phi}_i(\mathbf{r}) = & - \sum_j \frac{1}{\mu} \int d\mathbf{r}' \left(\left(\frac{\delta^2 E}{\delta\phi_i(\mathbf{r})\delta\phi_j(\mathbf{r}')} \right) + \lambda_{i,j} + \sum_{k,j,I} \frac{I}{M_I} \left(\frac{d\phi_i^0(\mathbf{r})}{dR_I} \right) \int d\mathbf{r}' d\mathbf{r}'' \right. \\
& \times \left. \left(\frac{d\phi_k^0(\mathbf{r}')}{dR_I} \right) \left(\frac{\delta^2 E}{d\phi_k^0(\mathbf{r}')\delta\phi_j(\mathbf{r}'')} \right) \right) \Big|_{\{\mathbf{R}_I\}, \{\phi_i^0\}} \delta\phi_j \\
& + \sum_{I,J} \frac{1}{M_I} \left(\frac{d\phi_i^0(\mathbf{r})}{dR_I} \right) \left(\frac{d^2 E}{dR_I dR_J} \right) \Big|_{\{\mathbf{R}_I\}, \{\phi_i^0\}} \delta R_J
\end{aligned} \tag{11.2}$$

From Eqs. 11.1 and 11.2, we see that the nuclear and orbital motions in Car-Parrinello molecular dynamics have the same form as linearly coupled oscillators when the system is sufficiently close to the ground state. Thus, the combined system of ionic and orbital degrees of freedom does not stay on the Born-Oppenheimer surface unless μ , which controls the coupling strength between the ionic and orbital degrees of freedom, is zero. Further from the ground state higher-order terms in the displacements become important, and the coupling is not linear.

Using the form of Eqs. 11.1 and 11.2 above, it is easy to understand the effect of μ on an ionic normal vibration frequency by turning on the ion-orbital interaction between one ionic normal mode with frequency ω_{0M} to one $\delta\phi$ orbital normal mode with frequency $\omega_{0\mu}$:

$$\begin{aligned}
\delta\ddot{\mathbf{R}} &= -\omega_{0M}^2 \delta\mathbf{R} + \omega_1^2 \delta\phi \\
\delta\ddot{\phi} &= -\omega_{0\mu}^2 \delta\phi + \omega_2^2 \delta\mathbf{R}
\end{aligned}$$

We note a couple of points here. From our analysis above, each of the coupling constants ω_1^2 and ω_2^2 is proportional to M^{-1} , ω_{0M}^2 is proportional to M^{-1} , and $\omega_{0\mu}^2$ is proportional to μ^{-1} . From Eq. 11.2 the coefficient $\omega_{0\mu}^2$ of the orbital-orbital coupling term has two contributions, one of which is proportional to $(\mu M)^{-1}$ which we neglect relative to the contribution proportional to μ^{-1} . In the limit of weak coupling and small μ/M the coupled ion-orbital normal modes have the frequencies, to first-order in μ/M :

$$\omega_M = \omega_{0M} \left(1 - \frac{\mu}{M} \frac{k_1 k_2}{2k_\mu k_M} \right) \tag{11.3}$$

$$\omega_\mu = \omega_{0\mu} \left(1 + \left(\frac{\mu}{M} \right)^2 \frac{k_1 k_2}{2k_\mu^2} \right) \tag{11.4}$$

The classic explanation for why CPMD works is that on a sufficiently long (ionic) time scale the errors in the ionic force due to the fictitious orbital dynamics average to zero [6, 7]. However, it has been shown that the ionic force averaged over a

time scale that is long compared to the timescale of the fast orbital motion deviates from the ground state force by an amount proportional to μ [9]. This is not difficult to understand from our analysis since each dynamical mode in CPMD is really a normal mode (at least close to the ground state) that consists of both orbital and ionic degrees of freedom. Further from the ground state the non-linear terms in the dynamics dropped in deriving Eqs. 11.1 and 11.2 become important. Then the orbital dynamics are expected to be chaotic, and a statistical averaging over the “frictional” effects of the orbital motion is an approach to understanding the dynamics [6]. From our results, it can be seen that the coupling strength between the orbital and the ionic degrees of freedom depend upon μ/M . Thus, the greater flow of energy from ionic modes into the fictitious orbital modes [11, 12] as μ increases can be understood. This highlights the importance of selecting a value of μ that is not too high, a point that has long been recognized.

11.3 Numerical Methodology

11.3.1 Basic Considerations

We explore in detail the interactions between the ionic and the orbital degrees of freedom with numerical CPMD simulations performed using the PWSCF code [15]. These calculations are done by first bringing the electronic structure (close) to the ground state for a fixed ionic geometry displaced slightly away from the equilibrium bond length to give potential energy to the ionic degree of freedom. The system is then allowed to evolve with zero initial ionic and orbital kinetic energies. We used orbital kinetic energy, total energy, and force convergence tolerances of 10^{-8} , 10^{-8} , and 10^{-4} Ry/bohr, respectively, to obtain the initial electronic orbitals. These convergence tolerances give sufficiently small initial displacements $\delta\phi_i$ so that a major component of the orbital motion is accounted for by ϕ_i^0 . We report only results for the nitrogen dimer, but similar results were obtained for the tin dimer and the silicon-hydrogen bond for adsorbed hydrogen atoms on the silicon surface [13].

It is useful to explore the dynamics of the system starting with the same initial structures and zero kinetic energies, but with small initial random displacements of the electronic structure away from the ground state. Such initial random orbital displacements are not appropriate in a “production” Car-Parrinello calculation, but allow us to quantify the effect of the deviation $\delta\phi_i$ from the ground-state. We also investigate higher than first-order interactions between the ionic and orbital degrees of freedom by starting with different values of the initial ionic displacements. Ionic oscillations are quantified using bond-length oscillations, while oscillations in the orbital degrees of freedom are quantified using oscillations in the KS eigenvalues. In all our simulations, care was taken in selecting the time-step so that the fictitious total energy of the system is conserved to within 0.03%.

11.3.2 Ionic Oscillations

We consider first the simulations where we do not apply an initial random perturbation to the electronic structure. The ionic vibrational frequencies calculated are plotted in Fig. 11.1a for ionic mass M from 1 to 28 amu, and orbital mass from 10 to 1,000 au. (We also include in Fig. 11.1 curves (in red) for $M = 1, 2,$ and 7 where an initial random perturbation is applied; these results are discussed later.) These frequencies are obtained from the rather stable sinusoidal oscillations in the bond length illustrated in the inset of Fig. 11.1a for an ion mass $M = 1$ amu and orbital mass μ equal to 10 and 1,000 au. The nitrogen pseudopotential is used so the electronic interaction is that for nitrogen even though we have set the ionic masses to a range of different values. For small values of the orbital mass μ , the ionic frequency increases linearly as μ decreases. This linear increase in the ionic vibrational frequency has been observed previously in CPMD calculations of a series of diatomic molecules [16]. Our results show that it is valid only for small μ/M . Extrapolating the frequency to zero orbital mass gives the parameter ω_{0M} in our analysis above, i.e., the actual ionic vibrational frequency. Figure 11.1b shows that the calculated value of ω_{0M} is linearly proportional to $M^{-1/2}$ as expected. From Eqs. 11.3 and 11.4 above, we expect the rescaled frequency ω_M/ω_{0M} to depend upon μ and M only through the ratio μ/M . We show that this is consistent with our numerical data by plotting ω_M/ω_{0M} against μ/M in Fig. 11.2, whereupon the data points all collapse onto a single curve. In the inset of Fig. 11.2, we plot $1 - (\omega_M/\omega_{0M})$ against μ/M using logarithmic axes to illustrate more clearly the correspondence of the data for different ionic masses at small μ/M values. We also see from the slope of this graph that the dependence of ω_M/ω_{0M} upon μ/M is indeed linear for μ/M smaller than about 20 au/amu. The calculated vibrational frequencies ω_{0M} are in reasonable agreement with previously calculated values for nitrogen [16] although we note that our goal here is to investigate the dynamics in CPMD rather than the properties of N_2 . We use a BLYP [17] norm-conserved Troullier-Martins [18] pseudopotential with a wavefunction (density) cutoff of 60 (240) Ry.

Assuming a rigid-ion approximation it can be shown that time has to be rescaled by a factor of $[M/(M+\Delta M)]^{1/2}$ to better describe the dynamics in CPMD [7]. This gives an ionic vibrational frequency that depends upon the ionic mass of a form similar to Eq. 11.3. Empirically, the appropriate mass correction ΔM can be determined by minimizing the average difference between the CPMD force and the ground state force [9, 10]. However, it was found that even with mass rescaling there are errors in the forces [9]. A constant value of the mass correction ΔM , in particular, seems problematic to us because each ionic mode that involves any particular atom in a system has a different force constant and requires a different time-scale correction. Rather than determining a correction ΔM empirically for each species in the system by minimizing the deviation of the CPMD force from the ground state force and then using that to correct the dynamics, our results show that doing a series of calculations at different orbital masses μ and extrapolating to zero orbital mass is a direct and rigorous method to extract dynamical quantities.

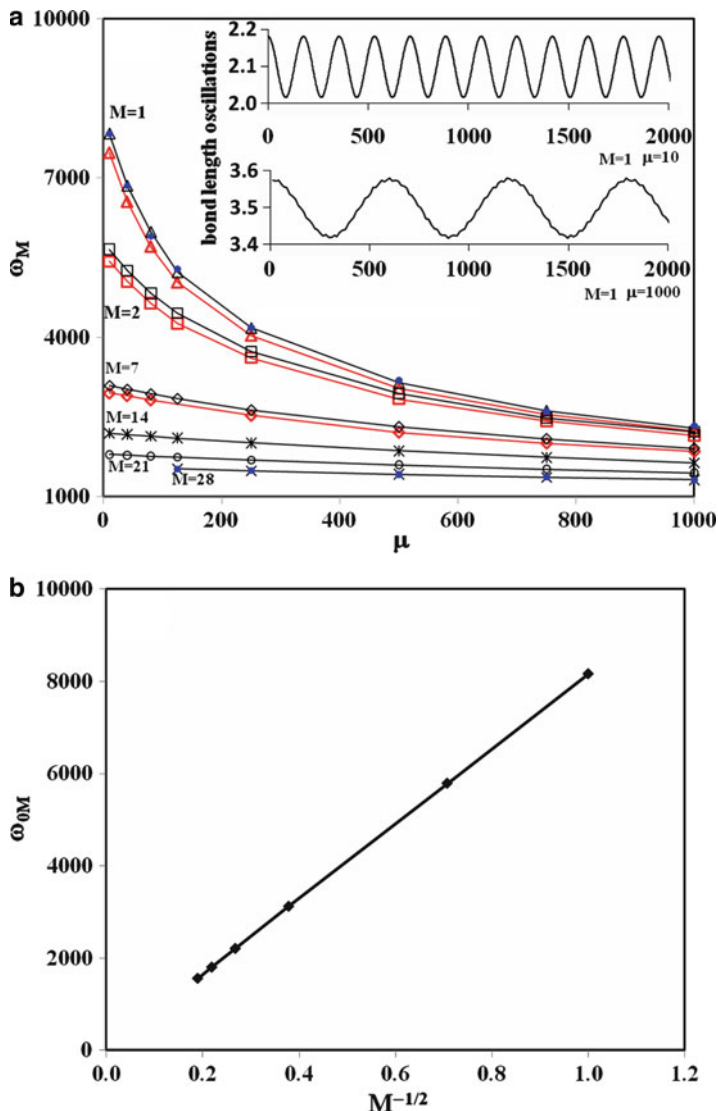


Fig. 11.1 In panel (a), the ion-vibrational frequency ω_M (in cm^{-1}) is plotted against the orbital mass μ (in au) for the nitrogen dimer. For ion mass $M = 1, 2,$ and 7 amu, we also plot the ionic frequency with an initial orbital perturbation (red lines). For $M = 1$ and $M = 28$, we also plot the ϕ_i^0 oscillation frequency (data points denoted by small solid blue circles) to show that it is equal to the corresponding ionic frequency (triangles for $M = 1$ and crosses for $M = 28$). The inset shows bond-length oscillations (in bohr) as a function of time (in au) for $M = 1$ amu, and $\mu = 10$ and $\mu = 1000$ au illustrating the higher-frequency oscillations that are observed as μ/M increases. In panel (b) the frequency ω_{0M} (obtained from the intercepts of the frequencies in panel (a), and corresponding to the ionic frequency in the adiabatic limit) is plotted against $M^{-1/2}$, showing that ω_{0M} is linearly proportional to $M^{-1/2}$ as it should.

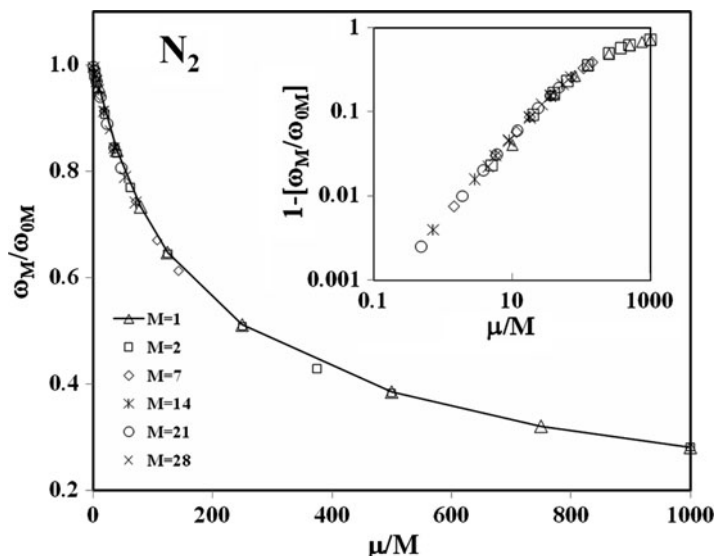


Fig. 11.2 The rescaled frequency ω_M/ω_{0M} for the nitrogen ionic vibrations in Fig. 11.1 is plotted against μ/M (in au/amu). The inset is the same data plotted logarithmically to better resolve the data points at small μ/M , demonstrating that the data for different μ and M fall on the same curve, and the linear dependence of the ionic frequency upon μ/M

The rigid-ion approximation is not necessary to obtain our results. For vibrational frequency, the extrapolation is linear in the mass ratio μ/M for small μ/M . This need not be true for other dynamical quantities, and it would be useful to investigate the dependence upon mass ratio of other dynamical quantities such as diffusion and reaction rates.

11.3.3 Orbital Oscillations

Since ϕ^0 is parametrically determined by ionic degrees of freedom, the oscillation in the bond length should be accompanied by an oscillation of the same frequency in the orbital degrees of freedom. This is easily observed in the oscillations of the KS eigenvalues. To illustrate this, we plot in Fig. 11.3a the oscillations in ε_1 the eigenvalue of the lowest KS orbital ($ss\sigma$) for nitrogen along with corresponding oscillations in the bond length. The data plotted is for an orbital mass of 125 au, and for ion mass equal to 1, 2, 7, and 21 amu. From this data the frequency of oscillations in ϕ_1^0 can be readily extracted. In Fig. 11.1a, we have also plotted these frequencies for the largest ($M = 28$ amu) and the smallest ($M = 1$ amu) ionic masses in order to show that they match the frequencies from the bond-length oscillations. The data in Fig. 11.3a shows that the lowest KS eigenvalue ε_1 ($ss\sigma$ orbital) oscillates

in phase with the ionic vibrations. We also find that the second lowest KS eigenvalue ϵ_2 (antibonding $s\sigma^*$ orbital) oscillates exactly out of phase with the ionic vibration as expected.

For the larger ion masses of 7 and 21 amu the oscillations in the KS eigenvalue show only one sinusoidal mode. At the smaller ion masses of 1 and 2 amu, in addition to oscillations in ϕ_i^0 , a higher frequency mode with smaller amplitude is observed for $\mu = 125$ au. This higher frequency mode is also present in the corresponding bond length oscillations plotted in Fig. 11.3b but with considerably smaller amplitude than the ϕ_i^0 mode. It is also observed in the bond-length oscillations in the inset of Fig. 11.1a for $\mu = 1,000$ au but not for $\mu = 1$ au. That is, the amplitude of the higher frequency oscillation in bond-length and KS-eigenvalues increases with μ/M , consistent with these oscillations being due to normal modes arising from ion-orbital coupling. This dependence of the ion-orbital strength upon μ/M can be understood as follows. The first term in Eq. 11.2 which accounts for orbital-orbital interactions is proportional to μ^{-1} , whereas the second term which accounts for ion-orbital interactions is proportional to M^{-1} . Thus, the amplitude dependence upon μ/M in the numerical data in Fig. 11.3, and the inset of Fig. 11.1a is consistent with these high frequency oscillations in the KS eigenvalues and the bond length being due to $\delta\phi_i$ displacements that are coupled to the ionic degree of freedom.

Larger ionic displacements should lead to larger amplitudes of orbital oscillations in ion-orbital coupled modes. Thus, we consider the orbital oscillations in Fig. 11.3 more closely by plotting in Fig. 11.4 the frequency spectra obtained by taking a Fourier transform of the oscillations in the KS eigenvalues. The data shown is for $\mu = 125$ au. For $M = 1$ amu we find a high intensity peak at about $5,250\text{ cm}^{-1}$. This is the ϕ_i^0 oscillation. In addition, we also find a smaller peak at a frequency of $43,500\text{ cm}^{-1}$. The corresponding peaks for $M = 2$ are at lower frequencies. In Fig. 11.5 we plot the orbital vibrational spectra also for $M = 1$ amu and $\mu = 125$ au, but with increasing initial ionic displacements from the equilibrium bond length. As the initial ionic displacement increases the intensities of both peaks increase significantly. The inset in Fig. 11.5 shows the corresponding increase in the oscillation amplitude of the KS eigenvalue ϵ_1 . For the largest ionic displacement, harmonics of the ϕ_i^0 oscillation are clearly observed showing that higher-order terms in δR_I have become rather important at this displacement. Thus, the results in Fig. 11.5 provide direct evidence that the $\delta\phi_i$ peak at $43,500\text{ cm}^{-1}$ is an orbital mode coupled to the ionic vibration. (The corresponding peak is not seen in the spectra for the larger ion masses $M = 7$ and 21 amu. From our results discussed below we expect the minimum frequency for this peak in the limit of large ion mass to be approximately $36,000\text{ cm}^{-1}$ for orbital mass of 125 au.)

Since it is due to ion-orbital coupling, we would also expect to see it in the frequency spectrum for ionic vibration. As we have pointed out above, in the inset of Fig. 11.1a we see a higher frequency mode in the bond length oscillation for $M = 1$ amu and $\mu = 1,000$ au. To illustrate this further, we plot in Fig. 11.6 the ionic frequency spectra for $M = 1$ amu and μ from 80 to 1,000 au showing just the high frequency peak. The ion-coupled $\delta\phi_i$ peak is indeed observed in the ionic

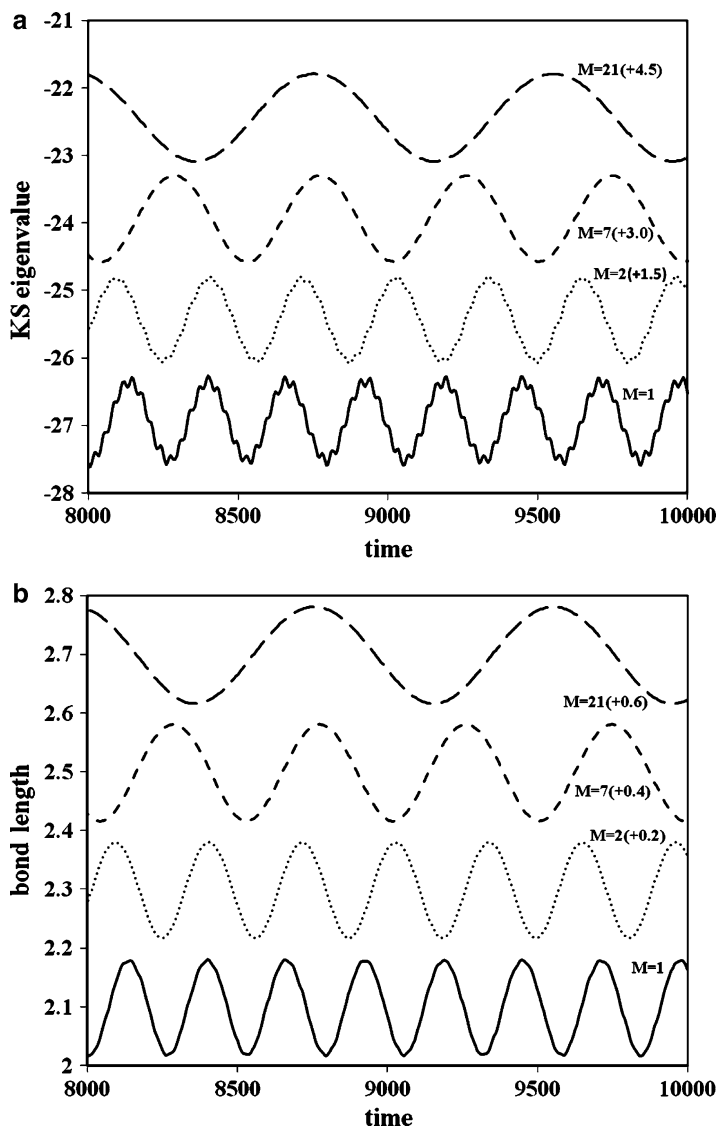


Fig. 11.3 Oscillations in the lowest KS eigenvalue ϵ_1 (in Ry) (panel (a)) and the bond length (in bohr) (panel (b)) plotted against time (in au) for the nitrogen dimer. The data shown is from simulations with orbital mass $\mu = 125$ au and ionic mass $M = 1, 2, 7,$ and 21 amu. For clarity the curves have been displaced vertically by the amounts indicated in brackets. This data shows the expected dependence of the KS energy upon the ionic degree of freedom since the ground state orbitals are parametrically dependent upon the latter. Note however the smaller amplitude and higher frequency oscillations which are especially clear in panel (a) for the largest values of μ/M

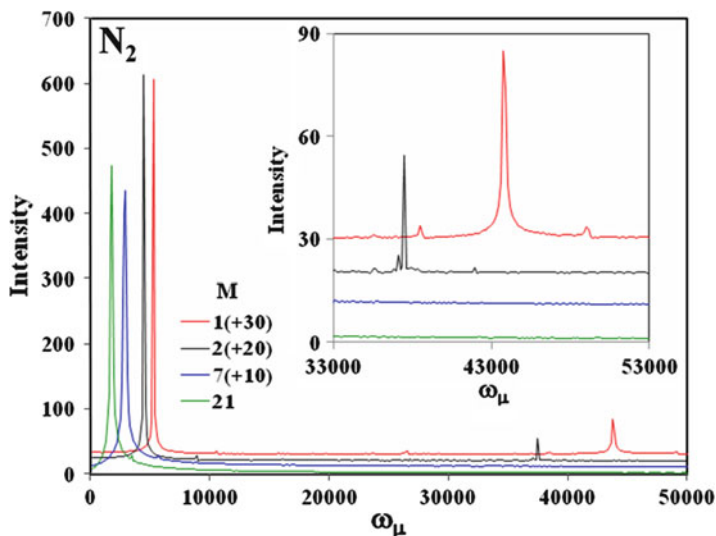


Fig. 11.4 Plots of the nitrogen dimer orbital frequency ω_μ (in cm^{-1}) spectra obtained from the Fourier transform of the lowest KS eigenvalue ϵ_1 showing orbital oscillation in ϕ_i^0 and a smaller intensity higher frequency peak. The region from 30000 to 50000 cm^{-1} is enlarged in the inset. This higher frequency peak corresponds to the faster orbital oscillations that are observed in panel a). Satellite peaks of the higher frequency peak can be clearly seen for $M = 1$ indicating anharmonic interactions with oscillations in ϕ_i^0 . Curves are displaced vertically for clarity

frequency vibration although the intensity is much smaller than the peak for ϕ_i^0 (not shown in Fig. 11.6). In the inset of Fig. 11.6 we show that the frequencies of the $\delta\phi_i$ peak obtained from both KS eigenvalue oscillations and bond-length oscillations are indeed the same.

11.3.4 Effect of Initial Orbital Perturbation

The intensity of the ion-orbital coupled $\delta\phi_i$ mode is not large in calculations of Figs. 11.3–11.6. It is also clear that besides oscillations due to the ion-coupled $\delta\phi_i$ and ϕ_i^0 (or anharmonic interactions of these modes) no other orbital vibrational modes are observed in the spectra in Figs. 11.4–11.6, suggesting that our initial electronic states are close to the ground state and have small orbital oscillation amplitudes. In order to better probe other possible orbital vibrations, we perform calculations where an initial random perturbation is applied to the orbital. This is done by adding an initial random perturbation to each orbital and reorthogonalizing the orbitals. The effect of these initial random perturbations can be seen in the frequency spectra for $M = 1$ amu and $\mu = 125$ au plotted in Fig. 11.7 for the

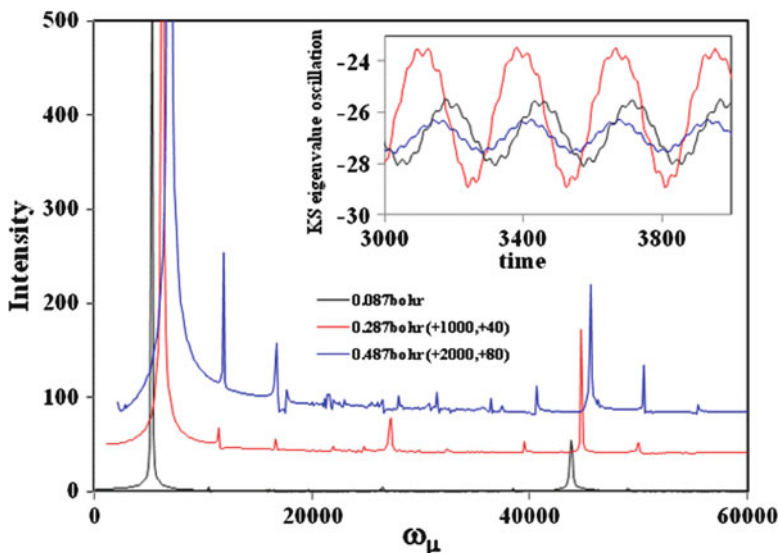


Fig. 11.5 Frequency spectra of oscillations in the KS eigenvalue ε_1 for initial ionic displacements larger than the equilibrium bond length by 0.087 bohr (black), 0.287 bohr (red), 0.487 bohr (blue) for the nitrogen dimer with $M=1$. For clarity the curves are shifted both horizontally and vertically by the indicated amounts in the brackets. The intensity of the oscillations increases with the initial ionic displacement. For the larger ionic displacements, harmonics of ϕ_i^0 can also be easily seen. The inset shows the corresponding oscillations of KS eigenvalue (in Ry) as a function of time (in au)

lowest and second lowest KS eigenvalue oscillations, and in Fig. 11.8 for the bond-length oscillations. We plot the data for perturbation amplitudes of 0.004, 0.008, 0.01 and 0.025. A perturbation of 0.01 means the original orbital is normalized to 0.99, and a random component is added to form a new orbital normalized to unity. These simulations ran for 4×10^5 steps with a time step of 0.05 au, and the frequency spectra are obtained from the last 1.6×10^5 steps when steady state has been reached, giving us a frequency resolution of about 175 cm^{-1} which is sufficient here. As we expect, the intensity of the peak at $43,500 \text{ cm}^{-1}$ is significantly increased when we perturb the orbitals away from the ground state. The intensity of the ϕ_i^0 ($5,250 \text{ cm}^{-1}$) peak, relative to the intensity of the other orbital modes, decreases with increasing initial displacement from the ground state. This is clearly seen in Fig. 11.7b where the most intense peak in the spectrum for a 0.025 initial perturbation is at $19,270 \text{ cm}^{-1}$.

Two points can be observed from the results in Figs. 11.7 and 11.8. First, as the size of the random perturbation increases, many orbital vibrational modes appear. Even for a perturbation of 0.004 numerous closely-spaced orbital peaks are observed from 2×10^4 to $4 \times 10^4 \text{ cm}^{-1}$, although the peak at $43,500 \text{ cm}^{-1}$ remains well-defined up to a perturbation of 0.01. A strong peak at $31,500 \text{ cm}^{-1}$ and its first harmonic are seen even at a perturbation of 0.004. The third and the

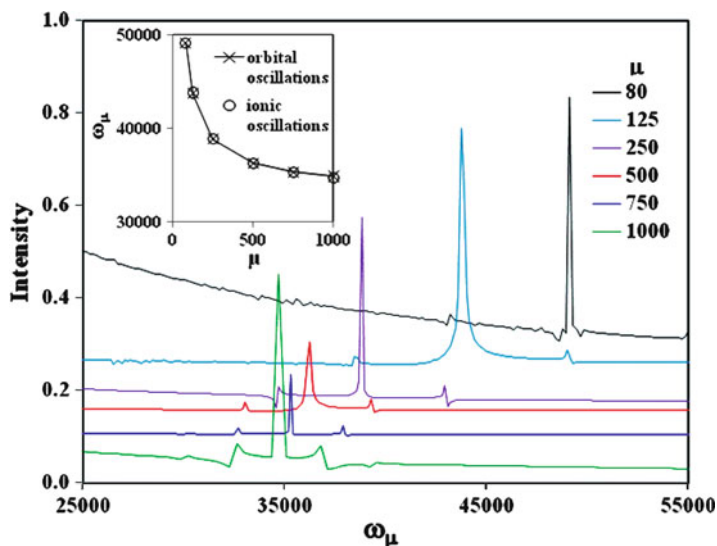


Fig. 11.6 The nitrogen dimer frequency spectra for $M = 1$ amu and μ from 80 au to 1000 au obtained from bond-length oscillations. We plot the region from 2.5×10^4 to 5.5×10^4 cm^{-1} showing that the ion-coupled $\delta\phi_i$ orbital mode is present in bond-length oscillations. In the inset we show that the frequency of the peak observed here matches that obtained from orbital oscillations

fourth harmonics can be seen for a perturbation of 0.01. For perturbation amplitudes of 0.01 and higher, the higher harmonics increase in intensity, the widths of the peaks increase, and the orbital spectra become considerably noisier. Therefore, as the initial displacement away from the ground state increases, non-linear coupling quickly becomes important. Second, Figs. 11.7a and 11.8 show that the frequency of the $\delta\phi_i$ peak at $43,500 \text{ cm}^{-1}$ decreases slightly as the random perturbation amplitude increases. For a perturbation equal to 0.025, Fig. 11.8 clearly shows that the frequency has decreased considerably. We also observed that the frequency of the ϕ_i^0 peak decreases slightly with the initial perturbation although this is not readily apparent from Fig. 11.8. This is more clearly observed if we consider the corresponding bond length oscillations in Fig. 11.9. For small perturbations (Fig. 11.9b) the oscillation period clearly increases with the amplitude of the perturbation. As the initial perturbation from the ground state increases (Fig. 11.9c), the equilibrium bond length can be significantly changed. For initial perturbations larger than approximately 0.025, the bond length appears to change considerably from an equilibrium value of about 2.2 to about 4.9 bohr. The behavior at a perturbation of 0.025 is particularly interesting because the system takes a considerably longer time than the other cases, at both smaller and larger perturbations, to settle into the new, incorrect equilibrium bond length. Our results show that non-linear effects become important, and ionic structures can be incorrectly predicted if the system is too far from the ground state. Since a larger orbital mass increases the coupling strength,

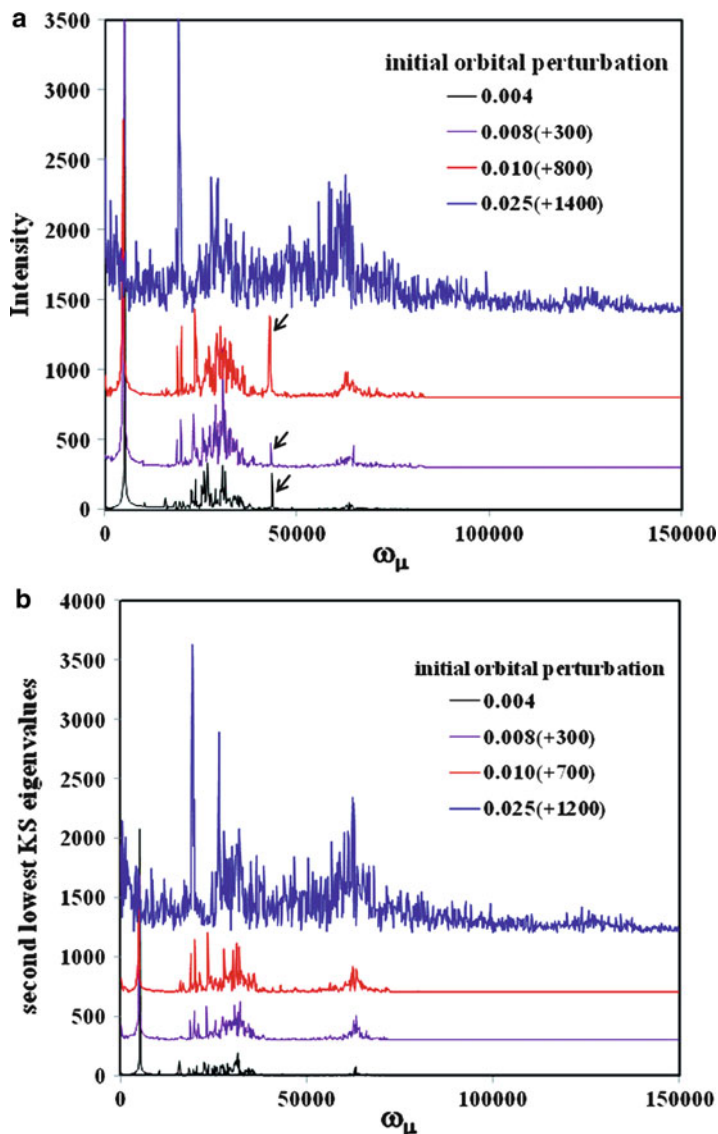


Fig. 11.7 Frequency spectra obtained from oscillations of the lowest (panel (a)) and second lowest (panel (b)) KS eigenvalues for $M = 1$ and $\mu = 125$ for the nitrogen dimer. Each curve is for a different value of the initial random perturbation to the wavefunction as indicated. We shift the graphs vertically by amounts indicated in brackets for clarity. The corresponding data for bond-length oscillations is shown below in Fig. 11.8

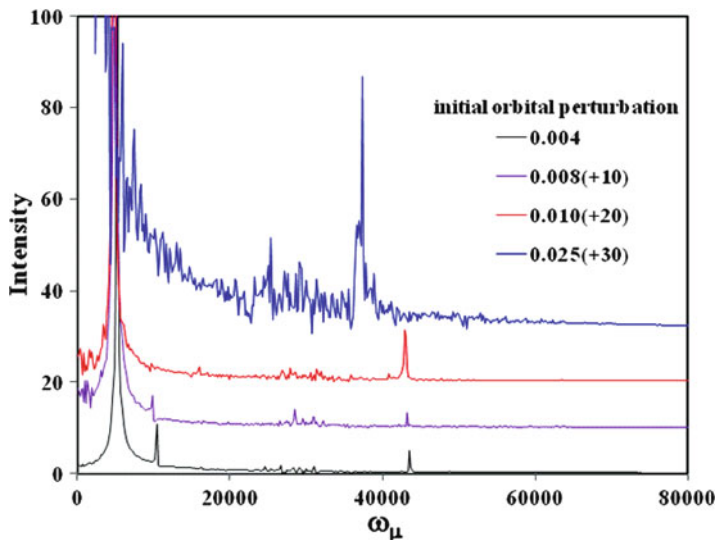


Fig. 11.8 Frequency spectra obtained from oscillations of the bond length for $M = 1$ and $\mu = 125$ for the nitrogen dimer. Each curve is for a different value of the initial random perturbation to the wavefunction as indicated, and shifted vertically by amounts indicated in brackets for clarity. The corresponding data for KS orbital oscillations is shown above in Fig. 11.7

this effect becomes more important for large orbital masses. It is thus important to stay sufficiently close to the Born-Oppenheimer surface in CPMD, particularly when a large orbital mass is used.

11.3.5 Departure from Linearity

The results in Figs. 11.7 and 11.8 show that to study $\delta\phi_i$ modes we need to be sufficiently far from the ground state such that enough energy is put into these modes but, on the other hand, not too far off that noisy spectra result from non-linear effects. We use an initial orbital perturbation of 0.01, ion mass equal to 1, 2 and 7 amu, and orbital masses ranging between 10 and 1,000 au. To illustrate the results, we show in Fig. 11.10 the orbital vibration spectra for M equal to 1 amu and orbital mass from 80 to 1,000 au for the nitrogen dimer. The abscissa is the rescaled frequency $\omega_\mu\mu^{1/2}$ which is independent of orbital mass for peaks that are not coupled to ionic vibrations. We identify from such plots a number of modes and the rescaled frequencies for these modes are plotted against μ/M in Fig. 11.11. From the results in Figs. 11.10 and 11.11a we find peaks for which the rescaled frequency $\omega_\mu\mu^{1/2}$ is independent of μ , for example at about 2×10^5 , 3.5×10^5 , and $7 \times 10^5 \text{ cm}^{-1}\text{au}^{1/2}$ for nitrogen, the last probably being a harmonic of the second. We deduce from our analysis that these peaks indicate orbital modes that are not coupled

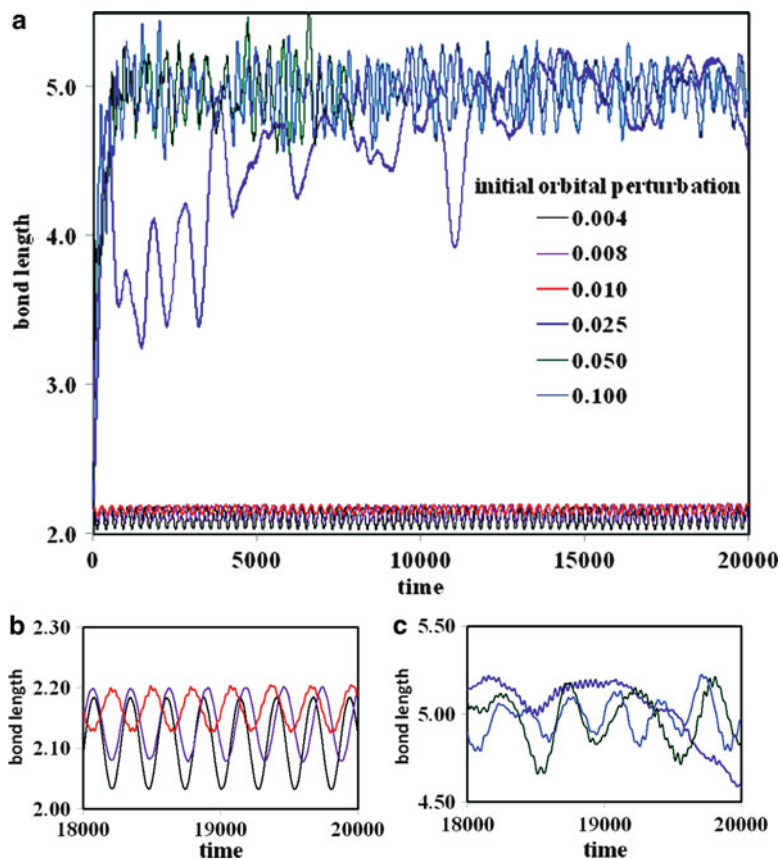


Fig. 11.9 The bond-length oscillations corresponding to the frequency spectra in Figs. 11.7 and 11.8. For small initial perturbations the oscillation frequency decreases with the amplitude of the initial perturbation. For larger initial perturbations the system has a different equilibrium bond-length when sufficiently perturbed away from the ground state. Panels b and c show the oscillations for small and large initial perturbations, respectively on a magnified scale. Time is in units of au

or only weakly coupled to the ionic vibration. We have excited these modes because our initial electronic structure includes sufficiently large random displacements $\delta\phi_i$ away from the ground state.

We also see two peaks in Fig. 11.10 for which the rescaled frequency changes significantly with μ . These are the (relatively low frequency) oscillations in ϕ_i^0 and the high frequency oscillations in the ion-coupled $\delta\phi_i$ mode. The latter is indicated by arrows in Fig. 11.10. The frequency change in ϕ_i^0 oscillations with μ is more clearly seen in Fig. 11.11a than in Fig. 11.10. The ionic (and hence ϕ_i^0) frequency in these calculations is slightly lower than the corresponding frequency for calculations without a random initial perturbation, consistent with the results in Fig. 11.9. In Fig. 11.1a, we have plotted (in red) the ionic frequencies from

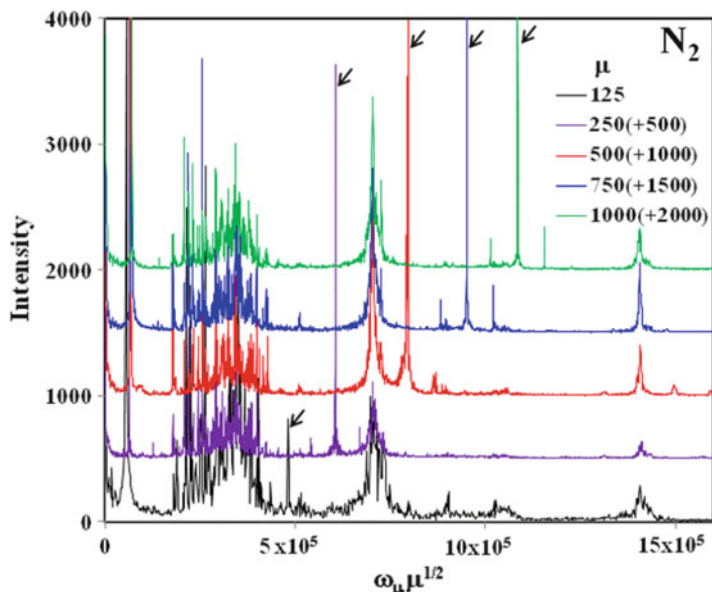


Fig. 11.10 The orbital frequency spectra obtained from oscillations of the KS eigenvalues for nitrogen in simulations with an initial random perturbation amplitude of 0.01. The intensity is plotted against the rescaled frequency $\omega_\mu \mu^{1/2}$ (in $\text{cm}^{-1} \text{au}^{1/2}$) so that orbital oscillations that are not coupled to the ion mode do not shift in position for different values of μ (in au). To guide the eye, each ion-coupled $\delta\phi_i$ peak is indicated with an arrow, and for clarity curves are shifted vertically by the amounts indicated in the brackets

the nitrogen data in Fig. 11.10 to indicate the magnitude of these differences. For $M = 1, 2,$ and $7,$ respectively, these are about $380, 235,$ and 152 cm^{-1} lower than the frequencies in simulations without the initial perturbation. That is, for the same initial perturbation, the difference decreases with ion mass. In Fig. 11.9, we plot the ionic frequency for $M = 1 \text{ amu}$ and $\mu = 125 \text{ au},$ as a function of the amplitude of the initial random perturbation from 0.004 to 0.01. For initial perturbations larger than 0.01, the spectrum becomes too noisy. This data shows that ionic frequency can be significantly underestimated if the system is not close to the ground state and μ/M is large. Importantly, it is clear from Fig. 11.11a that the rescaled frequency of each orbital mode can be collapsed onto one curve for all values of μ and $M.$ In particular, this is true for the ion-orbital coupled $\delta\phi_i$ mode even in the μ/M regime where the rescaled frequency changes rapidly with the mass ratio.

The results in Figs. 11.10 and 11.11 allow us to identify the ion-orbital coupled $\delta\phi_i$ mode for orbital displacements about the ground state. For nitrogen this mode has a rescaled frequency equal to approximately $4 \times 10^5 \text{ cm}^{-1} \text{au}^{1/2}$ in the limit of large ion mass. For an orbital mass of $125 \text{ au},$ this gives a minimum frequency of about $3.6 \times 10^4 \text{ cm}^{-1}$ in the limit of large ion mass as we mentioned when discussing the absence of this mode from the data for $M = 1 \text{ amu}$ and $M = 21 \text{ amu}$ in Fig. 11.4.

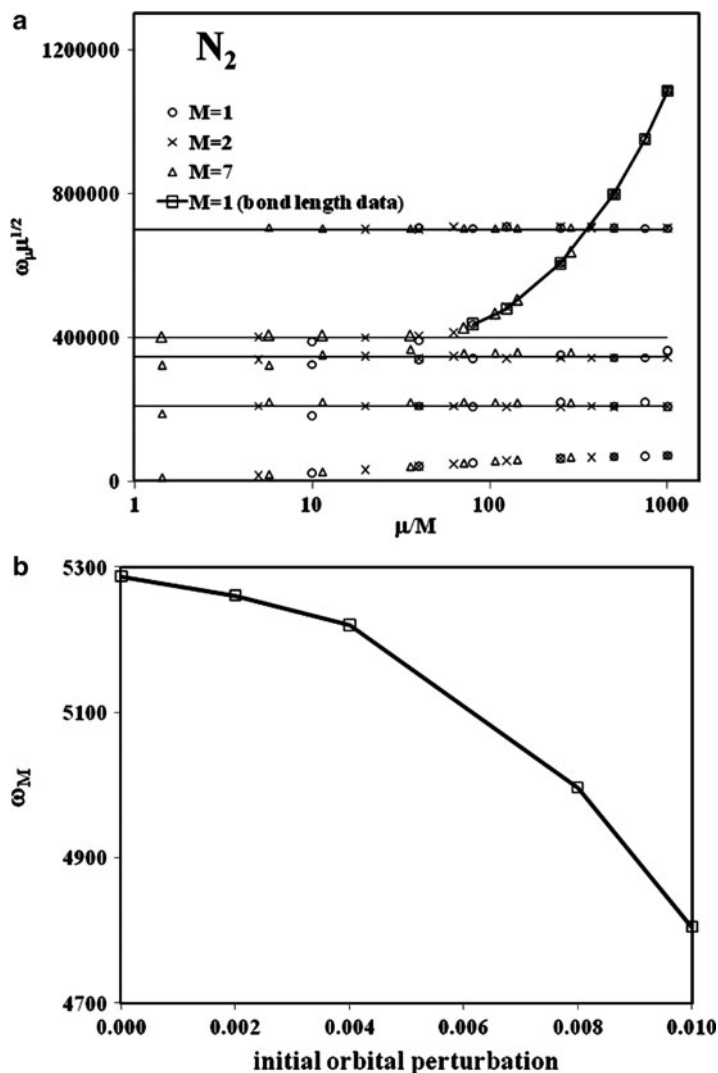


Fig. 11.11 Plots of the rescaled orbital frequency $\omega_\mu \mu^{1/2}$ (in cm^{-1}) against μ/M (in au/amu) for simulations with different values of M for simulations with an initial random perturbation amplitude of 0.01. The frequency spectra are shown in panel (a). These plots show that the dependence of the rescaled frequency upon the mass ratio is the same function even for different ionic masses. Horizontal lines are added to guide the eye. We also include data points (squares) for the frequency of the ion-coupled $\delta\phi_i$ oscillation obtained from the bond-length vibration data in Fig. 11.6 showing that the same mode is observed in both the orbital and the bond-length oscillations. In panel (b) we plot the ionic vibrational frequency for simulations with different initial random perturbation amplitude ranging from zero to 0.01

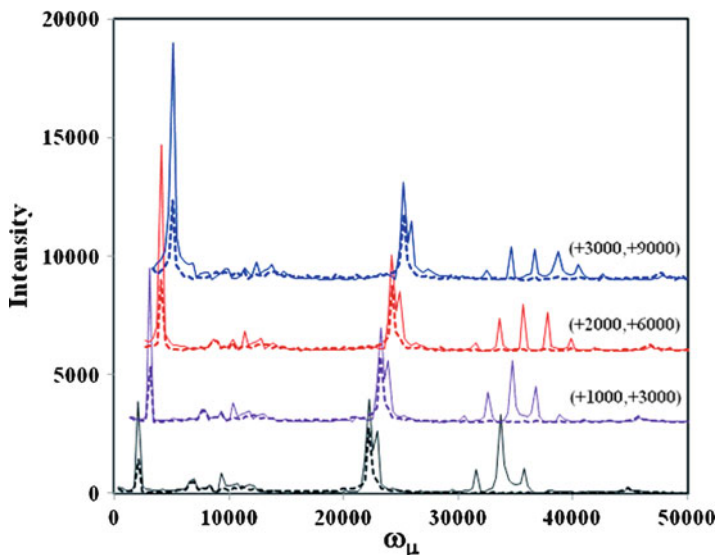


Fig. 11.12 Orbital frequency spectra with initial orbital perturbation amplitude of 0.01 at initial bond-lengths of 0.187 bohr (*black*), 0.287 bohr (*purple*), 0.387 bohr (*red*), and 0.487 bohr (*blue*). Solid lines are for ϵ_1 and dashed lines are for ϵ_2 , the lowest and second lowest KS ei-genvales, respectively. A higher order coupling of the ion-coupled $\delta\phi_i$ mode (in nitrogen) is observed as the initial bond length is increased. The two satellite peaks observed at small initial bond length, develop into a multiplet for larger initial ionic displacements. For clarity the frequency spectra are shifted both vertical and horizontally by the amount indicated in the brackets

We are able to see clearly the effect of ion-orbital coupling on the rescaled frequency because we have used μ/M ratios that are larger than typical; this increases the relative contribution of the second term in Eq. 11.2 to the first term. For nitrogen a typical value of $\mu = 500$ au has been used in CPMD calculations leading to ionic frequency that increases linearly as μ goes to zero [15]. We see from Fig. 11.11a that for the actual nitrogen mass $M = 14$, an orbital mass of 500 au is just at the point when the higher order correction terms in μ/M for the ionic frequency begins to be significant. That is, the results for nitrogen in Ref. [15] are just within the linear region of the curve for M equal to 14 au. Our own calculations for $M = 14$ in Fig. 11.1a show a small but observable departure of the ionic frequency from linearity for orbital masses larger than 200 au.

We consider again how the intensity of the ion-orbital coupled $\delta\phi_i$ mode is affected by the initial ionic displacement as in the calculations summarized in Fig. 11.5, but now for calculations where the system is also initially perturbed from the ground state. We performed calculations in which the initial random orbital perturbation is fixed at 0.01 as above and the initial ion bond length is gradually increased. The nitrogen dimer with an orbital mass of 1,000 au and an ion mass of 1 amu is used for these calculations. The frequency spectra for the lowest (solid line) and the second lowest (dashed line) KS eigenvalues are plotted in Fig. 11.12.

The ϕ^0 peak is at $2,083 \text{ cm}^{-1}$ and the ion-orbital coupled $\delta\phi_i$ peak is observed at about $33,680 \text{ cm}^{-1}$ for the lowest but not observed for the second-lowest KS eigenvalue. With the smallest initial ionic displacement, only two satellite peaks at $\pm 2,083 \text{ cm}^{-1}$ from the ion-orbital coupled peak cm^{-1} are observed as in similar orbital vibration data in Fig. 11.6. With both the orbital perturbation away from the ground state and the larger ionic displacement, we expect a larger ion-orbital interaction. We observe in Fig. 11.12 an increase in the initial ionic displacement, and the appearance of a multiplet of peaks centred at $33,680 \text{ cm}^{-1}$ as the initial ionic displacement increases. The intensity of the satellite peaks increases while the intensity of the main peak decreases. The constant frequency interval between the peaks in the multiplet is equal to $2,083 \text{ cm}^{-1}$ indicating that the additional peaks are due to ion-orbital coupling that are higher order than ΔR . Thus, as the initial displacements in both δR_I and $\delta\phi_i$ increase, anharmonic ion-orbital interactions become important.

11.4 Conclusion

In summary, we have shown that ion-orbital interaction in CPMD is manifested in two ways: through the parametric dependence of ϕ_i^0 upon R_I , and through the dynamical coupling between $\delta\phi_i$ and δR_I . Close to the ground state this ion-orbital interaction can be treated like linearly-coupled oscillators. This leads to two ion-orbital coupled modes with the frequencies ω_M and ω_μ , the former due to a normal mode consisting mainly of bond-length (and, parametrically ϕ_i^0) oscillations, and the latter due to a normal mode consisting mainly of $\delta\phi_i$ oscillations. Approximations for these frequencies are given in Eqs. 11.3 and 11.4. This approximation is useful because it allows us to quantitatively understand the frequency dependence of the coupled modes upon the mass ratio μ/M . For small mass ratios this is given by $\omega_M = \omega_{0M}[1 - C(\mu/M)]$ where ω_M is the CPMD-calculated ionic frequency and ω_{0M} is the actual ionic frequency. This result is of practical importance in extracting ionic vibrational frequencies using CPMD. At larger mass ratios the dependence upon μ/M becomes non-linear. We have also examined in detail these non-linear effects when progressively larger initial random perturbations are applied to the orbitals and when ionic displacements become large. This picture of ion-orbital interaction close to the ground state is verified by our numerical simulations. Our theoretical description provides new insight on adiabatic decoupling in CPMD. The linear coupling leads to *normal* ion-orbital modes when the system is close to the ground state but with larger displacements in $\delta\phi_i$, and δR_I , non-linear effects come into play, underscoring the well-known point that the orbitals should be rather close to the ground state in order to extract accurate quantities from CPMD, but also the less well-known point that the magnitude of ionic vibrations can also lead to spurious effects arising from the non-linear coupling between ionic degrees of freedom and the orbital displacements from the ground state. Close to the ground state the

orbital mode with the highest amplitude is that due to ϕ_i^0 oscillating parametrically with the bond-length. The ion-orbital coupled $\delta\phi_i$ mode has considerably smaller intensity, and the other $\delta\phi_i$ modes that are not coupled or weakly coupled to the ionic displacement have even smaller intensity. This, however, breaks down further from the ground state when non-linear interactions between ion and orbital modes become important. Then the notion of normal modes is not valid any longer, and we expect adiabatic decoupling to break down. Thus, in metallic systems, or systems with smaller gaps (tin dimer compared to the nitrogen dimer), and therefore larger interactions between orbitals for the same $\delta\phi_i$, there is a narrower region around the ground state where adiabatic decoupling is valid. Our analysis is also consistent with adiabaticity breakdown occurring more readily at large μ/M because the ion-orbital coupling increases with the mass ratio.

References

1. Car R, Parrinello M (1985) Unified approach for molecular dynamics and density-functional theory. *Phys Rev Lett* 55:2471–2474
2. Field MJ (1990) Simulated annealing, classical molecule dynamics and the Hartree-Fock method: the NDDO approximation. *Chem Phys Lett* 172:83–88
3. Hartke B, Carter EA (1992) Spin eigenstate-dependent Hartree-Fock molecular dynamics. *Chem Phys Lett* 189:358–362; Gibson DA, Carter EA (1997) *Ab initio* molecular dynamics of pseudorotating Li_5 . *Chem Phys Lett* 271:266–272; Liu ZH, Carter LE, Carter EA (1995) Full configuration interaction molecular dynamics of Na_2 and Na_3 . *J Phys Chem* 99: 4355–4359
4. Sprik M, Klein M L (1988) *J Chem Phys* 89:7556–7560; Sprik M (1991) Computer simulation of the dynamics of induced polarization fluctuations in water. *J Phys Chem* 95:2283–2291
5. Rick SW, Stuart SJ, Berne BJ (1994) Dynamical fluctuating charge force fields: application to liquid water. *J Chem Phys* 101:6141–6156
6. Pastore G, Smargiassi E, Buda F (1991) Theory of *ab initio* molecular-dynamics calculations. *Phys Rev A* 44:6334–6347
7. Marx D, Hütter J (2000) *Ab initio* molecular dynamics: theory and implementation. In: Grotendorst J (ed) *Modern methods and algorithms of computational chemistry* (NIC, FZ Jülich 2000), pp 301–449
8. Car R, Angelis F, Giannozzi P, Marzari N (2005) Chapter 1.4 first-principles molecular dynamics. In: Yip S, Kaxiras E, Marzari N, Trout B (eds) *Handbook of materials modeling: methods and models*, vol 1. Springer, New York
9. Tangney P (2006) On the theory underlying the Car-Parrinello method and the role of the fictitious mass parameter. *J Chem Phys* 124:044111
10. Tangney P, Scandolo S (2002) How well do Car-Parrinello simulations reproduce the Born-Oppenheimer surface? Theory and example. *J Chem Phys* 116:14–24
11. Kuo IFW, Mundy CJ, McGrath MJ, Siepmann JI, VandeVondele J, Sprik M, Hutter J, Chen B, Klein ML, Mohamed F, Krack M, Parrinello M (2004) Liquid water from first principles: investigation of different sampling approaches. *J Phys Chem B* 108:12990–12998
12. Kuo IFW, Mundy CJ, McGrath MJ, Siepmann JI (2006) Time-dependent properties of liquid water: a comparison of Car-Parrinello and Born-Oppenheimer molecular dynamics simulations. *J Chem Theory Comput* 2:1274–1281
13. Ong SW, Tok ES, Kang HC (2010) Vibrational frequencies in Car-Parrinello molecular dynamics. *Phys Chem Chem Phys* 12:14960–14966

14. Tassone F, Mauri F, Car R (1994) Acceleration schemes for *ab initio* molecular-dynamics simulations and electronic-structure calculations. *Phys Rev B* 50:10561–10573
15. Giannozzi P et al (2009) Quantum ESPRESSO: a modular and open-source software project for quantum simulations of materials. *J Phys Condens Matter* 21:395502
16. Wathelet V, Champagne B, Mosley DH, Andre J, Massida S (1997) Vibrational frequencies of diatomic molecules from Car and Parrinello molecular dynamics. *Chem Phys Lett* 275:506–512
17. Becke AD (1988) Density-functional exchange-energy approximation with correct asymptotic behavior. *Phys Rev A* 38:3098–3100; Lee C, Yang W, Parr RC (1988) Development of the Colle-Salvetti correlation-energy formula into a functional of the electron density. *Phys Rev B* 37:785–789
18. Troullier N, Martins JL (1991) Efficient pseudopotentials for plane-wave calculations. *Phys Rev B* 43:1993–2006

Chapter 12

Novel Liquid Diffusion Tube Determines Electrolytes' Relative Free Diffusion Velocities, Hydration Numbers and Overwhelmingly Revalidates Electrolytic Diffusion Law

Abul Khair, Golam M. Golzar Hossain, Mohammad S. Alam, Mahammad M. Hossain, Mohammad H. Kabir, Mohammad H. Rahman, and Amal Halder

Abstract A novel liquid diffusion tube closed and cylindrical termed Diffusimeter was fabricated from glass tube and straight bore stopcocks to measure relative velocities of electrolytes in free diffusion. Solutions of two electrolytes known to give characteristic reaction were put one above each of two stopcocks and then released concurrently to diffuse head on through water in the diffusion path and finally to produce a precipitate or color as indicator at the encounter. Experimental objective required entry of time elapsed for the reaction mark to appear and the distances traveled by the electrolytes. The velocity ratio termed distance traveled ratio (DTR) was found to match with the Molar Mass Ratio Square Root (MMRSR) of the electrolyte pair taken in order. A direct proportionality between the velocity and the square root of molar mass was thus revalidated. The heavier electrolyte moved faster contrary to the gaseous diffusion. The results hinted hydration numbers of the diffusing electrolytes. Diffusion velocities of 30 salts were determined using this novel, innovative Diffusimetric Method named DTR model. Surprisingly NH_4Cl and NH_4SCN showed similar velocities. HCl and LiCl showed low diffusion rates due to their cations' high charge to size ratio. Apparently MgCl_2 , CaCl_2 , and SrCl_2 diffused with one H_2O each but BaCl_2 , AgNO_3 , and Fe^{III} alum with none. NaCl showed relatively high rate which traces its fitness as antibacterial agent and biosalt in human. Na_2SO_4 and K_2SO_4 showed identical velocities which together with metatheses hypothesize sylvite mineral formation mechanism over geological periods. Close diffusion rates of ZnCl_2 and CdCl_2 traced reasons for

A. Khair (✉) • G.M.G. Hossain • M.M. Hossain • M.H. Kabir • M.H. Rahman
Department of Chemistry, University of Dhaka, Dhaka 1000, Bangladesh
e-mail: profabulkhair@gmail.com; hafizur.rahman@iccs.edu

M.S. Alam
Department of Applied Chemistry & Chemical Engineering, Noakhali Science and Technology University, Sonapur, Noakhali 3802, Bangladesh

A. Halder
Department of Mathematics, University of Dhaka, Dhaka 1000, Bangladesh

cadmium's presence in zinc ores. Diffusion controlled effects are shown in Fe^{III} salts' reactions with NH₄SCN; the DTR reveals reactant pair's encounter nature at their conjunction. Manipulating electrolytes' concentrations, crystalline precipitates were obtained.

12.1 Introduction

Diffusion is a universal phenomenon, membrane diffusion being extensive in the living kingdom and free diffusion in the rest. The irreversible nature of diffusion in combination with the statistical probability of material transfer in the cell cytoplasm, substantiate a perspective for the evolution process. Molecules of gases move with very high speeds but collide with every molecule standing their way. The number of such collisions being very high, molecules do move exceedingly slowly.

Transfer of material in free diffusion was studied by Graham and Fick. Graham's Law of Diffusion states that the diffusion velocity, V_d , of a gas is inversely proportional to the square root of its molar mass, M . Mathematically the law is represented as $V_d \propto \sqrt{\frac{1}{M}}$ [1]. According to Fick's First Law [2–4], the amount of solute dm diffusing in the x direction across an area A in a time dt is proportional to the concentration gradient $\frac{dc}{dx}$ at that plane and is given by $dm = -DA \frac{dc}{dx} dt$, where D is the diffusion coefficient having the unit of m^2s^{-1} . The equation is also often represented by $J = -D \frac{\partial c}{\partial x}$, where J is the flux density diffusing parallel to the x -axis per unit time per unit area. J has the unit of $\text{mol m}^{-2} \text{s}^{-1}$ and measures the amount of substance that flows through a small area during a small time interval. The minus sign expresses that substances diffuse down concentration. Fick's Second Law [2–4] predicts how diffusion causes with time the concentration field to change which is represented by $\frac{\partial c}{\partial t} = D \frac{\partial^2 c}{\partial x^2}$. The diffusion coefficient D is not strictly a constant for it changes slightly with concentration.

It is known that the relative free diffusion velocity of an electrolyte is directly proportional to the square root of its molar mass. Mathematically $D\sqrt{M} = K$, where D is the same as before, K is the permeability constant defined as the relative rate of diffusion, and M the molar mass of an electrolyte [5]. This is the Law of Electrolytic Diffusion upon which the work is based. The law also holds good for membrane diffusion the most widespread cellular activity, examples of which are innumerable such as intravenous drug movement, osmosis, dialysis, Na⁺ and K⁺ ion transport across cell membranes etc.

12.2 Experimental Section: Diffusimeter and Methodology

The Diffusimeter was manufactured [6] by joining the ends of a glass tube to two straight bore stopcocks parallel to each other with their keys outward (Fig. 12.1). The length CF or CDEF is the diffusion path length (DPL) being measured by a

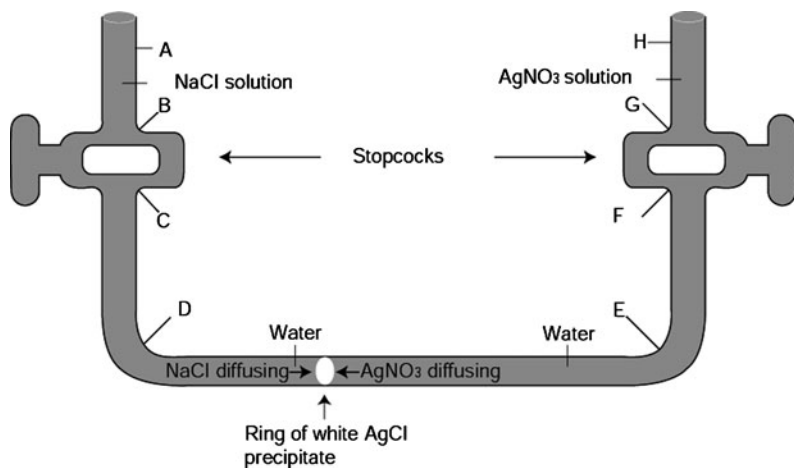


Fig. 12.1 The Diffusimeter

narrow paper strip held tight on to the points C and F of the tube and on the surface facing the observer. The lengths of the tube stems above the stopcocks, BA and GH, were left uncut so as to contain larger volume of reactant solutions as and when required. The bores of the stopcock stem and of the base tube were chosen identical.

An experimental run begins with mounting the Diffusimeter having its wide bottom rested on a dark, plane surface and the vertical arms held above each stopcock by clamps. A surveyor's level checks the Diffusimeter's horizontal alignment. The stopcocks are opened and water is poured in to fill up to a certain height of the stems, BA and GH. Any air bubbles seen in the diffusion path are removed by soft tapping and tilting the tube. The stopcocks are then closed and the excess water is poured off turning the Diffusimeter upside down. The residual water is removed by dropper. Reactant solutions are poured in AB and HG using separate graduated pipette. The stopcocks are then opened simultaneously making sure that their holes and the diffusion tube bore centers are aligned. The two reactants diffuse head on and meet and react after a time being recorded by a stop clock and at a point being marked by a fine scorer.

Distance traveled, DT, by one reactant measured by thin paper strip and centimeter scale is subtracted from the DPL to obtain distance traveled by the other. The Diffusimeter is then rotated by 180° and the experiment redone putting the reactant solutions in their same initial sides. The average time elapsed, distance traveled by each reactant, diffusion velocity of each, the distance traveled ratios, and the molar mass ratio square root are computed. This is one experimental run repetition of which gave precise results. It is to be noted that the diffusion path length does not include the two stopcock bore lengths and the tube heights the reactant solutions fill.

Compounds capable of giving a common product as precipitate or color with a single compound are named Congenous Compound and the single reactant Syngenous

Compound. The precipitate or color appearing as the product is termed Indicator. Ionic chlorides reacting with silver nitrate to give white silver chloride precipitate are congens, syngenus and indicator compound respectively. These reactions between congens and syngenus reactants were carried out at corresponding molar concentrations, instead of stoichiometry, to ensure same number of reactant particles start diffusing from either direction at zero time. The DTR values were calculated placing always the distance traveled by the congens electrolyte in the numerator. For NaCl – AgNO₃ reaction the $DTR = \frac{DT_{NaCl}}{DT_{AgNO_3}}$ and the Molar Mass Ratio Square Root, $MMRSR = \sqrt{\frac{M_{NaCl}}{M_{AgNO_3}}}$.

12.2.1 Reactions Carried Out to Determine Diffusion Velocities and Some General Enunciations

Reactions of congens chlorides of Group 1, 2, and 12 including NH₄Cl, AlCl₃, and FeCl₃ with syngenus AgNO₃, Group 1 sulfates and Fe^{III} alum with BaCl₂, and FeCl₃, Fe(NO₃)₃, and Fe^{III} alum with NH₄SCN at corresponding concentrations were carried out. Reactions of NaCl and AgNO₃ at constant AgNO₃ concentration but different NaCl concentrations are also reported.

The hydration number of a salt in the solid form and in diffusion may differ and for separate identity they, say Group 1 halides, were represented as MCl.YH₂O and MCl.yH₂O respectively. Y and y are either zero or small whole numbers and if zero were often omitted. Each Table shows the DTR and MMRSR values for a reacting salt pair and at the right the composition and molar mass of MCl.yH₂O. The plots are mostly the relative diffusion velocity V_d versus [salt] and in some cases V_d versus M_{salt} or V_d versus Z_M . Each reaction gave two relative velocities which were given abbreviated representation in the plot area. For Group 1 MCl and AgNO₃ reactions the relative velocities of AgNO₃ were represented by $V_{dAg^+ - MCl}$; few other abbreviations were also used. The x -axis in many cases shows both syngenus and congens reactant concentrations which are equal.

The work employed AR or R&D grade chemicals, 2.0 mL reactant solutions, corresponding concentrations unless otherwise mentioned, 0.40 cm stopcock bore diameter, and 33 cm DPL if not otherwise, and room temperatures ranging from 302 to 306 K. Narrow temperature gap was observed to have minor affect on the diffusion rates. The DTR for an electrolyte pair shows good agreement with their MMRSR which occasionally fitted well if yH₂O molecules were put in place with the diffusing electrolyte. Number y for the syngenus AgNO₃, BaCl₂, and NH₄SCN was found to be zero. Essential to note that salts MCl₂.YH₂O transform to MCl₂.yH₂O in solution and so [MCl₂.YH₂O] and [MCl₂.yH₂O] are the same but MCl₂.YH₂O and MCl₂.yH₂O are not.

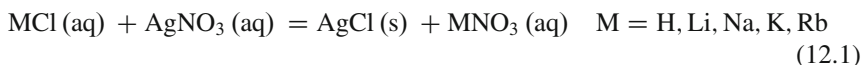
In aqueous medium the primary sphere of some cations contains definite number of water molecules strongly held to them thus increasing the molar mass of the salts and their velocities. Associated water molecules on the other hand in unspecified

numbers are weakly held to the ions in the secondary sphere thus adding to the volume of the salts and reducing their velocities. Hypothetically the velocity of a salt could be around 100 cms^{-1} or more, but in reality it is only a fraction of a centimeter. The high hydration radius of the ion associates and their collisions with the countless millions of surrounding water molecules make the electrolytes' movement incredibly slow.

Cleaning the diffusion tube was done using dilute ammonia to get rid of sticking AgCl , concentrated sulfuric acid to get rid of BaSO_4 , and dipping the Diffusimeter in acid bath taking care of the safety of the stopcock and its plastic cap if any.

12.3 Results and Discussion

12.3.1 Reactions of Group 1 Chlorides and AgNO_3



The average distance traveled ratio for each MCl-AgNO_3 pair is close to its molar mass ratio square root (Table 12.1) which ensures direct proportionality between electrolyte's diffusion velocity and square root of its molar mass. The new diffusimetric method or diffusimetry elegantly revalidates the law of electrolytic diffusion (Table 12.2).

The $V_{d\text{HCl}}$ show sudden fall (Fig. 12.2) from those of $V_{d\text{LiCl}}$ firstly due to the high hydration of H^+ ion caused by its smallest ion radius (10^{-5} pm) [7] and secondly

Table 12.1 DTR and MMRSR for diffusing MCl-AgNO_3 pairs; MCl being Group 1 chlorides

Congenus MCl.	FW, gmol^{-1}	DTR = $\frac{DT_{\text{MCl}}}{DT_{\text{AgNO}_3}}$								Average DTR	MMRSR = $\sqrt{\frac{\text{MCl}}{\text{AgNO}_3}}$
		0.1 M	0.2 M	0.3 M	0.4 M	0.5 M	0.6 M	0.7 M			
HCl	36.5	0.38	0.40	0.40	0.42	0.41	0.41	0.41	0.40	0.46	
LiCl.H ₂ O	60.41	0.47	0.45	0.47	0.49	0.48	0.49	0.53	0.48	0.50	
NaCl	58.44	0.62	0.60	0.62	0.59	0.63	0.64	0.63	0.62	0.59	
KCl	74.55	0.66	0.63	0.63	0.62	0.61	0.62	0.66	0.63	0.66	
RbCl	120.92	0.86	0.82	0.82	0.84	0.86	0.84	0.82	0.84	0.84	

Table 12.2 DTR at different $[\text{NaCl}]$ but constant $[\text{AgNO}_3] = 0.9 \text{ M}$ and MMRSR for NaCl-AgNO_3 pair

Congenus	FW, gmol^{-1}	DTR									MMRSR = $\sqrt{\frac{\text{NaCl}}{\text{AgNO}_3}}$ $\nu = 0$
		0.1 M	0.2 M	0.3 M	0.4 M	0.5 M	0.6 M	0.7 M	0.8 M	0.9 M	
NaCl	58.44	0.29	0.36	0.42	0.47	0.52	0.56	0.59	0.61	0.64	0.59

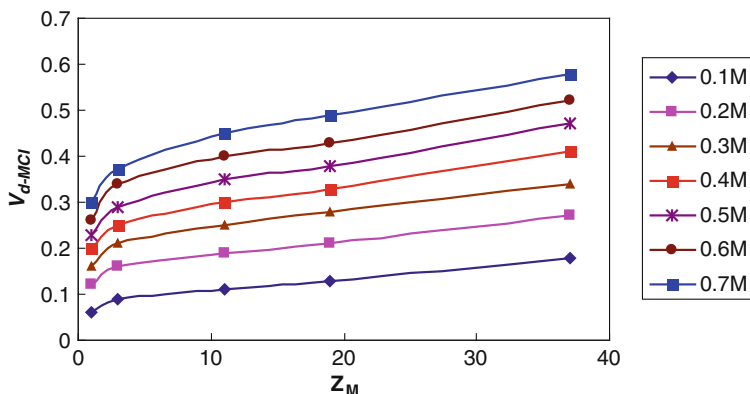


Fig. 12.2 Plots of V_{dMCl} versus Z_M for $MCl-AgNO_3$ reactions. M are Group 1 elements

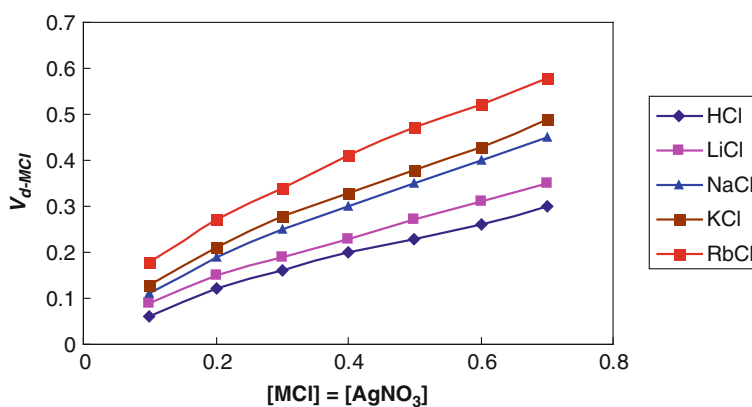


Fig. 12.3 Plots of V_{dMCl} versus $[MCl]$, MCl are Group 1 chlorides, for $MCl-AgNO_3$ reactions

for the high percent atomic number drop from Li to H. Plots of V_{dMCl} versus $[MCl]$ (Fig. 12.3) are in agreement with the Fick's first law and as such these observations are all Fickian. The plots of five MCl appear in order of their molar masses with the most massive one, RbCl, occupying the uppermost position and the least massive, HCl, the lowermost. The velocities converge at lower concentrations as though they are heading towards zero at zero concentration and diverge at higher for momentum. The NaCl plot rises up a little and comes closer to that of KCl leaving a noticeable gap between NaCl and LiCl lines. The comparative higher velocities of NaCl may be one of the reasons for its fitness as a biosalt in many living organisms including human and an antibacterial agent. The closer velocities of Na^+ and K^+ make the ion pumping across the cell membrane essential [8]. The narrowly differing $V_{dAg^+ - MCl}$ appeared twined at some points because of experimental flaw arising out of bare data collection process (Fig. 12.4).

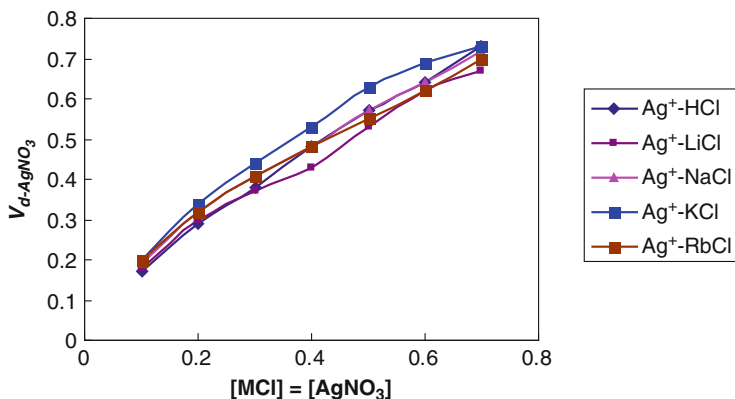


Fig. 12.4 Plots of $V_{d,AgNO_3}$ versus $[MCl]$ for $MCl-AgNO_3$ reactions

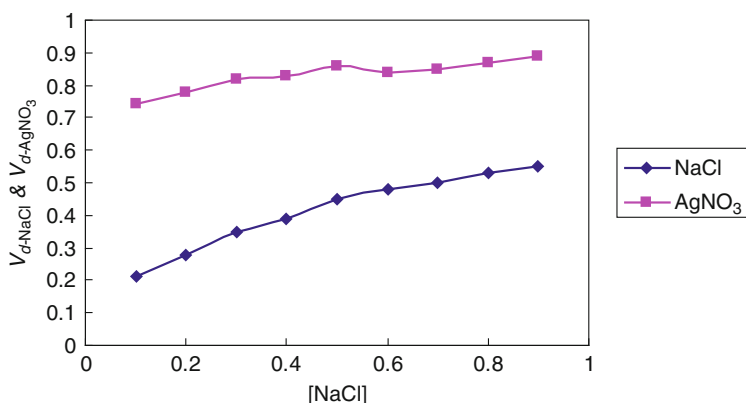


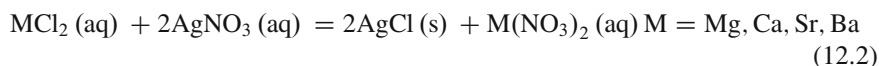
Fig. 12.5 Plots of $V_{d,NaCl}$ and $V_{d,AgNO_3}$ versus $[NaCl]$ for $NaCl-AgNO_3$ reaction at different $[NaCl]$ but constant $[AgNO_3] = 0.9$ M

Salt NaCl at 0.1 and 0.7 M shows diffusion velocities of 0.11 and 0.45 cm s^{-1} respectively. Calculations show the diffusing chlorides MCl hold no H_2O in the primary sphere though solid LiCl holds one in the sample used (Table 12.1). Cotton et al. speculated Na^+ and K^+ to have tetrahedrally arranged four H_2O in solution [9] but this is not evident in this study. At constant $[AgNO_3]$ but different $[NaCl]$ the quotient DTR (Table 12.2) increases with increasing $[NaCl]$ and maximizes at the corresponding concentration of 0.9 M. The DTR plot as a function of $[NaCl]$ gives a smooth, convex curve (not shown). The wide gap between NaCl and $AgNO_3$ plots (Fig. 12.5) is in keeping with their high molar mass difference.

Table 12.3 DTR and MMRSR for diffusing MCl_2-AgNO_3 pairs. M are Group 2 metals

Congenous $MCl_2 \cdot yH_2O$	FW, $g\text{mol}^{-1}$	DTR				Average DTR	MMRSR= $\sqrt{\frac{MCl_2 \cdot yH_2O}{AgNO_3}}$	FW, diffusing salt, $g\text{mol}^{-1}$
		0.1 M	0.2 M	0.3 M	0.4 M			
$MgCl_2 \cdot 6H_2O$	203.31	0.80	0.80	0.79	0.81	0.80	0.82 $y = 1$	$MgCl_2 \cdot H_2O$ 113.24
$CaCl_2$	110.99	0.89	0.85	0.84	0.86	0.86	0.87 $y = 1$	$CaCl_2 \cdot H_2O$ 129.01
$SrCl_2 \cdot 6H_2O$	266.62	1.1	1.0	0.99	1.0	1.0	1.0 $y = 1$	$SrCl_2 \cdot H_2O$ 176.55
$BaCl_2 \cdot 2H_2O$	244.28	1.1	1.1	1.1	1.1	1.1	1.1 $y = 0$	$BaCl_2$ 208.25

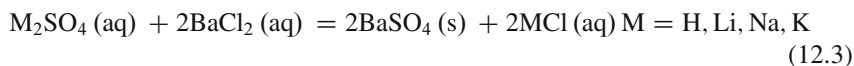
12.3.2 Reactions of Group 2 Chlorides and $AgNO_3$



Aqueous solutions of $MgCl_2$, $CaCl_2$, and $SrCl_2$ diffuse with one H_2O each but $BaCl_2$ with none (Table 12.3). Such observations are remarkable for Mg^{2+} is known to hold six water molecules though loosely in aqueous solution [10–13]. The lowermost position for magnesium chloride in Figs. 12.6 and 12.7 suggests that the diffusing species is not $MgCl_2 \cdot 6H_2O$ but $MgCl_2 \cdot H_2O$ the lowest molar mass electrolyte. The $Mg^{2+}-OH_2$ bond in solution being weak, some H_2O molecules break away in the rushing diffusion process making room for $[Mg-H_2O]^{2+}$ unit to spearhead less hindered. The diffusimetric method with digital recording system for time and length may be more rigorous in determining the hydration numbers of ions in solution.

12.3.3 Reactions of Group 1 Sulfates and $BaCl_2$

$[M_2SO_4] = [BaCl_2] = 0.2, 0.3, 0.4, \text{ and } 0.5 \text{ M}$



Salts Li_2SO_4 and Na_2SO_4 travel with one H_2O each (Table 12.4). Significantly it is noted that the sulfates of sodium and magnesium have the same velocities (Fig. 12.8). This is due partly to the extra mass contributed by the strong binding of one H_2O molecule to sodium sulfate and partly to the inherent higher Na^+ mobility (Fig. 12.3). Almost a linear progression of each of the plots in Fig. 12.8 justifies

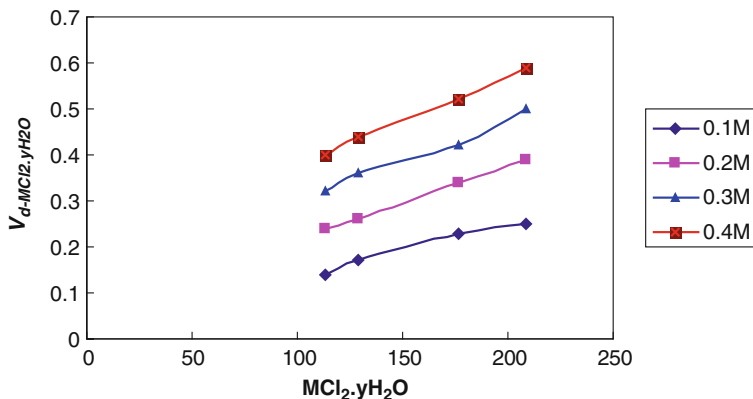


Fig. 12.6 Plots of $V_{dMCl_2.yH_2O}$, M are Group 2 metals, versus $MCl_2.yH_2O$ molar masses for $MCl_2^- AgNO_3$ reactions

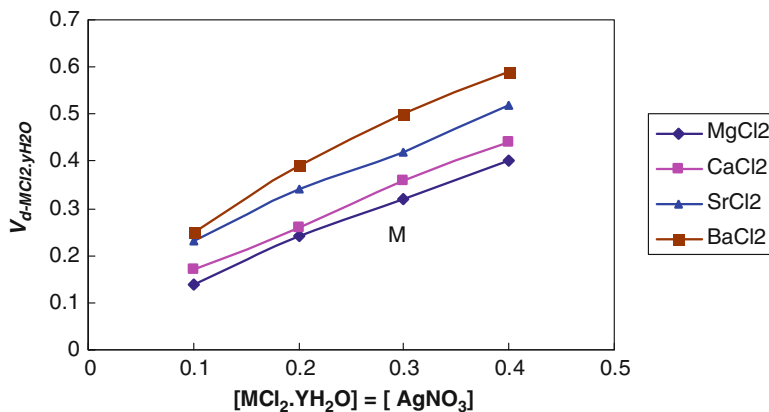


Fig. 12.7 Plots of $V_{dMCl_2.yH_2O}$, M are Group 2 metals, versus $[MCl_2.yH_2O]$ for $MCl_2^- AgNO_3$ reactions

y value assignments to $M_2SO_4.yH_2O$ (Table 12.4). Equal rates of $Na_2SO_4.H_2O$ and K_2SO_4 along with their metatheses with surrounding chlorides hypothesize the formation of mineral sylvite (consisting of 57% NaCl and 43% KCl) over geological periods [14].

12.3.4 Reactions of Group 12 Chlorides and $AgNO_3$

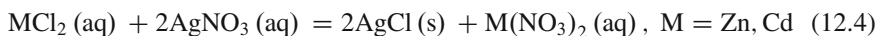
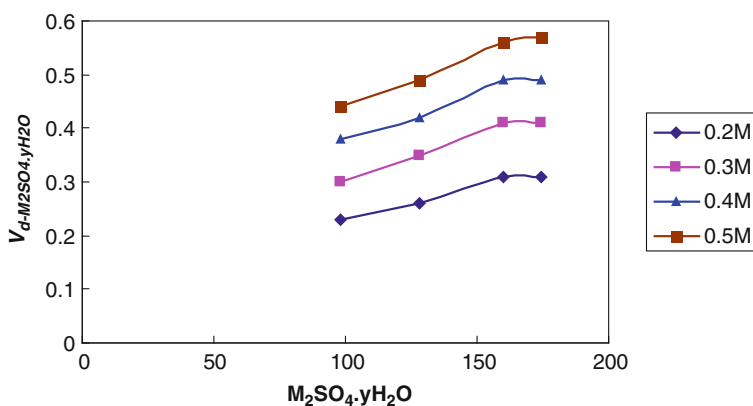


Table 12.4 DTR and MMRSR for diffusing M_2SO_4 - $BaCl_2$ pairs; M being Group 1 metals

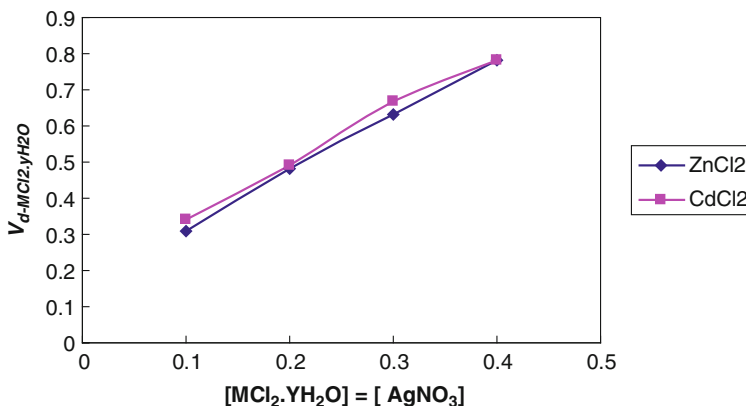
Congenous $M_2SO_4 \cdot yH_2O$	FW, $g\text{mol}^{-1}$	DTR				Average DTR	MMRSR = $\sqrt{\frac{M_2SO_4 \cdot yH_2O}{BaCl_2}}$	FW, diffusing congenus, $g\text{mol}^{-1}$
		0.2 M	0.3 M	0.4 M	0.5 M			
H_2SO_4	98.08	0.68	0.68	0.68	0.66	0.68	0.69 $y = 0$	H_2SO_4 98.08
$Li_2SO_4 \cdot H_2O$	127.96	0.78	0.75	0.79	0.80	0.78	0.78 $y = 1$	$Li_2SO_4 \cdot H_2O$ 127.95
Na_2SO_4	142.04	0.84	0.91	0.89	0.84	0.87	0.88 $y = 1$	$Na_2SO_4 \cdot H_2O$ 160.06
K_2SO_4	174.27	0.90	0.90	0.92	0.92	0.91	0.91 $y = 0$	K_2SO_4 174.27

**Fig. 12.8** Plots of $V_{dM_2SO_4 \cdot yH_2O}$ versus $M_2SO_4 \cdot yH_2O$ molar masses; M being the Group 2 metals

Zinc is an important bioelement; more than 100 zinc enzymes are performing crucial metabolic functions in the human alone. In concentrated solution $ZnCl_2$ exists as six coordinate $ZnCl_2 \cdot 4H_2O$ and $[Zn(H_2O)_6]^{2+}$ [15]. Zn^{2+} ion as a d^{10} system can hold two H_2O molecules with a linear geometry convenient to spearheading a nearby hole in the liquid structure during diffusion [16]. In fact $ZnCl_2$ in these observations appears to travel as a dihydrate (Table 12.5). A close difference (Fig. 12.9) between the velocities of the two chlorides traces the reason for cadmium's presence in most zinc ores [17]. The persistent narrow difference in diffusion rates for an $11.0 g\text{mol}^{-1}$ molar mass difference between $ZnCl_2 \cdot H_2O$ and $CdCl_2$ demonstrates good precision record of the new diffusimetric method. Coincidence in some of the average DTR values of the two chlorides (Table 12.5) is attributed to the value recording in two significant figures.

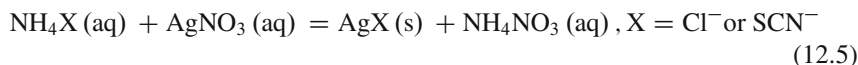
Table 12.5 DTR and MMRSR for MCl_2 - $AgNO_3$ pairs. M are Group 12 metals

Congenus $MCl_2 \cdot yH_2O$	FW, $g\text{mol}^{-1}$	DTR				Average DTR	MMRSR = $\sqrt{\frac{MCl_2 \cdot yH_2O}{AgNO_3}}$	FW, diffusing salt, $g\text{mol}^{-1}$
		0.1 M	0.2 M	0.3 M	0.4 M			
ZnCl ₂	136.39	0.96	1.0	0.93	1.0	1.0	1.0 y = 2	ZnCl ₂ ·2H ₂ O 172.40
CdCl ₂	183.40	0.96	1.0	1.0	1.0	1.0	1.0 y = 0	CdCl ₂ 183.40

**Fig. 12.9** Plots of $V_{dMCl_2 \cdot yH_2O}$ versus $[MCl_2 \cdot yH_2O]$ for MCl_2 - $AgNO_3$ reactions, M being Group 12 metals

12.3.5 Reactions of NH_4Cl and NH_4SCN with $AgNO_3$

Experiments carried out at 297 K



The dissociation constants of NH_4Cl , NH_4^+ , and $HSCN$ in water are infinity, 5.5×10^{-10} , and 0.014 respectively. Evidently hydration of NH_4Cl and NH_4^+ is complete and also that Cl^- is a weak base but SCN^- is strong which in turn suggests as having some covalence in NH_4SCN . Movement of a covalent compound in a polar solvent is sluggish. Hydration of the dissociated NH_4^+ and the covalence in NH_4SCN are both diffusion retarding. Indeed the relative velocities of NH_4SCN in NH_4SCN - $AgNO_3$ pair are significantly low and incidentally equal to those of the low molar mass NH_4Cl in NH_4Cl - $AgNO_3$ pair. Another notable point is that the rates of $AgNO_3$ in NH_4SCN - $AgNO_3$ pair are slightly higher than those in NH_4Cl - $AgNO_3$ pair (Fig. 12.10). It is apparent thus that a slow syngenus can make its congenus rates higher. Moreover in these diffusion controlled reactions

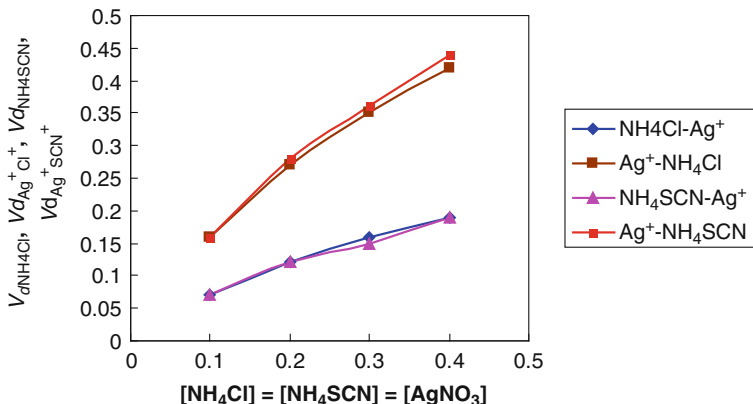


Fig. 12.10 Plots of V_{dNH_4Cl} and V_{dAgNO_3} in $NH_4Cl-AgNO_3$ pair and of V_{dNH_4SCN} and V_{dAgNO_3} in $NH_4SCN-AgNO_3$ pair versus corresponding concentrations of reactants. The expressions for example NH_4Cl-Ag^+ and $NH_4SCN-Ag^+$ on the right of the plot area refer to the relative velocities of NH_4Cl and NH_4SCN respectively with respect to syngenus $AgNO_3$

Table 12.6 DTR, MMRSR and percent DTR decrease from MMRSR for $NH_4X-AgNO_3$ reactions

Congenus NH_4X	FW, $gmol^{-1}$	DTR				Average DTR	MMRSR $= \sqrt{\frac{NH_4X}{AgNO_3}}$	Percent DTR decrease
		0.1 M	0.2 M	0.3 M	0.4 M			
NH_4Cl	53.49	0.44	0.44	0.45	0.45	0.45	0.56	20
NH_4SCN	76.12	0.43	0.44	0.42	0.43	0.43	0.67	36

the closest approach distance between $AgNO_3$ and NH_4SCN is less than that between $AgNO_3$ and NH_4Cl because $AgNO_3$ comes closer to the low outer electron density SCN^- group than it does to high electron density Cl^- ion. Indeed $AgSCN$ is more insoluble than $AgCl$. As such both kinetic and thermodynamic grounds suggest higher velocity to $AgNO_3$ in $NH_4SCN-AgNO_3$ pair than in the other pair (Table 12.6).

12.3.6 Reactions of Fe^{III} Salts with $BaCl_2$, $AgNO_3$, and NH_4SCN

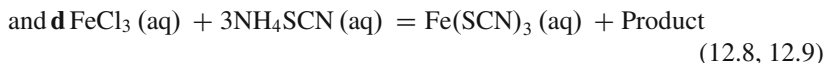
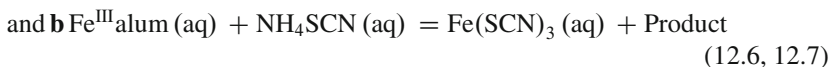


Table 12.7, Rows 1, 2 show that the Fe^{III} alum and FeCl_3 diffuse with no H_2O in keeping with which $\text{Fe}(\text{NO}_3)_3$ is also assigned as having no H_2O molecule (Row 4). For the reactions with syngenus NH_4SCN (Rows 3, 4, and 5) the DTR values are unusually high whereas with the other syngenus reactant NH_4Cl (Rows 1, 2) the values are closely normal. Higher DTR values are due to the lower rates of NH_4SCN (Fig. 12.10) the denominator reactant.

As is known the diffusion controlled reactions show almost similar reaction constants within the range of 10^9 – $10^{10} \text{M}^{-1} \text{s}^{-1}$ and depend little on the nature of the reactants [18]. The percent DTR rise over MMRSR in reactions of $\text{Fe}(\text{NH}_4)(\text{SO}_4)_2$ – NH_4SCN , FeCl_3 – NH_4SCN , and $\text{Fe}(\text{NO}_3)_3$ – NH_4SCN pairs (Table 12.7) are 52, 53, and 54 respectively. Almost similar values reflect the diffusion controlled nature of these reactions and the extent to which the closest approach distances differ. Visibly the closest approach distance is least in $\text{Fe}(\text{NH}_4)(\text{SO}_4)_2$ – NH_4SCN and most in $\text{Fe}(\text{NO}_3)_3$ – NH_4SCN with FeCl_3 – NH_4SCN pair in between. The closest approach distance is governed by factors like steric hindrance and charges on the approaching ions including their peripheral lone pairs in both attractive (Reactions **a** and **c**) and repulsive (Reactions **b** and **d**) encounters as in Figs. 12.11 and 12.12. In the plots (Fig. 12.13) the heavy weight Fe^{III} alum occupies the two upper positions and the comparative light weight FeCl_3 the two lower ones. Incidentally again the velocities of Fe^{III} alum with respect to NH_4SCN and of FeCl_3 with respect to AgNO_3 almost overlap. It may be mentioned that FeCl_3 has a planar structure [19].

12.4 Conclusions

The novel Diffusimeter is a straightforward glassware efficient in determining electrolytes' relative free diffusion velocities and discloses thus a host of their other properties and characteristics. This study observes *inter alia* that the velocity of a solute decreases with increasing diffusion path length and increases with its stopcock bore diameter and temperature. These measurements elegantly reconfirm the law of electrolytic diffusion which contrary to gaseous diffusion manifests direct proportionality between electrolyte's diffusion velocity and square root of its molar mass. It is apparent that a diffusing electrolyte may assume an altogether different hydration number and the orientation of the floating ions. The diffusimetric method termed DTR Model has the prospect of determining among other things the electrolyte concentration, molar mass of a salt, its purity, solvent polarity and diffusion rate, complex composition by continuous variation method, percent covalent character in an ionic compound and accomplishing precipitate crystallization and isotope separation. The closest approach distance between pairs of reacting electrolytes and throwing light on the nature of their electrostatic interactions. The instrument can be used to design interesting and thought inciting chemistry experiments of both qualitative and quantitative nature befitting all levels

Table 12.7 DTR and the molar mass ratio square root of Fe^{III} salt- BaCl_2 , Fe^{III} salt- NH_4SCN , and $\text{Fe}(\text{NO}_3)_3$ - NH_4SCN pairs

Sl	Reactions	FW, congenus	DTR			MMRSR =			FW, diffusing congenus
			0.1 M	0.2 M	0.3 M	0.4 M	$\sqrt{\frac{\text{Fe}^{\text{III}} \text{ salt} \cdot y \cdot H_2O}{\text{AgNO}_3 \cdot \text{BaCl}_2 \cdot \text{NH}_4\text{SCN}}} y = 0$		
1	$\text{Fe}(\text{NH}_4)(\text{SO}_4)_2 \cdot 12\text{H}_2\text{O} + \text{BaCl}_2$	482.25	1.02	1.04	1.05	1.04	1.04	1.04	$\text{Fe}(\text{NH}_4)(\text{SO}_4)_2$ $M = 265.95$
2	$\text{FeCl}_3 \cdot 6\text{H}_2\text{O} + \text{AgNO}_3$	270.30	0.94	0.95	0.92	0.93	0.94	0.94	FeCl_3 $M = 162.21$
3	$\text{Fe}(\text{NH}_4)(\text{SO}_4)_2 \cdot 12\text{H}_2\text{O} + \text{NH}_4\text{SCN}$	482.25	2.98	2.88	2.84	2.84	2.89	2.89	$\text{Fe}(\text{NH}_4)(\text{SO}_4)_2$ $M = 265.95$
4	$\text{Fe}(\text{NO}_3)_3 \cdot 9\text{H}_2\text{O} + \text{NH}_4\text{SCN}$	404.00	2.84	2.79	2.79	2.71	2.78	2.78	$\text{Fe}(\text{NO}_3)_3$ $M = 241.83$
5	$\text{FeCl}_3 \cdot 6\text{H}_2\text{O} + \text{NH}_4\text{SCN}$	270.30	2.37	2.40	2.24	2.14	2.29	2.29	FeCl_3 $M = 162.21$

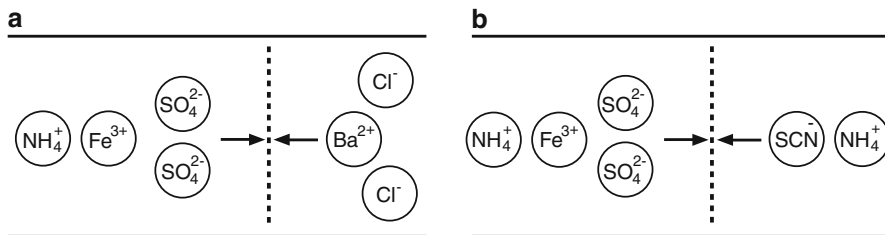


Fig. 12.11 Schematic encounters in diffusion controlled reactions: (a) for attractive encounter between Fe^{III} alum and BaCl_2 and (b) for repulsive encounter between Fe^{III} alum and NH_4SCN

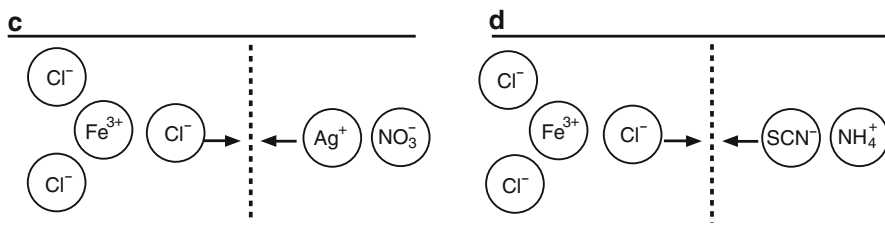


Fig. 12.12 Schematic encounters in diffusion controlled reactions: (c) for attractive encounter between FeCl_3 and AgNO_3 and (d) for repulsive encounter between FeCl_3 and NH_4SCN

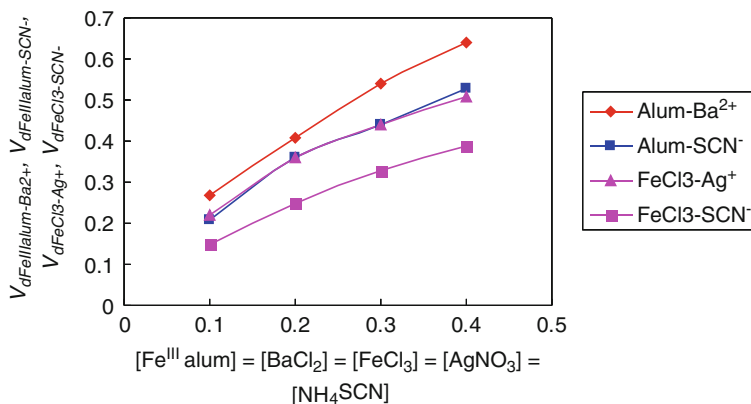


Fig. 12.13 Plots of $V_{d\text{Fe}^{\text{III}}\text{ alum}}$ and $V_{d\text{FeCl}_3}$ versus $[\text{Fe}(\text{NH}_4)(\text{SO}_4)_2]$ and $[\text{FeCl}_3]$ respectively. Velocities of $\text{Fe}(\text{NO}_3)_3$ with respect to NH_4SCN are excluded in the plot area for clarity

of chemistry education and making chemistry more computational. Finally the electrolytic diffusion law is not new but its exposition to a whole variety of chemical investigations is certainly novel.

References

1. Graham TH (1883) *Philos Mag J Sci* 175–191; 269–276; 351–358
2. Fick A (1855) *Philos Mag* 10:30
3. Narasimhan TN (2004) Fick's insights on liquid diffusion. *EOS Trans Am Geophys Union* 85(499):501
4. Shaw DJ (1992) *Introduction to colloid and surface chemistry*, 4th edn. Butterworth and Heinemann Ltd., London, 26
5. Jacobs MH (1967) *Diffusion processes*. McGraw-Hill, New York, p 1374
6. Khair A, Golzar Hossain GM, Saiful Alam M, Zakir Hossain Shaheen M (2010) Bangladesh Patent, Int. Cl⁵ G01N 13/00, 1004924, 18-Dec-2007
7. Emsley J (1991) *The elements*, 2nd edn. Oxford University Press, New York, p 88
8. Shriver DF, Atkins PW, Langford CH (1991) *Inorganic chemistry*. Oxford University Press, Oxford, p 608
9. Cotton FA, Wilkinson G, Gaus L (1987) *Basic inorganic chemistry*, 2nd edn. Wiley, New York, p 271
10. Cotton FA, Wilkinson G (1972) *Advanced inorganic chemistry*, 3rd edn. Interscience, New York, p 217
11. Matwiyoff NA, Taube H (1968) *J Am Chem Soc* 90:2796
12. Nakamura S, Meiboom S (1967) *J Am Chem Soc* 89:1765
13. Hatashi H, Sarkari M, Zeinali M, Zare Aliabadi H (2010) *Austr J Basic Appl Sci* 4:4766–4771
14. Lewis RJ Sr (1993) *Hawley's condensed chemical dictionary*, 12th edn. Van Nostrand Reinhold, New York, p 1110
15. Cotton FA, Wilkinson G, Murillo CA, Bochmann M (1999) *Advanced inorganic chemistry*, 6th edn. Wiley Interscience, New York, p 605
16. King EL (1964) *How chemical reactions occur*. W. A Benjamin, New York, p 65
17. Partington JR (1965) *A textbook of inorganic chemistry*, 6th edn. ELBS and Macmillan & Co Ltd., London, p 784
18. Katakis D, Gordorn G (1987) *Mechanisms of inorganic reactions*. Wiley, New York, p 72
19. Wells AF (1993) *Structural inorganic chemistry*, 5th edn. Oxford Science, New York, p 444

Chapter 13

Reverse Phase Extraction Chromatographic Separation of Trivalent Bismuth Using Liquid Anion Exchanger

Sachin R. Phule, Haribhau R. Aher, Shamrao P. Lawande,
and Shashikant R. Kuchekar

Abstract The extraction behavior of bismuth(III) was studied with *N-n*-octylaniline as a function of parameters viz. concentration of mineral acid, reagent, eluents and elution time. A selective, sensitive, less expensive and more precise method has been developed for the extraction chromatographic separation of bismuth(III) and its separation from several metal ions with *N-n*-octylaniline (liquid anion exchanger) as a stationary phase on silica as solid support. The quantitative extraction of bismuth(III) was found at 0.087 mol/L *N-n*-octylaniline and 0.7 mol/L hydrochloric acid media. The extracted bismuth(III) was eluted from the column with acetate buffer and analyzed spectrophotometrically with potassium iodide method. The proposed method is free from interferences from a large number of cations and anions. The method was applied for separation of bismuth(III) from binary mixtures with lead(II), copper(II) and manganese(II). The method was also extended for separation of bismuth(III) from synthetic alloy mixtures. The log-log plot of *N-n*-octylaniline concentration versus the distribution coefficient indicates that the probable extracted species is $[(RR'NH_2^+)_2BiCl_5^{2-}]_{(org)}$.

13.1 Introduction

Bismuth is one of the most abundant elements in the earth crust. The bismuth produced in the U.S. is obtained as a by-product in the refining of lead, copper, tin, silver and gold ores. Bismuth forms low melting alloys and these are widely

S.R. Phule • H.R. Aher • S.R. Kuchekar (✉)

P.G. Department of Analytical Chemistry, P. V. P. College Pravaranagar, At/Po. Loni (Kd), Tal. Rahata, Dist. Ahmednagar 413713, Maharashtra, India
e-mail: sachinphule55@yahoo.co.in; h_aher@yahoo.com; shashi17@gmail.com

S.P. Lawande

Department of Chemistry, Shri Chhatrapati Shivaji College, Shrigonda

used for safety devices in fire detection and extinguishing systems. The metal is used in the production of malleable iron and it is also used as a catalyst for making acrylic fibers. Bismuth and its compounds are used in semi-conductors, alloys and metallurgical additives.

The principal consumer of bismuth is the manufacture of pharmaceutical chemicals. Nearly 70% of its production is used for this purpose. Bismuth is the least toxic of all the heavy metals. Sub-carbonates and sub-gallates of bismuth are used in the treatment of diarrhea, dysentery and radiology. Bi-213 is used for cancer and leukemia treatment, because it has slight radioactive property. In view of its wide range of applications, it is essential to develop an innovative, fast, accurate and precise analytical method for its separation.

Reverse phase extraction chromatography is an extremely versatile technique and it has been applied successfully for the separation of various metals [1–4]. Liquid-liquid extraction is one of the most popular techniques employed for the recovery of bismuth(III). Extraction separation study of bismuth(III) from acidic media with *N-n*-octylaniline [5] and aliquot 336-S has been carried out [6, 7]. Bismuth(III) was extracted quantitatively from 0.004 to 0.007 mol/L sodium succinate solution at pH 2.5–10 using 0.036 mol/L 2-octylaminopyridine (2-OAP) in chloroform. The metal has been recovered by stripping with 3×10 mL 0.5 M nitric acid [8]. *N-n*-hexylaniline [9] in xylene was used for extraction separation studies of bismuth(III) from thiocyanate and sulphuric acid media, in a method where associated elements were not separated. Quantitative extraction of bismuth was achieved from 0.5 to 3.0 mol dm⁻³ in hydrochloric acid media with cyanex 301 in toluene [10]. Cyanex 302 in toluene was used as a extractant for the separation of antimony(III) from bismuth(III), lead(II), gallium(III), thallium(III), tellurium(IV) and tin(IV) [11]. Tetramethylammonium iodide in chloroform was used for the extraction of bismuth(III) before its oxidation to bismuthate with potassium periodate at pH 7.0–8.0 [12]. Quantitative separation of bismuth was observed from lead, cadmium and other elements by anion exchange chromatography, using hydrobromic acid-nitric acid for elution [13].

In our laboratory *N-n*-octylaniline was recently employed for solvent extraction separation of bismuth(III) [14] and lead(II) [15]. *N-n*-octylaniline was also used for reversed phase column chromatographic separation of zinc(II), cadmium(II), mercury(II) and bismuth(III) [16]. Mutual separation scheme has been developed for separation of palladium, platinum and iridium by taking advantage of strong acid and weak acid media [17]. Extraction chromatographic separation of platinum(IV) was achieved in ascorbic acid media at pH 1.0 [18]. Iridium was quantitatively extracted from 1.0 mol/L hydrochloric acid and was eluted using 2.0 mol/L hydrochloric acid [19]. Method was applied for separation of iridium from alloys. Manganese was separated from alloys in weak acid media at pH 10.5 and was eluted from column with 0.2 mol/L nitric acid [20].

The use of this reagent is found to be advantageous as it can be synthesized at low cost, with high yield and of best purity. In the present communication, a simple, selective, sensitive, less expensive and more precise method is developed

for the extraction chromatographic separation of bismuth(III) at 0.087 mol/L *N-n*-octylaniline in a 0.7 mol/L hydrochloric acid media and the metal was eluted with acetate buffer solution.

13.2 Experimental

13.2.1 Apparatus

An Elico spectrophotometer model SL-159 with 10 mm path length quartz cell was used for the absorbance measurements.

13.2.2 Reagents

The stock solution of bismuth(III) was prepared by dissolving 1.170 g bismuth(III) nitrate [Bi(NO₃)₃, Loba Chemicals] in 4.0 ml concentrated nitric acid and diluted to 100 ml using distilled water. The solution was standardized using gravimetric method [21]. A working solution containing 100 µg/mL bismuth(III) was prepared by further dilution. Analytical grade sodium acetate trihydrate, hydrochloric acid and acetic acid were used as per requirements. Other standard solutions of different metal ions used for study of effect of foreign ions were prepared by dissolving their corresponding salts in dilute hydrochloric acid. The solutions of anions were prepared by dissolving respective sodium salts in distilled water. The *N-n*-octylaniline was synthesized using the method reported by Gardlund et al. [22] and its dilutions were prepared in chloroform.

13.2.3 Preparation of Anion Exchange Material

Silica gel (60–120 mesh) obtained from British Drug House India Ltd., was dried at 120°C for 2–3 h and stored in desiccators. It was packed in a U-tube through which a stream of nitrogen gas has been passed and bubbled through a small Durand bottle containing about 20.0 ml dimethyldichlorosilane (DMCS) (Acros Organics, New Jersey, USA). The passage of DMCS vapors flowed continuously for 4 h. The silica gel was washed with anhydrous methanol and then dried [18]. A portion of 5.0 g silanated silica gel was soaked with 0.087 mol/L *N-n*-octylaniline which was previously equilibrated with 0.7 mol/L hydrochloric acid for 10 min, then solvent was evaporated to get a nearly dried gel. The slurry of *N-n*-octylaniline coated silica gel in distilled water was prepared by centrifugation at 2,000 r/min. Then the coated silica gel was packed into a chromatographic column made from borosilicate glass tube, having bore 8 mm, length 30 cm, fitted with glass-wool plug at the bottom, to give a bed height of 6.0 cm. The bed was then covered with a glass wool plug.

13.2.4 General Procedure for Extraction of Bismuth(III)

An aliquot solution containing 200 μg bismuth(III) was made up to 25.0 ml by adjusting the concentration of hydrochloric acid to 0.7 mol/L. It was passed through the column containing 0.087 mol/L *N-n*-octylaniline coated on silica gel at a flow rate of 1.0 ml/min previously equilibrated with 25 ml of 0.7 mol/L hydrochloric acid. After extraction, bismuth(III) was eluted with 25.0 ml acetate buffer and determined by spectrophotometric method [23].

13.3 Results and Discussion

13.3.1 Extraction as a Function of Acid Concentration

The effect of hydrochloric acid concentration on the percentage extraction of bismuth(III) was studied in the range 0.05–3.0 mol/L on the column coated with 0.087 mol/L *N-n*-octylaniline as the stationary phase (Fig. 13.1). The extraction of bismuth(III) was found to be quantitative from 0.7 to 3.0 mol/L hydrochloric acid. Therefore 0.7 mol/L concentration of hydrochloric acid was used throughout the work.

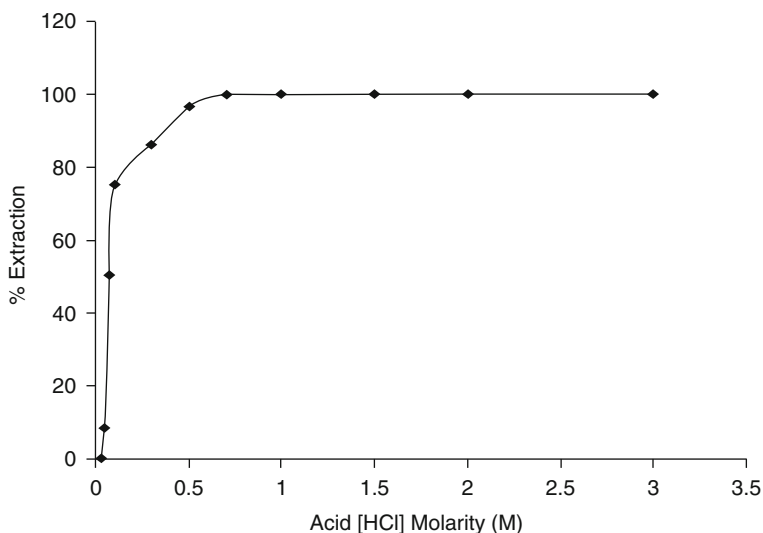


Fig. 13.1 Extraction of bismuth(III) as a function of hydrochloric acid concentration

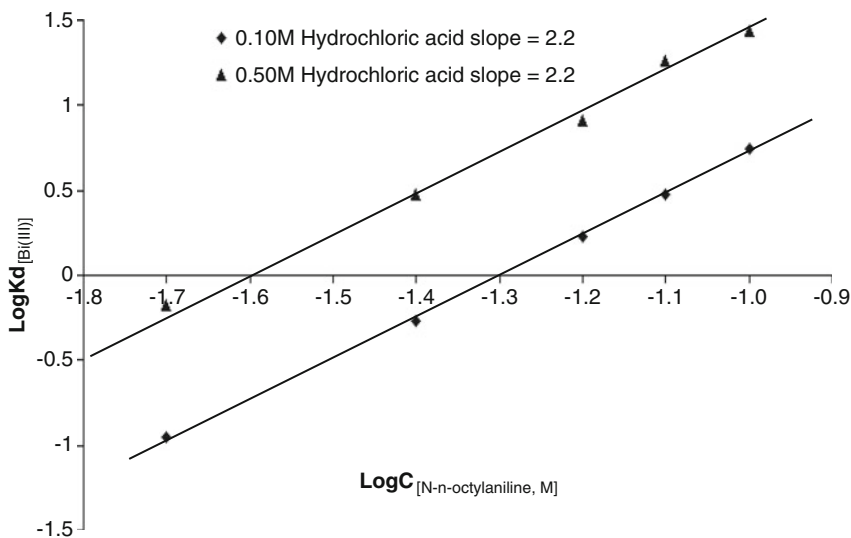


Fig. 13.2 Log-log plots of distribution coefficient versus *N-n*-octylaniline concentration at 0.1 and 0.5 mol/L hydrochloric acid

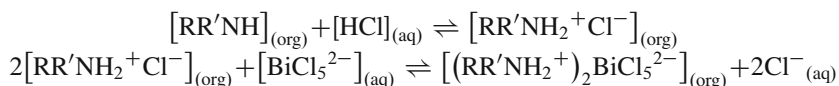
13.3.2 Extraction as a Function of Flow Rate

The effect of flow rate on percentage extraction of bismuth(III) was studied from 0.5 to 3.0 ml/min by keeping all other parameters constant. It was observed that the percentage extraction decreased with an increase in flow rate. Therefore the flow rate was kept at 1.0 ml/min for further extraction studies.

13.3.3 Extraction of Bismuth(III) as a Function of *N-n*-Octylaniline Concentration

The concentration of *N-n*-octylaniline in chloroform was varied from 0.022 to 0.109 mol/L while the concentration of hydrochloric acid was varied in the range from 0.03 to 3.0 mol/L for extraction of bismuth(III). It was found that for quantitative extraction of bismuth(III), 0.087 mol/L *N-n*-octylaniline was sufficient in 0.7 mol/L hydrochloric acid medium. The percentage extraction of bismuth(III) increases with increase in concentration of *N-n*-octylaniline. Log-log plot of *N-n*-octylaniline concentration versus distribution coefficient at 0.1 and 0.5 mol/L hydrochloric acid gives slopes of 2.2 and 2.2 respectively (Fig. 13.2). The probable

composition of extracted species was calculated as 1:2 (metal to amine ratio). The extraction mechanism can be explained as follows:



where $\text{R} = -\text{C}_6\text{H}_5$ and $\text{R}' = -\text{CH}_2(\text{CH}_2)_6\text{CH}_3$

13.3.4 Effect of Eluents

The elution of bismuth(III) was studied using various eluents. Metal ion was eluted quantitatively with acetate buffer. The elution of bismuth(III) was also studied with ammonia-ammonium chloride buffer, ammonia-ammonium nitrate buffer, sodium hydroxide (0.05–1.0 mol/L) and ammonia (0.1–0.3 mol/L). Maximum elution of bismuth(III) was observed in ammonia-ammonium chloride buffer 6.8%, ammonia-ammonium nitrate buffer 43.8%, sodium hydroxide 66.0% and ammonia 87.8%. Acetate buffer was used for elution of bismuth(III) in further studies.

13.3.5 Effect of Foreign Ions

Various quantities of foreign ions were added to a fixed amount of bismuth(III) (200 μg) to study the effect of interference according to the recommended procedure. The tolerance limit was set at the amount required to cause $\pm 1.5\%$ error in the recovery of bismuth(III) (Table 13.1). It was observed that the method was free from interference from a large number of cations and anions. The only cation showing interference in the method is chromium(VI).

13.4 Applications

13.4.1 Separation of Bismuth(III) from Synthetic Alloy Mixtures

The validity of the method was confirmed by applying it for the separation of bismuth(III) from synthetic alloy mixtures. The composition of alloys has been prepared for sealing alloy, wood-metal alloy, lead-bismuth alloy, bismuth solder alloy and tin bismuth alloy in laboratory. The proposed method has been applied for the separation of bismuth(III) (Table 13.2). The results obtained are in agreement with the certified values.

Table 13.1 Effect of foreign ions

Foreign ion	Added	Tolerance limit/ μg	Foreign ion	Added	Tolerance limit/ μg
Sb(III)	Sb_2O_3	300	Hg(II)	HgCl_2	300
Cu(II)	$\text{CuSO}_4 \cdot 5\text{H}_2\text{O}$	250	W(IV)	$\text{Na}_2\text{WO}_4 \cdot 2\text{H}_2\text{O}$	200
Mn(II)	$\text{MnCl}_2 \cdot 6\text{H}_2\text{O}$	300	In(III)	InCl_3	300
V(V)	V_2O_5	300	Ni(II)	$\text{NiCl}_2 \cdot 6\text{H}_2\text{O}$	300
U(VI)	$\text{UO}_2(\text{NO}_3)_2 \cdot 6\text{H}_2\text{O}$	150	Ir(III)	$\text{IrCl}_3 \cdot x\text{H}_2\text{O}$	250
Tl(III)	$\text{Tl}(\text{NO}_3)_3$	200	Fe(II)	$\text{FeSO}_4 \cdot 7\text{H}_2\text{O}$	300
Zn(II)	$\text{ZnSO}_4 \cdot 7\text{H}_2\text{O}$	300	Pb(II)	$\text{Pb}(\text{NO}_3)_2$	300
Cd(II)	$3\text{CdSO}_4 \cdot 8\text{H}_2\text{O}$	250	Os(VIII)	OsO_4	100
Sn(II)	SnCl_2	300	Rh(III)	$\text{RhCl}_3 \cdot x\text{H}_2\text{O}$	200
Mo(VI)	$(\text{NH}_4)_6\text{Mo}_7\text{O}_{24} \cdot 2\text{H}_2\text{O}$	300	Ru(III)	$\text{RuCl}_3 \cdot x\text{H}_2\text{O}$	250
Ag(I)	AgNO_3	300	EDTA	Disodium salt	250
Mg(II)	$\text{MgCl}_2 \cdot 6\text{H}_2\text{O}$	300	Tartrate	$\text{C}_6\text{H}_6\text{O}_6$	300
Fe(III)	FeCl_3	300	Malonate	$\text{CH}_2(\text{COONa})_2$	300
Co(II)	$\text{CoCl}_2 \cdot 6\text{H}_2\text{O}$	300	Oxalate	$(\text{COOH})_2 \cdot 2\text{H}_2\text{O}$	300
Ti(IV)	TiO_2	300	Succinate	$(\text{CH}_2\text{COONa})_2 \cdot 6\text{H}_2\text{O}$	300
Ga(III)	GaCl_3	300	Citrate	$\text{C}_6\text{H}_8\text{O}_7 \cdot \text{H}_2\text{O}$	300
Al(III)	AlCl_3	200	Thiourea	SCN_2H_4	300
Au(III)	$\text{HAuClO}_4 \cdot \text{H}_2\text{O}$	300			

Bi(III): 200 μg ; Hydrochloric acid 0.7 mol/L; Eluent: acetate buffer; *N-n*-octylaniline concentration 0.087 mol/L; Flow rate 1.0 mL/min

13.4.2 Separation of Bismuth(III) from Binary Mixtures ($n = 3$)

Synthetic binary mixtures of bismuth(III) with lead(II), copper(II) and manganese(II) were prepared. The separation of these mixtures was carried out using proposed method. The results are reported in Table 13.3.

13.5 Conclusions

The developed method is very simple, selective, reproducible and rapid. This method requires less time for separation of bismuth. It permits selective separation of bismuth(III) from other metals such as lead(II), copper(II) and manganese(II). Method is free from the interferences from a large number of foreign ions, which are associated with bismuth(III) in its natural occurrence. Low reagent and acid concentrations, small quantity of organic solvents are required for quantitative recovery of bismuth(III). Validity of method was confirmed by analyzing synthetic alloy mixtures and results were in good agreement with amount taken in synthetic mixture. Silica gel was used as good solid support because it was highly stable.

Table 13.2 Analysis of bismuth(III) from synthetic alloy mixtures

Composition of alloy/ μg	Bi(III) certified/ μg	Bi(III) found/ μg	Mean/ μg ($n = 3$)	Recovery/% ($n = 3$)	RSD/% ($n = 3$)
Sealing alloy Bi 58; Pb 36; Sb 6	58.0	57.8 57.8 57.9	57.8	99.7	0.10
Wood metal alloy Bi 50; Pb 26; Sn 13.3; Cd 10	50.0	49.7 49.8 49.8	49.8	99.6	0.12
Lead bismuth alloy Pb 84.6; Bi 15.4	15.4	15.2 15.3 15.3	15.3	99.4	0.38
Bismuth solder alloy Bi 27.5; Pb 27.5; Sn 45	27.5	27.4 27.3 27.3	27.3	99.3	0.21
Tin bismuth alloy Sn 75; Bi 25	25.0	24.8 24.9 24.7	24.8	99.2	0.40

Bi(III): (200 μg), Hydrochloric acid 0.7 mol/L; Eluent: Acetate buffer. *N-n*-octylaniline concentration 0.087 mol/L; Flow rate 1.0 mL/min

Table 13.3 Separation of bismuth(III) from binary mixtures

Mixture	Chromogenic ligand	Taken/ μg	Found/ μg	Recovery/%	% RSD
Bi(III) + Pb(II)	KI	200.0	199.78	99.9	0.13
	PAR	200.0	199.81	99.9	0.17
Bi(III) + Cu(II)	KI	200.0	199.24	99.6	0.31
	Rubeanic acid	200.0	199.81	99.9	0.19
Bi(III) + Mn(II)	KI	200.0	199.59	99.8	0.18
	Ammonium persulfate	200.0	199.69	99.8	0.15

*Bismuth(III) gets extracted and lead(II), copper(II) and manganese(II) remain in aqueous phase.

*Means *N-n*-octylaniline 0.087 mol/L; Eluent 25 mL acetate buffer; Hydrochloric acid 0.7 mol/L; Flow rate 1.0 mL/min

Acknowledgements The authors are thankful to the Management, Pravara Rural Education Society and Principal, P.V.P. College Pravaranagar for providing necessary facilities in the department. The authors are also thankful to BCUD University of Pune for providing financial assistance in the form of research project.

References

1. Mandal B, Ghosh N (2008) Extraction chromatographic separation of Ga(III) with the high molecular mass liquid cation exchanger SRS-100. *Indian J Chem A* 47:1041–1046
2. Mandal B, Roy US (2008) Extraction chromatographic method of preconcentration and separation of lead(II) with high molecular mass liquid cation exchanger, Versatic 10. *Indian J Chem A* 47:1497–1502

3. Kokate SJ, Kuchekar SR (2010) Reversed phase extraction chromatographic separation of ruthenium(III). *J Saudi Chem Soc* 14:41–47
4. Aher HR, Kuchekar SR (2008) Extraction chromatographic studies of gallium(III), indium(III) and thallium(III) with *n*-octylaniline. *Indian J Chem Technol* 15:403–408
5. Mulik GN, Kuchekar SR, Chavan MB (1986) Solvent extraction of zinc(II), indium(III), thallium(III) and bismuth(III) with *n*-octylaniline from hydrochloric acid media and their separation. *Indian J Chem A* 25:1073–1074
6. Sahoo SK (1991) Extractive-chromatographic separation of bismuth with aliquot 336S from citrate solutions. *Talanta* 38:789–792
7. Vibhute CP, Khopkar SM (1992) Separation of molybdenum as ascorbate complex by extraction with aliquot 336S from associated elements. *Fresen J Anal Chem* 344:555–556
8. Mane CP, Anuse MA (2008) Studies on liquid-liquid extraction and recovery of bismuth(III) from succinate media using 2-octylaminopyridine in chloroform. *J Chin Chem Soc* 55:807–817
9. Throat RB, Burungale AS, Patil NBK (2009) Liquid-liquid extraction and separation of bismuth(III) with *N-n*-hexylaniline. *Rasayan J Chem* 2:1–8
10. Argekar AP, Shetty AK (1995) Extraction and spectrophotometric determination of bismuth with cyanex 301. *Analyst* 120:1819–1822
11. Vartak SV, Gaudh JS, Shinde VM (1997) Analytical separation of antimony(III) from bismuth(III), lead(II), gallium(III), thallium(III), tellurium(IV) and tin(IV) with cyanex 302. *Mikrochim Acta* 127:41–44
12. El-Shahawi MS, Aldhaheeri SM (1996) Spectrophotometric determination of bismuth(III and V) in water after ion-pair liquid-liquid extraction using tetramethylammonium cation as counter ion. *Fresen J Anal Chem* 354:200–203
13. Strelow FEW, van der Walt TN (1981) Quantitative separation of bismuth from lead, cadmium and other elements by anion exchange chromatography with hydrobromic acid-nitric acid elution. *Anal Chem* 53:1637–1640
14. Kokate SJ, Shelar YS, Aher HR, Kuchekar SR (2010) Liquid-liquid extraction and recovery of bismuth(III) from hydrochloric acid media using *n*-octylaniline in chloroform. *Bulg Chem Commun* 42:107–112
15. Aher HR, Gunjal PS, Kuchekar SR, Chavan MB (1998) Solvent extraction of lead(II) and its separation from bismuth(III). *Asian J Chem* 10:43–45
16. Kuchekar SR, Aher HR, Chavan MB (2003) Solvent extraction of zinc(II), cadmium(II), mercury(II) and bismuth(III) from *n*-octylaniline and their separation. *Indian J Chem* 42A:1674–1676
17. Kokate SJ, Aher HR, Kuchekar SR (2009) Reversed phase extraction chromatographic separation of palladium(II) using liquid anion exchanger. *Bulg Chem Commun* 41:272–276
18. Kokate SJ, Kuchekar SR (2009) Extraction chromatographic separation of platinum(IV) from real samples and associated metals. *Chin J Chromatogr* 27:809–814
19. Kokate SJ, Aher HR, Kuchekar SR (2009) Reversed phase extraction chromatographic separation of trivalent iridium using liquid anion exchanger. *Anal Chem Indian J* 8:575–579
20. Phule SR, Shelar YS, Kuchekar SR (2010) Reversed phase partition chromatographic separation of divalent copper with *N-n*-octylaniline on silica gel. *Anal Chem Indian J* 15:209–213
21. Vogel AI (1961) A text book of quantitative inorganic analysis, 3rd edn. Longman, London, p 491
22. Gardlund ZG, Curtis RJ, Smith GW (1973) Influence of molecular structural changes on the mesomorphic behavior of benzilideneanilines. *Liq Cryst Ord Fluids* 2:541–556
23. Sandell EB (1965) In: Clarke BL, Elving PJ, Kolthoff IM (eds) Colorimetric determination of traces of metals, vol 3. Interscience, New York, pp 335–336

Chapter 14

Dry Sliding Wear Behavior of Ultrafine-Grained Mild Steel Processed Using Multi Axial Forging

Aditya K. Padap, Gajanan P. Chaudhari, and Sumeer K. Nath

Abstract Bulk nanostructured and ultra-fine grained (UFG) steels obtained by severe plastic deformation are of great interest for structural applications because of their enhanced hardness, strength and adequate ductility. For such steels to find wider applications, study of their wear behavior is necessary. In the present work, mild steel (MS) was severely deformed by warm multiaxial forging (MAF) technique using up to nine MAF passes in order to obtain UFG microstructure. After nine MAF passes, the initial ferrite grains of average 17 μm size reduced to about 0.5 μm . Change in strain paths and a higher strain rate employed in MAF resulted in fragmentation and refinement of pearlitic cementite to less than 200 nm size particles. The wear test results showed that strengthening of mild steel by warm MAF processing did not lead to any improvement in wear resistance. The results have been explained on the basis of its microstructural features and pull-off work.

14.1 Introduction

Severe plastic deformation (SPD) processes are used to develop UFG materials. These have much higher hardness when they possess UFG microstructure as compared to their coarse grained (CG) microstructure. Hence, they are expected to have higher wear resistance. These materials might be used as wear resistant parts like bearings, gears [1] and fasteners. But few existing studies [2, 3] have shown that there is no simple and direct relation between hardness and wear resistance. Kluge et al. [2] conducted experiments on six different steels having different microhardness and concluded that the wear resistance is not a simple function of the increase in microhardness. Similarly Kim and Kim [3] studied the effect of ductility

A.K. Padap • G.P. Chaudhari • S.K. Nath (✉)
Department of Metallurgical and Materials Engineering, Indian Institute of Technology, Roorkee,
247667 Uttarakhand, India
e-mail: chaudfmt@iitr.ernet.in; indiafmt@iitr.ernet.in

on dry sliding wear behavior of AISI 1045 steel and found that the specimen with higher ductility showed a higher wear resistance than the specimen with lower ductility though their hardness values are similar.

Since SPD of metals has an effect on hardness as well as on ductility, it is important to analyze critically all the literature related to wear behavior of metals that have undergone SPD. Only a few studies have been reported on wear behavior of UFG materials made by SPD. La et al. [1] in their work concluded that wear resistance of UFG Ti increased as compared to the CG counterpart while the friction coefficient is not affected much by the applied load. Higher strength, hardness, and lower ductility of UFG Ti, led to the wear mechanisms of micro-ploughing and delamination. In the ECAP processed UFG Ti, a lower adhesion component and lower friction coefficient and consequently a higher wear resistance are reported [4].

Higher strength and hardness of UFG Ti is also the reason for higher wear resistance as compared to CG Ti. Also, the dry sliding wear resistance of an Al-bronze alloy after equal channel angular extrusion (ECAE) was significantly improved [5]. This was ascribed to improved strength and hardness of the UFG material. Further, the wear mechanism changed from adhesive wear for CG material to abrasive wear for UFG Al bronze.

Wear resistance of UFG steel and cp aluminum obtained by equal channel angular processing (ECAP) and accumulative roll bonding (ARB), respectively was found to be lower than their CG as-received materials [6]. In another study on commercial 5052 and 5083 Al alloys refined by ARB to 200 nm grain size, the dry sliding wear resistance of the UFG Al alloys was lower than that of the as-received CG alloys [7]. This was attributed to non-equilibrium and unstable grain boundaries and low strain hardening capability of the UFG alloys. The ECAE processing of titanium improved the strength significantly; however, it had no significant effect on the dry sliding adhesive wear behavior of UFG Ti [8, 9].

In view of the contradictory observations on wear resistance of UFG materials, the primary focus of present study is to understand the role of microstructural changes in UFG steel on the friction and wear characteristics of mild steel. The tribological behavior of annealed and MAF processed mild steel has been investigated under dry sliding wear. The results have also been discussed to develop a coherent understanding of the tribological characteristics of this steel in terms of change in microstructure and mechanical properties resulting from the MAF process.

14.2 Experimental Procedure

14.2.1 *Multiaxial Forging*

AISI 1016 steel having chemical composition (wt percent) of 0.15 C, 0.87 Mn, 0.21 Si, 0.024 P, and 0.012 S and balance iron is used in the present study. Samples were machined into prismatic shape of size 20 mm × 16.33 mm × 13.33 mm. The

dimensional ratio of samples for MAF is 1.5:1.22:1.0. All samples were annealed at 920°C for 60 min to obtain uniform initial microstructure. Successive uniaxial compressions of $\epsilon = -0.4$ were applied to the longest side at each strain step. Assuming volume conservation and material isotropy, this procedure enables the initial dimensional ratio to be maintained at the end of each pass [10]. Samples were heated at 500°C before they were alternately forged, after furnace holding time of 50 min, with loading direction changed through 90°. Graphite powder was used for lubrication during forging. At large strains, use of graphite lubrication causes relatively homogeneous deformation [11]. Forging was performed at a strain rate of approximately 10 s⁻¹. Strain in each forging pass was about -0.4. The samples were quickly cooled in water after each pass of forging.

14.2.2 Microstructural Characterization

CG annealed sample was microstructurally characterized using a Leica DMI 5000M optical microscope. UFG material prepared by MAF was observed under a FEI Quanta 200 FEG scanning electron microscope (SEM). A FEI Tecnai 20 G² S-Twin transmission electron microscope (TEM) operated at 200 kV was used for TEM work. Thin foils for TEM investigation were twinjet electropolished in a 10% perchloric acid and 90% glacial acetic acid at room temperature.

14.2.3 Mechanical Characterization

Hardness tests were performed using a FIE-VM50 PC Vickers hardness tester by employing 30 kg load. At least five hardness readings were taken and the average is reported along with standard deviation. Tensile tests (H25 K-S Tinius Olsen) were performed on the small size samples with 8 mm gauge length and total length of 17 mm [12]. The width and thickness in the gauge length were 1.5 and 0.75 mm, respectively.

14.2.4 Dry Sliding Wear Test

Cylindrical pin samples (20 mm height, 5 mm diameter) were prepared from annealed material (CG) and the UFG material obtained by MAF (pass 9). Pin samples used for wear tests had flat surfaces in the contact region and were slightly rounded at the corner. These surfaces were polished using 4/0 grade of emery paper followed by cleaning with acetone.

A pin-on-disc machine (M/s DUCOM, Bangalore India) fitted with a hardened and polished disc made of En-32 steel (HRC 62–65 hardness) was used as a

counterface for dry sliding wear. Weight loss of pin samples was measured at different intervals of sliding time. Weight-loss data are converted to volume-loss data using a value of 7.88 g cm^{-3} for density of steel. The pin was removed from the holder after a definite sliding time interval, weighed, and fixed again in exactly the same position in the holder so that the orientation of the pin remained unchanged.

Weighing was performed using an electronic balance (Mettler AJ100) having an accuracy of 1×10^{-4} g. The weight of the test pin was measured after intervals of 10, 10, 10, 15, 30, and 45 min of sliding time. A constant sliding speed of 1 ms^{-1} was used. Pin samples were tested at three normal loads viz. 14.7, 24.5, and 34.3 N. The wear tests were performed in a room having relative humidity of 40–60%, at temperature of $24 \pm 1^\circ\text{C}$. Wear surfaces of the pins were observed under the SEM.

14.3 Results and Discussion

14.3.1 *Microstructural Evolution*

Optical microstructure of samples annealed at 920°C for 60 min is shown in Fig. 14.1a. It shows equiaxed ferrite grains with pearlite colonies. The average grain size of the annealed steel, determined using linear intercept method, is $17 \mu\text{m}$. Optical micrograph of steel sample MAFed using nine MAF passes is shown in Fig. 14.1b. In this UFG steel, several deformation features are observed in pearlite colonies. It shows extensive fragmentation of pearlitic cementite into ultrafine submicron size particles that also appear rounded in ferritic matrix. Bright field TEM micrograph of the specimen MAFed using nine MAF passes is shown in Fig. 14.1c. It shows that equiaxed ultrafine grains of average size $0.5 \mu\text{m}$ have been obtained. It shows that submicron size grains are obtained after nine passes of warm MAF.

14.3.2 *Mechanical Properties*

Vickers hardness was measured for MAFed samples. Hardness values at different locations on the samples were quite close, confirming a uniform development of microstructure after warm MAF. Hardness increases rapidly with increase in the number of MAF passes at an early stage of MAF, i.e. from 130 VHN at zeroth MAF pass (annealed) to 244 VHN at third MAF pass, an increase by about 90%. However, beyond third MAF pass, the hardness increased marginally with further increase in number of MAF strain steps.

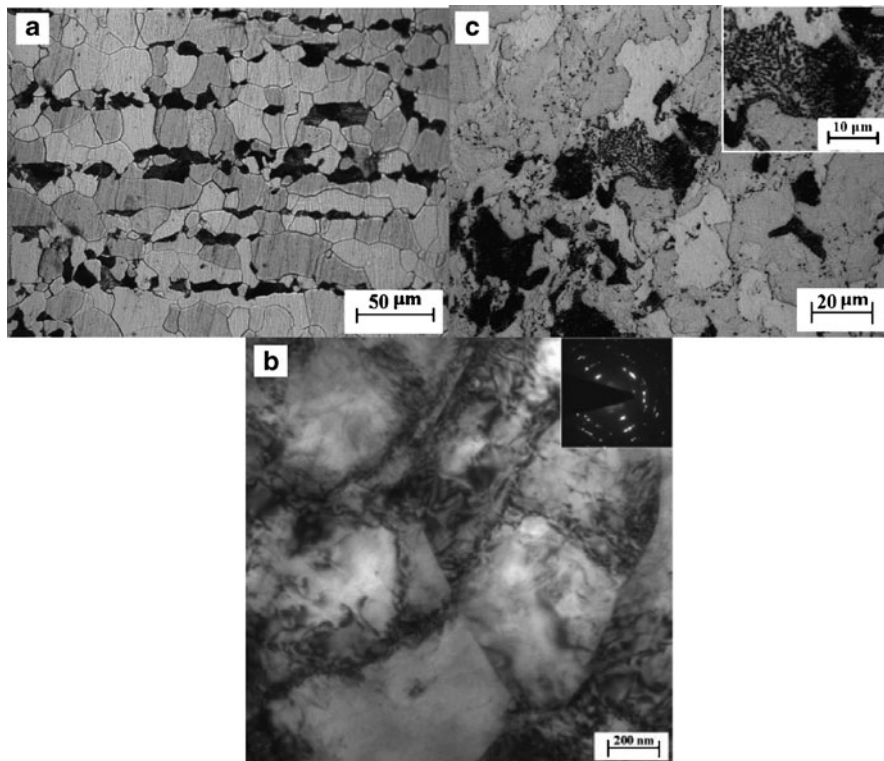


Fig. 14.1 Optical micrographs of (a) CG AISI 1024 steel annealed at 920°C for 60 min (b) UFG AISI 1016 steel MAFed using nine passes, (c) Bright field TEM micrograph of specimen MAFed using nine passes

14.3.3 Wear Behaviour

1. Variation of cumulative wear volume with sliding distance

The variation of cumulative wear volume with sliding distance under different normal loads of 14.7, 24.5 and 34.3 N at a fixed sliding velocity of 1 m/s for AISI 1016 steel is shown in Fig. 14.2a, b, c, d for annealed and MAF processed AISI 1016 steels using three, six, and nine MAF passes, respectively. It is observed that cumulative wear volume loss varies linearly with sliding distance. In both annealed (CG) and nine MAF passes (UFG) AISI 1016 steels, for a given sliding distance, cumulative wear volume increases with increase in normal load. Thus, cumulative wear volume is least for 14.7 N and maximum for 34.3 N normal loads.

2. Variation of wear rate with load

The wear rate (wear volume/sliding distance, V/S) for annealed and MAF processed AISI 1016 steel is calculated from the slope of the linear fit in Fig. 14.2. The variation of wear rate with normal load for CG, three, six and

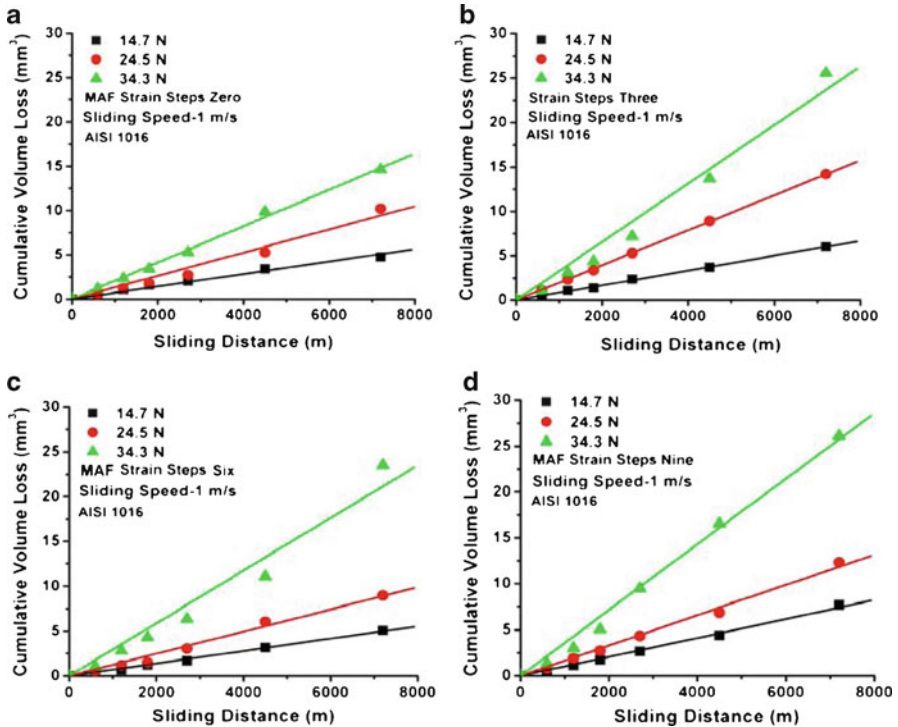


Fig. 14.2 Variation of cumulative wear volume with sliding distance at different loads for (a) CG AISI 1016 steel, and steel fabricated by warm MAF using after (b) three, (c) six, and (d) nine MAF passes

nine MAF passes UFG AISI 1016 steel is shown in Fig. 14.3. It can be observed that wear rate increases linearly with load and it (wear rate) is more for UFG material than for CG steel.

3. Variation of average friction coefficient

Average friction coefficient is calculated by averaging the measured friction force at least 15 times during each time span of test. Figure 14.4 shows the variation of average friction coefficient with sliding distance at different loads for AISI 1016 steel. It is seen that the fluctuation in the average friction coefficient is more during the initial period as compared to steady state in both the CG and UFG AISI 1016 steels. During steady state, the friction coefficient for CG AISI 1016 steel averages about 0.61 whereas that for UFG AISI 1016 steel averages about 0.6. It is observed that the average friction coefficient varies very little with normal load, and their average value for UFG AISI 1016 steel (0.6) and CG steel (0.61) are only marginally different.

4. Analysis of worn surfaces

The wear test results have been confirmed by scanning the worn surfaces of the pins by employing the SEM and AFM techniques. Figure 14.5a shows

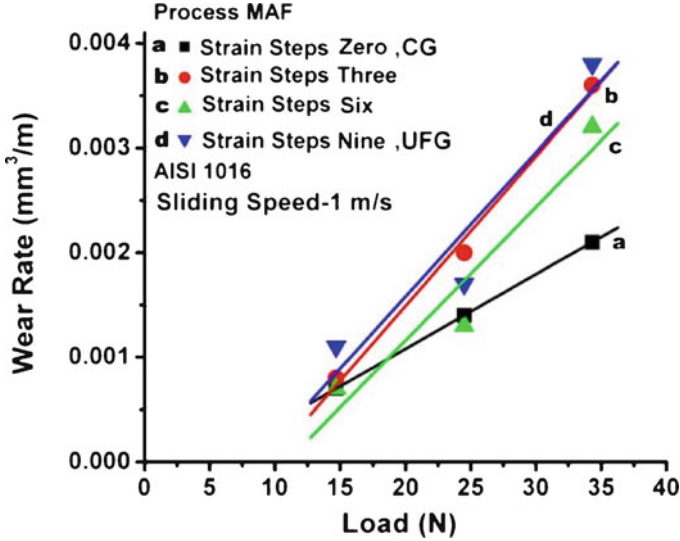


Fig. 14.3 Variation of wear rate with normal load for samples MAFed using zero, three, six, and nine passes

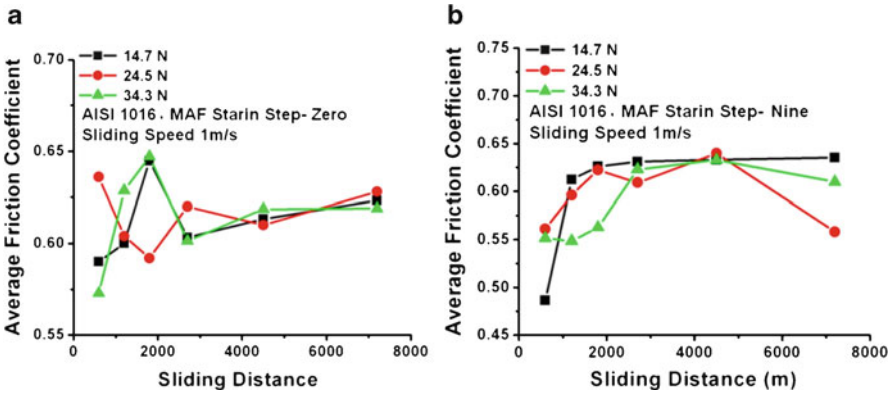


Fig. 14.4 Variation of average friction coefficient with sliding distance for (a) Zero or CG, (b) nine MAF passes

the SEM micrographs of worn surfaces of test pins of CG steel after a sliding distance of 7,200 m tested at a load of 34.3 N and Fig. 14.5b shows the SEM micrograph of UFG steel manufactured by MAF using 9 MAF passes after a sliding distance of 7,200 m at a load of 34.3 N. It is clear from the images that the UFG steel has deeper and wider scratches than the CG steel. Figures 14.6a, b, c, d show the AFM images of worn surfaces of CG and UFG steel samples, respectively. The wear grooves are not conspicuous because of smaller sampling area. 2D and 3D images of worn surfaces of CG steel subjected to 34.3 N are shown in Fig. 14.5a, b respectively.

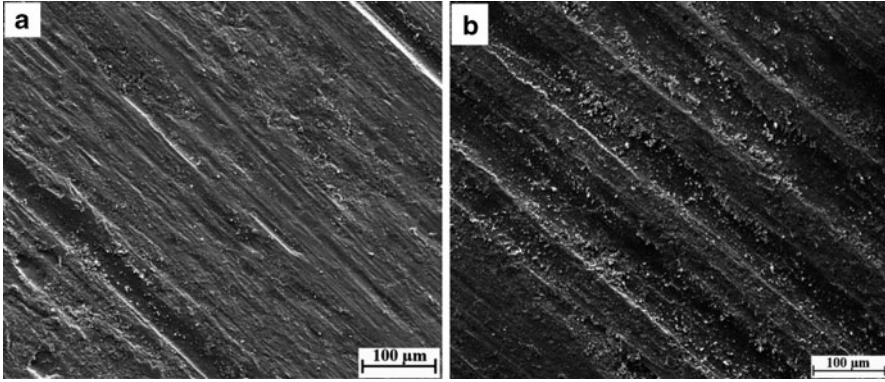


Fig. 14.5 Worn surfaces of wear samples, at a load of 14.7 N after a run of 7,200 m, for (a) CG and (b) UFG steel manufactured by MAF

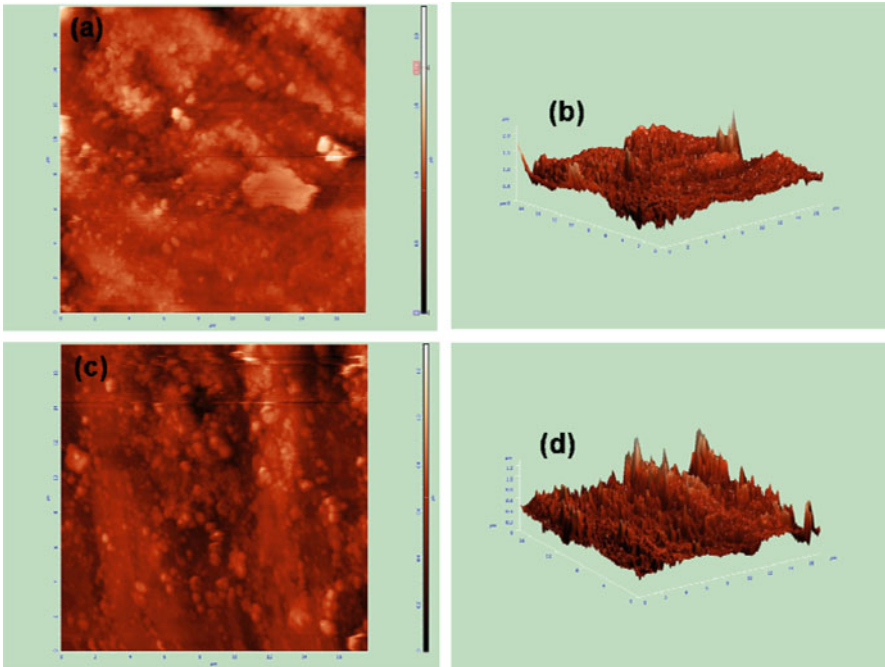
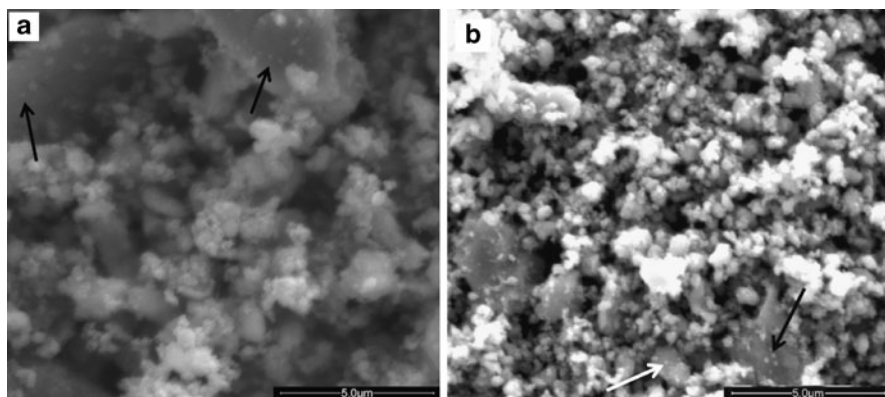


Fig. 14.6 AFM images of worn surfaces of CG AISI 1016 steel at 34.3 N load (a) 2-D and (b) 3-D image. AFM images of worn surfaces of UFG steel at 34.3 N load (c) 2-D and (d) 3-D image

Corresponding surfaces for UFG steel are shown in Fig. 14.6c, d, respectively. It is evident that the grooves on the surfaces are deeper for UFG steel as compared to CG steels for similar loads. Quantitative analysis of surface roughness in terms

Table 14.1 Roughness values of worn surfaces estimated using AFM, for CG and UFG steel samples at applied load of 34.3 N

Condition of steel samples	Roughness, RMS, nm
CG	119
UFG (after 9 MAF passes)	128

**Fig. 14.7** SEM micrograph of wear debris obtained from a wear test at a load of 34.3 N for MAFed samples after (a) zero and (b) nine passes

of root mean square value of roughness is summarized in Table 14.1. Surface roughness values for UFG steel are marginally higher than those for the CG steels at all the test loads employed in this study. Thus, worn surface morphology confirms the observed experimental data that UFG steel has lower wear resistance.

SEM micrographs of wear debris are shown in Fig. 14.7. Wear debris contain very fine particles of less than 100 nm size. XRD analysis of wear debris is shown in Fig. 14.8. Same oxide peaks obtained in all the samples processed using MAF suggests the same oxidative wear mechanism in all samples.

14.3.4 Discussion

The microstructural changes that occurred in the present study included refinement of ferrite grains from 17 to about 0.5 μm and fragmentation and spheroidization of pearlitic cementite to nanoscale dimensions. The increase in wear rate of the UFG steel fabricated by warm MAF is mainly due to the microstructural changes caused during the grain refinement process and the resulting mechanical properties. Pearlitic cementite is found to be dispersed throughout the ferrite matrix in UFG AISI 1016 steel. Observed nanoscale cementite particles could nucleate subsurface cracks and these might be responsible for the increased wear [13]. Worn surface morphology confirms the observed experimental data that UFG steel has lower wear resistance.

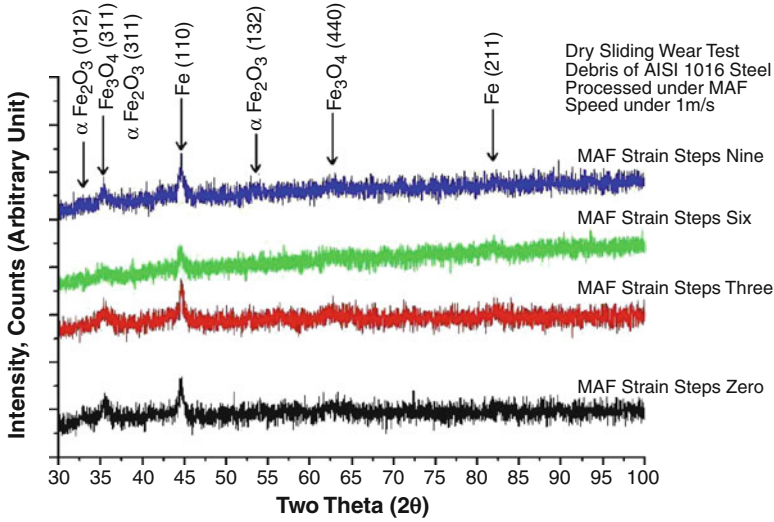


Fig. 14.8 X-ray analysis of debris collected from wear tests performed at a load of 34.3 N

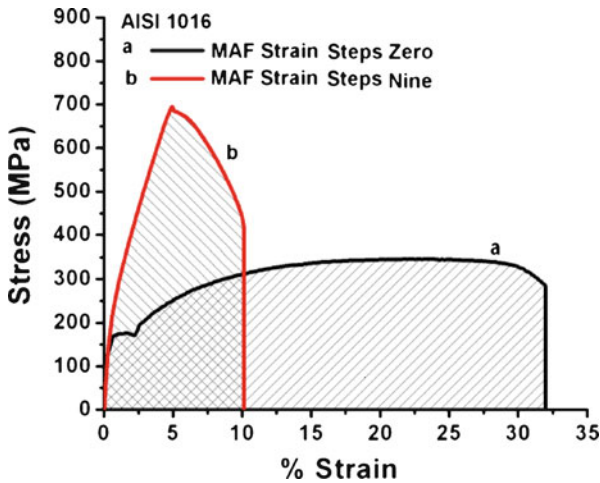


Fig. 14.9 Tensile curves for AISI 1016 steel showing mechanical behavior of zero (annealed, CG), and nine MAF strain steps (UFG) samples. Area under the curves is represented by hatched lines

Although the strength of the UFG steel increased, the wear resistance decreased. This is also due to the lower pull-off work (area under the stress strain curve, please refer Fig. 14.9) of UFG steel than that of CG steel. In UFG steel, although the strength increased, the total elongation decreased substantially and hence area under the stress–strain curve decreased. Pull-off work, which is calculated from area under

the stress–strain curves, is 0.52 MJ/m³ for UFG steel while it is 0.98 MJ/m³ in the CG steel. Thus, lower pull off work in UFG steel caused increased wear as compared to CG steel.

14.4 Conclusions

1. After multiaxial forging on AISI 1016 steel UFG microstructure containing submicron sized ferrite and nanosized cementite particles is developed.
2. The average friction coefficient of UFG steel and CG steel are quite close, i.e., 0.60 and 0.61, respectively. Average friction coefficient did not vary much with applied normal load.
3. Wear rate increases linearly with load and wear rate is more for UFG material than for CG steel. Thus UFG steel exhibits lower wear resistance.
4. The worn surface of UFG steel revealed deeper and wider grooves as compared to CG steel which showed shallow grooves.
5. The lower wear resistance of UFG steel as compared to CG steel is explained on the basis of its microstructural features and lower pull-off work.

References

1. La PQ, Ma JQ, Zhu YT, Yang J, Liu W, Xue Q, Valiev R (2005) Dry-sliding tribological properties of ultrafine-grained Ti prepared by severe plastic deformation. *Acta Mater* 53:5167–5173
2. Kluge A, Langguth K, Ochsner R, Kobs K, Ryssel H (1989) Examination of wear, hardness and friction of nitrogen-, boron-, carbon-, silver-, lead- and tin-implanted steels with different chromium contents. *Mater Sci Eng A* 115:261–265
3. Kim SH, Kim YS (1999) Effect of ductility on dry sliding wear of medium carbon steel under low load conditions. *Met Mater Int* 5:267–271
4. Stolyarov VV, Shuster LS, Migranov MS, Valiev RZ, Zhu YT (2004) Reduction of friction coefficient of ultrafine-grained CP titanium. *Mater Sci Eng A* 371:313–317
5. Gao LL, Cheng X (2008) Microstructure and dry sliding wear behavior of Cu–10%Al–4%Fe alloy produced by equal channel angular extrusion. *Wear* 265:986–991
6. Kim YS, Lee T, Park KT, Kim WJ, Shin DH (2002) Dry sliding wear behavior of commercial purity Aluminum and low carbon steel by severe plastic deformation techniques. In: *Proceeding of a symposium, TMS annual meeting, TMS (UFG materials II)*, Seattle, Washington, pp 419–428
7. Kim YS, Ha JS, Shin DH (2005) Sliding wear characteristics of ultrafine-grained non-strain-hardening aluminum-magnesium alloys. *Mater Sci Forum* 475–479:401–404
8. Garbacz H, Gradzka-Dahlke M, Kurzydłowski K (2007) The tribological properties of nano-titanium obtained by hydrostatic extrusion. *Wear* 263:572–578
9. Purcek G, Saray O, Kul O, Karaman I, Yapici G, Haouaoui M, Maier H (2009) Mechanical and wear properties of ultrafine-grained pure Ti produced by multi-pass equal-channel angular extrusion. *Mater Sci Eng A* 517:97–104
10. Lim SM, Wahabi ME (2007) The refinement of grain structure in a high purity α -iron base alloy under multiaxial compression. *Adv Mater Res* 15–17:900–905

11. Salishchev GA, Valiakhmetov OR, Galeyev RM (1993) Formation of submicrocrystalline structure in the titanium alloy VT8 and its influence on mechanical properties. *J Mater Sci* 28:2898–2902
12. Hyde TH, Sun W, Williams JA (2007) Requirements for and use of miniature test specimens to provide mechanical and creep properties of materials: a review. *Int Mater Rev* 52:213–255
13. Wayne S, Rice K (1983) The role of microstructure in the wear of selected steels. *Wear* 85: 93–106

Chapter 15

Thiocyanato Bridged Heterodinuclear Complex [Cu(bpy)₂(μ-NCS)Ru(bpy)₂(NO₃)](PF₆)₂ and Its Binding with Cd(II), Hg(II), Pb(II) and Ag(I) Ions

Niraj Kumari, Mudit Dixit, Herbert W. Roesky, and Lallan Mishra

Abstract The precursor complexes of composition [Cu(bpy)₂(H₂O)](PF₆)₂**1** and [Cu(bpy)₂(NCS)](PF₆)**2** (bpy = 2,2'-bipyridine) were initially prepared and characterized using spectroscopic (IR, UV-vis, ESR, Emission) along with their mass, elemental analysis, and single crystal X-ray crystallographic data. Complex **2** is linked with a known complex Ru(bpy)₂(NO₃)₂ prepared *in situ*. The resulting heterobimetallic complex of composition [Cu(bpy)₂(μ-NCS)Ru(bpy)₂(NO₃)](PF₆)₂**3** was isolated and characterized by its spectroscopic, mass, and elemental analysis data and its geometry is optimized without any constraint with plane-wave *ab initio* density functional theory using solid state package Abinit. The emission and electrochemical properties of these complexes are studied. The multiresponsive chemosensor property of complex **3** for Hg(II) ions as compared to Cd(II), Pb(II) and Ag(I) ions is monitored using UV-vis and fluorescence titrations.

15.1 Introduction

There is a great interest in sensing of cations especially toxic metal ions like Cd(II), Hg(II), and Pb(II). These metal ions are found common environmental pollutants as they damage the central nervous system and bring disorders in human being [1–3]. In this context, transition metal complexes have been reported with better sensitivity

N. Kumari • L. Mishra (✉)

Department of Chemistry, Banaras Hindu University, 221005 Varanasi, India
e-mail: nirajchem@gmail.com; lmishrabhu@yahoo.co.in

M. Dixit

Electronic Structure and Theory Group, National Chemical Laboratory, 441008 Pune, India
e-mail: dixitmuditk@gmail.com

H.W. Roesky

Institute of Inorganic Chemistry, Goettingen University, Goettingen, Germany
e-mail: hroesky@gwdgr.de

and functional ability as compared to organic molecules. The pyridine based complexes of Pt(II), Ru(II), and Ir(II) are reported as chemo sensors for cations, anions, and neutral molecules. However, polypyridyl complexes of ruthenium have been found more attractive owing to their potential photophysical and photochemical properties. A novel chemical sensor based on mesoporous nanocrystalline TiO₂ sensitized with a ruthenium complex bearing thiocyanato group as a co-ligand has been reported to bind selectively with mercuric salts [4]. It is outlined that changes in colour response could be considered as a promising approach for the analysis of Hg(II) ions especially in a biological sample. Recently Huang et al. [5] developed a terpyridyl ruthenium(II) complex bearing a thiocyanato ligand, and have used it in the colorimetric detection of Hg(II) ions. The binding studies are monitored using UV-vis absorption spectral titration. It is reported that naked eye detection of Hg(II) ions results in the interaction of the NCS group with Hg(II) via its sulfur atom. Therefore, with this precedence, we found interesting to synthesize a new heterodinuclear Ru(II) polypyridyl complex linked with Cu(II) polypyridyl complex via a NCS group. The selection of the heterobimetallic complex is made because heterodinuclear ruthenium based chemosensors are either rare or unknown. It is interesting to mention that clear detection of colour change upon binding of mercury(II) ion with such heterodinuclear complex is anticipated to make it a potential candidate as a chemosensor since it bears a platform of two coloured centers [Cu(II) and Ru(II)]. Thus upon binding of the Hg(II) ion, change in either of the two coloured centers could be exploited to differentiate from the original colour. As anticipated, the present complex is able to differentiate the colour of both centers without any interference by other cations like Cd(II), Pb(II) and Ag(I).

15.2 Methodology

15.2.1 Materials and Methods

RuCl₃·3H₂O purchased from Sigma-Aldrich was converted into cis-Ru(bpy)₂Cl₂·2H₂O using reported procedure [6] whereas Ru(bpy)₂(NO₃)₂ is prepared in solution by overnight stirring of Ru(bpy)₂Cl₂·2H₂O with two equivalents of silver nitrate and discarding the solid AgCl thus formed. The complex Cu(bpy)(MeCOO)₂·H₂O was also synthesized using the reported procedure [7]. Elemental analysis and mass spectral measurements were carried out using a Carbo-Erba elemental analyzer 1108, and JEOL SX-102 mass spectrometer respectively. IR spectra were recorded as KBr pellets on Varian 3100 spectrophotometer whereas ¹H NMR spectra were recorded on a JEOL AL 300 MHz instrument using DMSO-d₆ as solvent and TMS as internal reference. The UV-vis and luminescence measurements were made in the range 200–700 nm using Shimadzu UV-1701 spectrophotometer and Perkin Elmer LS-45 Luminescence spectrometer respectively. Cyclic voltammetric measurements were made on a CH instrument (USA) CH1660C.

15.2.2 Synthesis of Complexes

15.2.2.1 Synthesis of [Cu(bpy)₂(H₂O)](PF₆)₂ 1

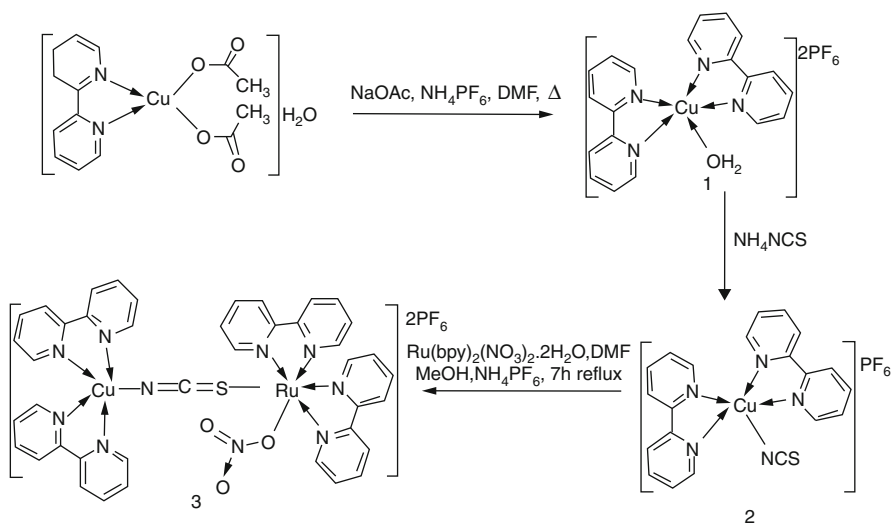
Complex **1** was synthesized using procedure reported earlier by Yi Shi et al. [8] and was characterized using spectroscopic and X-ray crystallographic techniques.

15.2.2.2 Synthesis of [Cu(bpy)₂(NCS)](PF₆) 2

Complex **1** (0.684 g, 1 mmol) was dissolved in minimum amount of DMF and to it a methanolic solution of ammonium thiocyanate was added slowly with stirring. After 0.5 h, the original blue colour of the reaction mixture changed to green. The green crystals obtained after slow evaporation were filtered off, washed with methanol followed by diethyl ether. Finally, crystals thus obtained were dried in *vacuo* and then characterized as [Cu(bpy)₂(NCS)](PF₆). Yield: 76%; m.p. >230°C. Elemental analysis calcd (%) for C₂₁H₁₆CuF₆N₅PS: C, 43.57; H, 2.79; N, 12.10. Found: C, 43.68; H, 2.80; N, 12.17. IR (KBr pellet, cm⁻¹): 2068 (νNCS), 1603 (νbpy), 842 (νPF₆), 768 (νbpy). FAB-MS: (m/z (%)): 577(43) [M]⁺, 432(38) [M - PF₆]⁺, UV-vis (DMSO, 10⁻⁴ M): λ_{max}/(nm) (ε_{max} × 10⁴ M⁻¹ cm⁻¹) 312 (3.6), 385 (1.98), 706 (0.18); λ_{em} at λ_{ex} 385 nm (DMSO, 10⁻⁴ M): λ_{max} (nm) (intensity in a.u.) 441 (25). Conductivity: Λ_m (DMSO, 10⁻⁴ M) 90 Ω⁻¹ cm² mol⁻¹. Crystallographic data: a/Å, 8.9568(9); b/Å, 10.3494(10); c/Å, 13.6735(14); α(°), 76.127(2); β(°), 75.438(2); γ(°), 72.658(2); V/Å³, 1152.2(2); R indices (all data) R₁, wR₂, 0.0526, 0.1413.

15.2.2.3 Synthesis of [Cu(bpy)₂(μ-NCS)Ru(bpy)₂(NO₃)](PF₆)₂ 3

Complex **2** (0.573 g, 1.0 mmol) was dissolved in DMF (5 mL) and added drop by drop to a solution of Ru(bpy)₂(NO₃)₂. The reaction mixture was then refluxed on a water bath for 7 h under N₂ atmosphere. A solid product was obtained after addition of an aqueous solution of NH₄PF₆ to the reaction mixture. It was filtered, washed with distilled water, methanol followed by diethyl ether and recrystallised from a mixture of DMSO/MeOH and dried in *vacuo* (Scheme 15.1). Yield: 60%, m.p.: >230°C, Elemental analysis calcd (%) for C₄₁H₃₂CuF₁₂N₁₀O₃P₂RuS: C, 41.06; H, 2.69; N, 11.68. Found: C, 40.93; H, 2.69; N, 11.73. IR (KBr pellet, cm⁻¹): 2100 (νNCS), 1602 (νbpy), 1383 (νNO₃), 842 (νPF₆), 778 (νbpy). FAB-MS: (m/z (%)): 908(24) [M - 2PF₆]⁺, 846(18) [M - 2PF₆ - NO₃]⁺, 410(69) [Ru(bpy)₂]⁺, 375(21) [Cu(bpy)₂]⁺. UV-vis (DMSO, 10⁻⁴ M): λ_{max}/(nm) (ε_{max} 10⁴ M⁻¹ cm⁻¹) 304 (3.65), 346 (1.78), 474(1.71), 756 (0.084); λ_{em} at λ_{ex} 346 nm (DMSO, 10⁻⁴ M): λ_{max} (nm) (intensity in a.u.) 414 (10), 604 (35). Conductivity: Λ_m (DMSO, 10⁻⁴ M) 170 Ω⁻¹ cm² mol⁻¹.



Scheme 15.1 Schematic diagram of the synthetic strategy of complexes

15.2.3 X-Ray Crystallographic Studies

Suitable crystals of complex **2** are grown directly from its reaction mixture in DMF/MeOH (5:2) at room temperature and X-ray crystallographic data are collected by mounting a single-crystal of the sample on glass fibers. Bruker SMART CCD area detector diffractometer equipped with LN₂ low-temperature attachment is used for the determination of cell parameters and intensity data collection. Appropriate empirical absorption corrections using the programs multi-scan are applied. Mo Kα ($\lambda = 0.71073 \text{ \AA}$) radiation has been used for the X-ray measurement of complex **2**. The crystal structure is solved by direct method [9] and refined by full matrix least squares SHELXL-97 [10]. Drawings were carried out using MERCURY [11] and special computations carried out with PLATON [12]. Since complex **3** results by the reaction between two known complexes so its structure is supported satisfactorily using spectroscopic data. The crystals suitable for X-ray diffraction measurement could not be obtained even after several months, its structure was therefore optimized using DFT calculation.

15.3 Results and Discussion

15.3.1 Spectroscopic Characterization

The synthetic strategy followed during the reaction is depicted in Scheme 15.1.

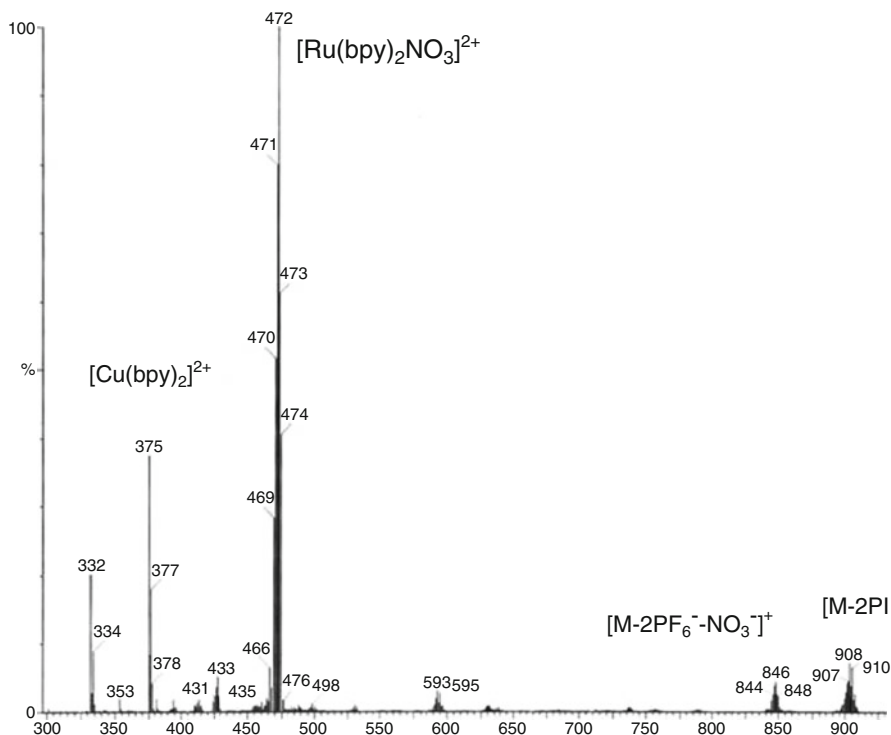


Fig. 15.1 ESI-MS of complex **3**

On the basis of elemental analysis and FAB-mass data, the composition of complex **3** is assigned to $[\text{Cu}(\text{bpy})_2(\mu\text{-NCS})\text{Ru}(\text{bpy})_2(\text{NO}_3)](\text{PF}_6)_2$. Its mass pattern shows the molecular ion peak at $m/z = 908$ $[\text{M}-2\text{PF}_6^-]$. Other peaks observed at m/z 375, 410, and 433 are assigned to $[\text{Cu}(2,2'\text{-bpy})_2]$, $[\text{Ru}(2,2'\text{-bpy})_2]$, and $[\text{Cu}(2,2'\text{-bpy})_2(\text{NCS})]$ fragments respectively. Thus FAB-mass data support the composition of complex **3**. ESI-MS of complex **3** also corroborates its composition (Fig. 15.1). Its mass pattern shows a peak at $m/z = 908$ $[\text{M}-2\text{PF}_6^-]$. Other ions are observed at m/z 375, 472 and 846 which are assigned to $[\text{Cu}(2,2'\text{-bpy})_2]$, $[\text{Ru}(2,2'\text{-bpy})_2\text{NO}_3]$, and $[\text{M}-2\text{PF}_6\text{-NO}_3]$.

Infrared spectrum of **2** shows a band at $2,068\text{ cm}^{-1}$ which we assign to the $\nu(\text{NCS})$ vibration whereas the $\nu(\text{NCS})$ vibration of **3** appears at $2,100\text{ cm}^{-1}$. It is a well-established criterion of infrared spectroscopy that $\nu_{\text{as}}(\text{NCS}) \geq 2,100\text{ cm}^{-1}$ indicates a thiocyanate bridge with a $\mu\text{-1,3}$ or $\mu\text{-1,1,3}$ bridging mode [13]. The strong $\nu_{\text{as}}(\text{NCS})$ absorption peak at $2,100\text{ cm}^{-1}$ in complex **3** shows the presence of $\mu\text{-1,3}$ thiocyanate ligand [14]. Therefore, we assume that the NCS group in **3** is in a bridging position.

The UV-vis spectra of complexes **1**, **2** and **3** depicted in Fig. 15.2a show bands for **1** and **2** at λ_{max} 311, 349^{sh} , and λ_{max} 312, 385 respectively. These absorptions

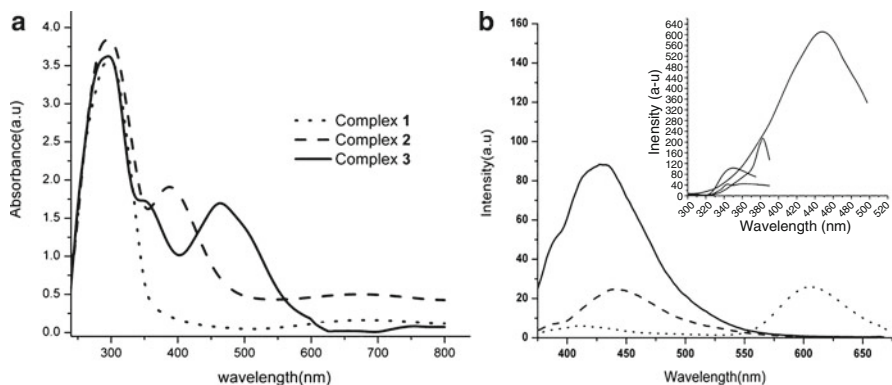


Fig. 15.2 (a) UV-vis spectra of complexes **1**, **2** and **3** in DMSO (10^{-4} M) solution (b) Emission spectra of complexes **1**, **2**, and **3** in DMSO solution [Inset: excitation spectrum of complexes]

are assigned to ligand centered (LC) $\pi \rightarrow \pi^*$ (bpy) transitions. However, absorptions observed at λ_{\max} 346 and 474 nm in the spectrum of complex **3** are assigned to $d\pi(\text{Ru}) \rightarrow \pi^*(\text{bpy})$ transitions [15]. A comparison of the positions in **3** with those of the corresponding parent complexes $\text{Ru}(\text{bpy})_2\text{Cl}_2 \cdot 2\text{H}_2\text{O}$ and $\text{Cu}(2,2'\text{-bpy})_2\text{NCS}$, leads to an appreciable decrease in $\text{Ru} \rightarrow \text{bpy}$ backbonding. This might be due to the fact that the $\text{Ru}(\text{bpy})_2$ unit links with the $\text{Cu}(2,2'\text{-bpy})_2$ part via a NCS group, with the result of a concomitant charge transfer from $\text{Ru} \rightarrow \text{NCS}$. Thus, owing to back bonding between $\text{Ru} \rightarrow \text{NCS}$ a blue shift in MLCT transition occurs [15]. This increase in back bonding between $\text{Ru} \rightarrow \text{NCS}$ gives rise to a concurrent red shift in d-d transition from the $\text{Cu}(\text{II})$ ion. The transition observed at λ_{\max} 706 nm in the spectrum of **2**, appears at λ_{\max} 746 nm for that of **3**. This observation also supports that the $[\text{Cu}(\text{bpy})_2]^{2+}$ unit is linked with the $[\text{Ru}(\text{bpy})_2]^{2+}$ part via the NCS group.

The emission spectra recorded in DMSO solution (10^{-4} M) show peaks at λ_{\max} 430 nm for complex **1** and 441 nm for complex **2**. In case of complex **3** two emission peaks are observed at λ_{\max} 414 and 604 nm. The emission at 414 nm arises from Cu – ligand charge transfer transition whereas emission at 604 nm arises from Ru – ligand charge transfer transition. Their excitation spectra (Fig. 15.2b) show absorption bands at 350 and 470 nm corresponding to their emission wavelengths λ_{\max} 414 and 604 nm respectively.

15.3.2 Structural Description of the Complexes

Selected bond lengths and bond angles with their estimated standard deviations are presented in Table 15.1 while selected parameters for weak interactions are listed in Table 15.2.

Table 15.1 Selected bond lengths (Å) and bond angles (°) for complex **2**

Cu(1)-N(2)	1.989(2)	N(2)-Cu(1)-N(4)	174.71(10)	N(2)-Cu(1)-N(5)	92.37(12)
Cu(1)-N(4)	1.996(2)	N(4)-Cu(1)-N(5)	92.70(11)	N(2)-Cu(1)-N(3)	95.99(9)
Cu(1)-N(3)	2.073(2)	N(4)-Cu(1)-N(3)	79.82(9)	N(5)-Cu(1)-N(3)	125.11(13)
Cu(1)-N(1)	2.091(3)	N(2)-Cu(1)-N(1)	79.63(9)	N(4)-Cu(1)-N(1)	99.28(9)
Cu(1)-N(5)	1.996(3)	N(5)-Cu(1)-N(1)	118.16(13)	N(3)-Cu(1)-N(1)	116.71(9)
N(5)-C(21)	1.148(4)	C(21)-N(5)-Cu(1)	156.8(3)	C(10)-N(2)-Cu(1)	123.9(2)
C(21)-S(1)	1.621(4)	C(11)-N(3)-Cu(1)	128.0(2)	C(15)-N(3)-Cu(1)	113.67(18)
N(3)-C(15)	1.344(3)	C(20)-N(4)-Cu(1)	124.4(2)	C(16)-N(4)-Cu(1)	115.98(19)
C(16)-C(15)	1.469(4)	C(5)-N(1)-Cu(1)	112.94(18)	C(1)-N(1)-Cu(1)	128.6(2)
P(1)-F(2)	1.525(3)	C(1)-N(1)-C(5)	118.6(3)	N(5)-C(21)-S(1)	178.3(3)

Table 15.2 Selected parameters for weak interactions in complex **2**

Cu(1)-N(2)	1.989(2)	N(2)-Cu(1)-N(4)	174.71(10)	N(2)-Cu(1)-N(5)	92.37(12)
Cu(1)-N(4)	1.996(2)	N(4)-Cu(1)-N(5)	92.70(11)	N(2)-Cu(1)-N(3)	95.99(9)
Cu(1)-N(3)	2.073(2)	N(4)-Cu(1)-N(3)	79.82(9)	N(5)-Cu(1)-N(3)	125.11(13)
Cu(1)-N(1)	2.091(3)	N(2)-Cu(1)-N(1)	79.63(9)	N(4)-Cu(1)-N(1)	99.28(9)
Cu(1)-N(5)	1.996(3)	N(5)-Cu(1)-N(1)	118.16(13)	N(3)-Cu(1)-N(1)	116.71(9)
N(5)-C(21)	1.148(4)	C(21)-N(5)-Cu(1)	156.8(3)	C(10)-N(2)-Cu(1)	123.9(2)
C(21)-S(1)	1.621(4)	C(11)-N(3)-Cu(1)	128.0(2)	C(15)-N(3)-Cu(1)	113.67(18)
N(3)-C(15)	1.344(3)	C(20)-N(4)-Cu(1)	124.4(2)	C(16)-N(4)-Cu(1)	115.98(19)
C(16)-C(15)	1.469(4)	C(5)-N(1)-Cu(1)	112.94(18)	C(1)-N(1)-Cu(1)	128.6(2)
P(1)-F(2)	1.525(3)	C(1)-N(1)-C(5)	118.6(3)	N(5)-C(21)-S(1)	178.3(3)

Molecular structure (Fig. 15.3) of **2** shows that it exhibits a triclinic space group *P*-1. It also features a distorted pentacoordinate geometry around the Cu(II) ion. The coordination core consists of four N-donor atoms from two 2,2'-bipyridine ligands and is completed by a N- of the thiocyanate group. In the trigonal bipyramidal geometry, the out-of-plane Cu(1)-N(2) and Cu(1)-N(4) distances are slightly different (1.989(2) Å and 1.996(2) Å), while the in-plane distances Cu(1)-N(1) and Cu(1)-N(3) are more distinct (2.091(3) Å and 2.073(2) Å). On average these distances are longer than out-of-plane Cu-N distances by 0.090 Å, a difference comparable with the 0.1 Å normally observed for trigonal bipyramidal copper(II) compounds [16]. The third in-plane Cu(1)-N(5) distance (N from the NCS ligand) of 1.996(3) Å is significantly shorter than the other two in-plane distances. The N(4)-Cu(1)-N(2) angle of 174.71(10)° shows an almost linear arrangement, while N(2)-Cu(1)-N(5) and N(4)-Cu(1)-N(5) amount to 92.37(12)° and 92.70(11)°, respectively. The chelating 2,2'-bipyridine makes bite angles of 79.81° (N3-Cu1-N4) and 79.64° (N2-Cu1-N1). Additionally, two 2,2'-bipyridine rings are inclined to each other with an angle of 64.80°. Thus replacement of coordinate water with a thiocyanate ligand has almost no effect on the bite angle of chelating 2,2'-bipyridine ligands. The Cu-N(bpy) distances vary from 1.989(3) to 2.091(3) Å which are again found in the range of values reported for similar complexes [17].

Fig. 15.3 ORTEP view of complex **2** with atom numbering scheme

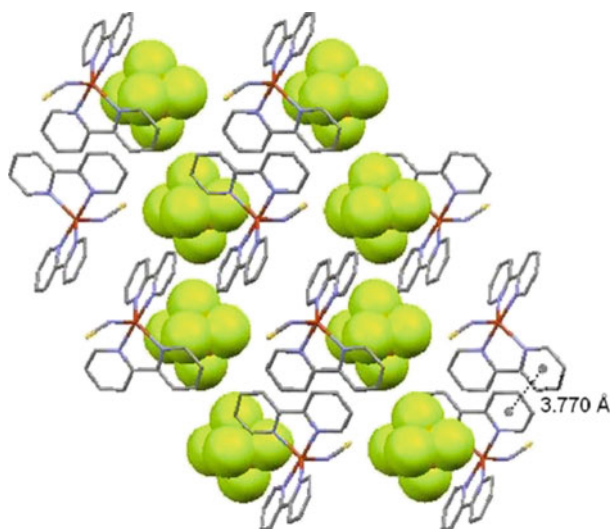
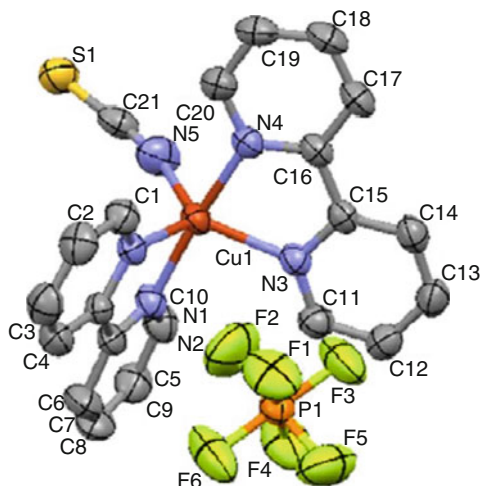


Fig. 15.4 A view of crystal packing of complex **2**, the packing is stabilized through π - π stacking between bipyridyl rings and C-H...F interactions

Weak force study using PLATON indicates the presence of four non conventional H-bonds in the packing diagram. These non conventional bonds involve C-H as donor and F as acceptor in all of the cases. There are no solvent accessible voids in the packing of this complex. The Kitaigorodskii packing index [18] was found to be 68.2% with the presence of five grid points. Non-conventional hydrogen bonds, in addition to π - π stacking interactions, provide a 3D supramolecular structure (Fig. 15.4). In the packing of the complex the structural units are arranged in a

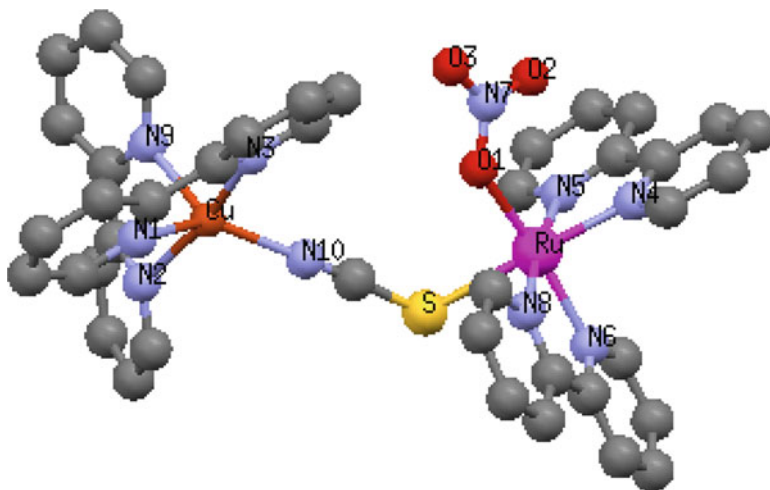


Fig. 15.5 Optimized structure of complex **3**. Hydrogen atoms are omitted for clarity

linear 2D fashion, in which counter PF_6^- anions are pillared. Two such chains are stabilized by C–H···F interactions as well as π – π stacking (3.770 Å) between the bipyridine rings.

15.3.3 Density Functional Theory Studies

To obtain improved insights on the structure and bonding in **3**, we have carried out density functional theory calculations. Geometry optimization of full molecule was carried out without any constraint with plane-wave *ab initio* density functional theory using solid state package Abinit [19]. The cubic unit cell was made longer enough that there must be no interaction with the other repeating units. Due to the longer size of cell only one k-point was used. We have used Fritz-Haber-Institute (FHI) pseudopotentials, generalized gradient approximation (GGA) [20], with in Perdew, Burke and Ernzerhof (PBE) [21] exchange correlation functional. All forces were calculated using Hellmann-Feynman theorem. Geometries were considered optimized when maximum forces found were smaller than 0.01 eV/Å. Geometry of the optimized structure of **3** is given in Fig. 15.5 and the important bond distances and bond angles around copper and ruthenium atom in **3** are listed in Table 15.3. The Cu(II) ion features a distorted trigonal bipyramid. It consists of four N-donor atoms of two 2,2'-bipyridine molecules and one N donor from bridging thiocyanate group. The bond lengths and bond angles are comparable with corresponding values reported in literature [17]. However, ruthenium is hexacoordinated with octahedral

Table 15.3 Selected bond lengths (Å) and bond angles (°) for complex **3**

Cu-N(10)	2.4312	N(1)-Cu-N(2)	97.93
Cu-N(9)	2.2934	N(3)-Cu-N(9)	104.33
Cu-N(3)	2.3070	N(3)-Cu-N(10)	99.02
Cu-N(1)	2.2688	N(6)-Ru-N(8)	77.02
Cu-N(2)	2.1784	N(4)-Ru-N(5)	76.74
Ru-N(5)	2.1560	O(1)-Ru-S	93.08
Ru-N(4)	2.1716	N(8)-Ru-S	87.27
Ru-N(6)	2.1607	O(1)-Ru-N(5)	94.57
Ru-N(8)	2.1524	O(2)-N(7)-O(3)	122.69
Ru-S	2.6395	N(10)-C(11)-S	176.98
Ru-O(1)	2.184	O(1)-Ru-N(4)	91.29

geometry. The coordination core consists of four N-donor atoms from two 2,2'-bipyridine ligands, one oxygen atom from nitrate ion and one sulfur from bridging thiocyanate group.

15.3.4 Electron Spin Resonance

The calculated g-tensor values found in the range of 2.11 ± 0.06 are in agreement with an orbitally non-degenerate ground state. However, in order to compare the studies between **2** and **3**, their ESR spectra are recorded both in solution (DMSO) and in powder form at room temp (Fig. 15.6). The parameter R defined by g_2-g_1/g_3-g_2 ranges from 1.3 to 1.4 (>1). It shows that dz^2 is the ground state as expected for Cu(II) complexes of trigonal bipyramidal geometry [22]. Thus, ESR spectral information shows that Cu(II) ion retains its trigonal bipyramidal geometry in **3**.

15.3.5 Electrochemistry

Redox behaviour of the complexes (10^{-4} M in DMF) containing tetrabutyl ammonium perchlorate (TBAP) as supporting electrolyte has been studied using cyclic voltammetric technique at scan rate of 50 mV/s using glassy carbon and Ag/AgCl as working and reference electrodes, respectively. A peak observed at -441 mV in complex **2** is assigned to copper based oxidation [23]. This peak position shifts at -305 mV for complex **3**. The ruthenium based oxidation with concomitant reduction is observed at $+771$ mV and $+858$ mV respectively (Fig. 15.7). Thus, ruthenium based oxidation is observed at lower potential as compared to its position observed from standard complexes [24]. The reductions of coordinate 2,2'-bpy moieties are observed at $-1,150$ and $-1,420$ mV for complex **2**, whereas corresponding peaks are observed at -920 and $-1,067$ mV in the cyclic voltammetry of complex **3**.

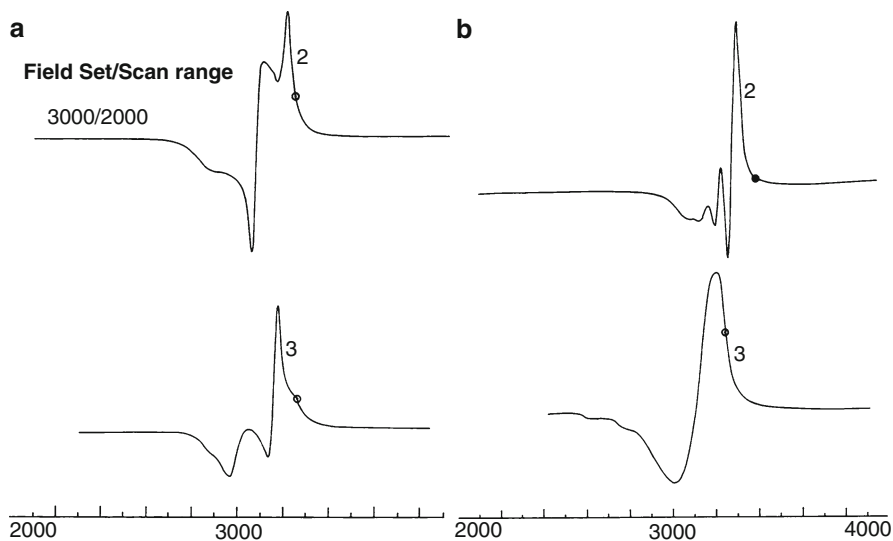


Fig. 15.6 ESR spectral pattern of complexes 2 and 3 in DMSO solution (a); solid (b)

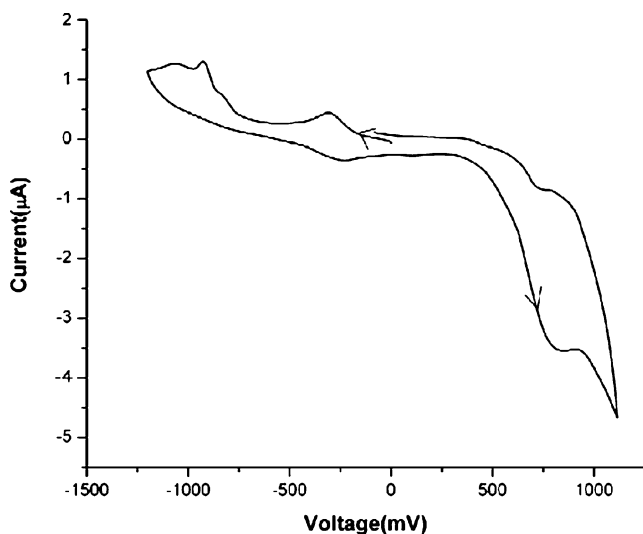


Fig. 15.7 Cyclic voltammogram of complex 3

15.3.6 Binding of Complex 3 with $\text{Hg}(\text{NO}_3)_2$

Initially the binding of $\text{Cd}(\text{II})$, $\text{Hg}(\text{II})$, $\text{Pb}(\text{II})$ and $\text{Ag}(\text{I})$ nitrate salts in the presence of 2 was monitored by UV-vis investigation. But the binding of these cations results in the formation of the corresponding thiocyanates with simultaneous formation

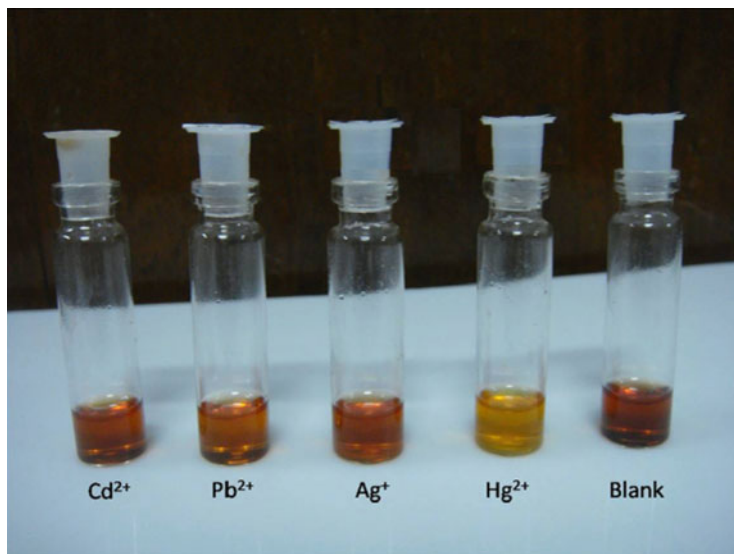


Fig. 15.8 Color variation observed in DMSO solutions of **3** in the presence of 1 equiv of Pb(II), Ag(I), Cd(II), and Hg(II) ions

of precursor cation **1** $[\text{Cu}(\text{bpy})_2(\text{H}_2\text{O})]^{2+}$. However, complex **3** shows significant change in its UV-vis spectral feature upon adding Hg(II) ion. Thus, an attempt was made to monitor this process colorimetrically. As depicted in Fig. 15.8, the presence of Hg(II) shows clear colour change from brown to yellow.

However, with Cd(II), Pb(II), and Ag(I) ions, no identifiable colour change was observed. Therefore complex **3** was found to be an appropriate colorimetric receptor for Hg(II). Perhaps binding of Hg(II) ion occurs via the sulfur atom of the bridged NCS group. An attempt was therefore made to calculate its binding constant by studying the variation in the spectral pattern of complex **3** upon incremental addition of Hg(II) ions as depicted in Fig. 15.9.

Incremental addition of aq. solution of $\text{Hg}(\text{NO}_3)_2$ (1×10^{-3} M) to a fixed concentration of **3** (10^{-5} M) in DMSO shows a blue shift of the MLCT band of **3** from λ_{max} 474 to λ_{max} 418 nm. This shift of 54 nm is quite significant and naked eye detection of corresponding colour change is possible. Various concentrations of Hg(II) ions plotted against the corresponding changes in absorbance are shown in Fig. 15.9. It clearly shows that as soon as the concentration of the Hg(II) ion addition reaches the initial concentration of complex **3** (1.0×10^{-5} M), the change in absorption intensity remains constant. This observation clearly shows that Hg(II) ion binds with complex **3** in 1:1 molar ratio. The blue shift of λ_{max} of the MLCT band of **3** is also an indication of Hg(II) binding through the NCS group. The value of the binding constant was calculated ($3.45 \times 10^4 \text{ M}^{-1}$) using the Benesi-Hildebrand equation [25].

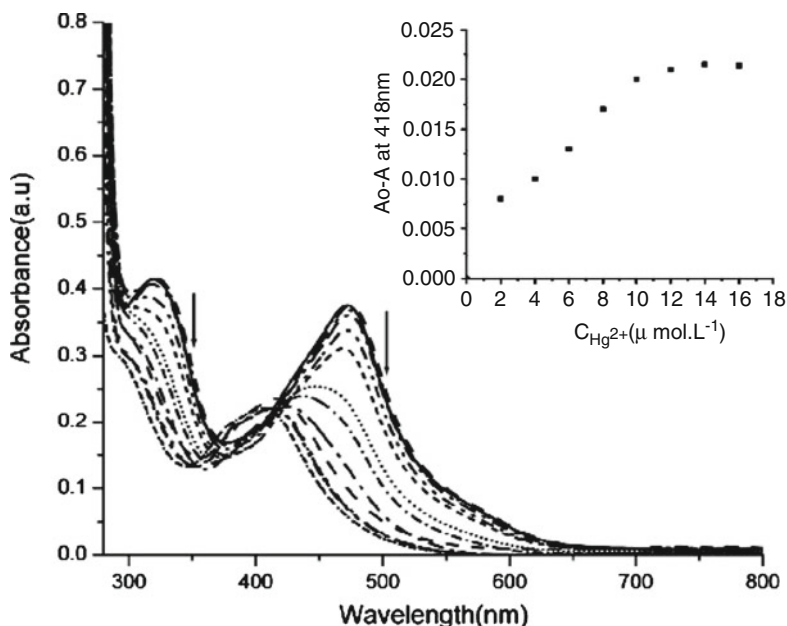


Fig. 15.9 Changes in the UV-vis absorption spectra of **3** (10 μM) in DMSO solution with incremental addition of Hg(II) ions (0–14 μM)

15.3.7 Luminescent Response of Complex **3** to Hg(II) Ions

Generally, emission spectroscopy is more sensitive toward small changes that affect the electronic properties of molecular receptors [26, 27]. Hence, the response of **3** to Hg(II) ions is also investigated by a photoluminescence technique. Complex **3** dissolved in DMSO shows dual emissions at λ_{max} 414 and 604 nm (Fig. 15.2b). Both emission peaks are lowered extensively (Fig. 15.10) upon addition of 1 equiv of Hg(II) ions. The decrease of the emission can be explained in terms of energy/electron transfer between the excited complex to the bound mercury cation [28, 29]. As determined by variations in the luminescent response of complex **3** in the presence of various amounts of Hg(II) ions, the stoichiometry of complex **3** with Hg(II) is found in a ratio of 1:1, which is consistent with the result obtained by the UV-vis absorption titrations.

This 1:1 stoichiometry for the **3**-Hg(II) coordination species is further confirmed by the ESI-MS of the titration solution (Fig. 15.11), which shows two peaks with (m/z) 1107 and 1147, corresponding to the species $[\mathbf{3}\text{-PF}_6\text{+Hg}]^+$ (m/z_{calcd} 1109.44) and $[\mathbf{3}\text{-PF}_6\text{+Hg}(\text{H}_2\text{O})_2]^+$ (m/z_{calcd} 1145.28), respectively. Other ions are observed at m/z 908 and 846 which are assigned to $[\mathbf{3}\text{-2PF}_6]$ and $[\mathbf{3}\text{-2PF}_6\text{-NO}_3]$.

A space filling model of Hg(II) bound complex **3** is depicted in Fig. 15.12.

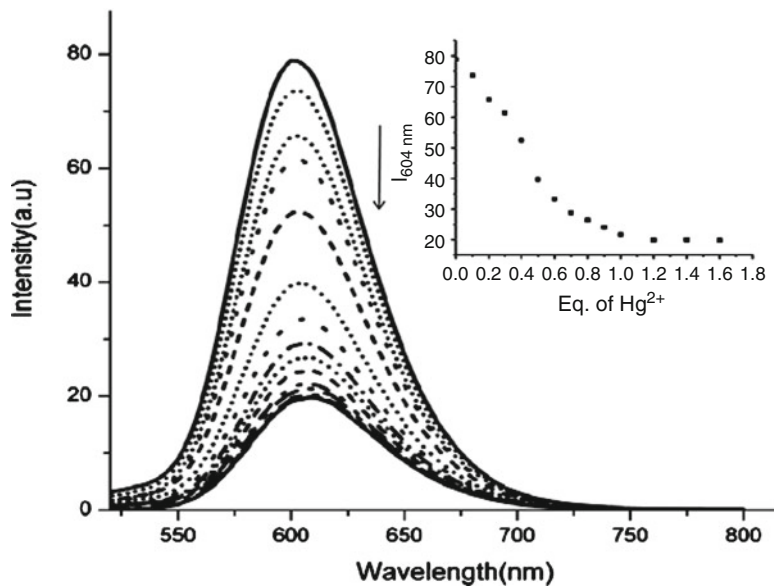


Fig. 15.10 Changes in the luminescence spectra of **3** (10 μ M) in DMSO solution with incremental various amounts of Hg^{2+} ions (0–18 μ M); $\lambda_{\text{ex}} = 474$ nm. Inset: titration curve of **3** with Hg^{2+} ions

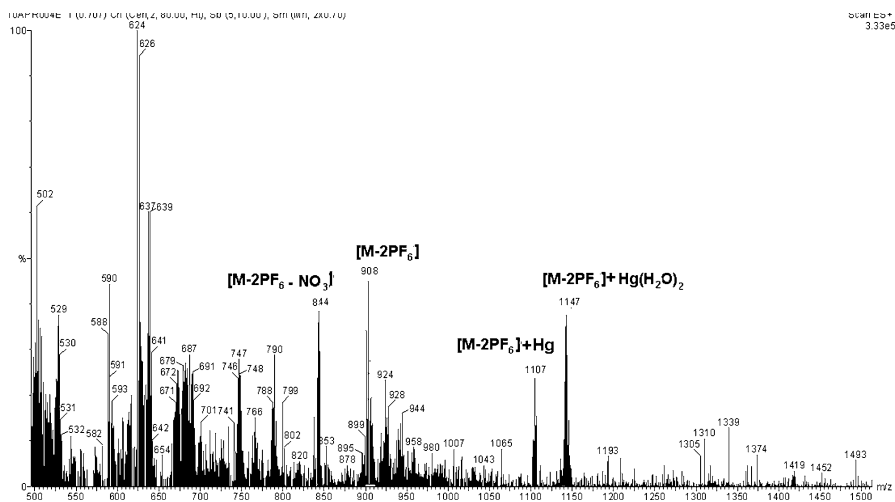


Fig. 15.11 ESI-MS of the titration solution of **3** upon the addition of $\text{Hg}(\text{II})$

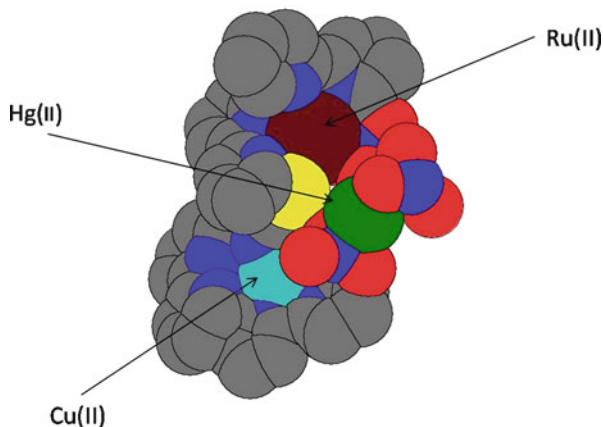


Fig. 15.12 Spacefilling model of **3** containing 1 equiv of Hg(II)

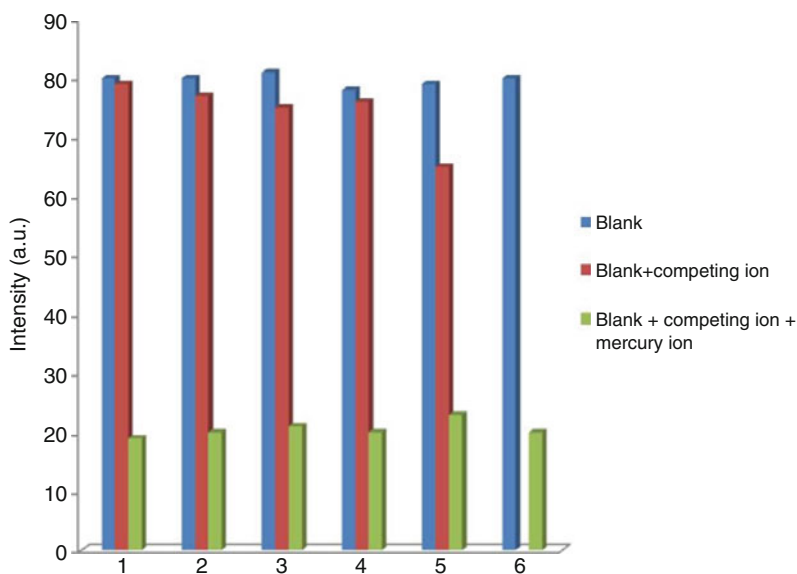


Fig. 15.13 Luminescent response of complex **3** ($10 \mu\text{M}$) in presence of various metal cations. *Red bars* represent luminescent intensity of complex after addition of excess of various metal cations. *Green bars* represent luminescent intensity after addition of Hg(II) 1 equiv to these solutions. 1. Zn(II), 2. Cu(II), 3. Pb(II), 4. Cd(II), 5. Ag(I)

15.3.8 Selective Optical Response of Complex 3 to Various Metal Ions

To verify a specific response to Hg(II), variations of luminescence spectra of complex **3** caused by other related transition metal ions were recorded. As shown

in Fig. 15.13, only the addition of Hg(II) resulted in a prominent luminescence change, whereas addition of a large excess of other competitive cations (such as Zn(II), Cd(II), Cu(II), Pb(II) and Ag(I)) caused only slight luminescent changes, confirming that complex **3** displayed a high selectivity in sensing Hg(II) ions. As shown in Fig. 15.13, in the absence and in the presence of competitive cations, the Hg(II) ions showed similar luminescence changes.

15.4 Conclusions

The brown coloured bimetallic complex $[\text{Cu}(\text{bpy})_2(\mu\text{-NCS})\text{Ru}(\text{bpy})_2(\text{NO}_3)](\text{PF}_6)_2$ turns to yellow upon addition of an equivalent aqueous solution of $\text{Hg}(\text{NO}_3)_2$ (1.0×10^{-5} M). It provides an opportunity to identify Hg(II) ion colorimetrically without interference by Ag(I), Cd(II) and Pb(II) ions. The colour change is also seen even at part per million dilution. The stoichiometry of Hg(II) bound complex is found to be 1:1 from its spectral as well as from ESI-MS data. In this stoichiometry, the fluorescence intensity of Hg(II) bound complex **3** is pronouncely lowered. Thus, **3** is considered as a potential multiresponsive receptor for Hg(II) ion.

Acknowledgements Authors thank authorities of CDRI Lucknow, India for providing analytical data. Authors (NK&LM) acknowledge the authorities of UGC and CSIR, New Delhi, India for the financial assistance.

References

1. Martinez R, Espinosa A, Tárraga A, Molina P (2005) New Hg^{2+} and Cu^{2+} selective chromo- and fluoroionophore based on a bichromophoric azine. *Org Lett* 7(26):5869–5872
2. Moon SY, Cha NR, Kim YH, Chang S-K (2004) New Hg^{2+} selective chromo- and fluoroionophore based upon 8-hydroxyquinoline. *J Org Chem* 69:181–183
3. Yang Y-K, Yook K-J, Tae J (2005) A Rhodamine-based fluorescent and colorimetric chemodosimeter for the rapid detection of Hg^{2+} ions in aqueous media. *J Am Chem Soc* 127:16760–16761
4. Palomares E, Vilar R, Durrant JR (2004) Heterogeneous colorimetric sensor for mercuric salts. *Chem Commun* 10:362–363
5. Li X-H, Liu Z-Q, Li F-Y, Duan X-F, Huang C-H (2007) Synthesis of N,N,N-4,4''-di-(4-methylphenyl)-2,2':6',2''-terpyridine-N,N,N-tris(isothiocyanato)ruthenium(II) and application to colorimetric Hg^{2+} sensor. *Chin J Chem* 25:186–189
6. Sullivan BP, Salmon DJ, Meyer TJ (1978) Mixed phosphine 2,2'-bipyridine complexes of ruthenium. *Inorg Chem* 17:3334–3341
7. Sen S, Mitra S, Kundu P, Saha MK, Krueger C, Bruckmann J (1997) Synthesis, characterization and structural studies of mono- and polynuclear complexes of zinc(II) with 1,10-phenanthroline, 2,2'-bipyridine and 4,4'-bipyridine. *Polyhedron* 16:2475–2481
8. Yi S, Toms BB, Dixit N, Kumari N, Mishra L, Goodisman J, Dabrowiak JC (2010) Cytotoxicity studies on Cu(II) and Zn(II) 2,2'-bipyridyl complexes as a function of recovery time. *Chem Res Toxicol* 23:1417–1426
9. Sheldrick GM (1997) SHELXS-97 Program for the Solution of Crystal Structures, University of Goettingen, Goettingen, Germany

10. Sheldrick GM (1990) Phase annealing in *SHELX-90*: direct methods for larger structures. *Acta Crystallogr A* 46:467–473
11. Bruno IJ, Cole JC, Edgington PR, Kessler M, Macrae CF, McCabe P, Pearson J, Taylor R (2002) *MERCURY*, new software for searching the Cambridge structural database and visualizing crystal structures. *Acta Crystallogr B* 58:389–397
12. Spek AL (2003) Single-crystal structure validation with the program *PLATON*. *J Appl Crystallogr* 36:7–13
13. Albada GAV, DeDraaff RAG, Haasnoot GA, Reedijk J (1984) Synthesis, spectroscopic characterization, and magnetic properties of unusual 3,5-dialkyl-1,2,4-triazole compounds containing N-bridging isothiocyanato ligands. X-ray structure of trinuclear bis [(mu-thiocyanato-N)bis(mu-3,5-diethyl-1,2,4-triazole-N1,N2)bis(thiocyanato-N)(3,5-diethyl-1,2,4-triazole-N1)nickel(II)-N,N1,N1']nickel(II) dihydrate. *Inorg Chem* 23:1404–1408
14. Shen L, Xu Y-Z (2001) Structure and magnetic properties of a novel two-dimensional thiocyanato-bridged heterometallic polymer $\{Cu(en)_2[Ni(en)(SCN)_3]_2\}_n$. *J Chem Soc Dalton Trans* 3413–3414
15. Ranjan S, Dikshit SK (1998) Synthesis, spectroscopic, photophysical and electrochemical properties of cyano-bridged copper(I)-ruthenium(II) complexes. *Polyhedron* 17:3071–3082
16. Potocnak I, Dunaj-Jurco M, Miklos D, Jager L (2001) Crystal structure of bis-(2,2'-bipyridine-N, N')-(dicyanamide-N)-copper(II) tricyanomethanide. Electronic and structural parameters describing the shape of coordination polyhedra in five-coordinated copper(II) compounds. *Monatshefte fur Chemie* 132:315–327
17. Carballo R, Castineiras A, Balboa S, Covelo B, Niclos J (2002) Solid state coordination chemistry of copper(II)/ α -hydroxycarboxylato/2,2'-bipyridine systems. *Polyhedron* 21: 2811–2818
18. Kitaigorodskii AI (1973) *Molecular crystals and molecules*. Academic, New York
19. Gonze X, Beuken JM, Caracas R, Detraux F, Fuchs M, Rignanese GM, Sindic L, Verstraete M, Zerah G, Jollet F, Torrent M, Roy A, Mikami M, Ghosez P, Raty JY, Allan DC (2002) First-principles computation of material properties: the ABINIT software project. *Comput Mater Sci* 25(3):478–492
20. Zhang Y, Pan W, Yang W (1997) Describing van der waals interaction in diatomic molecules with generalized gradient approximations: The role of the exchange functional. *J Chem Phys* 107:7921–7925
21. Perdew JP, Burke K, Ernzerhof M (1996) Generalized gradient approximation made simple. *Phys Rev Lett* 77:3865–3868
22. Bencini A, Gatteschi D (1977) Single-crystal polarized electronic and electron spin resonance spectra of the trigonal-bipyramidal complex aquobis(1,10-phenanthroline)copper(II) nitrate. *Inorg Chem* 16:1994–1997
23. Bhat IU, Tabassum S (2009) Synthesis of new piperazine derived Cu(II)/Zn(II) metal complexes, their DNA binding studies, electrochemistry and anti-microbial activity: validation for specific recognition of Zn(II) complex to DNA helix by interaction with thymine base. *Spectrochim Acta A* 72:1026–1033
24. Ghosh BK, Chakravorty A (1989) Electrochemical studies of ruthenium compounds Part I. Ligand oxidation levels. *Coord Chem Rev* 95:239–294
25. Benesi HA, Hildebrand JH (1949) A spectrophotometric investigation of the interact ion of iodine with aromatic hydrocarbons. *J Am Chem Soc* 71:2703–2707
26. Song KC, Kim JS, Park SM, Chung KC, Ahn S, Chang SK (2006) Fluorogenic Hg^{2+} selective chemodosimeter derived from 8-hydroxyquinoline. *Org Lett* 8:3413–3416
27. Mello JV, Finney NS (2005) Reversing the discovery paradigm: a new approach to the combinatorial discovery of fluorescent chemosensors. *J Am Chem Soc* 127:10124–10125
28. Varnes AW, Dodson RB, Wehry EL (1972) Interactions of transition-metal ions with photoexcited states of flavines. Fluorescence quenching studies. *J Am Chem Soc* 94:946–950
29. Ha-Thi M-H, Penhoat M, Michelet V, Leray I (2007) Highly selective and sensitive phosphane sulfide derivative for the detection of Hg^{2+} in an organoaqueous medium. *Org Lett* 9: 1133–1136

Chapter 16

Using Electrochemical Impedance Spectroscopy of Methylene Blue and Ferricyanide for DNA Sensing Surface Characterization

Suthisa Leasen, Kallaya Sritunyalucksana-Dangtip, Jose H. Hodak, Jiraporn Srisala, Chadin Kulsing, and Waret Veerasia

Abstract In pathogen diagnosis, a single stranded target DNA may be detected in a sensor carrying an active surface with a recognition layer of its complementary single stranded DNA (ssDNA probe). Such a surface may be the core of a specific DNA sensing electrode. The density of probe ssDNA should then be optimized to display the greatest sensitivity to the target DNA. In this work we utilize the electrochemical impedance spectroscopy (EIS) on the electrode reactions for ferri/ferricyanide ($[\text{Fe}(\text{CN})_6]^{3-/4-}$) and methylene blue (MB) to characterize different stages along the development of an indium tin oxide (ITO)-DNA sensor for target ssDNA after PCR amplification. In particular, we study the effects of applied DC potential pretreatments on the ferri/ferricyanide-electrode interaction.

S. Leasen (✉)

Department of Physics, Mahidol University, Rama VI Road Thung Phyathai Rachadevi, 10400 Bangkok, Thailand
e-mail: sainub@gmail.com

K. Sritunyalucksana-Dangtip

Centex Shrimp, Mahidol University, Rama VI Road Thung Phyathai Rachadevi, 10400 Bangkok, Thailand
e-mail: tekst@mahidol.ac.th

J.H. Hodak

Facultad de Ciencias Exactas y Naturales, Ciudad Univeritaria Pab, Universidad de Buenos Aires, 1428 Buenos Aires, Argentina
e-mail: josew3@yahoo.com

J. Srisala

National Science and Technology Development Agency, National Center for Genetic Engineering and Biotechnology, Klongluang Province, 12120 Pathumthani, Thailand
e-mail: jsrisala@gmail.com

C. Kulsing • W. Veerasia

IFEC-MU, Mahidol University, Rama VI Road Thung Phyathai Rachadevi, 10400 Bangkok, Thailand
e-mail: payoonum@yahoo.com; scwvr@mahidol.ac.th

The effect of the electrostatic repulsion by negative charges of single stranded DNA (ssDNA) was observed to affect the rate of the overall reaction rates for the redox couples. On one hand, EIS spectra for the $[\text{Fe}(\text{CN})_6]^{3-/4-}$ reaction on DNA modified ITO surfaces yielded time-independent fitting parameters which were consistent with the scanning electrochemical microscopy (SECM) images. On the other hand, MB species yielded time-dependent parameters due to adsorption and intercalation processes that take place on DNA. Models were proposed to explain such time-dependent behavior. The results of the impedance measurements were explained in terms of the variation of the surface charge for different densities of probe ssDNA.

16.1 Introduction

Single stranded deoxyribonucleic acid (ssDNA) immobilized on solid substrates has been utilized as platform of biosensors in the diagnosis of genetic or infectious diseases, for environmental monitoring, for detecting microorganism contaminants in food and beverages, and for national defense applications [1]. There are several measurement techniques that employ ssDNA bases. One of the simplest techniques uses electrochemical measurements which can respond to recognition and hybridization events. Since the electrochemical DNA sensors are low cost, easy-to-use, offer fast response with low limits of detection, and may be miniaturized, they have developed considerably in recent times. As a result of advances over traditional methods such as gel electrophoresis or membrane blots [2], electrochemical DNA sensors have replaced these techniques to some extent, especially in combination with polymerase chain reaction amplification (PCR) [3, 4], and microarray technology [5], achieving high sensitivity and real-time measurement capabilities.

An electrochemical system may be interrogated by measurements of its characteristic impedance when a small sinusoidal potential is applied. This is usually done by recording the magnitude of the impedance and the phase shift between applied potential and measured current, which are represented as a Nyquist plot (real against imaginary impedances) or as a Bode plot (frequency versus phase shift). These data provide valuable information about the kinetics of the electrode processes.

Dielectric layers created by surface modification of electrodes can be studied by electrochemical impedance spectroscopy. Single stranded DNA bound on an ITO surface for hybridization of a complementary target is a good example of a dielectric layer that is normally employed as platform in electrochemical DNA sensor [6–9]. In the case of an electrochemical DNA sensor, the interfacial regions of interest contain single stranded deoxyribonucleic acid (ssDNA) and double helix formed by recognition and complementary matching as well as non-complementary DNA hybridization (dsDNA). In this investigation ssDNA were immobilized at high density on ITO surfaces to achieve selectivity and to get the highest yield for complementary target DNA hybridization [10].

The surface coverage of the modified layer could be easily assessed from EIS which can quantify the immobilized DNA molecule density and confirm its

attachment. The appropriate surface density of the recognition molecules is also important for obtaining a high interaction signal from the target molecule [10]. Furthermore, from the estimated surface coverage or density, the different signals from various electroactive species [11, 12] from a set of layers may be used in the interpretation of the nature of the attached layer. The differences in the interactions of electroactive species can have physical or chemical origin and can be detected by electrochemical signals.

For noninvasive characterization of reversible and specific binding of DNA before and after hybridization, probe molecules such as iron or ruthinium metal complexes are commonly utilized [13–15]. One of the most widely used probes is the iron metal complex, ferri/ferrocyanide ion, which interacts reversibly with the electrode yielding time independent signals. Because of the charge-charge interactions, the negative metal complex such as ferri/ferrocyanide will be hindered by negative charge density conferred by other molecules such as single and/or double form of DNA. This hindrance will mainly affect the charge transfer process which is manifested by the semi-circle part of the Nyquist plot. Methylene blue is another valuable electroactive species due to its low reduction potential, and its specific interaction with certain biomolecules such as DNA. MB may interact with DNA via electrostatic fields with the negative backbone as well as intercalation into the double helix, and binding to the nitrogen base groups [16]. Thus, MB can be utilized as an indicator in electrochemical DNA sensors. Although MB has many useful properties, it has several drawbacks such as, adsorption on various substrates showing slowly varying interactions with the exposure time. However the time dependent behavior of MB could be described by a Langmuir isotherm which may be used to model the interaction with the DNA.

Despite of these drawbacks our results show that the time dependent EIS spectra of MB differ for each layer and may be used for their characterization. The behavior of the two electroactive species used as probes also showed significant differences detected by impedance spectroscopy. These results were confirmed by open circuit measurements and data on the rate of reaction through electron transfer resistance of MB and ferri/ferrocyanide redox couples.

16.2 Methodology

16.2.1 Chemicals and Reagents

Single stranded oligonucleotides (24-mer) were used as recognition and probe molecules. The sequence used was 5'-GATGGAAACGGTAACGAATCTGAA-3'. A 5'-disulfide bond modified probe ssDNA was reduced before immobilization by 1,4-dithio-DL-threitol (DTT). The complementary target was the PCR product obtained from shrimp samples at CENTEX. The thiol modified probe and the complementary target DNA were suspended in 2XSSC (0.3 M sodium chloride,

0.015 M sodium citrate). 1,4-Dithio-DL-threitol and 3-mercaptopropionic acid (MPA) were purchased from Fluka. Methylene blue and sodium citrate tribasic were purchased from Sigma-Aldrich and sodium chloride from Lab Scan. Sodium dodecyl sulfate (SDS) was purchased from BIOBASIC INC.

16.2.2 Cleaning and Patterning ITO

The substrate of sensor was Tin doped Indium Oxide (ITO) coated glass and it was obtained from Luminescence Technology Corp. The thickness of the ITO film was 140 nm with resistivity of $10^{-4} \Omega\cdot\text{cm}$. The ITO surface was cleaned in ultrasonic bath, once in detergent, twice in deionized water, acetone and isopropanol, respectively. The cleaned surface was patterned to have only a circular ITO coated spot of 8 mm in diameter in the center of the glass. This was accomplished by photolithographic masking followed by chemical etching of the surrounding ITO with HCl (37% w/w in water) to have a circular active area of 0.5 cm^2 .

16.2.3 Self Assembly of MPA onto ITO

The MPA modification onto ITO coated glass surface was carried out by self assembly technique following the work of Lee et al. [17]. The activated ITO was soaked in 5 mM MPA overnight, rinsed by deionized water and dried under a nitrogen gas stream. From previous investigations, the carboxylic end attaches to ITO and exposes a free thiol end that can be used for covalent immobilization of the thiol modified ssDNA via disulfide bonds [18]. In this work, we refer to the region of the ITO substrate that received the MPA surface modification as the “active surface”.

16.2.4 Immobilization of Probe ssDNA on MPA/ITO Surfaces

The MPA/ITO was equilibrated with 2XSSC (0.3 M sodium chloride, 0.015 M sodium citrate) for 5 min. A 50 μl aliquot of the thiol modified probe ssDNA was then applied on the active surface. The immobilized ssDNA surface was incubated at 37°C in a humidity chamber for 1 h. The unbound probe ssDNA was removed by rinsing with a mixture of 0.1% SDS (sodium dodecyl sulfate) and 2XSSC at 37°C . The complementary target was then hybridized in 2XSSC at 42°C for 1 h. The non-specific adsorption of target DNA was washed out with a rinsing sequence of 2XSSC, 1XSSC and 0.5XSSC solutions, respectively.

16.2.5 Electrochemical Impedance Spectroscopy

All the electrochemical impedances were obtained using a potentiostat/galvanostat (μ AutoLab type III equipped with FRA2 module). The counter and reference electrodes were a platinum rod and Ag/AgCl electrode in saturated 3 M KCl, respectively. The working electrodes were bare ITO, MPA/ITO, ssDNA-MPA/ITO and dsDNA-MPA/ITO. Before carrying the impedance measurements, they were pretreated with positive for ferri/ferrocyanide and negative DC potential for MB with a fixed period of time.

16.2.5.1 Ferri/Ferrocyanide Active Species

The supporting electrolyte for the experiments with ferri/ferrocyanide was tris-HCl:NaCl (10:1) at pH 7.0. The ferri/ferrocyanide ion concentration was 20 mM used for pretreatment of the surface at 0.1 V against Ag/AgCl reference electrode. The electrochemical impedance spectroscopy used sinusoidal wave with amplitude of 5 mV in the frequency range 10^{-1} – 10^4 Hz coupled on a DC potential 0.01 V versus Ag/AgCl reference electrode.

16.2.5.2 Methylene Blue Active Species

The same supporting electrolyte was employed in MB and ferri/ferrocyanide impedance measurements. MB impedance data were collected in the same frequency range as for ferri/ferrocyanide, except that the MB concentration was reduced to 20 μ M to minimize adsorption processes and measured EIS at -0.144 V DC coupling versus open circuit potential.

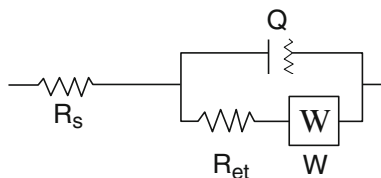
16.3 Results and Discussion

16.3.1 Electrochemical Impedance Spectroscopy of Ferri/Ferrocyanide Species

16.3.1.1 Different Densities of Probe ssDNA in Ferri/Ferrocyanide Solution

The impedance spectra for the samples having different probe ssDNA coverage densities, were measured in $[\text{Fe}(\text{CN})_6]^{3-/4-}$ couple at 0.01 V vs Ag/AgCl. To relate probe density with the EIS measurement, the experimental spectra were fitted with the same equivalent circuit used for modeling MB experiments (Fig. 16.1). Before the interaction with the probe ssDNA was characterized, two factors need to be controlled to give a reliable result: a pretreatment step [19, 20], and

Fig. 16.1 The Randle model equivalent circuit for the electrochemical impedance measurements



an MPA background to test for immobilization of the probe ssDNA. The effect of the pretreatment was investigated by in situ EIS measurement [21]. The use of a pretreatment at 0.1 V positive potential yielded more stable impedance and phase shift data over the measurement time. This is shown in Fig. 16.2, for impedance data observed at a fixed frequency of 58.9 Hz. Both the magnitude as well as the phase-shift for the $[\text{Fe}(\text{CN})_6]^{3-/4-}$ reaction increase up to a maximum at 48 s decaying thereafter (Fig. 16.2a). Furthermore, the data appear to drift even after 200 s. In contrast, a stable signal was achieved only after 100 s with a pretreatment at 0.1 V (Fig. 16.2b). When a 0.01 V pretreatment was applied, there was a slow process giving rise to a peak during the 0–100 s period which disappeared in the pretreatment at more positive potentials. This may be due to migration of $[\text{Fe}(\text{CN})_6]^{3-/4-}$ reaching the active site faster, where the electron transfer to the electrode occurs. Therefore, the negative ssDNA could hinder $[\text{Fe}(\text{CN})_6]^{3-/4-}$ from reaching the active site and this would lead to errors in the experiment if the pretreatment is omitted [12]. Thus, the different densities of probe ssDNA after the pretreatment were characterized by using various MPA background electrodes which produced the R_{et} values shown in Table 16.1. The constant phase element was characterized by two parameters n and Y_0 . The parameter n reflects the regularity of the charge on the surface [22], while Y_0 is related to the amount of charge on the surface [23]. Figure 16.3 shows that differences in the electrical regularity of the surfaces can be observed for different probe densities relative to a bare MPA layer. Thus, the dispersion in the parameter n or Δn was taken as an analytical measurement for the probe surface coverage. For ssDNA immobilized on MPA/ITO, the values of Δn for MPA were higher than for ssDNA layer, which suggests a higher level of electrochemical irregularity or greater electrochemical roughness [22] with increased probe DNA coverage. However, a non-linear relation with probe concentration was observed. This may be due to the random orientation that the probe ssDNA molecules can adopt by virtue of their flexibility. The hybridization of the probe to the target into a double helix is certainly more rigid and will tend to be oriented to a larger extent on the surface than ssDNA. As a result, this gives rise to a linear relation with probe concentration at fixed target concentration. The linear relationship between the values of Δn and ΔR_{ct} with probe concentration shown in Fig. 16.3a supports this conclusion. These assumptions are also consistent with the trend in the SECM results (Fig. 16.5a, b). Furthermore, Y_0 increased as more probes were immobilized, specifically Y_0 increased when the probe concentration increased from 0.03 fM to 3 pM as shown in Table 16.1. This would correspond to an accumulation of negative charges on the surface due to the increasing DNA

Table 16.1 Fitting parameters for ferri/ferrocyanide species at various probe ssDNA concentrations and fixed complementary target concentration

ssDNA concentration (fM)	Time constant dispersion (n)		Constant phase element coefficient Y_0 ($S^0/\Omega \cdot cm^2$)		Charge transfer resistance R_{ct} (Ω)	
	MPA	ssDNA	MPA	ssDNA	MPA	ssDNA
0.03	0.92	0.88	11×10^{-6}	11×10^{-6}	1,851	2,661
3	0.90	0.87	12×10^{-6}	11×10^{-6}	1,823	2,404
3,000	0.95	0.90	8×10^{-6}	14×10^{-6}	1,810	2,341

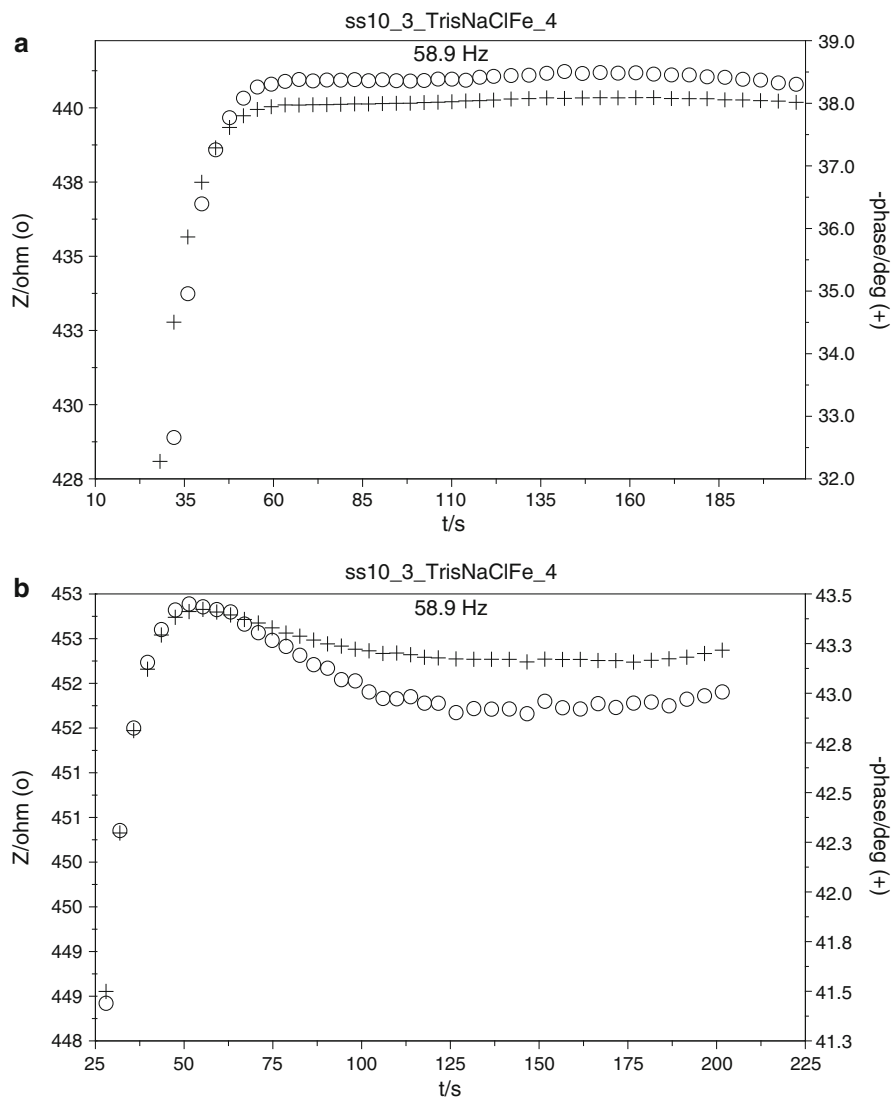


Fig. 16.2 Total impedance (O, *left axis*) and phase shift (+, *right axis*) profile as the time passed at 0.01 V using frequency 58.9 Hz in $[\text{Fe}(\text{CN})_6]^{3-/4-}$ solution, after (a) a pretreatment at 0.1 V for 30 s (b) a pretreatment at 0.01 V for 25 s

probe density. Although such probes can prevent the negative $[\text{Fe}(\text{CN})_6]^{3-/4-}$ from approaching the active surface [12], it can directly add negative charge to the surface thereby rising the Y_0 parameter as more probe molecules are immobilized. This was supported by the linear decrease in the value of R_{ct} with the logarithm of the probe concentration which is in contrast to the non linear increase observed in the value of Y_0 . Based on the assumption that R_{ct} was linearly proportional to the

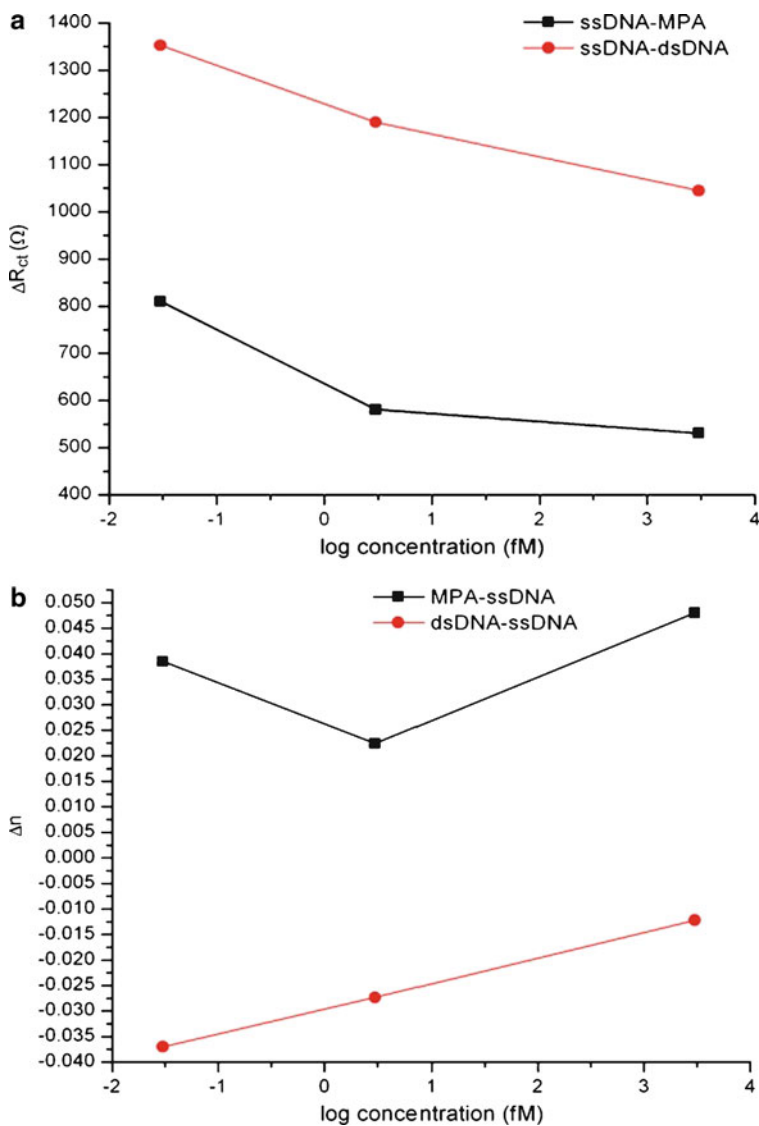


Fig. 16.3 Fitted constant phase element values, (a) differentiate R_{ct} and (b) no. of probe ssDNA having various densities; 0.03 fM, 3 fM and 0.3 pM in 20 mM $[\text{Fe}(\text{CN})_6]^{3-/4-}$ solution

surface concentration of $[\text{Fe}(\text{CN})_6]^{3-/4-}$, these results indicate that the effect of the reduction of negative charge preventing $[\text{Fe}(\text{CN})_6]^{3-/4-}$ from reaching the electrode had a smaller contribution than the increase of negative charge coming from higher DNA probe concentrations.

16.3.1.2 Single and Double Stranded DNA in Ferri/Ferrocyanide Electrochemical Impedance Spectra

After hybridization with complementary target DNA, Bode plots of three ssDNA modified electrodes, having different probe densities, showed a decrease in phase shift in $[\text{Fe}(\text{CN})_6]^{3-/4-}$ solution. Therefore the change in the phase shift was measured for discriminating double strand (ds) from single strand (ss) DNA (Fig. 16.4). In addition, the difference between the Bode peak height of ss and dsDNA decreased suggesting that more probe molecules interacted on MPA. The differences in R_{et} also had this trend. In this set of experiments we concluded that the best resolution was observed at 0.03 fM probe concentration (Fig. 16.4a–c).

16.4 Scanning Electrochemical Microscopy (SECM) Characterization

Since the surface properties in MB slowly changed with time, a long time scale measurement (more than 2 h) in SECM did not give consistent results. Therefore, only samples in ferri/ferrocyanide were characterized by SECM. The redox reaction of $[\text{Fe}(\text{CN})_6]^{3-/4-}$ for the probe ssDNA concentrations 3 pM and 300 pM, were mapped in two dimensions (Fig. 16.5a, b respectively). The results show that the electrochemical surface roughness at 300 pM was greater than that for 3 pM, which correlated well with a decrease in the parameter n in EIS as higher probe density was immobilized on the surface.

16.5 Electrochemical Impedance Spectroscopy in the Presence of MB Species

16.5.1 Open Circuit Potentials (OCP)

After the pretreatment step, a system containing ferri/ferrocyanide showed a stable OCP and it was possible to fit all the EIS components after measuring for three times (data not shown), this gave time-independent fitted parameters from EIS. In contrast, when MB was used as the active species unstable OCPs were observed, and time-dependent fitting parameters resulted from the analysis of the EIS data. There was a decrease in the OCP with time for all surfaces: ITO, MPA modified ITO (MPA/ITO) and ssDNA immobilized MPA/ITO, in the case of our experiments with MB (Fig. 16.6 second and third measurements). This indicated that the redox species or MB^+ accept electrons from the electrode surface and decreased the OCP with the exposure time. Bare ITO electrodes and those carrying ssDNA immobilized on MPA/ITO gave a faster decrease of their OCP than the MPA/ITO electrode

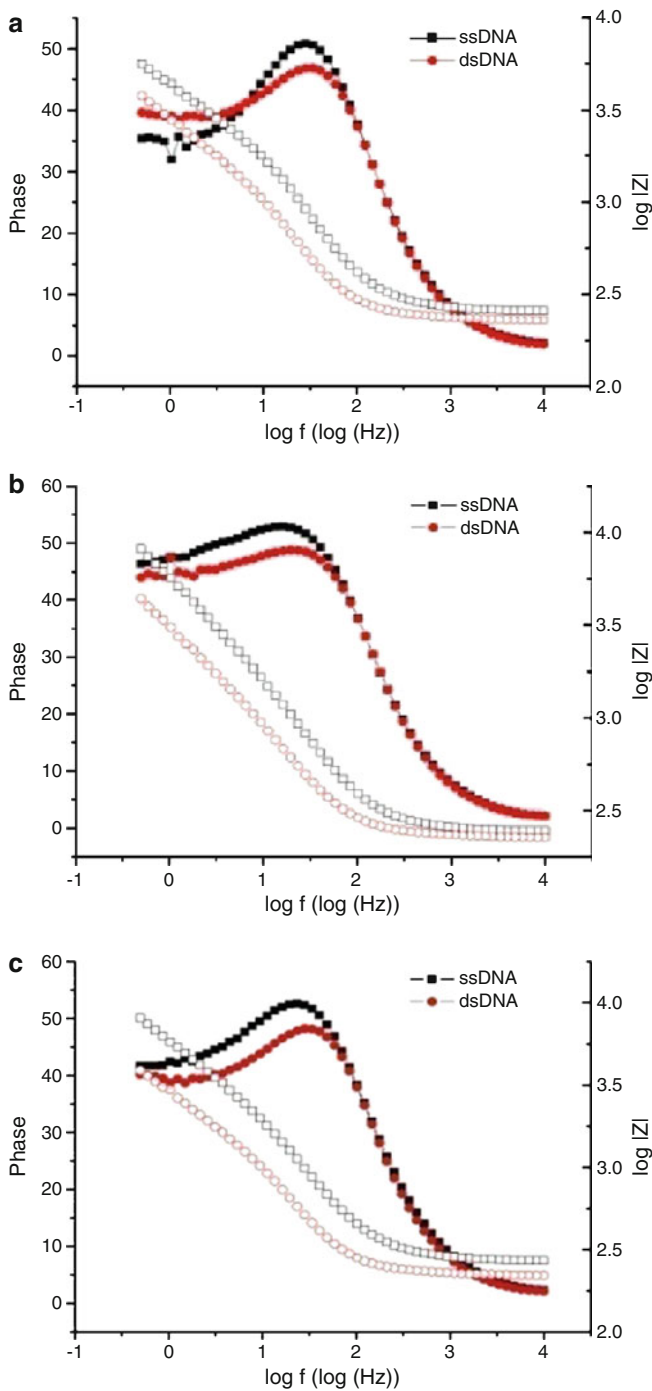


Fig. 16.4 Phase shift and total impedance in Bode plots of probe ssDNA (■, □) and dsDNA (●, ○), having various densities of probes in $[\text{Fe}(\text{CN})_6]^{3-/4-}$ solution; (a) 3 pM, (b) 3 fM, and (c) 0.03 fM respectively

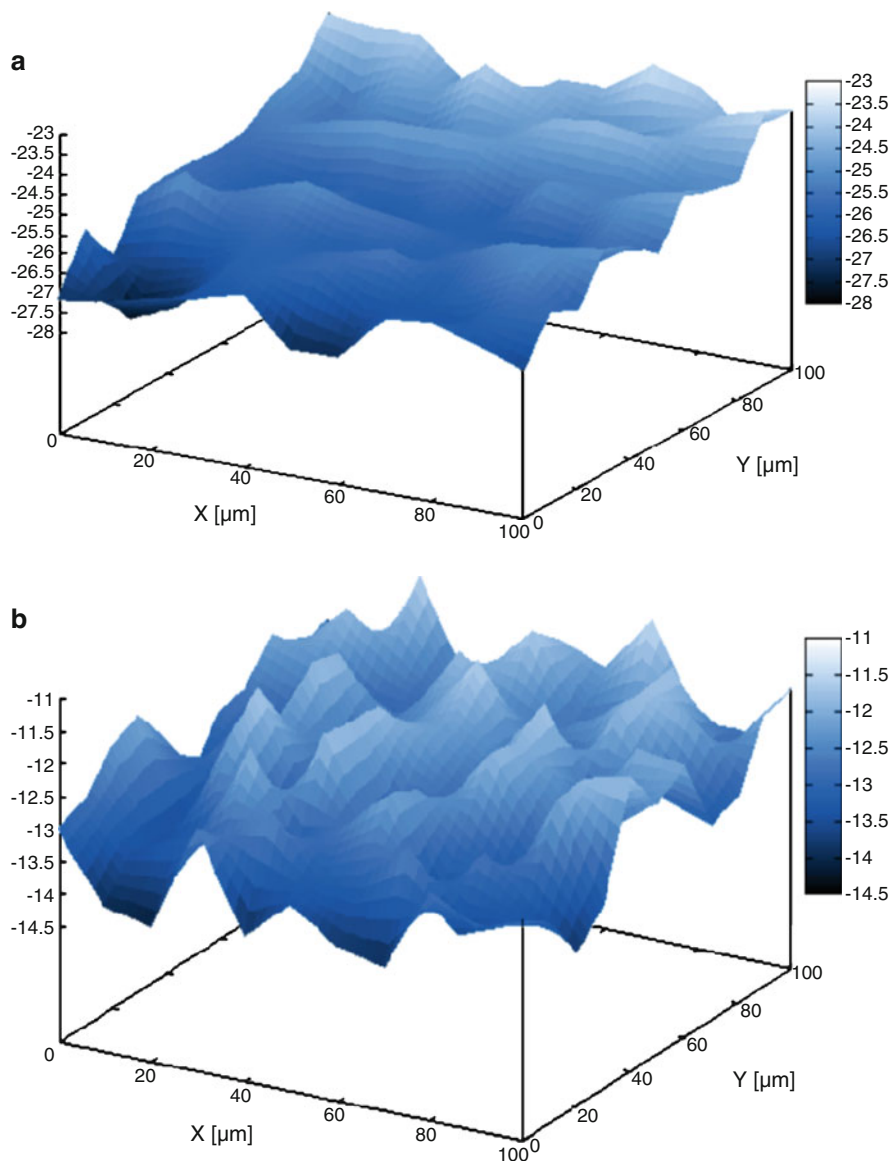


Fig. 16.5 Local (x and y-axis) SECM images of (a) 3 pM and (b) 33 nM of probe ssDNA in $[\text{Fe}(\text{CN})_6]^{3-/4-}$ solution, z-axis was the current from the redox reaction of $[\text{Fe}(\text{CN})_6]^{3-/4-}$

(Fig. 16.6) which may be due to MB binding at metal sites on the ITO itself and to nitrogenous base structures in ssDNA while MPA may act by blocking the active area of ITO metal sites.

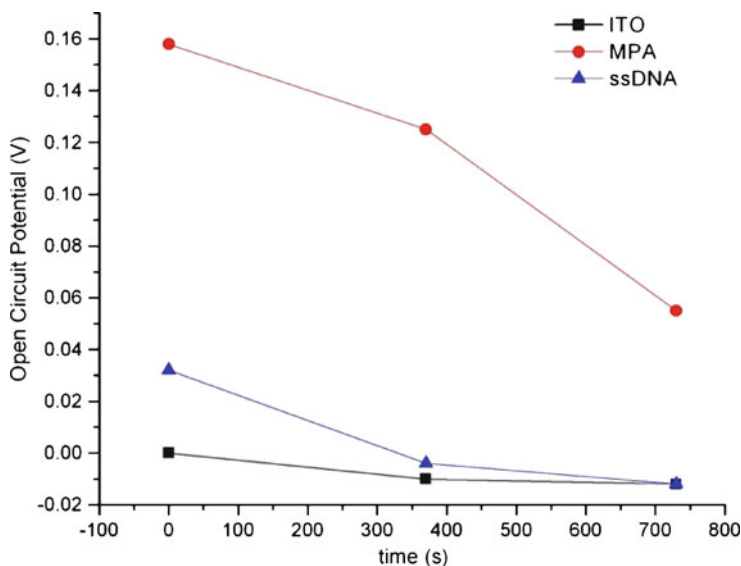


Fig. 16.6 Open circuit potentials OCP (V vs Ag/AgCl, y-axis) and repeated number of measurements (x-axis) in MB of ITO, MPA self assembled on ITO (MPA/ITO) and ssDNA immobilized MPA self assembled on ITO (ssDNA-MPA/ITO)

16.6 Electrochemical Impedance Measurements

From experiments of differential pulse voltammetry using MB as the active redox species we observed signs of intercalation in the DNA structure. The mechanisms of MB intercalation on the DNA platform change once hybridization take place due to the formation of double stranded DNA. Indeed, EIS spectra of MB for ITO, ssDNA and dsDNA showed significant changes during the probe exposure time, while the MPA/ITO surfaces only showed slight changes. From EIS theory the variation of the charge transfer resistance is related to the rate of the redox reaction for the active species [24]. Therefore, the experimental spectra were fitted to the Randle's equivalent circuit model [25], except that the double layer capacitor (C) was replaced with a constant phase element (Q) in the configuration shown in Fig. 16.2 [22]. The fitted parameters are the solution resistance (R_s), electron transfer resistance (R_{et}), the diffusion or Warburg impedance (W) and the constant phase element (Q). The fitted parameters for experiments on ITO, MPA and probe ssDNA are summarized in Table 16.2.

The values of n in Table 16.2 which are taken to describe electrochemical surface roughness decrease with increasing times after the end of the pre-treatment. For bare ITO using MB as the redox couple, we observe a fast initial roughness decrease remaining unchanged on subsequent measurements 6 and 12 min later. In contrast, when the electrode carries the MPA and ssDNA modifications, there are

Table 16.2 Fitting parameters from EIS for MB species for various surfaces: ITO, MPA, ssDNA

Measurement (min)	Time constant dispersion (n)			Constant phase element coefficient Y_0 ($S^0/\Omega \cdot cm^2$)			Charge transfer resistance R_{ct} ($k\Omega$)		
	ITO	MPA	ssDNA	ITO	MPA	ssDNA	ITO	MPA	ssDNA
	0-6	0.93	0.96	0.95	5.4×10^{-6}	3.7×10^{-6}	4.8×10^{-6}	682	N/A
6-12	0.90	0.92	0.92	6.8×10^{-6}	6.1×10^{-6}	7.0×10^{-6}	339	704	593
12-18	0.89	0.90	0.90	7.2×10^{-6}	7.2×10^{-6}	8.6×10^{-6}	303	419	310

noticeable changes during the entire experiment (12 min span). The concomitant kinetic parameters, the charge transfer resistance, for ITO and ssDNA had an abrupt decrease which was not resolved in the scale of our experiments. However, it appears to reach steady values on the second and third measurements (on a time scale longer than 6 min). These time dependencies are due to a reaction period where MB combines with metal sites in ITO and with nitrogenous base of ssDNA. In contrast, bare ITO directly reacted with MB, while MPA and ssDNA require traversing through organic layer that were deposited. The values of Y_0 also show similar trends as described for the other parameters. These results reveal increasing accumulated charge on surface that arises from adsorbed MB on the modified surface.

16.7 Conclusions

We have investigated the response of ITO electrodes modified with ssDNA for specific recognition of a target DNA. The properties of the modified interface were quantified by electrochemical impedance spectroscopy (EIS). We have found that the MPA layer provides an efficient platform for the immobilization of the probe ssDNA recognition layer. Among the active species ferri/ferrocyanide and methylene blue, it was found that either may be used to detect the immobilization of ssDNA on MPA. The EIS spectra were found to be a sensitive means of detecting the variation of probe ssDNA density giving results that are consistent with those from scanning electrochemical microscopy (SECM). Because EIS is much more simpler to implement than SECM, we conclude that DNA sensing could in principle be carried out using ssDNA/MPA modified ITO electrodes to construct specific sensing devices for DNA.

Acknowledgments Suthisa Leasen gratefully thanks for the financial support from Commission on Higher Education. The authors also thank Genome Institute of National Center for Genetic Engineering and Biotechnology for characterizing synthesized oligonucleotides.

References

1. Ronkainen NJ, Halsall HB, Heineman WR (2010) Electrochemical biosensors. *Chem Soc Rev* 39:1747–1763
2. Wang J (2005) Electrochemical nucleic acid biosensors. In: Paleček E, Scheller F, Wang J (eds) *Electrochemistry of nucleic acids and proteins: towards electrochemical sensors for genomics and proteomics*, 1st edn. Elsevier, Amsterdam
3. Ye Y, Ju H (2003) DNA electrochemical behaviors, recognition and sensing by combining with PCR. *Sensors* 3:128–145
4. Ferguson BS et al. (2009) Integrated microfluidic electrochemical DNA sensor. *Anal Chem* 81:6503–6508
5. Cagnin S et al. (2009) Overview of electrochemical DNA biosensors: new approaches to detect the expression of life. *Sensors* 9:3122–3148

6. Hleli S, Abdelghani A, Tlili A (2003) Impedance spectroscopy technique for DNA hybridization. *Sensors* 3:472–479
7. Fu Y et al. (2005) Electrochemical impedance behavior of DNA biosensor based on colloidal Ag and bilayer two-dimensional sol-gel as matrices. *J Biochem Biophys Methods* 62:163–174
8. Zhang S et al. (2007) A sensitive impedance immunosensor based on functionalized gold nanoparticle-protein composite films for probing apolipoprotein A-I. *Talanta* 71:874–881
9. Lisdat F, Schäfer D (2008) The use of electrochemical impedance spectroscopy for biosensing. *Anal Bioanal Chem* 391:1555–1567
10. Keighley SD, Li P, Estrela P, Migliorato P (2008) Optimization of DNA immobilization on gold electrodes for label-free detection by electrochemical impedance spectroscopy. *Biosens Bioelectron* 23:1291–1297
11. Kelley SO, Barton JK (1997) Electrochemistry of methylene blue bound to a DNA-modified electrode. *Bioconjug Chem* 8:31–37
12. Xu J et al. (2001) A novel DNA-modified indium tin oxide electrode. *Electrochem Commun* 3(11):665–669
13. Napier ME, Thorp HH (1997) Modification of electrodes with dicarboxylate self-assembled monolayers for attachment and detection of nucleic acids. *Langmuir* 13:6342–6344
14. Armistead PM, Thorp HH (2000) Modification of indium tin oxide electrodes with nucleic acids: detection of attomole quantities of immobilized DNA by electrocatalysis. *Anal Chem* 72:3764–3770
15. Yang IV, Thorp HH (2001) Modification of indium tin oxide electrodes with repeat polynucleotides: electrochemical detection of trinucleotide repeat expansion. *Anal Chem* 73:5316–5322
16. Pan D, Zuo X, Wan Y et al. (2007) Electrochemical interrogation of interactions between surface-confined DNA and methylene blue. *Sensors* 7:2671–2680
17. Lee TM, Li LL, Hsing IM (2003) Enhanced electrochemical detection of DNA hybridization based on electrode-surface modification. *Langmuir* 19:4338–4343
18. Gardner TJ, Frisbie CD, Wrighton MS (1995) Systems for orthogonal self-assembly of electroactive monolayers on Au and ITO: an approach to molecular electronics. *J Am Chem Soc* 117:6927–6933
19. Zhang W et al. (2008) Anodic electrochemical pretreatment time and potential affect the electrochemical characteristics of moderately boron-doped diamond electrode. *Collect Czech Chem Commun* 73(1):73–87
20. Shahin G (2008) A new pretreatment cycle for plating magnesium alloys. In: *Proceedings of the AESF SUR/FIN annual international technical conference, Washington, DC*, pp 373–388
21. Liu J et al (2005) In situ hybridization of PNA/DNA studied label-free by electrochemical impedance spectroscopy. *Chem Commun* 23:2969–2971
22. Ehrensberger MT, Gilbert JL (2010) A time-based potential step analysis of electrochemical impedance incorporating a constant phase element: a study of commercially pure titanium in phosphate buffered saline. *J Biomed Mater Res A* 94A(2):576–584
23. Brug GJ et al. (1984) The analysis of electrode impedances complicated by the presence of a constant phase element. *J Electroanal Chem Interfacial Electrochem* 176(1–2):275–95
24. Li D et al. (2007) Kinetic study of DNA/DNA hybridization with electrochemical impedance spectroscopy. *Electrochem Commun* 9:191–196
25. Yang L, Bashir R (2008) Electrical/electrochemical impedance for rapid detection of foodborne pathogenic bacteria. *Biotechnol Adv* 26:135–150

Chapter 17

An Investigation into the Use of the Concept Attainment Model in Teaching the “Periodic Table” at ‘O’-Level Through an Action Research

Mokshada Luckpoteea and Fawzia B. Narod

Abstract The present study was based on the use of the concept attainment model (CAM) in the teaching of the topic “Periodic Table” at the ‘O’-level, in an attempt to investigate its impact on students’ understanding and on students’ motivation and interest during the lessons. The research was carried out in a girls’ State Secondary School in a village located in the northern region of Mauritius. The sample consisted of 44 girls of age 14–15 years, who were preparing to sit for the ‘O’-level Cambridge International Examinations in November 2009. The study was carried out through an action research involving three cycles. Data were collected through observation checklists, achievement tests, students’ questionnaire and a group interview. Results from the study have revealed that use of CAM has motivated the students, and increased their level of participation during the lessons. Our findings have also shown that use of the model has enhanced conceptual understanding and helped to improve students’ performance in the topic “Periodic Table”. Most interestingly, we have also found that students were better able to identify the attributes of the concepts when varied resources and strategies were used to present the exemplars and non exemplars. Thus we would recommend that for successful implementation of the CAM in classroom teaching, educators should continuously vary the ways of presenting the exemplars and non-exemplars.

M. Luckpoteea

Simadree Virahsawmy State Secondary School, Rivière du Rempart, Mauritius

e-mail: mokshada25@hotmail.com

F.B. Narod (✉)

Department of Science Education, Mauritius Institute of Education, Réduit, Mauritius

e-mail: zia373@eudoramail.com

17.1 Introduction

Understanding the Periodic Table is critical for chemistry students since it is at the heart of all areas of chemistry. Perhaps it would be more appropriate to say that all of chemistry starts with the Periodic Table; it is the most significant tool that chemists use for organizing and recalling chemical facts about elements. Gallagher and Ingram [1] pinpointed that the Periodic Table is the most important chemistry reference that exists; it contains an enormous amount of important information and is very useful in the world of chemistry. The Periodic Table is also an extremely helpful tool when it comes to understanding why elements react the way they do. Elements interact differently with each other to produce simple everyday things such as table salt [2]. At a fundamental level, all of chemistry is contained in the Periodic Table. The structure of the table reflects the electronic structure of the elements, and hence their chemical properties and behavior. As rightly highlighted by Bouma [3], the Periodic Table is ubiquitous within the academic discipline of chemistry, providing an extremely invaluable framework to classify, systematize and compare all the many different forms of chemical behavior.

On the other hand, many students at “O”-level often perceive the topic “Periodic Table” as difficult and confusing, possibly because of inappropriate frameworks and lack of cognitive strategies. Furthermore, from recent Cambridge International Examinations (CIE) and previously University of Cambridge Local Examinations Syndicate (UCLES) “O”-level Examiners’ reports, it has been noted that many students failed to realize some prior concepts of the “Periodic Table” and this led to some misconceptions about the topic. The examiners also reported that a common reason for scoring poorly in questions that demand explanations was that many students gave general answers showing that these students have learned by rote. A general answer is unlikely to gain full marks because it indicates that the students cannot apply their knowledge. Some common mistakes reported include: (UCLES examination report–November 2005).

- Wrong observations, for example the production of the halogens as gases or solids rather than as colored aqueous solutions.
- Incorrectly balanced equations, or equations with wrong formulae. The same error was often repeated in every equation given, leading to a potential loss of several marks.
- Confusing the order of reactivity of halogens, believing that iodine is the most reactive.

Analysis of the CIE and UCLES Examiners’ reports has revealed that grasping the underlying concepts of the “Periodic Table” seems to be a problem for many students. They are often unable to apply their knowledge to given situations. Interpretative and analytical skills are often absent and students are unable to develop logical explanations and to draw valid inferences. Sevcik and co-workers [4] also reported that students often memorize facts about periodic table element arrangement without understanding the significance of the elements themselves.

In fact, one of the possible factors responsible for the misconceptions and problems encountered by students might be attributed to the way the topic is being taught: too much reliance on the traditional chalk and board method [5, 6]. For years, chemistry teachers have taught the topic “Periodic Table” using the traditional teacher-centered method. As a result, students have learnt the topic by the drill or rote approach whereby they could not really understand what was needed to be learnt [5, 6]. However, the “Periodic Table” is not a topic that can be learnt by heart or through drill-and-practice. It requires reasoning and commonsense that drill-and-practice and rote learning cannot inculcate. Furthermore, it is crucial for students to understand that Mendeleev [7] worked painstakingly hard and long to arrange the elements that form part of everything on earth, and that he was able to predict the existence of numerous elements that were not even discovered during his time.

It has also been noticed that many students lack the required critical thinking skills and problem-solving skills to solve problems on their own. As stated by Chuckowree [5], one of the factors responsible for the lack of skills could be that learners are groomed towards too much of the expository method and spoon-feeding. It is important for teachers to present data in an effective and interesting way through thoughtful selection and use of teaching aids where students are actively involved [8]. More engaging teaching approaches should be used to increase the involvement of students in the teaching/learning process. Fowler [9] suggested that students must be encouraged to ‘learn how to learn’ and ‘learning how to learn’ also requires pupils to use relationships as a means of bringing new opportunities to learning.

In view of the above discussions, an attempt has been made in the present study to use a different strategy to teach the “Periodic Table” to promote deep and meaningful learning of the topic. We wanted to shift from passive to active learning, and most importantly to create classroom situations where students would be encouraged to indulge in thinking and to seek hidden explanations. Indeed, we have used the Concept Attainment Model (CAM) as a strategy in the teaching and learning of the topic “Periodic Table” in view of studying its impact on pupils’ motivation, interest and conceptual acquisition. According to our knowledge, no research has been carried out on the use of the model in the teaching and learning of the “Periodic Table” at “O”-level.

17.1.1 Theoretical Framework – The Concept Attainment Model (CAM)

The Concept Attainment Model (CAM) is a technique of teaching and learning that helps to achieve a consistent understanding of important concepts and ideas [10]. The model is based on the works of Bruner [11] who believed that “to perceive is to categorize, to conceptualize is to categorize, to learn is to form categories, to make decisions is to categorize”. Bruner [11] stated people interpret the world in terms

of its similarities and differences and suggested a system of coding in which people form a hierarchical arrangement of related categories. Bruner et al. [12] qualified concept attainment as “the search for and listing of attributes that can be used to distinguish exemplars from non-exemplars of various categories”. According to Schunk [13], the CAM is built on the preposition that concepts involve the process of rule formation used to establish a concept’s critical features, in other words, its attributes. The model dictates a process in which students inductively learn a concept via the following process: the instructor selects the concept to be taught, determines the associated attributes and builds a list of examples (called exemplars) and non-examples (called non-exemplars) of the concepts. He then presents the exemplars and non-exemplars to learners, who are inductively brought to figure out the attributes of the concept by comparing and contrasting the exemplars and non-exemplars. Learners then separate them into groups and instructor develops a concept definition with interaction from the learners, provides additional examples and invites learners to suggest more examples [14]. The four-stage description of the CAM as per Klausmeier [14] is illustrated in Fig. 17.1. Moreover Driscoll [15] commented that teachers should provide opportunities for students to test other examples while implementing the CAM. According to Tennyson and Cocchiarella [16], teachers should be very careful while selecting and designing the exemplars and non-exemplars so that the attributes are clear.

Taba [17] reported that students can make generalizations after data are organized. She believed that students can be led towards making generalizations through concept development and concept attainment strategies. This is in line with Piaget’s work [18] in cognitive psychology; his ideas about assimilation, accommodation and schema have dramatically contributed to concept learning. More recently, Joyce and co-workers [19] have stated that the CAM requires a learner to figure out about the attributes of a category already formed in another person’s mind (the instructor) by comparing and contrasting examples that contain the characteristics of the concepts (the exemplars) with examples that do not contain those attributes (the non-exemplars). They also highlighted that selection of the negative examples (non-exemplars) is crucial in the implementation of the CAM as these would help learners identify the boundaries of the concept.

The CAM is reported to be an excellent evaluation tool when teachers want to determine whether important ideas introduced earlier have been mastered [20]. In addition, Bruner [21] stated that the model is particularly designed to clarify ideas and to introduce aspects of specific concepts and can be used to introduce or conclude a unit of study. He also highlighted that through data-collection and data-processing, students will not only be enhancing their observational skills but will also be extending their prior knowledge. According to literature, while implementing the CAM teachers should encourage students to work in cooperative groups to discuss the various characteristics of the objects presented [22]. Gagne [23] claimed that the model can promote active learning as learners are engaged in constructing their own knowledge. Most importantly, Joyce and co-workers [19] have shown that the CAM has a high tolerance for ambiguity. They pointed out that though in the initial stages of the model, learners might seem to be following

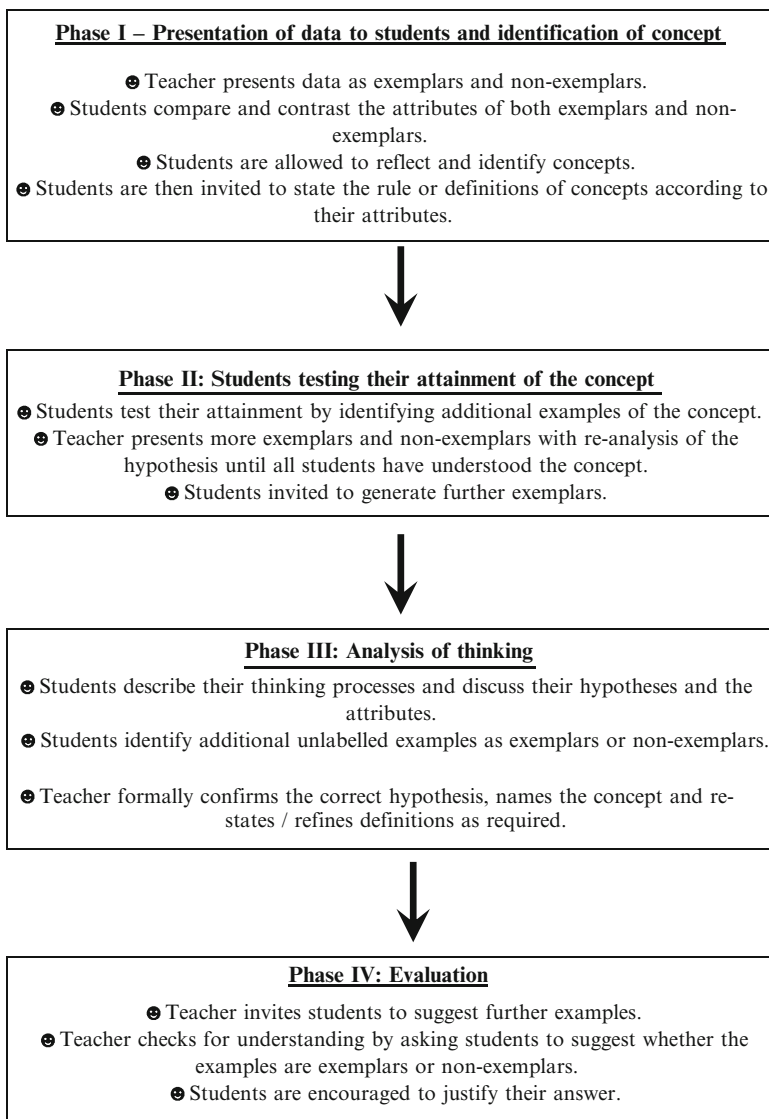


Fig. 17.1 Phases of the concept attainment model

the wrong path, they eventually would all come up to the expected results. In other words, the strategy nurtures an awareness of alternative perspectives, sensitivity to logical reasoning in communication and a tolerance of ambiguity. Thus the CAM as a teaching strategy can accomplish several instructional goals depending on the emphasis of the particular lesson. The model helps to provide practice in inductive reasoning and opportunities for altering and improving students' concept building strategies [24].

Thus, taking into account the difficulties encountered by students in the topic “Periodic Table”, we set about using the literature as a foundation to use the CAM as a strategy in the teaching and learning of the topic “Periodic Table” at “O”-level through an action research. This paper gives a detailed description of the implementation of the CAM in the teaching and learning of the “Periodic Table” and its impact on students’ motivation, interest and understanding of the topic. In addition, we also report here how presentation of exemplars and non-exemplars can be achieved through multiple paths.

17.2 Methodology

17.2.1 Sample

The present study was carried out in the period of July to September 2008 in a rural girls’ State Secondary School located in the North of Mauritius. The sample included 44 girls of mixed ability in the range of 14–15 years. The students are enrolled in the Form IV class which is the first preparatory year for the CIE “O”-level examinations; they were preparing to sit for the CIE “O”-level examinations in November 2009 (Students are usually prepared for the CIE “O”-level examinations over a period of 2 years).

17.2.2 Data Collection

The present study involved collection of both qualitative and quantitative data. Furthermore, to ensure reliability and validity, a variety of data-gathering tools were employed as described below.

17.2.2.1 Observations Checklists

Tilstone [25] defined observation as the systematic, and as accurate as possible, collection of usually visual evidence, leading to informed judgments and to necessary changes to accepted practices. Throughout the present study, students were observed at work to get a holistic picture of classroom events using appropriately designed checklists. The observation checklists included the following criteria:

- *students’ participation, interest and motivation*
- *students’ understanding of concepts*
- *use of CAM and the impact of the various ways of presenting the exemplars and non-exemplars.*

17.2.2.2 Student Achievement Tests

Three students' achievement tests were used during the action research namely Test 1, Test 2 and Test 3, which were administered after cycles 1, 2 and 3 respectively. The tests were used to gather information about students' understanding of concepts being taught by the CAM after each cycle. The achievement tests were non parametric tests designed by the teacher. They were criterion-referenced since they aimed to test whether students had achieved specific objectives during the lessons. The total number of marks achievable for each test was 35 and students were allocated 40 min to complete each test.

17.2.2.3 Student's Questionnaire

A questionnaire was administered to all students involved in the study to gather information about their attitudes and opinions regarding the use of the CAM in the teaching and learning of the topic "Periodic Table". The questionnaire included both close-ended and open-ended questions; the open-ended questions ensured qualitative dimensions to the student's views and opinions while the close-ended ones helped to achieve objectivity and to facilitate analysis. Before administering the questionnaire to the students, consent was gained from the participants who were assured confidentiality and anonymity. The questionnaire was administered to the participants at the end of the third cycle.

17.2.2.4 Interview

A semi structured group interview was conducted in conjunction with the other data collecting methods to find out facts which could not be observed or obtained from the questionnaire and also to triangulate the information collected. A list of questions related to issues of the present study was drawn focusing on the perceptions and attitudes of students towards the use of CAM in classroom teaching. The group interview was carried out on a sample of 10 students selected randomly.

17.2.3 Research Design

The present study was carried out through an action research over three cycles and comprised eight lessons ranging from 40 to 80 min. All the lessons were based on the use of the CAM to teach the "Periodic Table" in line with the CIE "O"-level syllabus. During the action research, CAM was implemented in the lessons as per the four-stage description of the CAM given in Fig. 17.1. Details of the use of the CAM in the three action research cycles are given in Table 17.1.

Table 17.1 Implementation of CAM in the lessons during the 3 cycles of the action research

Cycle	Lesson	Use of concept attainment model
One	1	• To introduce the terms period and group
	2	• To explain relationship between Group number and number of valence electrons
	3	• To show position of metals in the Periodic table
Two	1	• To illustrate Group I metals as soft metals
	2	• To highlight trend of reactivity of Group 1 metals with water
	3	• To deduce the order of reactivity of halogens through displacement reactions
Three	1	• To show lack of reactivity of the noble gases • To show that transition metals formed colored compounds
	2	• To illustrate that transition metals have having high melting points • To show that transition metals exhibit variable oxidation states in their compounds

17.2.3.1 Cycle 1 of the Action Research

Cycle 1 consisted of three lessons using the CAM. The first lesson dealt with an introduction to the history of the Periodic Table and to the terms groups and periods. Group number as well as the relationship between ionic charge and group number were covered in lesson two, while students were introduced to metallic and non-metallic characteristics in lesson three. The CAM was used in the first cycle to explain the following to students:

- The terms group and period
- Group number
- Position of metals in the Periodic Table.

In the first cycle of the action research, the implementation of the CAM was directed by the teacher. The chalk-board was used; a vertical line was drawn on board to have two separate columns, one marked **YES** and the other marked **NO**. Teacher presented exemplars in the **YES** column and non-exemplars in the **NO** column as illustrated in Fig. 17.2. Students were asked to observe and reflect on the examples given using the copy of the Periodic Table to find out about the attributes of the positive examples.

However, in the third lesson of Cycle 1 though presentation of exemplars and non-exemplars was again directed by teacher, a Bristol paper was affixed on board with two headings **YES** and **NO** instead of using the chalk-board. The exemplars and non-exemplars were written on learning cards which were stuck in the respective columns as shown in Fig. 17.3. As in the first two lessons, students were asked to observe and reflect on the examples given using the copy of the Periodic Table to look for the common characteristic among the exemplars.

YES	NO
Sodium	Nitrogen
Magnesium	Barium
Aluminium	Bromine
Silicon	Boron
Phosphorus	Hydrogen
Sulphur	Fluorine
Chlorine	Carbon
Argon	Beryllium

Fig. 17.2 Presentation of exemplars and non-exemplars using the chalk-board in Lesson 1 of Cycle 1 to introduce the term period through the CAM

Metals	NOT metals
YES	NO
Lithium	Fluorine
Magnesium	Xenon
Potassium	Helium
Sodium	Sulphur
Beryllium	Chlorine
Calcium	Iodine
Caesium	Oxygen
Strontium	

Fig. 17.3 Use of CAM in Lesson 3 of Cycle 1 to introduce the position of metals in the Periodic Table (exemplars and non-exemplars were presented on Bristol paper with colorful learning cards)

Table 17.2 Use of CAM in Lesson 1 of Cycle 2 to explain that Group I metals are soft – presentation of exemplars and non-exemplars using varied strategies and aids (Video clips retrieved from http://www.youtube.com/results?search_query=cutting+alkali+metal&searchtype)

Yes/positive	No/negative
<p data-bbox="202 310 373 336"><i>Viewing video clip</i></p>  <p data-bbox="202 543 283 569">Lithium</p>	 <p data-bbox="635 543 695 569">Gold</p>
<p data-bbox="202 578 373 605"><i>Viewing video clip</i></p>  <p data-bbox="202 804 279 830">Sodium</p>	<p data-bbox="635 578 806 605"><i>Hands-on activity</i></p>  <p data-bbox="635 804 686 830">Zinc</p>
<p data-bbox="202 843 373 869"><i>Viewing video clip</i></p>  <p data-bbox="202 1113 301 1139">Potassium</p>	<p data-bbox="635 843 806 869"><i>Hands-on activity</i></p>  <p data-bbox="635 1113 683 1139">Iron</p>

17.2.3.2 Cycle 2 of the Action Research

Cycle 2 consisted of three lessons during which Groups I and VII were studied using the CAM. In this second cycle, various teaching aids and strategies were used to present the exemplars and non-exemplars during the implementation of the CAM. The focus was on an attempt to increase motivation, interest and participation during the lessons based on CAM.

In Lesson 1 of Cycle 2, the CAM was used to explain that Group I metals are soft. The exemplars and non-exemplars were presented by a variety of teaching aids and strategies like hands-on activities, demonstrations and video clips as depicted in Table 17.2.



Table 17.3 Implementation of CAM in Lesson 2 of Cycle 2 to explain the trend in reactivity of Group I elements with water – presentation of exemplars and non-exemplars through video clips and hands-on activities (Video clips, retrieved from <http://www.youtube.com/watch?v=Ft4E1eCUItI&feature=related>)

Yes/positive	No/negative
<p data-bbox="202 299 376 335"><i>Viewing video clip</i></p> 	
<p data-bbox="202 529 376 564">Lithium in water</p> <p data-bbox="202 564 376 599"><i>Viewing video clip</i></p> 	<p data-bbox="623 529 799 564">sulfur in water</p> <p data-bbox="623 564 799 599">Hands-on activity</p> 
<p data-bbox="202 776 376 811">Sodium in water</p> <p data-bbox="202 811 376 846"><i>Viewing video clip</i></p> 	<p data-bbox="623 776 799 811">Iron in water</p> <p data-bbox="623 811 799 846">Hands-on activity</p> 
<p data-bbox="202 1023 376 1058">Potassium in water</p> <p data-bbox="202 1058 376 1093"><i>Viewing video clip</i></p> 	<p data-bbox="623 1023 799 1058">Zinc in water</p> <p data-bbox="623 1058 799 1093">Hands-on activity</p> 
<p data-bbox="202 1270 376 1305">Rubidium in water</p>	<p data-bbox="623 1270 799 1305">Magnesium in water</p>

(continued)

In the second lesson of Cycle 2, the CAM was used to explain the trend in reactivity of Group I elements with water. Exemplars and non-exemplars were presented through use of video-clips and hands-on activities as illustrated in Table 17.3.

Table 17.3 (continued)

Yes/positive	No/negative
<i>Viewing video clip</i>	<i>Hands-on activity</i>
	
Caesium in water	Gold in water

The third lesson of Cycle 2 dealt with Group VII elements. CAM was used to allow students to deduce the order of reactivity of halogens through displacement reactions of halogens by other halide ions. Exemplars and non-exemplars were presented by means of teacher demonstrations, hands-on activities and computer simulations as shown in Table 17.4.

17.2.3.3 Cycle 3 of the Action Research


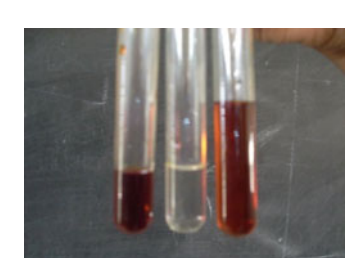
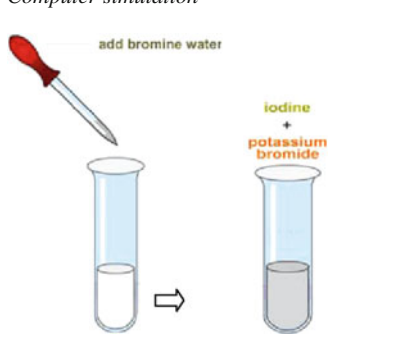
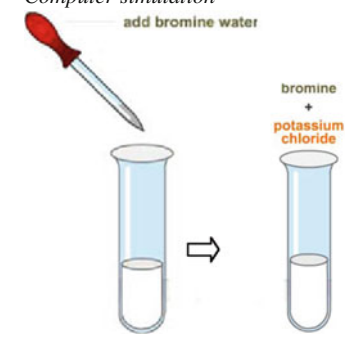
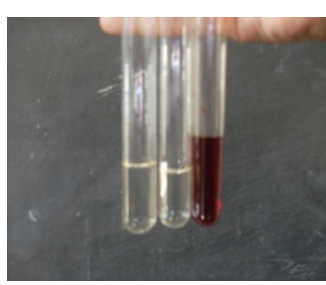

Cycle 3 comprised two lessons during which the noble gases and the transition metals were studied using the CAM. During the implementation of the CAM in the third cycle, students were involved in minds-on and hands-on activities; in addition, the CAM was used as a means to promote higher-order thinking among the students. In the first lesson of Cycle 3, the CAM was used to highlight the lack of reactivity of the noble gases. During the presentation of the exemplars and non-exemplars, students were required to draw the electronic configurations of different elements under the appropriate column on a Bristol paper. To show that transition elements form colored compounds, the CAM was implemented in such a way that students were involved in a hands-on activity that enabled them to observe and compare the salts of transition metals with salts of non transition metals as shown in Table 17.5.

In the second lesson of Cycle 3, which was indeed the last lesson of the action research, the CAM was used to allow students to deduce that transition metals

- have high melting points
- exhibit variable oxidation states in their compounds.

The students were required to indulge in minds-on activities to identify the exemplars and non-exemplars; they were required to calculate the oxidation states of different metals in compounds selected by teacher as depicted in Table 17.6.

Table 17.4 Implementation of CAM in Lesson 3 of Cycle 2 to explain order of reactivity of halogens through displacement reactions. Exemplars and non-exemplars were presented by means of teacher demonstrations, hands-on activities and computer simulations (Computer simulations, retrieved at <http://www.BBC-GCSE> Bitesize-Chemistry simulation Periodic table Halogen displacement reactions.mht)

Yes/positive	No/negative
<i>Teacher demonstration</i>	<i>Teacher demonstration</i>
	
$\text{Cl}_2 + \text{NaBr}$	$\text{I}_2 + \text{NaCl}$
<i>Computer simulation</i>	<i>Computer simulation</i>
	
Potassium iodide	Potassium chloride
$\text{Br}_2 + \text{KI}$	$\text{Br}_2 + \text{KCl}$
<i>Hands-on activity</i>	<i>Hands-on activity</i>
	
$\text{Cl}_2 + \text{KI}$	$\text{Cl}_2 + \text{NaCl}$

(continued)

Table 17.4 (continued)


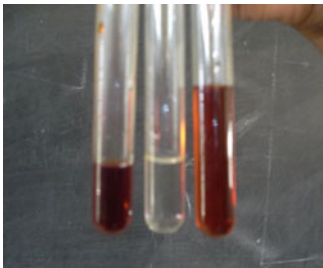






Yes/positive	No/negative
<i>Hands-on activity</i>	<i>Hands-on activity</i>
	
$\text{Cl}_2 + \text{KBr}$	$\text{I}_2 + \text{NaBr}$

Table 17.5 Implementation of CAM in lesson 1 of cycle 3 to show that transition elements form colored compounds

Yes/positive	No/negative
	
Copper(II) sulfate	Calcium sulfate
	
Potassium manganate(VII)	Potassium nitrate
	
Iron(III) chloride	Magnesium chloride

(continued)

Table 17.5 (continued)







Yes/positive	No/negative
	
Potassium chromate(VI)	Calcium chloride
	
Copper(II) carbonate	Sodium carbonate
	
Nickel(II) sulfate	Aluminium sulfate

Table 17.6 Implementation of CAM in Lesson 2 of Cycle 3 to illustrate that transition elements exhibit variable oxidation numbers (students were required to calculate the oxidation numbers of the metals to fill in the table)

Yes/positive	No/negative
Oxides of iron Oxidation number of iron can be +2 and +3	Oxides of calcium Oxidation number of calcium is +2
Oxides of copper Oxidation number of copper can be +1 and +2	Oxides of sodium Oxidation number of sodium is +1
Oxides of vanadium Oxidation number of vanadium can be +3, +4 and +5	Oxides of lithium Oxidation number of lithium is +1
Oxides of cobalt Oxidation number of cobalt can be +2 and +3	Oxides of magnesium Oxidation number of magnesium is +2
Oxides of manganese Oxidation number of manganese can be +4 and +6	Oxides of potassium Oxidation number of potassium is +1

17.3 Results and Discussion

In the current research, both quantitative and qualitative data were collected through use of observation checklists, students' achievement tests, students' questionnaire and interview. The data gathered are presented and discussed below.

17.3.1 Data gathered from Observation Checklists

17.3.1.1 Analysis of Data Obtained from Observation Checklists During Cycle 1

Observations during Lesson 1 of Cycle 1 have revealed that many students could not participate fully due to shyness or lack of communication skills. According to Murphy [26], in order to encourage students to participate in class, teachers should be friendly and supportive of their comments. This would help students to feel more comfortable and enhance their willingness to cooperate with the teacher. Thus during Lesson 2, more oral questions were being asked and it was found that students started to respond. During Lesson 2, many students had difficulties to observe and analyze the similarities and differences between the positive and negative exemplars. Students required many hints when analyzing the exemplars; this might be due to the fact it was their first exposure to the CAM. However, with teacher's guidance, students were able to deduce the concept under study. Observations in Lessons 1 and 2 have also revealed that students were not fully engaged and motivated when the exemplars were presented using the chalkboard. It was interesting to note that when colorful learning cards were used to present the exemplars in Lesson 3, students were more involved and motivated as the colorful cards provided visual stimuli and were more appealing. The major observation in Cycle 1 was that the lessons were mostly teacher-centered; the teacher herself was presenting the positive and negative exemplars and was leading the lesson. Students were not actively involved and engaged during presentation of exemplars. Thus in Cycle 2, it was decided to engage students in class activities during the presentation of the positive and negative exemplars while using the CAM.

17.3.1.2 Analysis of Data Obtained from Observation Checklists During Cycle 2

Observations gathered during the lessons of Cycle 2 have revealed that the atmosphere of the classroom has changed when varied strategies and resources were used to present exemplars and non-exemplars while employing the CAM. Student participation increased; students were less shy to talk and kept on asking questions. Indeed, presentation of positive and negative exemplars through varied resources

and strategies has involved creative and critical thinking and decision-making as learners were continuously guessing, looking for logical relationships, inventing, building and then testing them by considering attributes/features that characterize the concept under study. Students were also actively involved in the teaching and learning process during implementation of CAM promoting development of interpersonal and communications skills. During the lessons in Cycle 2, students were not bored as revealed by their facial expressions; they were actively participating and were engaged in constructing their own knowledge. Meyers and Jones [27] have indeed reported that active learning reduces boredom in the class. Indeed, the hands-on activities, computer simulations and You Tube videos used to present exemplars and non-exemplars have helped to render the classroom atmosphere livelier and to enhance students' interest and participation. Most importantly, observations during the lessons of Cycle 2 have revealed that students encountered less difficulty while comparing the positive and negative exemplars with the use of hands-on activities, interactive computer simulations and You Tube videos. Use of these varied resources and strategies has helped students to better perceive the similarities and differences between the positive and negative exemplars and to identify the attributes of the concepts under study. Our findings can be interpreted in line with findings from Fisher [28] who reported that when students see, they indulge in thinking and constantly connect their ideas to things they know about, thus encouraging them to seek hidden explanations. Thus, our results tend to point out that the implementation of CAM using a variety of strategies and resources while presenting the exemplars and non-exemplars has not only enhanced students' motivation and interest but has also promoted understanding of the concepts.

17.3.1.3 Analysis of Data Obtained from Observation Checklists During Cycle 3

In Cycle 3, the CAM was implemented by including some higher order level tasks while presenting the exemplars and non-exemplars in an attempt to engage students in higher order thinking. Observations during the lessons of Cycle 3 have revealed that all students were actively participating. Instead of teacher presenting the exemplars and non-exemplars directly, students were required to involve in minds-on activities to identify the exemplars and non-exemplars in Cycle 3. Thus Cycle 3 engaged students in self-learning and involved higher order skills to firstly find out the positive and negative examples and then to identify the attributes (Students were required to draw electronic configurations of elements and to calculate oxidation states of metals in compounds during the implementation of the CAM). This promoted the development of the learners' logico-mathematical intelligence, critical thinking and decision-making. According to Bloom's Taxonomy [29], higher order skills refer to students being able to do abstract thinking, applying, analyzing, synthesizing and evaluating. Moreover, students were highly motivated as they were discovering things on their own. Besides retention and cognitive learning outcomes, the CAM has also promoted other skills like decision-making, critical

and creative thinking, communication, and independent learning as students were encouraged to provide feedback and to make decisions based on facts and data collected throughout the activities.

17.3.2 Data Collected from Student's Achievement Tests

Three Students' Achievement Tests were administered during the present action research, namely Tests 1, 2 and 3 after Cycles 1, 2 and 3 respectively to test students' understanding and to obtain information about their performance after each Cycle. The maximum marks achievable for each of the three tests were 35; the marks and percentage marks scored by students in the three tests are shown in Table 17.7 while Fig. 17.4 highlights the performance of students in Tests 1, 2 and 3. Figure 17.5 gives a comparison of the minimum, maximum and average marks obtained by students in the three tests.

For Test 1, the maximum score was 31 while the minimum score obtained was 7. The mean was 20.5, median 22 and standard deviation 6.02. Considering students' performance in Cycle 1 of the study, it was found that 6 students out of 44 (13.6%) did not obtain pass marks (above 40%) and no one managed to obtain higher than 90%. Analysis of students' scripts has revealed that questions testing knowledge and comprehension were generally well answered; however, answers to questions where students were required to express themselves in words were very poor. For instance, many students could not suggest similarities and differences between elements found in the same group. This shows that students could not apply their knowledge to answer specific questions.

In Test 2, the maximum score was 32 while the minimum score was ten. The mean was 22.6, median 24 and standard deviation 5.67. Comparing the marks scored by students in Tests 1 and 2, it is noted that there was a slight improvement as the number of students who failed (scoring <40%) decreased from six (13.6%) in Test 1 to 3 (6.8%) in Test 2. It has also been noted that the number of students scoring less than 50% has decreased from 14 (32%) in Test 1 to 7 (16%) in Test 2. Moreover, while in Test 1 no one was able to score above 90%, in Test 2 one student scored 91%. The maximum score has thus increased from 31 in Test 1 to 32 in Test 2 while the minimum score has increased from seven (in Test 1) to ten (in Test 2). Results from Test 2 clearly show that students' performance has definitely improved compared to Test 1. This shows that implementing the CAM using a variety of resources and strategies to present the positive and negative exemplars has helped to improve the performance of students. According to Petty [30], learning is reinforced with different types of learning aids because they stimulate, motivate and capture learner's attention during the instructional process.

For Test 3, the maximum score was 33, the minimum score 17, the mean 26.1, the median 27 and the standard deviation was 4.57. Results from Test 3 have revealed that there was a slight but definite improvement in students' performance as

Table 17.7 Marks and percentage marks obtained by students in Tests 1, 2 and 3

Students' code	Scores out of 35 in Test 1 (%)	Scores out of 35 in Test 2 (%)	Scores out of 35 in Test 3 (%)
A1	15 (43%)	17 (49%)	26 (74%)
A2	19 (54%)	19 (54%)	25 (71%)
A3	24 (69%)	26 (74%)	30 (86%)
A4	25 (71%)	25 (71%)	29 (83%)
A5	22 (63%)	25 (71%)	29 (83%)
A6	24 (69%)	22 (63%)	29 (83%)
A7	10 (29%)	12 (34%)	18 (51%)
A8	8 (23%)	10 (29%)	19 (54%)
A9	16 (46%)	18 (51%)	23 (66%)
A10	15 (43%)	19 (54%)	17 (49%)
A11	31 (86%)	23 (66%)	32 (91%)
A12	30 (86%)	32 (91%)	33 (94%)
A13	24 (69%)	29 (83%)	31 (86%)
A14	25 (71%)	28 (80%)	28 (80%)
A15	25 (71%)	29 (83%)	28 (80%)
A16	24 (69%)	30 (86%)	29 (83%)
A17	30 (86%)	31 (86%)	32 (91%)
A18	29 (83%)	29 (83%)	27 (77%)
A19	21 (17%)	25 (71%)	29 (83%)
A20	23 (66%)	23 (66%)	26 (74%)
A21	15 (43%)	19 (54%)	28 (80%)
A22	18 (51%)	25 (71%)	29 (83%)
A23	22 (63%)	26 (74%)	33 (94%)
A24	25 (71%)	24 (69%)	27 (77%)
A25	12 (34%)	15 (43%)	19 (54%)
A26	14 (40%)	19 (54%)	21 (17%)
A27	29 (83%)	31 (86%)	32 (91%)
A28	28 (80%)	30 (86%)	30 (86%)
A29	18 (51%)	25 (71%)	27 (77%)
A30	24 (69%)	25 (71%)	29 (83%)
A31	22 (63%)	30 (86%)	31 (86%)
A32	20 (57%)	25 (71%)	24 (69%)
A33	25 (71%)	18 (51%)	20 (57%)
A34	23 (66%)	27 (77%)	29 (83%)
A35	24 (69%)	29 (83%)	31 (86%)
A36	22 (63%)	27 (77%)	28 (80%)
A37	15 (43%)	22 (63%)	24 (69%)
A38	18 (51%)	20 (57%)	21 (17%)
A39	7 (20%)	15 (43%)	18 (51%)
A40	23 (66%)	23 (66%)	29 (83%)
A41	18 (51%)	21 (17%)	23 (66%)
A42	17 (49%)	17 (49%)	21 (17%)
A43	11 (31%)	11 (31%)	20 (57%)
A44	15 (43%)	19 (54%)	23 (66%)

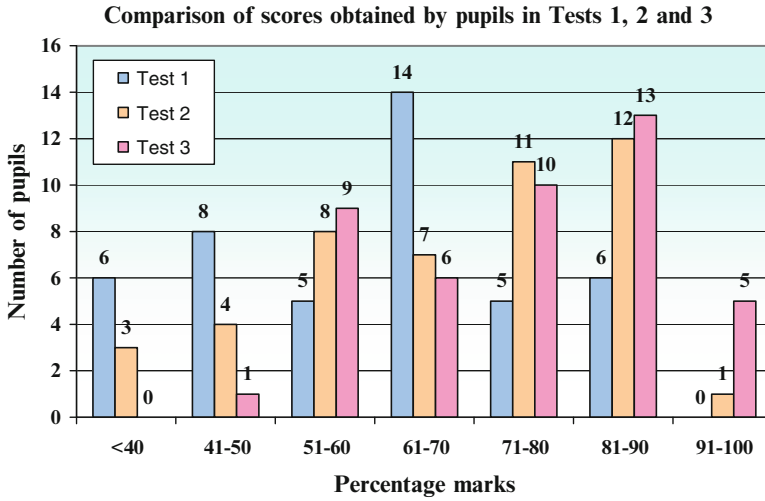


Fig. 17.4 Comparison of students’ performance in Tests 1, 2 and 3 in terms of percentage marks

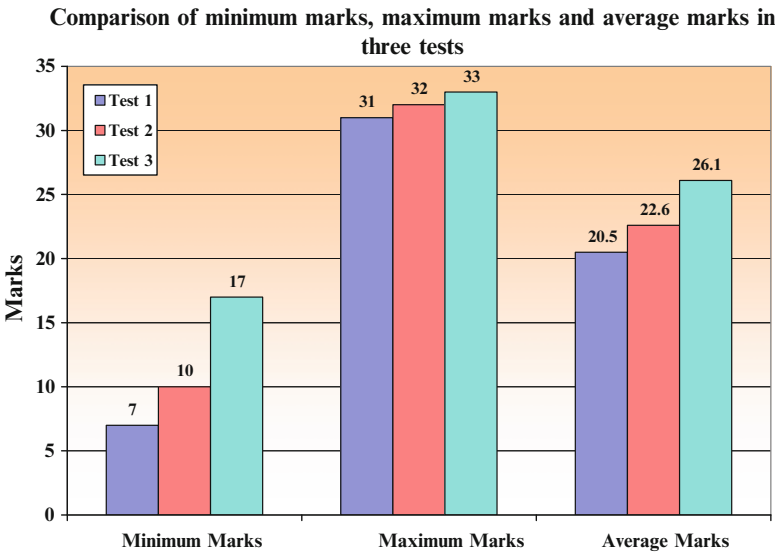


Fig. 17.5 Comparison of minimum, maximum and average marks obtained by students in Tests 1, 2 and 3

compared to Test 2. The maximum score has increased from 32 (in Test 2) to 33 (in Test 3) while the minimum score has increased from 10 (in Test 2) to 17 (in Test 3).

There has been a definite improvement of students’ performance from Test 1 to Tests 2 and 3 as depicted in Figs. 17.4 and 17.5. The minimum mark which was 7 in

Test 1 rose to 10 in Test 2 and reached 17 in Test 3. The tendency is the same for the maximum marks and average marks in all the three tests. The average marks scored by the students were 20.5 in Test 1, 22.6 in Test 2 and ultimately rose to 26.1 in Test 3. Further, the number of students who failed (less than 40% marks) has decreased from six (in Test 1) to three (in Test 2) while no student failed in Test 3. Moreover, while in Test 1, no one was able to score above 90%, in Test 2 one student scored more than 90% and in Test 3, 5 students out of 44 (11.4%) scored above 90%. Our findings are in line with Bruner et al. [12] who stated that CAM can help students to construct their own knowledge and retain it longer.

The percentage marks of most students in Test 3 have increased compared to Tests 1 and 2. Further, it has been noticed (Fig. 17.4) that the number of students obtaining low percentage marks (between 41% and 50%) has decreased from Test 1 to Test 3 whereas the number of pupils obtaining high percentage marks between (81–90%) has increased from Test 1 to Test 3. Thus data collected from the achievement tests clearly indicate that use of CAM throughout the three cycles has helped to promote conceptual understanding of the topic “Periodic Table”. Moreover, results obtained from the achievement tests also point out to the fact that use of varied strategies and resources (computer simulations, video clips, demonstration and hands-on-activities) while presenting the exemplars and non-exemplars during implementation of CAM has further enhanced conceptual understanding. Our findings are in line with Hong and Puck [31] who stated that during use of the CAM, students go beyond merely associating a key term or concept with a definition.

17.3.3 Data Gathered from Students’ Questionnaire

After completing the three cycles of the action research, a questionnaire was administered to all students involved in the study to gather feedback on their attitudes and opinions regarding use of CAM in the teaching and learning of the topic “Periodic Table”. In this section, we present the pertinent and salient findings gathered through the questionnaire.

17.3.3.1 Students’ Views on the Study of the “Periodic Table” in Lower Forms

Only 16 students (36%) out of the 44 found studying the “Periodic Table” in lower forms interesting while the majority (64%) found it boring. Some students commented that they found the Periodic Table interesting as it helped them to discover new “things”, while others who found the Periodic Table boring stated that they did not know how to use it properly. This might be due to the fact that they have learnt it by rote and were rarely involved in interactive experiences during its study in lower forms.

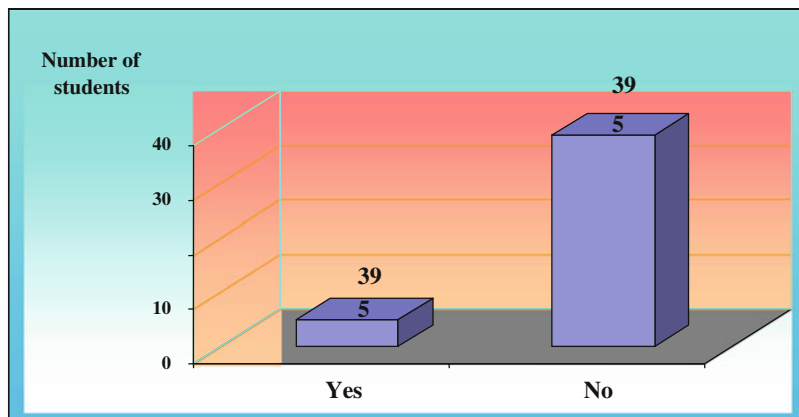


Fig. 17.6 Students's responses to whether use of chalk and board and teacher explanation are sufficient to understand the "Periodic Table"

17.3.3.2 Students' Opinions Regarding Use of Chalk-Board and Teacher Explanation

When asked whether use of chalk and board and teacher explanation are sufficient for understanding the topic "Periodic Table", most students (39, representing 88.6%) disagreed, while only five (11.3%) agreed as illustrated in Fig. 17.6. Students who disagreed claimed that chalk and board make the lessons passive, boring and dull; a few added that they used to feel sleepy when teacher is explaining using chalk and board. Our findings can be interpreted in line with those of Sobron [6], who argued that poor understanding of the topic "Periodic Table" could be due to the fact that our learners are groomed towards too much of expository method, chalk and board and spoon-feeding.

17.3.3.3 Prior Exposure to Use of CAM in Classroom Teaching

All students involved in the present study have never been exposed to the CAM in classroom teaching prior to this study. The present research thus constituted their first encounter with the CAM in the teaching/learning process.

17.3.3.4 Students' Views on the Use of CAM as a Strategy in Classroom Teaching

On the other hand, when students were asked whether use of CAM has helped them to better understand a concept, the majority (95.5%) agreed or strongly agreed, while 4.5% disagreed as depicted in Fig. 17.7. Students who answered positively

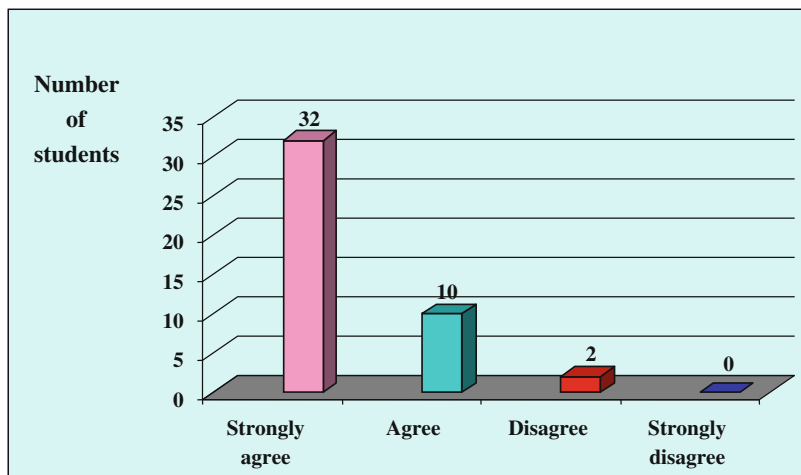


Fig. 17.7 Students' responses to whether use of CAM has helped them to better understand a concept as compared to usual teacher explanation

reported that use of CAM has helped them to understand and recall facts better. Our findings tend to confirm those of Tessmer and Meijer [32] who stated that CAM improved retention.

All students found use of CAM very interesting (77%) or interesting (23%) (Fig. 17.8). Further, all students agreed that use of CAM has helped to motivate them in learning about the "Periodic Table"; several students even acknowledged that they have started to like chemistry following use of CAM. These findings tend to confirm findings from Amirault [33] who reported that CAM has a positive impact on student learning and motivation.

When students were asked whether use of CAM has helped them to better understand specific subtopics in the "Periodic Table", the majority (95%) agreed while 5% disagreed (Fig. 17.9). Many students reported that they had better understood the concept of displacement reactions of halogens, as this is not an easy concept.

17.3.3.5 Students' Views on the Use of Positive and Negative Exemplars

Most students (89%) agreed that positive and negative exemplars are important for them to understand a particular concept (Fig. 17.10). They argued that analyzing and comparing the positive exemplars with the negative ones have not only helped them to understand concepts better but have also helped to promote retention. Surprisingly, the few students (11%) who answered negatively claimed that while being presented with positive and negative exemplars, they had a tendency to deduce

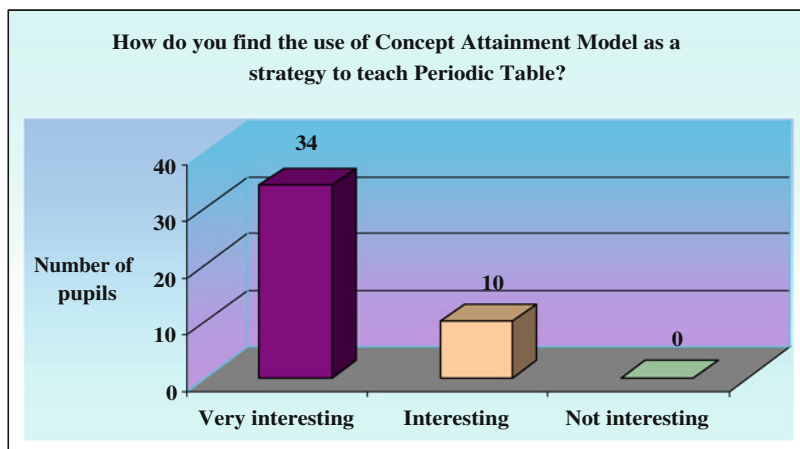


Fig. 17.8 Students' opinions about use of CAM as a strategy to teach the "Periodic Table"

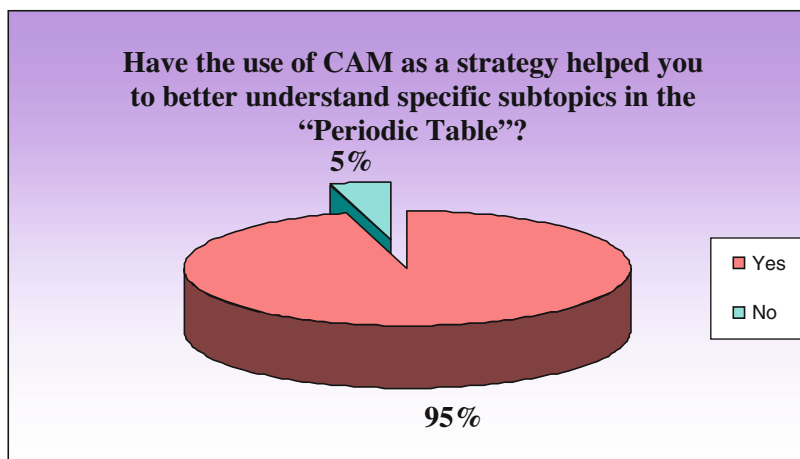


Fig. 17.9 Students' responses to whether use of CAM as a strategy has helped them to better understand specific subtopics in the topic "Periodic Table"

attributes that might belong to one or more negative exemplars. A few others also stated that at times, they were confused with the different exemplars presented.

Furthermore, when students were asked about the number of pairs of positive and negative exemplars that should be presented to allow them to identify a concept, the answers varied from more than five (46%) to five (18%), four (2%) and three (2%) as shown in Fig. 17.11. Thirty-two percent of students claimed that the number of exemplars and non-exemplars required would depend upon the concept being taught; this is especially true as very often the attributes of a concept may be easily identified from the exemplars while in some cases, attributes of a concept may not

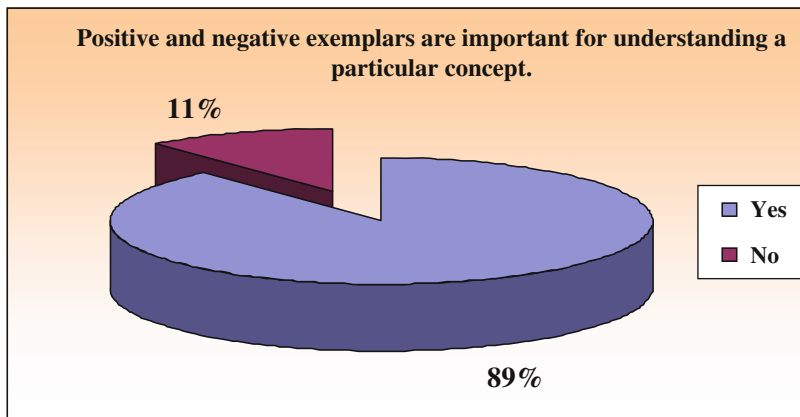


Fig. 17.10 Students’ responses to whether positive and negative exemplars are important to help them understand a particular concept

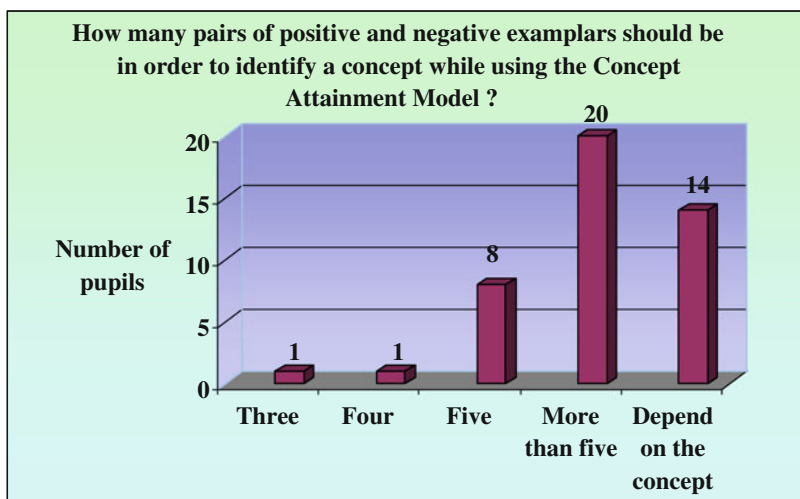


Fig. 17.11 Students’ responses when asked about the number of pairs of positive and negative exemplars that should be presented to identify a concept while using the CAM

be immediately obvious. Nevertheless, according to literature, presentation of more exemplars and non-exemplars to students would help them to better understand a concept and to improve thinking [12].

To a question regarding the importance of including negative exemplars in the CAM, it is worth noting that 35 students (80%) out of 44 claimed that negative exemplars are important while only nine (20%) answered negatively as shown in Fig. 17.12. This finding clearly highlights the relevance of negative exemplars in

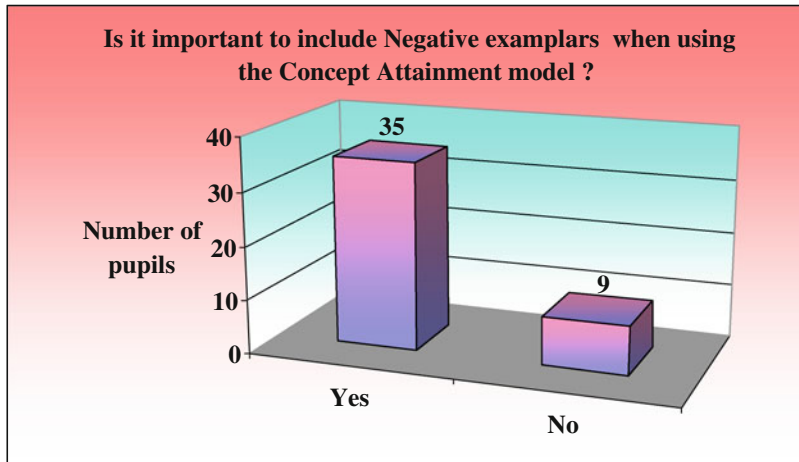


Fig. 17.12 Students' perception about the importance of including negative exemplars during implementation of the CAM

helping students to deduce the concept under study. Most students stated that use of negative exemplars has encouraged them to compare and analyze the attributes of the positive exemplars with them.

17.3.3.6 Students' Ratings of the Different Ways Used to Present the Positive and Negative Exemplars

When students were asked to rate the different ways used to present the positive and negative exemplars, all of them unanimously claimed that using chalk/board was very boring or boring (Fig. 17.13). None of them found the other teaching aids and strategies very boring as shown in Fig. 17.13. Besides, all students found use of flash movies and computer simulations interesting or very interesting. This is clearly in line with Kleinman and Dwyer [34] who stated that use of multimedia to present exemplars and non-exemplars in the CAM facilitate learning. Furthermore, Baker and Beisel [35] stated that visual treatments in lessons enhance learning with varying degrees of success. Use of varied teaching aids has also been reported to be a good means for gaining students' attention and for motivating them [5]. Findings from our study thus strongly support that for promoting students' motivation and interest during use of CAM, it is important for teachers to use a variety of teaching aids and strategies to present the positive and negative exemplars. In this perspective, increased motivation and interest would undoubtedly promote deep and meaningful learning of the concepts, as students would be more engaged in comparing and contrasting the positive and negative exemplars in view of identifying the correct attributes.

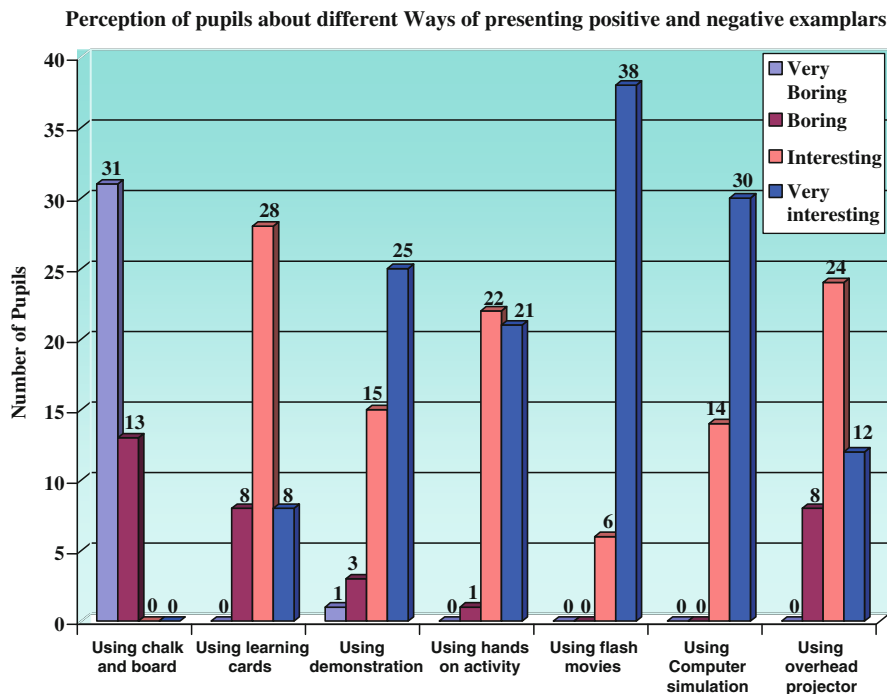


Fig. 17.13 Students' rating of the different ways of presenting positive and negative exemplars

17.3.3.7 Students' Views About Whether Use of CAM Is Time-Consuming

Most students (70%) claimed that use of CAM in classroom teaching is time-consuming as depicted in Fig. 17.14. Students argued that though CAM is a good strategy for teaching, teachers should not use it for all lessons; otherwise, it would be difficult to complete the syllabus. It is worth pointing out that though implementation of CAM in classroom teaching is time-consuming, teachers should decide when and how to use the model as our findings have revealed that the CAM helps learners to grasp concepts better and allows them to develop creative and critical thinking skills and leads to deeper meaningful understanding.

17.3.3.8 Students' Opinions Regarding Use of CAM in Other Topics in Chemistry and in Other Subjects

Most students (64%) stated that use of CAM should be extended to other topics in Chemistry as shown in Fig. 17.15. Reasons put forward include: CAM helps to motivate and make them more attentive and make learning meaningful; CAM promotes active learning and develops communication and higher order skills. Thus

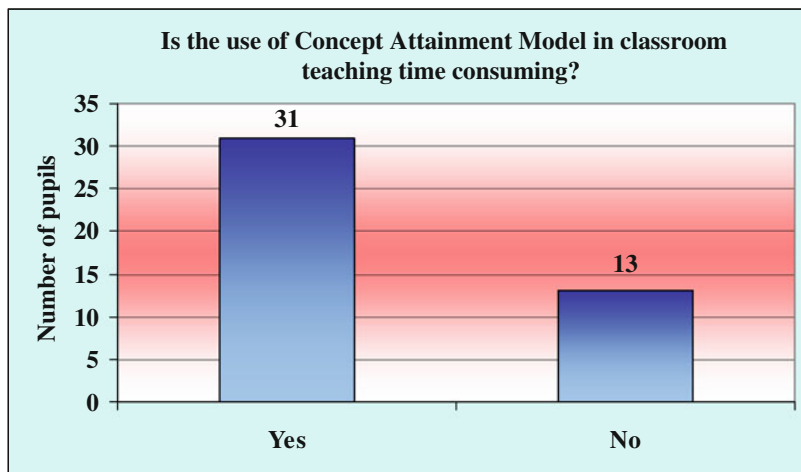


Fig. 17.14 Students' responses to whether use of CAM in classroom teaching is time consuming

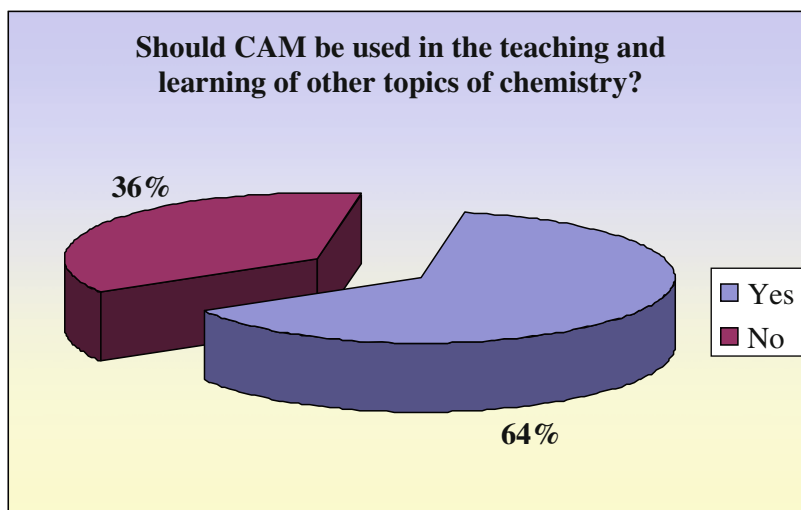


Fig. 17.15 Students' responses to whether CAM should be used in the teaching and learning of other topics of Chemistry

though students argued that use of CAM is time-consuming, they also agreed that the model enhances learning. These findings tend to confirm those of Bruner et al. [12], Joyce et al. [19] and Schunk [13] who reported that CAM promotes the development of inductive, critical, creative and higher-order thinking as well as independent learning.

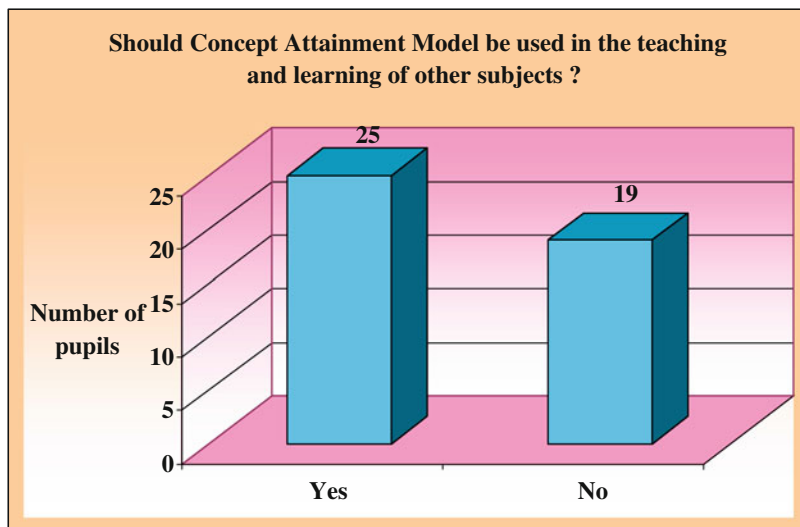


Fig. 17.16 Students' responses to whether CAM should be used in the teaching and learning of other subjects

When asked whether CAM should be used in the teaching and learning of other subjects, only 57% of students (Fig. 17.16) agreed and stated that CAM has promoted active learning and enhanced learning; these students also admitted that the strategy has helped them to better understand the concepts. Nevertheless, 43% of students answered negatively and stated that it might be difficult and sometimes impossible to find positive and negative exemplars.

17.3.3.9 Students' Own Comments on the Use of CAM in Classroom Teaching

In the last part of the questionnaire, students were invited to comment freely and to give their opinions on the use of CAM in classroom teaching. Some of the most pertinent comments include:

- *It is a very good method as it has helped us to recall many difficult concepts in the topic Periodic Table such as the displacement of halogens, the variable oxidation numbers of the transition metals.*
- *The lessons were very much interesting, interactive and motivating.*
- *More audio visuals aids should be included during the implementation of CAM as we learned better when we see.*
- *Class discussions during the implementation of CAM were very useful as it has helped us to clarify many important points.*

17.3.4 Data Gathered from Interview

After implementation of the action research, a semi-structured group interview was carried out on a sample of ten students selected randomly. Information gathered from the interview further confirms that the students have never been exposed to the CAM prior to this research. It is also interesting to note that all students interviewed asserted that use of CAM has increased their motivation in the lessons thus confirming data gathered from the questionnaire. Besides, all students unanimously stated that they preferred when exemplars and non-exemplars were presented through computer simulations or flash movies. This further triangulates data from the questionnaire where all students reported that use of computer simulations and flash movies was interesting/very interesting during the implementation of the CAM. Furthermore, all interviewed students affirmed that use of chalkboard was very boring during the CAM. All students claimed that use of CAM has rendered the lessons interesting. Thus, findings from the group interview have lent full support to the data gathered through questionnaire, especially with regard to the following:

- use of CAM has rendered the lessons more interesting.
- use of CAM has increased students' motivation.
- students' preference for use of varied strategies and resources like computer simulations and flash movies for presentation of exemplars and non-exemplars.

17.4 Conclusions

The present study was based on the use of the CAM in the teaching and learning of the "Periodic Table" at the Cambridge 'O'-level and aimed at investigating the impact of the CAM on student's motivation and conceptual understanding during the lessons on the "Periodic Table". It is widely acknowledged that education should be relevant and should have a clear immediate bearing upon students' current interests and aspirations. Thus, it is imperative for teachers to make use of a variety of strategies and resources to make sure that the teaching and learning processes appeal to students as relevant and meaningful.

Our results have shown that students were very enthusiastic and highly motivated during the lessons based on the use of CAM. This was evident from data gathered through observation and was further confirmed through the questionnaire. There was increased students' participation during the lessons; students were actively participating during the lessons. These findings lend support to those of Amirault [33] who reported that the CAM enhanced students' motivation and interest.

In addition, results from our study have shown that students were actively involved in the teaching/learning process during the implementation of the CAM thereby promoting development of interpersonal skills and communications skills. Students were actively involved in studying the exemplars and non-exemplars to identify their attributes and to communicate their findings and suggestions to

their friends and teacher; this had a positive impact on their interpersonal and communication skills. Gagné [23] indeed reported that the model encourages active learning as learners are engaged in constructing their own knowledge. Furthermore, Meyers and Jones [27] have argued that active learning reduces boredom in the class as students are constantly giving and receiving immediate feedback.

Our study has revealed that use of CAM in classroom teaching makes the lessons more interesting. All students in the present study have indeed acknowledged that the strategy has made the lessons more interesting. In fact, use of CAM requires active engagement from the part of students who are continuously challenged to “discover” the attributes of the concept under study.

Most importantly, our study has also shown that the CAM as a teaching/learning strategy involves creative and critical thinking and decision-making. When presented with the exemplars and non-exemplars, learners were continuously observing for attributes and characteristics, guessing, looking for logical relationships, formulating and building various categories and then testing them by considering attributes/features that characterize the concept under study. This clearly indicates that when using the CAM, students are encouraged to build an understanding of the concept under study by seeking for features that clearly distinguish exemplars from non-exemplars as previously highlighted by Bruner and co-workers [12] and more recently by Joyce et al. [19]. The latter also pointed out that the CAM, when properly planned and implemented, allows learners to work out and discover about the attributes of a concept by themselves. At this stage, it needs to be pointed out that the CAM is a strategy that is fully in line with the constructivist theory of learning [36] as students are actively involved in constructing knowledge and understanding about the concept under study. This was evident throughout the implementation of the CAM in the lessons during our research.

Furthermore, the present study has also revealed that the CAM has promoted thinking skills. Since exemplars and non-exemplars were presented in various ways, many avenues were opened for students to think in lateral and diverse ways. One of the major aims of using the model was to create a classroom situation in which students would have to indulge in thinking and to constantly connect their ideas to things they know about, encouraging them to seek hidden explanations and to reflect on their own thinking. We have indeed found that during the use of CAM, students were inductively thinking, observing, making connections in order to identify the attributes. In other words, students had to tap on their prior knowledge to form links with new ones. This is in line with Ausubel [37] who stated that prior knowledge is an important component to learning new complex topics. More recently, Rodgers [38] stated that activating learners’ prior knowledge encourages them to make connections with the new knowledge thereby increasing the motivation to learn.

Findings from our study have also revealed that use of CAM in the teaching and learning of “The Periodic Table” has helped to enhance students’ conceptual understanding, leading to an improvement in their performances throughout the three action research cycles. As highlighted in the previous section, there has been a slight but definite improvement in the performance of students from Tests 1 to 2 and 3. Although concepts taught in the topic became increasingly more difficult

from cycles 1 to 2 and 3, and in spite of the fact that in cycle 3, use of the CAM involved higher order skills, students performed better and better from Tests 1 to 2 and 3. Indeed, the CAM as a strategy encourages learners to construct knowledge about the concept being learnt by recalling, comparing, analyzing, classifying and discussing about assumptions, hypotheses and evidence [23]. In addition, as mentioned earlier, we have found that use of CAM has motivated and engaged the learners in the teaching/learning process; Blank and Harwell [39] have earlier reported that high motivation and engagement in learning are linked with increased levels of students' success. Thus, we would like to report here that the CAM has helped to enhance student's performance as its implementation not only engages and motivates learners but also provides them with the opportunity to construct knowledge resulting in enhanced conceptual understanding and improved retention.

One key aspect of the study was that there has been a continuous change in the ways in which exemplars and non-exemplars were presented to students, starting from writing on the board to use of flashcards, computer simulations, short movies, hands-on and minds-on activities. Our findings have revealed that students are more motivated when the exemplars and non-exemplars are presented through use of relevant visual aids and multimedia (computer simulations and movies). These eye-catching visual aids largely contributed to making the lessons more interesting and arousing students' motivation and awareness. Besides, when use of the CAM was coupled with hands-on and minds-on activities, students were actively engaged in comparing and contrasting the positive and negative examples, searching for attributes. This further encouraged students to examine a concept from several stances and to sort out relevant information from the different activities. Accordingly, students were able to develop deeper understanding of a concept leading to improved retention and comprehension. In consequence, using varied resources and strategies to present the positive and negative exemplars during implementation of the CAM not only helps students to learn about the concept but actually challenges them to build up knowledge about the concept from multiple angles. In this way, coupling use of CAM with different strategies and resources allows learners to go beyond their zone of proximal development [40].

Nonetheless, it needs to be pointed that though students fully agreed that the CAM has certain indisputable benefits like – increasing their motivation in the lessons, enhancing conceptual understanding and rendering the lessons more interesting, they conceded that implementing the strategy is time-consuming. Thus, it is important for teachers to decide when and how to implement the strategy to maximize learning of selected concepts, and at same time ensuring that students do not lag behind as far as syllabus and curriculum requirements are concerned.

To summarize, our findings have revealed that use of CAM as a strategy has been able to motivate the students, increase their level of participation, enhance conceptual understanding and help to improve performance of students in the topic "Periodic Table". The present study has also shown that use of varied resources and teaching aids while presenting the exemplars and non exemplars not only provides scope for further motivation and engagement of the learners but also enhances their

aptitudes and skills to analyze the positive and negative exemplars for similarities and differences promoting concept formation.

As a concluding remark, we would like to highlight that our present action research has proved to be a pioneering study affording an innovative way to teach the “Periodic Table” (a topic generally regarded as descriptive and learnt passively by students) through use of the CAM as a strategy. We have thus shown that the CAM can be *successfully and meaningfully incorporated in the teaching of concepts involved in the “Periodic Table”*. Our present study has also brought to light the *practicability of using the CAM* in classroom teaching and most importantly, the *flexibility of the model* as a strategy that conveniently accommodates the use of a whole gamut of *resources and strategies* in the teaching/learning process. We also report here that use of CAM coupled with varied resources and strategies further *increases students’ enthusiasm and motivation* and helps students to better detect similarities and differences between the positive and negative exemplars. Finally, we would recommend that teachers tap on their resourcefulness and creativity while using the CAM to ensure that presentation of exemplars and non-exemplars is not a passive classroom transaction, but actively engages learners.

References

1. Gallagher RM, Ingram P (2001) Chemistry for higher tier, 3rd edn. Oxford University Press, Oxford
2. Presscott C (1992) Comprehensive chemistry for O level. Federal Publications, Singapore
3. Bouma J (1989) An application oriented periodic table of the elements. J Chem Educ 66:741–745
4. Sevcik RS, McGinty RL, Alexander SV, Schultz LD (2008) Periodic table target: a game that introduces the biological significance of chemical element periodicity. J Chem Educ 85:516–517
5. Chuckowree V (2005) The use of pedagogical aids in the teaching of periodic table at form five level, an action research. PGCE dissertation, Mauritius Institute of Education, Réduit, Mauritius
6. Sobron S (2008) Use of games in the learning of periodic table at form four level, an action research. BEd dissertation, University of Mauritius and Mauritius Institute of Education, Réduit, Mauritius
7. Mendeleev D (1860) The periodic law of the chemical elements. J Chem Soc 55:634–56 (1889), <http://web.lemoye.edu/~giunta/MENDEL.HTML>. Accessed 23 June 2008
8. Barry K, King L (2000) Beginning teaching and beyond, 3rd edn. Social Science Press, Australia
9. Fowler G (1990) Decision making in British education. Open University Press, Buckingham
10. Kolb D (1976) Multimedia and concept attainment. <http://www.tcet.unt.edu/pubs/mul/mul04.pdf>. Accessed 28 Sept 2008
11. Bruner J (1966) Toward a theory of instruction. Harvard University Press, Cambridge
12. Bruner J, Goodnow JJ, Austin GA (1967) A study of thinking. Science Edns, New York. http://www.instructionalintelligence.ca/downloads/Montgomery%202005_Reflections%20on%20Concept%20Attainment.pdf. Accessed 16 June 2008
13. Schunk D (2000) Concept attainment model. <http://smtltd.wetpaint.com/page/08+Concept+Attainment+Model>. Accessed 16 Sept 2008

14. Klausmeir H (2000) Concept attainment model. In: Joyce B, Weil M, Calhoun E (eds) *Models of teaching*, 6th edn. A Pearson Education Company, Upper Saddle River
15. Driscoll MP (2005) *Psychology of learning for instruction*, 3rd edn. Pearson Company, New York
16. Tennyson RD, Cocchiarella MJ (1986) Concept attainment model. In: Joyce B, Weil M, Calhoun E (2000) *Models of teaching*, 6th edn. A Pearson Education Company, Englewood Cliffs
17. Taba H (1967) *Teachers' handbook for elementary social studies*. Addison-Wesley, Don Mill
18. Piaget J (1929) The child's conception of the world. In: Harcourt B (1952) *The origins of intelligence in children*. Cook M, London
19. Joyce B, Weil M, Calhoun E (2000) *Models of teaching*, 6th edn. A Pearson Education Company, Englewood Cliffs
20. Smith B, Ragan T (1999) Advantages of concept attainment model. In: Amirault RJ (2003) A study examining the effectiveness of two instructional treatments on student achievement, motivation, and cognitive reasoning processes in a complex concept domain. Dissertation, Department of Educational Psychology and Learning Systems, The Florida State University. http://etd.lib.fsu.edu/theses/available/etd-08312003-190047/unrestricted/Amirault_Dissertation_2003_submitted.pdf. Accessed 25 Sept 2008
21. Bruner J (1986) *Actual minds, possible worlds*. Harvard University Press, Cambridge
22. Baveja S, Sriwongjanya M (1985) Classification of plants. In: Joyce B, Weil M, Calhoun E (2000) *Models of teaching*, 6th edn. A Pearson Education Company, Englewood Cliffs
23. Gagné R (1992) Gagne's theory of instruction. In: Amirault RJ (2003) A study examining the effectiveness of two instructional treatments on student achievement, motivation, and cognitive reasoning processes in a complex concept domain. Dissertation, Department of Educational Psychology and Learning Systems, The Florida State University. http://etd.lib.fsu.edu/theses/available/etd-08312003-190047/unrestricted/Amirault_Dissertation_2003_submitted.pdf. Accessed 25 Sept 2008
24. Martindale T (1999) Alternate teaching models for non-classroom-based instruction. http://teachable.org/papers/1999_EdMedia_teachingmodels.htm. Accessed 6 Sept 2010
25. Tilstone C (1998) *Observing teaching and learning. Principles and Practice*, London
26. Murphy JJ (1988) Contingency contracting in schools: a review. *Educ Treat Child* 11:257–269
27. Meyers C, Jones TB (1993) Promoting active learning. Strategies for the college classroom. Jossey-Bass, San Francisco. http://www.uottawa.ca/academic/options/ActiveLearning_en.htm. Accessed 10 July 2008
28. Fisher R (1995) *Teaching children to learn*. Stanley Thornes Publisher Ltd, London
29. Bloom R (1974) *Taxonomy of educational objectives*. McKay, New York
30. Petty A (1998) Visual aids. <http://www.Britishcouncil.Britishcouncilorg/unit7.pdf>. Accessed 16 Aug 2008
31. Hong J, Puck J (1992) Long term memory. In: Amirault RJ (2003) A study examining the effectiveness of two instructional treatments on student achievement, motivation, and cognitive reasoning processes in a complex concept domain. Dissertation, Department of Educational Psychology and Learning Systems, The Florida State University. http://etd.lib.fsu.edu/theses/available/etd-08312003-190047/unrestricted/Amirault_Dissertation_2003_submitted.pdf. Accessed 25 Sept 2008
32. Tessmer JJ, Meijer A (1990) Concept attainment model. <http://carbon.cudenver.edu/~bwilson/construct.html>. Accessed 15 June 2008
33. Amirault RJ (2003) A study examining the effectiveness of two instructional treatments on student achievement, motivation, and cognitive reasoning processes in a complex concept domain. Dissertation, Department of Educational Psychology and Learning Systems, The Florida State University. http://etd.lib.fsu.edu/theses/available/etd-08312003-190047/unrestricted/Amirault_Dissertation_2003_submitted.pdf. Accessed 25 Sept 2008
34. Kleinman EB, Dwyer FM (1999) Analysis of computerized visual skills: relationships to intellectual skills and achievement. *Int J Instr Media* 26:53–69

35. Baker JD, Beisel RW (2001) An experiment in three approaches to teaching average to elementary school children. *Sch Sci Math* 101:23–31. http://gse.gmu.edu/cscvm/abs_doc/. Accessed 26 June 2008
36. Trowbridge LW, Bybee RW, Powell JC (2000) *Teaching secondary school science: strategies for developing scientific literacy*. Merrill and imprint of Prentice Hall. Pearson Education, Upper Saddle River
37. Ausubel D (1960) Use of organizers in the learning and retention of meaningful verbal material. *J Educ Psychol* 51:267–272
38. Rodgers EM (2004) Interactions that scaffold reading performance. *J Lit Res* 36:501–532. http://en.wikipedia.org/wiki/Instructional_scaffolding. Accessed 15 Aug 2008
39. Blank W, Harwell S (1997) Increasing Student Motivation. In: Amirault RJ (2003) A study examining the effectiveness of two instructional treatments on student achievement, motivation, and cognitive reasoning processes in a complex concept domain. Dissertation, Department of Educational Psychology and Learning Systems. http://etd.lib.fsu.edu/theses/available/etd-08312003-190047/unrestricted/Amirault_Dissertation_2003_submitted.pdf. Accessed 25 Sept 2008
40. Vygotsky LS (2000) *Mind in society: the development of higher psychological processes*. Harvard University Press, London/Cambridge

Chapter 18

Synthesis, Spectral Characterization and Anticancer Screening of Triorganotin(IV) Carboxylates

Mala Nath, Monika Vats, and Partha Roy

Abstract Triorganotin(IV) carboxylates of general formula, $R_3Sn(XA)$ [where $R = Me, n-Bu$ and Ph and $XA =$ anion of hippuric acid (HHA), lauric acid (HLA), stearic acid (HSA) and myristic acid (HMA)] have been synthesized. The bonding and coordination behavior in these derivatives are discussed on the basis of elemental analysis, FT-IR, 1H , ^{13}C and ^{119}Sn NMR spectroscopic studies, which suggest that the ligands are coordinated through COO^- group acquiring trigonal-bipyramidal geometry around tin with the R groups in the equatorial positions, the carboxylic oxygen and the carbonyl oxygen atom of adjacent molecule occupying the axial positions. These carboxylates have been screened *in vitro* against five cancer cell lines of human origin. Ph_3SnLA is the most active compound which exhibits potent anticancer activity against all the cell lines as compared to *cis*-platin. Furthermore, DNA ladder formation indicates that these compounds inhibit the cancer cell growth through apoptosis which has been confirmed by enzyme assays like lactate dehydrogenase, glutathione sulfur-transferase, glutathione reductase, glutathione-peroxidase, total glutathione content and lipid peroxidase assay.

18.1 Introduction

Organotins belong to the most widely used organometallic compounds which have emerged as a strongest area in the inter-disciplinary field owing to their wide spectrum of industrial, agricultural, and biological applications. Organotin carboxylates form an important class among the organotin compounds [1–3]. They

M. Nath (✉) • M. Vats

Department of Chemistry, Indian Institute of Technology Roorkee, Roorkee 247667, India
e-mail: malanfcy@iitr.ernet.in; mona2k42000@gmail.com

P. Roy

Department of Biotechnology, Indian Institute of Technology Roorkee, Roorkee 247667, India
e-mail: paroyfbs@iitr.ernet.in

possess rich structural diversity and biological applications. A range of mononuclear organotin carboxylates to complex polynuclear cages and clusters is formed [4]. One of the most important bioinorganic chemistry research areas with respect to the organotin compounds is the investigation of their cytotoxic/antitumor activities. Organotin complexes with a variety of ligands have been reported to exhibit *in-vitro* and *in-vivo* antitumor activity against several cell lines of human origin [5–9], and some of the complexes also showed cytotoxicity, including cellular apoptosis [10]. The *in-vitro* cytotoxicity of organotin camphorates steroid-carboxylates and carboxylates containing polyoxaalkyl moiety against a series of human cancer cell lines has been reported by Davies and coworkers [11]. This paper reports the synthesis, structural characterization, and *in vitro* anti-cancer activities of some triorganotin(IV) carboxylates.

18.2 Experimental

18.2.1 Materials

Solvents, *viz.* acetone (E. Merck), benzene (E. Merck), DMSO (E. Merck-HPLC grade), *n*-hexane (60–80°C fraction from petroleum) (E. Merck), petroleum benzene (60–80°C) (E. Merck) and petroleum ether (40–60°C) (E. Merck) were dried before use. Absolute methanol (specially dried) (s.d. fine-chemicals limited) employed for the synthesis work, was used as received. Triorganotin(IV) compounds, *viz.* trimethyltin(IV) chloride (TMC) (Sigma Aldrich), tri-*n*-butyltin(IV) chloride (TBC) (Merck-Schuchardt) and triphenyltin(IV) chloride (TPC) (E. Merck) were used as received. Carboxylic acids, *viz.* hippuric acid (HHA) (Sigma Aldrich), lauric acid (HLA) (Sigma Aldrich), stearic acid (HSA) (Sigma Aldrich), and myristic acid (HMA) (Sigma Aldrich) were used as received. For biological activities the following chemicals were used as received, such as 3-(4,5-dimethylthiazol-2-yl)-2,5-diphenyltetrazolium bromide (MTT) (Sigma Aldrich), Sorensen's buffer, PMSF, phosphate buffer saline (PBS), agarose gel, phenol (E. Merck), chloroform (E. Merck), isoamyl alcohol (E. Merck), EDTA, RNase, 50X TAE buffer, glacial acetic acid (s.d. fine-chemicals Ltd.), bromophenol blue, xylene cyanol FF, glycerol, Na-phosphate buffer, NADH, NADPH, Na-pyruvate, Ellman's reagent, glutathione reductase, CDNB (chlorodinitro benzene), GSH (reduced glutathione), sodium dodecyl sulphate (SDS) and thiobarbituric acid.

18.2.2 Synthesis of Triorganotin(IV) Derivatives of Carboxylic Acids by Sodium Salt Method

Fatty acid (HLA, HSA, HMA) (2.0 mmol) was dissolved in the minimum amount (20 mL) of specially dried methanol under dry nitrogen and added to sodium

methoxide, prepared by reacting sodium (0.058 g, 2.5 mmol) with dry methanol (25 mL). The resulting mixture was first stirred at room temperature for half an hour and then refluxed giving a clear solution of sodium salt of the acid within half an hour. Refluxing was continued for another 4–6 h with constant stirring. A hot methanol solution (20 mL) of trimethyltin(IV) chloride/tri-*n*-butyltin(IV) chloride/triphenyltin(IV) chloride (2.0 mmol) was added to the solution of the preformed sodium salt of the acid. The resulting solution was further refluxed with constant stirring for another 24–36 h for the tri-*n*-butyltin/triphenyltin(IV) derivatives, whereas for trimethyltin derivative only stirring was carried out at room temperature ($30 \pm 2^\circ\text{C}$) for 24–36 h, under dry nitrogen atmosphere. It was then centrifuged and filtered in order to remove sodium chloride formed. The excess of solvent was removed under reduced pressure and the solid product thus obtained was recrystallized either from methanol-hexane or methanol-petroleum ether (b.p. 40–60°C) mixture (1:3 v/v).

Sodium salt of hippuric acid (HHA), using HHA (5.0 mmol) in a mixture of 95.50% ethyl alcohol (10 mL) and benzene (30 mL) (hippuric acid is not soluble in absolute alcohol) was prepared as described above. To this solution triorganotin(IV) chloride (5 mmol) in ethanol (30 mL) was added. The reaction mixture was refluxed for 6–8 h during which sodium chloride separated out. The content was cooled and filtered under vacuum. To the filtrate benzene was added (30 mL) and the cycle of refluxing and filtration was repeated two or three times until all of the sodium chloride had been removed. The solvent was removed by distillation under reduced pressure to leave solid/syrup. Tri-*n*-butyltin(IV) complex was syrup and washed with petroleum ether (40–60°C), it solidified after about 4 months in a vacuum desiccator. Trimethyltin(IV) complex was a flocculent compound. Triphenyltin(IV) complex was recrystallized from absolute methyl alcohol [12].

18.2.3 Measurements

The melting points of the synthesized complexes were determined with a Toshniwal capillary melting point apparatus and are uncorrected. Carbon, hydrogen, and nitrogen analyses of the synthesized complexes were carried out on a Perkin-Elmer, CHNS-rapid elemental analyzer. The tin content in the synthesized complexes was determined gravimetrically as SnO_2 [13–15]. Molar conductance measurements were carried out on the Cyberscan 510-Eutech Instruments [13–15]. Near infrared and far-infrared spectra were recorded on a Thermo Nicolet Nexus FTIR spectrophotometer in KBr discs in the range 4,000–400 cm^{-1} and Thermo Scientific Nicolet 6700 FTIR in CsI discs in the range 600–200 cm^{-1} . Nuclear magnetic resonance (^1H , ^{13}C and ^{119}Sn) spectra were recorded on a Bruker AVANCE (500.13 MHz) spectrometer at the Institute Instrumentation Centre (IIC), IIT Roorkee using tetramethylsilane (TMS) as internal standard. Optical density (OD) was recorded on a Dynatech MR 5000 microplat reader at the Department of Biotechnology IIT Roorkee. The average IC_{50} was estimated via MTT assay and enzymes assays were done according to the procedures.

18.2.4 Anti-cancer Screening

The compounds were screened [16] *in-vitro* against five human cancer cell lines. Test and reference compounds were dissolved in dimethylsulfoxide (DMSO) or ethanol to form 4 mM stock solutions using a literature procedure [17, 18] by the microculture sulforhodamine B (SRB) test. The experiment was started on day 0. On day 0, 5×10^3 cells in 200 μL were placed in 96-wells flat-bottom microtitre plates (Griener, Germany). The plates were preincubated for 48 h at 37°C, 8.5% CO_2 , to allow the cells to adhere. On day 2, serial dilutions ranging from 5 to 2,000 μL using the stock solution in DMSO were prepared. On day 3, DMSO (same volume) used for all dilutions was used as vehicle control and every dilution (test and reference) was used in triplicate by adding 50 μL to a column of three wells. Cultures were incubated for 24 h at 37°C. On day 4, cultures were assayed by the addition of 25 μL of 5 mg/mL MTT and incubated for 4 h at 37°C. MTT containing media was aspirated and 200 μL of DMSO and 25 μL of Sorensen glycine buffer (0.1 M glycine and 0.1 M NaCl, pH 10.5) were added to lyse the cells and solubilize water insoluble formazon. The absorbance values (OD) of the lysates were determined using a Dynatech MR 5000 microplat reader at 570 nm. Data were used for the construction of concentration–percentage inhibition curves and determination of the IC_{50} values by using the graph pad prism, version 5.02 software (Graphpad Software Inc., CA, and USA). The percentage inhibition was calculated as:

$$\frac{\text{Mean OD of vehicle treated cells (negative control)} - \text{Mean OD of drug treated cells}}{\text{Mean OD of vehicle treated cells (negative control)}} \times 100$$

18.2.5 Enzyme Assays

18.2.5.1 Antioxidant Enzyme Activities

Lipid peroxidase, glutathione peroxidase, glutathione reductase, glutathione s-transferase and total glutathione assays were carried out to determine the effect of drug on antioxidant status of cancerous cell lines treated with the synthesized compound compared to control group of cells (non treated). In brief, tissue lysates were prepared in PBS pH 7.4, containing 2 mM (PMSF) with sonication (3 bursts of 20 s each). Equal amounts of protein samples were taken for all samples in each enzyme assay.

For the estimation of lipid peroxidase, 8.1% SDS, 20% acetic acid (pH 3.5) and thiobarbituric acid were added to the total protein and incubated at 95°C for 2 h. After cooling to RT, *n*-butanol and pyridine mixture (15:1 v/v) was added to the above incubated contents. It was centrifuged and OD was measured at 532 nm [19].

Glutathione reductase assay was performed according to the reported method [20]. 0.01 mL of 10 mM EDTA, 0.06 mL of 10 mM NADPH, 2 μ L β -mercaptoethanol, 0.1 mL of 250 mM GSSG (glutathione oxidized) were added to 0.778 mL of potassium phosphate buffer solution at pH 7.4 to which 0.05 mL of the total homogenate containing 0.5 mg total protein/mL was added and mixed thoroughly. After incubation for 5 min the absorbance of NADPH was measured at 340 nm.

Glutathione peroxidase activity [21] was measured by the method of Paglia and Valentine [22]. Reaction mixture was 0.2 mM NADPH, 4 mM GSH, 4 mM EDTA, 4 mM NaN_3 , 1 U of glutathione reductase, 0.2 mM H_2O_2 and the sample in 100 mM phosphate buffer pH 7.0. The assay was performed at 37°C and the rate of reduction of NADPH was followed at 340 nm.

Determination of glutathione-S-transferase (GST) activity was assayed in accordance with the protocol as reported earlier by Habig et al. [23]. Primarily potassium phosphate buffer, 20 mM CDNB (chlorodinitro benzene) was added to the protein sample and incubated at 37°C for 10 min. After the incubation, 30 mM GSH was added to each sample and absorbance was measured at 340 nm.

Total glutathione was determined according to the protocol described earlier by Pae et al. [24]. The protein was precipitated with 5% TCA and the supernatant was added in 96 wells plate in various dilutions. Ellman's reagent (12 mM DTNB), 5 nM EDTA, 0.4 unit of glutathione reductase in 125 mM PBS were added to the samples and the final reaction was started by addition of 5.6 mM NADPH. OD was then measured at 405 nm.

For measuring the LDH (enzyme involved in glycolytic pathways) [25], sodium phosphate buffer 0.1 M was added with 20 mM NADH and 10 mM Na pyruvate to the protein. The absorbance of NADH produced was estimated at 340 nm.

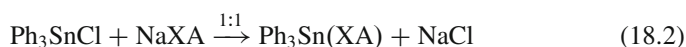
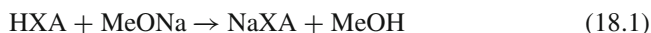
18.2.5.2 DNA Fragmentation Assay

The DNA cleavage pattern due to the synthesized compound was analyzed by agarose gel electrophoresis [26, 27]. 3×10^6 MCF-7 cells were exposed to the IC_{50} value of the synthesized compound. Cells were centrifuged and washed with PBS (phosphate buffer saline) and the pellet was lysed in 400 μ L with hypotonic buffer solution (10 mM tris pH 7.5, 1 mM EDTA and 0.2% triton X-100) for 15 min at room temperature, and then centrifuged for 15 min at 13,000 rpm. Three hundred and fifty microlitres of the supernatant was again lysed in 106 μ L of the second lysis buffer containing 150 mM NaCl, 10 mM Tris-HCl pH 8.0, 40 mM EDTA, 1% SDS and 0.2 mg/ml Proteinase K (at final concentration) for 4 h at 37°C. The DNA was extracted with phenol/chloroform/isoamyl alcohol (25:25:1 v/v/v) and the pellet obtained was washed with ethanol and resuspended for RNase digestion in 15 μ L of 10 mM tris, 1 mM EDTA pH 8.5, and 50 μ g/mL RNase for 1 h at 37°C. The DNA was analysed by running it at 50 V/cm in a 2% agarose gel in 0.5X TBE.

18.3 Results and Discussion

18.3.1 Synthetic Aspects

The reaction of triorganotin(IV) chloride with sodium salt (formed according to Eq. 18.1) of the acids in a 1:1 molar ratio led to the formation of the complex according to Eq. 18.2.



The reactions in Eqs. 18.1 and 18.2 required refluxing for 6–8 h in case of derivatives of hippuric acid and 24–26 h in case of other fatty acids used in the present study. The resulting solids were obtained in good yields. The complexes are stable towards air and moisture, soluble in methanol and DMSO, but sparingly soluble in chloroform and other organic solvents. The analytical data of the complexes are presented in Table 18.1. From the data it can be inferred that the resulting complexes crystallized with 1:1 stoichiometry independently of the

Table 18.1 Physical characteristic properties of triorganotin(IV) carboxylates

Complex (physical state)	Yield (%)	M.P. (°C)	MW	Analysis (%) observed (calculated)			
				Sn	N	C	H
Ph ₃ Sn(LA) C ₃₀ H ₃₈ O ₂ Sn (white solid)	52	120	564	21.62 (21.02)	—	65.57 (64.02)	6.29 (6.78)
Ph ₃ Sn(SA) C ₃₆ H ₅₀ O ₂ Sn (white solid)	55	47–50	634	18.75 (18.70)	—	68.31 (68.30)	7.89 (7.94)
Ph ₃ Sn(MA) C ₃₂ H ₄₂ O ₂ Sn (white solid)	48	320	577	20.57 (20.52)	—	66.55 (66.62)	7.27 (7.30)
Ph ₃ Sn(HA) C ₂₆ H ₂₁ O ₃ NSn (white solid)	51	160	515	22.32 (22.32)	2.65 (2.71)	59.15 (60.77)	3.98 (4.11)
Bu ₃ Sn(HA) C ₂₀ H ₃₃ O ₃ NSn (brown solid)	47	90	454	25.23 (26.14)	2.90 (3.10)	51.27 (53.03)	7.07 (7.32)
Me ₃ Sn(HA) C ₁₁ H ₁₅ O ₃ NSn (white solid)	60	200	328	35.12 (36.20)	4.08 (4.27)	38.52 (40.37)	4.37 (4.61)

M.P. Melting Point, MW Molecular Weight

Table 18.2 IR spectral data (cm^{-1}) of triorganotin(IV) carboxylates

Acid/complex	$\nu(\text{NH})$	$\nu(\text{CO}_{\text{amide}})$	$\nu_s(\text{COO})$		$\nu_{\text{as}}(\text{Sn-C})$	
			$\nu_{\text{as}}(\text{COO})$	$\Delta\nu$	$\nu_s(\text{Sn-C})$	$\nu(\text{Sn-O})$
HLA	–	–	1692	269	–	–
			1423		–	
$\text{Ph}_3\text{Sn}(\text{LA})$	–	–	1629	199	279	545
			1430		227	
HAS	–	–	1698	233	–	–
			1465		–	
$\text{Ph}_3\text{Sn}(\text{SA})$	–	–	1526	198	229	449
			1328		227	
HMA	–	–	1702	231	–	–
			1471		–	
$\text{Ph}_3\text{Sn}(\text{MA})$	–	–	1634	176	280	567
			1458		227	
HHA	3420	1745	1604	118	–	–
		1556	1416		–	
$\text{Ph}_3\text{Sn}(\text{HA})$	3490	1744	1600	174	280	536
		1559	1426		227	
$\text{Bu}_3\text{Sn}(\text{HA})$	3439	1649	1575	187	547	565
		1557	1388		515	
$\text{Me}_3\text{Sn}(\text{HA})$	3420	1636	1601	114	595	558
		1551	1487		579	

proportions of the organotin(IV) moiety and acid used. Very low molar conductance values of 10^{-3} M solutions of the complexes in methanol indicate their non-electrolytic nature.

18.3.2 IR Spectral Studies

Characteristic IR frequencies (cm^{-1}) and their assignments for the free carboxylic acids and their complexes are presented in Table 18.2. IR stretching frequencies ($\nu(\text{COO})$) for carboxylates have been utilised as a characteristic tool to confirm the mode of coordination through carboxylate oxygen, and also to identify the nature (monodentate, bidentate or bridging) of the bonding of the carboxylic group. The carboxylate groups in organotin(IV) carboxylates generally adopt a bridge structure in the solid state unless the organic substituents at the tin atom are bulky or carboxylate group is branched at the α -carbon [28].

The IR absorption spectra of the studied complexes indicate that the $\nu_{\text{as}}(\text{COO})$ values get shifted to lower frequencies in comparison with free acids (1604–1750 cm^{-1}), whereas the corresponding $\nu_s(\text{COO})$ absorption frequencies (1465–1390 cm^{-1}) either remain at the same value or move to lower frequencies than in the free acids (1467–1403 cm^{-1}). Strong interactions between the carboxylate carbonyl

Table 18.3 ^1H NMR spectral data of triorganotin(IV) carboxylates

Ligand/complex	Solvent	δ (ppm)
HLA	MeOD	12.60 (s, 1H, OH); 1.30–1.55 (mbr, 20H, CH ₂); 0.86 (t, 3H, CH ₃)
Ph ₃ Sn(LA)	MeOD	7.23 (mbr, 15H, Ph); 1.30–1.37 (mbr, 18H, CH ₂); 3.03 (t, 2H, CH ₂); 0.83 (t, 3H, CH ₃)
HAS	MeOD	12.29 (s, 1H, OH); 1.35–1.45 (mbr, 32H, CH ₂); 0.90 (t, 3H, CH ₃)
Ph ₃ Sn(SA)	MeOD	7.23 (mbr, 15H, Ph); 1.29–1.35 (mbr, 30H, CH ₂); 2.97 (t, 2H, CH ₂); 0.83 (t, 3H, CH ₃)
HMA	MeOD	12.60 (s, 1H, OH); 1.26–1.52 (mbr, 24H, CH ₂); 0.87 (t, 3H, CH ₃)
Ph ₃ Sn(MA)	MeOD	7.34 (mbr, 15H, Ph); 1.35–1.41 (mbr, 22H, CH ₂); 2.93 (t, 2H, CH ₂); 0.86 (t, 3H, CH ₃)
HHA	MeOD	12.83 (s, 1H, OH); 7.03–8.01 (mbr, 5H, Ph); 4.25 (d, 2H, CH ₂)
Ph ₃ Sn(HA)	MeOD	7.62–7.88 (mbr, 20H, Ph); 7.60–7.99 (m, 1H, C-NH); 4.15 (d, 2H, CH ₂)
<i>n</i> -Bu ₃ Sn(HA)	MeOD	7.30–8.27 (mbr, 5H, Ph); 4.23 (dbr, 2H, CH ₂); 1.23–1.99 (mbr, 12H, CH ₂); 1.15–1.18 (t, 6H, Sn-CH ₂); 0.54–1.10 (mbr, 9H, CH ₃); (2J (^1H – ^{119}Sn) = 71 Hz)
Me ₃ Sn(HA)	MeOD	7.23–7.93 (mbr, 5H, Ph); 4.01 (d, 2H, CH ₂); 0.47 (mbr, 6H, CH ₃); 0.07 (s, 3H, Sn-CH ₃); (2J (^1H – ^{119}Sn) = 64 Hz)

s singlet, *d* doublet, *t* triplet, *m* multiplet, *br* broad

and the tin atom can thus be ruled out on this basis [29]. The magnitude of the ($\nu_{\text{as}}-\nu_{\text{s}}$)COO ($\Delta\nu$) separation, which has been shown to be useful in identifying structural features [30] is $<200\text{ cm}^{-1}$ indicating that the carboxylate group is involved in bridging or chelation. Furthermore, the disappearance of a broad band in the spectra of the complexes in the region $2800\text{--}2200\text{ cm}^{-1}$, which was present in the free acids as a weak intensity band, suggests the deprotonation of the free COOH group upon complexation [31]. The appearance of a new band of medium intensity in the far IR spectra of all the complexes in the region $581\text{--}509\text{ cm}^{-1}$, which may be assigned to $\nu(\text{Sn-O})$, further supports the bonding of COO group to the tin atom [14, 30, 31] for these triorganotin carboxylates. The corresponding $\nu_{\text{as}}(\text{Sn-C})$ and $\nu_{\text{s}}(\text{Sn-C})$ stretching absorptions were observed at 270 and 220 cm^{-1} , respectively and are observed at 646 ± 23 and $563 \pm 54\text{ cm}^{-1}$ for tri-*n*-butyltin(IV) and at 630 ± 49 and $536 \pm 24\text{ cm}^{-1}$ for trimethyltin(IV) derivatives [32].

18.3.3 NMR Spectral Analysis

The ^1H NMR and ^{13}C NMR spectra of the complexes were recorded in MeOD and the data collected are presented in Tables 18.3 and 18.4. In the NMR spectra of the complexes studied, the OH signal ($\delta \sim 13.0\text{ ppm}$) of free acid is missing

Table 18.4 ^{13}C NMR spectral data of triorganotin(IV) carboxylates

Ligand/complex	Solvent	δ (ppm)
HLA	MeOD	177.08 (C(O)O); 22.77–31.70 (CH ₂) ₁₀ ; 13.52 (CH ₃)
Ph ₃ Sn(LA)	MeOD	176.88 (C(O)O); 22.77–31.70 (CH ₂) ₁₀ ; 13.09 (CH ₃); 126.00–127.01 (Sn-C α , -C β , -C γ); 139.54 (Sn-Ci, $^1J(^{13}\text{C}-^{119}\text{Sn}) = 469.62$ Hz)
HSA	MeOD	177.0 (C(O)O); 21.77–36.71 (CH ₂) ₁₆ ; 13.89 (CH ₃)
Ph ₃ Sn(SA)	MeOD	175.0 (C(O)O); 23.07–31.70 (CH ₂) ₁₆ ; 14.29 (CH ₃); 126.0–126.9 (Sn-C α , -C β , -C γ); 139.67 (Sn-Ci, $^1J(^{13}\text{C}-^{119}\text{Sn}) = 469.58$ Hz)
HMA	MeOD	174.98 (C(O)O); 22.65–32.41 (CH ₂) ₁₂ ; 13.88 (CH ₃)
Ph ₃ Sn(MA)	MeOD	174.0 (C(O)O); 22.64–32.07 (CH ₂) ₁₂ ; 112.89 (CH ₃); 126.07–127.11 (Sn-C α , -C β , -C γ); 139.03 (Sn-Ci, $^1J(^{13}\text{C}-^{119}\text{Sn}) = 469.58$ Hz)
HHA	MeOD	127.0–134.0 (Ph); 174.05 (C(O)O); 167.95 (CO-NH); 43.57 (CH ₂ -N)
Ph ₃ Sn(HA)	MeOD	127.01–131.0 (Ph); 176.05 (C(O)O); 167.05 (CO-N); 45.57 (CH ₂ -N); 126.0–127.01 (Sn-C α , -C β , -C γ); 139.00 (Sn-Ci)
<i>n</i> -Bu ₃ Sn(HA)	MeOD	128.01–136.0 (Ph); 175.05 (C(O)O); 167.0 (CO-N); 45.80 (CH ₂ -N); 25.0–27.10 (Sn-C β , Sn-C γ); 14.95 (Sn-C α); 13.06 (Sn-C δ)
Me ₃ Sn(HA)	MeOD	127.01–134.0 (Ph); 176.0 (C(O)O); 167.05 (CO-N); 46.07 (CH ₂ -N); -4.68 (Sn-C α)

which suggests deprotonation of the acid on complexation [33, 34]. All the carbons of alkyl or phenyl groups attached to the tin atom have also been identified and their chemical shift values are in close agreement with the reported values [32]. The heteronuclear coupling constant, *viz.* $^1J(^{13}\text{C}-^{119}\text{Sn})$ is very useful in providing information about the coordinating environment and geometry of the organotin complexes. The observed coupling constants $^2J(^1\text{H}-^{119}\text{Sn})$ and $^1J(^{13}\text{C}-^{119}\text{Sn})$ are 64–71 Hz and 476 ± 10 Hz, respectively for triorganotin(IV) derivatives, which lie in the range of penta-coordinate environment around the tin in a distorted trigonal-bipyramidal geometry (Fig. 18.1).

The ^{119}Sn NMR chemical shifts are very sensitive to coordination number of tin and are greatly shifted upfield on bonding to Lewis base. A typical range of chemical shifts ($\delta = -90$ to -330 ppm) has been reported [35] for coordination number five for organotin(IV) compounds. All the synthesized organotin(IV) carboxylates exhibit only one ^{119}Sn resonance which rules out the possibility of two different species (Table 18.5). The observed values clearly suggest five-coordination which corresponds to a distorted trigonal-bipyramidal geometry around the tin atom in the studied organotin(IV) carboxylates (Fig. 18.1).

R = Ph, *n*-Bu and Me;
 X = $-(\text{CH}_2)_{10}\text{CH}_3$ (LA);
 $-(\text{CH}_2)_{16}\text{CH}_3$ (SA);
 $-(\text{CH}_2)_{12}\text{CH}_3$ (MA);
 and $-(\text{CH}_2)\text{NHC}(\text{O})\text{C}_6\text{H}_5$ (HA)

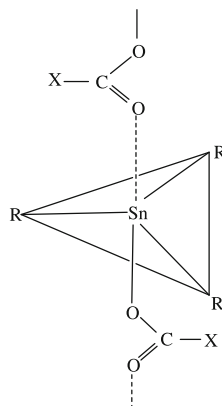


Fig. 18.1 Distorted trigonal bipyramidal structure of triorganotin(IV) carboxylates

Table 18.5 ^{119}Sn NMR spectral data of triorganotin(IV) carboxylates

Complex (CD_3OD , 500 MHz)	Solvent	δ (ppm)
$\text{Ph}_3\text{Sn}(\text{LA})$	MeOD	-184.6
$\text{Ph}_3\text{Sn}(\text{SA})$	MeOD	-172.5
$\text{Ph}_3\text{Sn}(\text{MA})$	MeOD	-190.4
$\text{Ph}_3\text{Sn}(\text{HA})$	MeOD	-181.7
<i>n</i> -Bu $_3\text{Sn}(\text{HA})$	MeOD	-130.0
$\text{Me}_3\text{Sn}(\text{HA})$	MeOD	-123.1

18.3.4 Biological Screening

18.3.4.1 Anti-cancer Activity

All of the studied triorganotin(IV) carboxylates along with parent organotin(IV) chlorides and standard drugs *viz.* *cis*-platin, 5-fluorouracil and methotrexate (Table 18.6) have been screened *in-vitro* against five cancer cell lines of human origin, *viz.* MCF-7 mammary cancer, HEK-293 kidney cancer, PC-3 prostate cancer, HCT-15 colon cancer and HepG-2 liver cancer. The cancer lines were purchased from NCCS Pune, India.

The IC_{50} values of the studied complexes as given in Table 18.6 are compared with those of some clinically used reference drugs, *cis*-platin (CPT), 5-fluorouracil (5FU) and methotrexate (MTX). Triphenyltin laurate, $\text{Ph}_3\text{Sn}(\text{LA})$ is the most active compound which exhibits potent anticancer activity against all the cell lines as compared to *cis*-platin. Further, it is even more active against MCF-7, HEK-293 and PC-3 as compared to 5-fluorouracil, and against HEK-293, PC-3 and HepG-2 in comparison to methotrexate. $\text{Ph}_3\text{Sn}(\text{HA})$ and $\text{Me}_3\text{Sn}(\text{HA})$ show comparable activity against HEK-293 and PC-3 as compared to *cis*-platin but they are less active as compared to 5-fluorouracil and methotrexate. $\text{Ph}_3\text{Sn}(\text{SA})$ and $\text{Ph}_3\text{Sn}(\text{MA})$ are

Table 18.6 *In-vitro* anti-cancer screening data (IC₅₀) of triorganotin(IV) carboxylates and reference drugs

Compound	MCF-7	HEK-293	PC-3	HCT-15	HepG-2
Ph ₃ SnLA	0.25 μM	0.45 μM	0.15 μM	3 μM	4 μM
Ph ₃ SnSA	150 μM	120 μM	100 μM	120 μM	150 μM
Ph ₃ SnMA	1 mM	2 mM	1 mM	5 mM	13 μM
Ph ₃ SnHA	100 μM	90 μM	120 μM	100 mM	100 mM
Bu ₃ SnHA	No effect at 1 mM	No effect at 2 mM	No effect at 3 mM	No effect at 1 mM	No effect at 4 mM
Me ₃ SnHA	100 μM	90 μM	100 μM	90 mM	10 mM
TPC	No effect at 4 mM	No effect at 6 mM	No effect at 1 mM	No effect at 1 mM	No effect at 1 mM
TBC	No effect at 5 mM	No effect at 1 mM	No effect at 1 mM	No effect at 1 mM	No effect at 1 mM
TMC	No effect at 1 mM	No effect at 1 mM	No effect at 1 mM	No effect at 1 mM	No effect at 1 mM
<i>Cis</i> -platin	60 μM	82 μM	100 μM	21.6 μM	42.8 μM
5-Fluorouracil	2.75 μM	18 μM	2.85 μM	1 μM	2.2 μM
Methotrexate	88 nM	124.6 μM	76 μM	80 nM	>500 μM

IC₅₀ values calculated by MTT assay in respective cell line

TPC triphenyltin chloride, TBC tributyltin chloride, TMC trimethyltin chloride

very active against HepG-2 in comparison to methotrexate and exhibit comparable activity against PC-3 as compared to *cis*-platin. *n*-Bu₃Sn(HA) is the least active among all the studied compounds.

18.3.4.2 Enzymatic Assays

The observed data of enzymatic assays of triphenyltin(IV) laurate against MCF-7 are presented in Table 18.7. Necrosis could be excluded by determination of extra cellular lactate dehydrogenase (LDH). The non-specific necrosis mediated through membrane toxicity is observed within short periods of time, which is responsible for the marginal increase in LDH concentration. This indicates that the cells are not dying by necrosis but the cell death is caused by apoptosis. Increase in other antioxidant enzymes suggests that reactive oxygen species have been produced in the cells which are responsible for causing apoptosis, and have led to the increase in the activities of the antioxidant enzymes. Results in Table 18.7, therefore, clearly indicate that the cytotoxic effect of the organotin(IV) carboxylates is selectively mediated through the induction of apoptosis.

18.3.4.3 DNA Fragmentation Assay

DNA extracted from MCF-7 was taken as control (lane 3) and added to triphenyltin(IV) laurate (lane 1), *cis*-platin (lane 2) and DNA ladder of 100 base pair (lane 4) as described in the experimental section. Gel electrophoresis experiment

Table 18.7 Enzymatic assays of triphenyltin(IV) laurate against MCF-7

Enzyme	Activity of triphenyltin(IV) laurate against MCF-7 cells		
	Untreated	Treated	Induction fold (treated/ untreated)
Lipid peroxidase	0.00035 $\mu\text{M}/\mu\text{g}$ protein	0.00745 $\mu\text{M}/\mu\text{g}$ protein	Increases by 24.00
Glutathione peroxidase	0.566 IU/mg protein	15.82 IU/mg protein	Increases by 27.90
Glutathione-s-transferase	0.790 IU/mg protein	31.81 IU/mg protein	Increases by 40.26
Total glutathione	0.0037 $\mu\text{M}/\mu\text{g}$ protein	0.0560 $\mu\text{M}/\mu\text{g}$ protein	Increases by 18.00
Glutathione reductase	0.162 IU/mg protein	3.54 IU/mg protein	Increases by 21.00
Lactate dehydrogenase	5.59 IU/mg protein	6.59 IU/mg protein	Increases by 1.18

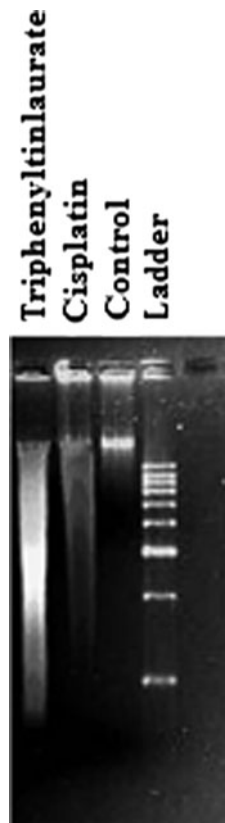
IU International Unit

was conducted and recorded on Biorad-UV-transilluminator after addition of ethidium bromide. The image was taken with the help of Gel Doc- software. The results are shown in Fig. 18.2. DNA fragmentation has long been used to distinguish apoptosis from necrosis, and is among the most reliable methods for detection of apoptotic cells. Figure 18.2 clearly shows formation of DNA-ladder which indicates that the DNA breakage or fragmentation has occurred which can only happen when cell apoptosis takes place. Therefore, the cytotoxic effect of the studied triorganotin(IV) carboxylates is selectively mediated through the induction of apoptosis.

18.4 Conclusions

Spectral analyses of the synthesised triorganotin(IV) carboxylates suggest a trigonal-bipyramidal geometry around tin for these carboxylates with the alkyl/aryl groups in the equatorial positions, while a carboxylic oxygen and the oxygen atom of the carbonyl group of adjacent molecule occupy the axial positions. *In-vitro* anti-tumor screening of these carboxylates suggests that triphenyltin laurate is the most active compound which exhibits potent anticancer activity against all the cell lines as compared to *cis*-platin. Further, it is even more active against MCF-7, HEK-293 and PC-3 as compared to 5-fluorouracil and against HEK-293, PC-3 and HepG-2 in comparison to methotrexate. $\text{Ph}_3\text{Sn}(\text{HA})$ and $\text{Me}_3\text{Sn}(\text{HA})$ show comparable activity against HEK-293 and PC-3 as compared to *cis*-platin but they are less active as compared to 5-fluorouracil and methotrexate. $\text{Ph}_3\text{Sn}(\text{SA})$ and $\text{Ph}_3\text{Sn}(\text{MA})$ are very active against HepG-2 in comparison to methotrexate and exhibit comparable activity against PC-3 as compared to *cis*-platin. *n*- $\text{Bu}_3\text{Sn}(\text{HA})$ is the least active among the studied compounds. Furthermore, DNA ladder formation indicates that these compounds inhibit the cancer cell growth through apoptosis which has

Fig. 18.2 DNA ladder formation through gel electrophoresis – *lane 1*: triphenyltin(IV) laurate; *lane 2*: *cis*-platin; *lane 3*: control (extracted DNA from MCF-7); *lane 4*: DNA Ladder of base pair 100



been confirmed by enzyme assays like lactate dehydrogenase, glutathione sulfur-transferase, glutathione reductase, glutathione-peroxidase, total glutathione content and lipid peroxidase assay.

Acknowledgement Ms. Monika Vats (JRF) is thankful to MHRD for the financial support.

References

1. Davies AG (2004) Organotin chemistry. Wiley-VCH, Weinheim
2. Chandrasekhar V, Nagendran S, Baskar V, Bergmeyer HU (2002) Organotin assemblies containing Sn–O bonds. *Coord Chem Rev* 235:1–52
3. Chandrasekhar V, Nagendran S, Gopal K, Saskumar P, Moorthi R (2005) Organotin assemblies from Sn–C bond cleavage reactions. *Coord Chem Rev* 249:1745–1765
4. Chandrasekhar V, Gopal K, Thilagar P (2007) Nanodimensional organostannoxane molecular assemblies. *Acc Chem Res* 40:420–434

5. Kemmer M, Dalil H, Biesemans M, Martins JC, Mahieu B, Horn E, de Vos D, Tiekink ERT, Willem R, Geielen M (2000) Dibutyltin perfluoroalkancarboxylates: synthesis, NMR characterization and *in vitro* anti-tumor activity. *J Organomet Chem* 608:63–70
6. Gielen M (2002) Review: organotin compounds and their therapeutic potential. *Appl Organomet Chem* 16:481–494
7. de Vos D, Willem R, Gielen M, van Wingerden KE, Nooter K (1998) Development of novel organotin anti-tumor drugs: structure and activity. *Met Based Drugs* 5:179–188
8. Zhou Y, Jiang T, Ren S, Yu J, Xia Z (2005) Synthesis, crystal structure and *in vitro* antitumor activity of di-*n*-butyltin 4⁻-(7-oxabicyclo[2,2,1]-5-heptane-2,3-dicarboximide) benzoates. *J Organomet Chem* 690:2186–2190
9. Tabassum S, Pettinari C (2006) Chemical and biotechnological developments in organotin cancer chemotherapy. *J Organomet Chem* 691:1761–1766
10. Perez-Rebolledo A, Ayala JD, de Lima GM, Marchini N, Bombieri G, Zani CL, Souza-Fagundes EM, Beraldo H (2005) Structural studies and cytotoxic activity of N(7) phenyl-2-benzoylpyridine thiosemicarbazone Sn(IV) complexes. *Eur J Med Chem* 40:467–472
11. Davies AG, Gielen M, Pannell KH, Tiekink ERT (Eds.) (2008) Tin chemistry: fundamentals, frontiers and applications. Wiley, New York
12. Sandhu GK, Kaur G (1990) Preparation, IR and ¹H NMR spectral studies of triorganotin(IV) complexes of N-benzoylglycine and N-benzoylglycylglycine. *J Organomet Chem* 388:63–70
13. Nath M, Pokharia S, Song X, Eng G, Gielen M, Kemmer M, Biesemans M, Willem R, de Vos D (2003) New organotin(IV) derivatives of dipeptides for metal-protein interactions: *in vitro* anti-tumor activity. *Appl Organomet Chem* 17:305–314
14. Nath M, Yadav R, Eng G, Nguyen TT, Kumar A (1999) Characteristic spectral studies, and anti-microbial and anti-inflammatory activities of diorganotin(IV) dipeptides. *J Organomet Chem* 577:1–8
15. Nath M, Pokharia S, Eng G, Song X, Kumar A (2003) Comparative study of structure-activity relationship of di- and triorganotin(IV) derivatives of amino acids and peptides. *J Organomet Chem* 669:109–125
16. Mosmann T (1983) Rapid colorimetric assay for cell growth and survival: application to proliferation and cytotoxicity assay. *J Immunol Methods* 65:55–63
17. De Vita Jr VT, Hellman S, Rosenberg SA (Eds.) (1997) Cancer: principles and practice of oncology. Lippincott-Raven Publications, Philadelphia
18. Keopers YP, Pizao PE, Peters GJ, Van Ark-Otte J, Winograd B, Pinedo HM (1991) Comparison of sulphorhodamine B protein and tetrazolium (MTT) assay for *in vitro* chemosensitivity testing. *Eur J Cancer* 27:896–903
19. Memduh K, Hakan E, Neslihan B, Ayse D, Gokhan K, Hatice P, Aydin P (2005) Effectiveness of FK506 on lipid peroxidation in the spinal cord following experimental traumatic injury. *Spinal Cord* 43:22–26
20. Bergmeyer HU, Garvehn P (1978) Glutathione reductase. In: Bergmeyer HU (ed) *Methods of enzymatic analysis*. Academic, New York
21. Kaji H, Kurasaki M, Ito K, Saito T, Saito K, Niioka T, Kojima Y, Ohsaki IY, Ide H, Tsuji M, Kondo T KSY (1985) Increased lipoperoxide value and glutathione peroxidase activity in blood plasma of the type 2 (non-insulin-dependent) diabetic women. *Klin Wochenschr* 63:765–768
22. Paglia DE, Valentine WN (1967) Studies on quantitative and qualitative characterization of erythrocyte glutathione peroxidase. *J Lab Clin Med* 70:158–169
23. Habig WH, Pabst MJ, Jakoby WB (1974) Glutathione S-transferases. The first enzymatic step in mercapturic acid formation. *J Biol Chem* 249:7130–7139
24. Pae HO, Oh GS, Choi BN, Seo EA, Oh H, Shin MK, Kim TH, Kwon TO, Chung HT (2003) Induction of apoptosis by 4-acetyl-12,13-epoxyl-9-trichothecene-3,15-diol from *isaria japonica yasuda* through intracellular reactive oxygen species formation and caspase-3 activation in human leukemia HL-60 cells. *Toxicol In Vitro* 17:49–57
25. Bergmeyer HU (ed) (1974) *Methods of enzymatic analysis*. Academic Press, New York
26. Sanchez-Alcazar JA, Khodjakov A, Schneider E (2001) Anticancer drugs induced increased mitochondrial cytochrome c expression that precedes cell death. *Cancer Res* 61:1038–1044

27. Sanchez-Alcazar JA, Ruiz-Cabello J, Hernandez-Munoz I, Pobre PS, de la Torre P, Siles-Rivas E, Garcia I, Kaplan O, Munoz-Yague MT, Sols-Herruzo JA (1997) Tumor necrosis factor- α increases ATP content in metabolically inhibited L929 cells preceding cell death. *J Biol Chem* 272:30167–30177
28. Ford BFE, Liengme BV, Sams JR (1969) Organotin carboxylates 1. Mössbauer and infrared study of triphenyltin carboxylates and the novel compounds $R\text{Sn}(\text{O})\text{OCOR}$. *J Organomet Chem* 19:53–65
29. Ho BYK, Zuckerman J (1973) Syntheses and crystal structures of triorganotin(IV) complexes based on mixed ligands of 2,4,5-trifluoro-3-methoxybenzoic acid and 4,4'-bipy. *Inorg Chem* 12:1552–1561
30. Nath M, Pokharia S, Yadav R (2001) Organotin(IV) complexes of amino acids and peptides: a review. *Coord Chem Rev* 215:99–149 (references cited therein)
31. Nath M, Yadav R (1998) Studies of organotin(IV) derivatives of DL-methionine and D-asparagine. *Bull Chem Soc Jpn* 71:1355–1362
32. Nath M, Goyal S (1996) Review on organotin(IV) complexes of Schiff bases. *Main Group Met Chem* 19:75–102
33. Sedaghat T, Menati S (2004) Synthesis and spectroscopic characterization of new adducts of diorganotin(IV) chlorides with an asymmetric Schiff base ligand. *Inorg Chem Commun* 7: 760–762
34. Nath M, Goyal S (1995) Spectral studies and bactericidal, fungicidal, insecticidal and parasitological activities of organotin(IV) derivatives of thio-Schiff bases having NO donor atoms. *Met Based Drugs* 2:297–309
35. Sarawat BS, Mason J (1986) Modes of coordination of 1,2-aminothiols in organotin(IV) complexes, as demonstrated by ^{119}Sn , ^{14}N and ^{13}C NMR spectroscopy. *Polyhedron* 5: 1449–1458

Chapter 19

Nonequilibrium Ultrafast Charge Transfer Reactions in Photoexcited Donor-Acceptor Pairs

Valentina A. Mikhailova, Sergey V. Feskov, Vladimir N. Ionkin,
Vladislav V. Yudanov, and Anatoly I. Ivanov

Abstract The ultrafast charge recombination kinetics in photoexcited donor-acceptor pairs in polar solvents has been explored. By using experimental data and theoretical modeling, the key role of medium nonequilibrium in ultrafast charge recombination has been elucidated. The influence of excitation pulse spectral characteristics as well as dynamic properties of solvent on the kinetics of such processes has been analyzed. The reorganization of high-frequency vibrational modes in hot electronic transitions has been shown to accelerate the charge recombination in the low exergonic region and to suppress it in the region of moderate exothermicity. The medium nonequilibrium can straighten the dependence of the logarithm of the charge recombination rate constant on the free energy gap to the form that can be well fitted to the experimental data. The kinetics of charge separation from the second excited state and subsequent charge recombination to the first excited state for a series of supramolecular systems have been quantitatively reproduced in the framework of stochastic multi-channel model.

19.1 Introduction

For last two decades charge transfer (CT) reactions proceeding on the femtosecond timescale have been intensively investigated [1–33]. In particular, systematic investigations of ultrafast charge recombination (CR) in excited donor-acceptor complexes (DAC) in polar solvents have uncovered a number of bright manifestations of nuclear nonequilibrium in CR kinetics [3, 6, 21, 25, 26, 29–31]. The nuclear nonequilibrium can be created by either short laser pulse excitation or

V.A. Mikhailova (✉) • S.V. Feskov • V.N. Ionkin • V.V. Yudanov • A.I. Ivanov
Physical-Technical Institute, Volgograd State University, University Avenue,
100 400062 Volgograd, Russia
e-mail: mikhailova_va@mail.ru; serguei.feskov@volsu.ru; ionya@mail.ru;
Yudanov-VolSU@yandex.ru; Anatoly.Ivanov@volsu.ru

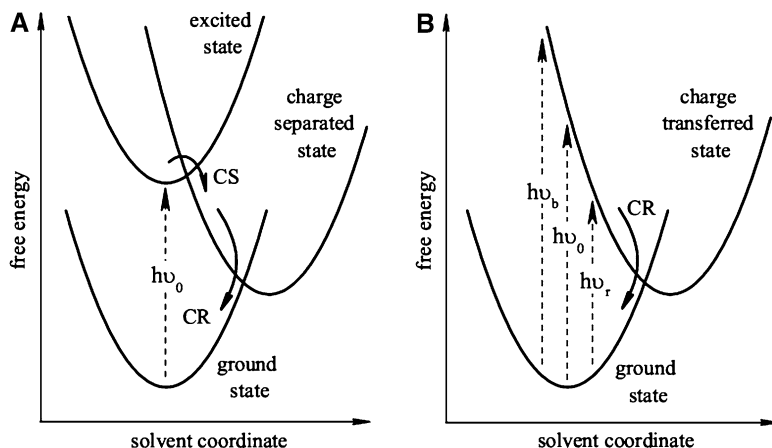


Fig. 19.1 Nonequilibrium nuclear state created by charge separation reaction (*panel A*) and by short laser pulse excitation (*panel B*)

chemical reaction itself (see Fig. 19.1). For example, photoinduced electron transfer proceeding in the vicinity of the term crossing of the excited and the ionic states produces a localized state that is far away from the product free energy surface minimum. Relaxation of such a state can result in hot backward transitions to the ground state. Upon laser pulse excitation, the excited DAC state is formed away from equilibrium and CR can proceed in parallel with nuclear relaxation. As a result in CR kinetics at least two (nonequilibrium (“hot”) and thermal) stages should appear. When the reaction is ultrafast the hot stage cannot be neglected. Moreover, if solvent relaxation time exceeds the characteristic timescale of electron transfer the thermal stage can be practically unobservable.

Most pronounced two stage kinetics of CR in excited DACs is expected for low exergonic reactions proceeding in the Marcus normal region. Such a behaviour was observed in DACs consisting of 1,2,4-trimethoxybenzene (TMB) and tetracyanoethylene (TCNE), but only in acetonitrile (ACN) [26]. In more viscous solvents the slow component of CR practically vanished and only the fast stage was observed. This can be thought as one more evidence in favour of nonequilibrium nature of the fast stage.

Another manifestation of nonequilibrium character of ultrafast CR in excited DACs is variation of the effective CR rate constant with the excitation pulse carrier frequency (so called spectral effect). This effect was observed for a few DACs in slowly relaxing solvents. In valeronitrile (VaCN), the spectral effect, measured between 480 and 620 nm, was (i) negative (decrease of the CR rate with increasing excitation pulse frequency) with isodurene (IDU)-TCNE, (ii) positive with hexamethylbenzene (HMB)-TCNE, and (iii) vanishingly small with pentamethylbenzene (PMB)-TCNE [26]. The origin of the spectral effect can be understood if we consider the excitation of DAC by short laser pulse in detail. As one can see in

Fig. 19.1 (panel B), excitation of these DACs at distinct wavelengths creates the nonequilibrium wave packets with different localization of particle density. These wave packets reach the CR reaction zone at different moments of time that leads to diversities in the CR kinetics.

Another bright manifestation of nuclear nonequilibrium was detected for the directly linked Zn-porphyrin-imide dyads [24]. Charge separation (CS) from the second excited state being much faster than radiationless deactivation results in low quantum yield of thermalized CT product. This fact directly reflects the crucial role of hot transitions into the first excited state. The CR into the first excited state is shown to proceed in a hot stage in parallel with the relaxation of both the medium and the intramolecular high-frequency vibrational modes. For these systems experimentally observed population kinetics of both the first and the second singlet excited states can be well reproduced within the multi-channel stochastic model [32].

It was found that reorganization of intramolecular high-frequency modes dramatically changes ultrafast CR in excited DACs. Moreover, when intramolecular reorganization is combined with ultrafast solvent relaxation, the excited state decay approaches to exponential regime [30, 31]. For relatively strong electronic coupling and moderate reorganization energy of quantum intramolecular vibrations (as it is, for example, in perylene-TCNE complex [30]) it was shown that the CR is monophasic because it is terminated at the nonthermal phase. Further it was also found that in the low exergonic region the multi-channel hot transitions enhance the CR rate overturning the ascending branch of the Marcus inverted parabola [30]. As a result, the CR rate constant monotonously decreases with the free energy gap in the solvent-controlled regime, that is, the Marcus normal region is absent in such reactions.

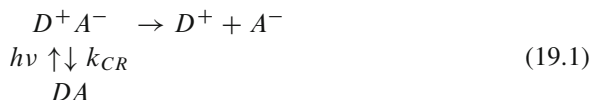
The results of numerous simulations indicate that the ultrafast CR kinetics are practically invariant with respect to high frequency vibrational spectrum provided the total reorganization energy of these modes is fixed and the mode number is no less than 5 [33]. In addition the fast relaxation of the intramolecular high-frequency vibrational mode was shown to considerably accelerate the CR of the excited DACs [30, 33, 34]. Simultaneous action of a large number of the hot transition channels along with the vibrational relaxation can provide practically complete transformation of the reactants into products at the hot stage in the wide range of parameters except for the weak electron transfer limit. In addition, it should be noted that the important role of nuclear nonequilibrium was theoretically predicted for the photoinduced CT [7, 12, 27, 35]. In particular, it was shown that, the dependence of ultrafast photoinduced electron transfer (ET) rate on the excitation pulse carrier frequency (the spectral effect) depends on the angle θ between the reaction coordinate directions corresponding to optical and charge transfer transitions. The dependence of photoinduced electron transfer dynamics on the angle θ is a direct evidence of nuclear nonequilibrium in the reaction [27, 35].

The main aim of this paper is to show that for CR in excited DACs the majority of experimentally observed manifestations of nuclear nonequilibrium can be reproduced within the framework of a single model. Until recently, one or another

theory explained only a single feature of ultrafast CR or calculate quantitatively the CR rate constant in specific systems. However the current level of research in the field of ultrafast photochemical processes requires a comprehensive approach in order to explain the whole set of experimental data within a single model. In the next sections we show that most of the above manifestations of nuclear nonequilibrium can be reproduced in framework of the multi-channel stochastic model [30–34], namely the charge transfer absorption band, the CR dynamics for a single excitation pulse carrier frequency in a single solvent, the spectral effect, the solvent effect, and free energy gap dependence of the CR rate.

19.1.1 Model

It is well known that CR in the DACs, which occurs after excitation by a short pulse at the frequency of the CT absorption band, can be described by the simplest scheme



where $h\nu$ indicates the photoexcitation, k_{CR} is the CR rate constant. In accordance with this scheme later we assume that only two electronic states of DAC (the charge transferred state $|e\rangle$ and the ground neutral state $|g\rangle$) can be populated. It is noted that the model is easily extended to three or more electronic states [32]. The system considered, initially in $|g\rangle$ -state with thermal equilibrium configuration of nuclear subsystem (solvent and intramolecular vibrational degrees of freedom), is transferred to the $|e\rangle$ -state with nonequilibrium nuclear subsystem by a short laser pulse (see Figs. 19.1 (panel B) and 19.2). The population of this nonequilibrium state is subjected to series of relaxation processes like the reorganization of solvent and intramolecular vibrational degrees of freedom. To account for the reorganization of high-frequency intramolecular vibrational modes, instead of one state U_g put a lot of vibrationally excited states $U_g^{(n)}$, separated by an amount equal to the energy of high frequency vibrational quantum $\hbar\Omega_\alpha$, where Ω_α is the frequency of the α th intramolecular quantum mode ($\alpha = 1, 2, \dots, M$). This leads to a problem with many channels of electronic transitions. Fig. 19.2 shows several vibrationally excited sublevels of ground state and also term intersection points in the case $M = 2$. Further for the enumeration of these points as well as the terms $U_g^{(n)}$ the same index n is used. Under the influence of a short laser pulse with a duration, τ_e , much shorter than the relaxation of the solvent, τ_L , the system vertically undergoes to the excited term (the vicinity of point B in Fig. 19.2).

Intuitively, this nonequilibrium nuclear configuration can be represented by a wave packet. It is located on the excited term over a minimum term of the ground state (the point A in Fig. 19.2). The subsequent movement of the wave package

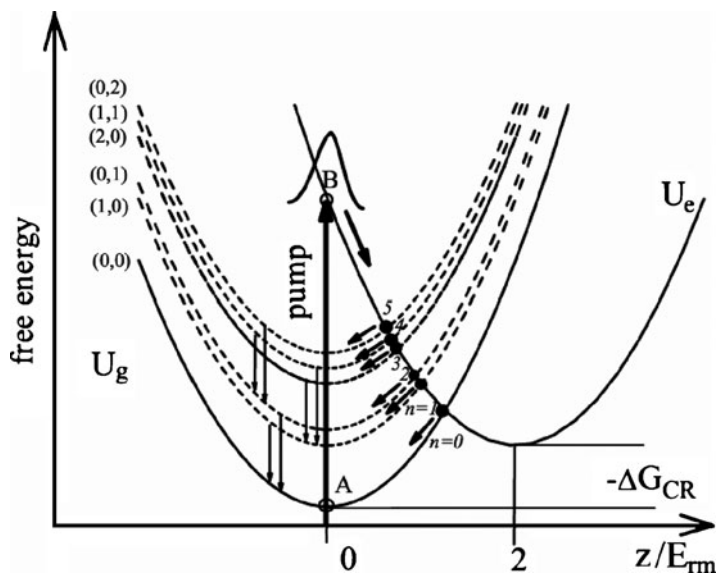


Fig. 19.2 Schematic representation of the multi-channel charge recombination after photoexcitation of DAC by pump pulse

toward a minimum term U_e reflects the reorganization of the classical degrees of freedom of the complex and the surrounding solvent, caused by the change of charge of the donor and acceptor, and corresponds to a transition of system to a new equilibrium position.

Relaxation of the system is characterized by the autocorrelation function $K(t) = \langle \Delta E(t) \Delta E(0) \rangle$, where the value $\Delta E(t) = U_g - U_e$ is a generalized reaction coordinate [36]. The autocorrelation function $K(t)$ is associated with the function of the relaxation of the solvent by a simple relation $K(t) = 2E_{rm}k_B T X(t)$, where E_{rm} is the reorganization energy of solvent, k_B is the Boltzmann constant and T is the temperature. Function $X(t)$ is directly related to time-dependent Stokes shift measured experimentally. For an ideal polar solvent, described by the Debye relaxation, $X(t)$ has the simple form [36] $X(t) = \exp(-t/\tau_L)$. Real polar solvents are characterized by not one but several relaxation times. These time scales are usually associated with different relaxation modes, as $X(t)$ written in the form [36, 37]

$$X(t) = \sum_{i=1}^N x_i e^{-t/\tau_i}, \quad \sum_{i=1}^N x_i = 1 \quad (19.2)$$

where N is the number of relaxation modes, $x_i = E_{ri}/E_{rm}$, E_{ri} and τ_i are the weight, the reorganization energy and the relaxation time of the i th medium mode, respectively. It is known that a random process with autocorrelation function of the

form (19.2) can be represented by a multidimensional Gaussian random process with a single exponential autocorrelation function $\exp(-t/\tau_i)$ in each dimension [38]. Each of them can be associated independent of reaction coordinate Q_j . This makes it possible to describe the stochastic dynamics by multi-dimensional equations of diffusion type. In this case the diabatic free energy surfaces of the ground and excited states can be represented as

$$U_g^{(n)} = \sum_{i=1}^N \frac{Q_i^2}{4E_{ri}} + \sum_{\alpha=1}^M n_\alpha \hbar \Omega_\alpha + \Delta G_{CR}, \quad U_e = \sum_{i=1}^N \frac{(Q_i - 2E_{ri})^2}{4E_{ri}} \quad (19.3)$$

Here n_α ($n_\alpha = 0, 1, 2, \dots$) is the quantum number of α th mode, ΔG_{CR} is the CR free energy.

The temporal evolution of the system considered can be described by a set of differential equations for the probability distribution functions for the excited state $\rho_e(t, Q_1, \dots, Q_N)$ and for the n th sublevel of the ground state $\rho_g^{(n)}(t, Q_1, \dots, Q_N)$

$$\frac{\partial \rho_e}{\partial t} = \hat{L}_e \rho_e - \sum_n k_n(Q_1, \dots, Q_N) (\rho_e - \rho_g^{(n)}) \quad (19.4)$$

$$\frac{\partial \rho_g^{(n)}}{\partial t} = \hat{L}_g \rho_g^{(n)} - k_n(Q_1, \dots, Q_N) (\rho_g^{(n)} - \rho_e) + \sum_{\alpha=1}^M \frac{1}{\tau_{v\alpha}^{(n\alpha+1)}} \rho_g^{(n'\alpha)} - \frac{1}{\tau_v^{(n)}} \rho_g^{(n)} \quad (19.5)$$

As noted above for the numbering of states with simultaneous excitation of different intramolecular quantum modes, instead of set of quantum numbers $(n_1, \dots, n_\alpha, \dots, n_M) \equiv \{n_\alpha\}$ we use a single index n ($0, 1, 2, \dots$). It implies that the set $\{n_\alpha\}$ is mapped in a one-to-one way onto the set of whole numbers n . The correspondence is fixed by the inequality $z_n^\dagger < z_{n+1}^\dagger$, where $z = \sum Q_i$ is the collective energy reaction coordinate, $z_n^\dagger = E_{rm} - \Delta G_{CR} - \sum_\alpha n_\alpha \hbar \Omega_\alpha$ are the intersection points of terms U_e and $U_g^{(n)}$. In Eq. 19.5 the index n'_α stands for the set of quantum numbers $\{n'_\alpha\} = (n_1, \dots, n_\alpha + 1, \dots, n_M)$.

We adopt here a single-quantum mechanism of high-frequency mode relaxation and the transitions $n_\alpha \rightarrow n_\alpha - 1$ proceed with the rate constant $1/\tau_{v\alpha}^{(n_\alpha)}$. Naturally, the ground vibrational state is stable and the equation $\tau_{v\alpha}^{(0)} = \infty$ must be fulfilled. This condition is met for the model $\tau_{v\alpha}^{(n_\alpha)} = \tau_{v\alpha}^{(1)}/n_\alpha$. The relaxation rate of the n -th state is determined by the equation

$$\frac{1}{\tau_v^{(n)}} = \sum_\alpha \frac{1}{\tau_{v\alpha}^{(n_\alpha)}} \quad (19.6)$$

In Eqs. 19.4 and 19.5 the Smoluchowski operators \hat{L}_g and \hat{L}_e describing diffusion on the U_g and U_e potentials have the form

$$\hat{L}_g = \sum_{i=1}^N \frac{1}{\tau_i} \left(1 + Q_i \frac{\partial}{\partial Q_i} + \langle Q_i^2 \rangle \frac{\partial^2}{\partial Q_i^2} \right) \quad (19.7)$$

$$\hat{L}_e = \sum_{i=1}^N \frac{1}{\tau_i} \left(1 + (Q_i - 2E_{ri}) \frac{\partial}{\partial Q_i} + \langle Q_i^2 \rangle \frac{\partial^2}{\partial Q_i^2} \right) \quad (19.8)$$

with $\langle Q_i^2 \rangle = 2E_{ri}k_B T$ being the dispersion of the equilibrium distribution along the i th reaction coordinate. Electronic transitions between the excited state $|e\rangle$ and the n th vibrational sublevels of the ground state $|g\rangle$ are described by parameters having the form [36, 39]

$$k_n = \frac{2\pi V_n^2}{\hbar} \delta(U_e - U_g^{(n)}) = \frac{2\pi V_n^2}{\hbar} \delta(z - z_n^\dagger), \quad V_n^2 = V_{el}^2 F_n, \quad F_n = \prod_{\alpha} \frac{S_{\alpha}^{n_{\alpha}} e^{-S_{\alpha}}}{n_{\alpha}!}. \quad (19.9)$$

F_n is the Franck-Condon factor, $S_{\alpha} = E_{rv\alpha}/\hbar\Omega_{\alpha}$ and $E_{rv\alpha}$ are the Huang-Rhys factor and the reorganization energy of the α -th high-frequency vibrational mode, respectively.

The system of Eqs. 19.4 and 19.5 with initial condition

$$\rho_e(t=0, Q_1, \dots, Q_N)$$

$$= Z^{-1} \sum_{n_{\alpha}} \left[\prod_{\alpha} \frac{S_{\alpha}^{n_{\alpha}} e^{-S_{\alpha}}}{n_{\alpha}!} \right] \exp \left[-\frac{(\hbar\delta\omega_e^{(n)} - \sum_i \tilde{Q}_i)^2 \tau_e^2}{2\hbar^2} - \sum_{i=1}^N \frac{\tilde{Q}_i^2}{4E_{ri}k_B T} \right] \quad (19.10)$$

is solved numerically using the Brownian simulation method [40]. In Eq. 19.10 the following designations are used: $\tilde{Q}_i = Q_i - 2E_{ri}$, $\hbar\delta\omega_e^{(n)} = \hbar\omega_e + \Delta G_{CR} - E_{rm} - \sum_{\alpha} n_{\alpha} \hbar\Omega_{\alpha}$, and Z is a factor determined by the initial population of the excited state. In next section a few of successful applications of this model and discussion of some of the brightest manifestations of nuclear nonequilibrium are analyzed.

19.2 Results and Discussion

In spite of the fact that very detailed experimental and theoretical studies of the CR kinetics have been performed with a large number of DACs, there are still several unresolved issues regarding the mechanism of ultrafast CR of excited DACs. One of the most important questions is the reaction regime that is realized in a specific

DAC. Indeed, a successful quantitative description of the CR rate constants can be obtained both in the weak [3, 4, 6, 15, 20, 21, 41] and the strong electronic coupling limit [18, 42, 43]. This fact clearly indicates that a good fit to the experimental rate constants within the framework of a specific theory is not a reliable evidence of its validity. A more rigorous test of the model should include the reproduction of at least a few dependencies of the rate constants on parameters that can be varied over a sufficiently large range.

19.2.1 Solvent and Spectral Effects in Excited DACs

Ultrafast CR processes in DACs present unique possibilities of experimental and theoretical studies. The absorption and resonance Raman spectra of DACs can give direct information on the CR reaction parameters in these chemical systems, since both optical and chemical processes proceed between the same free energy surfaces [3, 43–46].

By using Raman data for the HMB-TCNE, IDU-TCNE and PMB-TCNE complexes (intramolecular frequencies Ω_α and relative values of the Huang-Rhys factors S_α), the parameters E_{rm} , ΔG_{CR} , and the absolute values of S_α were determined from the fit to the experimental stationary CT absorption bands [31]. Thus, all parameters of the multi-channel stochastic model except for electronic coupling were obtained from spectral data. The value of electronic coupling was specified from the fit of the model to the CR dynamics for a single excitation pulse carrier frequency in a single solvent. So, investigations of the influence of dynamic solvent characteristics and excitation pulse carrier frequency, ω_e , on CR kinetics were fulfilled without any adjustable parameters. This is serious test of the model.

A good correlation between experimental and calculated results was obtained with IDU-TCNE in all solvents (ACN, VaCN, octanenitrile (OcCN)). With PMB-TCNE and HMB-TCNE on the other hand, the model describes correctly the variation of the effective time constant in ACN and VaCN but overestimates it noticeably in OcCN. The effective CR time constant was determined with the equation [31]

$$\tau_{eff} = \int_0^{\infty} \rho_e(t, Q_1, \dots, Q_N) dt dQ_1 \dots dQ_N$$

In the simulations, the relative weights of the fast and slow components in ACN and VaCN were set to $x_1 = x_2 = 0.5$. With such parameters, the CR time constant in OcCN is considerably underestimated. After having changed these parameters to $x_1 = 0.23$ and $x_2 = 0.77$, the solvent effect observed experimentally with the CR of IDU-TCNE upon 530 nm excitation could be well reproduced by the simulations in all three solvents [31].

Table 19.1 Effective CR time constants, τ_{eff} in ps, the wavelength of the pump pulse is 480 nm

DAC	Solvent	τ_{eff}^{exp}, ps [26]	τ_{eff}^{num}, ps [31]
HMB-TCNE	ACN	0.45	0.54
	VaCN	1.35	1.55
	OcCN	2.62	4.05
PMB-TCNE	ACN	0.55	0.74
	VaCN	1.95	2.25
	OcCN	3.8	5.04
IDU-TCNE	ACN	0.80	0.95
	VaCN	2.45	2.63
	OcCN	5.52	5.27

It was shown that there is also a really good accordance with the experimental data for PMB-TCNE and HMB-TCNE in ACN and VaCN (see Table 19.1). However, the CR time constant in OcCN is overestimated by a factor of 1.2–1.4. The discrepancy between experimental and theoretical results can be caused by the supposition that the energetic parameters of the electron transfer obtained from the fit to the stationary CT absorption band in ACN are the same in all three solvents. This assumption may be incorrect for OcCN, because it is noticeably less polar than ACN and VaCN. So the magnitude of $-\Delta G_{CR}$ for CR in OcCN is larger than in the other solvents. As a result, CR kinetics might be intrinsically slower. This difference has not been taken into account in the model, although it may play an important role in the solvent effect.

Thus, a comparison of the theoretical dependences with experimental kinetic data allows concluding: (i) the model provides a satisfactory description of the dependence of kinetics on the solvent characteristics for all complexes; (ii) the negative spectral effect (decrease of the effective CR rate constant with rise of ω_e) is satisfactorily reproduced for the IDU-TCNE complex; (iii) the positive spectral effect (increase of the effective CR rate constant with rise of ω_e) observed with the HMB-TCNE complex cannot be described within the framework of two-level models and the spectral dynamics of the excited state absorption, the stimulated emission, and the bleach should be taken into account. The charge redistribution in the excited complexes can also play an important role.

19.2.2 Free Energy Gap Dependences

One of unanswered questions of CR reaction concerns the free energy dependence of the CR rate constant, $k_{CR} = \tau_{eff}^{-1}$, in the DACs. The experimental investigations of CR in DACs after their photoexcitation by a short laser pulse at the carrier frequency of the CT band demonstrated unexpected dependence of k_{CR} on the reaction free energy in the weakly exergonic region [2, 21, 26]. The logarithm of the CR rate constant decreases monotonically, nearly linearly, with increasing the reaction exothermicity, $-\Delta G_{CR}$, whereas the standard equilibrium nonadiabatic

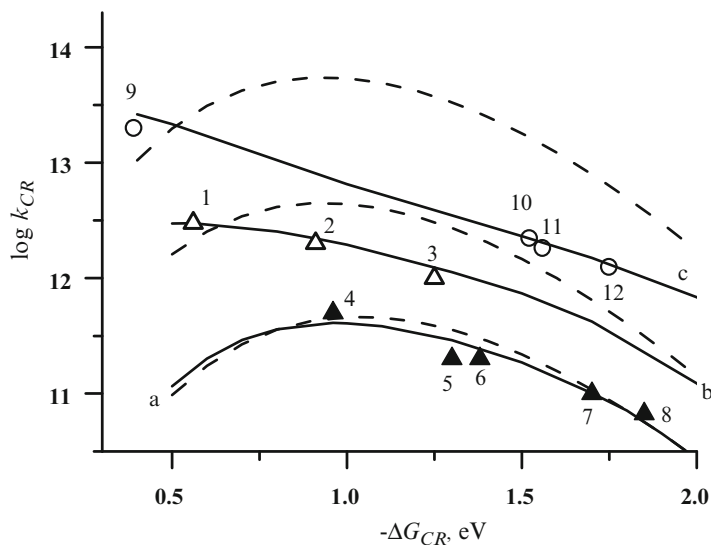


Fig. 19.3 The free energy dependence of the CR rate constant, k_{CR} in s^{-1} , in the excited DACs: 1 Per-TCNE, 2 Py-TCNE, 3 Nah-TCNE, 4 Py-TCNQ, 5 Nph-TCNQ, 6 Per-PMDA, 7 Py-PMDA, 8 Chr-PMDA, 9 TMB-TCNE, 10 HMB-TCNE, 11 PMB-TCNE, 12 IDU-TCNE. The experimental data and notations were taken from [2, 21, 26]. Solid curves (lines a, b, c) are result of numerical simulation. For comparison the thermal rate constant, k_{th} , is shown as dashed curve. The vibrational spectrum involving 5 high-frequency modes is employed [50]. Parameters used: $V_{el} = 0.0065$ eV, $E_{rm} = 0.6$ eV (lines a); $V_{el} = 0.02$ eV, $E_{rm} = 0.5$ eV (lines b); $V_{el} = 0.07$ eV, $E_{rm} = 0.51$ eV (lines c).

Marcus theory predicts a bell-shaped dependence. In the past few decades numerous attempts have been made to explain this dependence [6, 18, 41, 42]. In this subsection we propose and discuss another possible mechanism. This is the mechanism of hot electron transitions which could lead to straightening of the Marcus parabolic dependence in the weakly exergonic region. We also fit the available experimental data [2, 21, 26] on the free energy gap law in framework of the generalized multi-channel stochastic model.

The results of numerical simulation of the CR kinetics for a number of DACs are presented in Fig. 19.3. In weak exergonic range considerable difference between effective, k_{CR} , and thermal, k_{th} [3, 47], CR rates is demonstrated. The experimental data borrowed from [2, 21, 26] are pictured by different symbols. The behaviour of CR rate constant, k_{CR} , strongly depends on values of electronic coupling, V_{el} . For smaller values of electronic coupling the Marcus dependence of the effective rate constant on the reaction exothermicity has typical for thermal reactions a bell-shaped form with a small deviation from the thermal rate in the vicinity of the maximum (solid and dashed lines a, b in Fig. 19.3). However the curves with large V_{el} are characterized by large deviation especially in the weakly exothermic (solid and dashed lines c). For good approximation, the DACs should be separated

into a few groups with different values of electronic coupling. The nonequilibrium nature of the CR leads to the deviation of the effective CR rate constant from its thermal value. In strongly exothermic region the effective CR rate is close to the thermal one. In the region of moderate exothermicity k_{CR} is less than k_{th} and in the weakly exothermic region the inverse relation, $k_{CR} < k_{th}$, is fulfilled. The effective and thermal rate constants at $-\Delta G_{CR} = 0.56$ eV for the complex Per-TCNE in ACN solution have practically the same value (symbol 1, Fig. 19.3), the CR mainly proceeds in nonthermal regime. The exponential decay of the excited complexes is not direct evidence of the equilibrium regime of CR. For example, the CR in the excited Per-TCNE in ACN is known to proceed in exponential regime but CR reaction occurs mainly in nonthermal regime. In this area the thermal rate decreases because of the Marcus activation barrier and the effective rate constant can even rise since the wave packet is initially placed in the area of more powerful sinks so that the inequality $k_{CR} < k_{th}$ is held.

Although in framework of the model elaborated we were unable to reproduce the linear dependence of the logarithm of CR rate constant throughout the experimentally accessible region of the reaction free energies (-3 eV $< \Delta G_{CR} < -0.5$ eV) for the complexes studied in the work [2], nevertheless, it can be done for the other DACs [21, 26] (line c). This argues in favor of the proposed mechanism.

19.2.3 CR in Excited DACs with Two CT Absorption Bands

Within the framework of multi-channel stochastic model CR kinetics in the excited DAC, consisting of TMB as the electron donor and TCNE as electron acceptor in ACN, were investigated. The complex TMB-TCNE belongs to a very large group of DACs, showing two charge transfer absorption bands (CT1 and CT2) [26]. In order to separate the bands and to determine the contribution of each spectrum, the absorption spectrum was approximated by the sum of two asymmetric Gaussian functions. Then each of the absorption bands was approximated by the following expression

$$A = C \sum_{n_\alpha} \left[\prod_{\alpha} \frac{S_{\alpha}^{n_\alpha} e^{-S_{\alpha}}}{n_{\alpha}!} \right] \times \exp \left\{ -\frac{[\Delta G_{CR} - E_{rm} - \sum_{\alpha} n_{\alpha} \hbar \Omega_{\alpha} - \hbar \omega_e]^2}{4E_{rm}k_B T} \right\}$$

As in the previous section all electron-transfer energetic parameters have been determined from the stationary CT absorption band, the electronic coupling has been obtained from the fit to the CR dynamics in single solvent. Scheme of electronic terms involves three electronic states (ground, first and second excited) and transitions corresponding to CT1 and CT2 and radiationless transitions between the second and first excited states are treated. The excitation pulse with wavelength of 620 nm leads to population of the lowest excited electronic state [26]. A more complicated situation is realized when the excitation pulse wavelength is equal to 480 nm [26]. Such a pulse leads to the population of both excited states

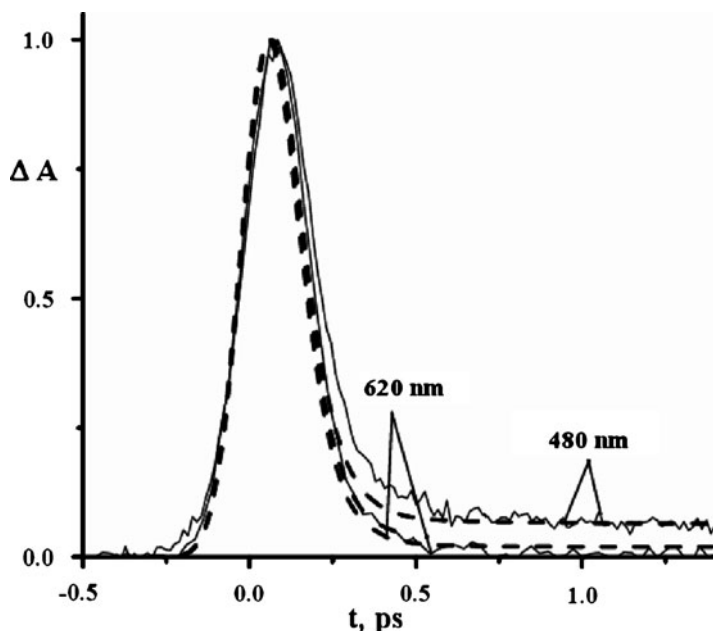


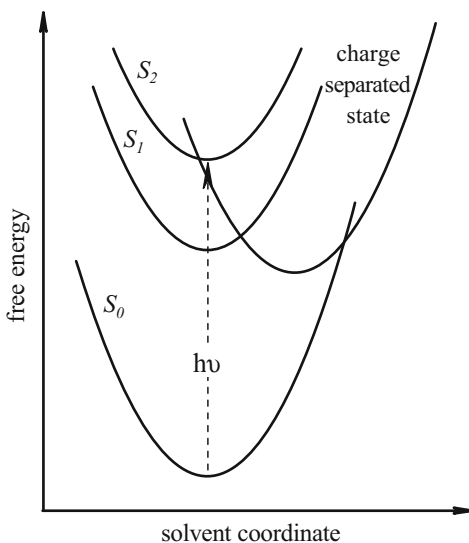
Fig. 19.4 Time dependence of the population of the excited state of TMB-TCNE in ACN. Experimental data are *thin solid lines*, results of numerical simulation are *dashed lines*. The numbers represent the wavelengths of the pump pulse

due to the overlapping of the CT1 and CT2 bands in this spectral region. The results of numerical calculations [33] agree well with experimental data [26]. Time dependence of the population of the first excited state of DAC induced by excitation pulses of different wavelengths is shown in Fig. 19.4. The model quantitatively reproduces the experimental data over the time interval presented in the figure. Note that, at times longer than 0.5 ps, a plateau appears which, in terms of the suggested approach, is treated as the thermal stage. The height of the plateau is determined by the relative number of complexes that avoided hot recombination. The thermal stage of the decay of the excited state has a much lower effective rate. Thus the CR in TMB-TCNE complex clearly demonstrates the biphasic behaviour.

19.2.4 Photochemical Processes from Higher Excited States

Charge separation from the second excited state due to relatively small energy gap between the second, S_2 , and the first, S_1 , singlet excited states is characterized by a series of peculiarities. First, the energy gap between S_2 and S_1 states is considerably smaller than that between S_1 and the ground S_0 states. As a result, the CR into the first excited state proceeds either in the Marcus normal region or in the endothermic

Fig. 19.5 Scheme of charge separation from the second excited state and ensuring CR into the first excited state



regime. This means that the kinetics and mechanism of photochemical processes started from the second excited state may differ dramatically from that started from the first excited state. The higher excited states are very difficult to detect in the condensed phase because most of them are very short-lived. As a result the internal conversion is the main channel of their primary transformation. Nevertheless, there are a few examples in which the kinetics of charge separation from S_2 state and ensuing CR have been investigated with high time resolution [24, 48, 49]. We have quantitatively reproduced the results of experimental studies of the kinetics of charge separation from the second excited state S_2 and the subsequent recombination of the first excited state S_1 for a series of zinc-porphyrins covalently bound to the electron-acceptor groups (series imides) in tetrahydrofuran solution [24, 32, 48, 50, 51]. For this system the charge separation, and the subsequent recombination and vibrational relaxation occur simultaneously (see Fig. 19.5). We have examined the mechanism of CS from the second excited state. A distinguishing feature of this process is effective hot recombination to the 1st excited state. This implies that charge separation and charge recombination are not separable and the time scale of the first excited state population rise is predetermined by the time scale of the second excited population decay. This regularity was deduced from the experimental data in refs [24, 32, 48, 49] and is quantitatively reproduced in the framework of the model considered here. The kinetics of S_1 state occupation depend not only on the decay rate of S_2 state but on the medium and intramolecular vibration relaxation timescales too. Moreover, there is a dependence on the distribution of the sink effectivenesses at the free energy surface of S_2 state.

In the framework of stochastic multi-channel models we were able to quantitatively reproduce the dynamics of populations of the two excited states S_1 and S_2 (see Fig. 19.6) [32]. Good agreement obtained in the fitting is a strong argument in favour of the adequacy of the nonequilibrium mechanism of CR in first excited state.

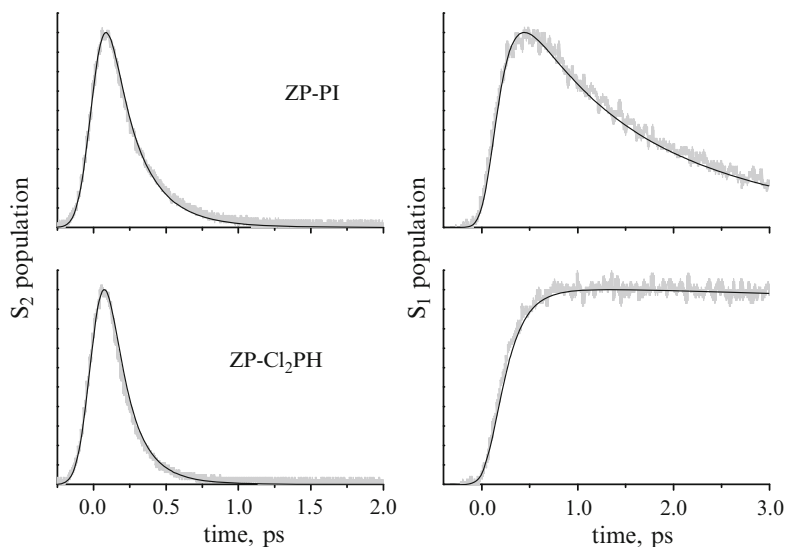


Fig. 19.6 Population kinetics of S_2 (left panel) and S_1 (right panel) states. The data are plotted with *light gray lines* (experimental results [24]) and *black lines* (simulation results [32]). The abbreviations for the supramolecular systems are borrowed from ref [24]. The values of model parameters are listed in ref [32]

19.3 Conclusions

We have considered some successful applications of the multi-channel stochastic model and discussed in detail some of the brightest manifestations of medium nonequilibrium. The results of these investigations prove a decisive role of medium nonequilibrium in ultrafast CT reactions. When hot CR is operative it can suppress the efficiency of photoinduced forward ET to great extent. For majority of photoinduced CT reaction applications the hot CR is waste process. On this point inhibition of hot CR becomes a vital problem. The investigations point out possible ways of its solution. The most obvious way is to reduce the magnitude of CR electronic coupling. However such a handling is difficult to implement because of symbate variation of electronic couplings of forward and backward reactions. In our opinion, more efficient hot CR control is based on the variation of solvent viscosity. The fact is that the rates of thermal forward ET and hot backward ET alter with solvent viscosity in opposite directions [14]. This opens up new opportunities of photoinduced CT control.

Acknowledgments This work was supported by the Ministry of Education and Science of the Russian Federation (contracts No. P1145 and No. 14.740.11.0374).

References

1. Najbar J, Dorfman RC, Fayer MD (1991) Solvent relaxation effects on the kinetics of photoinduced electron transfer reactions. *J Chem Phys* 94:1081–1092
2. Asahi T, Mataga N (1991) Femtosecond-picosecond laser photolysis studies on the dynamics of excited charge-transfer complexes: aromatic hydrocarbon-acid anhydride, -tetracyanoethylene, and -tetracyanoquinodimethane systems in acetonitrile solutions. *J Phys Chem* 95:1956–1963
3. Walker GC, Akesson E, Johnson AE, Levinger NE, Barbara PF (1992) Interplay of solvent motion and vibrational excitation in electron-transfer kinetics: experiment and theory. *J Phys Chem* 96:3728–3736
4. Tominaga K, Kliner DAV, Johnson AE, Levinger NE, Barbara PF (1993) Femtosecond experiments and absolute rate calculations on intervalence electron transfer of mixed-valence compounds. *J Chem Phys* 98:1228–1235
5. Jean JM (1994) Time- and frequency-resolved spontaneous emission as a probe of coherence effects in ultrafast electron transfer reactions. *J Chem Phys* 101:10464–10473
6. Tachiya M, Murata S (1994) Non-Marcus energy gap dependence of back electron transfer in contact ion pairs. *J Am Chem Soc* 116:2434–2436
7. Cho M, Silbey RJ (1995) Nonequilibrium photoinduced electron transfer. *J Chem Phys* 103:595–606
8. Yoshihara K, Tominaga K, Nagasawa Yu (1995) Effects of the solvent dynamics and vibrational motions in electron transfer. *Bull Chem Soc Jpn* 68:696–712
9. Reid PJ, Silva D, Barbara PF, Karki L, Hupp JT (1995) Electronic coherence, vibrational coherence, and solvent degrees of freedom in the femtosecond spectroscopy of mixed-valence metal dimers in H₂O and D₂O. *J Phys Chem* 99:2609–2616
10. Barbara PF, Meyer TJ, Ratner MA (1996) Contemporary issues in electron transfer research. *J Phys Chem* 100:13148–13168
11. Domcke W, Stock G (1997) Theory of ultrafast nonadiabatic excited-state processes and their spectroscopic detection in real time. *Adv Chem Phys* 100:1–168
12. Ando K, Sumi H (1998) Nonequilibrium oscillatory electron transfer in bacterial photosynthesis. *J Chem Phys* 102:10991–11000
13. Yoshihara K (1999) Ultrafast intermolecular electron transfer in solution. *Adv Chem Phys* 107:371–401
14. Ivanov AI, Potovoi VV (1999) Theory of non-thermal electron transfer. *Chem Phys* 247:245–259
15. Bagchi B, Gayathri N (1999) Interplay between ultrafast polar solvation and vibrational dynamics in electron transfer reactions: role of high-frequency vibrational modes. *Adv Chem Phys* 107:1–80
16. Cao J (2000) Effects of bath relaxation on dissipative two-state dynamics. *Chem Phys* 112:6719–6724
17. Mataga N, Shibata Y, Chosrowjan H, Yoshida N, Osuka A (2000) Internal conversion and vibronic relaxation from higher excited electronic state of porphyrins: femtosecond fluorescence dynamics studies. *J Phys Chem B* 104:4001–4004
18. Frantsuzov PA, Tachiya M (2000) Charge recombination in contact ion pairs. *J Chem Phys* 112:4216–4220
19. Denny RA, Bagchi B, Barbara PF (2001) Effects of vibrational energy relaxation and reverse reaction on electron transfer kinetics and fluorescence line shapes in solution. *J Chem Phys* 115:6058–6071
20. Morandeira A, Furstenberg A, Nicolet O, Pagès S, Lang B, Vauthey E (2002) Ultrafast photochemistry. *Chimia* 12:690–694
21. Nicolet O, Vauthey E (2002) Ultrafast nonequilibrium charge recombination dynamics of excited donor-acceptor complexes. *J Phys Chem A* 106:5553–5562
22. Koch CP, Klüner T, Kosloff R (2002) A complete quantum description of an ultrafast pump-probe charge transfer event in condensed phase. *J Chem Phys* 116:7983–7986

23. Kovalenko SA, Lustres JLP, Ernsting NP, Rettig W (2003) Photoinduced electron transfer in bianthryl and cyanobianthryl in solution: the case for a high-frequency intramolecular reaction coordinate. *J Phys Chem A* 107:10228–10232
24. Mataga N, Taniguchi S, Chosrowjan H, Osuka A, Yoshida N (2003) Ultrafast charge transfer and radiationless relaxation from higher excited state (S_2) of directly linked Zn-porphyrin (ZP)-acceptor dyads: investigations into fundamental problems of exciplex chemistry. *Chem Phys* 295:215–228
25. Fedunov RG, Feskov SV, Ivanov AI, Nicolet O, Pagès S, Vauthey E (2004) Effect of the excitation pulse carrier frequency on the ultrafast charge recombination dynamics of donor-acceptor complexes: stochastic simulations and experiments. *J Chem Phys* 121:3643–3656
26. Nicolet O, Banerji N, Pages S, Vauthey E (2005) Effect of the excitation wavelength on the ultrafast charge recombination dynamics of donor-acceptor complexes in polar solvents. *J Phys Chem A* 109:8236–8245
27. Fedunov RG, Ivanov AI (2005) Effect of the excitation pulse frequency on the ultrafast photoinduced electron transfer dynamics. *Chem Phys* 122:064501–0654508
28. Kuzmin MG, Soboleva IV, Dolotova EV (2008) Evolution of the reaction mechanism during ultrafast photoinduced electron transfer. *J Phys Chem A* 112:5131–5137
29. Bagchi B, Oxtoby DW, Fleming GR (1984) Theory of the time development of the Stokes shift in polar media. *Chem Phys* 86:257–267
30. Feskov SV, Ionkin VN, Ivanov AI (2006) Effect of high-frequency modes and hot transitions on free energy gap dependence of charge recombination rate. *J Phys Chem A* 110:11919–11925
31. Feskov SV, Ionkin VN, Ivanov AI, Hagemann H, Vauthey E (2008) Solvent and spectral effects in the ultrafast charge recombination dynamics of excited donor-acceptor complexes. *J Phys Chem A* 112:594–601
32. Ionkin VN, Ivanov AI (2009) Numerical simulations of ultrafast charge separation dynamics from second excited state of directly linked Zn-porphyrin-imide dyads and ensuing hot charge recombination into first excited state. *J Phys Chem A* 113:103–107
33. Ionkin VN, Ivanov AI (2009) Independence of the rate of the hot charge recombination in excited donor-acceptor complexes from the spectral density of high-frequency vibrations. *Chem Phys* 360:137–140
34. Mikhailova VA, Ivanov AI (2007) Effect of relaxation of intramolecular high frequency vibrational mode on nonthermal electron transfer probability. Stochastic point-transition approach. *J Phys Chem C* 111:4445–4451
35. Khohlova SS, Mikhailova VA, Ivanov AI (2006) Three-centered model of ultrafast photoinduced charge transfer: continuum dielectric approach. *J Chem Phys* 124:114507–114518
36. Zusman LD (1980) Outer-sphere electron transfer in polar solvents. *Chem Phys* 49:295–304
37. Garg S, Smyth C (1965) Microwave absorption and molecular structure in liquids. The three dielectric dispersion regions of the normal primary alcohols. *J Phys Chem* 69:1294–1301
38. Risken H (1989) The Fokker-Planck equation. Springer, Berlin
39. Yakobson BI, Burshtein AI (1980) Relaxation hindrance in nonadiabatic cage reactions. *Chem Phys* 49:385–395
40. Gladkikh V, Burshtein AI, Feskov SV, Ivanov AI, Vauthey E (2005) Hot recombination of photogenerated ion pairs. *J Chem Phys* 123:244510-1–244510-11
41. Gould IR, Noukakis D, Gomez-Jahn L, Goodman JL, Farid S (1993) Explanation of the driving-force dependence of return electron transfer in contact radical-ion pairs. *J Am Chem Soc* 115:4405–4406
42. Mikhailova VA, Ivanov AI, Vauthey E (2004) Nonequilibrium charge recombination from the excited adiabatic state of donor-acceptor complexes. *J Chem Phys* 121:6463–6469
43. Wynne K, Galli C, Hochstrasser RM (1994) Ultrafast charge transfer in an electron donor-acceptor complex. *J Chem Phys* 100:4797–4810
44. Gould IR, Noukakis D, Gomez-Jahn L, Young RH, Goodman JL, Farid S (1993) A quantitative relationship between radiative and nonradiative electron transfer in radical-ion pairs. *J Am Chem Soc* 115:3830–3831

45. Gould IR, Noukakis D, Gomez-Jahn L, Goodman JL, Young RH, Farid S (1993) Radiative and nonradiative electron transfer in contact radical-ion pairs. *Chem Phys* 176:439–456
46. Wynne K, Reid GD, Hochstrasser RM (1996) Vibrational coherence in electron transfer: the tetracyanoethylene–pyrene complex. *J Chem Phys* 105:2287–2297
47. Jortner J, Bixon M (1988) Intramolecular vibrational excitations accompanying solvent-controlled electron transfer reactions. *J Chem Phys* 88:167–170
48. Mataga N, Chosrowjan H, Taniguchi S, Shibata Y, Yoshida N, Osuka A, Kikuzawa T, Okada T (2002) Ultrafast charge separation from the S₂ excited state of directly linked porphyrin-imide dyads: first unequivocal observation of the whole bell-shaped energy-gap law and its solvent dependencies. *J Phys Chem A* 106:12191–12201
49. Morandeira A, Engeli L, Vauthey E (2002) Ultrafast charge recombination of photogenerated ion pairs to an electronic excited state. *J Phys Chem A* 106:4833–4837
50. Myers Kelly A (1999) Resonance Raman intensity analysis of vibrational and solvent reorganization in photoinduced charge transfer. *J Phys Chem A* 103:6891–6903
51. Mataga N, Chosrowjan H, Shibata Y, Yoshida N, Osuka A, Kikuzawa T, Okada T (2001) First unequivocal observation of the whole bell-shaped energy gap law in intramolecular charge separation from S₂ excited state of directly linked porphyrin-imide dyads and its solvent-polarity dependencies. *J Am Chem Soc* 123:12422–12423

Chapter 20

Adsorption Studies of Lead, Copper and Cadmium Ions in Aqueous Solution by Ethylene Diamine Modified Amberlite XAD-1180

Isaac W. Mwangi, Jane C. Ngila, Joseph Kamau, and Jonathan Okonkwo

Abstract This study reports on the synthesis of an adsorbent for the preconcentration of heavy metals at trace levels in environmental samples. Amberlite XAD resins are excellent support materials because of their high surface area and good mechanical stability. Ethylenediamine was chemically anchored on the resin to create active sites for metal adsorption. It was then employed for adsorption of lead, copper and cadmium ions in aqueous solution. Contact time flow rate and pH were optimized after which Langmuir and Freundlich isotherms, were applied on the experimental data to establish the mechanism of adsorption. The sorption capacity for the three metals under study (Cu^{2+} , Cd^{2+} and Pb^{2+}) were 61.49, 16.17 and 14.01 mg g^{-1} , respectively. It was observed that the resin adsorbed 95% of the metals in less than 10 min indicating that the affinity of the adsorbent to the analyte metals was high and adsorption took place instantly. The developed method was applied to an environmental water sample whose concentration was determined and thereafter spiked with Cd^{2+} , Cu^{2+} and Pb^{2+} at varying concentrations. The maximum percent recoveries were determined as 28, 98 and 90% for Cd^{2+} , Cu^{2+} and Pb^{2+} , respectively. This indicated that the adsorbent has a potential application as a tool for trace metal analysis in environmental samples.

I.W. Mwangi • J.C. Ngila (✉) • J. Kamau
University of Johannesburg, Department of Chemical Technology, Doornfontein Campus
P.O Box 17011, Doornfontein 2028, Johannesburg, South Africa

I.W. Mwangi
School of Chemistry, University of KwaZulu-Natal, University Road, Westville, P/Bag X45001,
Durban 4000, South Africa
e-mail: isaacwaweru2000@yahoo.co.uk

J. Okonkwo
Department of Environmental, Water and Earth Science, Faculty of Science, Tshwane University
of Technology, P/Bag X680, Pretoria 0001, South Africa
e-mail: OkonkwoOJ@tut.ac.za

20.1 Introduction

Industrial discharges into the water systems cause a serious concern to human populations as well as the flora and fauna. This leads to loss of biodiversity [1]. Furthermore, most heavy metals in the environment are in trace levels and are masked by matrices and therefore their direct determination may require sample pretreatment to eliminate matrices as well as effect preconcentration of the analyte. Methods applied for separation and preconcentration techniques include adsorption, membrane filtration, cloud point extraction, solvent extraction and co-precipitation [2]. Among these techniques, solid phase extraction (SPE) is an attractive technique based on the use of a sorbent that retains the analyte. SPE is a simple technique with numerous advantages. Several analytes can be enriched and separated simultaneously. The SPE material should have a high surface area, high purity and good sorption properties including porosity, durability, and uniform pore distribution [3–6]. The SPE sorption properties can be modified to enhance or enable the adsorption of the analyte of interest.

This paper reports on an analytical technique applied for the analysis of trace metals in environmental samples. The technique is both a cleanup and preconcentration tool. Functionalised amberlite XAD-1180 was used as a solid phase material. Amberlite XAD-1180 is one of the commonly used materials that contain a phenyl ring in its structure. This aromatic ring can be exploited by substituting hydrogen with various functional groups and attaching chelating agents to it. The hydrophilic end co-ordinates with metals in solution whereas the organic end remains insoluble. This mechanism is similar to that of detergent's action on dirt.

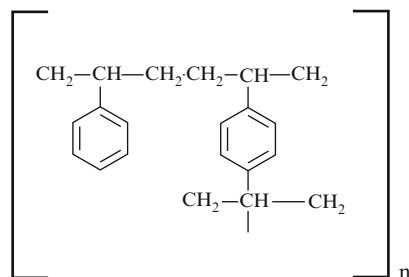
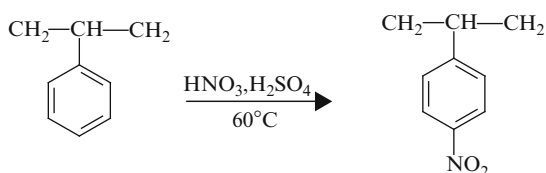
20.2 Material and Methods

20.2.1 Reagents

The solutions were prepared in double distilled water and all the reagents were of analytical grade. Nitric acid was of trace select ICP grade >69%, supplied by Fluka; XAD-1180 was sourced from Supelco Belfonte USA, its specifications were: surface area $500 \text{ m}^2 \text{ g}^{-1}$ and an average pore diameter of 300 \AA . Ethylenediamine was obtained from Riedel de Haen (Germany) while stannous chloride and sodium nitrite were supplied by Rochelle Chemicals Ltd (South Africa).

20.2.2 Instrumentation

The metal ions content in solution was determined by inductively coupled plasma optical emission spectrometry (ICP-OES; model OPTIMA 5300DV). Characterization of the attached functional groups was determined using Fourier transform

Scheme 20.1 Structure of amberlite XAD-1180**Scheme 20.2** Nitration of Amberlite XAD1180

infra red spectroscopy (Perkin Elmer 100). The thermal stability of the amberlite XAD-1180 adsorbent was determined using thermogravimetric analysis instrument (TGA) [7]. TGA gives information on the thermal stability of a material sample, thus determines degradation temperatures, absorbed moisture content of materials, the level of inorganic and organic components in materials, and decomposition points.

20.2.3 Procedures

20.2.3.1 Synthesis of Modified XAD-1180 EDA Chelating Resin

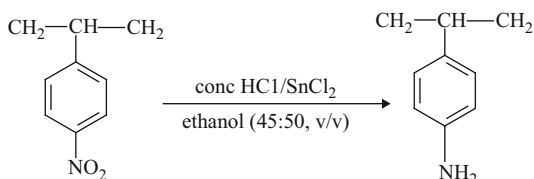
Amberlite XAD-1180 is a polymeric adsorbent resin with several uses [7, 8]. Scheme 20.1 shows the structure of amberlite XAD-1180.

Structurally XAD-1180 contains no functional groups (sites) for metal ion adsorption as observed in Scheme 20.1. The resin therefore requires a modification of its structure to create active sites for metal adsorption.

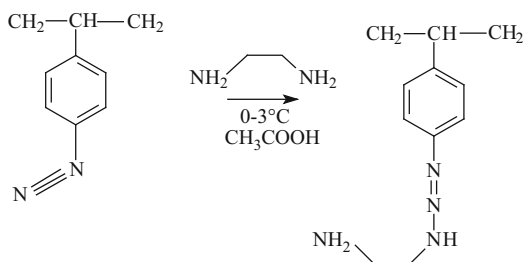
The modification process involved the attachment of EDA on XAD-1180. EDA is a bidentate ligand with a high metal affinity. The modification of XAD-1180 was achieved by transferring 5 g of Amberlite XAD-1180 resin into a 250 ml round bottomed flask containing 40 ml of concentrated nitric acid and 60 ml of concentrated sulfuric acid. The mixture was maintained at a temperature below 60°C for 1 h. Scheme 20.2 shows the nitration reaction [9].

The reaction mixture containing the nitrated resin was transferred into a beaker filled with ice water. The resin was then filtered with Whatman filter paper (\varnothing 42 cm) and washed with double distilled water until the solution attained a

Scheme 20.3 Reduction of the nitrated Amberlite XAD-1180



Scheme 20.4 Azotization and modification of XAD-1180 with ethylenediamine



pH 4–5. The nitrated resin (XAD-1180 -NO₂) was then reduced by refluxing at 90°C for 24 h in a mixture of conc HCl and ethanol (45:50, v/v) and 50 g of SnCl₂ as per Scheme 20.3 [10].

After cooling to ambient temperature, the product obtained from the reduction reaction was filtered and washed with a mixture of concentrated HCl and ethanol (45:50, v/v) followed by 2 M NaOH and then distilled water. The resultant amino product was diazotized by cooling it in an ice bath (0–3°C), thereafter 75 ml of 1 M NaNO₂ was added followed by 100 ml of 1 M HCl. The mixture was stirred and tested with iodide paper until the paper changed colour from white to violet [10] due to formation of diazotized resin. The latter was then washed with ice-cold water and coupled with ethylenediamine at a temperature below 3°C for 24 h in an acetic acid medium. The resulting brownish resin was filtered, washed with distilled water and air-dried. The modification reaction of aminated amberlite XAD-1180 is shown in Scheme 20.4 [11].

20.2.3.2 Optimization of pH on Modified Amberlite XAD-1180 Resin

Sorption of the metal under study was carried out in batch equilibrium experiments. Batches of 10 ml model solutions (40 ppm) prepared in buffered solutions of different pH (2–7) were dispensed into 100 ml polyethylene bottles containing approximately 0.04 g of the modified Amberlite XAD-1180. The mixtures were equilibrated for 2 h after which the metal in solution was analysed by ICP-OES.

20.2.3.3 Optimization of Adsorption Time

Batches of 10 ml model solutions (40 ppm) were dispensed into 100 ml polyethylene bottles containing approximately 0.04 g of the modified Amberlite XAD-1180. The initial pH of the model solutions was adjusted to the appropriate pH value for each metal under study. The mixture was allowed to equilibrate and removed from the shaker at different time intervals. The resin was filtered off by suction and the concentration of metal ions in the filtrate determined by ICP-OES.

20.2.3.4 Determination of Adsorption Capacity of EDA Modified Amberlite XAD 1180

The adsorption capacity was determined by varying initial metal ion concentration contained in batches of 10 ml model solutions containing approximately 0.04 g of the modified Amberlite XAD-1180. The pH was adjusted to the desired value for each metal solution. The mixtures were agitated for 1 h on a mechanical shaker and the resin was thereafter filtered and analyzed by ICP-OES.

20.2.3.5 Preparation of Solid-Phase Extraction (SPE) Columns

The modified XAD-1180 (0.25 g) was packed in 6 ml polyethylene tubes; a frit was inserted before and after packing the adsorbent. The packed columns were washed successively with water, preconditioned and buffered to the desired pH before use. After conditioning the columns were used to optimize pH, sample loading flow rate and determining the ideal eluent.

20.2.3.6 Effect of Flow Rate on Adsorption

The flow rate was optimised by loading the column with 100 ml of model solution (0.25 ppm). Elution was carried out at various flow rates. The retained metal ions were subsequently eluted and their concentrations analysed.

20.2.3.7 Effect of Sorbent Dose on Adsorption

Several SPE columns were packed with varying weights of the resin. The columns were washed with 10 ml HNO₃ (0.1 M) rinsed with 20 ml double distilled water then buffered to the desired pH before loading at a flow rate of 3 ml min⁻¹. The retained metal ions were stripped using 10 ml of 1 M HNO₃ and analyzed by ICP-OES.

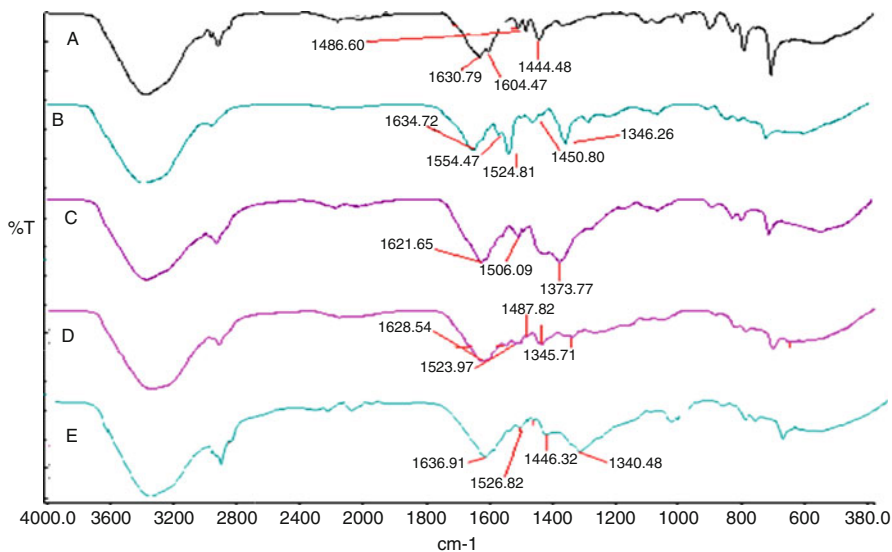


Fig. 20.1 Spectrum of the parent amberlite XAD-1180 and its functionalised forms overlaid. (A) Un-modified amberlite XAD-1180; (B) Nitrated amberlite XAD-1180; (C) Aminated amberlite XAD-1180; (D) Azotized amberlite XAD-1180; (E) Modified amberlite XAD-1180

20.2.3.8 Effect of the Eluent Type on Recovery of Metal Ions

The model solution (0.2 ppm) was loaded on the packed column at a fixed flow rate of 3 ml/min. The adsorbed metals were then stripped by eluting with 10 ml solutions of 0.5 M HNO_3 , 1 M HNO_3 , and 3 M HNO_3 . The % recoveries for each metal were then determined.

20.3 Results and Discussion

20.3.1 Characterization of the Chelating Resin

The parent XAD-1180 resin and its functionalized forms were characterized using FTIR. All the spectra were overlaid to give a contrast of the various peaks with respect to their functional groups as shown in Fig. 20.1.

As expected, the XAD-1180 material showed no peaks around the 1500 cm^{-1} region. But when a nitro group was introduced in the ring, a peak was observed at 1524.81 cm^{-1} which is characteristic of a nitrogen substituted ring. A second peak was observed at 1346.26 cm^{-1} which was absent in the original compound as shown in spectrum A.

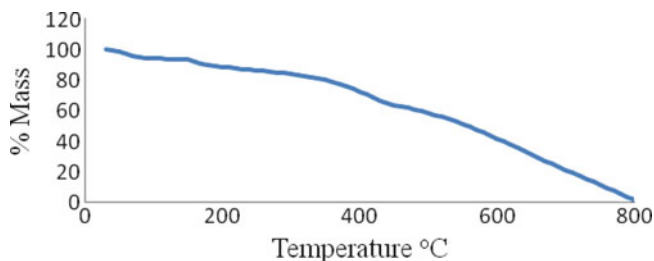


Fig. 20.2 Thermogram of the modified amberlite XAD-1180

After the reduction of the nitro compound, the peak at 1524.81 cm^{-1} (spectrum B) disappeared due to the formation of an amine group. It was observed that the peak at 1346.26 cm^{-1} shifted to 1373.77 cm^{-1} (spectrum C) suggesting a modification of the attached functional group. Both the nitro and amine groups have a nitrogen atom attached to a carbon (C–N). However the nitro group is heavier than the amino group and as such requires more energy to resonate. This explains the shift from 1346.26 to 1373.77 cm^{-1} . On the latter peak, there is a shoulder, which is characteristic of $-\text{NH}_4^+$ functional groups [12].

When the compound was azotized, the peak at 1373.77 cm^{-1} shifted to 1340.48 cm^{-1} suggesting the presence of C–N stretching vibration but a slight shift due to the effect of the azo functional group which is relatively a bigger group that requires more energy to vibrate as can be seen in spectrum D [12].

When the azo compound was treated with EDA, the peak at 1373.77 cm^{-1} found in the aminated compound disappeared as the functional group was bulky. However, the peaks in the 1500 cm^{-1} region still remained but with a lower intensity indicating the presence of nitrogen substitution on the ring as shown in spectrum E [12].

20.3.2 Thermal Stabilities and Moisture Content

The results of TGA data of the modified amberlite XAD-1180 are presented in Fig. 20.2. The thermogram shows the percentage mass as a function of sample temperature under a nitrogen purge. Approximately 10 mg of sample was heated at a rate of $20^\circ\text{C}/\text{min}$ with the Perkin Elmer TGA.

It was observed that the adsorbent undergoes a very slow but steady weight loss and was completely denatured at a temperature of 800°C . A similar analysis was carried out by Metilda et al. (2004) as they characterised Amberlite XAD-4 resin functionalized with succinic acid [13]. They observed that thermal analysis of the XAD-4 resin showed a complete weight loss by 510°C . They attributed region between 100°C and 120°C to the water molecules whereas the other weight loss ($\sim 400\text{--}500^\circ\text{C}$) was attributed to the dissociation of chemically immobilized succinic acid resin. In this study, the overall thermal stability of the investigated

amberlite modified with ethylenediamine may be said to be more stable than the immobilized succinic acid resin reported by Metilda et al. in 2004 [13].

20.3.3 Effect of pH on the Adsorption of Metal Ions

Adsorption of metal ions by sorbents is pH dependent as it influences the charge of the binding sites of the sorbent and the chemistry of the metal ion [14]. In this study, the optimum pH for metal ions uptake was determined by loading model solutions buffered at various pH values into a SPE column. The column retained metal ions were stripped using 1 M nitric acid solution and the metal ion concentration determined by ICP-OES.

Figures 20.3–20.5 show the effect of pH on preconcentration of metals on functionalised Amberlite. It was observed that the maximum sorption of Cd, Pb and Cu was at pH 4.80, 5.40 and 4.50, respectively. From the observed optimum pH values, other subsequent experiments were carried out for each metal respectively.

Other researchers have reported similar findings as they investigated on the feasibility of using phosphatic clay, a waste by-product of the phosphate mining industry, as an effective sorbent for lead ions from aqueous effluents [15]. A possible reason for the poor adsorption at low pH is the fact that protons competed with metal cations for adsorption sites and the sorbent was not a good remover of metal ions as shown in Eq. 20.1.

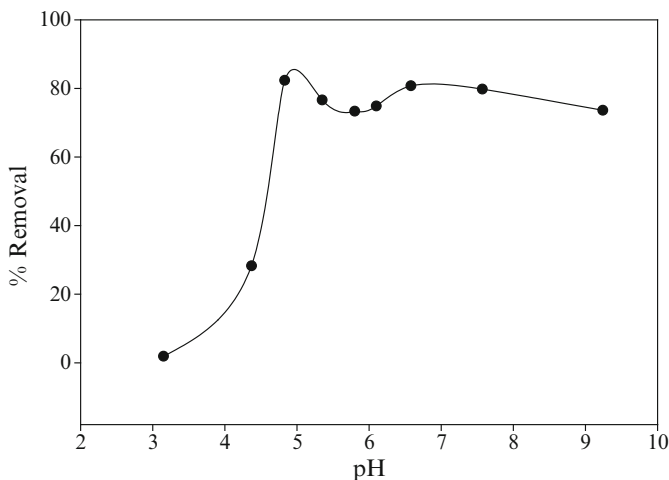
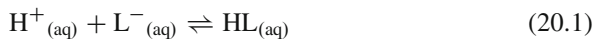


Fig. 20.3 Effect of pH on adsorption of cadmium

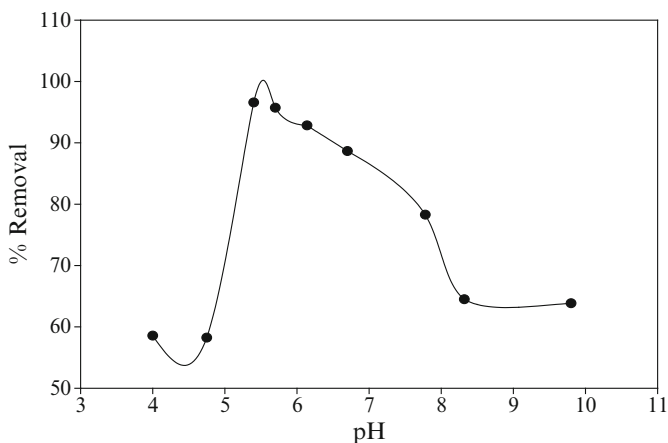


Fig. 20.4 Effect of pH on adsorption of lead ions

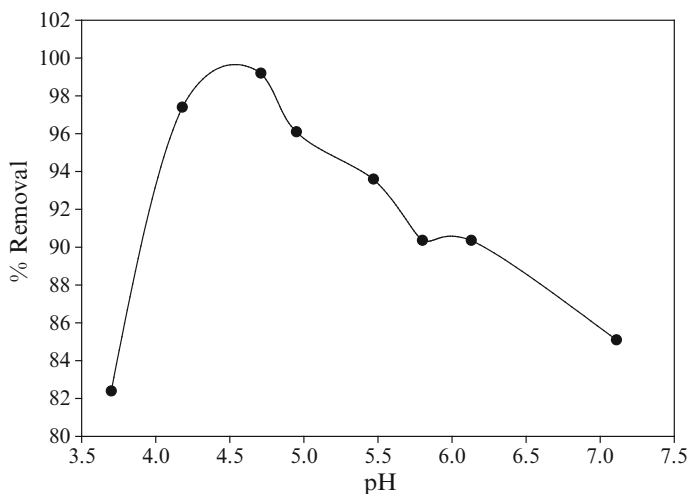


Fig. 20.5 Effect of pH on adsorption of copper

From the equation (20.1), an increase of protons shifts the equilibrium to the right. The sorbent is positively charged at $\text{pH} < \text{PZC}$ (point of zero charge) and lower adsorption and at pH equal or greater than PZC and negative at $\text{pH} > \text{PZC}$ high adsorption [15]. When the metal is in solution, it is positively charged and will be attracted to the surface of the negatively charged adsorbent at that pH ($\text{pH} > \text{PZC}$) favouring adsorption. At $\text{pH} > 6$, there is hydrolysis of metal leading to precipitation due to formation of hydroxyl metal species [16].

Table 20.1 Effect of the eluent type on recovery of metal ions

Eluent	Copper (%)	Recovery Cadmium (%)	Lead (%)
3 M Nitric acid	100	97	93
1 M Nitric acid	98	93	80
0.5 M Nitric acid	95	92	78
Sodium acetate buffer	Under 10	–	–

Equations 20.2 and 20.3 show the hydrolysis of metal ions resulting in the formation of metal-ligand; metal-hydroxyl species (MOH: M-XAD).



It has been observed that that the concentration of $PbOH^+$ is relatively negligible relative to Pb^{2+} over the studied pH ranges [15]. For the metal-hydroxyl species to be adsorbed onto resin, it must possess exceptional affinity for the surface that will drive the metal hydrolysis reactions in Eqs. 20.2 and 20.3 above to the right, maintaining Le Chatelier's principle of equilibrium [17].

It can, therefore, be generalised that the adsorption of Cu^{2+} , Pb^{2+} and Cd^{2+} is pH dependent as observed. This is explained by competition by the positively charged ion to the active sites and as such, the presence of counter ions might influence adsorption in a similar manner that may result in lower efficiency of adsorption [18].

20.3.4 Effect of Flow Rate: Metal Recovery

The effect of flow rate on the adsorption of metals ions was studied. The results presented in Fig. 20.6 show that flow rate had little or no observed effect on the adsorption of the metal ions. This implies that the affinity of the adsorbent to the analyte metals was high such that adsorption of the metals took place almost instantly.

20.3.5 Effect of Eluent Type

The effect of eluent type on the recovery of metal ions was studied. The elutions were performed using 0.5 M HNO_3 , 1 M HNO_3 , 3 M HNO_3 and 0.1 M CH_3COONa solutions. The results are presented in Table 20.1.

The 3 M HNO_3 eluent stripped more metals than the other dilute acids (0.5 and 1.0 M HNO_3). This is possibly due to presence of a bond between the metal

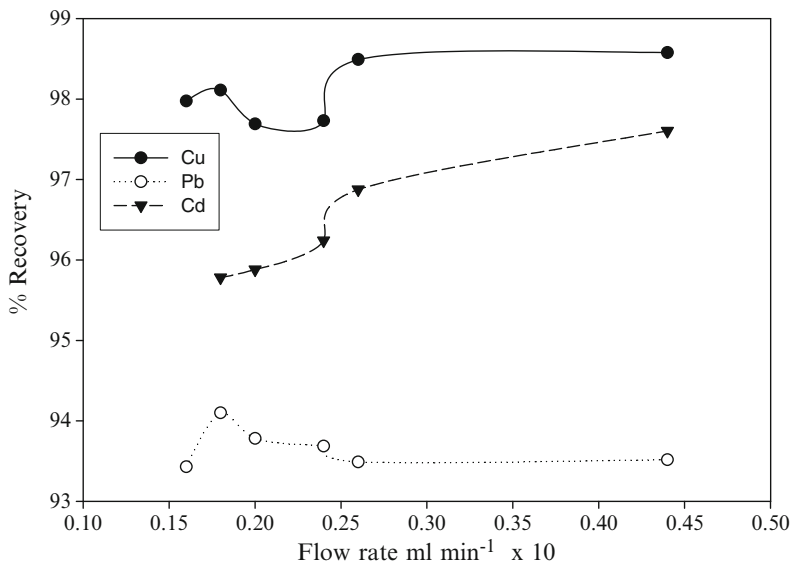


Fig. 20.6 The effect of the flow rate on adsorption of the metal ions

and adsorbent that required a high conc. of H^+ ions to dislodge the metal ions on the adsorbent. The high positive charge environment for the adsorbent (due to H^+ ions), $pH < PZC$ (point of zero charge) creates a relatively lower metal adsorption environment [15].

20.3.6 Determination of Adsorption Capacity

In order to investigate the adsorption capacity, model solutions (20 ml) 40–200 $mg\ l^{-1}$ were transferred into 100 ml polystyrene screw cap bottles containing approximately 0.0400 g of resin and placed on a mechanical shaker. A fast adsorption was observed such that 90% of the adsorption happened within 15 min followed by a steady state adsorption. The mixture was allowed to equilibrate for 1 h then filtered and the resulting solution analysed for lead by ICP-OES.

Figure 20.7 shows a plot of mg of metal per gram of adsorbent (q_e) against initial lead concentration in solution C_0 .

The amount of lead adsorbed (q_e value) is shown to increase linearly to a saturation point at around 12 $mg\ g^{-1}$ which corresponds to the adsorption capacity (q_{max}) [19]. Thus the Pb adsorption capacity obtained experimentally was 12.40 $mg\ g^{-1}$, a value lower than the theoretical adsorption capacity calculated by the Langmuir model [20]. Similar experiments were performed for copper and cadmium.

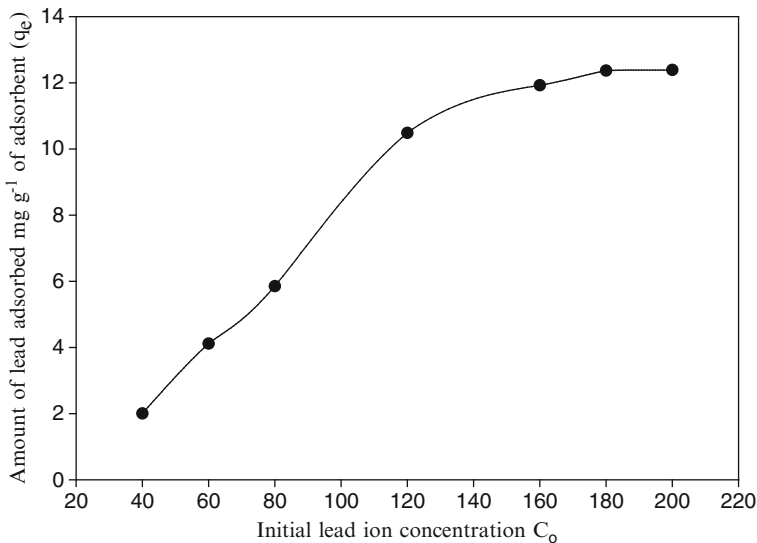


Fig. 20.7 Graph of initial concentration against adsorption per gram of adsorbent

20.3.7 Adsorption Isotherms: Langmuir and Freundlich

Adsorption isotherms describe how adsorbates interact with adsorbents. With the isotherms, it is possible to design sorption systems by determining factors such as adsorption capacity. The adsorption models applied in this study were Langmuir [20], Freundlich [21] and Lagergren [22] isotherms.

Langmuir isotherm, derived by Gibbs approach [23] is in the form given by Eq. 20.4, and assumes that adsorption can only occur at fixed sites with one adsorbate molecule (monolayer) occupying equivalent sites with no interaction between adsorbed molecules [20].

$$q_e = \frac{K_L C_e}{1 + a_L C_e} \quad (20.4)$$

The linearised form is given in Eq. 20.5, where K_L is the equilibrium constant and α_L is a constant of the Langmuir equation [20].

$$\frac{C_e}{q_e} = \frac{1}{K_L} + \frac{a_L C_e}{K_L} \quad (20.5)$$

From Eq. 20.5, a plot of C_e/q_e against C_e will give a straight line whose gradient (α_L/K_L) will be the adsorption capacity [20, 24].

Table 20.2 Adsorption models and kinetics for Pb, Cu and Cd

Metal	Langmuir		Freundlich		Best model	Lagergren
	R ²	Adsorption capacity	R ²	Adsorption capacity		
Lead	0.973	14.03	0.233	2.218	Langmuir	0.969 ^a
Copper	0.541	198.5	0.696	61.49	Freundlich	0.891 ^a
Cadmium	0.875	16.17	0.783	9.507	Langmuir	0.696 ^a

^aPseudo first order

On the other hand, Freundlich isotherms describe multi-site adsorption process for heterogeneous surfaces and have the general form given by Eq. 20.6:

$$q_e = K_L C_e^{bF} \quad (20.6)$$

The linearised equation (by taking logarithms) is applied to determine if the systems are heterogeneous with highly interactive species [21].

Table 20.2 shows the adsorption of both Pb and Cd fitting better with Langmuir model ($R^2 = 0.973$ for Pb and 0.875 for Cd) but not so good fit with Freundlich model ($R^2 = 0.233$ Pb and 0.783 for Cd). This implies that both lead and Cd are possibly chemically attached on this adsorbent [25]. Contrary to Pb and Cd, Cu fitted better with the Freundlich model ($R^2 = 0.696$) compared to Langmuir (0.541).

The adsorption capacity data show Cu to have a larger value compared to Pb and Cd. This may imply that the species involved are highly interactive with the sorbent [24]. A similar observation was made by Huang and Vansant (1973) as they studied adsorption of ammonia in Cu(II)Y zeolites gravimetrically [26]. They observed a large ammonia uptakes in Cu(II) samples than other cations studied, a phenomenon attributed to the formation of copper(II)-ammine complexes, in the form of $[\text{Cu}(\text{NH}_3)_4]^{2+}$. A possible explanation is the high interaction between copper and ammonia, arising from lanthanide contraction due to a high polarizing ability of copper compared to the other cations [27].

Huang and Vansant study concluded that the electrostatic components, polarization energy and field-dipole energy were also important contributors to the above phenomenon [26]. The sorption of copper, therefore, could be a result of more than one mechanism and that a degree of heterogeneity is possible for ionic species involved in the solution and on the surface [24].

20.3.8 Effect of Resin Amount (Sorbate Dose) on the % Recovery of Metal Ions

Varying weights of the modified XAD-1180 resin were packed in a 6 ml polystyrene column. Model solutions buffered at optimized pH value were passed through the column at 3 ml min⁻¹ flow rate. The adsorbed metal ions were eluted from the

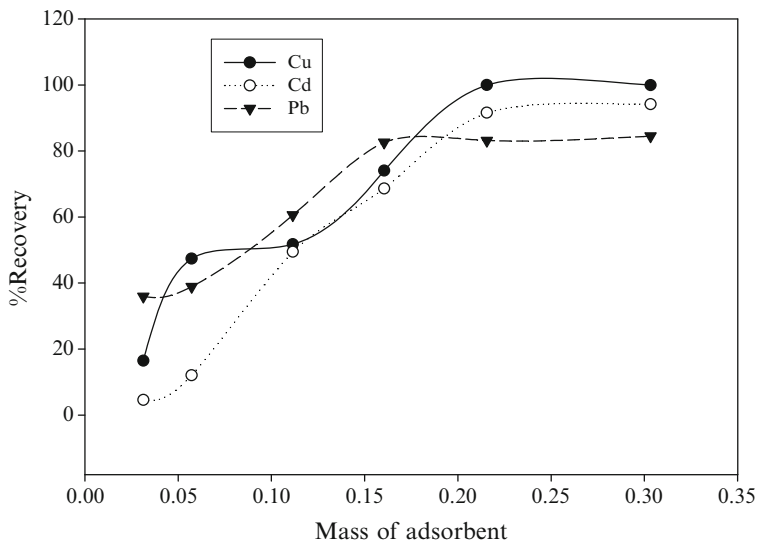


Fig. 20.8 Effect of mass of adsorbent on adsorption of cadmium, copper and lead

column using 10 ml 1 M HNO_3 /methanol and analysed for the content of the metals in the solution. Figure 20.8 represents the effect of the mass of resin adsorbent against adsorption. It was observed that $\sim 95\%$ of the Cd ions and $>95\%$ of Cu ions were adsorbed by the resin if its mass was >0.20 g. However, Cd and Cu required 0.25 g while Pb needed only 0.15 g of adsorbent for a point of inflection (Fig. 20.8) to be observed. The general observation made for all the metals is that the percentage adsorption increased with an increase in sorbate concentration. After all the binding sites are occupied, a plateau appears where there is no significant metal removal. The explanation has been suggested [28].

20.3.9 Effect of Metal Ion Concentration on % Recovery

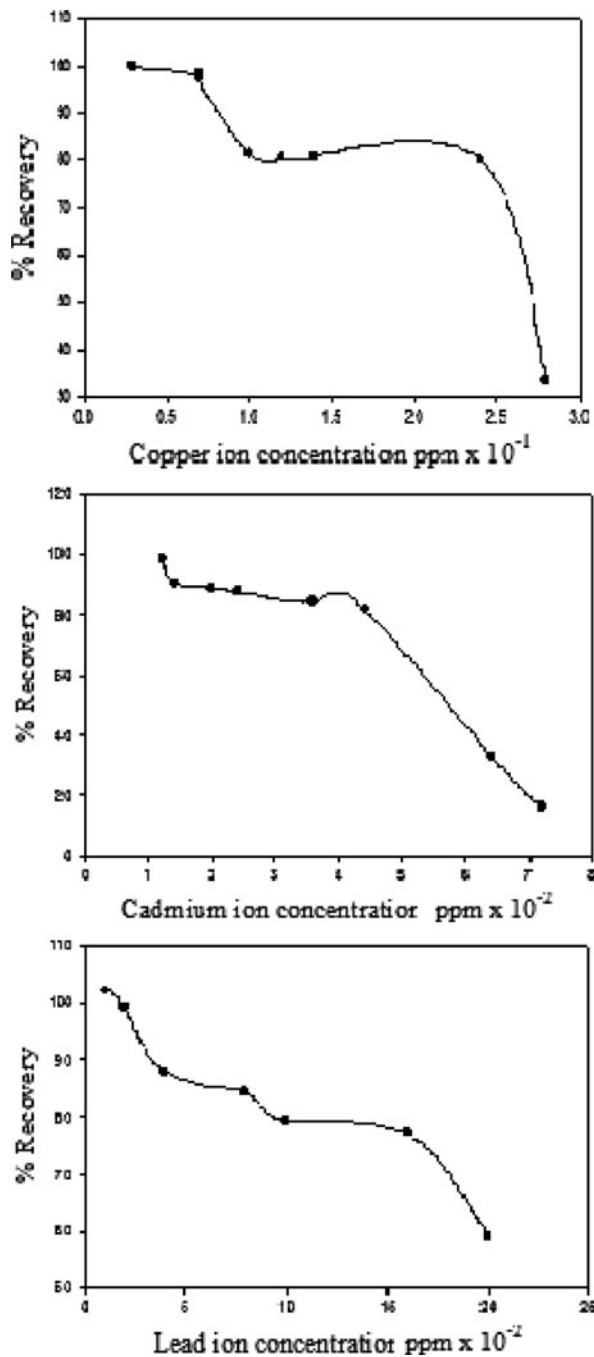
Several solutions of different metal ion concentration were loaded into the SPE column. The recovery of the metals retained on the sorbents was obtained using dilute nitric acid (1.0 M) and the fraction recovered calculated using Eq. 20.7 below;

$$\% \text{ Recovery} = \frac{C_e}{C_o} \times 100\% \quad (20.7)$$

where C_e is the amount of metal retained and C_o is the quantity of metal loaded.

Figure 20.9 shows that the profile of copper reached a plateau at 80% removal when the concentration was between 0.10 and 0.25 mg l^{-1} after which the recovery

Fig. 20.9 Effect of metal ion concentration on % recovery



went below 40%. This may be due to the fact that the concentration surpassed the adsorption capacity of the adsorbent. In the case of Cd, the plateau was observed at 80% when the concentration levels of the solutions to be preconcentrated were between 0.01 and 0.04 mg l⁻¹.

20.3.10 Performance of the Sorbent in Real Water Samples

The modified resin was applied in environmental water samples (50 ml) spiked with known concentrations of Pb, Cu and Cd ions. The mixture was loaded in to the SPE column and the retained metal was later stripped with 1 M nitric acid. The results obtained were recorded in Table 20.3.

20.4 Conclusions

The functionalization of Amberlite XAD-1180 with ethylenediamine was confirmed by FTIR results with the presence of the functional groups providing the binding sites for adsorption of metals. The functionalized material exhibited a good capacity for adsorption of Cu²⁺, Cd²⁺ and Pb²⁺ as 61.49, 16.17 and 14.01 mg l⁻¹, respectively. These values compare well with those of other solid phase adsorbents. Langmuir model fitted well for adsorption of Cu and Pb while Cd is better described the Freundlich model. The pH values for adsorption of the various metals in the batch equilibrium experiments agrees well with results obtained in the SPE preconcentration column. The rate of adsorption was quite fast as >90% of the sorbate was taken up within less than 10 min. The thermal stability of the modified resin in this work was relatively higher compared to other modified amberlite series

Table 20.3 Content of metal ions in water samples

Metal	Added	Found	% Recovery
Cadmium	0.00	0.0063	N/A
	0.20	0.058 ± 0.01	28.5% ± 0.57*
	0.40	0.104 ± 0.01	25.5% ± 1.68
	0.60	0.137 ± 0.01	21.7% ± 0.09
Lead	0.00	0.027	N/A
	0.20	0.244 ± 0.05	90.9% ± 0.12
	0.40	0.325 ± 0.04	70.5% ± 1.04
	0.60	0.46 ± 0.02	74.7% ± 4.31
Copper	0.00	0.029	N/A
	0.20	0.249 ± 0.03	98.5% ± 1.30
	0.40	4.196 ± 0.01	97.9% ± 0.65
	0.60	6.077 ± 0.5	96.4% ± 0.89

*Recovery means amount of metal retained in the adsorbent

reported in the literature. A pre-concentration factor of 20 for all the metals was achieved with the recovery values as high as 98.5% for Cu. Thus the modified resin could be employed for solid phase extraction for metal clean up as well as preconcentration of trace levels of Cu and Pb from real environmental samples prior to analysis.

Acknowledgements Isaac Mwangi is grateful to OPCW for financial support, ANEMAS research group at UKZN Westville, and Kenyatta University for study leave.

References

1. Srivastava N, Majumder CB (2008) Novel biofiltration methods for the treatment of heavy metals from industrial wastewater. *J Hazard Mater* 151:1–8
2. Saracoglu S, Soylak M, Elci L (2001) Preconcentration of Cu(II), Fe(III), Ni(II), Co(II) and Pb(II) ions in some manganese salts with solid phase extraction method using chromosorb-102 resin. *Trace Elem Electrolyte* 18:129–133
3. Chaudhari AR, Nagpurkar LP, Ekhe JD (2003) Uptake of heavy metal ions by carbonaceous material obtained from industrial waste lignin using microwave irradiation. *Asian J Chem* 15:917–924
4. Rao TP, Daniel S (2003) Preconcentration of trace and ultratrace amounts of platinum and palladium from real samples. *Rev Anal Chem* 22:167–189
5. de Alcântara IL, Roldan PS, Margionte MAL, Castroa GR, Padilha CCF, Florentino AO, Padilha PM (2004) Determination of Cu, Ni and Pb in aqueous medium by FAAS after preconcentration on 2-aminothiazole modified silica gel. *J Braz Chem Soc* 15:366–371
6. Godlewska-Zylkiewicz B (2004) Preconcentration and separation procedures for the spectrometric determination of platinum and palladium. *Microchim Acta* 147:189–210
7. Pielichowski J, Pielichowski K (2007) Application of thermal analysis for the investigation of polymer degradation processes. *J Therm Anal Calorim* 43:1388–6150
8. Fisher J, Maikner J and Gehris, (2008) A new cost effective adsorbent for the capture and purification of antibiotics. *Advanced biosciences and Haas company*, <http://www.rohmhaas.com/ionexchange/pharmaceuticals/xad.htm> last visited on 8th May 2010.
9. Lemos VA, Baliza PX (2005) Amberlite XAD-2 functionalized with 2-aminothiophenol as a new sorbent for on-line preconcentration of cadmium and copper. *Talanta* 67:564–570
10. Tashiro T, Shimura Y (1982) Removal of mercuric ions by systems based on cellulose derivatives. *J Appl Polym Sci* 27:747–756
11. Pearson DE, Greer CM (1949) Rearrangement of hydrazones. *J Am Chem Soc* 71:1895–1896
12. Reusch W (1999) *Virtual text of organic chemistry*. Michigan State University, East Lansing
13. Metilda P, Sanghamitra K, Gladis JM, Naidu GRK, Rao TP (2004) Amberlite XAD-4 functionalized with succinic acid for the solid phase extractive preconcentration and separation of uranium(VI). *Talanta* 62:207–213
14. Ünlü N, Ersoz M (2006) Adsorption characteristics of heavy metal ions onto a low cost biopolymeric sorbent from aqueous solutions. *J Hazard Mater* 136:272–280
15. Singh SP, Ma LQ, Hendry MJ (2006) Characterization of aqueous lead removal by phosphatic clay: equilibrium and kinetic studies. *J Hazard Mater* 136:654–662
16. Li X, Tang Y, Cao X, Lu D, Luo F, Shao W (2008) Preparation and evaluation of orange peel cellulose adsorbents for effective removal of cadmium, zinc, cobalt and nickel. *Colloids Surf A Physicochem Eng Asp* 317:512–521
17. Kathrine C, Hans C (2007) Sorption of zinc and lead on coir. *Bioresour Technol* 98:89–97
18. Yu B, Zhang Y, Shukla A, Shukla SS, Dorris KL (2001) The removal of heavy metals from aqueous solutions by sawdust adsorption – removal of lead and comparison of its adsorption with copper. *J Hazard Mater* 84:83–94

19. Benhima H, Chiban M, Sinan F, Seta P, Persin M (2008) Removal of lead and cadmium ions from aqueous solution by adsorption onto micro-particles of dry plants. *J Colloids Surf B Biointerfaces* 61:10–16
20. Langmuir I (1918) The adsorption of gases on plane surfaces of glass, mica and platinum. *J Am Chem Soc* 40:1362–1403
21. Freundlich H (1906) Over the adsorption in solution. *Z Phys Chem* 57:385–470
22. Lagergren S (1898) Zur theorie der sogenannten adsorption gelöster stoffe. *Kungliga Svenska Vetenskapsakademiens. Handlingar*
23. Markham AC, Benton AF (1931) The adsorption of gas mixtures by silica. *J Am Chem Soc* 53:497–506
24. Ng JCY, Cheung WH, McKay G (2003) Equilibrium studies for the sorption of lead from effluents using chitosan. *Chemosphere* 52:1021–1030
25. Deng S, Bai R, Chen PJ (2003) Aminated polyacrylonitrile fibers for lead and copper removal. *Langmuir* 19:5058–5064
26. Huang YY, Vansant EF (1973) Adsorption of ammonia in copper(II) Y zeolites. *J Phys Chem* 77:663–667
27. Johnson AR, McQueen TM, Rodolfa KT (2005) Species distribution diagrams in the copper-ammonia system: an updated and expanded demonstration illustrating complex equilibria. *J Chem Educ* 82:408
28. Ilhan S, Noubakhsh MN, Kilicarslan S, Ozdag H (2004) Removal of chromium, lead and copper from industrial waste by *Staphylococcus saprophyticus*. *Turk Electron J Biotechnol* 2:50–57

Chapter 21

Theoretical Study of Structure, Vibration Spectra and Thermodynamic Properties of Cluster Ions in Vapors over Potassium, Rubidium and Cesium Chlorides

Tatiana P. Pogrebnaya, Jean B. Hishamunda, Camille Girabawe,
and Alexander M. Pogrebnoi

Abstract The geometrical structure, the frequencies of normal vibrations, and the thermodynamic characteristics of tri- and pentaatomic cluster ions M_2Cl^+ , MCl_2^- , $M_3Cl_2^+$, and $M_2Cl_3^-$ ($M = K, Rb, \text{ or } Cs$) existing in saturated vapors over potassium, rubidium, and cesium chlorides have been calculated by nonempirical methods. According to the calculations, the triatomic ions have a linear equilibrium configuration of $D_{\infty h}$ symmetry. For the pentaatomic ions $M_3Cl_2^+$ and $M_2Cl_3^-$, three isomeric forms were considered. The most abundant isomer in saturated vapor was found to be the linear one ($D_{\infty h}$) for $K_3Cl_2^+$, $Rb_3Cl_2^+$, $K_2Cl_3^-$, $Rb_2Cl_3^-$ and $Cs_2Cl_3^-$, and the angular V-shaped (C_{2v}) for $Cs_3Cl_2^+$. The concentration of the other two isomers, cyclic and bipyramidal, is negligible. The energies and enthalpies of dissociation of the ions have been found. The enthalpies of formation of the ions, $\Delta_f H^\circ(0 \text{ K})$ in kJ/mol, were obtained: 116 ± 3 (K_2Cl^+), -623 ± 3 (KCl_2^-), -228 ± 7 ($K_3Cl_2^+$), -971 ± 6 ($K_2Cl_3^-$), 91 ± 3 (Rb_2Cl^+), -620 ± 3 ($RbCl_2^-$), -256 ± 5 ($Rb_3Cl_2^+$), -967 ± 4 ($Rb_2Cl_3^-$), 51 ± 4 (Cs_2Cl^+), -622 ± 3 ($CsCl_2^-$), -301 ± 8 ($Cs_3Cl_2^+$), -975 ± 6 ($Cs_2Cl_3^-$).

T.P. Pogrebnaya
Ivanovo State University of Chemical Technology, Ivanovo, Russia

A.M. Pogrebnoi (✉)
Department of Applied Physics, Kigali Institute of Science and Technology, Kigali, Rwanda
e-mail: pgamtp@mail.ru

J.B. Hishamunda • C. Girabawe
Physics Department, Brandeis University, Waltham, MA 02453, USA

21.1 Introduction

The M_2X^+ , MX_2^- , $M_3X_2^+$ and $M_2X_3^-$ type ions (M is an alkali metal; X is halogen) were recorded in vapors over alkali metal halides in mass spectrometric studies [1–5]. Similar ions are of great importance in different applications: ionic implantation, ion thrusters, MHD generators, aerospace investigations, etc. Experimental data about the structure and spectra of these cluster ions are unavailable. Previously, nonempirical investigations of structure and properties had been done for the ions existing in vapors over sodium halides [6–8]. At present work, quantum chemical study has been performed for tri- and pentaatomic ions M_2Cl^+ , MCl_2^- , $M_3Cl_2^+$ and $M_2Cl_3^-$ where $M = K, Rb$ or Cs . Our aims were as follows: to determine the equilibrium geometrical structure of the ions; to compute the normal vibrational frequencies, to find out the possible isomeric configurations of the pentaatomic ions and the relative concentration in saturated vapors. Based on the molecular parameters determined in this work, together with equilibrium constants taken from high temperature mass spectrometric investigations [1–5], thermodynamic functions and thermodynamic properties of the ions were to be found.

21.2 Methodology

The calculations were performed using the GAMESS program [9] (PC GAMESS version 7.1.C [10]) implementing the following methods: electron density functional theory (DFT) with the Becke–Lee–Yang–Parr functional (B3LYP5), second order and fourth order Möller–Plesset perturbation theory (MP2 and MP4).

To choose the appropriate theory level, the calculations of properties of the diatomic alkali metal chloride molecules were performed using DFT and MP2 methods in two basis sets. The first basis set was constricted and the second was extended, we denoted them as B1 and B2 respectively. The basis set B1 was the McLean–Chandler full-electron basis set (6s5p1d) augmented with diffuse functions of the s- and p-type for Cl [9]; and the relativistic effective core potential with cc-pVTZ basis set (5s4p1d) for valence shells [11] was used for K, Rb, Cs. The extended basis set B2 was the full-electron basis set cc-pVTZ (5s4p2d1f) augmented with diffuse functions of the s, p, d, and f type for Cl [11] and the relativistic effective core potentials [11] for K, Rb, Cs. The valence shells of the metal atoms were described by correlation consistent basis sets cc-pVTZ [11]: (5s4p2d1f) on K, (7s5p4d1f) on Rb, and (6s5p4d1f) on Cs.

The optimization of the geometric parameters of the ions and the calculations of vibrational frequencies in the harmonic approximation were carried out by the methods implemented in the GAMESS program. In the calculations by MP2 and MP4 methods, the 1s, 2s, 2p orbitals of Cl were frozen.

21.3 Results and Discussion

21.3.1 Diatomic Molecules KCl, RbCl, and CsCl

The equilibrium internuclear distance, the normal vibration frequency, and the ionization potential are given in Table 21.1 for KCl, RbCl, and CsCl molecules. These calculated values are compared with the reference data.

As it is seen from Table 21.1, the results obtained with MP2 method and the extended basis set B2 are better to correspond to the reference data than the results obtained with the other three methods. Therefore we have chosen the theory level MP2 B2 for further computation of the properties of the ions. The internuclear distances calculated for KCl, RbCl, and CsCl molecules are systematically overrated about 0.03–0.06 Å and the frequencies are underrated by 2–3% compared with the experimental data. We expect the similar uncertainties in the values of R_e and ω_i for the tri- and pentaatomic ions. The results represented below for the ions correspond to the MP2 B2 calculations.

Table 21.1 Calculated and experimental parameters for KCl, RbCl and CsCl molecules

	$R_e(\text{M-Cl}), \text{Å}$	ω_e, cm^{-1}	μ_e, D	IP, eV
Method	KCl			
DFT B1	2.746	255	11.3	5.6
MP2 B1	2.750	257	11.7	9.0
DFT B2	2.722	268	10.5	5.7
MP2 B2	2.709	272	10.7	9.1
Experimental	2.667 [12]	280 [12]	10.2 [13]	8.3 ± 0.2 [14]
	RbCl			
DFT B1	2.889	218	11.5	5.5
MP2 B1	2.877	223	11.8	8.9
DFT B2	2.864	219	10.8	5.6
MP2 B2	2.849	225	11.1	9.0
Experimental	2.787 [12]	233 [12]	10.5 [15]	8.2 ± 0.2 [14]
	CsCl			
DFT B1	3.001	202	11.3	5.5
MP2 B1	3.001	205	11.7	8.9
DFT B2	2.954	206	10.4	5.7
MP2 B2	2.937	209	10.7	9.1
Experimental	2.906 [12]	214 [12]	10.5 [15]	8.1 ± 0.2 [14]

$R_e(\text{M-Cl})$ is the equilibrium internuclear distance, ω_e is the frequency of normal vibration, μ_e is the dipole moment, IP is the ionization potential. The calculated value of IP was taken as the energy of the highest occupied MO

21.3.2 Triatomic Ions M_2Cl^+ , MCl_2^- ($M = K, Rb, \text{ or } Cs$)

According to the calculations, the structure of all triatomic ions is linear with $D_{\infty h}$ symmetry. The properties, namely the equilibrium internuclear distances, the total electron energies, the frequencies of normal vibrations, the intensities of vibrations in IR spectra are represented in Table 21.2.

As is seen in Table 21.2, the increase in the internuclear distances $R_e(M-Cl)$ in series K–Rb–Cs either in positive or in the negative ions is similar to those in the MCl molecules given in Table 21.1. It is evident also that increase of the values $R_e(M-Cl)$ correlates with the enlarging of the ionic radius in the series $K^+ - Rb^+ - Cs^+$. As concerns frequencies, the stretching symmetric vibration frequency ω_1 is smaller than the antisymmetric ω_2 in all cases. For the positive ions, the stretching vibration ω_1 may be considered to be close to the frequency ω_e in the diatomic molecules respectively. For the K_2Cl^+ and KCl_2^- ions, the frequencies are similar to each other respectively, while for the other two pairs, Rb_2Cl^+ and $RbCl_2^-$, Cs_2Cl^+ and $CsCl_2^-$, the corresponding frequencies are markedly different. In addition, the intensities of the vibrations ω_2 and ω_3 active in IR spectra are of the same magnitude approximately.

21.3.3 Pentaatomic Ions $M_3Cl_2^+$ and $M_2Cl_3^-$ ($M = K, Rb, \text{ or } Cs$)

Several probable geometric configurations of the pentaatomic ions $M_3Cl_2^+$ and $M_2Cl_3^-$ ($M = K, Rb, \text{ or } Cs$) were considered: $D_{\infty h}$ linear symmetry, C_{2v} planar cyclic symmetry, and D_{3h} bipyramidal symmetry (Fig. 21.1). For each configuration the geometric parameters were optimized, and the frequencies of normal vibrations were calculated.

The obtained parameters of the linear structure are given in Table 21.3. According to the calculations performed, the equilibrium structure of ions $K_3Cl_2^+$, $K_2Cl_3^-$, and $Rb_2Cl_3^-$ found to be linear. As concerns the other three ions, the imaginary frequencies were found: $\omega_7(\Pi_u)$ for $Rb_3Cl_2^+$, $Cs_3Cl_2^+$, and $Cs_2Cl_3^-$ and $\omega_5(\Pi_g)$ for $Cs_2Cl_3^-$.

In the case of $Rb_3Cl_2^+$ and $Cs_2Cl_3^-$, the optimization procedure showed the “slightly distorted linear” configuration of C_2 symmetry. Meanwhile, no energy decrease of this distorted configuration compared with the linear structure was observed. Note that DFT method indicated the linear structure of these two ions also. Therefore we assumed that the equilibrium structure of $Rb_3Cl_2^+$ and $Cs_2Cl_3^-$ must be linear. The imaginary deformation frequencies were substituted by the values given in Table 21.3 between the parentheses. These frequencies were estimated by the comparative method based on the tendency in frequency change in the series $K_3Cl_2^+ - Rb_3Cl_2^+ - Cs_3Cl_2^+$ and $K_2Cl_3^- - Rb_2Cl_3^- - Cs_2Cl_3^-$.

As to $Cs_3Cl_2^+$ ion, the optimization procedure gave the V-shaped angular structure with C_{2v} symmetry shown in Fig. 21.1. The geometric parameters

Table 21.2 Properties of the triatomic ions

Property	K_2Cl^+	Rb_2Cl^+	Cs_2Cl^+	KCl_2^-	$RbCl_2^-$	$CsCl_2^-$
$R_e(M-Cl)$	2.827	2.978	3.100	2.878	3.038	3.178
E	-516.08762	-507.65320	-499.77527	-947.84470	-943.62018	-939.67506
$\omega_1 (\Sigma_g^+)$	153	98	77	155	147	143
$\omega_2 (\Sigma_u^+)$	261	226	209	239	179	150
$\omega_3 (\Pi_u)$	43	38	38	50	29	15
A_2	2.10	1.66	2.08	2.06	1.90	2.30
A_3	2.02	1.24	0.91	2.17	1.96	1.84

$R_e(M-Cl)$ is the equilibrium internuclear distance, Å; E is the total electron energy, au; ω_i are the frequencies of normal vibrations, cm^{-1} ; A_i are the IR intensities, $D^2 amu^{-1} \text{Å}^{-2}$

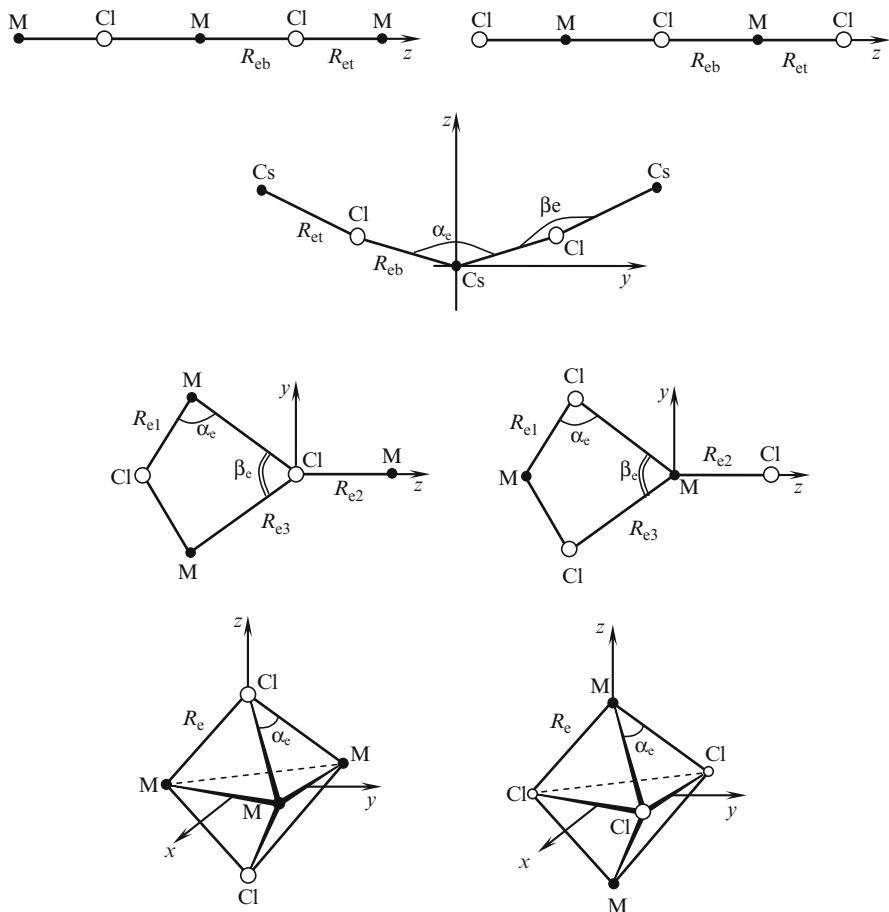


Fig. 21.1 Isomers of the pentaatomic ions: linear, angular, cyclic, and bipyramidal

and vibration frequencies are given in Table 21.4. As is seen from the data, the central fragment Cl-Cs-Cl was specified by the angle $\alpha_e = 141^\circ$ whereas the Cs-Cl-Cs fragments were found almost linear. The energy was decreased by $h = E(C_{2v}) - E(D_{\infty h}) = -0.5$ kJ/mol. Thus among the number of considered pentaatomic ions the only one was not found to be linear but definitely bent.

The other two structures, cyclic (C_{2v}) and bipyramidal (D_{3h}), were found to be equilibrium as well. The valence angles α_e and β_e of the cyclic isomer and α_e of the bipyramidal isomers were close to 90° . The values of relative energy h_{iso} of these two types of isomers with respect to linear (or angular V-shaped for $Cs_3Cl_2^+$) are given in Table 21.5. All the ions, except the cyclic $K_3Cl_2^+$ and $K_2Cl_3^-$, have the negative value of h_{iso} . That means that the bipyramidal isomers of all ions and the cyclic isomers of $Rb_3Cl_2^+$, $Cs_3Cl_2^+$, $Rb_2Cl_3^-$, and $Cs_2Cl_3^-$ are energetically more stable than those of linear structure (or angular V-shaped for $Cs_3Cl_2^+$).

Table 21.3 Properties of the pentaatomic ions of D_{och} symmetry

Property	K_3Cl_2^+	Rb_3Cl_2^+	Cs_3Cl_2^+	K_2Cl_3^-	Rb_2Cl_3^-	Cs_2Cl_3^-
$R_{\text{et}}(\text{M}-\text{Cl})$	2.793	2.941	3.051	2.833	2.988	3.117
$R_{\text{eb}}(\text{M}-\text{Cl})$	2.910	3.074	3.228	2.927	3.096	3.256
E	-1004.13243	-991.47513	-979.65415	-1435.88960	-1427.44184	-1419.55305
$\omega_1 (\sum_g^+)$	254	222	206	238	183	162
$\omega_2 (\sum_g^+)$	89	61	49	88	71	53
$\omega_3 (\sum_u^+)$	265	221	200	252	197	172
$\omega_4 (\sum_u^+)$	176	112	84	184	171	158
$\omega_5 (\Pi_g)$	32	31	27	37	18	(15)
$\omega_6 (\Pi_u)$	52	38	28	53	33	23
$\omega_7 (\Pi_u)$	12	(9)	10i	9	9	(9)
A_3	4.07	3.35	4.27	3.94	2.98	1.44
A_4	0.02	0.00	0.01	0.10	0.61	2.98
A_6	3.01	2.24	1.66	3.35	2.54	1.55
A_7	0.52	-	-	0.34	0.53	-

$R_{\text{et}}(\text{M}-\text{Cl})$ and $R_{\text{eb}}(\text{M}-\text{Cl})$ are the terminal and bridge internuclear distances respectively, Å; E is the total electron energy; ω_i are the frequencies of normal vibrations, cm^{-1} ; A_i are the IR intensities, $\text{D}^2\text{amu}^{-1}\text{Å}^{-2}$

Table 21.4 Properties of the Cs_3Cl_2^+ ion of V-shape

Property	$\text{Cs}_3\text{Cl}_2^+ (C_{2v})$
$R_{\text{et}}(\text{Cs}-\text{Cl})$	3.052
$R_{\text{eb}}(\text{Cs}-\text{Cl})$	3.213
$\alpha_e(\text{Cl}-\text{Cs}-\text{Cl})$	141.1
$\beta_e(\text{Cs}-\text{Cl}-\text{Cs})$	179.7
E	-979.65434
$E - E(D_{\infty h})$	-0.5
$\omega_1 (A_1)$	208
$\omega_2 (A_1)$	56
$\omega_3 (A_1)$	35
$\omega_4 (A_1)$	35
$\omega_5 (A_1)$	10
$\omega_6 (A_2)$	86
$\omega_7 (A_2)$	28
$\omega_8 (B_1)$	201
$\omega_9 (B_1)$	28
μ_e	6.1

$R_{\text{et}}(\text{M}-\text{Cl})$ and $R_{\text{eb}}(\text{M}-\text{Cl})$ are the terminal and bridge internuclear distances respectively, Å; α_e and β_e are the valence angles in degrees; E is the total electron energy, au; $E - E(D_{\infty h})$ is the relative energy, kJ/mol. ω_i are the frequencies of normal vibrations, cm^{-1} ; μ_e is the dipole moment, D. The vibrational representation is $\Gamma = 5A_1 + 2A_2 + 2B_1$. Analysis of vibrational modes was performed using the SHRINK software [16]; the Q2SHRINK program [17] was used for building the input for SHRINK

In order to draw the final conclusion about the content of the isomers of pentaatomic ions in saturated vapor, it is necessary to take into account the entropy factor. To evaluate the relative isomer contents in saturated vapor over alkali metal chlorides, we performed thermodynamic calculations. We considered the isomerization reactions from the linear into cyclic or bipyramidal configurations:



Instead of linear, the equilibrium angular V-shaped structure was considered for the Cs_3Cl_2^+ . To calculate the relative concentration of the isomers we used the following formula

$$\Delta_r H^\circ (0 \text{ K}) = RT \ln(p_{\text{iso}}/p) + T \Delta_r \Phi^\circ (T) \quad (21.3)$$

Table 21.5 Enthalpies of isomerization reactions and relative concentrations of the isomers at 1,000 K

Isomerization reaction	h_{iso} , kJ/mol	$\Delta\varepsilon$, kJ/mol	$\Delta_r H^\circ(0\text{ K})$, kJ/mol	$\Delta_r \Phi^\circ(T)$, J/(mol·K)	p_{iso}/p
K_3Cl_2^+ (linear) = K_3Cl_2^+ (cyclic)	1.8	0.8	2.6	-22.925	0.047
K_3Cl_2^+ (linear) = K_3Cl_2^+ (bipyramidal)	-16.4	1.7	-14.7	-56.593	0.007
K_2Cl_3^- (linear) = K_2Cl_3^- (cyclic)	2.7	0.8	3.5	-37.590	0.007
K_2Cl_3^- (linear) = K_2Cl_3^- (bipyramidal)	-14.2	1.6	-12.6	-70.040	0.001
Rb_3Cl_2^+ (linear) = Rb_3Cl_2^+ (cyclic)	-1.0	0.7	-0.3	-21.573	0.077
Rb_3Cl_2^+ (linear) = Rb_3Cl_2^+ (bipyramidal)	-21.1	1.6	-19.5	-55.312	0.014
Rb_2Cl_3^- (linear) = Rb_2Cl_3^- (cyclic)	-2.5	0.9	-1.6	-32.698	0.024
Rb_2Cl_3^- (linear) = Rb_2Cl_3^- (bipyramidal)	-23.4	1.5	-21.9	-67.040	0.004
Cs_3Cl_2^+ (angular) = Cs_3Cl_2^+ (cyclic)	-6.1	0.6	-5.4	-22.162	0.134
Cs_3Cl_2^+ (angular) = Cs_3Cl_2^+ (bipyramidal)	-27.7	1.1	-26.6	-55.433	0.031
Cs_2Cl_3^- (linear) = Cs_2Cl_3^- (cyclic)	-12.3	0.9	-11.4	-34.855	0.060
Cs_2Cl_3^- (linear) = Cs_2Cl_3^- (bipyramidal)	-39.5	1.5	-38.0	-71.501	0.018

h_{iso} is the relative energy of the isomer, $\Delta\varepsilon$ is zero point vibrational energy, $\Delta_r H^\circ(0\text{ K})$ is the enthalpy of the reaction, $\Delta_r \Phi^\circ(T)$ is the reduced Gibbs energy of the reaction, p_{iso}/p is relative concentration of the isomer

where p_{iso}/p is the ratio between the pressure p_{iso} of the ions of the cyclic or bipyramidal isomeric form and the pressure p of linear (or angular for Cs_3Cl_2^+) isomer; $\Delta_r\Phi^\circ(T)$ is a change in the reduced Gibbs energy of the isomerization reactions.

The enthalpies of the isomerization reactions $\Delta_r H^\circ(0\text{ K})$ were obtained on the basis of the relative energy of isomers h_{iso} and the zero point vibration energy correction $\Delta\varepsilon$:

$$\Delta_r H^\circ(0\text{ K}) = h_{\text{iso}} + \Delta\varepsilon. \quad (21.4)$$

The zero point vibration energy correction was calculated using the formula

$$\Delta\varepsilon = 1/2hc \left(\sum \omega_{\text{iproduct}} - \sum \omega_{\text{ireactant}} \right) \quad (21.5)$$

where h is the Planck's constant, c is the speed of light in free space, $\sum \omega_{\text{iproduct}}$ and $\sum \omega_{\text{ireactant}}$ are the sums of the vibrational frequencies of the products and reactants, respectively. According to calculations this correction was small and negative, did not exceed 1.7 kJ/mol. The values of the reduced Gibbs energy were calculated in the rigid rotator–harmonic oscillator approximation using the geometrical parameters and vibration frequencies found in this work. The results of calculations are given in Table 21.5 for the temperature of 1,000 K, common in the mass spectrometric investigations of alkali metal halides.

As it was mentioned above, the relative energy h_{iso} for the majority of isomers (excluding the cyclic isomer of K_3Cl_2^+ and K_2Cl_3^-) is negative. That means that these isomers are energetically more stable than those of the linear structure (angular in the case of Cs_3Cl_2^+). Nevertheless, the calculations show that the relative amount of either cyclic or bipyramidal isomers in vapors is small. The largest value of $p_{\text{iso}}/p = 13.4\%$ is predicted for Cs_3Cl_2^+ (cyclic).

The low amount of the cyclic and bipyramidal isomeric forms may be explained by the prevailing effect of the entropy factor. The considerable decrease in entropy and hence in the reduced Gibbs energy $\Delta_r\Phi^\circ(T)$ in the isomerization reaction dominate over the energy factor and lead to a higher concentration of linear isomer (angular for Cs_3Cl_2^+). The concentration of the cyclic and bipyramidal isomers is decreased when the temperature is increased. As an example, the temperature dependence of the isomer concentration is presented for Cs_3Cl_2^+ and Cs_2Cl_3^- in Fig. 21.2.

21.3.4 Enthalpies of Ion Molecular Reactions and Enthalpies of Formation of the Ions

The dissociation energies of ions ΔE were calculated with MP2 and MP4 methods. For pentaatomic ions the energies of the reactions were calculated for the linear isomers (angular for Cs_3Cl_2^+) because they dominate in the equilibrium vapor.

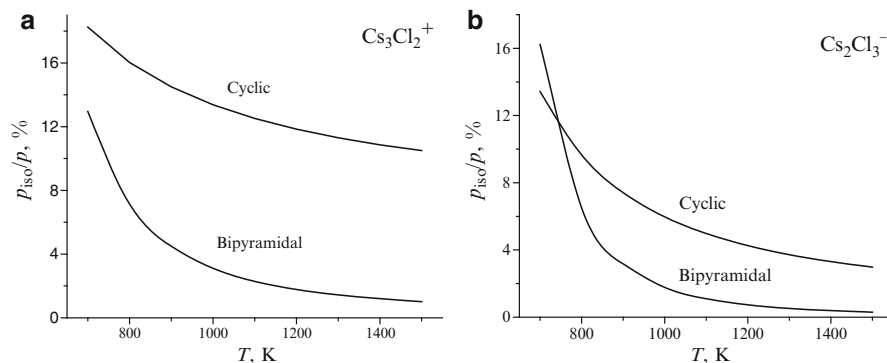


Fig. 21.2 Temperature dependence of the relative amount of the isomers of Cs_3Cl_2^+ (a) and Cs_2Cl_3^- (b) ions

Moreover, the ion dissociation energies were calculated taking into account the basis set superposition error (BSSE) by the counterbalance method [18] using the procedure proposed by Solomonik and co-workers [19]. The energies of the reactions obtained with MP4 method and BSSE corrections are denoted as ΔE_c (Table 21.6). The BSSE correction equals to the difference of the values ΔE and ΔE_c , it was not big here but allowed us to obtain more reliable results of the dissociation energy values. The values of enthalpies of the reactions $\Delta_r H^\circ(0 \text{ K})$ called the “theoretical” in Table 21.6 were calculated using the formula

$$\Delta_r H^\circ(0 \text{ K}) = \Delta E_c + \Delta \varepsilon \quad (21.6)$$

where $\Delta \varepsilon$ is the zero point vibration energy correction.

The values of $\Delta_r H^\circ(0 \text{ K})$ called “based on experiment” were calculated using the equilibrium constants K_p° for the heterophase reactions from [3–5] and the procedure of the third law of thermodynamics:

$$\Delta_r H^\circ(0 \text{ K}) = -RT \ln K_p^\circ + T \Delta_r \Phi^\circ(T). \quad (21.7)$$

The thermodynamic functions of atomic ions M^+ , Cl^- , alkali metal chlorides MCl in the condensed and in gaseous phase were taken from [21]. The thermodynamic functions of the cluster ions M_2Cl^+ , MCl_2^- , M_3Cl_2^+ , and M_2Cl_3^- were calculated using the molecular constants obtained in this work and listed in Tables 21.2–21.4. In order to converse the enthalpies of heterophase reactions into the enthalpies of gas phase reactions, we used the sublimation enthalpies of MCl from [21]. The enthalpies of the reactions are given in Table 21.6.

The uncertainties in the theoretical enthalpies of the reactions were estimated from the comparison of MP2 and MP4 results. The uncertainties of the dissociation enthalpies “based on experiment” included errors in equilibrium constants [3–5],

Table 21.6 Energies and Enthalpies of dissociation reactions and enthalpies of formation of ions (in kJ/mol)

Reaction	ΔE	ΔE_c	$\Delta \varepsilon$	$\Delta_r H^\circ(0)$		Reference
				Theoretical	Based on experiment	
$K_2Cl^+ = KCl + K^+$	184.0	181.8	-1.36	180 ± 3	175 ± 5	113 ± 5 [1], 109 ± 10 [2]
$KCl_2^- = KCl + Cl^-$	184.8	182.5	-1.33	181 ± 3	185 ± 8	-623 ± 3
$K_3Cl_2^+ = KCl + K_2Cl^+$	139.0	131.9	-1.21	131 ± 6	128 ± 8	-263 ± 30 [2]
$K_2Cl_3^- = KCl + KCl_2^-$	139.2	135.6	-1.10	135 ± 5	120 ± 10	-971 ± 6
$Rb_2Cl^+ = RbCl + Rb^+$	175.7	174.1	-0.99	173 ± 3	169 ± 5	94 ± 10 [2], 98 ± 5 [1]
$RbCl_2^- = RbCl + Cl^-$	171.4	170.3	-0.95	169 ± 2	No data	-620 ± 3
$Rb_3Cl_2^+ = RbCl + Rb_2Cl^+$	130.0	126.5	-0.86	126 ± 4	124 ± 8	-276 ± 30 [2]
$Rb_2Cl_3^- = RbCl + RbCl_2^-$	129.3	127.0	-0.80	126 ± 3	No data	-256 ± 5
$Cs_2Cl^+ = CsCl + Cs^+$	166.9	163.8	-0.90	163 ± 4	153 ± 7	-967 ± 4
$CsCl_2^- = CsCl + Cl^-$	154.5	153.3	-0.68	153 ± 3	142 ± 7	51 ± 4
$Cs_3Cl_2^+ = CsCl + Cs_2Cl^+$	118.6	112.8	-0.71	112 ± 7	110 ± 8	57 ± 20 [2], 36 ± 14 [20]
$Cs_2Cl_3^- = CsCl + CsCl_2^-$	116.5	113.2	-0.53	113 ± 5	104 ± 10	-622 ± 3
						-301 ± 8
						-975 ± 6

ΔE is the energy of the reaction, ΔE_c is the energy of the reaction when the BSSE correction has been taken into account, $\Delta \varepsilon$ is the zero point vibration energy correction, $\Delta_r H^\circ(0)$ theoretical is the enthalpy of the reaction equal to $\Delta E_c + \Delta \varepsilon$, $\Delta_r H^\circ(0)$ based on experiment was obtained by the third law of thermodynamics using the equilibrium constants from [3-5]

the standard deviation in the $\Delta_r H^\circ(0\text{ K})$ values calculated by the third law of thermodynamics, and the uncertainties in the reduced Gibbs energy caused by errors in frequencies which were accepted to be 10%.

The theoretical values of $\Delta_r H^\circ(0\text{ K})$ and the values “based on experiment”, as seen in Table 21.6, agree between each other within the uncertainty limits. For the triatomic ions, the enthalpy of dissociation of positive M_2Cl^+ ions is very close to that of the negative MCl_2^- ions respectively. For the pentaatomic positive and negative ions, the values of $\Delta_r H^\circ(0\text{ K})$ are very close to each other also and less than those of the triatomic ions. For all ions, the decrease of the dissociation enthalpies from potassium to cesium is observed.

The enthalpies of formation of M_2Cl^+ , MCl_2^- , $M_3Cl_2^+$, and $M_2Cl_3^-$ ions were calculated on the basis of the theoretical values of $\Delta_r H^\circ(0\text{ K})$. The required enthalpies of formation of M^+ , Cl^- , and MCl were taken from [21]. Our values of $\Delta_f H^\circ(0\text{ K})$ of the ions are in good agreement with the available reference data (Table 21.6), but obtained with much less uncertainties.

21.4 Conclusions

The MP2 method with the extended basis set was accepted for the calculations of geometrical parameters and vibrational frequencies of the cluster ions as the more reliable method because it gives better agreement with available reference data for the diatomic molecules KCl , $RbCl$ and $CsCl$.

Geometrical structure, vibrational spectra and thermodynamic properties of the ions M_2Cl^+ , MCl_2^- , $M_3Cl_2^+$, and $M_2Cl_3^-$ ($M = K, Rb, Cs$) have been determined. The equilibrium structure of the triatomic ions M_2Cl^+ and MCl_2^- is the linear of $D_{\infty h}$ symmetry. For the pentaatomic ions $M_3Cl_2^+$ and $M_2Cl_3^-$, three isomeric forms were considered. The most abundant isomer in saturated vapor was found to be the linear one ($D_{\infty h}$) for $K_3Cl_2^+$, $Rb_3Cl_2^+$, $K_2Cl_3^-$, $Rb_2Cl_3^-$ and $Cs_2Cl_3^-$, and the angular V-shaped for $Cs_3Cl_2^+$. The other two forms, cyclic and bipyramidal, correspond to minima at the potential energy surface of the ion and have the comparable or even lower energy than the first isomer; nevertheless, according to the calculations, the relative amount of cyclic and bipyramidal isomers in saturated vapor is negligible.

The geometrical parameters and vibrational frequencies of the cluster ions vary regularly in K – Rb – Cs series.

The enthalpies of the dissociation of the ions $\Delta_r H^\circ(0\text{ K})$ were found by quantum chemical calculation and also on the basis of available equilibrium constants of reactions. The theoretical and the “based on experiment” values of $\Delta_r H^\circ(0\text{ K})$ agree between each other within the uncertainty limits. That confirms the reliability both the experiment and theoretical results.

The enthalpies of the dissociation reactions of the ions are higher for triatomic ions than those for the corresponding pentaatomic ions. The $\Delta_r H^\circ(0\text{ K})$ values decrease monotonically from K to Cs for both negative and positive ions. The enthalpies of formation of the ions were determined.

Acknowledgements We gratefully acknowledge the financial support from Government of Rwanda.

References

1. Chupka WA (1959) Dissociation energies of some gaseous alkali halide complex ions and the hydrated ion $K(H_2O)^+$. *J Chem Phys* 10:458–465
2. Gusarov AV (1986) Equilibrium ionization in vapors of inorganic compounds and the thermodynamic properties of ions. Chemical sciences doctoral dissertation, Moscow
3. Kudin LS, Burdukovskaya GG, Krasnov KS, Vorob'ev OV (1990) Mass spectrometric study of the ionic composition of saturated potassium chloride vapour. Enthalpies of formation of the K_2Cl^+ , $K_3Cl_2^+$, KCl_2^- , and $K_2Cl_3^-$ ions. *Russ J Phys Chem* 64:48–489
4. Motalov VB, Pogrebnoi AM, Kudin LS (2001) Molecular and ionic associates in vapor over rubidium chloride. *Russ J Phys Chem* 75:1407–1412
5. Pogrebnoi AM, Kudin LS, Kuznetsov AYu (2002) Enthalpies of formation of ions in saturated vapor over Cesium Chloride. *Russ J Phys Chem* 74:1930–1932
6. Pogrebnaya TP, Pogrebnoi AM, Kudin LS (2008) Calculation of the thermodynamic characteristics of ions in vapor over sodium fluoride. *Russ J Phys Chem* 82:84–92
7. Pogrebnaya TP, Pogrebnoi AM, Kudin LS (2007) Theoretical study of structure and stability of Na_2Cl^+ , $NaCl_2^-$, $Na_3Cl_2^+$ and $Na_2Cl_3^-$ ions. *Russ J Struct Chem* 48:1053–1061
8. Pogrebnaya TP, Pogrebnoi AM, Kudin LS (2010) Structural and thermodynamic characteristics of ionic associates in vapors over sodium bromide and iodide. *Russ J Struct Chem* 51:231–237
9. Schmidt MW, Baldrige KK, Boatz JA, Elbert ST, Gordon MS, Jensen JH, Koseki S, Matsunaga N, Nguyen KA, Su SJ, Windus TL, Dupuis M, Montgomery JA (1993) The general atomic and molecular electronic structure system. *J Comput Chem* 14:1347–1363
10. Granovsky AA (2010) <http://classic.chem.msu.ru/gran/games/index.html>. Accessed 16 Mar 2010
11. EMSL Basis Set Library (2010) www.emsl.pnl.gov/forms/basisform.html. Accessed 28 Sept 2010
12. Krasnov KS (1979) *Molekulyarnye postoyannye neorganicheskikh soedinenii*. Khimiya, Leningrad
13. NIST Diatomic Spectral Database (www.physics.nist.gov/PhysRefData/MolSpec/Diatomic/index.html). Accessed 23 Nov 2010
14. Kondrat'ev VN (1974) Chemical bond dissociation energies. Ionization potentials and electron affinity. Nauka, Moscow
15. Batzanov SS (1976) Structural refractometry. Vysshaja Shkola, Moscow
16. Sipachev VA (1985) Calculation of shrinkage corrections in harmonic approximation. *J Mol Struct (Theochem)* 121:143–151
17. Zakharov AV, Shlykov SA, Danilova EA, Krasnov AV, Islyaikin MK, Girichev GV (2009) Thiadiazole-containing expanded heteroazaporphyrinoids: a gas-phase electron diffraction and computational structural study. *Phys Chem Chem Phys* 11:8570–8579
18. Boys SF, Bernardi F (1970) The calculation of small molecular interactions by the differences of separate total energies. Some procedures with reduced errors. *Mol Phys* 19:553–566
19. Solomonik VG, Smirnov AN, Mileev MA (2005) Structure, vibrational spectra, and energetic stability of LnX_4^- ($Ln = La, Lu; X = F, Cl, Br, I$) ions. *Koordinats Khim* 31:218–228
20. Berkowitz J (1969) Photoionization of high temperature vapors. Cesium halides, chemical shift of autoionization. *J Chem Phys* 50:3503–3515
21. Gurvich LV, Yungman VS, Bergman GA, Veitz IV, Gusarov AV, Iorish VS, Leonidov VYa, Medvedev VA, Belov GV, Aristova NM, Gorokhov LN, Dorofeeva OV, Ezhov YuS, Efimov ME, Krivosheya NS, Nazarenko II, Osina EL, Ryabova VG, Tolmach PI, Chandamirova NE, Shenyavskaya EA. Thermodynamic properties of individual substances. IVTANTHERMO for Windows database on thermodynamic properties of individual substances and thermodynamic modeling software, Version 3.0. (1992–2000). Glushko Thermocenter of RAS, Moscow

Chapter 22

Environmental Threat to Photochemical and Photobiological Reactions

Rafia Azmat

Abstract Photochemical and photobiological reactions are under consideration from the beginning of the world when man started to think about the changes occurring around him. The fact is that there is a deep relationship between man and the plants and no doubt that human life is based on oxygen and the plants are the providers of fresh oxygen. In fact this oxygen is produced when plant leaves harvest the solar radiation and major portion of this light is absorbed by the different pigments present in the leaf where CO_2 and H_2O in presence of this absorbed light react together and a glucose molecule is produced with the release of oxygen as a byproduct through biological (system) reaction which is the result of photochemical reaction. Oxygen production industry is placed naturally in plant leaves and termed as photosynthetic apparatus where various pigments through absorption of photon of light produced the food which is responsible to provide the energy for the plants survival. The photosynthetic apparatus is directly placed at open atmosphere therefore any change in the atmosphere can easily be detected by the change in the working capability of apparatus.

The change in the working capability of photosynthetic apparatus will automatically reflect on photobiological reactions. Today both photochemical and photobiological reactions are under threat of urbanization, industrialization and developments of various fields. The decline in ozone layer and presence of various pollutants may interfere in light harvesting by scattering the light before absorption in light harvestings pigments of plants. The pollutants are responsible for the disorder in normal natural processes by activating the enzymatic activity, proteins decline and metabolic variations. These changes are marked by monitoring as a bio-monitor of photochemical and photobiological reactions.

R. Azmat (✉)

Department of Chemistry, University of Karachi, 75270 Karachi, Pakistan

e-mail: rafiasaeed200@yahoo.com

22.1 Introduction

Photobiology and photochemistry of all biological reactions is a rapid developing subject and helps the understanding of photosynthesis, photophysics, phototaxis, photoiodism, photo dynamics actions, vision and mutagenic effects. In doing so it tries to integrate the knowledge of physics, chemistry and biology. Photochemistry is a branch of science which deals with reactions which are initiated electronically by excited molecule by the absorption of radiation (200–800 nm) in the visible and near ultraviolet region.

Photochemistry is basic to the world we live in. As sun is the central figure, the origin of life itself must have been a photochemical act. In the primitive earth conditions radiations from the sun were the only energy source. Through the ages nature has perfected her machinery for utilization of solar energy for all photo biological phenomena and providing food for propagation of life itself [1].

Contamination of soil and water by heavy metals is of widespread occurrence due to human and industrial activities. Many environmental pollutants like Al, Cd, Cr, Cu, Hg and Pb were targeted to check the effect of these metals on plant photo system which ultimately related with nutrition's for sustainable life and development [2–7]. A general increase in the level of heavy metals poses a pervasive threat to the natural ecosystem. Although many heavy metals when in trace amounts are essential for various metabolic processes in organisms, they create physiological stress leading to generation of free radicals when in high concentration [8–12].

Some important crops like bean and pulses were taken as a bio-monitor of photochemical and photobiological reactions, continuously taking place in the plants [2–10].

It was observed that the unrestricted developmental activities (such as industrialization and urbanization) carried out during the past few years have given rise to serious problems of environmental contamination [2]. Plants exposed to stressing agents such as drought, salinity, excess of heavy metals, air pollutants, or pathogens have developed strategic defense mechanisms that vary between species to species and the nature of stressing agent [12, 13].

Lead usually enters in plants by similar pathways as micro- and macronutrients. However, the metabolic pathways underwent by this element within plant cells are not fully understood [14]. Toxic effects include inhibition of stem leaf elongation, thickening, and dryness in plants [15, 16]. Germination of seeds and growth as a biomarker of environmental threat metal toxicity inhibits germination of seeds and seedling growths. It decreases germination percent, germination index, root/shoot, length, tolerance index and dry mass of roots and shoot [2–6].

Changes in solar UV radiation and climate change are to a great extent caused by changes in the concentration of atmospheric compounds (gases and aerosols). Atmospheric compounds not only affect solar UV radiation and climate but can have direct effects on human health, and terrestrial and aquatic ecosystem [17].

One of the most important threats is the translocation of water. Metal puts obstruction in the imbibitions of water due to which plant growth was affected.

Plant lost its immune system owing to the accumulation of metal [18]. It damages the root hairs and affects on cuticle which prevents the plant from metal toxicity. It also affects the morphology of leaves and reduce leaves expansion which ultimately related with the photosynthesis of plant. Because reduced leaf area is directly related with the absorption of CO₂ and in such a way a chain link was observed which first affects the carbohydrate metabolism, then nitrogen metabolism and mineral metabolism [19–22].

22.2 Photochemical Apparatus Under Environmental Threat

Heavy metal pollution in the aquatic systems has become a serious threat today. The chemical processes that exist are not economical for treating a large volume of water bodies of dilute metal concentration. Aquatic resources are polluted by the industrial sewage sludge, which contain high percentages of toxic metals. The polluted water used for irrigation purpose, produced bad effect on the crops [10]. The photosynthetic pigments are some of the most important internal factors, which in certain cases are able to limit the photosynthesis rate. There is a considerable decrease of chlorophyll and caretonoid content under metals and UV radiation. A reduction of the pigment content in the case of increasing levels of heavy metals and metalloids was also established [10, 11]. This may be due to the accumulation of metal in porphyrin ring of the chlorophyll where metal displaced the Mg due to which processes of the photosynthesis was affected because light energy absorbed by chloroplast pigments is transferred to chlorophyll then it activates photosynthesis. It may reduce the quantum yield of oxygen which is released after the quanta of light absorbed and this decrease in quantum yield of oxygen may affect the environment [23, 24].

Metal/UV radiation changes morphology of plant. It was more green in presence of Cr [3] as compared to control one while more dark green in presence of Pb [10, 11] and yellow green in presence of Cd [5, 7] whereas it turned black in presence of Cu and red in case of UV radiation. The root and shoot length are decreased with the increase in the concentration of metal.

When spectral analysis of chloroplast pigments were performed under the stress of UV and metals, the resultant spectrum demonstrates intermediate characteristics, of changes due to stress depending on the particular peak under consideration (the blue maximum or the red maximum). Results showed that seedlings receiving the lowest supplemental UV-C irradiance showed reduction in growth and photosynthetic capacity instantly after receiving first initial dose of only one min of irradiation and pots left for normal growth by placing them into normal sunlight. But the effect was deleterious and persisted to results in lower biomass production, with an increase in UV-C absorbing compounds in seedlings [17].

22.3 Environmental Threat to N Metabolism

It is generally accepted that heavy metals can be major toxicants in plant cells due to their potential inhibitory effects on many physiological and biochemical processes. The toxicity of heavy metals may arise as a result of the generation of ROS that may cause wide-ranging damage to proteins, nucleic acids and lipids, eventually leading to cell death [25].

Protein content may be considered a reliable *indicator* of oxidative *metal stress* in plants. Increase in protein content under heavy metal (Al and Cu) stress in beans indicates that it may contain a larger proportion of proline. Binding with metal ions due to the chelating ability of proline (an amino acid) can also be a defense mechanism for survival. In case of Cd, protein content decreased from 19.0–71.4% in metal exposed plants at metal concentrations equivalent to those found in polluted soil. Diverse biochemical changes in observed plants in response to metals leading to reduction in protein and nitrogen contents of plants suggested that affects of metal on plant were related with the type of plant and metal [23].

In case of Al, protein was found to increase whereas in all other toxic metals protein degraded due to an increase in protease activity or role of plant metallothioneine – like protein and phytochelatin which showed strong interaction towards metals. These changes suggested that plant system reworks in stress environment where adaptation leads to survival in many cases but these adaptations may be a cost to health of plant animal, or human being [24].

22.4 Environmental Threat ions is Mineral Metabolism

It has been observed that uptake of heavy metals by plant may interfere the plant mineral metabolism through reduction of essential mineral ions due to which cutback in plant growth was observed.

Significant reduction in contents of essential Ca, Mg, Na, K, Mn, and Fe were recorded in the three species of *Vigna radiate*, *Phaseolus mungo* and *Lens culinaris* due to elevated concentration of Cr and Pb. The probable mechanism of disturbance in uptake of these mineral by physical blocking from absorption sites of root which ultimately lead to decrease of the root growth due to inhibition of cell division. The decrease in concentration of Mg and Ca was probably a result of osmotic adjustment with the cost of photosynthesis. A deficiency of K results in depletion in protein synthesis, quality of fruits and size of leaves [3, 18].

Calcium deficiency is generally a result of an imbalance of K and Mg contents due to which demorphology in leaves and shape was observed. Mn is involved in enzymes activity like synthesis of fatty acid, DNA, RNA formation for plants growth. A lowering in concentration of these biocatalytic trace metals like Fe, Mn, Zn, Co results in overall decrease in healthy crop production for safe life on earth [18, 24–26].

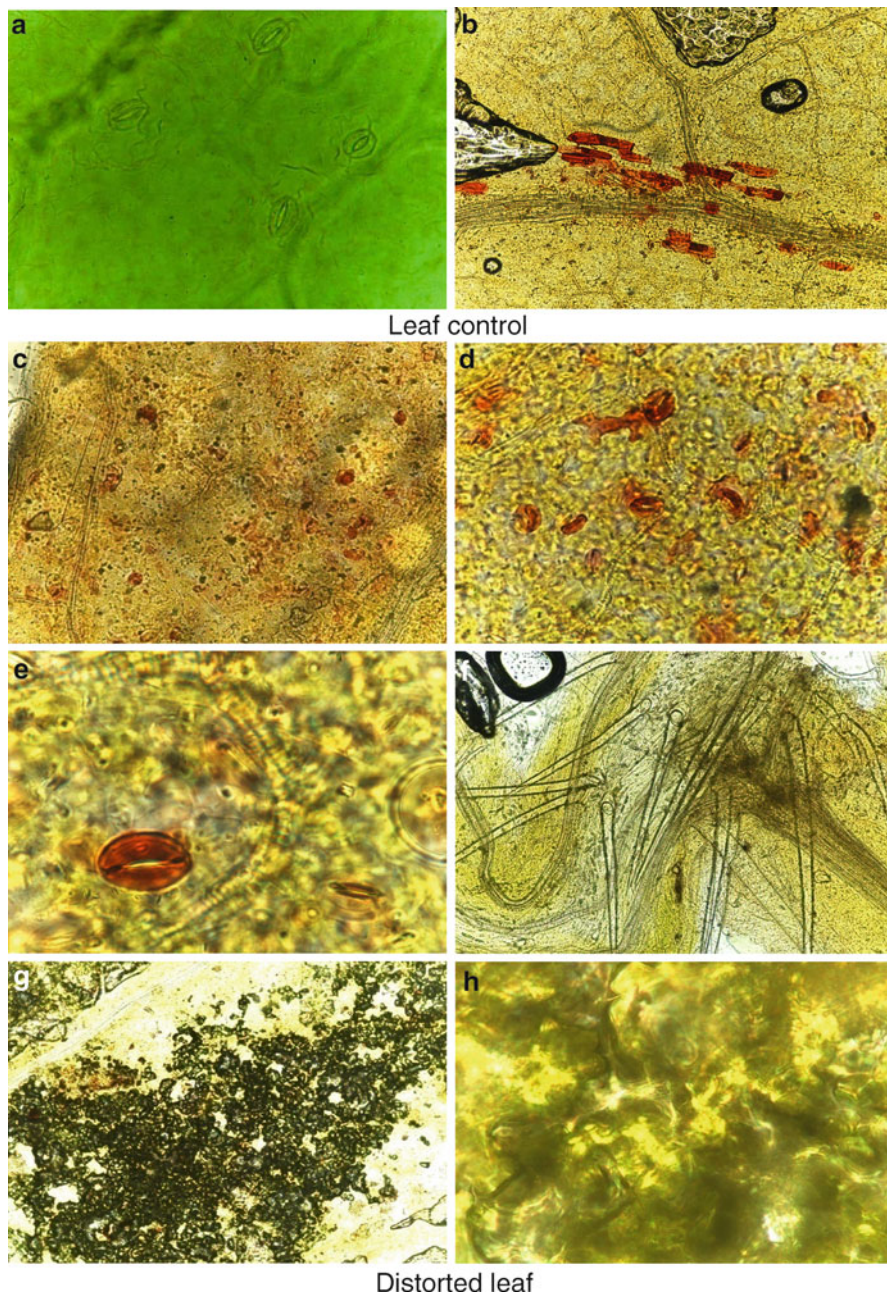


Fig. 22.1 Morphology of leaf under metal (Pb) stress (by light camera microscope) (a) morphology of control leaf, (b) red pigmentation due to metal/UV stress, (c) metal accumulation and changes in chloroplast pigment, (d) red pigments around stomata, (e) changes in red pigmentation and metal accumulation, (f) leaf hair formation, (g) metal ion deposition, (h) complete destruction of photosynthetic apparatus, (i) stem of control plant, (j) movement of metal, (k) loosening of vascular tissues, (l) damage of vascular bundles, (m) destruction of vascular bundle, (n) complete breakdown of vascular tissues

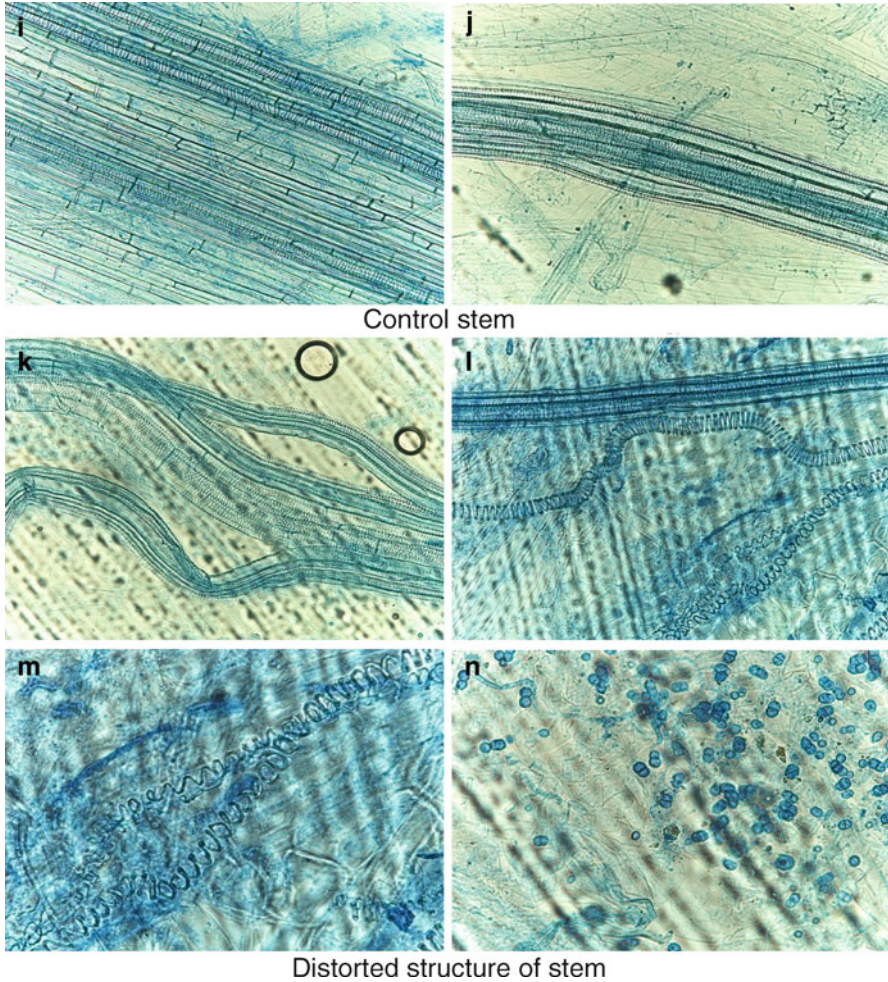


Fig. 22.2 (continued)

22.5 Mechanism of Metal Accumulation

Mechanism of metal accumulation is not fully understood. Metal ions send the false signal to the plant [10] and the absorption of metals followed the same role of absorption as the essential mineral ions. It depends upon time and is dose dependent varying from species to species. Sometimes it stimulates the growth but sometimes reduced the growth but after sometime plant dies. Mechanism has been suggested for the Pb that Pb replaced the Mg in the porphyrin ring of chlorophyll due to their higher entropy of activation.

Photosynthetic apparatus is a group of the collaborating molecules of pigments of biological system which is essential for photochemical phase. When photon of light is absorbed it migrates through these collaborating molecules to the reaction center or trapping center with release of an electron. It is possible that released electron may be trapped by the toxic metal due to which photosynthesis was reduced.

It was suggested for probable mechanism of metal accumulation that high optical density (absorbance of solution) observed during analysis of chlorophyll, might indicate the maximum concentration of heavy metal in leaves (Fig. 22.1a–h) which could lead to decrease chlorophyll contents. That was also supported by the reduced leaves size and growth of seedlings length due to distorted structure of stem (Fig. 22.1i–n) [24].

22.6 Conclusions

The results of research of last few years on trace metal accumulation in plants suggested that metals as environmental pollutants are threats to the life via food chain. New technologies should be developed and encouraged by the state to save the life on surface of earth.

Acknowledgment Author is very thankful to the organizers of ICPAC for providing the financial assistance through OPCW to attend the conference to share the views at international forum with the scientists of repute countries.

References

1. Rohatgi-Mukherjee KK (1986) Fundamentals of photochemistry, Revised edn. New age International publisher, New Delhi
2. Azmat R, Naz F, Khanum T, Hayat A (2005) Persistence of pathogens in heavy metal contaminated environment. Pak J Biol Sci 8:235–238
3. Azmat R, Hayyat A, Khanum T, Talat R, Uddin F (2006) The inhibition of bean plant metabolism by Cd metal and atrazin III. Effect of seaweed *Codium iyengarii* on metal, herbicide toxicity and rhizosphere of the soil. Biotechnology 5:85–89
4. Azmat R, Parveen R, Naqvi II, Shoukat S (2005) Effect of Cr(III) combine with atrazine on protein, carbohydrate, amino acid and chlorophyll content in *Vigna radita* (L.) Wilczek International. J Biol Biotechnol 2:433–439
5. Azmat R, Khanum R (2005) Effect of chromium on uptakes of minerals in bean plant. Pak J Biol Sci 8:281–283
6. Azmat R, Zill-e-Huma HA, Khanum T, Talat R (2005) The inhibition of bean plant metabolism by cadmium metal I: effect of Cd metal on physiological process of bean plant and rhizobium species. Pak J Biol Sci 8:401–404
7. Azmat R, Iftikar B, Khanum T, Hayyat A, Talat R, Uddin F (2005) The inhibition of bean plant metabolism by cadmium metal II: the inhibition of mineral acquisition in heavy metal contaminated environments. Pak J Biol Sci 8:748–750

8. Azmat R, Akhtar Y, Talat R, Uddin F (2005) The inhibition of bean plant metabolism by Cd metal and atrazine: I. Effect of atrazine with Cd metal on growth, photosynthesis, nutritional level and rhizosphere of soil. *Biotechnology* 4:238–242
9. Azmat R, Uddin F (2005) The inhibition of bean plant metabolism by Cd metal and atrazine: II. The inhibition of bioremediation of atrazine in heavy metal environment and its effect on mineral nutrients of bean plant. *Biotechnology* 4:262–266
10. Azmat R, Hayat A, Khanum T, Talat R, Uddin F (2006) Effect of micronutrients of *Codium iyengarii* on metal toxicity in bean plants. *J Biol Sci* 6:173–177
11. Azmat R, Askari S, Haider S (2006) Effect of toxic metal mercury on histomorphology of *Cymopsis tetragoloba*. *Asian J Cell Biol* 1:34–39
12. Shamsi IH, Wei K, Jilani G, G-ping Z (2007) Interactions of cadmium and aluminum toxicity in their effect on growth and physiological parameters in soybean. *J Zhejiang Univ Sci B* 8:181–188
13. Sharma P, Dubey RS (2005) Lead toxicity in plants. *J Plant Physiol* 17:35–52
14. Patra M, Bhowmik N, Bandopadhyay B, Sharma A (2004) Comparison of mercury, lead, and arsenic with respect to genotoxic effects on plant systems and the development of genetic tolerance. *Environ Exp Bot* 52:199–223
15. Azmat R, Haider S, Askari S (2006) Phytotoxicity of Pb I : effect of Pb on germination, growth, morphology and histomorphology of *Phaseolus mungo* and *Lens culinaris*. *Pak J Biol Sci* 9:979–984
16. Haider S, Kanwal S, Uddin F, Azmat R (2006) Phytotoxicity of Pb: II. Changes in chlorophyll absorption spectrum due to toxic metal Pb stress on *Phaseolus mungo* and *Lens culinaris*. *Pak J Biol Sci* 9:2062–2068
17. Azmat R, Nasreen H (2010) Marine green algae as the supplement of chlorophyll and other nutrients in the stress of UV-C radiation in *Vigna radiate*. *J Chem Chem Eng* 4:1–9
18. Azmat R, Uzma UF (2007) Biosorption of toxic metals from solid sewage sludge by marine green algae. *Asian J Plant Sci* 6:42–45
19. Azmat R, Haider S (2007) Effect of Pb stress on phytochemistry of *Phaseolus mungo* and *Lens culinaris*. *Asian J Plant Sci* 6:332–337
20. Azmat R, Talat R, Qurashi S, Mahmood SJ (2007) Metal and herbicide toxicity effect on crops, rhizosphere. *Saudi J Chem Soc* 11:101–110
21. Azmat R, Parveen R, Naqvi II (2007) Effect of chromium combined with atrazine on potassium, sodium, manganese, iron and phosphate in roots and shoots in bean *Vigna radiata* (L.) Wilczek. *Saudi J Chem Soc* 11:111–120
22. Askari S, Uddin F, Azmat R (2007) Biosorption of Hg: I. Significant improvement with marine green algae in the anatomy of hypocotyls of *Trigonella foenumgracum* under Hg stress. *Pak J Bot* 39:1089–1096
23. Azmat R, Hasan S, Uddin F (2007) Aluminium stress induced alteration in seedling growth and alleviation in protein and amino acid contents of *Lens culinary*. *Asian J Plant Sci* 6:1246–1250
24. Azmat R, Hasan S (2008) Photochemistry of light harvesting pigments of *Lens culinaris* under Al stress. *Pak J Bot* 40:779–784
25. Azmat R, Haider S, Riaz M (2009) An inverse relation in between Pb^{2+} and Ca^{2+} ions accumulation in *Phaseolus mungo* and *Lens culinaris* under Pb stress. *Pak J Bot* 41:2289–2295
26. Azmat R, Riaz M, Nasreen H, Aziz F, Haider S (2009) A viable alternative mechanism in adapting the plants to heavy metal environment. *Pak J Bot* 41:2729–2738

Chapter 23

Neutral-Neutral Direct Hydroamination Reactions of Substituted Alkenes: A Computational Study on the Markovnikov Selection Rule

Sanyasi Sitha and Linda L. Jewell

Abstract We have carried out a detailed computational study on the neutral-neutral direct hydroamination reactions between various substituted ethylene derivatives with ammonia, using the density functional theory based on B3LYP/6-31++G(2df,2p) level of theory. Analysis of the potential energy surfaces for all these reactions shows that in all these cases, thermodynamically the Markovnikov product is more stable than the anti-Markovnikov product. Analysis of the transition states for all these reactions shows that kinetically in some cases the Markovnikov product is preferable whereas other cases the anti-Markovnikov product is preferable. This gives a clear indication on how to control the selectivity in these reactions by mere alteration of the substituent. We observed that, in the case of ethylene with an electron withdrawing substituent (i.e. $\text{CH}_2=\text{CH}-\text{NO}_2$) reacting with ammonia, the barrier height is reduced by approximately 70 kJ/mol and at the same time the anti-Markovnikov product is preferred kinetically. This situation clearly mimics the general catalytic hydroamination reaction where the ethylene is being activated by the catalyst. Also, this suggests that a stronger electron withdrawing group than $-\text{NO}_2$ will possibly be able to reduce the barrier height further and ultimately a non-catalytic neutral-neutral direct hydroamination reaction will be physically attainable.

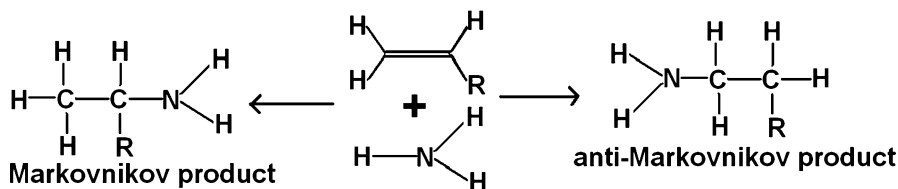
23.1 Introduction

The hydroamination of alkenes, which proceeds through the formal addition of an N–H bond across a carbon-carbon double bond, is an elegant synthetic organic transformation, which offers an attractive route to numerous classes of

S. Sitha (✉) • L.L. Jewell

School of Chemical and Metallurgical Engineering, University of the Witwatersrand,
Private Bag 3, Wits 2050 Johannesburg, South Africa

e-mail: sanyasi.sitha@wits.ac.za; linda.jewell@wits.ac.za



Scheme 23.1 Hydroamination reaction of substituted ethylene with ammonia

organo-nitrogen molecules such as alkylated amines, enamines or imines [1–15]. The synchronous direct addition of ammonia to an alkene to produce the amine is of seemingly fundamental simplicity and is highly desirable from an industrial point of view, as several tons of amines are produced worldwide every year [1, 2, 8]. From a thermodynamic standpoint the reaction is exothermic under standard conditions and feasible [7]. But, a large activation barrier and large negative reaction entropy make the reaction very difficult and a detailed description can be found in our previous work [16]. In our previous work we have shown that in fact the reaction has a very large activation barrier of 274.0 kJ/mol and a very large negative reaction entropy of $-138.9 \text{ J/mol}\cdot\text{K}$ and are mainly responsible for forbidding the reaction from proceeding in the forward direction [16].

Now, it will be of interest to see how these key factors will be affected in the case of neutral-neutral direct hydroamination reaction between a “*substituted alkene and ammonia*”. Once the ethylene is substituted with a suitable substituent in one side, the molecular symmetry of the ethylene will be completely lost. Hence, unlike the earlier case of reaction between $\text{CH}_2=\text{CH}_2$ and NH_3 where one can get only a single product, in the case of the reaction of a substituted ethylene with NH_3 there is a possibility of two different products, based on the direction of approach of NH_3 towards the substituted ethylene moiety. The two reaction paths leading to two different products are shown in Scheme 23.1, one is the Markovnikov and other is the anti-Markovnikov product.

In our earlier work we have shown that the neutral-neutral direct hydroamination reaction between the $\text{CH}_2=\text{CH}_2$ and NH_3 proceeds through a concerted type of mechanism with a four centred transition state [16]. Analysis of the TS showed that the N-H bond of the ammonia is aligned parallel to the C=C of the ethylene and at the same time NH_2 -fragment of the NH_3 reacts with one of the carbon atoms of the ethylene and the H-fragment of the NH_3 reacts with the other carbon atom of the ethylene, simultaneously [16]. As $\text{CH}_2=\text{CH}_2$ is symmetric in nature, the approach of the NH_3 unit from either side of the ethylene will have no effect and ultimately lead to only one product. On the other hand, once the ethylene is substituted, the approach of the NH_3 molecule from the side of unsubstituted C-atom of ethylene will definitely result a different interaction than the approach of the NH_3 from the substituted C-atom of the ethylene. This type of situation ultimately will lead to two different types of products as shown in Scheme 23.1. The Markovnikov rule says that if the addition reaction proceeds through a carbocation

intermediate, the Markovnikov product will be dominant and for other type of mechanism mostly the anti-Markovnikov product will be preferable [17]. As the neutral-neutral hydroamination reaction between the $\text{CH}_2=\text{CH}_2$ and NH_3 proceeds through a concerted type of mechanism, a similar kind of mechanism can be predicted for substituted ethylenes reacting with ammonia. Now it will be interest to see whether the reaction between the substituted ethylene and ammonia shows preference for the Markovnikov or anti-Markovnikov product. So, in this work we have carried out a detailed computational study for the analysis of the neutral-neutral hydroamination reaction between substituted ethylene and ammonia, using density functional theory.

23.2 Computational Methods

In our earlier work related to the hydroamination reaction we have shown that the MP2 and B3LYP methods are equally suitable for mapping the reaction surface [16]. Hence, keeping eye on the computational time, we have carried out all the calculations using B3LYP/6-31++G(2df,2p) [henceforth referred as B3LYP] level of theories, implemented in the Gaussian 03 program package [18]. A very large basis set like 6-31 Pople's basis set combined with double diffuse functions, with the addition of two sets of d-functions and one set of f-functions on the C and N atoms, and 2 sets of p-functions on the hydrogens, to obtain a high level of accuracy in the energetic results. All the energetics reported in this work are ZPE corrected values. For the molecules with iodine substitution we have used an extra basis "MidiX" over the iodine atom(s). The true minima and the transition states were confirmed from analysis of frequencies by ensuring that all frequencies were positive for a minimum, and with only one imaginary frequency for the transition state. We have also carried out the analysis of the displacement vectors for the imaginary frequency to ascertain that the TS is a structurally true TS. All the thermodynamic quantities were calculated from the zero point energy corrected energies of the reactants, transition states and products.

23.3 Results and Discussion

As discussed above, the neutral-neutral hydroamination reaction between the substituted ethylene and ammonia proceeds through two different reaction paths, ultimately leading to the formation of either Markovnikov or anti-Markovnikov products. Although the Markovnikov and anti-Markovnikov products are isomers their stabilities in the PES can be expected to be different due to the presence of intramolecular interactions. This results in thermodynamic selection either towards the Markovnikov or anti-Markovnikov product. In addition, the potential barrier associated with the reaction, will control the selection of the reaction paths via

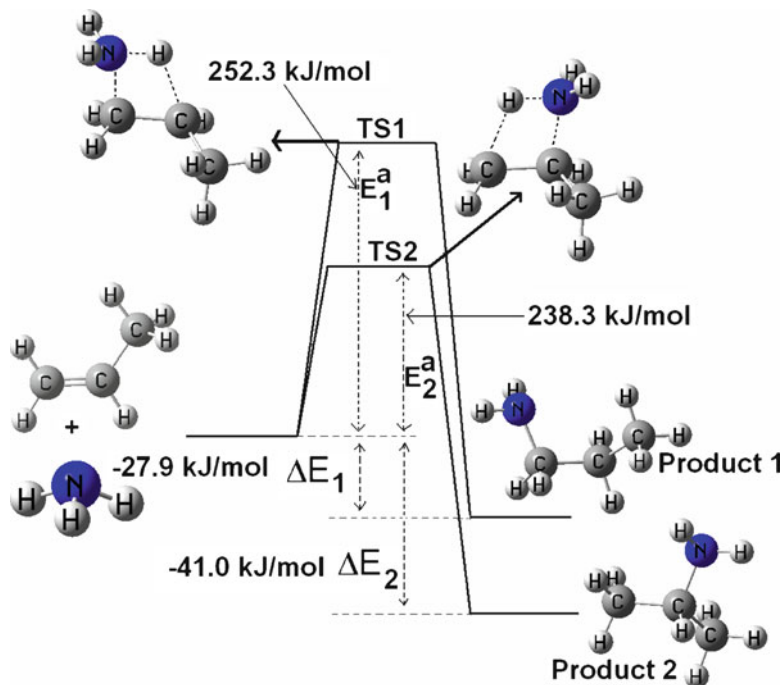


Fig. 23.1 Potential energy surface of the neutral-neutral hydroamination reaction between methyl substituted ethylene and ammonia. All the energies are ZPE corrected. Energy levels are not to scale

kinetics. Hence, to account for these effects we have carried out the neutral-neutral hydroamination reaction between ethylene with various substituents and ammonia. According to the chemical nature of those substituents, they can be classified as neutral or alkyl substituents ($-\text{CH}_3$ and $-\text{C}_2\text{H}_5$), halogen substituents ($-\text{F}$, $-\text{Cl}$, $-\text{Br}$ and $-\text{I}$), electron donating substituents ($-\text{OH}$ and $-\text{OCH}_3$), and electron withdrawing substituents ($-\text{CN}$ and $-\text{NO}_2$).

23.3.1 Alkyl Substituted Ethylene + Ammonia

The PES of the hydroamination reaction between methyl substituted ethylene and ammonia calculated using the B3LYP method is shown in Fig. 23.1. The details of the structural parameters and other properties of the reactants, products and the transition states are given in the supporting information (available from the author). As shown in Fig. 23.1, the reaction proceeds through two different paths. Path 1, proceeds through TS1 and ends in Product 1, and Path 2 proceeds through TS2 to give the Product 2 (The same convention is applied throughout the article). Product 1 is the anti-Markovnikov product and Product 2 is the Markovnikov product.

Comparing the product energies with the reactant energies it can be seen that the anti-Markovnikov product is -27.9 kJ/mol more stable, while product 2 which is the Markovnikov product is -41.0 kJ/mol more stable than the reactants. This indicates that the reaction leading to the formation of a Markovnikov product is thermodynamically preferable to the reaction leading to the formation of the anti-Markovnikov product. Analysis of TS1 and TS2 shows that they are true transition states structurally as well as energetically. Comparing the energy of TS1 and TS2 with the reactants shows that the reaction Path 1 proceeds through a barrier of 252.3 kJ/mol, whereas reaction Path 2 proceeds through a barrier of 238.3 kJ/mol. This indicates that reaction Path 2, which leads to the formation of the Markovnikov product (Product 2), is kinetically preferable to reaction Path 1 which leads to the formation of an anti-Markovnikov product (Product 1). Thus in the neutral-neutral hydroamination reaction of methyl substituted ethylene with ammonia, the formation of a Markovnikov product is thermodynamically as well as kinetically preferred over the formation of an anti-Markovnikov product. Another important factor affecting the direct hydroamination reaction is the ΔS_R value (difference between the entropy of the product and total entropies of the reactants). In the case of the simple $\text{CH}_2=\text{CH}_2 + \text{NH}_3$ reaction, the ΔS_R value is highly negative and thus prohibits the reaction from occurring at high temperature (yet reaction at high temperature is needed due to the high reaction barrier height) [16]. ΔS_R values for the reaction leading to the formation of Product 1 and Product 2 were calculated and are found to be -152.9 and -157.2 J/mol-K respectively. This clearly indicates that, the high value of entropy will also prevent this reaction from moving in the forward direction.

Similar to the above reaction, we have also carried out calculations for the PES of the hydroamination reaction between ethyl substituted ethylene and ammonia using the B3LYP method. The PES obtained for this reaction is similar to the PES of Fig. 23.1. The details of the structural parameters and other properties of the reactants, products and the transition states are given in the supporting information. Comparing the product energies with the reactant energies it can be seen that the anti-Markovnikov product (Product 1) is -21.1 kJ/mol more stable, while product 2 (which is the Markovnikov product) is -38.4 kJ/mol more stable than the reactants. This indicates that the reaction leading to the formation of a Markovnikov product is thermodynamically preferable to the reaction leading to the formation of the anti-Markovnikov product. Analysis of TS1 and TS2 for this reaction also shows that they are true transition states structurally as well as energetically, and are geometrically similar to the transition states shown in Fig. 23.1. Comparing the energy of TS1 and TS2 with the reactants shows that reaction Path 1 proceeds through a barrier of 249.5 kJ/mol, whereas reaction Path 2 proceeds through a barrier of 236.3 kJ/mol. This indicates that the reaction Path 2 which leads to the formation of a Markovnikov product (Product 2) is kinetically preferable over the reaction Path 1 which leads to the formation of an anti-Markovnikov product (Product 1). Thus in the neutral-neutral hydroamination reaction of ethyl substituted ethylene with ammonia, the formation of a Markovnikov product is also both thermodynamically and kinetically preferred over the formation of the anti-Markovnikov product.

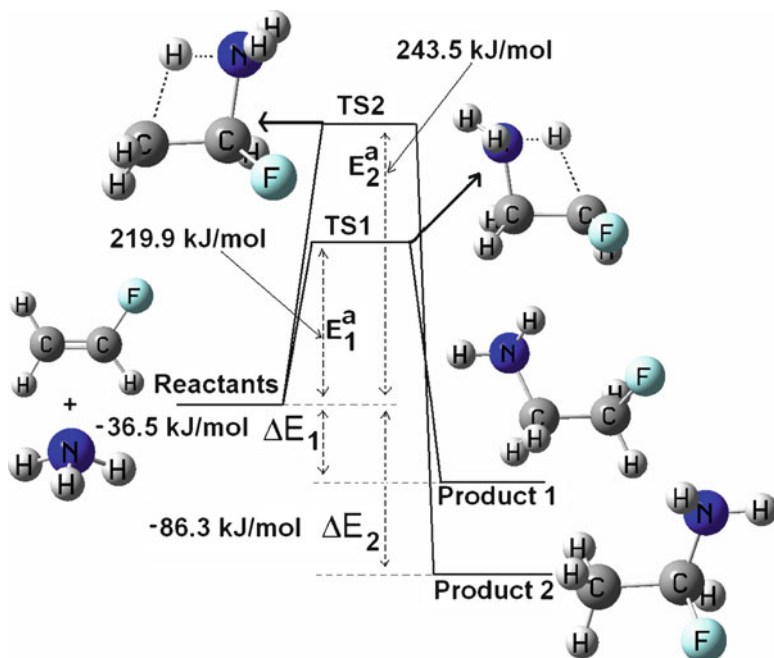


Fig. 23.2 Potential energy surface of the neutral-neutral hydroamination reaction between fluorine substituted ethylene and ammonia. All the energies are ZPE corrected. Energy levels are not to scale

We have also calculated the ΔS_R values for the reaction leading to the formation of Product 1 and Product 2 which were found to be -159.9 and -157.5 J/mol-K respectively. This clearly indicates that, entropy will also forbid this reaction moving in the forward direction at high temperatures.

Analysis of the PESs for methyl and ethyl substituted ethylene shows that, both the surfaces are similar and also the reaction energetics are almost same. This gives an indication that substitution of a higher alkyl group does not have much effect on the reaction PES.

23.3.2 Halogen Substituted Ethylene + Ammonia

The PES of the hydroamination reaction between fluorine substituted ethylene and ammonia calculated using the B3LYP method is shown in Fig. 23.2. For the chlorine and the bromine substituted ethylene case, we got similar PESs to that of the fluorine case (as shown in Fig. 23.2). However for the iodine case a slightly different picture was observed. Also, these surfaces are different from the PES shown in Fig. 23.1. The details of the structural parameters and properties

of the other reactants, products and transition states are given in the supporting information. From Fig. 23.2, comparing the reactant energies with product energies it can be seen that Product 1 is -36.5 kJ/mol more stable, while product 2 is -86.3 kJ/mol more stable than the reactants. This indicates that the reaction leading to the formation of a Markovnikov product is thermodynamically preferable to the reaction leading to the formation of the anti-Markovnikov product. For the chlorine, bromine and iodine substituted cases we have observed similar situations, indicating that the Markovnikov product is thermodynamically preferable to the anti-Markovnikov product. The stabilization energies for Product 1 and Product 2 are -41.7 and -76.2 kJ/mol respectively for chlorine substitution, -45.2 and -77.8 kJ/mol respectively for bromine substitution, and -48.0 and -74.6 kJ/mol respectively for the iodine substitution.

Analysis of TS1 and TS2 in all the reaction surfaces shows that they are true transition states structurally as well as energetically. Also, structurally TS1 and TS2 for all these halogen substituted cases are similar and look similar to the transition states shown in Fig. 23.2. From Fig. 23.2, it can be seen that reaction Path 1 proceeds through a barrier of 219.9 kJ/mol, whereas reaction Path 2 proceeds through a barrier of 243.5 kJ/mol. This indicates that reaction Path 1 which leads to the formation of the anti-Markovnikov product (Product 1) is kinetically preferable over reaction Path 2 which leads to the formation of the Markovnikov product (Product 2). Thus in the neutral-neutral hydroamination reaction of fluorine substituted ethylene with ammonia, the formation of a Markovnikov product is thermodynamically preferable, whereas the formation of an anti-Markovnikov product is kinetically preferable. We observed a similar kind of trend for the bromine and iodine substituted cases, but unlike the fluorine case the TS1 and TS2 energies are quite close in the hydroamination of chlorine and bromine substituted ethylene. The activation energies for the TS1 and TS2 are 219.7 and 220.4 kJ/mol respectively for the chlorine case, and 213.5 and 214.1 kJ/mol respectively for the bromine case. The PES of the iodine case showed a different trend than the above three cases. The barrier heights of TS1 and TS2 with respect to the reactants for the iodine case are 211.9 and 211.2 kJ/mol respectively indicating that TS2 is slightly more stable than TS1. The reason for this behavior for the iodine case is quite unclear at this time. For the iodine case, instead of the standard 6-31++G(2df,2p) basis set applied to the entire system, an extra basis set 'MidiX' was applied over the iodine atom. Hence, this is due to the basis set or some other factor may be affecting this reaction; this phenomenon needs further investigation.

We have also calculated the ΔS_R values for the reaction leading to the formation of Product 1 and Product 2. We found that the ΔS_R values are -152.8 and -156.0 J/mol·K respectively for the fluorine case; -153.7 and -154.8 J/mol·K respectively for the chlorine case; -153.4 and -154.7 J/mol·K for the bromine case and -155.1 and -154.8 J/mol·K for the iodine case. This clearly indicates that, the high value of entropy will prevent all these reactions from moving in the forward direction at high temperatures.

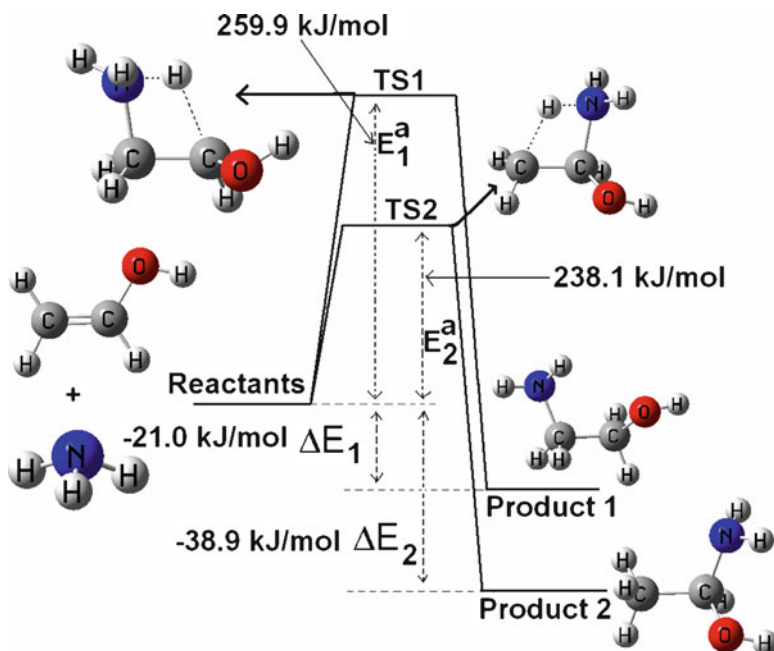


Fig. 23.3 Potential energy surface of the neutral-neutral hydroamination reaction between hydroxy substituted ethylene and ammonia. All the energies are ZPE corrected. Energy levels are not to scale

23.3.3 *Electron Donating Group Substituted Ethylene + Ammonia*

The PES of the hydroamination reaction between ethylene with a hydroxy group substituent (i.e. an electron donating group) and ammonia calculated using the B3LYP method is shown in Fig. 23.3. For the methoxy case we got a similar PES to that shown in Fig. 23.3. The details of the structural parameters and other properties of the reactants, products and the transition states are given in the supporting information. From analysis of the PES for the hydroxy case, it can be seen that the anti-Markovnikov product (Product 1) is -21.0 kJ/mol more stable, and Product 2 (Markovnikov product) is -38.9 kJ/mol more stable than the reactants. Similarly, analysis of the PES for the methoxy case shows that Product 1 is -23.9 kJ/mol more stable, while Product 2 is -55.5 kJ/mol more stable than the reactants. This indicates that in both hydroxy and methoxy substitution cases, the reaction leading to the formation of a Markovnikov product is thermodynamically preferable to the reaction leading to the formation of the anti-Markovnikov product.

Analysis of TS1 and TS2 for both of the surfaces shows that they are true transition states structurally as well as energetically and the transition states for

the methoxy surface are geometrically similar to TS1 and TS2 respectively of the hydroxy surface (Fig. 23.3). In the hydroxy case, comparing the energy of TS1 and TS2 with the reactants shows that the reaction Path 1 proceeds through a barrier of 259.9 kJ/mol, whereas reaction Path 2 proceeds through a barrier of 238.1 kJ/mol. This indicates that reaction Path 2 which leads to the formation of a Markovnikov product (Product 2) is kinetically preferred over reaction Path 1 which leads to the formation of an anti-Markovnikov product (Product 1). Thus in the neutral-neutral hydroamination reaction of hydroxy substituted ethylene with ammonia, the formation of a Markovnikov product is thermodynamically as well as kinetically preferable to the formation of an anti-Markovnikov product. Similar behavior was observed for the methoxy case. The calculated barrier height for TS1 was found to be 256.2 kJ/mol and for that of the TS2 is 230.9 kJ/mol.

We have also calculated the ΔS_R values for both the surfaces. For the hydroxy surface, the ΔS_R values are -153.5 and -163.4 J/mol·K respectively for Product 1 and Product 2. Similarly, for the methoxy surface, the ΔS_R values are found to be -169.4 and -171.2 J/mol·K respectively for Product 1 and Product 2. This clearly indicates that the entropy will forbid the reactions from moving in the forward direction at high temperatures.

23.3.4 *Electron Withdrawing Group Substituted Ethylene + Ammonia*

The PES of the hydroamination reaction between ethylene with a cyano group substituent (an electron withdrawing group) and ammonia calculated using the B3LYP method is shown in Fig. 23.4. We got a similar surface for the nitro case. The details of the structural parameters and other properties of the reactants, products and the transition states are given in the supporting information. In the cyano case, the PES shows that, the anti-Markovnikov product (Product 1) is -36.2 kJ/mol more stable, while the Markovnikov product (Product 2) is -37.8 kJ/mol more stable than the reactants. Product 2 is only 1.6 kJ/mol more stable than Product 1. On the other hand, from analysis of the PES for the nitro case, it can be seen that Product 2 is -73.8 kJ/mol and Product 1 is -43.9 kJ/mol more stable than the reactants and at the same time Product 2 is around 30 kJ/mol more stable than Product 1. This indicates that in these two cases the reaction leading to the formation of the Markovnikov product is thermodynamically preferred to the reaction leading to the formation of the anti-Markovnikov product. At the same time the effect is more distinct in the case of nitro substitution than cyano substitution.

Analysis of TS1 and TS2 for both the cyano and the nitro cases shows that the TSs obtained are true transition states structurally as well as energetically. For the cyano case, analysis of the PES shows that the barrier heights leading to TS1 and TS2 are 178.5 and 243.3 kJ/mol respectively with respect to the reactants. This indicates that reaction Path 1 which leads to the formation of the anti-Markovnikov

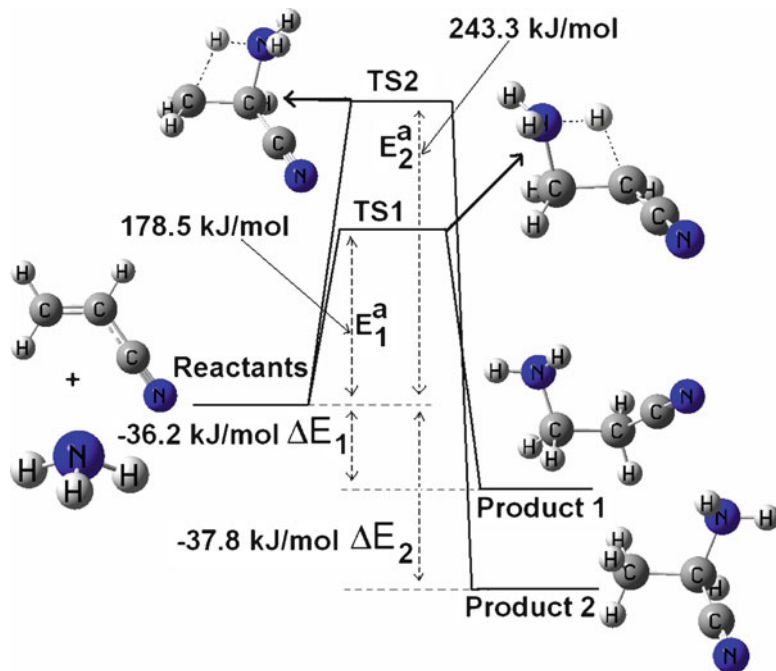


Fig. 23.4 Potential energy surface of the neutral-neutral hydroamination reaction between cyano substituted ethylene and ammonia. All the energies are ZPE corrected. Energy levels are not to scale

product (Product 1) is kinetically preferable to reaction Path 2 which leads to the formation of the Markovnikov product (Product 2). Note that the barrier height for the reaction path is drastically reduced and is now around 175 kJ/mol. We also observed a similar situation for the nitro case, where the barrier height for reaction Path 1 is now 145.8 kJ/mol and at the same time the barrier height for reaction Path 2 is around 216.1 kJ/mol. This drastic decrease in the barrier heights for these cases is significant for the reaction kinetics. Thus in the neutral-neutral hydroamination reaction of ethylene with an electron withdrawing substituent with ammonia, the formation of the Markovnikov product is thermodynamically preferable, but kinetically the formation of an anti-Markovnikov product is preferable.

We have also calculated the ΔS_R values for these two reaction surfaces. For the cyano surface, the ΔS_R values are -151.8 and -153.5 J/mol·K respectively for Product 1 and Product 2. For the nitro surface, we found the ΔS_R values to be -150.6 and -150.7 J/mol·K respectively for Product 1 and Product 2. As for all the earlier cases, this clearly indicates that the entropy will forbid these two reactions from moving in the forward direction at high temperatures.

23.4 Conclusions

In summary, we have carried out a computational study on the PESs of neutral-neutral hydroamination reactions between various substituted ethylenes and ammonia, using the B3LYP/6-31++G(2df,2p) level of theory. It is well known that Markovnikov addition proceeds through a carbocation intermediate to give the Markovnikov product. On the other hand if the reaction proceeds through a mechanism other than carbocation intermediate one gets the anti-Markovnikov product. Contrary to this, analysis of all these reaction surfaces confirms that though the neutral-neutral direct hydroamination reaction is going through a four-centre (concerted type of reaction mechanism) transition state, thermodynamically the Markovnikov product is preferred over the anti-Markovnikov product. Also, we observed that, like that of the simple $\text{CH}_2=\text{CH}_2 + \text{NH}_3$ reaction, the large negative values of the reaction entropies will prohibit the reactions in moving in the forward direction as temperature increases. Analysis of the reactions between the alkyl group substituted ethylene and ammonia shows that thermodynamically as well as kinetically the Markovnikov product is preferred over the anti-Markovnikov product. Similar behaviour was observed for the reactions between the electron donating group substituted ethylene and ammonia. On the other hand, a different type of behaviour was observed for the reactions between the electron withdrawing group substituted ethylene and ammonia. In these reactions it was observed that kinetically the anti-Markovnikov product is preferred, whereas thermodynamically the Markovnikov product is more stable. We observed more or less similar behaviour for the reactions between the halogen substituted ethylene and ammonia, where the Markovnikov product is preferable thermodynamically and anti-Markovnikov product is preferable kinetically. The iodine case is anomalous in that the Markovnikov product is thermodynamically more stable but the barrier heights (which control the kinetics) of TS1 and TS2 are almost the same in energy. This behaviour might be due to the use of MidiX extra basis for the iodine or some other factors might be contributing to this and needs further investigation. Interestingly, in case of the reactions between the electron withdrawing group substituted ethylene with ammonia, we found a drastic decrease in the reaction barrier of the order of 70 kJ/mol and the preference is kinetically towards the anti-Markovnikov product. This behaviour clearly mimics the catalytic process, where barrier height is sufficiently low for the reaction to proceed and at the same time the product in most cases is the anti-Markovnikov product [1, 2, 19, 20]. In the catalytic process, the catalyst activates the ethylene, thus resulting in a decrease in the electron density on the ethylene (or substituted ethylene) reactant and in this case, for example the nitro group substituted case, a similar decrease in the electron density in the ethylene carbons can be expected due to the presence of the electron withdrawing group. This clearly indicates that for the realisation of the neutral-neutral direct hydroamination reaction without a catalyst, one needs to have very strong electron withdrawing groups directly attached to the ethylene unit.

Acknowledgements SS thanks Claude-Leon foundation of South Africa for the postdoctoral fellowship. This material is based on work supported by the National Research Foundation, South Africa. This publication was made possible (in part) by a grant from the Carnegie Corporation of New York. The statements made and views expressed are, however, solely the responsibility of the author

References

1. Pohlki C, Doye S (2003) The catalytic hydroamination of alkynes. *Chem Soc Rev* 32:104–114
2. Muller TE, Beller M (1998) Metal-initiated amination of alkenes and alkynes. *Chem Rev* 98:675–803
3. Brunet JJ, Neibecker D, Philippot K (1993) Rhodium-mediated 100% regioselective oxidative hydroamination of α -olefins. *Tetrahedron Lett* 34:3877–3880
4. Trost BM (1991) The atom economy: a search for synthetic efficiency. *Science* 254:1471–1477
5. Roundhill DM (1997) Homogeneously catalyzed amination of alkenes. *Catal Today* 37:155–165
6. Senn HM, Blochl PE, Togni A (2000) Toward an alkene hydroamination catalyst: static and dynamic ab initio DFT studies. *J Am Chem Soc* 122:4098–4107
7. Taube R (1996) Reaction with nitrogen compounds: hydroamination. In: Cornils B, Herrmann WA (eds) *Applied homogeneous catalysis with organometallic compounds*, vol 1. VCH, Weinheim, pp 507–520
8. Heilen G, Mercker HJ, Frank D, Reck RA, Jackh R (1985) Amines, aliphatic. In: Gerhartz W (ed) *Ullmann's encyclopedia of industrial chemistry*, vol A2. VCH, Weinheim, pp 1–56
9. Gagne MR, Stern CL, Marks TJ (1992) Organolanthanide-catalyzed hydroamination. A kinetic, mechanistic, and diastereoselectivity study of the cyclization of N-protected amino olefins. *J Am Chem Soc* 114:275–294
10. Roundhill DM (1992) Transition metal and enzyme catalyzed reactions involving reactions with ammonia and amines. *Chem Rev* 92:1–25
11. Brunet JJ, Neibecker D, Niedercorn F (1989) Functionalisation of alkenes: catalytic amination of monoolefins. *J Mol Catal* 49:235–259
12. Dorta R, Egli P, Zurcher F, Togni A (1997) The $[\text{IrCl}(\text{Diphosphine})_2/\text{Fluoride}]$ System. Developing catalytic asymmetric olefin hydroamination. *J Am Chem Soc* 119:10857–10858
13. Gase MB, Lattes A, Perie JJ (1983) Amination of alkenes. *Tetrahedron* 39:703–731
14. Coulson DR (1971) Catalytic addition of secondary amines to ethylene. *Tetrahedron Lett* 12:429–430
15. Hamann T, Bohler E, Swiderek P (2009) Low-energy-electron-induced hydroamination of alkene. *Angew Chem Int Ed (English)* 48:4643–4645
16. Sitha S, Jewell LL (2010) Non-catalytic hydroamination of alkenes: a computational study. *Tetrahedron* 66:3030–3036
17. McMurry JE (2008) *Organic chemistry*, 7th edn. Brookscole, Pacific Grove
18. Frisch MJ, Trucks GW, Schlegel HB, Scuseria GE, Robb MA, Cheeseman JR, Montgomery JA Jr, Vreven T, Kudin KN, Burant JC, Millam JM, Iyengar SS, Tomasi J, Barone V, Mennucci B, Cossi M, Scalmani G, Rega N, Petersson GA, Nakatsuji H, Hada M, Ehara M, Toyota K, Fukuda R, Hasegawa J, Ishida M, Nakajima T, Honda Y, Kitao O, Nakai H, Klene M, Li X, Knox JE, Hratchian HP, Cross JB, Adamo C, Jaramillo J, Gomperts R, Stratmann RE, Yazyev O, Austin AJ, Cammi R, Pomelli C, Ochterski JW, Ayala PY, Morokuma K, Voth GA, Salvador P, Dannenberg JJ, Zakrzewski VG, Dapprich S, Daniels AD, Strain MC, Farkas O, Malick DK, Rabuck AD, Raghavachari K, Foresman JB, Ortiz JV, Cui Q, Baboul AG, Clifford S, Cioslowski J, Stefanov BB, Liu G, Liashenko A, Piskorz P, Komaromi I, Martin RL, Fox DJ, Keith T, Al-Laham MA, Peng CY, Nanayakkara A, Challacombe M, Gill PMW, Johnson B, Chen W, Wong MW, Gonzalez C, Pople JA (2004) *Gaussian 03, Revision C.01*. Gaussian, Inc., Wallingford

19. Beller M, Trauthwein H, Eichberger M, Breindl C, Muller TE, Zapf A (1998) New cationic rhodium-amine complexes and their implication in the catalytic anti-Markovnikov oxidative amination of styrene. *J Organomet Chem* 566:277–285
20. Beller M, Trauthwein H, Eichberger M, Breindl C, Herwig J, Muller TE, Thiel OR (1999) The first rhodium-catalyzed anti-Markovnikov hydroamination: studies on hydroamination and oxidative amination of aromatic olefins. *Chem A Eur J* 5:1306–1319

Chapter 24

Preparation and Characterization of TiO₂–ZrO₂ Mixed Oxide Catalysts for Photocatalytic Reduction of Carbon Dioxide

Simona Krejčikova, Kamila Koci, Lucie Obalova, Libor Capek,
and Olga Solcova

Abstract Seven pure and mixed oxides TiO₂, ZrO₂ catalysts with the mole fraction of TiO₂ in the range 0–1 were prepared by a sol-gel process controlled in the reverse micellar environment. Triton X114 was used as the nonionic surfactant and titanium(IV) isopropoxide and/or zirconium(IV) propoxide were used as the metal precursors. As treatment method the calcination at temperature of 400°C in air was applied. The effect of ZrO₂ on photocatalytic properties of prepared mixed-oxide catalysts was evaluated. Textural properties, structural properties, morphology and purity of prepared catalysts were characterized by nitrogen physisorption at 77 K, advanced XRD analysis, TEM, XRF, UV-VIS and organic elemental analysis. For testing of photocatalytic activity the photocatalytic reduction of carbon dioxide was chosen with methane and methanol as the main reduction products.

24.1 Introduction

Titania (TiO₂) is a well-known material especially owing to majority of its applications based on its excellent physical and chemical properties [1]. Titania similarly as the other ordered mesoporous structures of metal oxides are commonly prepared by

S. Krejčikova • O. Solcova (✉)

Department of Catalysis and Reaction Engineering, Institute of Chemical Process Fundamentals of the ASCR, v.v.i., Rozvojova, 135, Prague 6, Czech Republic
e-mail: krejcikova.simona@icpf.cas.cz; solcova@icpf.cas.cz

K. Koci • L. Obalova

Department of Physical Chemistry and Theory of Technological Processes, Technical University of Ostrava, 17. Listopadu, 15, Ostrava, Czech Republic
e-mail: kamila.koci@vsb.cz; lucie.obalova@vsb.cz

L. Capek

Faculty of Chemical Technology, University of Pardubice, Studentská, 95, Pardubice, Czech Republic
e-mail: libor.capek@upce.cz

sol-gel routes using the ionic or nonionic surfactants as a structure-directing agent and metal precursors.

TiO₂ has been traditionally applied as a pigment giving whiteness and/or opacity into paints, plastics and paper. Photo-catalysis using semiconductor particles have found increasing interest to solve global pollution problems. Recently, TiO₂ has been employed as an efficient photocatalyst in such reactions as the ecological liquidation (oxidation) of organic pollutants in waste water and/or air, as an inactivator of microorganisms, *etc.* [2–6].

Nowadays a lot of studies dealing with modification and/or tuning of TiO₂ characteristics [7, 8] by doping of a second metal oxide [9–12], or metal (nonmetal) element [13] have occurred. It is well established that titanium oxide and related nanostructure materials in the presence of UV light (in dependence of condition also in the presence of visible light) can create very active species that are able to restore and preserve a clean environment by decomposing harmful organics, killing bacteria and viruses and being easily self-cleaned.

One of the promising metal oxides seems to be zirconia (ZrO₂), which is mainly used as a carrier of metal species in catalytic processes (volatile organic compounds (VOC) oxidation *etc.*). In mixture with TiO₂ it can increase the solidity of final material due to crystal properties [14] and it can be effective for improvement of thermal stability and photocatalytic activity. Details concerning syntheses of these mixed oxides by various methods and their characterization by various techniques are partially summarized in the first review of TiO₂-ZrO₂ mixed oxides [15].

Our study tried to bring some light into mutual relationships between mixed oxides preparation, properties and activity in further applications. Therefore a set of titanium, zirconium dioxides and their mixture powders with various molar ratios prepared by sol-gel methods was thoroughly characterized. For comparison of their activity, photoreduction of carbon dioxide was employed as carbon dioxide is supposed to be the most important greenhouse gas and the reduction of CO₂ is an issue drawing the attention of many researchers [16, 17]. The reduction of CO₂ by photocatalysts is one of the most promising methods since CO₂ can be reduced to useful compounds by irradiating it with UV light at room temperature and constant pressure. The possible products of CO₂ reduction are methane, ethane and carbon monoxide in gas phase and methanol, ethanol, formaldehyde and formic acid in liquid phase.

24.2 Experimental

24.2.1 Preparation of Powders

A set of powder samples (titanium(IV) dioxide, zirconium(IV) dioxide and their mixtures) was prepared by a sol-gel process controlled in the reverse micellar environment. The molar ratios of Ti/Zr in mixed samples were 9:1, 7:3, 5:5, 3:7 and 1:9.

Cyclohexane as a solvent was mixed with the nonionic surfactant, Triton X114 (TX-114) and water. Metal precursor (Titanium(IV) isopropoxide (Ti(OCH(CH₃)₂)₄), Aldrich, 99.999% and/or Zirconium(IV) propoxide (Zr(OCH₂CH₂CH₃)₄), Aldrich, 70 wt.% solution in 1-propanol) was added after micelles formation. In the typical synthesis the molar ratio of cyclohexane/TX-114/water/Ti(OC₃H₇)₄ was kept at 11/1/1/1 with volume ratio TX-114/C₆H₁₂ = 0.49 [18]. Sol was dried in air at laboratory conditions for 24 h. The transparent amorphous gel was treated by calcination at 400°C for 4 h (temperature ramp 1°C/min) in air.

24.2.2 Sample Characterization

Textural properties of samples (S_{BET} , S_{meso} , V_{micro} , pore-size distribution) were evaluated from nitrogen physical adsorption-desorption isotherms at 77 K obtained with the ASAP2020M instrument (Micromeritics, USA) where S_{BET} = specific surface area, S_{meso} = specific surface area of mesopore and V_{micro} = volume of micropore. Before analysis samples were dried at 105°C at least for 12 h *in vacuo* (1 Pa). S_{meso} and V_{micro} were evaluated from measured nitrogen physical adsorption-desorption isotherms by two independent methods, modified BET equation [19] and t-plot constructed with the use of nonporous TiO₂ standard isotherm [20]. Results from both methods were identical. Pore-size (r_p) was determined by BJH method using nonporous TiO₂ standard.

The purity (carbon content in %) of oxide materials was specified on the Elementar vario EL III (Elementar Comp.). TiO₂ and/or ZrO₂ powders (approximately 5 mg) were burnt in oxygen atmosphere at high temperature (up to 1,200°C). Gaseous products (N₂, CO₂, H₂O and SO₂) were purified, separated to individual components and analyzed on a thermal conductivity detector (TCD). Each sample was analyzed three times for the reliability of results. The detection limit of the analysis was 0.1%.

X-ray diffraction (XRD) measurements for the powder characterization (crystal-lite size, phase composition) were performed on the Panalytical-XRD laboratory diffractometer in the parallel beam geometry with a Cu anode, with a Goebel mirror in the incident beam and a parallel plate collimator in the diffracted beam. The X-ray patterns were obtained as simple detector 2Q scans with a constant incidence angle of the X-ray beam of 1.5°.

An ARL 9400 XP sequential WD-XRF (X-ray fluorescence) spectrometer was used for determination of real molar content of TiO₂ and/or ZrO₂ in all prepared samples. The analyzed powders were pressed into pellets about 5 mm thick and diameter of 40 mm without any binding agent (or with Dentakryl as binding agent) and covered with 4 μm supporting polypropylene (PP) film. The time of measurement was about 15 min.

Transmission electron micrographs were determined from unstained ultrathin sections with the Philips CM100 electron microscope.

Fractions of prepared granulated samples in the range 0.25–0.50 mm were used for obtaining UV-Vis diffuse reflectance spectra that were recorded using GBS CINTRA 303 spectrometer equipped with a diffuse reflectance attachment with a spectralon-coated integrating sphere against a spectralon reference. The reflectances were re-calculated to the absorption using the Schuster-Kubelka-Munk equation, $F(R_\infty) = (1-R_\infty)^2/2R_\infty$, where R_∞ is the diffuse reflectance from a semi-infinite layer.

24.2.3 Photocatalytic Testing

The photocatalytic reduction of carbon dioxide was carried out in a homemade apparatus. The photocatalytic reduction of carbon dioxide was carried out in a stirred batch annular reactor with a suspended catalyst illuminated by a UV 8 W Hg lamp (254 nm). GC/FID/TCD was used for the analysis of gas and liquid reaction products. The details of the photocatalytic CO₂ reduction experiment, scheme of reactor and analytical methods were described in [17].

24.3 Results and Discussion

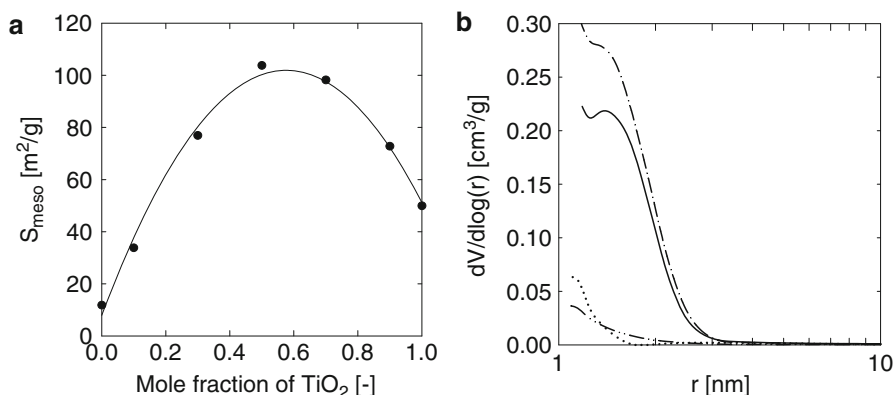
Textural characteristics of synthesized TiO₂ and/or ZrO₂ samples together with their molar content are summarized in Table 24.1. It is seen that pure TiO₂ possesses approximately four times higher surface area than pure ZrO₂ with lower portion of micropores. Similarly, the effect of TiO₂/ZrO₂ molar ratio on the surface area and partially on the portion of micropores is noticeable. Dependence of surface area on the TiO₂ molar fraction in the synthesized mixed oxides is more clearly illustrated in Fig. 24.1a. Sample with equal content of TiO₂ and ZrO₂ reveals the highest surface area of all prepared mixed oxides. The correlation can be described as quadratic $S_{\text{meso}} = y_0 + a \cdot x + b \cdot x^2$ with $y_0 = 7.93 \text{ m}^2/\text{g}$, $a = 326.1$ and $b = -282.8$, standard error = 3.7 and index of determination 0.99. The amount of micropores grows insignificantly with increasing surface area. A real molar content of TiO₂ and/or ZrO₂ in all prepared samples (shown in Table 24.1) corresponds with the originally required values. The minimal deviations can be ascribed to undetected impurities.

Content of organic impurities in all samples was under detectable limit, which means smaller than 0.1%.

The pore-size distributions (PSD) evaluated from the adsorption branch of the adsorption-desorption isotherm are shown in Fig. 24.1b. It can be seen that for two samples with the highest content of titania (pure TiO₂ and 0.9TiO₂-0.1ZrO₂) the pore radii lay in the range 1.3–3 nm with maximum about 1.7 nm. The other mixed-oxides samples revealed nearly the same pore-size distribution with wide broadening and without characteristic peaks similarly as pure ZrO₂ catalyst. It is shown in Fig. 24.1b for the 0.9ZrO₂-0.1TiO₂ sample.

Table 24.1 Textural properties and molar contents of metal oxides of prepared TiO₂ – ZrO₂ powders

Sample identification	S _{BET} [m ² /g]	S _{meso} [m ² /g]	V _{micro} [mm ² (liq)/g]	TiO ₂ [mol.%]	ZrO ₂ [mol.%]
TiO ₂	67.6	49.9	13.9	99.7	0.0
0.9Ti ₂ 0.1Zr	99.9	72.8	21.4	93.5	7.2
0.7Ti ₂ 0.3Zr	137.9	98.2	33.8	67.7	30.4
0.5Ti ₂ 0.5Zr	175.2	103.8	40.9	45.5	51.3
0.3Ti ₂ 0.7Zr	136.7	76.9	30.8	29.5	68.3
0.1Ti ₂ 0.9Zr	51.4	33.8	10.9	8.0	89.0
ZrO ₂	16.6	11.8	3.5	0.0	97.4

**Fig. 24.1** (a) Dependence of the surface area on TiO₂ mole fraction; (b) the pore-size distribution curves — — TiO₂; — · — 0.9TiO₂-0.1ZrO₂; ··· 0.1TiO₂-0.9ZrO₂; — · — ZrO₂

Presence of the crystalline phases was evaluated by XRD analysis. Diffraction patterns for pure TiO₂ and ZrO₂ together with diffraction patterns for mixed-oxides are shown in Fig. 24.2. It is seen that anatase is the dominant crystalline phase in pure TiO₂ and 0.9TiO₂-0.1ZrO₂ samples. Conversely, for pure ZrO₂ and 0.9ZrO₂-0.1TiO₂ samples the zirconia crystalline phase can be described as the face centered cubic with relatively wide peaks which complicate the precise determination of their position. The other mixed-samples revealed only amorphous character without presence of crystalline phase. This fact is demonstrated for 0.5TiO₂-0.5ZrO₂ (dashed line).

Presence of crystalline phases was corroborated by the TEM (transmission electron microscopy) analysis (Fig. 24.3). The amorphous character of mixed-oxides is demonstrated in Fig. 24.3a for 0.5TiO₂-0.5ZrO₂ sample. In Fig. 24.3b the presence of the crystalline phase for 0.9TiO₂-0.1ZrO₂ is confirmed. It can be easily seen that the regular shape of anatase crystallites and their size correspond with the crystallite-size evaluated from XRD analysis, which was determined at 6 ± 2 nm.

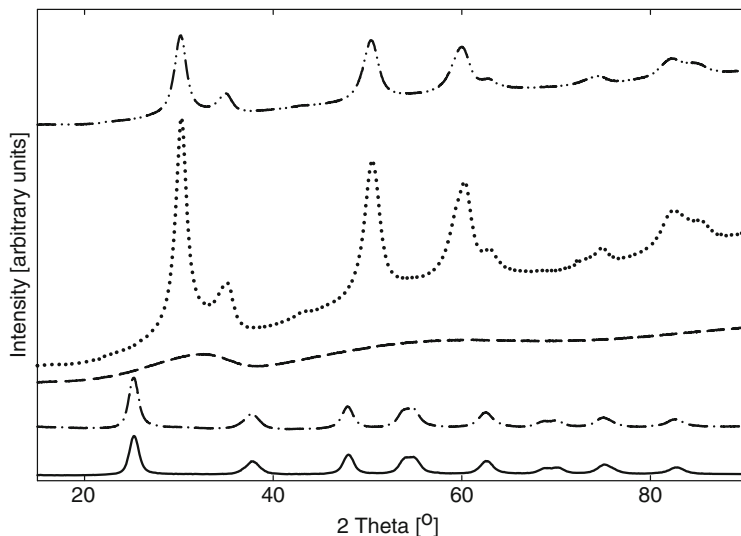


Fig. 24.2 X-ray diffraction patterns: ---- TiO_2 ; - · - 0.9 TiO_2 -0.1 ZrO_2 ; ··· 0.5 TiO_2 -0.5 ZrO_2 ; ···· 0.1 TiO_2 -0.9 ZrO_2 ; - - - ZrO_2

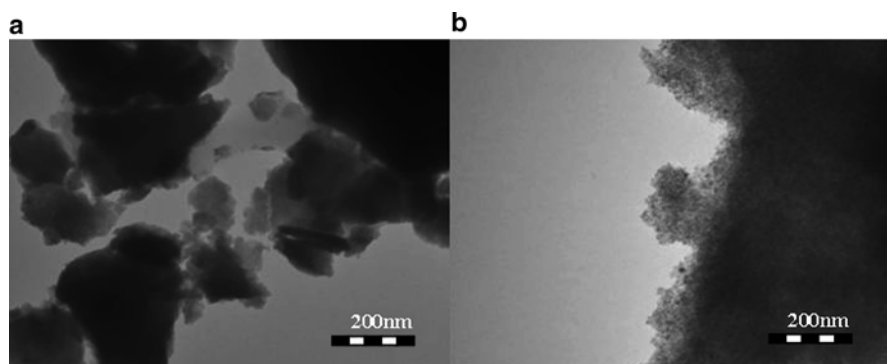


Fig. 24.3 TEM analysis: (a) 0.5 TiO_2 -0.5 ZrO_2 ; (b) 0.9 TiO_2 -0.1 ZrO_2

The ZrO_2 crystallite size could be obtained with the lower accuracy owing to the wide peak broadening. It was determined at 5 ± 3 nm.

The normalized UV-Vis spectra for pure TiO_2 and ZrO_2 samples together with two spectra for TiO_2 - ZrO_2 mixed samples (0.5 TiO_2 -0.5 ZrO_2 and 0.9 ZrO_2 0.1 TiO_2) are shown in Fig. 24.4.

A sharp intense band was observed in the UV-Vis spectrum of TiO_2 due to a charge-transfer transition between the lattice oxygen ligands and a central titanium ion. The maximum of this band was observed at 360 nm. On the other hand, a broad band was observed in the UV-Vis spectrum of ZrO_2 with a maximum at 292 nm.

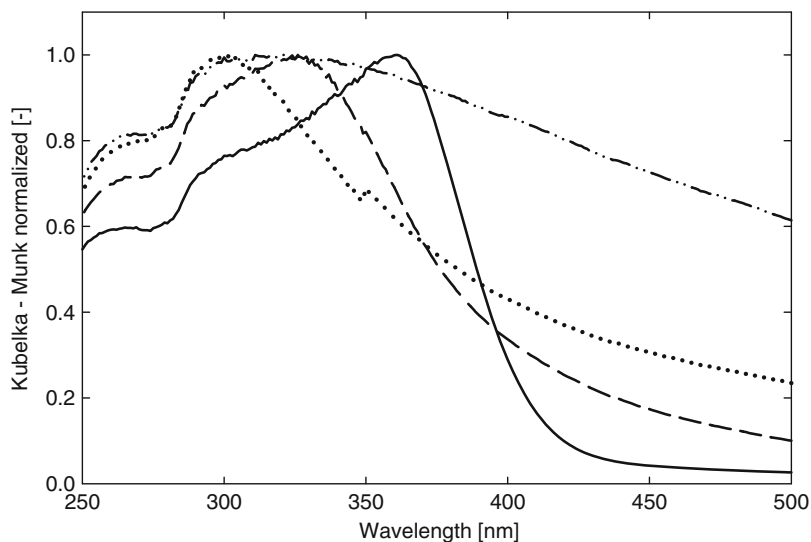


Fig. 24.4 UV-vis spectra: ---- TiO₂; - · - · 0.5TiO₂-0.5ZrO₂; ···· 0.1TiO₂-0.9ZrO₂; — — — ZrO₂

The wavelength of the maxima of the UV-Vis band was shifted for TiO₂-ZrO₂ catalysts with the increasing amount of ZrO₂ into lower wavelength and thus to higher energies (Fig. 24.4). However, the shoulder of the UV-Vis band was shifted to the visible region and thus to lower energies with increasing amount of ZrO₂ in the TiO₂-ZrO₂ mixture. The dependence of the wavelength maximum and the band gap energy on TiO₂ mole fraction is shown in Fig. 24.5. Both dependences are linear with the standard deviation 5% for wavelength maximum and 3.5% for band gap energy, respectively.

For the fast photocatalytic activity appraisal of prepared mixed oxides, the reduction of CO₂ during irradiation was applied. The effect of irradiation time on the formation of CO₂ photocatalytic reduction products was investigated over a period of 0–24 h on the commercial Degussa catalyst and two laboratory prepared catalysts: pure TiO₂ and TiO₂ doped by the lowest content of zirconia – 0.9TiO₂-0.1ZrO₂.

Two main products were detected: methane in the gas phase and methanol in the liquid phase together with low amounts of carbon monoxide and hydrogen. (However, hydrogen concentration was under the detection limit during the first 8 h). Other products such as formic acid, formaldehyde, ethane and ethylene were not detected.

In Fig. 24.6a the time dependence of the methane yields over the pure TiO₂ catalyst and Degussa catalyst is compared. An increase of methane yield was observed after 5 h of irradiation for the pure titania catalyst, whereas for Degussa catalyst the substantial increase of methane yields started after 8 h. During the whole period the prepared titania catalyst produced higher methane yields than the Degussa catalyst. The steepest increase stopped after 18 h for both catalysts and the

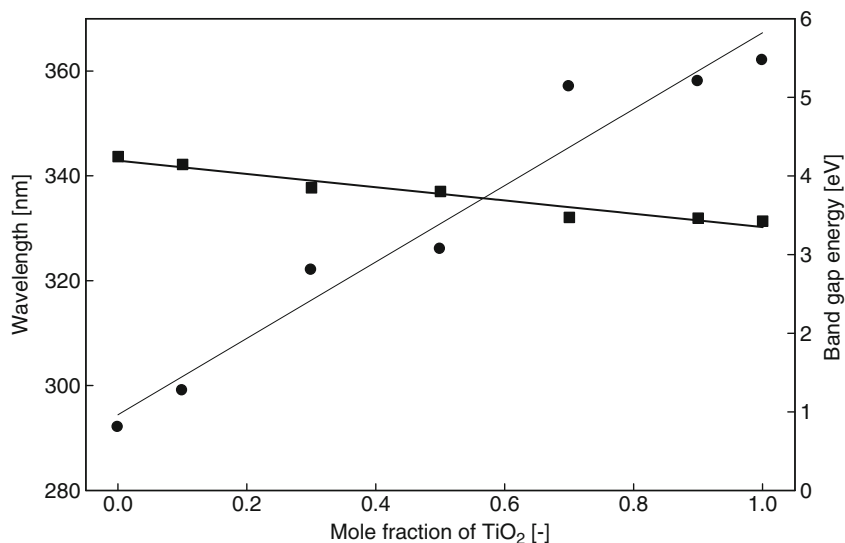


Fig. 24.5 Wavelength of maximum (●) and Band gap energy (■) depending on content of TiO₂

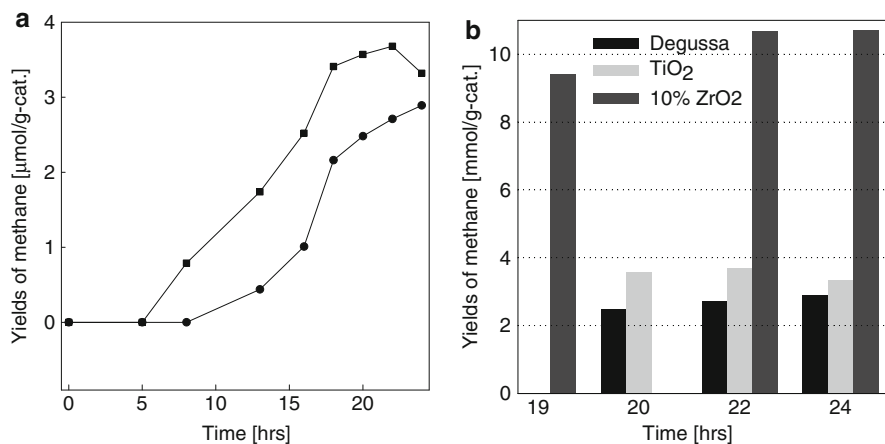


Fig. 24.6 (a) (●) Degussa (■) TiO₂; (b) Comparison of methane yields over the commercial catalyst, laboratory prepared TiO₂ catalyst and titania – zirconia mixed oxide (0.9TiO₂-0.1ZrO₂)

decrease of the methane yields was detected after 24 h for the laboratory prepared pure TiO₂ catalyst. Therefore, the doping effect of ZrO₂ on TiO₂ photocatalytic activity was mainly investigated during the last 5 h of the time period. Comparison of the methane yields of the pure TiO₂ and Degussa catalyst together with the mixed-oxide TiO₂ doped by 10% of ZrO₂ (0.9TiO₂-0.1ZrO₂) is shown in Fig. 24.6b.

It is obvious that during the whole period the photocatalytic activity of the TiO₂-ZrO₂ mixed oxides (with respect to yields of methane) is three times higher than for the laboratory prepared pure titania catalyst and more than four times higher than for the Degussa catalyst.

24.4 Conclusions

The pure and mixed-oxides TiO₂, ZrO₂ catalysts with the mole fraction of TiO₂ in the range 0–1 were successfully prepared by the sol-gel method. Anatase was the dominant crystalline phase in the pure TiO₂ and 0.9TiO₂-0.1ZrO₂ catalysts with the crystallite size 6 ± 2 nm, while the crystalline phase in the pure ZrO₂ and 0.9ZrO₂0.1TiO₂ catalysts was determined as the face centered cubic with relatively wide peaks and the crystallite size 5 ± 3 nm. The other mixed-oxides possess amorphous character with the high surface area.

For comparison of photocatalytic properties of the prepared nanocrystalline TiO₂ and/or ZrO₂ catalysts with the commercial Degussa catalyst the photocatalytic reduction of CO₂ was used. Prepared mixed-oxide catalyst – TiO₂with 10% of ZrO₂ revealed 3–4 times higher photocatalytic activity than the laboratory prepared pure TiO₂ or Degussa catalysts. This corroborated the positive effect of ZrO₂ on the mixed-oxide photocatalytic activity, which can be ascribed to enlarged surface area of 0.9TiO₂-0.1ZrO₂ catalysts and the higher zirconia photoactivity under the UV lamp 254 nm.

Acknowledgements The financial support of the Grant Agency of the Czech Republic, projects 104/09/0694 and 203/08/H032, and the Czech Ministry of Education, Youth and Sports, project MSM 6198910019 is gratefully acknowledged.

References

1. Diebold U (2003) Structure and properties of TiO₂ surfaces: a brief review. *Appl Phys A* 76:681–687
2. Peral J, Ollis DF (1993) Photocatalytic deactivation oxidation of decamethyl tetrasiloxane, pyrrole, indol and dimethyl sulphide. In: Ollis DF, Alekabi H (Eds) *Trace Metals in the Environment*. Elsevier Science Publ BV, London
3. Legrini O, Oliveros E, Braun A (1993) Photochemical processes for water treatment. *Chem Rev* 93:671–698
4. Lukac J, Klementova M, Bezdicka P, Bakardjieva S, Subrt J, Szatmary L, Bastl Z, Jirkovsky J (2007) Influence of Zr as TiO₂ doping ion on photocatalytic degradation of 4-chlorophenol. *Appl Catal B* 74:83–91
5. Yuan Q, Liu Y, Li LL, Li ZX, Fang CJ, Duan WT, Li XG, Yan CH (2009) Highly ordered mesoporous titania-zirconia photocatalyst for applications in degradation of rhodamine-B and hydrogen evolution. *Microporous Mesoporous Mater* 124:169–178

6. Karunakaran C, Dhanalakshmi R (2008) Semiconductor-catalyzed degradation of phenols with sunlight. *Sol Energy Mater Sol Cells* 92:1315–1321
7. Assefa Z, Haire RG, Raison PE (2004) Correlation of the oxidation state of cerium in sol-gel glasses as a function of thermal treatment via optical spectroscopy and XANES studies. *Spectrochim Acta A* 60:89–95
8. Tian G, Pan K, Fu H, Jing L, Zhou W (2009) Enhanced photocatalytic activity of S-doped TiO₂-ZrO₂ nanoparticles under visible-light irradiation. *J Hazard Mater* 166:939–944
9. Reddy BM, Sreekanth PM, Reddy EP, Yamada Y, Xu Q, Sakurai H, Kobayashi T (2002) Surface characterization of La₂O₃-TiO₂ and V₂O₅/La₂O₃-TiO₂ catalysts. *J Phys Chem B* 106:5695–5700
10. Hong S, Lee MS, Park SS, Lee G (2003) Synthesis of nanosized TiO₂/SiO₂ particles in the microemulsion and their photocatalytic activity on the decomposition of p-nitrophenol. *Catal Today* 87:99–105
11. Wang XC, Yu JC, Chen YL, Wu L, Fu XZ (2006) ZrO₂-modified mesoporous nanocrystalline TiO₂-xNx as efficient visible light photocatalysts. *Environ Sci Technol* 40:2369–2374
12. Fresno F, Hernandez-Alonso MD, Tudela D, Coronado JM, Soria J (2008) Photocatalytic degradation of toluene over doped and coupled (Ti, M)O-2 (M = Sn or Zr) nanocrystalline oxides: influence of the heteroatom distribution on deactivation. *Appl Catal B Environ* 84:598–606
13. Lucky RA, Charpentier PA (2010) N-doped ZrO₂/TiO₂ bimetallic materials synthesized in supercritical CO₂: morphology and photocatalytic activity. *Appl Catal B Environ* 96:516–523
14. Hidalgo MC, Colon G, Navio JA, Macias M, Kriventsov VV, Kochubey DI, Tsodikov MV (2007) EXAFS study and photocatalytic properties of un-doped and iron-doped ZrO₂-TiO₂ (photo-) catalysts. *Catal Today* 128:245–250
15. Reddy BM, Khan A (2005) Recent advances on TiO₂-ZrO₂ mixed oxides as catalysts and catalyst supports. *Catal Rev* 47:257–296
16. Koci K, Obalova L, Matejova L, Placha D, Lacny Z, Jirkovsky J, Solcova O (2009) Effect of TiO₂ particle size on the photocatalytic reduction of CO₂. *Appl Catal B Environ* 89:494–502
17. Koci K, Mateju K, Obalova L, Krejčíková S, Lacny Z, Placha D, Capek L, Hospodkova A, Solcova O (2010) Effect of silver doping on the TiO₂ for photocatalytic reduction of CO₂. *Appl Catal B Environ* 96:239–244
18. Kluson P, Kacer P, Cajthaml T, Kalaji M (2001) Preparation of titania mesoporous materials using a surfactant-mediated sol-gel method. *J Mater Chem* 11:644–651
19. Schneider P (1995) Adsorption isotherms of microporous-mesoporous solids revisited. *Appl Catal A Gen* 129:157–165
20. Matejova L, Solcova O, Schneider P (2008) Standard (master) isotherms of alumina, magnesia, titania and controlled-pore glass. *Microporous Mesoporous Mater* 107:227–232

Chapter 25

Modification of Anthraquinone-2-Carboxylic Acid with Multiwalled Carbon Nanotubes and Electrocatalytic Behavior of Prepared Nanocomposite Towards Oxygen Reduction

Ida Tiwari, Manorama Singh, and Mandakini Gupta

Abstract We herein report a simple method for the preparation of multiwalled carbon nanotubes-anthraquinone-2-carboxylic acid (AQ-COOH-AMWCNTs) nanocomposite. For the preparation of the composite, multiwalled carbon nanotubes have been functionalized with amino group (AMWCNTs) using 3-aminopropyltrimethoxysilane. Then, anthraquinone-2-carboxylic acid is coupled to amino functionalized multiwalled carbon nanotubes (AMWCNTs) by carbodiimide coupling. Characterization of the material has been performed with scanning electron microscopy (SEM), transmission electron microscopy (TEM), fourier transform IR (FTIR) and cyclic voltammetry (CV). The prepared material exhibited electrocatalytic behavior towards the reduction of oxygen to hydrogen peroxide with a detection limit of 0.02 ppm. The prepared material was stable with no leaching observed of the mediator.

25.1 Introduction

The field of nanoscience and nanotechnology has been the most identifiable activity in modern era of materials science. There are two main attributes of nanomaterials, i.e. reduced size and high surface area which make these highly useful for molecular-recognition properties. Nanocomposites are engineered materials made from two or more dissimilar constituent materials mixed at nanoscale having significantly different physical and chemical properties and the advantage of nanocomposite preparation is due to its high surface to volume ratio of reinforcing phase and they also have improved properties from their macro composite counterparts. It has been proved that nanoscale materials can dramatically enhance electrochemical sensitivity over their larger scale analogues [1, 2]. As a new

I. Tiwari (✉) • M. Singh • M. Gupta

Department of Chemistry, Faculty of Science, Banaras Hindu University, Varanasi 221005, India
e-mail: datiwari_2001@rediffmail.com; manoramabhu@gmail.com; mandakini1710@gmail.com

and interesting member of nanomaterials, carbon nanotube (CNT) is an equally attractive material for the development of nanocomposite because of its capability to provide strong electrocatalytic activity and to minimize surface fouling of the sensors, high chemical stability, low resistance and extremely high mechanical strength and modulus [3]. CNTs have been found to promote electron transfer reactions when used as electrode materials. Charge transfer reactions at CNTs were found to occur at a faster rate than those at traditional carbon electrodes [4]. The electrochemical reduction of oxygen on carbon electrode is desirable due to its importance in hydrogen-oxygen fuel cells where there is a requirement of high surface area carbon materials as supports for noble metal catalysts. There is also a need for electrode catalysts which can promote oxygen reduction with high efficiency with long operating lifetimes. These catalysts reduce the large overpotential required at electrode surface. Hence CNTs based carbon materials are very desirable.

Quinones are a series of widespread compounds found in the living organisms performing a variety of biochemical and physiological functions [5]. A relatively small number of *p*-quinones have been recognized as biological electron carriers. The main activity of these compounds arises from their reversible electron transfer behaviour [6, 7]. Anthra-9,10-quinones (AQNEs) are interesting compounds for investigations in electro analytical chemistry due to the fact that they contain the reducible *p*-quinone system and also form conductive, electro active films and monolayers [8], so they can be used as surface modifier and redox mediator [9–17]. It has been shown that adsorption of quinones on the electrode surface enhances the rate of O₂ reduction [17, 18]. However they can desorb from surface in long term operation, especially in alkaline solution [19]. This problem can be overcome by attaching AQ covalently [20–22], but only a few O₂ reductions have been explored due to lack of simple grafting [19].

Therefore, it is fascinating to prepare material based on anthraquinone and carbon nanotubes which shows electrocatalytic activity towards oxygen reduction on carbon electrode. Much work has been done based on anthraquinone and its derivatives and previously it has been used in O₂ reduction to water or H₂O₂ [11, 17–19]. The electrochemical reduction of O₂ on glassy carbon electrode modified with anthraquinone-2-carboxylic acid in DMSO was done by Maia et al. [18]. Wilson et al. [23] reported newly synthesized anthraquinone-2-carboxylic-allyl ester which can strongly adsorb on the graphite electrode, and catalyze the two-electron reduction of oxygen to produce H₂O₂ with high current efficiency. Anthraquinone-2-carboxylic acid was also used as electron shuttling mediator and attached relay for H₂O₂ [19]. But all these works have their drawbacks as discussed.

In our new piece of work, we have prepared a new nanocomposite based on anthraquinone-2-carboxylic acid (AQ-2-COOH). In this nanocomposite multiwalled carbon nanotubes (MWCNTs) increase the electro catalytic activity and AQ-2-COOH functions as redox mediator at a much reduced overpotential than bare glassy carbon electrode in the reduction of oxygen.

25.2 Methodology

25.2.1 Materials

Multiwalled carbon nanotubes (diam. 110–170 nm, length 5–9 μm , purity 90+ %), 1-ethyl-3-(3-dimethylaminopropyl) carbodiimide (EDC), N-hydroxysuccinimide (NHS) and anthraquinone-2-carboxylic acid were purchased from Aldrich (USA). 3-Aminopropyltrimethoxysilane (3-APTMS) was purchased from Alfa Aesar (UK). The aqueous solutions were prepared using triple distilled water. All other chemicals employed were of analytical grade.

25.2.2 Preparation of Anthraquinone-2-Carboxylic Acid/Amino Functionalized Multiwalled Carbon Nanotubes (AQ-2-COOH-AMWCNTs) Nanocomposite

Step 1. Purification of MWCNTs:

MWCNTs (4 mg) were purified by ultrasonication for 4 h with 0.5 M HCl. It was thoroughly washed with water to give neutral state and centrifuged for separation. Finally it was dried under vacuum at 50°C overnight to obtain the purified MWCNTs.

Step 2. Amino functionalization of MWCNTs for preparation of amino functionalized multiwalled carbon nanotubes (AMWCNTs):

Purified MWCNTs (2.5 mg) was ultrasonicated in 1 ml water for 1 min. 250 μl of 3-APTMS was added and ultrasonicated for 15 min. A homogeneous suspension was prepared. 0.02 ml of 0.1 N HCl was added and stirred for 5 min.

Step 3. Preparation of the AQ-2-COOH-AMWCNTs nanocomposite via carbodiimide coupling:

AQ-2-COOH (11.6 mg) was suspended in 700 μl of 0.1 M, pH 7.4 HEPES buffer + 44 mg NHS + 60 mg EDC. The mixture was stirred for 45 min. 100 μl AMWCNTs were then added drop by drop to the mixed solution under continuous stirring and left at room temperature for 24 h. After completion of the incubation, the produced conjugates were centrifuged and washed with water several times and dried for 24 h in a vacuum oven at 70°C.

25.2.3 *Fabrication of the AQ-2-COOH-AMWCNTs Modified Electrode*

AQ-2-COOH-AMWCNTs (1 mg) composite was dissolved in 150 μl acetonitrile. The solution was ultrasonicated for 2 min. 8 μl of this solution was deposited on GC electrode and dried for 0.5 h at room temperature.

25.2.4 *Electrochemical Characterization*

The electrochemical measurements were performed with CHI 630°C series (USA) electrochemical system. Cyclic voltammetry studies were done with a three electrode system comprising of the AQ-2-COOH-AMWCNTs modified glassy carbon (GC) electrode as a working electrode, an Ag/AgCl reference electrode and platinum wire as counter electrode. All electrochemical measurements were carried out in 15 mL 0.1 M phosphate buffer solution (pH 6.5).

The AQ-2-COOH-AMWCNTs nanocomposite was pressed in KBr pellets for FTIR measurements (Varian 3100). SEM of nanocomposite film has been performed with JEOL 840A, Japan and TEM measurements were performed on a Tecnai G2 instrument. For TEM measurements the composite material was dispersed in distilled water and deposited onto a formvar/carbon coated copper grid.

25.3 Results and Discussion

25.3.1 *Synthesis of the AQ-2-COOH-AMWCNTs Composite*

The scheme followed in the synthesis of AQ-2-COOH-AMWCNTs composite is illustrated in Fig. 25.1. It is proposed that siloxane micelles of 3-APTMS were wrapped around the MWCNTs with amino group site outside and alkoxy silane site inside in aqueous solution. The siloxane will be attached to nanotubes surfaces via hydrophobic interactions and then polymerized simply through acid catalysis. Thus MWCNTs were enveloped in polysiloxane shell with amino groups extruding outside. A large number of amino groups were present on the surface of purified dispersed AMWCNTs in 0.1 M PBS buffer (pH 6.5). Further in this mechanism, the carboxyl group of AQ-2-COOH was successfully activated in the presence of EDC and NHS to form an NHS-ester as an intermediate and chemically conjugated to the amino group of AMWCNTs by hydrolysis in buffer solution.

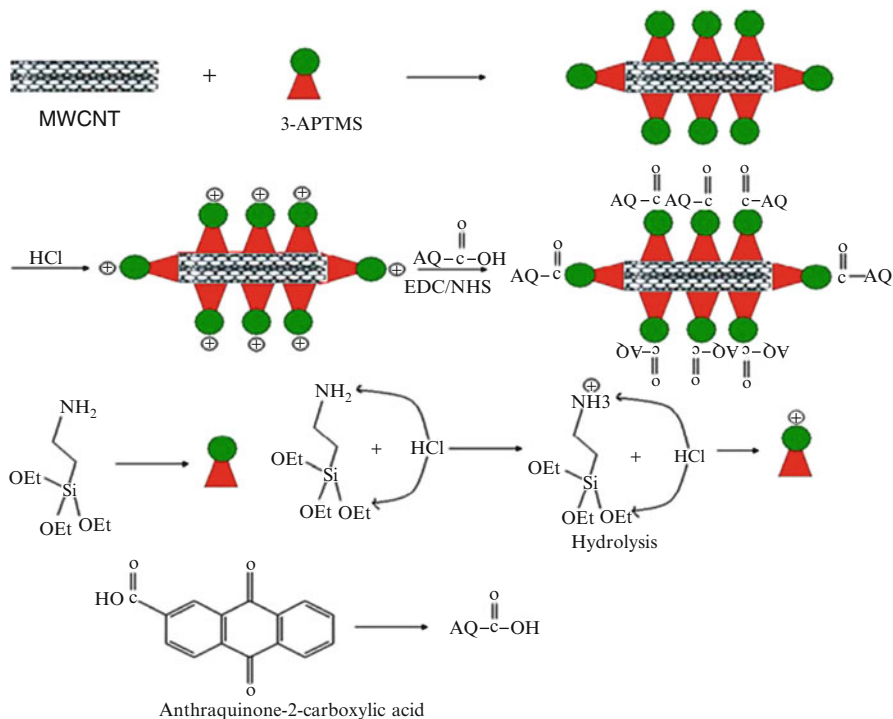


Fig. 25.1 Schematic diagram of the preparation of AQ-2-COOH-AMWCNTs nanocomposite via carbodiimide coupling

25.3.2 Characterization of AQ-2-COOH-AMWCNTs Composite

25.3.2.1 Morphological Characterization of the AQ-2-COOH-AMWCNTs Composite

Figure 25.2a shows TEM images of plain MWCNTs dispersed in aqueous solution and Fig. 25.2b shows TEM images of AQ-2-COOH-AMWCNTs nanocomposite. The walls of plain MWCNTs appear very smooth (cf. Fig. 25.2a) but after covalent interaction of anthraquinone-2-carboxylic acid (AQ-2-COOH) via carbodiimide coupling (cf. Fig. 25.2b), became coarse. The presence of AQ-2-COOH is indicated by appearance of plenty of small features superposed over plain fiber and covering its maximum area. It is predicted that clusters of linked anthraquinone-2-carboxylic acid appear on AMWCNTs which probably increase the surface area of the AMWCNTs.

Figure 25.2c shows the SEM image of the AQ-2-COOH-AMWCNTs nanocomposite. The SEM photograph of the prepared nanocomposite material shows a uniform pattern.

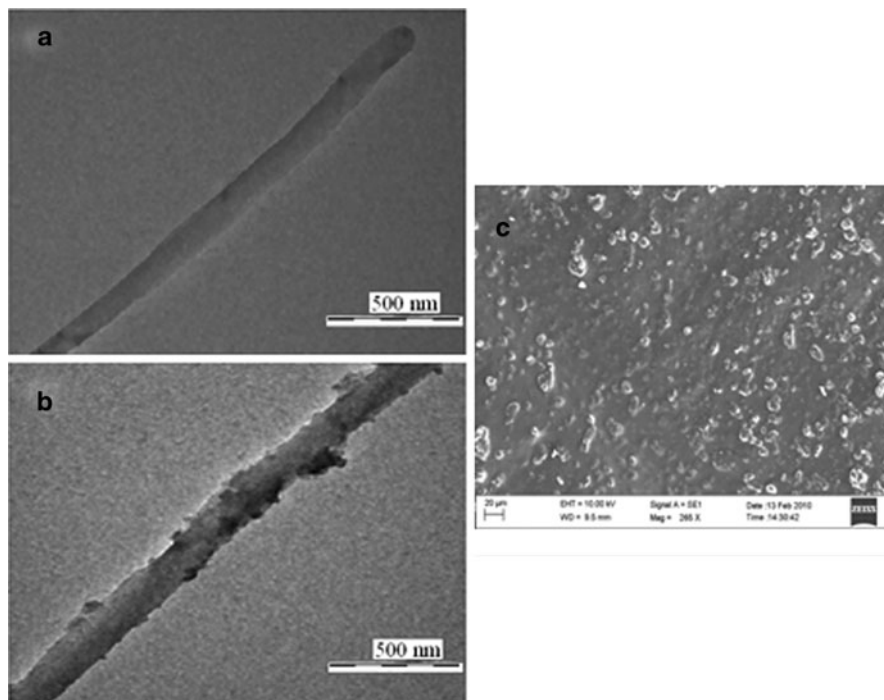


Fig. 25.2 (a) TEM image of plain MWCNTs dispersed in aqueous solution, (b) TEM image of AQ-2-COOH-AMWCNTs nanocomposite and (c) SEM image of the AQ-2-COOH-AMWCNTs nanocomposite

25.3.2.2 FTIR Studies

The FTIR spectra of AMWCNTs showed a peak at $3,360\text{ cm}^{-1}$ due to $-\text{NH}_2$ symmetric stretch indicating the functionalization of MWCNTs with amino group of 3-APTMS whereas FTIR data of MWCNTs did not show any remarkable peaks (results not shown).

Figure 25.3 shows the FTIR data of the AQ-2-COOH-AMWCNTs nanocomposite. The formation of composite of AQ-2-COOH with AMWCNTs was confirmed by FTIR. The characteristic peak of $\text{C}=\text{O}$ stretching vibration and $\text{N}-\text{H}$ stretching of $-\text{CONH}$ group at 1739.8 and 3452.7 cm^{-1} appears in the spectrum of prepared nanocomposite. The characteristic absorption of ring stretching appeared at 1589.4 cm^{-1} and $\text{C}=\text{C}$ appeared at 1674.2 cm^{-1} in the spectrum of AQ-2-COOH-AMWCNTs nanocomposite. These results confirmed that AMWCNTs successfully reacted with AQ-2-COOH to form AQ-2-COOH-AMWCNTs composite. Moreover, the characteristic peaks of $\text{C}-\text{N}$ stretching vibration appear at 1288.5 cm^{-1} which can be ascribed to their overlap with strong absorbance of the $\text{Si}-\text{O}-\text{Si}$ bond in the composite. The hydrogen bonded silanol groups show the absorbance at 3444.0 cm^{-1} .

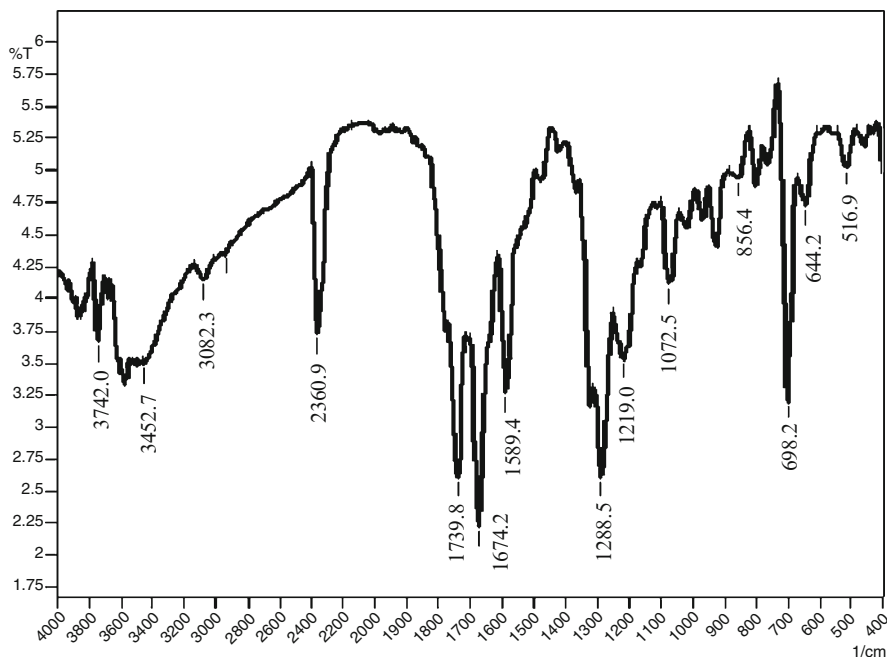


Fig. 25.3 FTIR spectrum of the AQ-2-COOH-AMWCNTs nanocomposite

25.3.3 Surface Electrochemistry of AQ-2-COOH-AMWCNTs Composite Modified Glassy Carbon Electrode

Inset (a) to Fig. 25.4 shows cyclic voltammograms of AQ-2-COOH (0.2 mg/ml) on a GC electrode in an aqueous solution of 0.1 M, pH 6.5 phosphate buffer solution at different scan rates (10, 20, 50 and 100, 200 mV/s). The electrode reaction involves two-electron and two-proton reduction of AQ-2-COOH to dihydroanthraquinone and subsequent reoxidation of dihydroanthraquinone back to AQ-2-COOH as already reported [24]. The reaction is, however, quasi reversible since an increase in peak separation with sweep rates is observed [25]. The formal potential E^0 calculated from the midpoint between the cathodic and anodic waves was found to be -0.422 mV vs. Ag/AgCl reference electrode at scan rate of 20 mV/s.

Figure 25.4 shows the cyclic voltammograms of AQ-2-COOH-AMWCNTs composite modified GC electrode in a potential range of 0.3 to -1.0 V at different scan rates (10, 20, 50, 100, 200 mV/s) in 0.1 M phosphate buffer solution (pH 6.5). After modifying the electrode with the composite, 50 cycles were scanned in the potential range from 0.3 to -1.0 V in 0.1 M phosphate buffer solution at a scan rate of 20 mV/s (result not shown). The composite formed provided a stable electrochemical response indicating the stability of the modified electrode. The cathodic and anodic potential are -0.518 and -0.378 V at the scan rate of

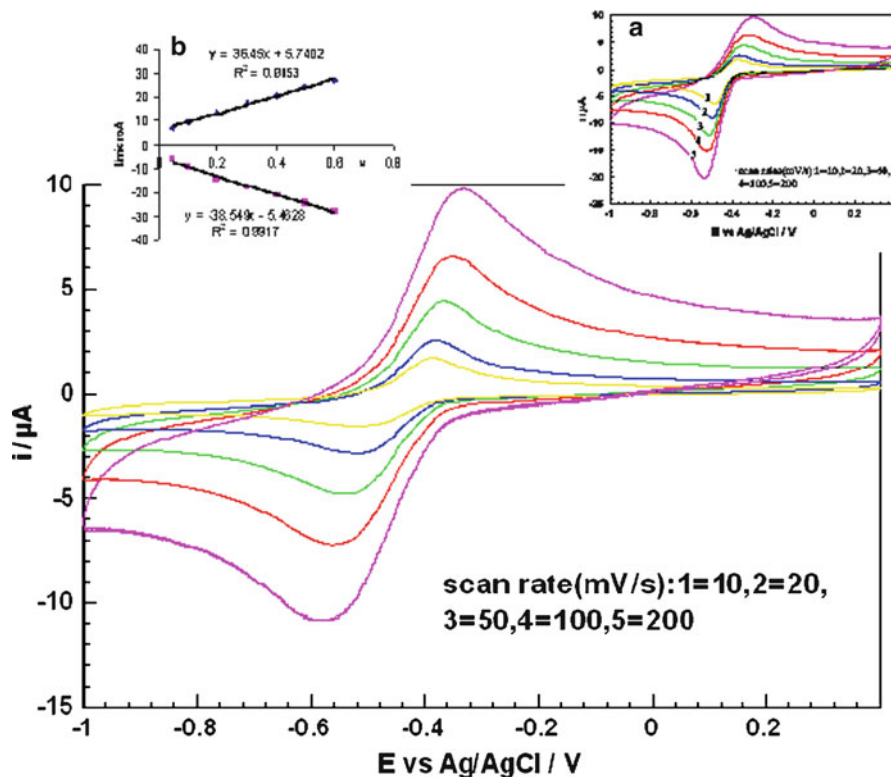


Fig. 25.4 Cyclic voltammograms of AQ-2-COOH-AMWCNTs composite modified GC electrode in 0.1 M PBS (pH 6.5) at different scan rates; Inset (a): Cyclic voltammograms of anthraquinone-2-carboxylic acid in 0.1 M PBS (pH 6.5) and Inset (b): Randles-Sevcik plot of AQ-2-COOH-AMWCNTs composite modified GC electrode

20 mV/s, which were ascribed to the reduction and oxidation potentials of the multiwalled carbon nanotubes modified AQ-2-COOH mediator. It shows a quasi-reversible behavior of the mediator with the formal potential of -0.448 V. The E^0 calculated from the midpoint between the cathodic and anodic waves was found to be -0.424 mV vs. Ag/AgCl reference electrode at scan rate of 20 mV/s. It is evident that on coupling of AQ-2-COOH with MWCNTs, $E_{1/2}$ has not significantly changed as compared to that obtained of AQ-2-COOH in solution which justifies the suitability of system for further analysis. The effect of varying the scan rates (v) on the peak currents (i_{p_a} and i_{p_c}) was investigated in the range of 5–200 mV/s. According to Randles-Sevcik plot [inset (b) to Fig. 25.4], the cathodic and anodic peak currents increased linearly with the increase of the scan rates, suggesting that the electrochemical reaction on AQ-2-COOH-AMWCNTs composite modified GC electrode is typical of surface confined electroactive reactant [26, 27].

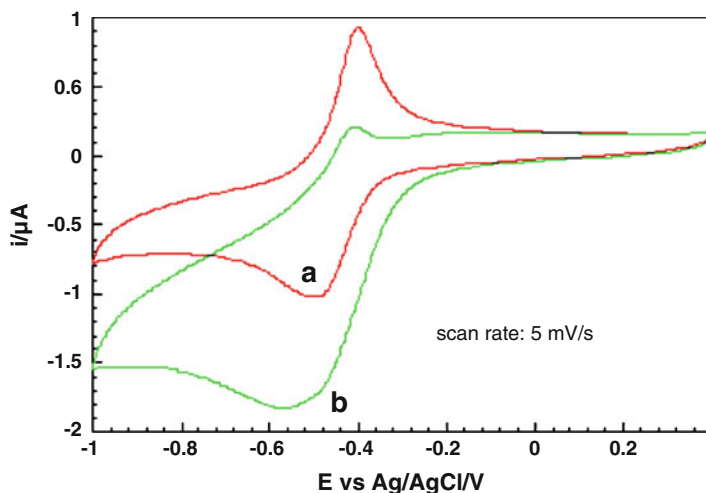


Fig. 25.5 Electrocatalytic oxygen reduction on AQ-2-COOH-AMWCNTs composite modified GC electrode in (a) absence and (b) presence of 0.19 ppm oxygen in 0.1 M PBS (pH 6.5)

The surface coverage area (Γ_{aq}) for the electroactive species was estimated by using Eq. $\Gamma_{aq} = Q/nFA$ [25], where Q is the charge obtained by integrating the cathodic peak at low scan rate (10 mV/s), n is the number of electrons involved per AQ molecules ($n = 2$) and A (cm^2) is the geometric electrode area. In the present case, the value of Γ_{aq} was determined to be $2.5 \times 10^{-7} \text{ mol cm}^{-2}$.

25.3.4 *Electrocatalytic Activity of AQ-2-COOH-AMWCNTs Composite Towards the Reduction of Oxygen*

The response of AQ-2-COOH-AMWCNTs composite modified GC electrode was examined in an oxygen saturated solution by cyclic voltammetry, with typical results as shown in Fig. 25.5.

From the Fig. 25.5 it is evident that the prepared AQ-2-COOH-AMWCNTs composite gives large enhancement in cathodic peak current under oxygen aerated condition while corresponding anodic peak diminishes which clearly indicates the electrocatalytic reduction of oxygen. From the fig. it is also clear that reduction starts at -0.3 V and attains a maximum at -0.56 V even in slight presence of oxygen (0.19 ppm) indicating significant electrocatalytic activity for oxygen reduction in the range of potentials coinciding with the formation of anthraquinone semiquinone radical. It is believed that such a large increase in reduction current results from attached anthraquinone groups and multiwalled carbon nanotubes indicating a synergic effect in the catalysis for oxygen reduction. The modified electrode promotes an increase in the reduction current, with a shift of about 556 mV

Table 25.1 Influence of different 0.1 M buffer solutions on the peak current obtained by CV for 0.19 ppm O₂ on AQ-2-COOH-AMWCNTs composite modified GC electrode

Buffer solution	−I _p (μA)
Phosphate buffer	1.97
Tris buffer	1.76
Hepes buffer	1.82

Table 25.2 Influence of the phosphate buffer concentration on the peak current obtained by CV on AQ-2-COOH-AMWCNTs composite modified GC electrode for 0.19 ppm O₂ in pH 6.5

Buffer (M)	−I _p (μA)
0.05	1.85
0.1	1.91
0.2	1.87

towards positive potential when compared to the bare graphite paste electrode on which oxygen reduction occurs at -1.097 V in present case as already reported [28]. The detection limit for the estimation of oxygen using the AQ-2-COOH-AMWCNTs composite modified GC electrode is 0.02 ppm which is to the best of our knowledge the lowest as compared to other results [29, 30] justifying the novelty of the prepared composite.

The determination of kinetic parameters of oxygen reduction on GC electrode modified with AQ-2-COOH-AMWCNTs composite was outside the scope of this article. A detailed kinetic analysis including one done at various pHs is being carried out and will be reported in a separate piece of work.

Finally the influence of the nature of the buffer and its concentration were also investigated. These studies indicated that 0.1 M phosphate buffer solution gives the best response as indicated in Table 25.1. The peak current reached a maximum value at pH 6.5 as shown in Table 25.2. Accordingly, 0.1 M phosphate buffer solution of pH 6.5 was used for the studies.

25.4 Conclusions

A nanocomposite has been prepared by coupling of the anthraquinone-2-carboxylic acid with amino functionalized multiwalled carbon nanotubes via carbodiimide coupling. The prepared composite was characterized by SEM, TEM, FTIR and CV.

The results indicated the formation of AQ-2-COOH-MWCNTs conjugates which prevented the leakage of the anthraquinone-2-carboxylic acid and acted as an electron transfer mediator. A synergic effect in the catalysis for oxygen reduction due to presence of multiwalled carbon nanotubes was evident from large increase in response in presence of oxygen. It is demonstrated that the AQ-2-COOH – AMWCNTs nanocomposite modified glassy carbon electrode could be effectively employed for the oxygen reduction.

Acknowledgements The authors are grateful to BRNS, DAE for financial support. One of the authors Manorama is grateful to CSIR, New Delhi for award of SRF.

References

1. Menon VP, Martin CR (1995) Fabrication and evaluation of nanoelectrode ensembles. *Anal Chem* 67:1920–1928
2. Martin CR (1994) Nanomaterials: a membrane based synthetic approach. *Science* 266: 1961–1966
3. Baughman RH, Zakhidov AA, DeHeer WA (2002) Carbon nanotubes-the route toward applications. *Science* 297:787–792
4. Britto PJ, Santhanam KSV, Ajayan PM (1996) Carbon nanotube electrode for oxidation of dopamine. *Bioelectrochem Bioenerg* 41:121–125
5. Reza O, Jahanbakhsh R, Manochehr E (2001) A cyclic voltammetric study of the aqueous electrochemistry of some anthraquinone derivatives on carbon paste electrode. *Iran J Chem Chem Eng* 20:75
6. *Elektrokhimicheskie svoistva obratimnykh biologicheskikh redoks-sistem (Electrochemical properties of reversible biological redox systems)*. O.S. Ksenzhek, S.A. Petrova; Published 1986 Nauka, Moskva” (written in Russian)
7. Petrova SA, Kolodyazhny MV, Ksenzhek OS (1990) Electrochemical properties of some naturally occurring quinines. *J Electroanal Chem* 277:189–196
8. Zon A, Palys M, Stojek Z, Sulowska H, Ossowski T (2003) Supramolecular derivatives of 9,10 anthraquinone. Electrochemistry of regular and low ionic strength and complexing properties. *Electroanalysis* 15:579–585
9. Hu SS, Xu CL, Wang GP, Cui DF (2001) Voltammetric determination of 4-nitrophenol at a sodium montmorillonite-anthraquinone chemically modified glassy carbon electrode. *Talanta* 54:115–123
10. Soriaga MP, Hubbard AT (1982) Determination of the orientation of adsorbed molecules at solid-liquid interfaces by thin layer electrochemistry: aromatic compounds at platinum electrodes. *J Am Chem Soc* 104:2735–2747
11. He P, Crooks RM, Faulkner LR (1990) Adsorption and electrode reactions of disulfonated anthraquinones at mercury electrodes. *J Phys Chem* 94:1135–1141
12. Zhang J, Anson FC (1992) Voltammetry and in-situ fourier transform IR spectroscopy of two anthraquinone disulfonates adsorbed on graphite electrode. *J Electroanal Chem* 331:945–957
13. McDermott MT, Kneten K, McCreery RL (1992) Anthraquinonedisulfonate adsorption, electrode –transfer kinetics and capacitance on ordered graphite electrodes: the important role of surface defects. *J Phys Chem* 96:3124–3130
14. Mohan TM, Gomathi H, Rao GP (1990) Quinone-hydroquinone modified glassy carbon electrode. *Bull Electrochem* 6:630–632
15. Gomathi H, Rao GP (1985) Chemical and electrochemical modification of the glassy carbon surface with quinhydrone. *J Electroanal Chem* 190:85

16. Manisankar P, Gomathi A (2005) Electrocatalytic reduction of dioxygen at the surface of carbon paste electrodes modified with 9,10-anthraquinone derivatives and dyes. *Electroanalysis* 17:1051–1057
17. Salimi A, Eshghi H, Sharghi H, Golabi SM, Shamsipur M (1999) Electrocatalytic reduction of dioxygen at the surface of glassy carbon electrodes modified by some anthraquinone substituted podands. *Electroanalysis* 11:114–119
18. Maia G, Maschion FC, Tanimoto ST, Vaik K, Mäeorg U, Tammeveski K (2007) Attachment of anthraquinone derivatives to glassy carbon and the electrocatalytic behavior of the modified electrodes toward oxygen reduction. *J Solid State Electrochem* 11:1411–1420
19. Mogharrab N, Ghourchian H (2005) Anthraquinone-2-carboxylic acid as an electron shuttling mediator and attached electron relay for horseradish peroxidase. *Electrochem Commun* 7: 466–471
20. Calabrese GS, Buchanan RM, Wrighton MS (1983) Mediated electrochemical reduction of oxygen to hydrogen peroxide via a surface confined naphthoquinone reagent and the mediated electrochemical reduction of a naphthoquinone redox reagent anchored to high surface area oxides. *J Am Chem Soc* 105:5594–5600
21. Delamar M, Hitmi R, Pinson J, Saveant JM (1992) Covalent modification of carbon surfaces by grafting of functionalized aryl radicals produced from electrochemical reduction of diazonium salts. *J Am Chem Soc* 114:5883–5884
22. Allongue P, Delamar M, Desbat B, Fagebaume O, Hitmi R, Pinson J, Saveant JM (1997) Covalent modification of carbon surfaces by grafting of functionalized aryl radicals generated from electrochemical reduction of diazonium salts. *J Am Chem Soc* 119:201–207
23. Wilson T, Zhang J, Oloman CC, Wayner DDM (2006) Anthraquinone-2-carboxylic acid –allyl ester as a new electrocatalyst for dioxygen reduction to produce H₂O₂. *Int J Electrochem Sci* 1:99–109
24. Susan MABH, Begum M, Takeoka Y, Watanabe M (2000) Effect of pH and the extent of micellization on the redox behavior of non-ionic surfactants containing an anthraquinone group. *J Electroanal Chem* 481:192–199
25. Bard AJ, Faulkner LR (2001) *Electrochemical methods, fundamentals and applications*, 2nd edn. Wiley, New York
26. Brown AB, Anson FC (1977) Cyclic and differential pulse voltammetric behavior of reactants confined to the electrode surface. *Anal Chem* 49:1589–1595
27. Bard AJ, Faulkner LR (1980) *Electrochemical methods, fundamentals and applications*. Wiley, New York
28. Manishanker P, Gomathi A, Velayutham D (2005) Oxygen reduction at the surface of glassy carbon electrodes modified with anthraquinone derivative and dyes. *J Solid State Electrochem* 9:601–608
29. Damos FS, Luz RCS, Tanaka AA, Kuboto LT (2010) Dissolved oxygen amperometric sensor based on layer by layer assembly using host-guest supramolecular interactions. *Anal Chim Acta* 664:144–150
30. Duarte JC, Luz RCS, Damos FS, Tanaka AA, Kuboto LT (2008) A highly sensitive amperometric sensor for oxygen based on iron(II)tetrakisulfonated phthalocyanine and iron (III)tetra-(N-methyl-pyridyl)-porphyrin multilayers. *Anal Chim Acta* 612:29–36

Chapter 26

Synthesis and Biological Activity of Derivatives of 2,2'-Dithiobisbenzamides

Roumilla Gungah, Salma Moosun, Sabina Jhaumeer-Laulloo,
and Minu G. Bhowon

Abstract The dithiobisbenzamides **1–4** were synthesised using 2,2'-dithiosalicylic acid with ammonia/ethylamine/benzylamine and 1,2-diaminopropane under different reaction conditions such as grinding, microwave irradiation and conventional heating which yielded the same products but in different yields. The synthesised compounds were subjected to antibacterial screening against both Gram-positive (*S. aureus*, *B. cereus*, *E. faecalis*) and Gram-negative (*E. coli*, *S. typhi*, *P. aeruginosa*, *K. pneumoniae*, *Shigella*) bacteria. The acyclic amides **1–3** showed activity against gram-positive bacteria while no activity was observed for Gram-negative bacteria. On the other hand cyclic amide, **4** was completely inactive against both types of bacteria. The synthesised benzamides were also screened for their anti-HIV activity.

26.1 Introduction

Compounds containing both sulfur and amide functional groups are an important category of pharmaceutical compounds with a broad spectrum of biological activities [1–8]. The synthesis of amides from carboxylic acids or esters is a transformation of general synthetic interest which in many cases needs harsh conditions (temperature, reaction periods) or the use of strong catalysts.

The concept of green chemistry constitutes a good example of solvent free reaction with minimum environmental impact [9–11]. Apart from providing solvent free conditions, microwave and grinding methods are known to provide efficient and safe technology conforming to “green chemistry” requirements. The advantages of performing synthesis in dry medium are: (i) short reaction times, (ii) increased

R. Gungah • S. Moosun • S. Jhaumeer-Laulloo • M.G. Bhowon (✉)
Department of Chemistry, Faculty of Science, University of Mauritius, Reduit, Mauritius
e-mail: rumilla_777@yahoo.com; salma2410@gmail.com; sabina@uom.ac.mu;
mbhowon@uom.ac.mu

safety, (iii) economic advantages due to the absence of solvent. Microwave activation has been used with a great deal of success in various amide syntheses [12–14].

In the present study a few derivatives of amides were synthesised by grinding and microwave irradiation as well as by conventional method and their yields and spectral data were compared. The synthesised compounds were screened for their antibacterial and anti-HIV activities.

26.2 Methodology

26.2.1 General

All chemicals were purchased either from Aldrich or BDH Chemicals and were used without further purification, with the only exception of thionyl chloride which was distilled prior to use. Infrared spectra were measured on a Mattson 1000 FT IR spectrometer in the range of 4,000–400 cm^{-1} using KBr pellets. ^1H NMR and ^{13}C NMR spectra were obtained from a 250 MHz Bruker spectrometer. The elemental analysis was determined on a LECO-932 analyzer. Reaction mixtures were subjected to microwave irradiation by making use of the LG 700 W microwave. The melting points of all samples were determined using a Stuart Scientific Electric Melting point apparatus.

26.2.2 Synthesis of Compounds 1–4

26.2.2.1 Conventional Method

2,2'-Dithiosalicylic acid (1 mmol) was converted into its corresponding bis-acid chloride by refluxing with excess freshly distilled thionyl chloride (10 ml) for 1 h under anhydrous conditions. The excess of thionyl chloride was removed by distillation and 2,2'-dithiobis(benzoyl chloride) was obtained as a brown solid. The bis-acid chloride was stirred for 5 min with triethylamine in dioxane (25 ml) in which ammonia or ethylamine or benzylamine or 1,2-diaminopropane (2 or 1 mmol) dissolved in dioxane (15 ml) was added. The reaction was refluxed for 2 h. The excess solvent was removed which resulted in a brown gum which was purified using $\text{MeOH}/\text{H}_2\text{O}$.

26.2.2.2 Grinding Method

A mixture of 2,2'-dithiosalicylic acid (1 mmol) and concentrated ammonia/ethylamine/benzylamine/1,2-diaminopropane (2 or 1 mmol) in the presence of

thionyl chloride (1 ml) were ground in a mortar and pestle for about 15–20 min. The crude product obtained was thoroughly washed with diethyl ether/ethanol to yield the product.

26.2.2.3 Microwave Method

A mixture of 2,2'-dithiosalicylic acid with ammonia/ethylamine/benzylamine/1,2-diaminopropane in 1:1 or 1:2 ratio in the presence of thionyl chloride (1 ml) was ground for 15–20 min and subjected to microwave irradiation at 350 W, for 7 min. After washing the crude product with diethyl ether/ethanol, the brown solid was obtained.

26.2.2.4 Biological Screening

The benzamides **1–4** were tested in-vitro to assess the growth inhibitory activity against 8 pathogenic clinical isolates namely *Staphylococcus aureus*, *Bacillus cereus*, *Enterococcus faecalis*, *Escherichia coli*, *Salmonella typhi*, *Pseudomonas aeruginosa*, *Klebsiella pneumoniae* and *Shigella* using the Disc diffusion technique. The test organisms were grown on nutrient Muller Hinton agar. The amides solutions of 100 mg/ml in DMSO were prepared and solutions were diluted accordingly. 10 μ L of solution was soaked in the filter paper disc of 5 mm diameter and paper discs were transferred onto the surface of the previously seeded plates and incubated at 37°C for 24 h. The tests were carried out in duplicate. Nalidixic acid (10 mg/ml) and DMSO were used as positive and negative control respectively. The diameter of the inhibition zone was measured after 24 h.

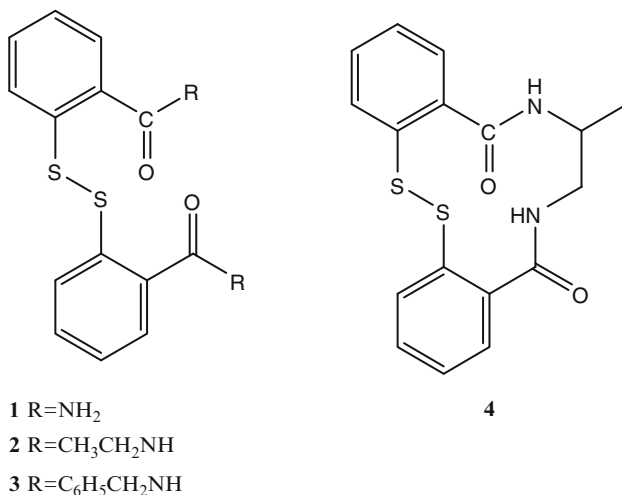
26.3 Results and Discussion

The syntheses of benzamides, **1–4**, by the reaction of dithiosalicylic acid with ammonia, ethyl amine, benzyl amine and 1,2-diaminopropane (Scheme 26.1) were carried out successfully by using conventional, grinding and microwave methods. Compounds **1** and **4** have been reported earlier [15–17] while **2** and **3** are unreported.

The reaction of **1** using microwave irradiation at 350 W was monitored using IR at different time intervals (1–7 min). From the IR spectra, it was found that the reaction started after 5 min of irradiation due to the appearance of the peak at 1,631 cm^{-1} . The reaction reached completion after 7 min with complete disappearance of the peak at 1,681 cm^{-1} .

A comparison of the melting points obtained from the different methods suggested the formation of the same compound, but in different yields (Table 26.1).

The synthesised compounds **1–4** were characterized on the basis of their spectral data (IR, ^1H NMR and ^{13}C NMR) which were compared with data obtained from



Scheme 26.1 Structures of the compounds 1–4

Table 26.1 Yield and melting points of the compounds 1–4

Compd	Grinding		Microwave		Classical	
	Yield %	m.p.(°C)	Yield %	m.p.(°C)	Yield %	m.p.(°C)
C ₁₄ H ₁₂ O ₂ N ₂ S ₂ 1	31	234–240	48	239–241	86	243–244
C ₁₈ H ₂₀ O ₂ N ₂ S ₂ 2	34	141–146	75	143–148	87	149–152
C ₂₈ H ₂₄ O ₂ N ₂ S ₂ 3	51	162–166	83	167–169	91	168–171
C ₁₇ H ₁₆ O ₂ N ₂ S ₂ 4	30	143–147	68	148–152	94	150–154

classical method. The ¹H NMR spectrum of **2** showed a triplet and a quartet at δ 0.6 and 2.3 ppm respectively corresponding to two CH₃CH₂ moieties. The peak at δ 3.5 in compound **3** was attributed to the 4 benzylic protons. These data confirmed the presence of two ethyl amine and benzylamines in compounds **2** and **3**. The structure of **3** was further confirmed by mass spectral data which showed molecular ion peak of C₂₈H₂₄O₂N₂S₂ at m/z 484 (Table 26.2).

26.4 Biological Screening

The antibacterial activities of 2,2'-dithiosalicylic acid and the synthesised compounds 1–4 have been assayed against 8 pathogenic bacteria (Table 26.3). All the compounds showed negligible inhibition against gram-negative bacteria. The

Table 26.2 Spectral and analytical data of compounds **1–4**

Compd	IR $\nu(\text{C=O})$	$^1\text{H NMR}$	$^{13}\text{C NMR}$
1	1,640	8.1(4H, s), 7.9(2H, d, J = 8 Hz), 7.6(2H, d, J = 8 Hz), 7.4(2H, t, J = 7 Hz), 7.2(2H, t, J = 7 Hz)	–
2	1,633	7.4(2H, d, J = 8 Hz), 7.0(2H, d, J = 8 Hz), 6.8(2H, t, J = 7 Hz), 6.7(2H, t, J = 7 Hz), 2.3(4H, q, J = 7 Hz), 0.6(6H, t, J = 7 Hz)	171.1, 139.9, 137.9, 132.3, 131.4, 126.2, 125.9, 32.4, 14.4
3	1,632	7.4(2H, d, J = 7 Hz), 7.0(6H, m), 6.9(6H, m), 6.8(2H, t, J = 7 Hz), 6.6(2H, t, J = 7 Hz), 3.5(4H, s)	171.8, 139, 138, 136.6, 132.3, 131.4, 130.6, 130.4, 130.3, 130.2, 130, 129.7, 126.3, 42.1
4	1,633	7.4(2H, d, J = 6 Hz), 7.0(2H, d, J = 6 Hz), 6.8(2H, t, J = 6 Hz), 6.6(2H, t, J = 6 Hz), 3.0(2H, s), 2.6(2H, d), 1.6(1H, m), 0.8(3H, d)	172.1, 139.7, 137.1, 132.5, 132.0, 126.6, 126.0, 47.4, 44.7, 18.7

Table 26.3 Antibacterial activity of compounds **1–4**

Compd	Conc (mg/ml)	Gram- +ve bacteria			Gram –ve bacteria		
		<i>S. aureus</i>	<i>B. cereus</i>	<i>E. faecalis</i>	<i>E. coli</i>	<i>K. pneumoniae</i>	<i>Shigella</i>
DTSA	100	9 8	– –	– –	8 8	8 8	8 8
	50	– –	– –	– –	7 7	7 7	7 7
1	100	6 6	8 8	– –	– –	– –	– –
	100	7 8	14 14	– –	– –	– –	– –
3	50	– –	8 8	– –	– –	– –	– –
	100	24 24	28 28	20 20	– –	– –	– –
	25	19 19	22 21	16 17	– –	– –	– –
	1	15 16	18 17	12 13	– –	– –	– –
	0.075	9 8	14 13	7 7	– –	– –	– –
	0.05	7 7	12 12	– –	– –	– –	– –
4	0.0125	– –	8 7	– –	– –	– –	– –
	100	– –	– –	– –	– –	– –	– –

DTSA 2,2'-dithiosalicylic acid, – no activity

antibacterial activities of **1–4** and **DTSA** against the bacteria *Salmonella typhi* and *Pseudomonas aeruginosa* were negligible and the data are not reported.

Compound **3** was found to be the most active against all the Gram-positive bacteria with MIC values of 0.05 mg/ml with *Staphylococcus aureus*, 0.0125 mg/ml with *Bacillus cereus* and 0.075 mg/ml with *Enterococcus faecalis*. Compound **4**, a cyclic amide, was found to be ineffective against both Gram negative and Gram positive bacteria.

2,2'-Dithiobisbenzamide, **4** has been reported to possess good anti-HIV activity [17]. The compounds **2** and **3** were tested against the replication of HIV-1(III_B) and HIV-2(ROD) in acute MT-4 cells. Compound **2** was almost inactive with IC₅₀ value

of 123 $\mu\text{g/ml}$ and selectivity index of 1. Compound **3** showed better activity with an IC_{50} of 0.49 against HIV-2 (ROD) with selectivity index of 8.

26.5 Conclusions

In this work, we have been able to synthesize successfully the dithiobisbenzamides derivatives using green protocols. The microwave irradiation gave higher yields in shorter reaction time compared to grinding method. However, the conventional method gave purer products and in higher yields. The acyclic amides showed moderate activity against gram-positive bacteria while no activity was observed for cyclic amide.

Acknowledgements The authors thank Prof De Clerq of Leuven University for anti-HIV activity and the Victoria Hospital, Candos, Mauritius for providing the strains of bacteria.

References

1. Koz'minykh VO (2006) Synthesis and biological activity of substituted amides and hydrazides of 1,4-dicarboxylic acids (a review). *Pharmaceut Chem J* 40:8–17
2. Negwer M, Scharnow HG (2001) *Organic-chemical drugs and their synonyms*, 8th edn. Wiley-VCH, Weinheim, 4680
3. Mishra A, Kaushik NK, Verma AK, Gupta R (2008) Synthesis, characterization and antibacterial activity of cobalt(III) complexes with pyridine-amide ligands. *Eur J Med Chem* 43:2189–2196
4. Patel NB, Patel SD, Patel JN, Patel JC, Gorgamwala YS (2011) Synthesis and antibacterial activity of thioureido amide of fluoroquinolone. *Int J Biochem* 5:37–45
5. Xy L, Farthing AK, Dropinski JF, Meinke PT, McCallum C, Leavitt E (2009) Nocathiacin analogs: synthesis and antibacterial activity of novel water-soluble amides. *Bioorg Med Chem Lett* 19:3531–3535
6. Husain A, Ahmad A, Mujeeb M, Akhter M (2010) New amides of sulphonamides: synthesis and biological evaluation. *J Chil Chem* 55:74–77
7. Medou M, Priem G, Rocheblave L, Pepe G, Meyer M, Chermann JC, Kraus JL (1999) Synthesis and anti-HIV activity of alpha-thiophenoxy-hydroxyethylamide derivatives. *Eur J Med* 34:625–638
8. Domagal JM, Bader JP, Gogliotti RD, Sanchez JP, Stier MA, Song Y, Va JVN (1997) A new class of anti-HIV agents targeted toward the nucleocapsid protein NCp7: the 2,2'-dithiobisbenzamides. *Bioorg Med Chem* 5:569–579
9. Comerford JW, Clark JH, Macquarrie DJ, Breeden SW (2009) Clean, reusable and low cost heterogeneous catalyst for amide synthesis. *Chem Commun* 18:2562–2564
10. Uppiah DJN, Bhowon MG, Jhaumeer-Laulloo S (2009) Solventless synthesis of imines derived from diphenyldisulphide diamine or *p*-vanillin. *J Chem* 6(S1):S195–S200
11. Ancker TRV, Cave GWV, Raston CL (2006) Benign approaches for the synthesis of bis-imine Schiff bases. *Green Chem* 8:50–53
12. Perreux L, Loupy A, Volatron F (2002) Solvent-free preparation of amides from acids and primary amines under microwave irradiation. *Tetrahedron* 58:2155–2162

13. Gopalakrishnan M, Sureshkumar P, Kanagarajan V, Thanusu J, Govindaraju R (2006) A simplified green chemistry approach to organic synthesis in solid media. Activated fly ash, an industrial waste (pollutant) as an efficient and novel catalyst for some selected organic reactions in solvent free conditions under microwave irradiation. *ARKIVOC* 2006:130–141
14. Nomura E, Hosoda A, Mori H, Taniguchi H (2005) Rapid base-catalyzed decarboxylation and amide-forming reaction of substituted cinnamic acids via microwave heating. *Green Chem* 7:863–866
15. Bhowon MG, Jhaumeer-Laulloo S, Rungasami P (2003) Synthesis and characterization of some transition metal chelates of 2,2'-dithiobenzoic acid. *Asian J Chem* 15:1008–1012
16. Witrouw M, Balzarini J, Pannecouque C, Jhaumeer-Laulloo S, Este JA, Schols D, Chereanov P, Schmit JC, Debyser Z, Vandamme AM, Desmyter J, Ramadas SR, De Clercq E (1997) SRR-SB3, a disulphide-containing macrolide that inhibits a late stage of the replicative cycle of human immunodeficiency virus. *Antimicrob Agents Chemother* 41:262–268
17. Jhaumeer-Laulloo S, Ramadas SR (1999) Synthesis and anti-HIV activity of macrocyclic dilactams containing disulphide bridge. *Indian J Heterocycl Chem* 9:01–06

Chapter 27

Spectral Studies of Solar Radiation Induced Dye Decoloration in Aqueous Solution

Fahim Uddin, Rafia Azmat, and Tehseen Ahmed

Abstract Currently extensive researches are in progress for the development of de-coloration techniques for the control of textile industries effluents. The dye waste water is hazardous to the environment and the presence of many anions like Cl^- , Br^- , I^- and NO_3^- increases the risk. This research is in continuation of first report which is based on the photolytic decoloration of methylene green (MG) with urea (which is commonly used in dye industry) as a powerful reductant by the natural light photon as a simulating source to ascertain the role of light for the cleaning of environment. The different concentrations of MG with urea as a reductant were placed under solar radiation for approximately 5 h with variable concentration of these ions and their spectra were recorded before and after irradiation with induced solar radiation. It was found that maximum de-coloration was observed with solar radiations using optimal operational parameters and radiations safely play an effective role in minimizing the color of dye industrial wastes. Results showed that an initial rate of decolorization depends strongly on incident photon energy when full sun rays emitted photon was used (at 12 noon). Thus it was concluded that natural solar light induced treatment may be helpful in cleaning the environment.

27.1 Introduction

The control of water pollution has become of increasing importance in recent years. The release of dyes into the environment constitutes only a small proportion of water pollution, but dyes are visible in small quantities due to their brilliance. Due to large degree of chemical complexity, diversity and stability of the compounds contained in these waste waters, conventional treatment methods are ineffective for their decolorization. Tightening government legislation is forcing textile industries to

F. Uddin (✉) • R. Azmat • T. Ahmed

Department of Chemistry, University of Karachi, Karachi 75270, Pakistan

e-mail: fahim.Uddin01@yahoo.com; rafiasaeed200@yahoo.com; chemist_physical@yahoo.com

treat their waste effluent to an increasingly high standard. Currently, removal of dyes from effluents is by physico-chemical means. Such methods are often very costly and although the dyes are removed, accumulation of concentrated sludge creates a disposal problem [1]. Xiong et al. [2] reported two kinds of coagulation methods, ferrous-mediated coagulation and electrocoagulation as a pretreatment. The overall COD and color removal efficiencies reached as high as 99% and 87%, respectively, by ferrous coagulation (molar rate of Fe(II)/dye: 0.5) and 30-min electrolysis (cell voltage: 20.0 V and airflow: $0.1 \text{ m}^3 \text{ h}^{-1}$). Lee et al. [3] reported the extremely high activities of the Pd–Pt/Al₂O₃ catalysts which may be due to the combined effects of the faster redox cycle resulting from the increased reducibility of Pt surface and the additional oxidation of the reactive dyes with hydroxyl radical. Arslan-Alaton [4] observed the effect of dye-assisting chemicals which were commonly used in the reactive dyeing process (i.e. chloride, carbonate and sulphate sodium salts) on the kinetics, reaction mechanism and efficiency of advanced oxidation processes. There is a need to find alternative treatments that are effective in removing dyes from large volumes of effluents and are low in cost, such as biological or combination systems with various visible/UV resources [5–7]. This article proposes spectral information about the decoloration of methylene green by urea in presence of different ions and specially emphasizes on the effect of incident solar light energy on the apparent color removal of dye waste water as compared to the current available technologies and suggests an effective, cheaper alternative for dye removal and decolorization applicable on large scale by considering the diversity of the effects of solar radiation.

27.2 Material and Methods

All reagents obtained from E-Merck were used as received. MG was obtained from Fluka, Switzerland. The experiment was divided into different sessions. This includes preparation of solutions, spectral measurements, data analysis. All solutions were prepared in de-ionized water and diluted before use. Spectral changes were monitored on UV/Visible Shimadzu 160A Spectrophotometer [8–11].

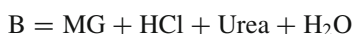
27.3 Preparation of Sample Solutions

MG stock solution of $1 \times 10^{-4} \text{ mol.dm}^{-3}$ was prepared in 250 mL of de-ionized water. Dilutions of this stock solution were made with de-ionized water to obtain a series of dye solutions with varying concentration of reagents [11].

27.4 Spectral Measurements

Spectral changes were monitored before and after absorption of light were recorded by preparing eight sets (A–H) of reaction mixtures according to following reaction scheme.

27.5 Reaction Scheme



The contents were mixed together according to the scheme given and the progress of the (inlets) reaction was monitored by recording the overlay of spectrum after each half hour at $\lambda_{\text{max}} = 652.8$ nm on the UV/Visible spectrophotometer. The O.D (optical density) was also recorded by peak pick in the spectrum obtained after every half hour for every set of reactions. Percent decrease in absorbance was calculated by using the formula [11]

$$\% \text{ decrease in absorption} = \left(1 - \frac{A_f}{A_i} \right) \times 100$$

where A_f = Absorbance after 5 h or final absorbance.

A_i = Absorbance at 0 h or initial absorbance.

The initial absorbance (before placing the sets in the sunlight) and final absorbance (the sets after placing 5 h in the sunlight) were recorded with the wavelength.

Concentration of MG was kept low to avoid the aggregation or degradation of dye which produced sludge in the environment which in turn is carcinogenic itself. The sets prepared were put in sunlight for 5 h (9 am–2 pm) before and after this time no remarkable difference in spectra was observed.

27.6 Results and Discussion

The textile industries are very complex in nature as far as varieties of products, processes and raw materials are concerned and considered in the context of recalcitrant xenobiotics compounds in water and soil ecology. Currently extensive researches are in progress for the development of de-coloration techniques for the control of textile industries effluents. This research is based on the photolytic decoloration of methylene green (MG) with urea (which is commonly used in dye industry) as a powerful reductant by the natural light photon as a simulating source to ascertain the role of light for the cleaning of environment. When only visible solar radiation was used, one might expect the rate of decoloration to be proportional to the amount of dye interaction with photon of light absorbed and there was a significant correlation between dye and photon of light ($r^2 = 0.9165$) which showed that dye could be reduced in the presence of solar radiation. The different concentrations of MG with urea as a reductant were placed under solar radiation for approximately 5 h with variable concentration of these ions and their spectra were recorded before and after irradiation with induced solar radiation. It was found that maximum de-coloration was observed with solar radiations using optimal operational parameters and radiations safely play an effective role in minimizing the color of dye industrial wastes. Spectral changes monitored after each 30 min were reported in the Tables 27.1–27.9.

Initially when spectra were scanned to record the change in optical density only with dye and reductant (Table 27.2) mixture, no significant change in absorbance value indicated that solar radiation was not effective in reduction of MG with urea alone with the observed wavelength of 668 nm(set A). After 5 h no significant shift in wavelength with non significant absorbance change showed that dye and reductant alone are not enough colour for reduction in the presence of natural visible radiation in the atmosphere. Spectral changes of set A are shown in Fig. 27.1 in which dye and reductant were placed alone in presence of solar radiation. Figure 27.1 reflects no significant effect of solar radiation on dye decoloration which may be due to the presence of oxygen that shifts the equilibrium towards reverse side where dye oxidizes and a blue appeared. Solar radiation induced therapy of dye and reductant in open atmosphere represents the significant role of oxygen and

Table 27.1 Spectral changes under solar radiation for 5 h

Set	Initial O.D	Final O.D	% Decoloration
A	1.998	1.986	0.601
B	2.000	1.980	1.00
C	1.413	0.645	54.35
D	1.332	0.530	60.21
E	1.374	0.591	56.99
F	1.507	0.587	61.05
G	1.278	0.534	58.22
H	1.454	0.588	59.56

Table 27.2 Natural solar radiation induced changes in optical density and wavelength of MG with urea

Set A	Time (min)	λ_{\max} (nm)	Absorbance at λ_{\max}
[MG] = 2.8504×10^{-5} M	0	668	2.000
	30	668	2.000
	60	667	2.000
	90	668	2.000
[Urea] = 0.2 M	120	667	2.000
	240	666	1.996
	300	666	1.996

Table 27.3 Natural solar radiation induced changes in optical density and wavelength of MG with urea in presence of HCl

Set B	Time (min)	λ_{\max}	Absorbance at λ_{\max}
[MG] = 2.8504×10^{-5} M	0	671	2.000
	30	672	2.000
	60	672	2.000
	90	673	2.000
[Urea] = 0.2 M	120	673	2.000
	240	673	1.984
[HCl] = 0.1 M	300	674	1.984

Table 27.4 Natural solar radiation induced changes in optical density and wavelength of MG with urea in presence of NaOH

Set C	Time (min)	λ_{\max}	Absorbance at λ_{\max}
[MG] = 2.8504×10^{-5} M	0	570	1.413
	30	568	1.364
	60	568	1.285
[Urea] = 0.2 M	90	568	1.221
	120	570	1.036
	240	567	0.673
[NaOH] = 0.02 M	300	562	0.645

Table 27.5 Natural solar radiation induced changes in optical density and wavelength of MG with urea in presence of NaOH and HCl

Set D	Time (min)	λ_{\max}	Absorbance at λ_{\max}
[MG] = 2.8504×10^{-5}	0	586	1.332
	30	577	1.278
	60	578	1.217
[HCl] = 0.1 M	90	577	1.193
	120	578	1.018
	240	574	0.596
[NaOH] = 0.02 M	300	571	0.530
[Urea] = 0.2 M			

Table 27.6 Natural solar radiation induced changes in optical density and wavelength of MG with urea in presence of NaOH, HCl and Cl⁻ ions

Set E	Time (min)	λ_{\max}	Absorbance at λ_{\max}
[MG] = 2.8504×10^{-5} M	0	594	1.374
	30	577	1.343
	60	576	1.287
[HCl] = 0.1 M	90	575	1.255
	120	574	1.060
	240	571	0.649
[NaOH] = 0.02 M	300	570	0.591
[Urea] = 0.2 M			
[Cl ⁻] = 0.02 M			

Table 27.7 Natural solar radiation induced changes in optical density and wavelength of MG with urea in presence of NaOH, HCl and Br⁻ ions

Set F	Time (min)	λ_{\max}	Absorbance at λ_{\max}
[MG] = 2.8504×10^{-5} M	0	580	1.507
	30	577	1.449
	60	575	1.370
[HCl] = 0.1 M	90	572	1.306
	120	574	1.108
	240	571	0.643
[NaOH] = 0.02 M	300	571	0.587
[Urea] = 0.2 M			
[Br ⁻] = 0.02 M			

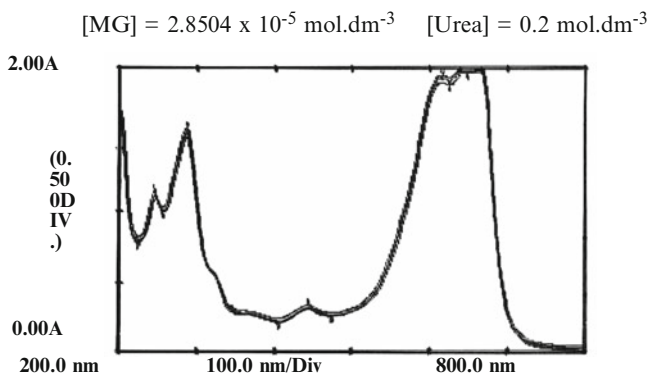
Table 27.8 Natural solar radiation induced changes in optical density and wavelength of MG with urea in presence of NaOH, HCl and I⁻ ions

Set G	Time (min)	λ_{\max}	Absorbance at λ_{\max}
[MG] = 2.8504×10^{-5} M	0	587	1.278
	30	578	1.223
	60	578	1.157
[HCl] = 0.1 M	90	575	1.114
	120	577	0.955
	240	572	0.586
[NaOH] = 0.02 M	300	569	0.534
[Urea] = 0.2 M			
[I ⁻] = 0.02 M			

also showed the Chemical Oxygen Demand (COD) in the open atmosphere. This indicated that only reductant or radiation is not effective for de-coloration even at very low concentration of dye in open atmosphere [12]. When spectra were scanned (Fig. 27.1) in only dye and reductant mixture there was no significant change in absorbance initially and no change in wavelength (Table 27.2). It was 668 nm initially and after 5 h it was 666 nm.

Table 27.9 Natural solar radiation induced changes in optical density and wavelength of MG with urea in presence of NaOH, HCl and NO_3^- ions

Set H	Time (min)	λ_{max}	Absorbance at λ_{max}
[MG] = 2.8504×10^{-5} M	0	580	1.454
	30	573	1.386
	60	572	1.300
[HCl] = 0.1 M	90	574	1.242
	120	574	1.056
	240	569	0.640
[NaOH] = 0.02 M	300	571	0.588
[Urea] = 0.2 M			
[NO_3^-] = 0.02 M			

**Fig. 27.1** Solar radiation induced spectral changes of MG decoloration in presence of urea as a reductant and water (set A)

Reaction mixture containing MG, urea and HCl (Table 27.3) marked as a set B, when placed in solar radiation also showed no significant change in absorbance but non significant shifts in λ_{max} towards longer wavelength region i.e. 671 nm. This shift in wavelength showed that reverse side reaction was dominant in the presence of air. Spectral changes of set B which contain HCl as a medium to optimize decoloration were recorded and the presented in Fig. 27.2. No significant shift in the peaks after induced radiation showed that in acidic medium the decoloration is suppressed that may be related with that the urea in acidic medium abstracts proton according to the following reaction [11].



and the protonated form of $\text{NH}_2\text{CONH}_3^+$ does not undergo the reduction of dye; consequently the oxidized form of MG will remain in the reaction mixture as reported in first paper [11] while addition of alkali shift the wavelength toward

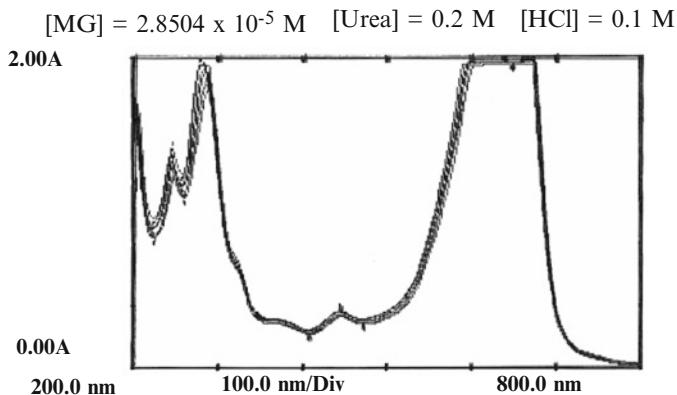


Fig. 27.2 Solar radiation induced spectral changes of MG decoloration in presence of urea as a reductant, HCl and water (set B)

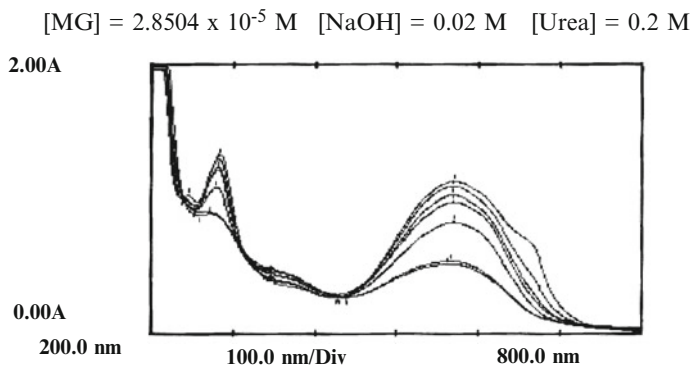


Fig. 27.3 Solar radiation induced spectral changes of MG decoloration in presence of urea as a reductant in alkaline medium (Table 27.3)

smaller region. This may be due to OH radical generated and may cause the bleaching due to degradation (Fig. 27.3). When solution was adjusted to certain pH by adding appropriate amount of acid and base wavelength was 586 nm and absorbance decreases from 1.332 to 0.530 indicate that dye reduction with degradation.

A marked variation in optical density (54.35%) was recorded when methylene green and urea was placed in solar radiation with alkali where wavelength shifts toward shorter region from 670 to 570 nm which reflects the role of OH⁻ ion generation in dye reduction, as observed by earlier investigators [13–16]. Significant (60.21%) decrease in absorbance was measured by natural solar induced photon when reaction mixture contains both NaOH and HCl with MG and urea as compared to other three remaining sets with shift in wavelength towards longer region

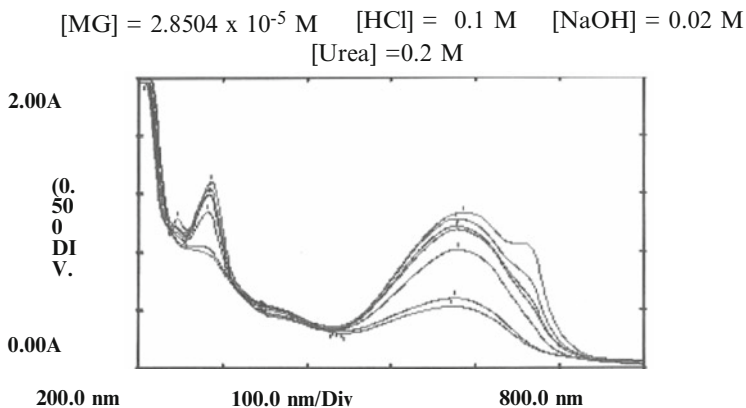
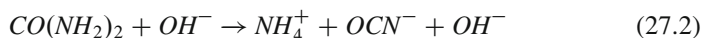
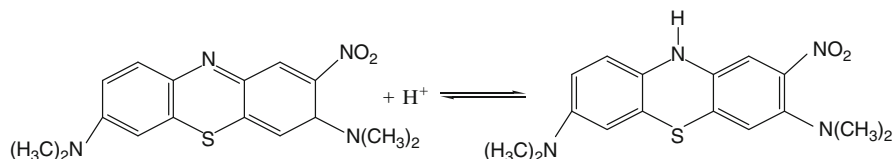


Fig. 27.4 Solar radiation induced spectral changes of MG decoloration in presence of urea as a reductant (set D)

(Table 27.5). Spectral shift in peaks in alkaline medium were recorded after each half hour and shown in Fig. 27.3. Absorption spectrum of dye after 30 min showed the decrease in absorption of dye indicating that the bleaching of dye take place in basic medium through solar therapy. This may be related with OH radicals generated in alkaline medium



The powerful reducing reactive species of urea in alkaline medium [(NH₂)₂COH⁺] after hydrolysis generates one proton as mentioned in first report [11] (Eq. 27.3) which is believed to be abstracted by dye and therefore reduction of dye easily takes place in alkaline solution according to the following reaction



Approximately same spectral peaks were observed in set D when dye mixture with alkali and acid was placed in solar radiation (Fig. 27.4) but % de-coloration is found to be 60.21% which was highest as compared to all studied sets of A, B and C reflecting the simultaneous role of proton and OH ions in dye bleaching.

As the textile effluent is complex in nature and contains many types of ions (Tables 27.5–27.9), the role of additive ions in dye bleaching was monitored as an environmental influence of ions present in aquatic resources and it was found

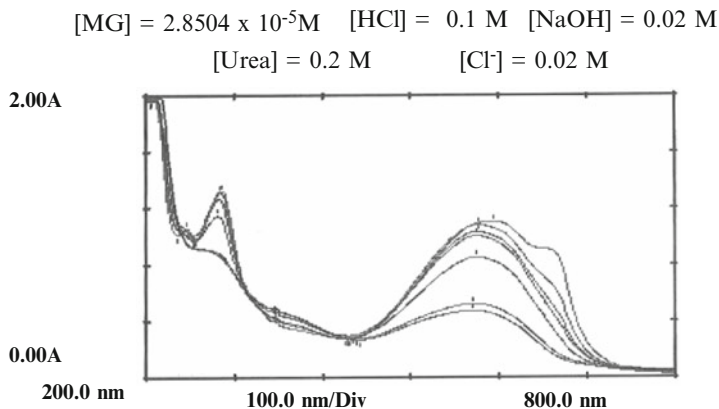


Fig. 27.5 Solar radiation induced spectral changes of MG decoloration in presence Cl^- ions (set E)

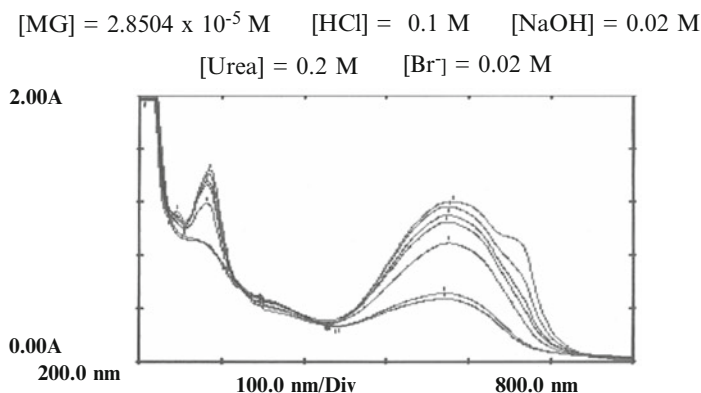


Fig. 27.6 Solar radiation induced spectral changes of MG decoloration in presence Br^- ions (set F)

that these ions play an effective function in dye decoloration. The addition of chloride (Table 27.6) initially effects the absorption with non-significant shift in the wavelength, it was 594 nm when reaction mixture was placed in the solar radiation but after 5 h it was shifted to a shorter region with 61.04% decrease in absorbance. This decrease in optical density supports that dye industrial effluents have complex nature with complex continuous reaction which may be helpful for color loss of dye. With bromide (Table 27.7) and iodide (Table 27.8) treatment of MG showed variation in optical density before and after solar radiation treatment with approximate same wavelength after 5 h. This wavelength supports the decoloration of the dye with reduction with no significant shift in λ_{max} . The role of nitrate was monitored in presence of solar radiation and followed the same pattern as bromide,

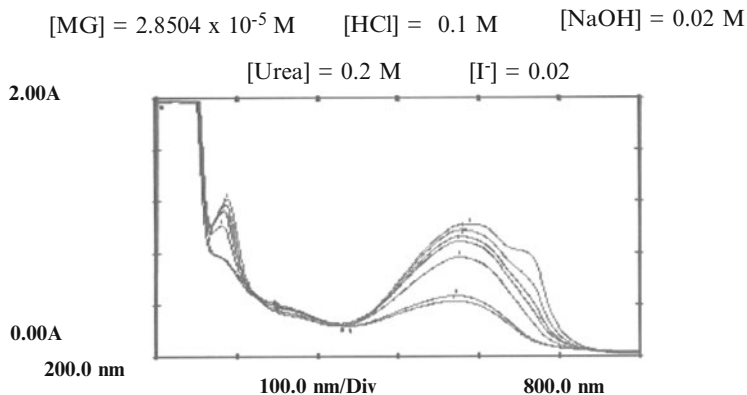


Fig. 27.7 Solar radiation induced spectral changes of MG decoloration in presence I^- ions (set G)

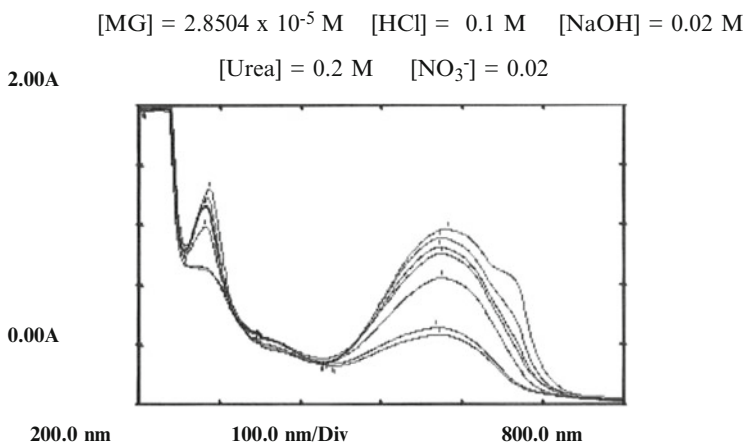


Fig. 27.8 Solar radiation induced spectral changes of MG decoloration in presence of NO_3^- ions (set H)

iodide, and chloride with approximately same wavelength and optical density where decrease in absorbance after 5 h was 59.56% in bleaching the MG solution under the visible solar radiation. The % decoloration was found to be 56.99% in set E, in which Cl^- ions were present with MG and urea (Fig. 27.5). Results showed that % decoloration is slightly decreased as compared to that in the absence of Cl^- ions (set D) showing the inhibitory effect of the anion on dye bleaching may be due to some other secondary reaction of Cl^- ion in reaction mixture while reaction mixture containing Br^- as anion in water showed highest bleaching power of dye which also reflects the oxidizing nature of Br^- in reaction mixture (Set F). The % decoloration was found to be 61.05%. This showed that presence of Br^- ions helps in decoloration of MG or % decoloration of MG is enhanced in the presence of Br^-

ion (Fig. 27.6). In presence of I^- % decoloration (Fig. 27.7) was found to be 58.22% (Set G). The decoloration followed the order $Br^- > I^- > Cl^-$. In the presence of NO_3^- % decoloration (Fig. 27.8) was found to be 59.55% (Set H) (Table 27.9).

27.7 Conclusions

Results showed that an initial rate of decolorization depends strongly on incident photon energy when full sun rays emitted photon was used (at 12 noon). Both solar light illumination and ions present in the dye mixture were more effectively eliminated than with either solar light or ions alone. Thus it was concluded that natural solar light induced treatment may be helpful in cleaning the environment. Basically this research was launched due to the fact that all dye industrial effluents were dumped in the sea-water which have high salinity and ions like Cl^- , Br^- , I^- and NO_3^- which help in bleaching the dye solution or this showed that treatment of NATURE may be helpful in cleaning the environment to certain extent but continuous discharge should be monitored by biological or chemical treatment.

References

1. Robinson T, Mc-Mullan G, Marchant R, Nigam P (2001) Remediation of dyes in textile effluent: a critical review on current treatment technologies with a proposed alternative. *Bioresour Technol* 77:247–255
2. Xiong Y, Strunk PJ, Xia H, Zhu X, Karlsson HT (2001) Treatment of dye wastewater containing acid orange II using a cell with three-phase three-dimensional electrode. *Water Res* 35:4226–4230
3. Lee DK, Cho IC, Lee GS, Kim SC, Kim DS, Yang YK (2004) Catalytic wet oxidation of reactive dyes with H_2/O_2 mixture on Pd-Pt/ Al_2O_3 catalysts. *Sep Purif Technol* 34:43–50
4. Arslan-Alaton A (2003) A review of the effects of dye-assisting chemicals on advanced oxidation of reactive dyes in wastewater. *Color Technol* 119:345–353
5. Azmat R, Ahmed S, Qureshi S, Mohammed FV, Uddin F (2006) Aerobic oxidation of D-glucose by methylene green in alkaline aqueous solution by visible spectrophotometry. *J Appl Sci* 6:2784–2788
6. Azmat R, Yasmeen B, Uddin F (2007) Kinetics of methylene blue reduction with oxalic acid by visible spectrophotometric method. *Asian J Chem* 19:1115–1121
7. Azmat R (2009) Reduction of methylene blue with reducing sugars: kinetics of reduction of methylene blue with organic reductants. VDM Verlag Dr. Müller e.K., Saarbrücken. Paperback, 248 p, ISBN 978-3-639-14715-5
8. Azmat R, Qamar N, Saeed A, Uddin F (2008) Spectrophotometric studies of reduction of methylene green with EDTA in alkaline medium. *Chin J Chem* 26:631–634
9. Ahmed K, Uddin F, Azmat R (2009) Reduction kinetics of thionine in aerobic condition with D-galactose. *Chin J Chem* 27:1232–1236
10. Azmat R, Uddin F (2009) Photo decoloration of methylene blue with ribose at optimum condition by visible radiation. *Chin J Chem* 27:1237–1243
11. Ahmed T, Uddin F, Azmat R (2010) Kinetics and mechanism study of chemical treatment of methylene green by urea. *Chin J Chem* 28:748–754

12. Styliidi M, Kondarides DI, Verykios XE (2003) Mechanistic and kinetic study of solar-induced photocatalytic degradation of acid orange 7 in aqueous TiO₂ suspensions. *Int J Photoenergy* 5:59–67
13. Fox MA, Dulay MT (1993) Heterogeneous photocatalysis. *Chem Rev* 93:341–357
14. Goncalves MST, Oliveira-Campos AMF, Pinto EMMS, Plasencia PMS, Queiroz MJRP (1999) Photochemical treatment of solutions of azo dyes containing TiO₂. *Chemosphere* 39:781–786
15. Bauer C, Jacques P, Kalt A (1999) Investigation of the interaction between a sulfonated azo dye (AO7) and a TiO₂ surface. *Chem Phys Lett* 307:397–406
16. Vautier M, Guillard C, Herrmann JM (2001) Photocatalytic degradation of dyes in water: case study of indigo and of indigo carmine. *J Catal* 201:46–59

Chapter 28

Optimization of Process Parameters for Enhanced Decolorization of NOVASOL Direct Black Textile Dye by *Agaricus bitorqus*

Haq N. Bhatti and Ismat Bibi

Abstract Dyes released by the textile industries pose a threat to the environment safety. Recently, dye decolorization through biological means has gained momentum as these are cheap and can be applied to wide range of dyes. The current project focused on the ability of two strains of *Agaricus bitorqus* for the decolorization of four direct dyes. In the initial time course study maximum decolorization (77.42%) of NOVASOL direct black by *Agaricus bitorqus* A66 was observed after 4 days. Various process parameters like pH, temperature, carbon and nitrogen supplements and C:N ratio were optimized. The effects of Tween-80, metal ions, veratryl alcohol on enzyme synthesis and dye decolorization were also investigated. The process optimization enhanced enzyme biosynthesis and dye removal. Maximum activity of lignin peroxidase (855 IU/ml) and enhanced dye decolorization (99.7%) was achieved only in 5 h. Lignin peroxidase (LiP) was found to be the major enzyme secreted by *Agaricus bitorqus* A66.

28.1 Introduction

A wide variety of textiles dyes are being synthesized and used in textile industry to develop different colors and shades according to the desire of the people [1]. Huge volumes of dye-containing effluents are being released into the environment by textile industries. Such effluents discolor water bodies and increase biochemical oxygen demand of contaminated water. Textile dyes are potentially toxic, carcinogenic and mutagenic because of their low removal rate [2]. Textile dyes and other commercial colorants have emerged as a focus of environmental remediation efforts [3].

H.N. Bhatti (✉) • I. Bibi

Department of Chemistry & Biochemistry, University of Agriculture, Faisalabad 38040, Pakistan
e-mail: hnbhatti2005@yahoo.com; ismat16.08.1982@yahoo.com

Conventional methods are available for treatment of textile wastewater, but most of the processes are either not very effective or environmentally compatible [4]. Microbial degradation of environmental pollutants such as dyes has been proposed as a cheaper and environmentally friendly alternative [5]. In the recent past an intensive work has been carried out regarding the biodegradation and decolorization of dyes using white rot fungi [1, 6–8]. White rot fungi can mineralize xenobiotics/dyes to carbon dioxide and water through their oxidative and non-specific ligninolytic enzyme system. The main objective of this investigation was to observe the decolorization potential of least studied fungus *Agaricus bitorqus* for decolorization of some direct dyes. This study may form the basis of using *Agaricus bitorqus* for development of effective decolorization process for textile industry real effluents.

28.2 Experimental

The direct dyes NOVASOL Direct Black, NOVASOL Direct Blue GL, NOVASOL Direct Red 2BL and NOVASOL Direct Flavin were gifted by Huntsman Pakistan Ltd. for research purposes. All the reagents used were of analytical grade.

Pure culture of *Agaricus bitorqus* was obtained from Institute of Horticultural Sciences, University of Agriculture Faisalabad Pakistan. The inoculum was prepared by adding fungal spores to the sterilized inoculum medium (pH 5) having composition of modified Kirk's medium [9]. The inoculum flasks were incubated (30°C) in an orbital shaker (Gallen-Kemp, UK) at 120 rpm to get homogenous spore suspension.

Experiments were performed using 250 mL flasks in a temperature controlled incubator. Each flask contained 100 mL of 0.01% respective direct dye solutions prepared in Krik's basal medium (pH 5). The flasks were sterilized for 15 min at 121°C, allowed to cool and then inoculated with 2 mL homogenous conidia of *Agaricus bitorqus*. The inoculated flasks were incubated for 5 days at 30°C in orbital shaker at 120 rpm. Samples (2 mL) were removed after every 24 h and centrifuged at 10,000 rpm for 15 min. The supernatants were used to determine the extent of dye decolorization and enzyme assay.

The extent of dyestuff decolorization was determined by measuring the absorbance of each dye by UV/Visible spectrophotometer (Hitachi U2001, Tokyo, Japan). The wavelength resulting in maximum absorbance (λ_{\max}) for Direct Blue (578 nm), Direct Red (357 nm), Direct Black (499 nm) and Direct Flavin (468 nm) was used for the estimation of % dye decolorization.

The ligninolytic enzymes profile in the culture supernatants was determined by standard methods. Manganese peroxidase (MnP) activity was determined by monitoring the oxidation of 1 mM MnSO₄ in 50 mM sodium malonate buffer (pH 4.5) in the presence of 0.1 mM hydrogen peroxide [10]. Laccase activity was determined following the oxidation of 2,2-azinobis (3-ethyl-benzo-thiazoline-6-sulphonic acid (ABTS) at 420 nm [10]. Lignin peroxidase (LiP) was assayed by

determining the oxidation rate of veratryl alcohol to veratraldehyde in the presence of 10 mM sodium tartrate buffer (pH 3.0) and H_2O_2 [11].

The most decolorized dye NOVOSOL Direct black by *Agaricus bitorqus* A66 was used to find out the most suitable culture conditions like pH, temperature, medium composition, dye concentration, C/N ratio, the effect of metal ions and mediators etc. The classical approach was adopted for the optimization of different parameters [1, 12].

28.3 Results and Discussion

The initial time course study for decolorization of four direct dyes viz. NOVASOL Direct Black, NOVASOL Direct Blue GL, NOVASOL Direct Red 2BL and NOVASOL Direct Flavin by *Agaricus bitorqus* A66 was carried out for 4 days using medium I. Results of screening study are shown in Fig. 28.1. The screening results of direct dyes showed varying extent of decolorization by the fungus. There was a gradual increase in the decolorization of all direct dyes with time. The result showed that *Agaricus bitorqus* A66 showed more decolorization trend (77.42%) for the NOVASOL Direct Black dye on the 4th day as compared to other direct dyes. The results of ligninolytic enzymes involved in decolorization of direct dyes such as LiP, MnP and laccase are shown in Fig. 28.2. Maximum lignin peroxidase (LiP) activity (377 IU/mL) was observed in the flask containing NOVASOL Direct Black while minimum LiP activity (204 IU/mL) was observed in flask having NOVASOL Direct Flavin. Based on maximum decolorization trend and involvement of LiP as major enzyme, the NOVASOL Direct Black dye was selected for further process optimization for enhanced decolorization.

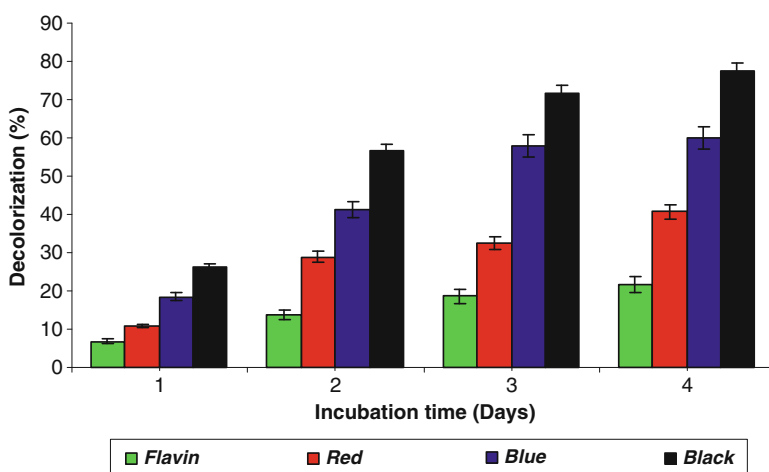


Fig. 28.1 Decolorization of different dyes by *Agaricus bitorqus* A66

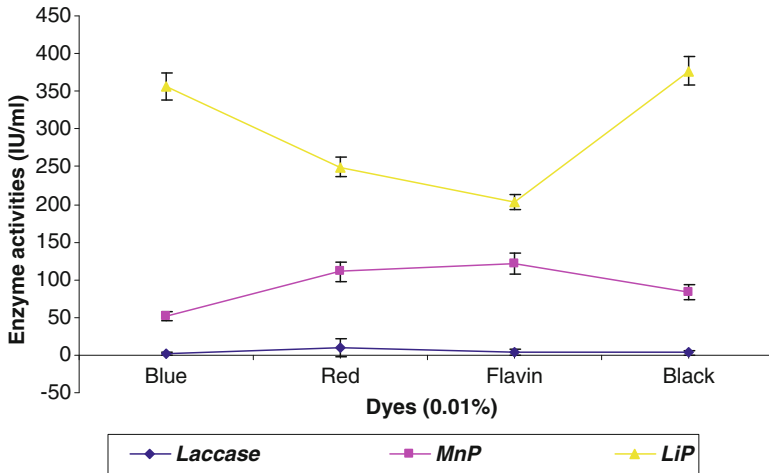


Fig. 28.2 Production of ligninolytic enzymes during decolorization of direct dyes by *Agaricus bitorques* A66

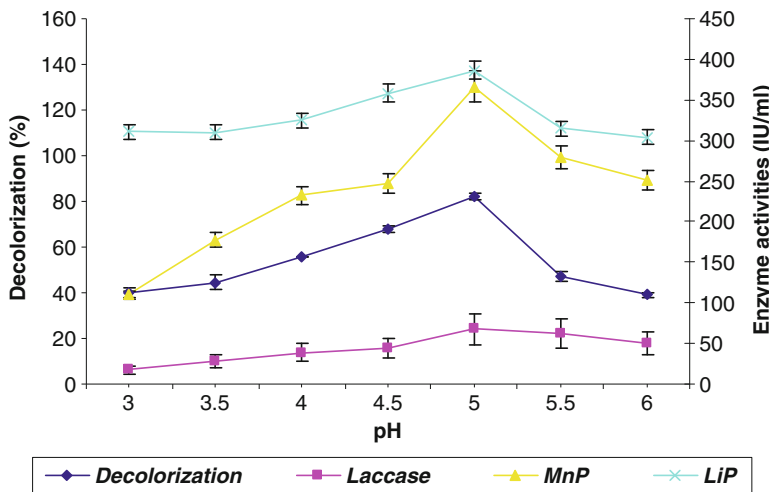


Fig. 28.3 Effect of pH on dye decolorization and enzymes activity by *Agaricus bitorques* A66

Triplicate flasks containing medium modified Kirks, medium having pH from 3 to 6 were inoculated and incubated at 30°C for 24 h. The decolorization and production of ligninolytic enzymes as a function of pH has been represented in Fig. 28.3. The results indicated that with increase in pH of the medium the decolorization potential of the fungus also increased. Maximum dye decolorization (82.25%), LiP (386.6 IU/ml) and MnP (130.3 IU/ml) activities were observed at pH 5.0. A further increase in pH lowered the decolorization efficiency and LiP activity

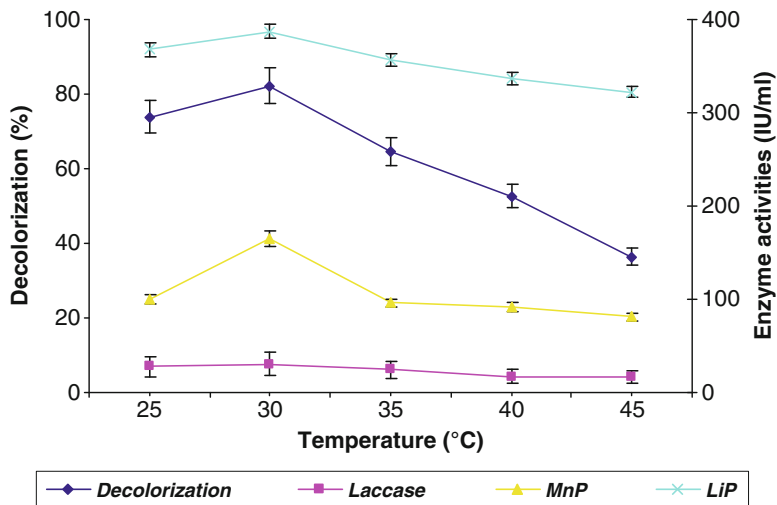


Fig. 28.4 Effect of temperature on dye decolorization and enzymes activity by *Agaricus bitorquis* A66

of *Agaricus bitorquis* A66. Ligninases production increased with increase in pH of the medium, but as the pH increased above 5.0, the enzyme activities decreased. The pH of the basal nutrient medium plays a significant role in biodegradation of dyes and other recalcitrant compounds by white rot fungi. The pH is a very important parameter for the proper functioning of enzymes which show maximum activity at optimal pH.

In order to study the effect of temperature on the biodegradation of NOVA-SOL Direct Black by *Agaricus bitorquis* A66 inoculated flasks were subjected to different temperatures (25°C, 30°C, 35°C, 40°C and 45°C). The results indicated that maximum decolorization (82.26%), LiP (387.18 IU/ml) and MnP activity (165.58 IU/ml) were observed in flasks incubated at 30°C followed by 73.87% decolorization and LiP activity (367.7 IU/ml) at 25°C (Fig. 28.4). Low activity of laccase (30.66 IU/ml) was also observed at this temperature. The decolorization efficiency as well as ligninases activity of the fungus decreased above 30°C. The enhanced decolorization of the dye can be correlated to high ligninases activity at 30°C. There was no significant difference in the final pH. However dry cell biomass increased with an increase in the temperature and could not be correlated with maximum decolorization and enzyme production.

In order to enhance the decolorization of NOVASOL Direct Black by *Agaricus bitorquis* A66 different carbon sources like glucose, fructose, maltose, sucrose, molasses & starch (1%) were added in growth medium under optimum conditions. The results indicated that maximum dye decolorization (90.64%) was observed in flasks receiving fructose followed by sucrose (87.10%), and minimum color removal (47.74%) was observed with molasses in 24 h (Fig. 28.5). Ligninolytic

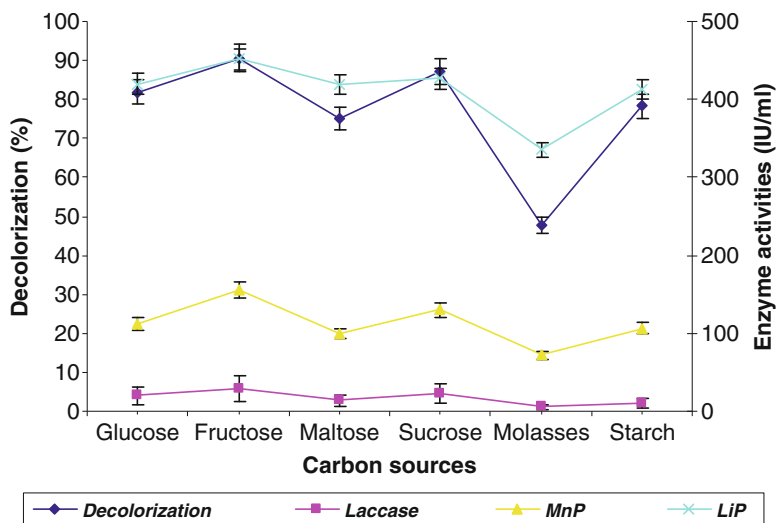


Fig. 28.5 Effect of carbon additives on dye decolorization and enzymes activity by *Agaricus bitorqus* A66

profiles of *Agaricus bitorqus* A66 with various carbon additives were also consistent with the decolorization pattern of NOVASOL Direct Black. Again LiP was the major enzyme (451.4 IU/ml) produced in flasks receiving fructose as compared to MnP (155.2 IU/ml) and laccase (29.54 IU/ml). Generally the addition of carbon supplements to basal media have been reported to increase the fungal growth and enzyme biosynthesis of white rot fungi to achieve enhanced decolorization of different dyes [8, 13–15].

In order to study the stimulating/inhibitory effect of nitrogen, different nitrogen sources like ammonium nitrate, ammonium sulphate, ammonium tartrate, peptone and urea (0.02%) were added to the culture media under optimum conditions for 24 h. The results (Fig. 28.6) showed that maximum decolorization (93.87%) was observed with ammonium nitrate followed by urea (91.29%) and ammonium sulphate (88.71%). All the nitrogen sources tested exerted stimulatory effect on the decolorization of NOVASOL Direct Black along with ligninolytic profiles of *Agaricus bitorqus* A66; LiP (503.3 IU/ml), MnP (282.6 IU/ml) and laccase (33.76 IU/ml). Our findings are in line with the earlier reported results in which higher growth and ligninolytic activities have been reported in nitrogen rich media for decolorization of different types of dyestuff by WRF [16–18].

For efficient decolorization the growth medium was further supplemented with different C/N ratios (15:1, 20:1, 25:1, 30:1 and 35:1) of selected carbon and nitrogen sources under preoptimized conditions. Maximum color removal (98%) was observed for 20:1 C/N ratio after 24 h. By increasing the C/N ratio from optimum, less color removal was achieved. This enhanced decolorization of the dye may be attributed to higher LiP activity (587.5 IU/ml) of the fungus.

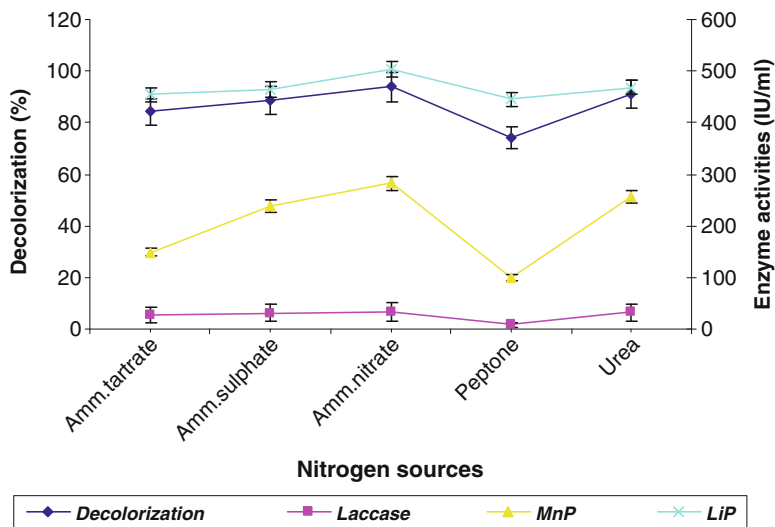


Fig. 28.6 Effect of nitrogen additives on dye decolorization and enzymes activity by *Agaricus bitorquus* A66

Various redox mediators like MnSO_4 , ABTS, veratryl alcohol, glyoxylate and guaiacol were added (1 ml of 1 mM mediator solution) to the growth medium under optimum conditions. It was noted that different mediators showed different effects on decolorization as well as enzyme production. The flasks receiving veratryl alcohol exhibited almost complete decolorization (99.7%) and maximum LiP activity (855 IU/ml) in only 5 h. Moreover, it was observed that veratryl alcohol had no significant effect on MnP and laccase production. MnSO_4 had a stimulatory influence on MnP activity with non-significant effect on other two enzymes whereas, ABTS increased laccase production but had little or no affect on LiP and MnP activities.

The decolorization potential of *Agaricus bitorquus* A66 was checked using different concentrations of NOVASOL Direct Black (0.01–0.030%) under pre-optimized conditions. The results showed that almost complete decolorization (99.34%) of the dye was observed with 0.01% dye in 5 h only (Fig. 28.7). With an increase in dye concentration a gradual decrease in dye decolorization was observed. High concentration of the dye was not tolerated by the fungus and consequently less decolorization was observed in flasks receiving higher (>0.01%) concentration of the dye. Lignin peroxidase was observed to be the major enzyme (855 IU/ml) involved in the decolorization of NOVASOL Direct Black followed by MnP (305 IU/ml).

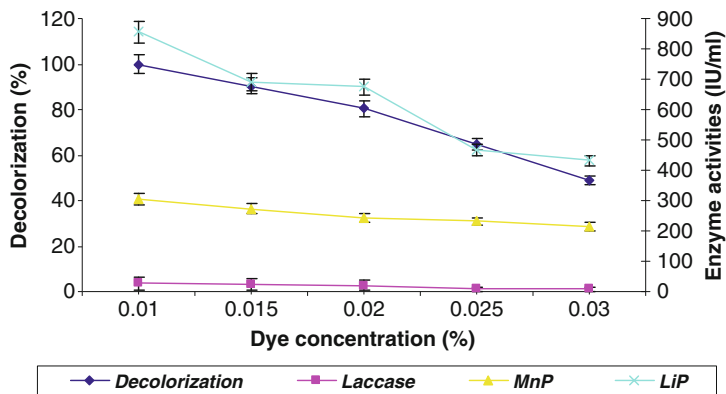


Fig. 28.7 Effect of dye concentration on decolorization and enzymes activity by *Agaricus bitorques* A66

28.4 Conclusions

The white rot fungus *Agaricus bitorques* A66 had variable decolorization potential towards direct dyes commonly used in the textile industry. It can efficiently decolorize and degrade textile dye NOVASOL Direct Black using suitable nutrient growth medium under acidic pH. Decolorization potential of the fungus was enhanced to 99.7% in 5 h by the addition of veratryl alcohol as mediator. Lignin peroxidase (LiP) was found to be the major enzyme activity during the dye decolorization. The fungus seems to be highly promising for development of effective bioremediation process for real industrial effluents that contain other structurally related dyes.

Acknowledgements The authors are thankful to Higher Education Commission of Pakistan (HEC) for financial support.

References

1. Kanwal N, Asgher M, Bhatti HN, Sheikh MA (2010) Ligninase synthesis and decolorization of Drimarine Blue K2RL by *Pleurotus ostearatus* IBL-02 in carbon and nitrogen sufficient shake flask medium. *Fresenius Environ Bull* 19:63–68
2. Zollinger H (2003) *Color chemistry: syntheses, properties and applications of organic dyes and pigments*, 3rd edn. Wiley – VCH, Weinheim, p 36
3. Weber EJ, Adams RL (1995) Chemical and sediment-mediated reduction of the azo Dye. *Environ Sci Technol* 29:1163–1170
4. Seshadri S, Bishop PL, Agha AM (1994) Anaerobic/aerobic treatment of selected azo dyes in waste water. *Waste Manag* 14:127–137
5. Poonum N, Banat IM, Singh D, Marchant R (1996) Microbial process for the decolorization of textile effluent containing azo, diazo and reactive dyes. *Process Biochem* 31:435–442

6. Bhatti HN, Akram N, Asgher M (2008) Optimization of culture conditions for enhanced decolorization of Cibacron Red FN-2BL by *Schizophyllum commune* IBL-06. *Appl Biochem Biotechnol* 149:255–264
7. Asgher M, Azim N, Bhatti HN (2009) Decolorization of practical textile industry effluents by white rot fungus *Coriolus versicolor* IBL-04. *Biochem Eng J* 47:61–65
8. Bibi I, Bhatti HN, Asgher M (2009) Decolorization of direct dyes with manganese peroxidase from white rot basidiomycetes *Ganoderma lucidum*-IBL-5. *Can J Chem Eng* 87:435–440
9. Asgher M, Asad MJ, Legge RL (2006) Enhanced lignin peroxidase synthesis by *Phanerochaete chrysosporium* in solid state bioprocessing of a lignocellulosic substrate. *World J Microbiol Biotechnol* 22:449–453
10. Wariishi H, Vali K, Gold MH (1992) Manganese (II) oxidation by manganese peroxidase from basidiomycete *Phanerochaete chrysosporium*. *J Biol Chem* 267:23688–23698
11. Tien M, Kirk TK (1988) Lignin peroxidase of *Phanerochaete chrysosporium*. *Methods Enzymol* 161:238–249
12. Hafiz I, Asgher M, Bhatti HN (2008) Optimization of Cibacron Turquoise P-GR decolorization by *Ganoderma lucidum*-IBL-05. *Fresenius Environ Bull* 17:1987–1993
13. Selvam KA, Swaminathan KB, Rasappan KC, Rajendran RA, Pattabhi SD (2006) Decolorization and dechlorination of pulp and paper industry effluent by *Thelephora* sp. *Ecol Environ Conserv* 12:223–226
14. Chander M, Arora DS (2007) Evaluation of some white-rot fungi for their potential to decolorize industrial dyes. *Dyes Pigments* 72:192–198
15. Asgher M, Kausar S, Bhatti HN, Shah SAH, Ali M (2008) Optimization of medium for decolorization of solar golden yellow R direct textile dye by *Schizophyllum commune* IBL-06. *Int Biodeterior Biodegrad* 61:189–193
16. Kaal EEJ, Field JA, Joyce TW (1995) Increasing ligninolytic activities in several white-rot basidiomycetes by nitrogen-sufficient media. *Bioresour Technol* 53:133–139
17. D'Souza TM, Merrit CS, Reddy CA (1999) Lignin-modifying enzymes of the white-rot basidiomycete *Ganoderma lucidum*. *Appl Environ Microbiol* 65:5307–5313
18. Rigas F, Dritsa V (2006) Decolourization of a polymeric dye by selected fungal strains in liquid cultures. *Enzyme Microb Technol* 39:120–124

Chapter 29

Chemical Composition and Antimicrobial Activity of Comorian *Ocimum canum* Essential Oil Harvested in the Region of Maweni Dimani-Grande Comoros

S.O.S. Hassane, A. Farah, B. Satrani, M. Ghanmi, N. Chahmi, S.H. Soidrou, and A. Chaouch

Abstract This work aims to study antibacterial and antifungal activities and chemical composition of *Ocimum canum* Sims essential oil, harvested in the region of Maweni Dimani on the island of Grande Comore. The yield of *O. canum* essential oil from Maweni-Dimani was 2.06%. This essential oil comprises 1,8-cineole (46.88%), camphor (14.98%), α -pinene (5.71%), β -pinene (4.66%) and γ -elemene (3.91%) as predominant constituents. The antibacterial and antifungal activities of this essential oil have been studied against four bacteria (*Escherichia coli*, *Bacillus subtilis*, *Staphylococcus aureus*, *Micrococcus luteus*) and three fungi (*Aspergillus niger*, *Penicillium expansum*, *Penicillium digitatum*). Bioassays showed that *Ocimum canum* Sims essential oil has bactericidal and fungicidal activities.

S.O.S. Hassane (✉)

Faculty of Science and Technology, University of the Comoros, BP 2585 Moroni, Comoros
e-mail: said.omar2000@yahoo.fr

B. Satrani

Centre de recherche forestière, BP 763, Agdal, 10050 Rabat, Morocco

M. Ghanmi

Laboratoire de Chimie des Plantes et Synthèse organique et Bioorganique, Faculté des Sciences, Université Mohammed V-Agdal, BP1014 Rabat, Morocco

A. Farah • N. Chahmi • S.H. Soidrou

National Institute of Medicinal and Aromatic Plants – Taounate, BP 159, Tounate Principale, Sidi Mohamed Ben Abdallah University, Fes Maroc

A. Chaouch

Laboratory of Applied Chemistry and Quality Control, Faculty of Science, Université Ibn Tofail, BP133 Kenitra, Morocco

29.1 Introduction

The genus *Ocimum* belonging to the *Lamiaceae* comprises annual and perennial herbs and shrubs native to the tropical and subtropical regions of Asia, Africa and South America [1–3]. Worldwide, the genus includes about 150 species. These species are small annual Labiates seldom reaching over 40 cm in height and are very common in villages. The taxonomy of *Ocimum* is complex due to interspecific hybridization and polyploidy of the species in the genus.

In the Comoros Islands, there are four species of *Ocimum*: *Ocimum canum* Sims, *Ocimum basilicum* L., *Ocimum suave* L. and *Ocimum grantissimum* L. [4]. Their presence is usually indicated on the volcanic soil and they grow well in forest medium and high altitude [5].

The *Ocimum canum* (basil with small leaves) is a very fragrant plant that grows only by seeds. It is also considered as a source of aroma compounds, and it possesses a range of biological activities. It is an adventitious species which grows on the wet clay-loam. Its growth and germination are respectively rapid and short [2, 6–8].

The whole plant is used as a medicinal herb in medical treatments such as for headaches, coughs, diarrhoea, worms, and kidney malfunctions. It is also used to relieve shortness of breath, aches, and ear washes for mumps. Several *Ocimum* species (*Ocimum gratissimum*, *Ocimum basilicum*, *Ocimum viridae*, *Ocimum suave*, *Ocimum canum*) are used to treat central nervous system (CNS) disorders in various parts of the world and its depressive activity is frequently reported. Leaves from *Ocimum* species release a pleasing odor when squashed between the fingers and could be used as a culinary condiment. This fragrant herb is used as an ornamental and it allows the extraction by hydro-distillation of essential oils [3, 9–11]. These essential oils are recommended against insomnia and anxiety [12–14].

Moreover, several studies have shown that the essential oil of *O. canum* has antibacterial, antifungal, insecticidal and larvicidal activities [11, 15–18]. Several chemotypes of the essential oil of *O. canum* are listed in the literature: fenchone [19], eugenol [20], terpineol [21], 1,8-cineole [22], β -caryophyllene/(E) α -bergamotene/bicyclogermacrene [23], methyl cinnamate [24], methyl chavicol/ α -terpineol [25], camphre [26] and linalol [27].

The aim of this study is to determine the yield of essential oil, to characterize its chemical composition and to study its antibacterial and antifungal activity against four bacterial strains and three fungal species. This work is part of the agreement established between the National Institute of Medicinal and Aromatic Plants (Morocco), Faculty of Science and Technology of the Comoros and Forest Research Centre.

29.2 Material and Methods

29.2.1 Plant Material

The samples of *O. canum* (leaves and flowers) were collected in Maweni – Dimani (east of Grande Comoros, on the cliff of Karthala volcano) in May 2008. The samples were previously subjected to dry in the shade for 15 days to facilitate storage.

29.2.2 Extraction of Essential Oil

The plant materials were subjected to hydro-distillation for 2 h using a modified Clevenger-type apparatus [28]. In every test, 250 g of fresh leaves have been treated. The oils obtained were separated from water by decantation, and dried over anhydrous sodium sulphate (20% of the total mass essential oil), filtered and stored at 4°C and analyzed by GC and GC-MS. The oil yields were expressed in ml/100 g dry plant material.

29.2.3 Chemical Analysis

GC analyses were performed on a Hewlett-Packard (HP 6890) gas chromatograph (FID), equipped with a HP-5 capillary column (30 m × 0.25 mm × 0.25 μm). The temperature was programmed from 50°C after 5 min initial hold to 250°C at 4°C/min. Gas chromatography conditions were as follows: N₂ as carrier gas (1.8 ml/min); split mode was used (Flow: 72.1 ml/min, ratio: 1/50); temperature of injector and detector was 275°C. The machine was led by a computer system type “HP ChemStation”, managing the functioning of the machine and allowing to follow the evolution of chromatographic analyses. Diluted samples (1/50 in hexane) of 1.2 μl were injected manually.

GC/MS analyses were performed on a Hewlett-Packard equipped with a HP-5MS (Crosslinked 5% PHME Siloxane) capillary column (30 m × 0.25 mm i.d, 0.25 μm film thickness) and coupled with a mass spectrometer (HP 5973). The temperature was programmed 50–250°C at 2°C/min. The carrier gas was He (1.5 ml/min) and split mode was used (Flow: 112 ml/min, ratio: 1/74.7). The different compounds were confirmed by reference to their MS identities (Library of NIST98 Spectra). MS operating parameters were: ionization voltage 70 eV, ion source temperature 230°C, scan mass range 35–450 amu.

Oils constituents were identified by their retention indices relative to *n*-alkanes (C8-C24) and by comparison of their mass spectral fragmentation patterns with those reported in literature [29].

29.3 Antimicrobial Activities of Essential Oil

29.3.1 Bacteria

The bacterial strains (*Bacillus subtilis* (ATCC 6633), *Escherichia coli* (ATCC 25922), *Micrococcus luteus* (ATCC 4698) and *Staphylococcus aureus* (ATCC 25923)) were selected in this study for their high pathogenicity. These strains were provided by ATCC (American Type Culture Collection) and they were maintained by subculture on nutrient agar supported growth for 24 h in the dark at 37°C.

29.3.2 Fungi

The three strains of fungi (*Aspergillus niger*, *Penicillium expansum* and *Penicillium digitatum*) used in this work belong to the collection of the mycological herbarium of the Mycology Laboratory of the Research Center Forest – Rabat (Morocco). In the dark, these fungi were grown on nutrient medium PDA (Potato Dextrose Agar) for 7 days at 25°C.

29.3.3 Antimicrobial Assays

The Minimal Inhibitory Concentration (MIC) tests of essential oil were determined according to the method reported by Remmal et al. [30].

The essential oils are not miscible in water and culture medium. An emulsion from this oil was realized using solution of agar in 0.2%. The aim of this technique is to obtain a homogeneous distribution of essential oil to increase the contact germ/compound. Various dilutions (1/10th, 1/25th, 1/50th, 1/100th, 1/200th, 1/300th and 1/500th) were prepared from the solution. In test tubes containing each 13.5 ml of the solid medium PDA for fungi, sterilized in the autoclave during 20 min in 121°C and cooled in 45°C, 1.5 ml of each of the dilutions was added aseptically so as to obtain the final concentrations (1/100, 1/250, 1/500, 1/1,000, 1/2,000, 1/3,000 and 1/5,000 v/v). The tubes were shaken to scatter well the essential oil in the culture medium before pouring them into Petri dishes. The control, containing the culture medium and solution of agar in 0.2% only, were also prepared.

Streaking was done with a platinum loop calibrated to remove the same volume of inocula from a 24 h for bacteria, or for fungi, from a suspension of spores in saline solution from a culture of 7 days in the PDA. For fungi, seeding is done by depositing fragments of 1 cm³ in diameter, taken from the periphery of a mycelia mat and from a culture of 7 days in malt extract. For bacteria, the incubation was performed for 24 h at 37°C and 7 days at 25°C for fungi.

29.4 Results and Discussion

29.4.1 Essential Oil Yield

The yield of *Ocimum canum* essential oil from Maweni-Dimani (Grande Comoros) is 2.06%. This yield is higher than Cameroon *Ocimum canum* essential oil (0.59%) [11, 31], but substantially equal to those from Burkina Faso and Brazil (1–2.02%) [18, 32, 33]. We can explain this difference by climatic and soil conditions of each region, and the vegetative stage of the plant [34].

29.4.2 Chemical Composition of *Ocimum canum* Essential Oil

The essential oil was analyzed by gas chromatography (GC-FID) and gas chromatography coupled with mass spectrometry (GC-MS). The results obtained are summarized in Table 29.1.

A total of 30 constituents representing approximately 99.95% of the essential oil were identified. The abundant compounds are: 1,8-cineole (46.88%), camphor (14.98%), α -pinene (5.71%), β -pinene (4.66%), γ -elemene (3.91%), limonene (3.42%), α -terpineol (3.37%) and camphene (2.18%).

This oil was characterized by high amounts of 1,8-cineole and camphor, with 46.88% and 14.98% respectively. The major fraction is constituted by monoterpenes (91.38%), against sesquiterpene compounds 8.57% (Table 29.2).

Tchoumboungang et al. [11] reported a different result for Cameroonian *O. canum* essential oil, as compared to obtained results in this study. He showed that linalool (56.3%) and limonene (10.9%) were the dominant components.

The essential oil extracted from the leaves of *O. canum* from Burkina Faso is dominated by 1,8-cineole (60.1%) [18, 35]. According to Wossa et al. [35], this same species from Papua New Guinea is mainly constituted of eugenol (35.3%) and linalool (27.2%).

Comparing our results and those from literature, there is a very large chemical variability of essential oils extracted from *O. canum*. This result shows that quality of essential oils depends on a number of factors including origin, environmental conditions (temperature, light, rainfall) and soil [34–40]. Other factors (culture conditions, treatment plant, harvesting techniques) can influence the chemical composition of essential oils [40, 41].

29.4.3 Antimicrobial Activities

The results of antimicrobial activity of the essential oil *Ocimum canum* are summarized in Table 29.3.

Table 29.1 Chemical composition of Comorian *Ocimum canum* essential oil

N°	KI	Constituents	%
1	926	Tricylene	0.06
2	931	α -Thujene	0.11
3	939	α -Pinene	5.71
4	953	Camphene	2.18
5	976	Sabinene	1.11
6	980	β -Pinene	4.66
7	991	Dihydro-1,8-cineole	0.81
8	995	Myrcene	2.11
9	1005	α -Phellandrene	0.28
10	1011	δ -3-Carene	0.08
11	1018	α -Terpinene	0.24
12	1031	Limonene	3.42
13	1033	1,8-Cineole	46.88
14	1062	γ -Terpinene	0.75
15	1068	cis- Sabinene-hydrate	1.45
16	1088	Terpenolene	0.47
17	1098	Linalool	0.36
18	1143	Camphor	14.98
19	1156	Isoborneol	0.13
20	1165	Borneol	1.62
21	1177	Terpinen-4-ol	0.60
22	1189	α -Terpineol	3.37
23	1418	E-caryophyllene	1.07
24	1433	γ -Elemene	3.91
25	1454	α -Humulene	0.17
26	1491	Neryle isobutyrate	1.50
27	1499	α -Muurolene	1.08
28	1452	δ -Cadinene	0.16
29	1581	Caryophyllene oxide	0.51
30	1596	14-Hydroxy-9-epi-(E)caryophyllene	0.17
Total			99.95

N° Number of peak, **KI** Kovàts Indices

Table 29.2 Composition of monoterpenes and sesquiterpenes of Comorian *Ocimum canum* essential oil

	Hydrogenated compounds (%)	Oxygenated compounds (%)	Total (%)
Monoterpenes	21.18	70.20	91.38
Sesquiterpenes	6.39	2.18	8.57

Essential oil of *O. canum* from Maweni-Dimani inhibited growth of *E. coli*, *M. luteus* and *S. aureus* at concentration of 1/100 v/v. Only *B. subtilus* was more sensitive against this essential oil with a concentration of 1/250 v/v. *P. expansum* and *A. niger* were also inhibited at concentration of 1/250 v/v. However *P. digitatum*, less sensitive, was inhibited at 1/100 v/v.

Table 29.3 Antibacterial and antifungal activity of Comorian *Ocimum canum* essential oil

	1/100	1/250	1/500	1/1000	1/2000	1/3000	1/5000	Control
	v/v	v/v	v/v	v/v	v/v	v/v	v/v	
Bacteria								
<i>E. coli</i>	-	-	+	+	+	+	+	+
<i>B. subtilis</i>	-	-	-	-	+	+	+	+
<i>M. luteus</i>	-	-	+	-	+	+	+	+
<i>S. aureus</i>	-	-	+	-	+	+	+	+
Fungi								
<i>A. niger</i>	-	-	-	-	+	-	+	+
<i>P. expansum</i>	-	-	-	-	+	-	+	+
<i>P. digitatum</i>	-	-	+	-	+	-	+	+

(-) inhibition, (+) development

The essential oil of *O. canum* from Maweni Dimani showed antibacterial and antifungal properties for the seven microorganisms tested. These effects can be explained probably by the presence of 1,8-cineole, camphor, α -pinene and β -pinene as major components. These components have been demonstrated as exhibiting antimicrobial activities in other studies [42–46].

In this study, the antimicrobial activities of *O. canum* essential oil can be attributed mainly to the terpene alcohols representing 51.15% of the total of essential oil. As demonstrated in other studies, the antimicrobial properties of essential oils from several aromatic and medicinal plants have been attributed to their terpene alcohols components [47–50].

In general, the antibacterial and antifungal activity of this essential oil of *O. canum* can be explained by the presence of major components. But, it can also be due to the presence of interaction between different volatile constituents [51–55].

29.5 Conclusions

In this work, the essential oil yield obtained was 2.06%. This study has shown the composition of the essential oil of *O. canum* Sim growing in Comoros Island. The qualitative and quantitative analysis of this essential oil has identified two major compounds: 1,8-cineole and camphor.

This oil showed antibacterial and antifungal activities against the seven microorganisms tested. This activity was attributed to its chemical composition, essentially to major compounds and the presence of interactions between all different volatile constituents.

It was concluded that essential oils examined in the present study could be used as antimicrobial agents in pharmaceutical and cosmetic products and also against food spoilage.

In Comoros Islands, *O. canum* is a plant widely used in traditional medicine. This work may justify the use of the plants in treatment of some diseases.

References

1. Guenther E (1974) Oil of *Boronia megastigma* (*Boronia* flower oil). In: Guenther E (ed) *The Essential Oils, Vol 3 – Individual Essential Oils of the Plant Families Rutaceae and Labiatea*. R. E. Krieger Publishing Company, pp 364–367
2. Paton A (1992) A synopsis of *Ocimum* L. (*Labiatea*) in Africa. *Kew Bull* 47:403–435
3. Edmond D, Hladik A, Hladik CM (1996) De la ressource disponible à la ressource exploitée: méthodes de quantification des ressources alimentaires dans les régions forestières et les savanes du Cameroun. In: Froment A, de Garine I, Binam Bikoi C, Loung J-F (eds) *Bien manger et bien vivre. Anthropologie alimentaire et développement en Afrique intertropicale: du biologique au social*. L'Harmattan/ORSTOM, Paris, pp 55–66
4. Guenther E (1949) *The essential oils, vol 3*. D Van Nostrand Company Inc, New York, 777p
5. DGE (2000) Stratégie nationale et plan d'action pour la conservation de la diversité biologique en RFI des Comores du PROJET PNUD/FEM/COI/97/GEF. 31:39–40
6. Hutchinson J, Dalziel JM, Keay RWJ, Hepper FN (1963) *Flora of west tropical Africa, vol 2, 2nd edn*. The Whitefriars Press, London/Tonbridge, 544p
7. Berhaut J (1967) *Flore du Sénégal, 2ème éd. Clairafrique éd, Dakar, 485*
8. Berhaut J (1975) *Flore illustrée du Sénégal, vol 4. Clairafrique éd., Dakar, 625*
9. Morales MR, Simon JE (1996) New basil selections with compact inflorescence for the ornamental market. In: Janick J (ed) *Progress in new crops*. ASHS Press, Alexandria, pp 543–546
10. Morales MR, Simon JE (1997) Sweet Dani: a new culinary and ornamental lemon basil. *HortScience* 32:148–149
11. Tchoumboungang F, Dongmo PMJ, Sameza ML, Mbango EGN, Fotso GBT, Zolla PHA, Chantal M (2009) Activité larvicide sur *Anopheles gambiae* Giles et composition chimique des huiles essentielles extraites de quatre plantes cultivées au Cameroun. *Biotechnol Agron Soc Environ* 13(1):77–84
12. Adjanohoun EJ, Ake Assi L, Ali A, et al (1982) Contribution aux études ethnobotaniques et floristiques aux Comores. ACT, Paris, 216p
13. Monjoin M (1981) Possibilité d'utiliser la médecine traditionnelle pour améliorer les soins de santé primaire aux Comores. Université de Bordeaux II, Thèse, 340 p
14. Kaou AM, Mahiou-Leddé V, Hutter S, Ainouddine S, Hassani S, Yahaya I, Azas N, Ollivier E (2008) Antimalarial activity of crude extracts from nine African medicinal plants. *J Ethnopharmacol* 116(4):74–83
15. Albuquerque UP (1996) de Taxonomia e ethnobotânica gênero *Ocimum* L. Nordeste Brasil – referência especial para Pernambuco. Recife. Dissertação, Centro de Ciências Biológicas, Univ Fed de Pernambuco. Masterado, 125 p
16. Karaman S, Digrak M, Ravid U, Ilcim A (2001) Antibacterial and antifungal activity of the essential oils of *Thymus revolutus* Celak from Turkey. *J Ethnopharmacol* 76:183–186
17. Kouamé RO, Yolou S, Boti JB, Guessenn KN, Kanko C, Ahibo C, Casanova J (2008) Etude chimique et activité antidiarrhéique des huiles essentielles de deux plantes aromatiques de la Pharmacopée ivoirienne. *Eur J Sci Res* 1–24(1):94–103
18. Bassole IHN, Nebie R, Savadogo A, Ouattara CT, Barro N, Traore SA (2005) Composition and antimicrobial activities of the leaf and flower essential oils of *Lippia chevalieri* and *Ocimum canum* from Burkina Faso. *Afr J Biotechnol* 4(10):1156–1160
19. Lawrence BM, Powel RH, Peele DM (1980) Variation in the genus *Ocimum*. In: *Proceedings of the eighth international congress on essential oils*. FEDAROM, Grasse, pp 109–117

20. Kundayo O, Laakso I, Hiltunen R (1989) Constituents of the volatile oil from leaves of *Ocimum canum* Sims. *Flavour Fragr J* 4:17–18
21. Chalchat JC, Garry RP, Sidibe L (1996) Aromatic plants of Mali. *Ocimum basilicum* and *Ocimum canum* Sims. *Riv Ital EPPPOS* 7(spec. Num.):618–626
22. Amvam Zollo PH, Biyiti L, Tchoumboungang F, Menut C, Lamaty G, Bouchet P (1998) Aromatic plants of tropical central Africa, Part XXXII: chemical composition and antifungal activity of thirteen essential oils from aromatic plant of Cameroon. *Flavour Fragr J* 13:107–114
23. Sanda K, Koffi K, Nambo Ph, Gaset A (1998) Chemical investigation of *Ocimum* species growing in Togo. *Flavour Fragr J* 13(4):226–232
24. Martins AP, Salgueiro L, Vila R, Tomi F, Caniguera S, Casanova J, Proença Da Cunha A, Adzet T (1999) Composition of the essential oil of *O. canum*, *O. gratissimum* and *O. minimum*. *Planta Med* 65:187–189
25. Chalchat JC, Garry RP, Sidibe L, Harama M (1999) Aromatic plants of Mali (II): chemical composition of oil of *Ocimum canum* Sims. *J Essent Oil Res* 11:473–476
26. Chagonda LS, Makanda CD, Chalchat JC (2000) The essential oils of *Ocimum canum* Sims (basilic camphor) and *Ocimum urticifolia* Rothf from Zimbabwe. *Flavour Fragr J* 15:23–26
27. Yayi E, Moudachirou M, Chalchat JC (2001) Chemotyping of three *Ocimum* species from Benin: *O. basilicum*, *O. canum*, *O. gratissimum*. *J Essent Oil Res* 13:13–17
28. Clevenger JF (1928) Apparatus for the determination of volatile oil. *J Am Pharm Assoc* 17(4):346–351
29. Adams RP (1995) Identification of essential oil components by gas chromatography – mass spectroscopy. Allured, Carol Steam, 302 p
30. Remmal A, Bouchikhi T, Rhayour K, Ettayebi M (1993) Improved method for determination of antimicrobial activity of essential oils in agar medium. *J Essent Oil Res* 5(2):179–184
31. Tchoumboungang F, Amvam Zollo PH, Dagne E, Mekonnen Y (2005) *In vivo* antimalarial activity of essential oils from *Cymbopogon citratus* and *Ocimum gratissimum* on mice infected with *Plasmodium berghei*. *Planta Med* 71:20–23
32. Alfa K, Abdoul DS, Mouhoussine N (2003) Composition chimique de l'huile essentielle d'*Ocimum americanum* Lin. Syn. *O. canum* Sims. *C R Chim* 7:1033–1037
33. Silva MG, Vieira IG, Mendes FN, Albuquerque IL, dos Santos RN, Silva FO, Morais SM (2008) Variation of Ursolic acid content in eight *Ocimum* species from Northeastern Brazil. *Molecules* 13:2482–2487
34. DGE-MPARME (1999) Rapport intermédiaire sur l'élaboration d'une stratégie nationale et d'un Plan d'action en matière de biologie en R F I des Comores
35. Wossa SW, Rali T, Leach DN (2008) Volatile chemical constituents of three *Ocimum* species (Lamiaceae) from Papua New Guinea. *S Pac J Nat Sci* 26:25–27
36. Rajeswara Rao BR, Kaul PN, Mallavarapu GR, Ramesh S (1996) Effect of seasonal climatic changes on biomass yield and terpenoid composition of rosescented geranium. *Biochem Syst Ecol* 24:627–635
37. Boira H, Blanquer A (1997) Environmental factors affecting chemical variability of essential oils in *Thymus piperella* L. *Biochem Syst Ecol* 26:811–822
38. Randrianalijaona JA, Ramanoelina PAR, Rasoarahona JER, Gaydou EM (2005) Seasonal and chemotype influences on the chemical composition of *Lantana camara* L. essential oils from Madagascar. *Anal Chim Act* 545:46–52
39. Curado MA, Oliveira CBA, Jesus JG, Snotos S, Seraphin J, Ferri PH (2006) Environmental factors influence on chemical polymorphism of the essential oils of *Lychnophora ericoides*. *Phytochemistry* 67(21):2363–2369
40. Rajeswara Rao BR (2002) Biomass yield, essential oil yield and essential oil composition of rose-scented geranium (*Pelargonium* species) as influenced by row spacings and intercropping with commint (*Mentha arvensis* L; *piperascens* Malinv. Ex Holmes). *Ind Crop Prod* 16:133–144
41. Anton R, Lobstein A (2005) Plantes aromatiques. Épices, aromates, condiments et huiles essentielles. Tec & Doc, Paris, 522p

42. Obeng-Ofori D, Reichmuth CH, Bekele J, Hassanali A (1997) Biological activity of 1,8 cineole, a major component of essential oil of *Ocimum kenyense* (Ayobeingira) against stored product beetles. *J Appt Ent* 121:237–243
43. Prates HT, Santos JP, Waquil JM, Fabris JD, Oliveira AB, Foster JE (1998) Insecticidal activity of monoterpenes against *Rhyzopertha dominica* F. and *Tribolium castaneum* H. *J Stored Prod Res* 34:243–249
44. Senatore F, Napolitano F, Apostolides AN, Bruno M, Herz W (2005) Composition and antimicrobial activity of the essential oil of *Achillea falcalata* L. *Flavour Fragr J* 20(3):291–294
45. Malecky M (2007) Métabolisme des terpénoïdes chez les caprins. Institut des Sciences et Industries du Vivant et de l'Environnement (AgroParisTech) thèse, 205 p
46. Smirnov V, Bondarenko AS, Prikhodkov VA (1998) Antimicrobial activity of sesquiterpene phenol from *Bidens cernua*. *Fitoterapia* 69(1):7–12, 84–85
47. Kurita N, Koike S (1982) Synergistic antimicrobial effect of sodium chloride and essential oils components. *Agric Bio Chem* 46:159–165
48. Bouchikhi T (1994) Activité antimicrobienne de quelques huiles essentielles. Thèse de Doctorat d'Etat. Université Blaise Pascal, Clermont-Ferrand, 132 p
49. Faid M, Charal M, Mosaddak M (1996) Chemical composition and antimicrobial activities of two aromatic plants: *Origanum majorana* L and *O. compactum* Benth. *J Essent Oil Res* 8:57–664
50. Satrani B, Aberchane M, Farah A, Chaouch A, Talbi M (2006) Composition chimique et activité antimicrobienne des huiles essentielles extraites par hydrodistillation fractionnée du bois de *Cedrus atlantica* Manetti. *Act Bot Galla* 153(1):97–104
51. Franchomme P (1981) L'aromatologie à visée anti-infectieuse. *Phytomédecine* 1(2):25–47
52. Gueldener RC, Wilson DM, Heidt A (1985) Volatile compounds inhibiting *Aspergillus's flavus*. *J Agric Food* 33:413–419
53. Burt S (2004) Essential oils: their antibacterial properties and potential applications in foods. *J Food Microbiol* 94:223–253
54. Lee KH, Ibuka T, Wur Y, Geissman TA (1985) Structure-antimicrobial activity relationships among the sesquiterpenes lactones and related compounds. *Phytochemistry* 16:1171–1181
55. Lahlou M (2004) Methods to study the phytochemistry and bioactivity of essential oils. *Phytother Res* 18:435–448
56. Satrani B, Farah A, Fechtal M, Talbi M, Blaghen M, Chaouch A (2001) Composition chimique et activité antimicrobienne des huiles essentielles de *Satureja calamintha* et *Satureja alpina* du Maroc. *Ann Fals Exp Chim* 94(956):241–250

Chapter 30

Synthesis of Five-, Six- and Seven-Membered Hetero Ring Annulated Imidazo[4,5-b] carbazoles and Azacarbazoles of Medicinal Interest

Bhawani Singh, Bharti Vashishtha, and D. Kishore

Abstract Application of Japp-Klingemann reaction with benzimidazolyl diazonium chloride (**4**) on 2-hydroxymethylidene cyclohexanone (**6a**) and *N*-benzyl-3-hydroxymethylidene-4-piperidone (**6b**) yielded the corresponding hydrazones (**7a-b**) which underwent facile Fischer-indolization in acid to give the imidazo condensed oxocarbazole and imidazo condensed oxoazacarbazoles (**8a-b**). Subsequent treatment of (**8a-b**) with (i) HCOOEt, NaOEt (ii) Me₂NCH(OMe)₂ (iii) CS₂, CH₃I, t-BuOK and (iv) C₆H₅CHO yielded in succession the corresponding enolic ethers (**9a-b**), dimethylaminomethylene ketones (**10a-b**), oxoketenedithioacetals (**11a-b**) and α,β -unsaturated ketones (**12a-b**) respectively. Interaction of (**9a-b**), (**10a-b**), (**11a-b**) and (**12a-b**) with bidentate nucleophiles such as hydroxylamine hydrochloride and hydrazine hydrate afforded the corresponding isoxazolo and pyrazolo incorporated derivatives of imidazo condensed carbazoles and azacarbazoles (**13a-l**). Similar interaction with urea and thiourea yielded corresponding pyrimido incorporated imidazo condensed carbazoles and azacarbazoles (**14a-r**). Reactions of these intermediates with *o*-phenylenediamine, *o*-aminophenol and *o*-aminothiophenol produced benzodiazepino, benzoxazepino and benzothiazepino incorporated imidazo condensed carbazoles and azacarbazoles (**15a-r**) respectively. Structures of all the compounds have been unequivocally established on the basis of their elemental and spectral data. Antifungal and antibacterial activities of some of the synthesized compounds have been carried out.

B. Singh (✉) • B. Vashishtha • D. Kishore
Department of Chemistry, Banasthali University, Banasthali, Rajasthan 304022, India
e-mail: bsyadav2000@gmail.com; bhartivashishtha.chem@gmail.com;
kishoredharma@yahoo.co.in

30.1 Introduction

Condensed heterocyclic systems containing pyrazole, isoxazole, pyrimidine, diazepine, oxazepine, thiazepine nuclei have attracted the attention of chemists on account of the significant medicinal properties associated with them. In view of the prodigious range of activities of these compounds, it was considered worthwhile in the present work to undertake investigation on the synthesis of condensed nitrogen heterocyclic systems containing above nuclei fused to the benzimidazole framework. It is expected that synthesis of these condensed heterocyclic systems and evaluation of their biological properties would provide a rational approach to the study of structure activity relationship of these molecules.

A large number of benzimidazole derivatives are reported to possess trypanosomocidal properties and are found to be active against disease caused by protozoa [1]. Carbazoles and carbazole fused heterocyclic ring are of special interest and of contemporary importance on account of the variety of carbazole alkaloids showing antimicrobial, anti-tumor and cytotoxic properties [2–4]. Indole group of plant alkaloids ellipticine and olivacine have been known since a long time to exhibit anti-cancer and DNA intercalating properties [5–7]. In view of this, selectively functionalized and annelated carbazoles are interesting targets for the development of anti-tumor and antibiotically active drugs [8]. Azacarbazoles also seem to have great potential for the development of compounds with analgesic and hypotensive activity. It is reported that in presence of stobadine, an azacarbazole, the blood platelets have been aggregated [9] and the stobadine has proved effective against atherosclerosis, myocardial stroke and neurodegenerative diseases [10]. Azacarbazole derivatives also show such widely differing activities as bacteriostatic [11], anti-plasmodial and anti-trypanosomal [12], anti-viral [13], anti-cancer [14, 15], anti-tumor activities [16–18] and psychopharmacologically active biological profiles [19]. A recent demonstration that these compounds can be used as potential anti-HIV agents has stimulated further interest in these molecules from yet another perspective.

Pyrazoles belong to an important group of heterocyclic compounds which have aroused much interest owing to their valuable pharmacological properties [20–22] and therefore, extensively explored for their application in the field of medicine. In addition to medicinal importance, pyrazole derivatives also find application in agriculture and horticulture. Isoxazole represents one of the most active classes of compounds possessing a broad spectrum of pharmacological properties [23]. Isoxazole nucleus is present in a number of drugs, including the COX-2 inhibitor valdecoxib. On account of the interesting medicinal properties shown by isoxazole derivatives, the chemical literature is replete with the chemistry and pharmacological properties of these materials and an impressive armory of synthetic routes have been developed for these compounds. Based on such precedence in the literature on the pharmacological activity of pyrazoles and isoxazole it was assumed that incorporation of the pyrazole or isoxazole moiety on to the benzimidazole condensed carbazole and azacarbazole could produce interesting series of compounds with enhanced biological activities.

Pyrimidines play a vital role in many biological processes since this ring system is present in several vitamins, coenzymes, nucleic acids. Synthetic members of these groups are also important as chemotherapeutic agents. The pyrimidine nucleus also occurs in a considerable number of natural products of vital importance to living organisms. As a structural component of key biomolecules, the pyrimidine moiety is widely incorporated in the design of privileged structures. In view of the impressive pharmacodynamic applications of pyrimidine and condensed pyrimidine derivatives, it is considered worthwhile to synthesize pyrimidine ring fused derivatives from enolic ethers, chalcone analogues, dimethyl aminomethylene ketones, and oxoketene dithioacetals derived from benzimidazolo condensed carbazoles and azacarbazoles.

The broad spectrum of biological properties exhibited by [1,5]-benzodiazepines has triggered the development in this field and caused the chemistry of these azepines to evolve into a major area of research in heterocyclic chemistry. The pace of research and development in this area is accelerating and there seem to be virtually no limit to the number of interesting ring systems that can be created in the laboratory to day by the combination of ingenuity and perseverance. The practical importance of azepines is by no means limited to their application as psychopharmacological or anti-neoplastic agents alone but their additional novel applications are continuously emerging. Recent demonstrations that some of these compounds can be used as anti-HIV agents have stimulated research in this area with yet another perspective.

30.2 Materials and Methods

30.2.1 Synthesis and Characterization

All solvents and reagents were of analytical reagent grade and were dried in advance and redistilled before use. Melting points of all the synthesized compounds were determined by open capillary method without correcting the thermometer. The purity of synthesized compounds was checked by thin layer chromatography. The reaction was monitored by ascending thin layer chromatography (TLC). Spots were visualized under UV light as well as in iodine chamber. ^1H NMR spectra were scanned at 300 MHz in CDCl_3 and DMSO-d_6 using TMS as an internal reference. Chemical shift values (δ) are given in parts per million (ppm). IR spectra were recorded on Shimadzu 8,000 C FT-IR using KBr and peaks are presented in cm^{-1} .

30.2.2 Preparation of 6-Nitro-1H-Benzo[d]imidazole (2)

A mixture of 4-nitro-*o*-phenylenediamine (0.004 mol) and 90% formic acid (6 ml) was refluxed for 3 h. The flask was then cooled and 10% sodium hydroxide solution

was added slowly with constant stirring until the mixture was just alkaline. The solid was filtered off, washed with cold water and dried. Recrystallization with methanol yielded the product in 70% yield with mp 196°C.

30.2.3 Preparation of 6-Amino-1H-Benzo[d]imidazole (3)

A stirred mixture of (2) (0.004 mol), Fe powder (1 g) and ethyl acetate (10 ml) in acetic acid (35 ml) was heated at 60°C for 2 h. The reaction mixture was then basified with NaOH and extracted with ethyl acetate. The combined extracts were washed with aqueous solution of saturated sodium bicarbonate and sodium chloride. The organic layer was dried with sodium sulphate and filtered. The filtrate was concentrated under reduced pressure and the resultant solid was collected by filtration. The solid was dried to give 6-Amino-1H-Benzo[d]imidazole (3). IR (KBr) cm^{-1} : 3201 (NH str), 2923 (CH str), 1650 (C=N str), 1110 (CN str), 1257 (NH def), 800 (CH def). ^1H NMR (δ ppm): 12.36 (1H, s, NH), 8.19 (1H, s, CH), 7.34 (1H, d, CH₂), 6.90 (1H, s, CH), 6.46 (1H, d, CH), 5.32 (2H, s, NH₂).

30.2.4 General Method for the Preparation of 3-Hydroxymethylidene Cyclohexanone and N-Benzyl-3-Hydroxymethylidene-4-Piperidone (6a-b)

A mixture of EtONa (0.01 mol), dry ether (10 ml), redistilled cyclohexanone or N-benzyl piperidone (0.01 mol) ethyl formate (10 ml) was stirred for 6–8 h. After standing overnight, 2.5 ml of ethanol was added. The mixture was stirred for additional 1 h. Water was added and aqueous extracts were washed with ether. The aqueous layer was acidified with 5 ml of 6 N HCl and the mixture was extracted twice with ether. The ether solution was washed with 5 ml saturated NaCl solution. The solution was dried over anhydrous MgSO₄.

30.2.5 General Method for the Preparation of Imidazo[4,5-b]carbazol/Azacarbazol-(3H)-ones (8a-b)

30.2.5.1 Preparation of Hydrazones (7a-b)

A solution of (3) (0.005 mol) in aqueous hydrochloric acid (0.5 ml conc. HCl in 1 ml water) was treated with a cold saturated solution of sodium nitrite (0.1 g in 1 ml water) while the temperature was kept at 0–5°C. It was then added portion wise to an ice cooled mixture containing (6a-b) (0.05 ml), sodium acetate trihydrate (0.3 g), methanol (1.5 ml) and water (1 ml) over a period of 0.5 h with stirring.

The contents were allowed to stand for further 0.5 h and the resulting solid mass was filtered, washed with water, dried and recrystallized from ethanol to give the hydrazones. The hydrazones were used as such in the second step without further purification.

30.2.5.2 Cyclisation of Hydrazones (**8a-b**)

A solution of hydrazones (**7a-b**) (0.005 mol) in a mixture of acetic acid (0.5 ml) and hydrochloric acid (0.2 ml) was refluxed on an oil bath preheated to 125–130°C for 0.5 h. The content were then cooled and poured in ice cooled water with continuous stirring. The separated brown solid was purified by passing through a column of silica gel using 50% benzene in petroleum ether as eluant. (**8a**) IR (KBr) cm^{-1} : 3109 (NH str), 2920 & 2850 (CH str), 1712 (C=O str), 1650 (C=N str), 1072 (CN), 1342 (NH def), 948 (CH def). ^1H NMR (δ ppm): 12.36 (1H, s, NH), 11.96 (1H, s, NH), 8.19 (1H, s, CH), 7.70 (2H, s, CH_2), 3.01 (2H, t, CH_2), 2.58 (2H, t, CH_2), 2.11 (2H, m, CH_2). (**8b**) IR (KBr) cm^{-1} : 3100 (NH str), 2930 & 2810 (CH str), 1710 (C=O str), 1650 (C=N str), 1070 (CN), 1332 (NH def), 945 (CH def). ^1H NMR (δ ppm): 12.36 (1H, d, NH), 11.63 (1H, s, NH), 8.19 (1H, s, CH), 7.70 (2H, s, ArH), 7.26–7.23 (5H, m, ArH), 4.51 (2H, s, CH_2), 3.39 (2H, t, CH_2), 2.63 (2H, t, CH_2).

30.2.6 General Method for the Preparation of (Z)-7-(Ethoxymethylene)-5,7,8,9-Tetrahydroimidazo[4,5-b]carbazol/Azacarbazol-(3H)-ones (**9a-b**)

To a solution of 10% EtONa (10 ml) in benzene (50 ml) at 0°C, a solution of ethyl formate (10 ml) in dry benzene (25 ml) was added. To this mixture (**8a-b**) (10 mmol) in benzene (25 ml) was added. The mixture was stirred for 4–6 h at room temperature and allowed to stand overnight. It was then diluted with cold water, acidified with dil. HCl and extracted with ether. The solvent was evaporated and the resultant compound was recrystallised from ethanol to give pure product. (**9a**) IR (KBr) cm^{-1} : 3450 (NH str), 2980 & 2850 (CH str), 1610 (C=O str), 1550 (C=N str), 1350 (CN def). ^1H NMR (δ ppm): 12.36 (1H, s, NH), 11.19 (1H, s, NH), 8.19 (1H, s, CH), 7.70 (2H, s, ArH), 6.99 (1H, s, CH), 4.49 (2H, q, CH_2), 3.03 (2H, t, CH_2), 2.83 (2H, t, CH_2), 1.21 (3H, t, CH_3). (**9b**) IR (KBr) cm^{-1} : 3440 (NH str), 2970 & 2860 (CH str), 1600 (C=O str), 1550 (C=N str), 1370 (CN def). ^1H NMR (δ ppm): 12.36 (1H, s, NH), 11.63 (1H, s, NH), 8.19 (1H, s, CH), 7.70 (1H, s, ArH), 7.33–7.23 (5H, m, ArH), 7.11 (1H, s, CH), 4.71 (1H, s, CH_2), 4.49 (2H, q, CH_2), 3.73 (1H, s, CH_2), 1.21 (3H, t, CH_3).

30.2.7 *General Method for the Preparation of 7-(Dimethylaminomethylene)-5,7,8,9-Tetrahydroimidazo [4,5-b]carbazol/Azacarbazol-(3H)-ones (10a-b)*

The compounds (**8a-b**) (15.7 mmol) were dissolved in *N,N*-dimethylformamide dimethyl acetal (15 ml) and the solution was heated under reflux for 4–6 h and concentrated. The residue was triturated with hexane, filtered and washed with hexane to give (**10a-b**). (**10a**) IR (KBr) cm^{-1} : 3010 (CH str), 1630 (C=O str), 1550–1450 (C=C str), 1020 (CN str). $^1\text{H NMR}$ (δ ppm): 12.36 (1H, s, NH), 11.19 (1H, s, NH), 8.19 (1H, s, CH), 7.70 (2H, s, ArH), 3.04 (6H, s, CH_3), 3.22 (2H, t, CH_2), 2.26 (1H, s, CH). (**10b**) IR (KBr) cm^{-1} : 3000 (CH str), 1620 (C=O str), 1550–1450 (C=C str), 1120 (CN str). $^1\text{H NMR}$ (δ ppm): 12.36 (1H, s, NH), 11.63 (1H, s, NH), 8.19 (1H, s, CH), 7.70 (2H, s, ArH), 7.26–7.23 (5H, m, ArH), 7.61 (1H, s, CH), 4.71 (2H, s, CH_2), 3.73 (2H, s, CH_2), 3.04 (6H, s, CH_3).

30.2.8 *General Method for the Preparation of 7-(Bis(methylthio)methylene)-5,7,8,9-Tetrahydroimidazo [4,5-b]carbazol/Azacarbazol-(3H)-ones (11a-b)*

A mixture of compound (**8a-b**) (0.003 mol) and CS_2 (3 ml) was added to a well stirred and cooled suspension of *t*-BuOK (0.006 mol) in dry benzene (15 ml) and DMF (10 ml). The reaction mixture was allowed to stand at room temperature for 4 h. Methyl iodide (3 ml) was gradually added with stirring and with external cooling. The reaction mixture was allowed to stand for further 4 h at room temperature with occasional shaking. It was then refluxed on a water bath for 3 h. The mixture was poured on crushed ice and the benzene layer was separated. The aqueous portion was extracted with benzene and the combined extracts were washed with water and dried over anhydrous sodium sulphate to give (**11a-b**). (**11a**) IR (KBr) cm^{-1} : 2950 (CH str), 1620 (C=O str), 1550–1450 (C=C str), 800 (CH def). $^1\text{H NMR}$ (δ ppm): 12.36 (1H, s, NH), 11.19 (1H, s, NH), 8.19 (1H, s, CH), 7.70 (2H, s, ArH), 3.03 (2H, t, CH_2), 2.83 (2H, t, CH_2), 2.80 (6H, s, CH_3). (**11b**) IR (KBr) cm^{-1} : 2970 (CH str), 1660 (C=O str), 1550–1450 (C=C str), 880 (CH def). $^1\text{H NMR}$ (δ ppm): 12.36 (1H, s, NH), 11.63 (1H, s, NH), 8.19 (1H, s, CH), 7.70 (2H, s, ArH), 7.26–7.23 (5H, m, ArH), 4.71 (2H, s, CH_2), 3.73 (2H, s, CH_2), 2.80 (3H, s, CH_3).

30.2.9 *General Method for the Preparation of 7-Benzylidene-5,7,8,9-Tetrahydroimidazo [4,5-b]carbazol/Azacarbazol-(3H)-ones (12a-b)*

A mixture of (**8a-b**) (0.01 mol), benzaldehyde (0.01 mol) and fused sodium acetate (0.015 mol) in glacial acetic acid was refluxed for 5 h. The reaction mixture

was cooled in ice water. The resulting solid was filtered, washed with water and recrystallised from aq. ethanol to give pure compounds (**12a-b**). (**12a**) IR (KBr) cm^{-1} : 3460 (NH str), 2950 & 2830 (CH str), 1650 (C=O str), 1370 (CN def), 750 (CH def). $^1\text{H NMR}$ (δ ppm): 12.36 (1H, s, NH), 11.19 (1H, s, NH), 8.19 (1H, s, CH), 7.70 (2H, s, ArH), 7.60–7.33 (5H, m, ArH), 7.25 (1H, s, CH), 3.03 (2H, t, CH_2), 2.83 (2H, t, CH_2). (**12b**) IR (KBr) cm^{-1} : 3460 (NH str), 2960 & 2830 (CH str), 1670 (C=O str), 1370 (CN def), 770 (CH def). $^1\text{H NMR}$ (δ ppm): 12.36 (1H, s, NH), 11.63 (1H, s, NH), 8.19 (1H, s, CH), 7.70 (2H, s, ArH), 7.60–7.23 (10H, m, ArH), 7.45 (1H, s, CH), 4.71 (2H, s, CH_2), 3.73 (2H, s, CH_2).

30.2.10 General Method for the Preparation of Imidazo[4,5-a]pyrazolo/Isoxazolo[3,4-a]carbazoles/Azacarbazoles (**13a-d** and **13e-l**)

A solution of (**9a-b**) or (**10a-b**) or (**11a-b**) or (**12a-b**) (10 mmol) in glacial acetic acid (25 ml) was stirred with hydrazine hydrate/hydroxylamine hydrochloride (15 mmol) for 6–8 h at 70–80°C. The solvent was removed under reduced pressure and the residue was diluted with water. It was extracted with ethyl acetate, washed with saturated NaHCO_3 solution, water, brine solution and dried over Na_2SO_4 . The solvent was removed and the crude product was recrystallised from ethanol. (**13a**) IR (KBr) cm^{-1} : 2930 & 2890 (CH str), 1695 (C=N str), 790 (CH def). $^1\text{H NMR}$ (δ ppm): 12.51 (1H, s, NH), 12.36 (1H, s, NH), 11.34 (1H, s, NH), 8.19 (1H, s, CH), 7.70 (2H, s, CH), 7.56 (1H, s, CH), 2.87 (2H, t, CH_2), 2.83 (2H, t, CH_2). (**13b**) IR (KBr) cm^{-1} : 2940 & 2880 (CH str), 1690 (C=N str), 770 (CH def). $^1\text{H NMR}$ (δ ppm): 12.36 (1H, s, NH), 11.34 (1H, s, NH), 8.19 (1H, s, CH), 8.1 (1H, s, CH), 7.70 (2H, s, CH), 2.93 (2H, t, CH_2), 2.87 (2H, t, CH_2). (**13c**) IR (KBr) cm^{-1} : 2940 & 2890 (CH str), 1675 (C=N str), 1540–1450 (C=C str.), 780 (CH def). $^1\text{H NMR}$ (δ ppm): 12.51 (1H, s, NH), 12.36 (1H, s, NH), 11.34 (1H, s, NH), 8.19 (1H, s, CH), 7.70 (2H, s, CH), 7.56 (1H, s, CH), 7.33–7.23 (7H, m, ArH), 4.71 (2H, s, CH_2), 4.32 (2H, s, CH_2). (**13d**) IR (KBr) cm^{-1} : 2920 & 2890 (CH str), 1685 (C=N str), 1540–1450 (C=C str), 1290 (CN str), 790 (CH def). $^1\text{H NMR}$ (δ ppm): 12.36 (1H, s, NH), 11.34 (1H, s, NH), 8.19 (1H, s, CH), 8.1 (1H, s, CH), 7.70 (2H, s, CH), 7.33–7.23 (5H, m, ArH), 4.71 (2H, s, CH_2), 4.32 (2H, s, CH_2). (**13e**) IR (KBr) cm^{-1} : 2990 & 2895 (CH str), 1680 (C=N str), 1510–1400 (C=C str), 1330 (CN str), 780 (CH str). $^1\text{H NMR}$ (δ ppm): 13.7 (1H, s, NH), 12.36 (1H, s, NH), 11.34 (1H, s, NH), 8.19 (1H, s, CH), 7.70 (2H, s, CH), 2.93 (4H, t, CH_2), 2.87 (2H, t, CH_2), 2.53 (3H, s, CH_3). (**13f**) IR (KBr) cm^{-1} : 2980 & 2895 (CH str), 1620 (C=N str), 1510–1400 (C=C str), 1310 (CN str), 780 (CH str). $^1\text{H NMR}$ (δ ppm): 13.7 (1H, s, NH), 12.36 (1H, s, NH), 11.34 (1H, s, NH), 8.19 (1H, s, CH), 7.70 (2H, s, CH), 7.79–7.41 (5H, m, ArH), 2.93 (4H, t, CH_2), 2.87 (2H, s, CH_2). (**13g**) IR (KBr) cm^{-1} : 2980 & 2895 (CH str), 1640 (C=N str), 1510–1400 (C=C str), 1330 (CN str), 790 (CH str). $^1\text{H NMR}$ (δ ppm): 12.36 (1H, s, NH), 11.34 (1H, s, NH), 8.19 (1H, s, CH), 7.70 (2H, s, CH),

2.93 (4H, t, CH₂), 2.87 (2H, t, CH₂), 2.53 (3H, s, CH₃). **(13h)** IR (KBr) cm⁻¹: 3132 (NH str), 3010 (CH str), 2983 & 2854 (CH str), 1728 (C=N str), 1604–1450 (C=C str), 1342 (CH def), 1337 (CN str). ¹H NMR (δ ppm): 12.36 (1H, s, NH), 11.34 (1H, s, NH), 8.19 (1H, s, CH), 7.70 (2H, s, CH), 7.41–8.1 (5H, m, ArH), 2.93 (4H, t, CH₂), 2.87 (2H, s, CH₂). **(13i)** IR (KBr) cm⁻¹: 2980 & 2895 (CH str), 1640 (C=N str), 1510–1400 (C=C str), 760 (CH str). ¹H NMR (δ ppm): 13.7 (1H, s, NH), 12.36 (1H, s, CH), 11.34 (1H, s, NH), 8.19 (1H, s, CH), 7.70 (2H, s, CH), 7.33–7.23 (5H, m, ArH), 4.71 (2H, s, CH₂), 4.32 (2H, s, CH₂), 2.53 (3H, s, CH₃). **(13j)** IR (KBr) cm⁻¹: 2980 & 2890 (CH str), 1640 (C=N str), 1510–1400 (C=C str), 790 (CH str). ¹H NMR (δ ppm): 13.7 (1H, s, NH), 12.36 (1H, s, NH), 11.34 (1H, s, NH), 8.19 (1H, s, CH), 7.70 (2H, s, CH), 7.79–7.23 (10H, m, ArH), 4.71 (2H, s, CH₂), 4.32 (2H, s, CH₂). **(13k)** IR (KBr) cm⁻¹: 2970 & 2890 (CH str), 1680 (C=N str), 1500–1400 (C=C str), 770 (CH str). ¹H NMR (δ ppm): 12.36 (1H, s, NH), 11.34 (1H, s, NH), 8.19 (1H, s, CH), 7.70 (2H, s, CH), 7.33–7.23 (5H, m, ArH), 4.71 (2H, s, CH₂), 4.32 (2H, s, CH₂), 2.53 (3H, s, CH₃). **(13l)** IR (KBr) cm⁻¹: 2880 & 2890 (CH str), 1600 (C=N str), 1530–1450 (C=C str), 770 (CH str). ¹H NMR (δ ppm): 12.36 (1H, s, NH), 11.34 (1H, s, NH), 8.19 (1H, s, CH), 7.23–8.10 (10H, m, ArH), 7.70 (2H, s, CH), 4.71 (2H, s, CH₂), 4.32 (2H, s, CH₂).

30.2.11 Preparation of Imidazo[4,5-a]pyrimido[7,6-a]carbazoles/Azacarbazoles (14a-f and 14g-r)

A mixture of **(9a-b)** or **(10a-b)** or **(11a-b)** or **(12a-b)** (0.02 mol) and urea/thiourea/guanidine (0.02 mol) was refluxed in an oil bath for 4–6 h with constant stirring. The temperature was raised and finally the mixture was refluxed for 4–6 h. On cooling the product solidified which was recrystallised from DMF-EtOH mixture. **(14c)** IR (KBr) cm⁻¹: 3448–3170 (NH str), 1696 (C=N str), 1600 (C=C str). ¹H NMR (δ ppm): 12.36 (1H, s, NH), 11.34 (1H, s, NH), 8.56 (1H, s, CH), 8.19 (1H, s, CH), 7.70 (2H, s, CH), 7.18 (2H, s, NH₂), 2.87 (2H, t, CH₂), 2.83 (2H, t, CH₃). **(14f)** IR (KBr) cm⁻¹: 3300 (NH str), 2950 & 2860 (CH str), 782 (C=S str). ¹H NMR (δ ppm): 12.36 (1H, s, NH), 11.63 (1H, s, NH), 8.19 (1H, s, CH), 8.00 (1H, s, NH), 7.70 (2H, s, CH), 3.03 (2H, t, CH₂), 2.83 (2H, t, CH₂), 2.43 (3H, t, CH₃). **(14g)** IR (KBr) cm⁻¹: 1580 (C=C str), 1560 (C=N str), 770 (C=S str). ¹H NMR (δ ppm): 12.36 (1H, s, NH), 11.36 (1H, s, NH), 8.19 (1H, s, CH), 8.00 (1H, s, NH), 7.70 (2H, s, CH), 7.71–7.33 (5H, m, ArH), 3.03 (2H, t, CH₂), 2.83 (2H, t, CH₂). **(14h)** IR (KBr) cm⁻¹: 2956 & 2884 (CH str), 1600 (C=C str), 780 (C=S str). ¹H NMR (δ ppm): 12.36 (1H, s, NH), 11.63 (1H, s, NH), 8.19 (1H, s, CH), 7.70 (2H, s, CH), 3.03 (2H, t, CH₂), 2.83 (2H, t, CH₂), 2.43 (3H, s, CH₃), 2.0 (1H, s, NH). **(14i)** IR (KBr) cm⁻¹: 2950 & 2860 (CH str), 1575 (C=C str), 1570 (C=N str), 780 (C=S str). ¹H NMR (δ ppm): 13.04 (1H, s, NH), 12.36 (1H, s, NH), 11.63 (1H, s, NH), 8.19 (1H, s, CH), 7.70 (2H, s, CH), 7.71–7.33 (5H, m, ArH), 3.03 (2H, t, CH₂), 2.83

(2H, t, CH₂). **(14j)** IR (KBr) cm⁻¹: 3230 (NH str), 1580 (C=C str), 1560 (C=N str). ¹H NMR (δ ppm): 12.36 (1H, s, NH), 11.63 (1H, s, NH), 8.19 (1H, s, CH), 8.00 (1H, s, NH), 7.26–7.33 (5H, m, ArH), 7.70 (2H, s, CH), 4.71 (2H, s, CH₂), 3.73 (2H, s, CH₂), 2.43 (3H, s, CH₃). **(14m)** IR (KBr) cm⁻¹: 3230 (NH str), 1670 (C=O str), 1590 (C=N str). ¹H NMR (δ ppm): 12.36 (1H, s, NH), 11.63 (1H, s, NH), 8.19 (1H, s, CH), 8.00 (1H, s, NH), 7.70 (2H, s, CH), 7.71–7.23 (10H, m, ArH), 4.71 (2H, s, CH₂), 3.73 (2H, s, CH₂). **(14n)** IR (KBr) cm⁻¹: 3448–3170 (NH str), 1596 (C=N str). ¹H NMR (δ ppm): 12.36 (1H, s, NH), 11.63 (1H, s, NH), 8.19 (1H, s, CH), 8.00 (1H, s, NH), 7.26–7.33 (5H, m, ArH), 7.70 (2H, s, CH), 4.71 (2H, s, CH₂), 3.73 (2H, s, CH₂), 2.43 (3H, s, CH₃), 2.0 (1H, s, NH). **(14o)** IR (KBr) cm⁻¹: 3230 (NH str), 1595 (C=N str), 1497 (C=C str), 780 (C=S str). ¹H NMR (δ ppm): 13.04 (1H, s, NH), 12.36 (1H, s, NH), 11.63 (1H, s, NH), 8.19 (1H, s, CH), 7.70 (2H, s, CH), 7.71–7.23 (10H, m, ArH), 4.71 (2H, s, CH₂), 3.73 (2H, s, CH₂). **(14p)** IR (KBr) cm⁻¹: 1597 (C=N str), 1600–1550 (C=C str). ¹H NMR (δ ppm): 12.36 (1H, s, NH), 11.63 (1H, s, NH), 8.19 (1H, s, CH), 7.70 (2H, s, CH), 7.40–7.29 (5H, m, ArH), 7.09–6.89 (4H, m, ArH), 4.0 (1H, s, NH), 3.9 (1H, d, CH), 2.73 & 2.63 (2H, dd, CH₂), 2.1 (1H, q, CH), 1.7 & 1.4 (2H, dd, CH₂).

30.2.12 Preparation of Imidazo[4,5-*a*]benzodiazepine/ Oxazepino/Thiazepino[6,7-*a*]carbazoles/Azacarbazoles (15a-f and 15g-r)

A mixture of *o*-phenylenediamine / *o*-aminophenol / *o*-aminothiophenol (0.005 mol) and **(9a-b)** or **(10a-b)** or **(11a-b)** or **(12a-b)** (0.005 mol) was refluxed in DMF (5 ml) for 10–15 h. The reaction mixture was cooled to room temperature and solid was collected by filtration and washed thoroughly with water. Recrystallization from aqueous DMF gave the compounds. **(15b)** IR (KBr) cm⁻¹: 3100 (NH str), 1580 (C=N str), 680 (C=S str). ¹H NMR (δ ppm): 12.36 (1H, s, NH), 11.63 (1H, s, NH), 8.19 (1H, s, CH), 7.70 (2H, s, CH), 7.40–7.29 (5H, m, ArH), 7.09–6.89 (4H, m, ArH), 4.0 (1H, s, NH), 3.9 (1H, d, CH), 2.73 & 2.63 (2H, dd, CH₂), 2.1 (1H, q, CH), 1.7 & 1.4 (2H, dd, CH₂). **(15c)** IR (KBr) cm⁻¹: 3200 (NH str), 1580 (C=N str), 700 (C=S str). ¹H NMR (δ ppm): 12.36 (1H, s, NH), 11.63 (1H, s, NH), 8.19 (1H, s, CH), 7.70 (2H, s, CH), 7.33–7.23 (5H, m, ArH), 7.40–7.27 (5H, m, ArH), 7.39–7.21 (4H, m, ArH), 4.32 (2H, s, CH₂), 3.8 (1H, d, CH), 3.2 & 2.9 (2H, dd, CH₂), 2.4 (1H, q, CH). **(15e)** IR (KBr) cm⁻¹: 3100 (NH str), 1620 (C=N str). ¹H NMR (δ ppm): 12.36 (1H, s, NH), 11.63 (1H, s, NH), 8.19 (1H, s, CH), 7.70 (2H, s, CH), 7.33–7.23 (5H, m, ArH), 7.40–7.27 (5H, m, ArH), 7.09–6.89 (4H, m, ArH), 4.0 (1H, s, NH), 3.2 & 2.9 (2H, dd, CH₂), 2.3 (1H, q, CH). **(15f)** IR (KBr) cm⁻¹: 3200 (NH str), 1570 (C=N str), 660 (C=S str). ¹H NMR (δ ppm): 12.36 (1H, s, NH), 11.63 (1H, s, NH), 8.19 (1H, s, CH), 7.70 (2H, s, CH), 7.39–7.17 (4H, m, ArH), 2.83 (2H, t, CH₂), 3.03 (2H, t, CH₂), 2.80 (3H, s, CH₃). **(15i)** IR (KBr) cm⁻¹:

3400 (NH str), 1600 (C=N str). $^1\text{H NMR}$ (δ ppm): 12.36 (1H, s, NH), 11.63 (1H, s, NH), 8.19 (1H, s, CH), 7.70 (2H, s, CH), 7.09–6.86 (4H, m, ArH), 4.0 (1H, s, NH), 2.83 (2H, t, CH_2), 3.03 (2H, t, CH_2), 2.43 (3H, s, CH_3). (**15k**) IR (KBr) cm^{-1} : 3200 (NH str), 1580 (C=N str), 710 (C=S str). $^1\text{H NMR}$ (δ ppm): 12.36 (1H, s, NH), 11.63 (1H, s, NH), 8.19 (1H, s, CH), 7.70 (2H, s, CH), 7.33–7.23 (5H, m, ArH), 7.39–7.17 (4H, m, ArH), 4.71 (2H, s, CH_2), 3.73 (2H, s, CH_2), 2.80 (3H, s, CH_3). (**15o**) IR (KBr) cm^{-1} : 3200 (NH str), 1580 (C=N str). $^1\text{H NMR}$ (δ ppm): 12.36 (1H, s, NH), 11.63 (1H, s, NH), 8.19 (1H, s, CH), 7.70 (2H, s, CH), 7.33–7.23 (5H, m, ArH), 7.20–6.81 (4H, m, ArH), 4.71 (2H, s, CH_2), 4.0 (1H, s, NH), 3.73 (2H, s, CH_2), 2.43 (3H, s, CH_3).

30.3 Antimicrobial Activity

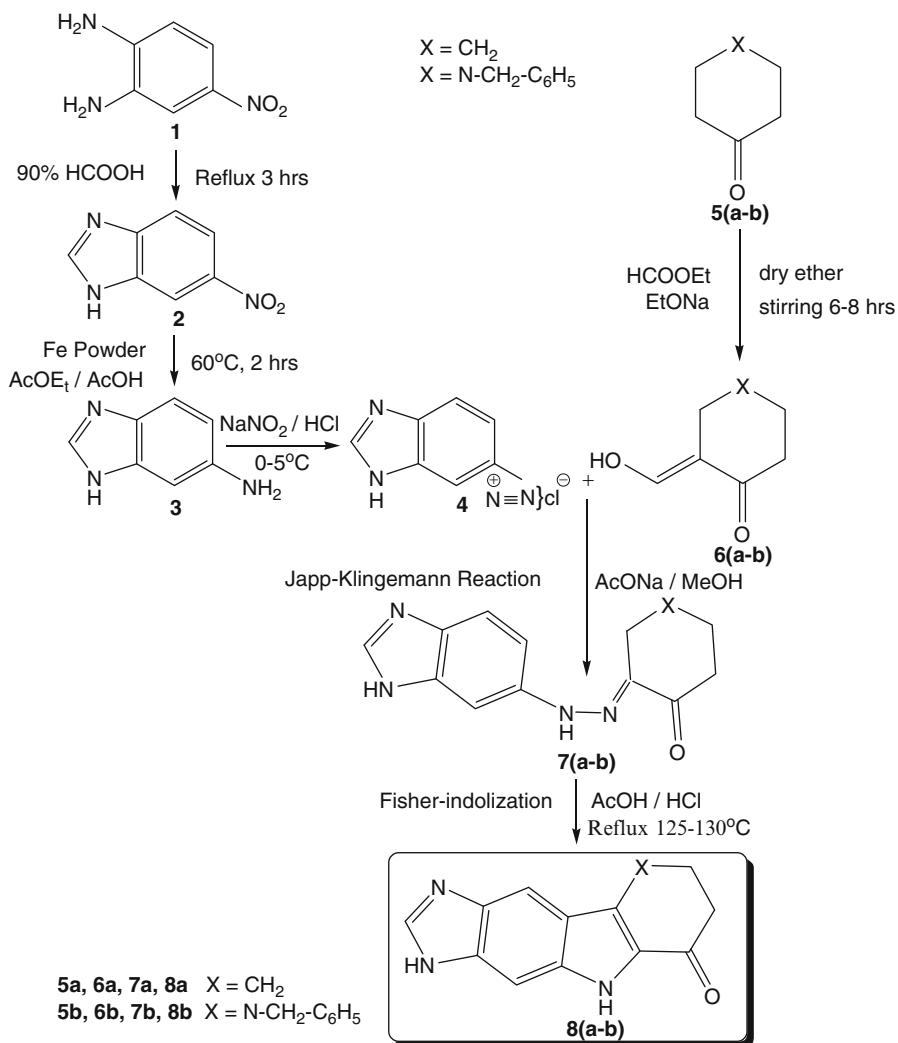
Pure culture of pathogenic bacteria (*Escherichia coli* and *Bacillus subtilis*) and fungi (*A. niger* and *A. flavus*) were procured from the Microbiology Research Laboratory, Department of Bioscience and Biotechnology, Banasthali University, Banasthali (Rajasthan). These were sub-cultured and characterized by standard methods of identification [24]. The zone of inhibition was determined in comparison to the standard drugs ciprofloxacin for antibacterial activity and fluconazole for antifungal activity.

Nutrient agar was developed for the microbes to grow by settling over Petri dishes. To develop nutrient agar peptone (5 g), NaCl (5 g) and meat extract (3 g) were dissolved in 1000 ml distilled water to prepare growth medium for antibacterial activity whereas glucose (20 g), peptone (10 g) and agar-agar (15 g) were dissolved to prepare growth medium for antifungal activity. The media were then sterilized in the autoclave along with the glasswares, Petris dishes, pipettes etc. at 15 psi pressure and 120°C for half an hour. The sterilized nutrient agar solution was taken out by micro-pipettes and a large number of Petri's dishes were prepared by pouring growth medium in Laminar Air Flow. The solution gradually solidified to a thickness of around 0.5–0.3 cm. The plates were then tightly tapped and kept at room temperature. Under aseptic conditions, the sterilized filter paper discs were dipped in the diluted test solutions with different concentrations in DMF. This was again done in Laminar Air Flow (LAF). All the agar plates with different organisms and discs of test solutions were accordingly utilized. Then the plates, properly cupped, were placed in an incubator at 37°C for 6 h for bacteria and $28 \pm 2^\circ\text{C}$ at 48 h for fungi. 10 mg of the test compounds was dissolved in DMF to make necessary dilutions at 400, 200, 100 $\mu\text{g/ml}$ to form the stock solutions of the compounds. After 24 h of incubation, the plates were analyzed and the diameter of the zones of complete inhibition was measured to the nearest whole millimeter with a sliding caliper.

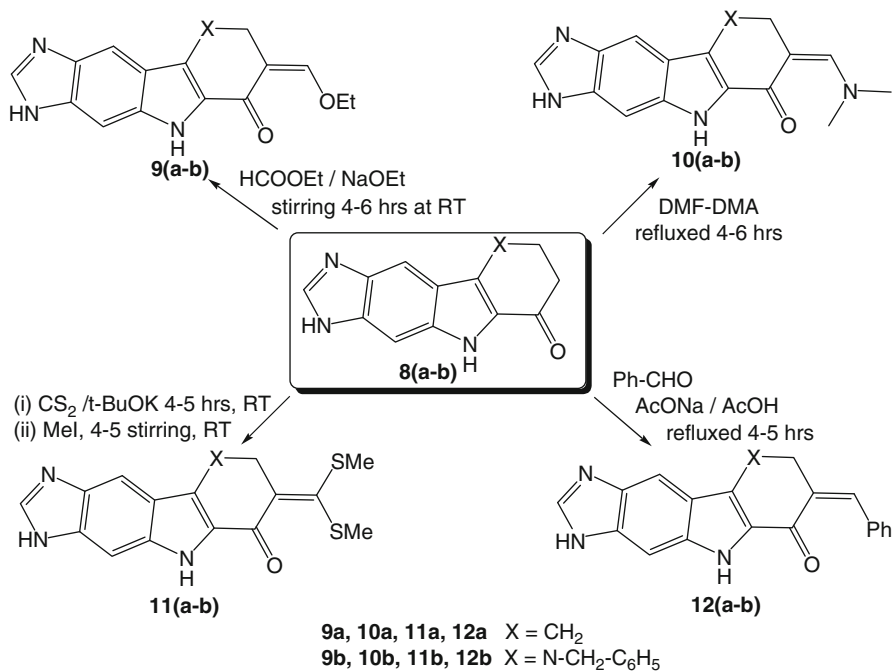
30.4 Results and Discussion

30.4.1 Synthesis of Compounds

4-Nitro-*o*-phenylenediamine (**1**) was treated with HCOOH shown in Scheme 30.1. The synthesis of 6-nitrobenzimidazole (**2**) from (**1**) was straightforward and the procedure reported in the literature [25, 26] was employed for its preparation. Diazoized aryl amines have been known to undergo Japp-Klingemann reaction [27] with



Scheme 30.1 Synthesis of 8,9-dihydroimidazo[4,5-b]carbazol-6-ones and azacarbazol-6-ones

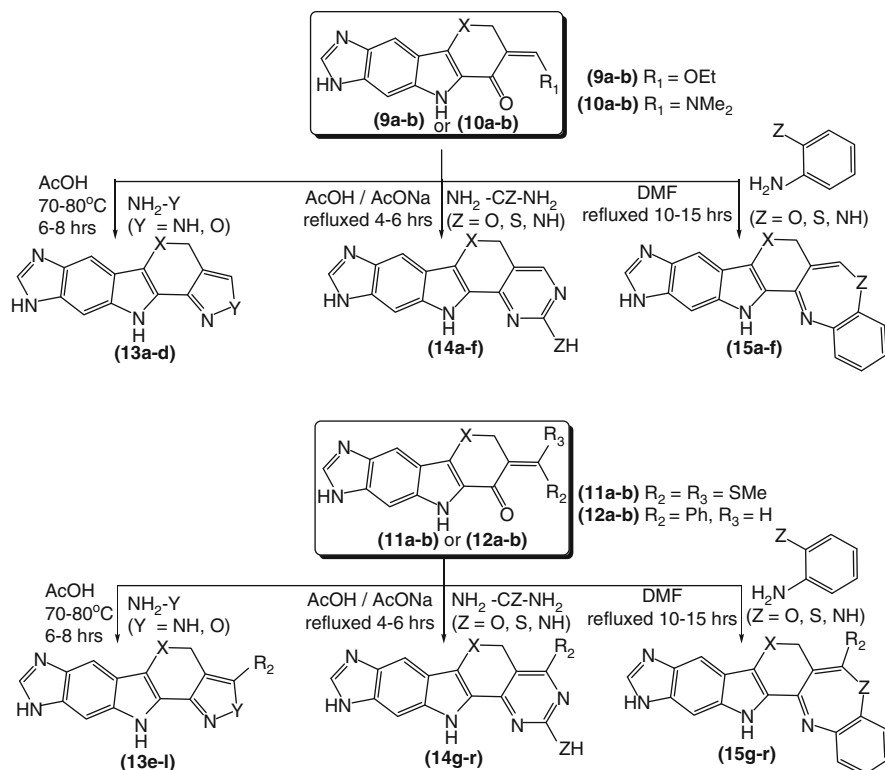


Scheme 30.2 Synthesis of intermediates: enolic ethers, chalcone analogues, dimethyl aminomethylene ketones, oxoketene dithioacetals

2-hydroxymethylened cyclohexanone (**6a**) or *N*-benzyl-3-hydroxymethylidene-4-piperidone (**6b**) (generated *in situ* from the reaction of cyclohexanone or *N*-benzyl-4-piperidone with ethyl formate in the presence of EtONa) to give corresponding hydrazones (**7a-b**). The same methodology was applied on the diazotized amino substituted benzimidazole (**4**) to generate (**7a-b**). The compounds (**7a-b**) were cyclised using Fischer indolization [28] to give (**8a-b**).

It is evident from the strategy depicted in Scheme 30.2 that the compounds (**8a-b**) are the key intermediates in the formation of (**9a-b**), (**10a-b**), (**11a-b**) and (**12a-b**). The reaction of (**8a-b**) with ethyl formate in the presence of a base [29] furnished (**9a-b**). It has been reported recently that carbonyl compounds containing an adjacent CH_2 group react smoothly with commercial *N,N*-dimethyl formamide dimethylacetal [30] to afford the reactive intermediates 2-dimethylaminomethylene ketones (**10a-b**). The compounds (**8a-b**) gave oxoketenedithioacetals (**11a-b**) on the reaction with CS_2 and CH_3I [31] whereas it gave α,β -unsaturated carbonyl compounds (**12a-b**) on the reaction with aromatic aldehydes [32].

The intermediates (**9a-b**), (**10a-b**), (**11a-b**) and (**12a-b**) are useful 1,3-dipolarophiles which have been extensively employed in the literature in the preparation of five-, six- and seven-membered heterocyclic rings from their reaction with bidentate nucleophiles such as hydrazine hydrate, hydroxylamine hydrochloride,



Scheme 30.3 Synthesis of five-, six- and seven-membered hetero ring fused imidazo[4,5b]carbazoles /azacarbazoles

urea, thiourea, guanidine, *o*-phenylenediamine, *o*-aminophenol and *o*-aminothiophenol [31, 33, 34]. The same methodology was applied on the intermediates **(9a-b)**, **(10a-b)**, **(11a-b)** and **(12a-b)** to prepare five-membered **(13a-d)** and **(13e-l)**, six-membered **(14a-f)** and **(14g-r)** and seven-membered compounds **(15a-f)** and **(15g-r)** shown in Scheme 30.3. The spectral data are given along with compounds preparation in Materials and Methods.

Physical and analytical data of all the compounds are given in Table 30.2.

30.4.2 Antimicrobial Activity

30.4.2.1 Antibacterial Activity

On comparing the antibacterial activity of the synthesized compounds (shown in tabular form in Table 30.3), the following conclusion was drawn:

Table 30.1 Various substituents of the compounds synthesized

S.No.	Compound Code	X	Y	R ₂
1.	(13a)	CH ₂	N H	-
2.	(13b)	CH ₂	O	-
3.	(13c)	N-CH ₂ - C ₆ H ₅	N H	-
4.	(13d)	N-CH ₂ - C ₆ H ₅	O	-
5.	(13e)	CH ₂	N H	S Me
6.	(13f)	CH ₂	N H	C ₆ H ₅
7.	(13g)	CH ₂	O	S Me
8.	(13h)	CH ₂	O	C ₆ H ₅
9.	(13i)	N-CH ₂ - C ₆ H ₅	N H	S Me
10.	(13j)	N-CH ₂ - C ₆ H ₅	N H	C ₆ H ₅
11.	(13k)	N-CH ₂ - C ₆ H ₅	O	S Me
12.	(13l)	N-CH ₂ - C ₆ H ₅	O	C ₆ H ₅

1. The results clearly indicated that increase in the concentration of compounds increased the antimicrobial activity. A regular fall in antimicrobial activity was recorded when the concentration of compounds was decreased.
2. The results of antimicrobial activity revealed that all the compounds showed higher antimicrobial activity with *B. subtilis* as compared to *E. coli*.
3. 400 µg/ml concentration maximum antibacterial activity was observed with compound (15l) followed by compound (14i) and compound (14l) with *B. subtilis* while highest antimicrobial activity against *E. coli* was observed with compound (15l) followed by compound (14i) and compound (14l).
4. At 200 µg/ml concentration, however, reduction in antimicrobial activity was observed, but at 200 µg/ml concentration highest antimicrobial activity was

Table 30.1 (continued)

S.No.	Compound Code	X	Z	R ₂
1.	(14a), (15a)	CH ₂	O	-
2.	(14b), (15b)	CH ₂	S	-
3.	(14c), (15c)	CH ₂	N H	-
4.	(14d), (15d)	N- CH ₂ - C ₆ H ₅	O	-
5.	(14e), (15e)	N- CH ₂ - C ₆ H ₅	S	-
6.	(14f), (15f)	N- CH ₂ - C ₆ H ₅	N H	-
7.	(14g), (15g)	CH ₂	O	S M e
8.	(14h), (15h)	CH ₂	O	C ₆ H ₅
9.	(14i), (15i)	CH ₂	S	S M e
10.	(14j), (15j)	CH ₂	S	C ₆ H ₅
11.	(14k), (15k)	CH ₂	N H	S M e
12.	(14l), (15l)	CH ₂	N H	C ₆ H ₅

Table 30.1 (continued)

13.	(14m), (15m)	N- CH ₂ - C ₆ H ₅	O	S M e
14.	(14n), (15n)	N- CH ₂ - C ₆ H ₅	O	C ₆ H ₅
15.	(14o), (15o)	N- CH ₂ - C ₆ H ₅	S	S M e
16.	(14p), (15p)	N- CH ₂ - C ₆ H ₅	S	C ₆ H ₅
17.	(14q), (15q)	N- CH ₂ - C ₆ H ₅	N H	S M e
18.	(14r), (15r)	N- CH ₂ - C ₆ H ₅	N H	C ₆ H ₅

found with compound (8a) followed by compound (14c) and compound (14i) against *B. subtilis*. Further, compound (8a) showed maximum antimicrobial activity against *E. coli* followed by compound (11a).

5. Similarly at 100 µg/ml concentration maximum antimicrobial activity was observed with compound (8a) followed by compound (14l), (15l), and (14c) against *B. subtilis*.

30.4.2.2 Antifungal Activity

On comparing the antifungal activity of the synthesized compounds (shown in tabular form in Table 30.3), the following conclusion was drawn:

1. At 400 µg/ml concentration compound (14c) showed maximum antifungal activity followed by compound (14i). The growth of *A. flavus* was maximum inhibited by compound (14c) followed by compound (14i), compound (15l) and compound (11a).
2. At 200 µg/ml concentration compound (14i) showed more inhibition against *A. flavus* followed by compound (14l) and (8a).
3. 100 µg/ml concentration maximum antifungal activity shown against *A. flavus* by compound (15l) and compound (14i). Similarly at the same concentration compound (15l) showed maximum antifungal activity against *A. niger*.

Table 30.2 Physical and analytical data of the synthesized compounds

S. No.	Compounds code	Molecular formula	M.W.	Yield		Elemental analysis	
				(%)	mp (°C)	N (cal/found)	S (cal/found)
1.	(3)	C ₇ H ₇ N ₃	133	70	102	32.08/31.56	–
2.	(8a)	C ₁₃ H ₁₁ N ₃ O	225	66	295–296	19.13/18.66	–
3.	(8b)	C ₁₉ H ₁₆ N ₄ O	316	50	315–316	18.32/17.71	–
4.	(9a)	C ₁₆ H ₁₅ N ₃ O ₂	281	50	299–300	15.56/14.94	–
5.	(9b)	C ₂₂ H ₂₀ N ₄ O ₂	372	60	288–290	15.46/15.04	–
6.	(10a)	C ₁₇ H ₁₈ N ₄ O	294	68	255–256	20.61/19.09	–
7.	(10a)	C ₂₂ H ₂₁ N ₅ O	371	58	280–282	19.28/18.85	–
8.	(11a)	C ₁₆ H ₁₅ N ₃ OS ₂	329	70	270–272	13.25/12.76	19.99/19.47
9.	(11b)	C ₂₂ H ₂₀ N ₄ OS ₂	420	71	297–299	13.81/13.32	15.78/15.25
10.	(12a)	C ₂₀ H ₁₅ N ₃ O	313	65	300–302	13.99/13.41	–
11.	(12b)	C ₂₆ H ₂₀ N ₄ O	404	72	260–261	14.54/13.85	–
12.	(13a)	C ₁₄ H ₁₁ N ₅	249	52	230–232	28.79/28.10	–
13.	(13b)	C ₁₄ H ₁₀ N ₄ O	250	50	220–222	22.91/22.39	–
14.	(13c)	C ₂₀ H ₁₆ N ₆	340	57	300–302	25.31/24.69	–
15.	(13d)	C ₂₀ H ₁₅ N ₅ O	341	55	315–316	21.05/20.52	–
16.	(13e)	C ₁₅ H ₁₃ N ₅ S	295	60	295–296	24.33/23.71	11.42/10.82
17.	(13f)	C ₂₀ H ₁₅ N ₅	325	71	245–246	22.14/21.52	–
18.	(13g)	C ₁₅ H ₁₂ N ₄ OS	296	62	300–301	19.36/18.91	11.42/10.82
19.	(13h)	C ₂₀ H ₁₄ N ₄ O	326	67	250–252	17.74/17.17	–
20.	(13i)	C ₂₁ H ₁₈ N ₆ S	386	65	245–247	22.32/21.75	08.90/08.30
21.	(13j)	C ₂₆ H ₂₀ N ₆	416	70	275–276	20.64/20.18	–
22.	(13k)	C ₂₁ H ₁₇ N ₅ OS	387	66	260–262	18.75/18.08	08.87/08.28
23.	(13l)	C ₂₆ H ₁₉ N ₅ O	417	67	310–312	17.26/16.78	–
24.	(14c)	C ₁₅ H ₁₂ N ₆	276	71	270–272	30.89/30.42	–
25.	(14f)	C ₂₂ H ₁₈ N ₆	366	66	318–320	22.96/22.94	–
26.	(14g)	C ₁₆ H ₁₃ N ₅ OS	323	62	278–280	22.12/21.66	10.42/09.92
27.	(14h)	C ₂₁ H ₁₅ N ₅ O	353	75	280–282	20.28/19.82	–
28.	(14i)	C ₁₆ H ₁₃ N ₅ S ₂	339	67	250–253	21.12/20.63	19.47/18.89
29.	(14j)	C ₂₁ H ₁₅ N ₅ S	369	76	290–293	19.38/18.96	09.17/08.68
30.	(14m)	C ₂₂ H ₁₈ N ₆ OS	414	69	260–261	20.83/20.28	08.33/07.74
31.	(14n)	C ₂₇ H ₂₀ N ₆ O	444	67	300–302	19.37/18.91	–
32.	(14o)	C ₂₂ H ₁₈ N ₆ OS ₂	430	60	322–325	19.99/19.52	15.38/14.89
33.	(14p)	C ₂₇ H ₂₀ N ₆ S	460	69	270–273	19.74/18.25	07.50/06.96
34.	(15b)	C ₂₆ H ₂₀ N ₄ S	420	65	220–222	13.75/13.32	08.02/07.62
35.	(15c)	C ₂₆ H ₂₁ N ₅	403	67	274–275	17.89/17.36	–
36.	(15e)	C ₃₂ H ₂₅ N ₅ S	511	71	250–252	14.11/13.69	06.81/06.27
37.	(15f)	C ₃₂ H ₂₆ N ₆	494	76	290–292	17.46/16.99	–
38.	(15i)	C ₂₁ H ₁₆ N ₄ S ₂	388	65	255–256	14.42/14.90	16.98/16.51
39.	(15k)	C ₂₁ H ₁₇ N ₅ S	371	75	260–262	19.25/18.85	09.12/08.63
40.	(15o)	C ₂₇ H ₂₁ N ₅ S ₂	479	77	240–242	15.02/14.60	13.79/13.37
41.	(15q)	C ₂₇ H ₂₂ N ₆ S	462	62	230–231	18.69/18.17	07.42/06.93

Table 30.3 Antimicrobial activity of some of the synthesized compounds (diameter of the disc = 80 mm)

S. No.	Level of conc.	Conc. (in $\mu\text{g/ml}$)	Zone of inhibition (in mm) (<i>E. coli</i>)	Zone of inhibition (in mm) (<i>B. subtilis</i>)	Zone of inhibition (in mm) (<i>A. niger</i>)	Zone of inhibition (in mm) (<i>A. flavus</i>)
(8a)	1	400	7.0	10.0	8.0	11.0
	2	200	8.0	9.0	6.0	7.0
	3	100	5.0	6.0	4.0	4.0
(11a)	1	400	8.0	11.0	13.0	12.0
	2	200	7.0	7.0	6.0	7.0
	3	100	4.0	3.0	4.0	4.0
(14c)	1	400	9.0	13.0	16.0	15.0
	2	200	6.0	8.0	7.0	6.0
	3	100	4.0	4.0	5.0	3.0
(14i)	1	400	13.0	15.0	15.0	13.0
	2	200	6.0	8.0	7.0	8.0
	3	100	5.0	4.0	5.0	5.0
(14l)	1	400	11.0	14.0	11.0	14.0
	2	200	5.0	6.0	7.0	7.0
	3	100	3.0	4.0	5.0	4.0
(15l)	1	400	15.0	17.0	12.0	13.0
	2	200	5.0	7.0	7.0	6.0
	3	100	2.0	4.0	6.0	5.0
Ciprofloxacin	1	400	4.0	4.2	3.9	4.4
	2	200	3.4	3.6	3.1	3.2
	3	100	2.7	2.4	2.3	2.6
Fluconazole	1	400	3.5	3.2	3.3	3.1
	2	200	2.4	2.3	2.9	2.8
	3	100	1.6	1.9	2.2	1.9

30.5 Conclusions

Finally, on the basis of the above results it was concluded that when the concentration of compound was increased, its antimicrobial activity also increased. From the above results the following trend of antimicrobial activity was observed: **400 > 200 > 100 $\mu\text{g/ml}$** . It had also been observed that compound no. (**14i**), (**14l**) and (**15l**) gave best results against all the pathogens.

Acknowledgement Authors are thankful to CURIE (Consolidation of University Research for Innovation and Excellence in Women's University) programme of the Department of Science and Technology (DST), Government of India for funding.

References

1. Alvarez F, Ghérardi A, Nebois P, Sarciron M-E, Pétavy A-F, Walchshofer N (2002) Benzimidazole-4,7-diones as inhibitors of protozoal (*Toxoplasma gondii*) purine nucleoside phosphorylase. *Bioorg Med Chem Lett* 12:977–979
2. Mahata G, Hayat M, De Vessel F, Schwargenberg L, Schneider M, Schlumberger JR, Jasmin C, Rosefeld C (1970) Methoxy-9-ellipticine-lactate-III: clinical screening and its action in acetate myeloblastic leukemia. *Rev Eur Etudes Clin Biol* 15:541–545
3. Werbel LM, Angelo M, Fry DW, Worth LM (1986) Basically substitutes ellipticine analogues as potential anti-tumor agents. *J Med Chem* 29:1321–1322
4. Tse-lok H, Hsieh SY (2006) Regioselective synthesis of ellipticine. *Helv Chem Acta* 89:111–114
5. Gilbert HK (2001) Heterocyclic analogues of carbazole alkaloids. *Curr Org Chem* 5:507–518
6. Crol WM, Osborne PC, Edward MA, Leen G (1995) Preparation and antitumour activity of olivacine and some new analogues. *J Med Chem* 9:237–241
7. Guilbaud N, Kraus-Berthier L, Saint-Dizier D, Rouillon M-H, Jan M, Burbridge M, Visali M, Bisagni E, Pierre A, Atassi G (1996) *In vivo* antimicrobial activity of S16020-2: a new olivacine derivative. *Cancer Chemother Pharmacol* 38:513–521
8. Jaszold-Howorko R, Croisy A, Carrez D, Jaroszewicz I, Nasulewicz A, Pełczyńska M, Opolski A (2004) Synthesis, structure and cytostatic properties of new olivacine derivatives. *Arch Pharm* 337:599–604
9. Janinová V, Nosál R, Danihelová E (1999) Aggregation of human blood platelets in the presence of the pyridoindole stobadine. *Life Sci* 65:1983–1986
10. Stole S, Snirc V, Majekova M, Gasparova Z, Gajdosikova A, Stvrtina S (2006) Development of the new group of indole-derived neuroprotective drugs affecting oxidative stress. *Cell Mol Neurobiol* 26:1495–1504
11. Rocca P, Marsis F, Godard A, Quiguiner G (1993) A short synthesis of the antimicrobial marine sponge pigment fascaplysin. *Tetrahedron Lett* 34:7917–7918
12. Arzel E, Rocca P, Grellier P, Labaëid M, Frappier F, Guéritte F, Gaspard C, Marsais F, Godard A, Quéguiner G (2001) New synthesis of benzo- δ -carbolines, cryptolepines, and their salts: *in vitro* cytotoxic, antiplasmodial, and antitrypanosomal activities of δ -carbolines, benzo- δ -carbolines, and cryptolepines. *J Med Chem* 44:949–960
13. Molinski TF (1993) Marine pyridoacridine alkaloids: structure, synthesis, and biological chemistry. *Chem Rev* 93:1825–1838
14. Takenaga N, Ishii M, Nakajima S, Hasegawa T, Iwasa R, Ishizaki H, Kamei T (1999) *In vivo* metabolism of a new anticancer agent, 6-*N*-formylamino-12,13-dihydro-1,11-dihydroxy-13-(β -D-glucopyranosyl)-5*H*-indolo [2,3-*a*]pyrrolo [3,4-*c*]carbazole-5,7(6*H*)-dione (NB-506) in

- rats and dogs: pharmacokinetics, isolation, identification, and quantification of metabolites. *Drug Metab Dispos* 27:205–212
15. Mukherjee AK, Basu S, Sarkar N, Ghosh AC (2001) Advances in cancer therapy with plant based natural products. *Curr Med Chem* 8:1467–1486
 16. Dalton LK, Demerac S, Elmes BC, Loder JW, Swan JM, Teitei T (1967) Synthesis of the tumour-inhibitory alkaloids, ellipticine, 9-methoxyellipticine, and related pyrido[4,3-b]carbazoles. *Aust J Chem* 20(12):2715–2727
 17. Dalton LK, Demerac S, Teitei T (1969) Synthesis of pyridocarbazoles for anti-tumour studies. *Aust J Chem* 22:185–195
 18. Asche C, Demeunynck M (2007) Antitumor carbazoles. *Anti Cancer Agents Med Chem* 7:247
 19. Both FL, Meneghini L, Kerber VA, Henriques AT, Elisabetsky E (2006) Role of glutamate and dopamine receptors in the psychopharmacological profile of the indole alkaloid psychollatine. *J Nat Prod* 69:342–345
 20. Farghaly AM, Soliman FS, Semary MM, Rostom AF (2001) Polysubstituted pyrazoles, part 4: synthesis, antimicrobial and anti-inflammatory activity of some pyrazoles. *Pharmazie* 56:28–32
 21. Wang AX, Xie Q, Lane B, Mollison KW, Hsieh GC, Marsh K, Sheets MP, Luly JR, Coghlan MJ (1998) Synthesis and immunosuppressant activity of pyrazole carboxamides. *Bioorg Med Chem Lett* 8:2787–2792
 22. Bouabdallah I, Mbarek LA, Ziad A (2006) Anticancer effects of three pyrazol derivatives. *Nat Prod Res* 20:1024–1030
 23. Naohiko Y, Iwagami H, Sasaki Y (2006) Synthesis and antibacterial activity of triazole and isoxazole derivatives of ampicillin. *J Antibiot* 36:1516–1524
 24. Black JG (1999) In: Schreiber L (ed) *Microbiology principles and explorations*, 4th edn. Prentice Hall, New Jersey, 363
 25. Bloom A, Day AR (1939) The preparation of 2-alkylaminobenzimidazoles. *J Org Chem* 4:14–19
 26. Roeder CH, Day AR (1941) Benzimidazole studies: the mechanism of benzimidazole formation from *o*-phenylenediamine. *J Org Chem* 6:29–35
 27. (a) Japp FR, Klingemann F (1887) *Ber Deutschen Chem Gesell* 20:2942–2944, 3284–3286, 3398–4301; (1888) *Liebigs Ann Chem* 247:190–225; (b) Prasad KJ, Vijayalakshmi CS (1994) Synthesis of 4-methyl-1-oxotetrahydrocarbazoles. *Indian J Chem* 33B:481–482
 28. Fischer E, Jourdan F (1883, 1884) *Ber Deutschen Chem Gesell* 16:2241 & 17:1184
 29. Padmawati V, Reddy BJM, Balaiah A, Reddy VK, Reddy DB (2000) Synthesis of some fused pyrazoles and isoxazoles. *Molecules* 5:1281–1286
 30. Fukui H, Inoguchi K, Nakano J (2002) Synthesis of the bicyclic secondary amines via dimethylaminomethylene ketones from 3-pyrrolidone and 4-piperidone. *Heterocycles* 56:257–264
 31. Chauhan SMS, Junjappa H (1976) Ketene-S, S-acetals-V, the reaction of α -keto and α -cyanoketene-S, S-acetals with guanidine and thiourea: a new general synthesis of alkoxy-pyrimidine. *Tetrahedron* 32:1779–1787
 32. Singh B, Mehta D, Baregama LK, Talesara GL (2004) Synthesis and biological evaluation of 7-(*n*-alkoxyphthalimido)-2-hydroxy-4-aryl-6-aryliminothiazolidino[2,3-*b*]pyrimidine and related compounds. *Indian J Chem* 43B:1306–1313
 33. Singh G, Ila H, Junjappa H (1987) Polarised ketene dithioacetals. Part 50. Reactions of α -aroyl- α -bromoketene dithioacetals with hydrazine hydrate: formation of rearranged pyrazoles. *J Chem Soc Perkin Trans 1*:1945–1949
 34. Claramunt RM, Sanz D, Aggarwal S, Kumar A, Prakash O, Singh SP, Elguero J (2006) The reaction of *o*-phenylenediamine with α,β -unsaturated carbonyl compounds. *ARKINOC XIV*:35–45

Chapter 31

Screening Biochemical Markers for the Prevention of Coronary Heart Disease

Deepuk Albana and Marie Chan Sun

Abstract Coronary heart disease (CHD) is among one of the major causes of deaths in Mauritius. It is important to screen biochemical markers, amongst other clinical and para-clinical tests, in view of the prevention of the disease. The study consisted of screening a random sample of 300 employees for total cholesterol above the desirable range (>5.17 mmol/l). A second fasting blood test was performed in those who had high total cholesterol. The lipid profile was performed using commercially available kits. The *Total Cholesterol to High Density Lipoprotein Cholesterol* ratio was calculated for identification of those at risk of CHD.

The findings showed an important prevalence of blood lipid abnormalities in the studied population, thus highlighting the need for screening for abnormal levels of these biochemical markers.

31.1 Introduction

Cardiovascular disease is ranked by the World Health Organization (WHO) as the world's top cause of death, causing one third of all deaths globally [1]. Each year, more than 17 million people die from cardiovascular disease, mainly heart disease and stroke [2]. Coronary Heart Disease (CHD), of which dyslipidaemia is a significant feature, continues to be the single leading cause of death globally among both males and females, underscoring the tremendous need for the successful identification and management of CHD risk factors [3].

Moreover, it is evident from studies in the literature review that when the total cholesterol concentration is high, the incidence and prevalence of CHD are also high

D. Albana
Huddlesfield Royal Infirmary, Leeds, United Kingdom
e-mail: yoyo_17@yahoo.com

M. Chan Sun (✉)
Department of Medicine, University of Mauritius, Réduit, Mauritius
e-mail: lan.sun@uom.ac.mu

[4–10]. Increased cholesterol is a causative factor in the etiology of atherosclerotic disease [11]. The association between serum cholesterol and atherosclerosis was first suggested in 1938, when Thanhauser and Muller each demonstrated familial aggregation of hypercholesterolemia and CHD [12].

Heredity, a diet rich in saturated fat content, and various metabolic conditions such as diabetes mellitus influence an individual's level of cholesterol [13]. Cholesterol levels usually rise steadily with age, more steeply in women, and stabilize after middle age [13]. Mean cholesterol levels vary moderately between regions, although never more than 2.0 mmol/l in any age group [13]. More than 60% of the global burden of coronary heart disease occurs in developing countries [1]. Coronary heart disease is decreasing in many developed countries, but is increasing in developing and transitional countries, partly as a result of increasing longevity, urbanization, and lifestyle changes [1].

Mauritius, situated in the Indian Ocean, is changing from an agro-based economy to the Information and Communication Technology sector. The Mauritian population is thus experiencing a considerable change in lifestyle patterns, such as adopting fast food eating habits. This lifestyle trend with a high consumption of fast food, high content of salts and fats, poor consumption of fruits and vegetables constitute an important risk factor that contributes to lipid imbalances.

During the Mauritius Non Communicable Diseases survey carried out by the Ministry of Health and Quality of Life (MoH&QL), which used the ethnic specific BMI cut-points, the prevalence of obesity was found to be 43.3% and the prevalence of overweight was 22.3%. Thus, the prevalence of overweight or obesity was 65.6%. The prevalence of hypertension was 37.9%. Moreover, almost 1 in 2 Mauritians 25–74 years has either diabetes or impaired glucose metabolism, a pre-diabetic condition, which is associated with substantially increased risk of developing heart disease [14].

Coronary heart disease is among one of the major causes of deaths in Mauritius [14]. The current mortality rate and the overwhelming presence of CHD risk factors highlight the need to screen biochemical markers, among other clinical and para-clinical tests, for early detection of dyslipidaemia for the prevention of the disease. The U.S. Preventive Services Task Force (USPSTF) strongly recommends screening men aged 35 and older for lipid disorders and men aged 20–35 for lipid disorders if they are at increased risk for coronary heart disease. However, the major change in the current recommendation is that adult women at any age should be screened only if other risk factors for cardiovascular disease are present [15].

Lipid profiling, or coronary risk profile, is a battery of blood tests to determine a person's risk of coronary heart disease. The blood tests include the measurement of a person's total cholesterol and triglyceride levels as well as the determination of Low density lipoprotein (LDL or "bad" cholesterol), High density lipoprotein (HDL or "good" cholesterol), and Very low density lipoprotein (VLDL cholesterol, though this is often calculated from the triglyceride level) [15].

Healthy adults should be screened for cholesterol and HDL every 5 years. However, shorter intervals are advised for persons consuming fatty and cholesterol-rich meals and presenting risk factors such as diabetes, hypertension and smoking status to have the full lipid profiling [16].

In light of the above, this research work was designed with the aim to prevent CHD in an employee population of Mauritius by early screening of biochemical risk factors. The main objectives of this study were to analyze the lipid profile of a randomly selected employee population of an institution and to identify individuals at risk of CHD in view of counseling or referral.

31.2 Methodology

31.2.1 Sample Population

Participants were recruited from an employee population of an institution. The study comprised screening of 300 participants who were randomly selected (irrespective of sex, age and ethnic origin) from the registry of staff workers of the institution. Total cholesterol and triglycerides levels in the blood, as well as glycemia and uricemia were performed.

Upon receipt of the results of the biochemical markers, participants with total cholesterol and triglycerides levels beyond the normal range were invited to undergo a full lipid profile in order to identify those at risk for CHD. Levels of serum total cholesterol (TC), its sub-fractions: low density lipoprotein (LDL) cholesterol, high density lipoprotein (HDL) cholesterol and triglycerides were measured using commercially available kits (RANDOX, Crumlin UK). The TC/HDL ratio for predicting risk of CHD was calculated and those at risk identified.

31.2.2 Ethical Considerations

Prior to start of this project work, ethical clearance was obtained from the relevant health authorities. Employees who were randomly selected were provided with an information sheet on the project being carried and asked to sign a consent form prior to their participation. Participation was purely on a voluntary basis and participants could withdraw at any time during the research process. Each participant was assured of the strict confidentiality of data collected and this aspect was maintained all throughout the study.

31.2.3 Blood Collection

Blood collection was performed by specialized nursing officers from participants after an overnight fasting period of 12 h for the required lipid profile. The blood samples were obtained from the ante-cubital vein while participants were in a sitting

position. Amounts of 5 ml of whole blood were removed in sterile plastic tubes that contained EDTA and heparin for the required analyses. The plasma samples were first allowed to thaw by allowing them to stand at room temperature for about 30 min and then used for determination of different lipid levels.

31.2.4 Statistical Analysis

Collected data was analyzed using the EpiInfo 2002 and Excel (Microsoft Office 2000). Means were compared by simple analysis of variance (ANOVA) and association between pairs was performed using the Chi-squared test as well as Fisher's tests. Differences were considered significant for a two-sided p-value < 0.05. Mantel-Haenszel statistics were also used.

31.3 Results

The response rate for the initial blood test was 74%. Among the respondents, 35% had TC level above desirable range and 23% had abnormal levels of TG. The response rate for the second blood test was 77%. Among these respondents who had abnormal lipid level(s), there were 53 (67.9%) men and 25 (32.1%) women. The mean age \pm SD was 41.81 ± 8.80 years and was 42.26 ± 8.08 years for men versus 40.84 ± 10.26 years for women.

Based on the findings of the second blood test, the sex specific distribution of lipid levels is shown in Table 31.1.

Table 31.1 Serum lipid distribution according to sex

Serum lipid	Female	Male	Total
Total cholesterol (mmol/l)			
0–5.17 (desirable)	8	19	27
5.18–6.18 (borderline)	7	18	25
6.19– (high)	10	16	26
LDL-Cholesterol (mmol/l)			
0–3.36 (desirable)	8	22	30
3.37–4.14 (borderline)	7	13	20
4.15– (high)	10	17	27
HDL-Cholesterol (mmol/l)			
0–1.03 (low)	3	19	22
1.04–1.55 (normal)	18	29	47
1.56– (high)	4	5	9
Triglycerides (mmol/l)			
0–1.70 (normal)	25	37	62
1.71–2.26 (borderline)	0	15	15
2.27– (high)	0	1	1

Table 31.2 Lipid abnormalities according to sex

	Men	Women	Total
TC/HDL-C ratio ≥ 5	31	6	37
TC ≥ 5.18 mmol/l and TG ≥ 2.26 mmol/l	1	0	1
TC ≥ 5.18 mmol/l and LDL-C ≥ 4.15 mmol/l	17	10	27
HDL-C < 1.04 mmol/l and TG ≥ 2.26 mmol/l	10	0	10

Table 31.3 Risk factors for CHD among participants

Variable	LDL-C ≤ 3.36 mmol/l		LDL-C > 3.36 mmol/l	
	TC/HDL-C < 5 n = 21	TC/HDL-C ≥ 5 n = 10	TC/HDL-C < 5 n = 20	TC/HDL-C ≥ 5 n = 27
Age	39.95 \pm 9.62	40.90 \pm 6.89	43.25 \pm 9.61	42.52 \pm 8.30
TC (mmol/l)	4.50 \pm 0.62	5.03 \pm 0.55	5.96 \pm 0.53	6.63 \pm 1.20
HDL-C (mmol/l)	1.30 \pm 0.39	0.85 \pm 0.10	1.39 \pm 0.19	1.16 \pm 0.15
LDL-C (mmol/l)	2.65 \pm 0.64	2.81 \pm 0.32	3.94 \pm 0.42	4.62 \pm 1.03
TG (mmol/l)	1.22 \pm 0.81	3.15 \pm 1.15	1.39 \pm 0.43	1.86 \pm 0.69
TC/HDL-C ratio	3.68 \pm 0.87	5.92 \pm 0.60	4.34 \pm 0.46	5.73 \pm 0.61

The mean \pm SD total cholesterol levels were 5.70 \pm 1.29 mmol/l in men and 5.65 \pm 1.06 mmol/l in women. The mean LDL-cholesterol levels were 3.67 \pm 1.20 mmol/l in men and 3.74 \pm 0.93 mmol/l in women while the mean HDL-cholesterol levels were 1.17 \pm 0.31 mmol/l in men and 1.32 \pm 0.22 mmol/l in women.

The mean triglycerides levels were 1.94 \pm 1.05 mmol/l in men and 1.30 \pm 0.46 mmol/l in women, the mean fasting blood sugar levels 5.31 \pm 2.27 mmol/l in men and 5.18 \pm 1.48 mmol/l in women, the mean uric acid levels 297.13 \pm 78.85 μ mol/l in men and 209.44 \pm 55.95 μ mol/l in women, and the mean TC/HDL ratio 5.05 \pm 1.11 in men and 4.41 \pm 1.07 in women.

Further findings on the lipid abnormalities are shown in Table 31.2. Table 31.3 shows the risk factors for CHD among respondents categorized by LDL-Cholesterol levels and TC/HDL-C ratios.

31.4 Discussion

The respondents of this study were classified according to the recommendations of the US National Cholesterol Education Programme Adult Treatment Panel III for the determination of the prevalence of hyperlipidaemia, therefore the cut-off point of LDL-Cholesterol levels of 3.36 mmol/l and the cut-off point of TC/HDL-C ratio of 5 were used [11].

The present findings highlight an important number of respondents with one or more elevated lipid parameters. This is in line with the Mauritius Non Communicable Diseases survey which reported that one out of two Mauritians had

at least one abnormality in one of the four lipids, putting them at increased risk of cardiovascular disease [14]. According to this report, the prevalence, in adult Mauritian population aged 25–74 years, of elevated total cholesterol (≥ 5.2 mmol/l) was 34.7%; the prevalence of elevated triglycerides (≥ 2.0 mmol/l) was 16.9% [14].

The comparison of the findings of this study and especially those of the NCD report with the prevalence of dyslipidaemia in Africa, China, India and the United States shows that Mauritius has the highest prevalence of hyperlipidaemia (51%), followed by the Punjabi people of North India (48.9%). The Mauritian prevalence of dyslipidaemia is also higher than the US (17%), which is closely followed by South Africa (13%), while the Beijing population seems to have the lowest prevalence of same for this set of data (9.3%) [17–20].

On the other hand, the levels of HDL-cholesterol for 71.8% of the sample population in this study fall in the favourable range (> 1.03 mmol/l). However, 36% of these respondents had a TC/HDL-C ratio of high coronary risk. A favorable HDL-Cholesterol level does not necessarily imply low CHD risk. Numerous studies show that TC/HDL ratio is a better predictive value for CHD risk [21–23]. Wang et al. (2001) put forward that the total cholesterol/HDL ratio is the most powerful lipoprotein discriminator for future CHD events, irrespective of age, sex, and various cardiovascular risk factors. Moreover, compared with using the LDL cholesterol level of 3.36 as the cut-off point, using the total cholesterol/HDL cholesterol ratio of 5 was associated with significantly higher specificity and accuracy and similar sensitivity [8].

Based on the specificity of the total cholesterol/HDL cholesterol ratio and on the high prevalence of dyslipidaemia in Mauritius, the primary prevention of CHD, through the determination of the lipid profile of employees, should become a priority for all work organizations. There is need for the annual provision of facilities on the workplace for regular screening and monitoring of abnormal levels of these biochemical markers which expose employees to an increased risk of CHD. Lifestyle modification supported by the workplace environment is the key for controlling these biochemical markers and for the prevention of CHD.

The theme for 2010 World Heart Day “Workplace Wellness: Take Responsibility for Your Own Heart Health” builds on 2009 healthy workplace theme [24]. Leading a healthy lifestyle, on an individual level, involves eating a healthy diet, maintaining a healthy weight, exercising regularly and limiting alcohol use as well as quitting tobacco. Engaging in healthy behaviour helps to control certain risk factors such as high blood cholesterol and prevent CHD [24].

At an employer level, there are simple ways to foster and promote healthy lifestyles around the workplace, thereby creating a healthier workplace for employees. These include the provision of a canteen/cafeteria where healthy and affordable food can be consumed and where healthy food choices will be identified with signs or menu labeling. The provision of facilities and incentives for performing leisure-time physical activities is also to be considered. Employers can have recourse on an annual basis to clinicians to encourage employees presenting cardiovascular risk factors to undergo on the workplace a medical examination along with a lipid profile. This will definitely contribute to the primary prevention of CHD.

Good health is essential to human welfare and to sustained economic and social development [13]. Employers and decision makers in the workplace organization have an important role to play with respect to healthy workplace policies to be adopted so as to provide a supportive environment for healthy lifestyle. Otherwise, through strengthening of community/workplace action, trade unions and employees will have to advocate for healthy supportive environments so that the paradigm shift to healthy behaviours can occur at the workplace level extending progressively to national level. Workplaces with healthy policies can provide welfare and health services which are crucial in Mauritius to curb the incidence of CHD.

31.5 Conclusions

This research work carried out in a workplace setting has revealed a high prevalence of blood lipid abnormalities in the studied employee population. This study therefore highlights the need for screening in the workplace setting for abnormal levels of the biochemical markers which expose employees to an increased risk of CHD. The identification of cardiovascular risk factors is of major importance in the evaluation of the need for treatment. Lifestyle modification of employees supported by the workplace environment remains nonetheless the key for controlling dyslipidaemia and for the prevention of CHD. Emphasis is laid on the need for supportive environment to be provided by workplace settings. Workplaces with healthy policies can provide the necessary supportive environment for successful behaviour change and health improvement.

Acknowledgements The authors are thankful to the staff of the Department of Medicine, University of Mauritius for technical support provided.

References

1. World Health Organization (2004) The atlas of heart disease and stroke, Part 3: the burden. World Health Organization, Geneva. http://www.who.int/cardiovascular_diseases/resources/atlas/en/. Accessed 8 Sept 2010
2. World Health Organization (2005) Preventing chronic diseases: a vital investment. World Health Organization, Geneva. <http://www.who.int/>. Accessed 8 Sept 2010
3. Brewer HB (2004) A new dawn in the treatment of Dyslipidaemia: cardiovascular risk reduction through emerging science and proven clinical results. *Am Heart J* 148:S1–S2
4. Gupta R, Gupta HP, Kumar N, Joshi AK, Gupta VP (1994) Lipoprotein lipids and the prevalence of hyperlipidaemia in rural India. *J Cardiovasc Risk* 1:179–184
5. Rafiei M, Boshtam M, Sarraf-Zadegan N (1999) Lipid profiles in the Isfahan population: an Isfahan cardiovascular disease risk factor survey, 1994. *East Mediterr Health J* 5:766–777
6. Foucan L, Kangambega P, Koumavi Ekouevi D, Rozet JE, Bangou-Brédent J (2000) Lipid profile in an adult population in Guadeloupe. *Diabetes Metab* 26:473–480

7. Yarzebski J, Spencer F, Goldberg RJ, Lessard D, Gore JM (2001) Temporal trends (1986–1997) in cholesterol level assessment and management practices in patients with acute myocardial infarction. *Arch Intern Med* 161:1521–1528
8. Wang TD, Chen WJ, Chien KL, Su SS, Hsu HC, Chen MF, Liao CS, Lee YT (2001) Efficacy of cholesterol levels and ratios in predicting future coronary heart disease in a chinese population. *Am J Cardiol* 88:737–743
9. American Association of Clinical Endocrinologists (AACE) (2002) AACE lipid guidelines. *Endocr Pract* 6:4–52
10. Eghan BA Jr, Acheampong JW (2003) Dyslipidaemia in outpatients at General Hospital in Kumasi, Ghana: cross-sectional study. *Croat Med J* 44:576–578
11. National Cholesterol Education Program Expert Panel (2001) Executive summary of the third report of the National Cholesterol Education Program (NCEP) expert panel on detection, evaluation and treatment of high cholesterol in adults (Adults Treatment Panel III). *J Am Med Assoc* 285:2486–2497
12. Rifai N, Bachorik PS, Albers JJ (1999) Lipids, lipoproteins & apolipoproteins. In: Burtis CA, Ashwood ER (eds) *Tietz textbook of clinical chemistry*, 3rd edn. Saunders, Philadelphia, pp 809–861
13. World Health Organization (2010) Health systems financing: the path to universal coverage. The world health report 2010. World Health Organization, Geneva. <http://www.who.int/whr/2010/en/index.html>. Accessed 8 Sept 2010
14. Ministry of Health and Quality of Life, Republic of Mauritius (2009) The trends in diabetes and cardiovascular disease risk in Mauritius. Mauritius non communicable diseases survey report
15. United States Preventive Services Task Force (2008) Screening for lipid disorders in adults: recommendation statement. <http://www.uspreventiveservicestaskforce.org/uspstf08/lipid/lipidrs.htm>. Accessed 8 Sept 2010
16. United States Preventive Services Task Force (2002) Screening for lipid disorders in adults: recommendations and rationale. *Internet J Intern Med* 3(2). <http://www.ispub.com/ostia/index.php?xmlFilePath=journals/ijim/vol3n2/lipid.xml>. Accessed 8 Sept 2010
17. Sliwa K, Wilkinson D, Hansen C, Ntyintyane L, Tibazarwa K, Becker A, Stewart S (2008) Spectrum of heart disease and risk factors in a black urban population in South Africa (the Heart of Soweto Study): A cohort study. *Lancet* 371:915–922
18. Cheng J, Zhao D, Zeng Z, Critchley JA, Liu J, Wang W, Sun J, Capewell S (2009) The impact of demographic and risk factor changes on coronary heart disease deaths in Beijing (1999–2010). *BMC Public Health* 9:30–36
19. Gupta R, Kaul V, Bhagat N, Agrawal M, Gupta VP, Misra A, Vikram NK (2008) Trends in prevalence of coronary risk factors in an urban Indian population: Jaipur Heart Watch-4. *Indian Heart J* 156:112–119
20. Ghandehari H, Kamal-Bahl S, Wong ND (2008) Prevalence and extent of dyslipidemia and recommended lipid levels in US adults with and without cardiovascular comorbidities: the National Health and Nutrition Examination Survey 2003–2004. *Am Heart J* 156:112–119
21. Lemieux I, Lamarche B, Couillard C, Pascot A, Cantin B, Bergeron J, Dagenais GR, Despres JP (2001) Total cholesterol/HDL cholesterol ratio vs LDL cholesterol/HDL cholesterol ratio as indices of ischemic heart disease risk in men. *Arch Intern Med* 161:2685–2692
22. Bersot TP, Pépin GM, Mahley RW (2003) Risk determination in populations characterised by low levels of high-density lipoprotein cholesterol. *Am Heart J* 146:1052–1060
23. Natarajan S, Glick H, Criqui M, Horowitz D, Lipsitz SR, Kinoshian B (2003) Cholesterol measures to identify and treat individuals at risk for coronary heart disease. *Am J Prev Med* 25:50–57
24. Centers for Disease Control. Heart Disease (On line). Available at <http://www.cdc.gov/Features/WorldHeartDay/>. Accessed 30 Sept 2010

Index

A

Abinit, 239
Ab initio, 44, 45, 172, 239
Absorption, 58, 63, 104, 116, 232, 234–236, 242, 243, 307, 308, 320, 324, 325, 327–328, 367–370, 372, 392, 404, 421, 427, 428
Acetonitrile, 318, 402
Action research, 265–297
Active learning, 267, 268, 281, 291, 293, 295
Addition reaction, 83, 95–99, 144, 376
Adiabatic decoupling, 190, 191
Adsorption
 capacity, 339, 345–347, 350
 isotherms, 346–347
Agaricus bitorqus, 433–440
Agrochemicals, 104, 122
Alloys, 103, 209, 210, 214–216, 220
Allylic halide, 144
 α -pinene, 447–449
Amberlite, 335–351
Amic acid, 103–116
Ammonia, 197, 214, 347, 376–385, 412, 413
Amphiphilic, 81, 82, 94
Analgesic, 104, 454
Analysis, 5, 9, 13, 14, 33, 37, 59–62, 70, 84, 91, 92, 100, 107, 127, 129, 173–176, 185, 191, 216, 224–228, 232, 233, 235, 258, 266, 269, 271, 280–282, 306, 308–310, 336, 337, 341, 351, 360, 369, 373, 376, 377, 379–383, 385, 391–394, 406, 408, 412, 420, 445, 449, 469, 476
Analytical, 84, 107, 108, 124–126, 128, 129, 148, 210, 211, 254, 266, 306, 336, 392, 400, 401, 415, 434, 455, 465, 469
Angular distribution studies, 50, 54
Anharmonic coupling, 181, 190

ANOVA, 476
Antibacterial, 100, 104, 116, 122, 128, 129, 198, 412, 414, 415, 444, 449, 462, 465, 466, 468, 470
Anticancer, 301–313
Anticonvulsant, 104
Anti-diabetic, 121
Antifungal, 104, 129, 444, 449, 462, 468, 470
Anti-HIV, 412, 415, 454, 455
Anti-inflammatory, 121, 122
Anti-Markovnikov, 376–379, 381–385
Antimicrobial, 121–140, 443–450, 454, 462, 465, 466, 468, 470, 471
Antioxidant, 304–305, 311
Antitumor, 104
 activity, 122, 302
Aspergillus
 A. flavus, 462, 468, 470
 A. niger, 128, 129, 446, 448, 449, 462, 468, 470
Asymmetry, 51, 53
Atmospheric chemistry, 35, 36, 55
Attributes/characteristics of a concept, 268, 269, 288, 295
Azacarbazoles, 453–471
Azotized, 340, 341

B

Bacillus subtilis, 128, 446, 462, 466, 468, 470
Backbonding, 236
Bacterial cultures, 116
Baylis-Hillman, 81–100
Benzaldehyde, 83, 89, 94, 95, 100, 149, 458
Benzamides, 413
Benzylamine, 412–414
Benzylidene, 145, 146, 148, 150, 458–459

- β -amino alcohols, 83
 β -pinene, 447–449
 Bimetallic complex, 246
 Biochemical, 370, 400, 433, 473–479
 Biodegradable, 69, 434, 437
 Biodiversity, 336
 Biological, 7, 74, 91, 122, 232, 301, 302,
 310–313, 368, 373, 400, 420, 430, 444,
 454, 455
 activity, 83, 84, 93, 100, 411–416
 Biosynthesis, 438
 Blood, 454, 474–479
 Blue shift, 63, 236, 242
 Bond energies, 39
 Buffer, 211, 212, 214–216, 302, 304, 305, 344,
 401, 402, 405, 408, 434, 435
- C**
- Cage complex, 13, 18, 23–25, 30, 32, 33
 Cage effect, 11–33, 82
 Camphor, 447–449
 Cancer, 210, 302, 304, 310, 312
 Carbazoles, 453–471
 Cardiovascular, 473, 474, 478, 479
 Car-Parrinello molecular dynamics (CPMD),
 171–191
 Catalysis, 82, 95, 402, 407, 409
 Catalyst, 82, 83, 89, 91, 94–100, 103, 143, 144,
 146, 147, 150, 210, 385, 389–397, 400,
 411, 420
 Cementite, 222, 227, 229
 Cesium chloride, 353–365
 Chalcone, 145–147, 150, 455, 464
 Charge transfer, 116, 236, 251, 317–330,
 394, 400
 resistance, 255, 261–263
 Chemical kinetics, 11–15, 18, 19, 23, 24, 30,
 33
 Chloramphenicol, 128, 129
 Chlorophyll, 369, 372, 373
 Cholesterol, 473–478
 Chromatography, 84–90, 124, 128–130, 134,
 148, 149, 210, 445, 447, 455
 Cineole, 444, 447–449
 Cinnamaldehyde, 146, 150
Cis-platin (CPT), 310–313
 Classical, 172, 173, 321, 414, 435
 Climate change, 2, 368
 Cluster ions, 353–365
 Coagulation, 420
 Co-doped-TiO₂, 60–62, 65–67
 Collision theory, 11, 13, 14, 32
- Complexes, 5, 13, 18, 23–25, 30, 32, 33,
 103–116, 148, 205, 231–246, 251, 295,
 302, 303, 306–310, 317, 319, 321, 324,
 325, 327, 328, 347, 422, 427, 428, 444
 Computational, 122, 172, 207, 375–385
 Concept, 12, 18, 19, 24, 32, 166, 411
 attainment model, 265–297
 Conductivity, 104, 107, 113–116, 233, 391
 Configuration interaction (CI), 154–159,
 161–168
 Congenous Compound, 195–197, 200, 202, 204
 Constant-ionic-state (CIS) spectroscopy, 36,
 50–52
 Coordination, 104, 111, 115, 237, 240, 243,
 307, 309
 Coronary heart disease, 473–479
 Correlation energy, 155, 156
 Correlations, 6–8, 93, 153–168, 239, 321, 322,
 324, 354, 392, 422
 Coulomb hole, 154, 160–162, 165, 166, 168
 Critical micelle concentration (CMC), 82, 83
 Cyclic voltammetry, 240, 402, 407
- D**
- De-coloration, 422, 424, 427
 Degrees of freedom, 172–175, 178, 190, 320,
 321
 Denitrification, 3, 6, 8
 Density functional theory, 172, 239–240, 354,
 377
 Diamagnetic susceptibility, 159
 1,2-Diaminopropane, 412, 413
 Diatomic molecules, 176, 355, 356, 365
 Diet, 474, 478
 Diffraction, 59–60, 234, 391, 393, 394
 Diffusimeter, 194–197, 205
 Diffusion law, 193–207
 Dihydroanthraquinone, 405
 Diisopropyl ethylamine, 127, 128, 138, 140
 Dimethyl formamide, 126, 140, 464
 Dipolar addition, 99, 100
 Dissociation reactions, 364, 365
 Distance traveled ratio (DTR), 195–197, 199,
 200, 202–206
 Dithiosalicylic acid, 412–415
 DNA, 249–263, 313, 370, 454
 fragmentation, 305, 311–313
 sensor, 250, 251
 Donor-acceptor complexes (DACs), 317–321,
 323–328
 Donor-acceptor pairs, 317–330
 Drug, 82, 121, 194, 211, 304, 310, 311, 454,
 462

Ductility, 219, 220
Dye, 3, 5, 123, 419–430, 433–440
 effluent, 420, 422, 427, 428, 430, 433, 434, 440
Dysdercus koenigii, 69–78
Dyslipidaemia, 473, 474, 478, 479

E
Eigen state, 155
Electrochemical, 249–263, 399, 400, 402, 405, 406
Electrode, 240, 250, 251, 253, 254, 257, 258, 261, 263, 400, 402, 405–409
Electrolytes, 193–207, 240, 253
Electronic structure, 39, 172, 175, 176, 186, 266
Electron microscope, 221, 391
Electron microscopy, 61, 62, 393
Electrophilic reagents, 144
Eluent, 214–216, 339, 340, 344, 345
Emission, 2, 61, 236, 243, 325, 336
Enantioselectivity, 82–84, 96, 98
Encounter theory, 13, 14, 18–20, 24, 25, 32
Enolate, 143–150
Enthalpies of formation, 362–365
Enthalpies of the isomerisation, 362
Enzymes, 104, 202, 303–305, 311–313, 370, 434–440
Escherichia Coli, 116, 128, 413, 415, 446, 448, 449, 462, 466, 468, 470
Ethylamine, 85–87, 89, 92, 93, 127, 128, 412, 413
Ethylene, 335–351, 376–385, 395
Exemplars, 268–270, 272–277, 280–282, 285, 287–291, 294–297
Expectation values, 154, 159–161, 164–167
Extraction, 209–216, 336, 339, 351, 444, 445

F
Fatty acid, 302, 306, 370
Fauna, 2, 3, 336
Fermi and Coulomb holes, 160, 162
Ferri/ferrocyanide, 251, 253–260, 263
Ferrite, 222, 227, 229
Fertilisers, 2, 4, 8, 9
Flora, 2, 3, 336
5-Fluorouracil (5FU), 310–312
Fourier transform, 179, 181, 336
Franck-Condon factors, 323
Freundlich isotherms, 347
Friction, 220, 224, 225, 229

Fuel cells, 400
Fungal species, 129, 444

G

γ -elemene, 447, 448
Gas sensor, 57, 58
Gaussian, 322, 327, 377
Gilman double titration method, 148
Glucose, 437, 462, 474
Glutathione reductase assay, 305
Gram-negative bacteria, 414
Gram-positive bacteria, 415, 416
Graphite, 221, 400, 408
Gravimetric, 211
Green chemistry, 411
Greenhouse gas, 390
Grinding, 411–414, 416
G-tensor, 240

H

Haemocyte count, 69–78
Hartree-Fock (HF), 154–159, 161–168
Hellmann-Feynman theorem, 239
Heterocycles, 121, 122, 124
Heterocyclic, 104, 115, 122, 454, 455, 464
 rings, 115, 454, 464
Hexamethylbenzene (HMB), 318, 324–326
High density lipoprotein (HDL), 474–478
Homogeneous, 12, 47, 221, 401, 446
Hydration number, 193–207
Hydrazides, 125
Hydrazine, 70, 71, 73, 74, 77, 78, 121–124, 130, 133, 140, 459, 464
Hydrazones, 122, 124, 125, 130, 456–457, 464
Hydroamination, 375–385
Hydrogen sulfide, 58
Hydrothermal, 58, 68
Hyperlipidaemia, 477, 478

I

Imidazole, 103, 454–456, 463, 464
Impedance, 249–263
 spectroscopy, 249–263
Indium oxide, 252
Indolization, 464
Inductive reasoning, 269
Industrial waste, 422
Infrared spectroscopy, 235
Insect, 69–78
In-vitro cytotoxicity, 302

Ionic displacement, 173, 175, 179, 182, 189–191

Ionic oscillation, 175–178

Ionization energies, 36, 37, 43, 44, 51

Ion-orbital coupling, 179, 181, 187, 189–191

Irreversible reaction, 12–27, 29, 30, 32, 33

Isodurene (IDU), 318, 324–326

Isotropy, 221

K

Kinetics, 11–16, 18–20, 23–31, 33, 37, 47, 48, 172, 175, 204, 250, 263, 317–319, 323–327, 329, 330, 347, 378, 384, 385, 408, 420

 scheme and equation, 11–14, 18–20, 23–25, 27, 29–31, 33

Knorr reaction, 122

Knowledge construction, 268, 281, 285, 295, 296

L

Laccase, 434, 435, 437–439

Langmuir model, 345, 347

Lanthanide contraction, 347

Le Chatelier's principle, 344

Leukemia, 210

Ligand, 82, 104–107, 111, 113, 115, 116, 216, 232, 235–237, 240, 302, 308, 309, 337, 344, 394

Ligninolytic, 434–438

Lignin peroxidase (LiP), 434–440

Lipid, 82, 304, 312, 313, 370, 474–479

Low cost, 210, 250

Low density lipoprotein, 474, 475

M

Magnetic moment, 104, 107, 113–116

Mammalian, 69

Mannich bases, 144

Markovnikov, 375–385

Mauritius, 1–9, 270, 474, 475, 477–479

Medicinal, 444, 449, 453–471

Methylene blue, 249–263

Methylene green (MG), 420–429

Micellar, 81–83, 91, 95, 390

Micelles, 82, 391, 402

Michael-addition, 95–98

Micrococcus luteus, 446, 448, 449

Microorganisms, 128, 250, 390, 449

Misconceptions, 266, 267

Molar mass ratio square root (MMRSR), 195–197, 200, 202–206

Möller–Plesset perturbation theory, 354

Monitoring, 50, 51, 250, 367, 434, 478

Morphology, 61, 227, 369, 371, 403–404

Motivation, 267, 270, 274, 281, 287, 290, 294–297

Multistage reaction, 11–13, 30–33

N

Nanocrystalline, 232, 397

Nanoscale, 227, 399

Nanoscience, 399

Nanotechnology, 399

Nano-TiO₂, 66

Nanotubes, 399–409

Nitrate, 3, 5–9, 196, 211, 214, 232, 240, 241, 278, 337, 428, 438

Non-equilibrium, 220, 317–330

Non-exemplars/negative exemplars, 268–270, 272–276, 280, 281, 285, 288–290, 294–297

Non-linear coupling, 183, 190

Normalization, 156, 160

Normal mode, 174, 175, 179, 190, 191

NOVASOL, 433–440

Nuclear magnetic resonance, 303

Nutrients, 1–9, 413, 437, 440, 446, 462

O

Ocimum canum, 443–450

Open circuit potential, 253, 258, 260, 261

Optical density, 303, 373, 421–426, 428, 429

Orbital mass, 171–191

Orbital oscillation, 177–183, 185, 187

Organocuprate, 144

Organomanganese, 143–150

Organometallic, 148, 301

Organotins, 301, 302, 307, 309–311

P

Partial distribution function, 162–163, 167, 168

Pathogens, 91, 368, 471

Penicillium

P. digitatum, 446, 448, 449

P. expansum, 446, 448, 449

Pentaatomic ions, 354–356, 358–363, 365

Periodic table, 265–297

Pharmaceutical, 121–123, 210, 411, 449
Phenylalanine, 81–100
Phosphate, 3, 5–9, 302, 305, 342, 402, 405, 408
Phosphorylation, 122, 144
Photobiology, 368
Photocatalytic, 389–397
Photochemical, 232, 320, 328–330, 367–373
Photochemistry, 368
Photoelectron spectroscopy (PES), 36–50, 377–383, 385
Photoexcited, 317–330
Photoionization, 35–55
Photoluminescence, 243
Photolytic, 422
Photophysics, 368
Physiological, 368, 370, 400
Pollutants, 3, 231, 367, 368, 373, 390, 434
Pollution, 2, 3, 369, 390, 419
Polymer, 103
Polynuclear cages, 302
Polynuclear clusters, 302
Polysiloxane, 402
Population, 2, 319, 320, 323, 327–330, 336, 474, 475, 478, 479
Positive exemplars, 280–282, 287–291, 293, 296, 297
Potassium chloride, 277, 353–365
Potential energy surfaces, 365, 378, 380, 382, 384
Protein, 304, 305, 312, 367, 370
Pyrazoles, 121–140, 454

Q

Quantum chemistry calculations, 365
Quantum yield, 319, 369

R

Radial distance, 162
Radiation, 50–54, 60, 234, 368, 369, 419–430
Radioactive, 210
Rate coefficient measurement, 44, 46–49
Reactive intermediates, 35–55, 464
Redox, 240, 250, 251, 258, 260, 261, 400, 420, 439
Reverse micellar, 390
Reverse phase, 129, 209–216
Rubidium chloride, 353–365
Runoff, 2, 4, 8, 9

S

Salinity, 368, 430
Scanning electrochemical microscopy (SECM), 250, 254, 258, 260, 263
Semiconductors, 57, 65, 210, 390
Separation, 40, 43, 50, 160–162, 205, 209–216, 308, 318, 319, 328, 329, 336, 401, 405
Sewage, 9, 369
Slater-type-orbital's (STO's), 156
Sol-gel method, 58, 67, 390, 397
Solid phase extraction (SPE), 336, 339, 342, 348, 350, 351
Spectroscopy, 36, 37, 54, 61, 235, 243, 249–263, 337
Spin-orbital, 155
Standard deviation, 6, 164, 166, 167, 221, 236, 282, 365, 395
Standard isotherm, 391
Staphylococcus aureus, 100, 116, 128, 413, 415, 446, 448, 449
Steel, 219–229
Structure-activity, 74, 454
Substituted ethylene, 376–385
Summer, 3, 6–9
Surfactants, 81–83, 89, 91–94, 96, 99, 100, 390, 391
Synchrotron radiation, 36, 50–54
Syngenus compound, 195–196, 204, 205
Synthetic, 71–73, 81, 144, 214–216, 234, 306–307, 375, 411, 454, 455

T

Tanabe–Sugano, 115
Teaching, 265–297
 strategies, 269
Tetracyanoethylene (TCNE), 318, 319, 324–328
Textile, 419, 422, 427, 433–440
Thermal stability, 337, 341, 350, 390
Thermodynamic, 14, 36, 37, 204, 354, 360, 363, 365, 376, 377
 properties, 353–365
Thermogravimetric analysis, 337
Thiourea, 69–78, 215, 460, 465
Threshold photoelectron spectroscopy (TPES), 36, 50, 54
Time dependent EIS, 251
Titanium oxide, 57–68, 390
Toxicity, 69, 70, 104, 123, 311, 368–370
Transition metal, 122, 231, 245, 272, 276, 293

Transmission, 62, 221, 391, 393
Triatomic ions, 356, 357, 365
Triazole, 103–116
Tribological, 220
Triglycerides, 474–478
1,2,4-Trimethoxybenzene (TMB), 318,
326–328
Triorganotin (IV) carboxylates,
301–313
Triphenyltin laurate, 310, 312
Tyrosine, 81–100, 127

U

Ultrafast charge transfer, 317–330
Ultra-violet, 84, 368
Urea, 69–78, 128, 140, 420–427, 429, 438,
460, 465
UV spectrophotometry, 63
UV-visible, 104

V

Valeronitrile (VaCN), 318, 324,325
Variation theorem, 156
Veratraldehyde, 435
Veratryl alcohol, 435, 439, 440
Vibrational frequency, 173, 176–178, 188, 190,
354, 362, 365
Vibration spectra, 185, 353–365

W

Wave functions, 153–156, 158, 161, 163–168
Winter, 3, 6–9

X

X-ray, 59–60, 228, 233, 234, 391, 394

Z

Zn-porphyrin-imide, 319